Computational and optical approaches for fluorescence lifetime imaging of intrinsic cellular metabolism

By

Md Abdul Kader Sagar

A dissertation submitted in partial fulfillment of the requirement for the degree of

Doctor of Philosophy

(Biomedical Engineering)

at the

UNIVERSITY OF WISCONSIN- MADISON

2020

Date of final oral examination: 12/9/2019

The dissertation is approved by following members of the Final Oral Committee:
Kevin Eliceiri, PhD, Assoc Professor, Biomedical Engineering
Jyoti Watters, PhD Professor, Comparative Biosciences
Justin Williams, PhD, Professor, Biomedical Engineering
Melissa Skala, PhD, Assoc Professor, Biomedical Engineering
Elizabeth Meyerand, PhD, Professor, Biomedical Engineering
Vikash Singh, PhD, Professor, Biostatistics

Table of contents

Acknowledgement

In this thesis, I developed various tools and methods to improve fluorescence lifetime imaging microscopy, apply them to study microglia cell and collaborate with other labs to apply my FLIM expertise to answer other biological questions. Because of the inherent nature of this work, it required a very collaborative environment and helpful colleagues who have expertise in different areas. But first and foremost, it took a lot of effort by my advisor Dr Kevin Eliceiri to create such an environment where we can thrive. I would like to thank him for giving me the opportunity to start my graduate work in UW Madison and believing that the I would be a good fit for this lab. I would also like to thank my amazing co-mentors, LOCI-colleagues, collaboration lab members.

I have been fortunate to be co-mentored by Dr Kevin Eliceiri, Dr Jyoti Watters and Dr Justin Williams for my microglia related projects. I learnt a lot during this project about microglia biology, technical and biological challenge associated with them. I also learnt formulating research problem and best ways to address them and I believe that the research expertise obtained from the project would help me throughout my research career. I am also thankful to Dr Kevin Cheng and Jonathan Ouellette for helping me in this project.

Without the helpful guidance and collaboration from LOCI staff members a lot of projects would not have been possible. I would like to express my sincerest gratitude towards, Dr Bing Dai, Dr Jenu Chacko, Dr Joshua Webers for the countless number of times they have helped and collaborated with me. Dr John White, despite not being present here in Madison, but guided us

with our project and whenever possible, helped us with in person meeting during his visits to Madison, and I offer my sincerest gratitude towards him. Specially, in the spectral lifetime project, they have been incredibly helpful. I would also like to specially thank Dr Jenu chacko for all the FLIM related discussion and co-authored paper. In all the programming related project, Curtis Rueden have been very helpful and I thank him for that. Dr Jayne Squirrel also have been helpful in many aspects during my tenure in LOCI. And last but not the least, I would like to thank Adib Keikhosravi who have been incredibly helpful in many LOCI projects.

My parents have set the vision in me at a very young age, that I should pursue the noble profession of a scientific career and try to solve problems those help other. Without their help throughout my life, I do not believe I could have come this far. They have always believed in me and that helped me through the harder times. And for the last 5 year, my wife Nafisah have been beside me though every ups and downs which helped me manage the challenges of PhD. I am grateful to her for being there for me even when I was trying maintaining coherence between various challenges of life.

Finally, I would like to express my sincerest gratitude towards the other committee members Dr. Melissa Skala and Dr. Elizabeth Meyerand and Dr. Vikash Singh for providing their valuable guidance towards finishing my thesis.

ABSTRACT

Computational and optical approaches for fluorescence lifetime imaging of intrinsic cellular metabolism

Md Abdul Kader Sagar

Under the supervision of Dr Kevin Eliceiri

At the university of Wisconsin-Madison

Fluorescence Lifetime Imaging Microscopy (FLIM) based visualization of endogenous autofluorescence can provide a plethora of information about cellular biochemical microenvironment. In particular, FLIM of autofluorescent metabolic coenzyme NADH and its relative binding status has been shown to be highly sensitive to fluxes in cellular microenvironment. Accurate estimation of lifetime changes can help us better understand response of biological system to external stimuli, for exampling creating metabolic maps of NADH fluxes during a cellular wounding event. There has been significant improvement in FLIM instrumentation, analysis in the last decade and it has been applied to range of biological applications such as cancer detection, imaging metabolism, protein-protein interaction, tissue characterization, etc. Much of this work has been using FLIM as a contrast to compare normal and diseased conditions. However, there is growing interest in using FLIM to help characterize cellular identity and functional state. There is great need for new and ideally label-free approaches that could distinguish cell types. This is especially of need with immune cell types where it can be very challenging to discern identity and function. Here, we have investigated NADH FLIM as potential

biomarker for microglia activation to characterize its functional state. Additionally, we have developed instrumentation and software-oriented technique to augment existing FLIM imaging and analysis methods. In this thesis, we aim to address various aspects of FLIM imaging which can be divided in three broad areas. i) Novel application of NADH FLIM in biology, ii) advanced quantitative analysis to improve FLIM based post-processing, iii) develop novel FLIM based instrumentation. First, we explore NADH FLIM as a potential tool to develop label free probing technique for characterizing microglia in the context of the Central Nervous System (CNS). Using NADH FLIM to compare lifetime of surveillant versus activated microglia, we found that, activated microglia has significantly different NADH lifetime compared to resting microglia cell. Second, we developed a label free technique to identify surveillant microglia in mixed cell culture and brain tissue using FLIM combined with Artificial Neural Network (ANN). Third, we developed hardware and software to improve FLIM acquisition which could lead to better FLIM based characterization and develop cellular signature in future. We demonstrated that using an optical fiber to introduce dispersion to existing multiphoton FLIM system can add simultaneous spectral/lifetime acquisition capability reducing the need to add additional detection pathway for spectra/lifetime imaging. Additionally, we developed open source FLIM acquisition software which can be eventually extended to add runtime FLIM analysis or custom FLIM acquisition. In future, these microglia visualization technique along with machine learning approach can be used to probe microglia in CNS associated diseases such as Alzheimer's disease, Parkinson's disease, and better understand their role in those diseases and might lead to better therapeutic technique.

Chapter 1

Introduction

1. Introduction

In recent years, imaging and visualization techniques that can quantitate biological fluorescence have been increasingly used to understand biological phenomena at the cellular and subcellular scale. With the increased sensitivity, depth, and automation of modern optical microscopy scientists have been able to gather more and more information from cellular interactions, functional state and response to external stimuli. Laser scanning microscopy methods such as confocal and multiphoton microscopy technique offer better resolution over traditional fluorescence microscopy and enables going deeper into a sample imaging subcellular features (Denk et al., 1990; Durr et al., 2011; White et al., 1987). With multiphoton microscopy, built on the principle of two-photon absorption first discovered by Maria Goeppert-Mayer (Göppert-Mayer, 1931) and later realized in its microscopy form (Denk et al., 1990b)(ref), scientists are able visual subcellular fluorescently labeled structures up to a millimeter deep into both fixed and live tissues. This methodology is very useful for biologists studying dynamic cellular processes in living cell and tissues without significant alteration or damage to the sample. In the past decade, there has been great advances in multiphoton microscopy for biomedical research (Hoover and Squier, 2013; Jiang et al., 2017, 2014; Wang et al., 2010; Yamada et al., 2014). With the advent of modern electronics able to control all aspects of laser scanning microscopy, it now possible to image and quantify larger samples all while extracting more information from a single pixel.

Whether it be conventional widefield or the more advanced laser scanning microscopy methods, Fluorescence has played a substantial role in this progress as a powerful tool for identifying biomolecules. The applications of fluorescence imaging span from studying small molecules inside a cell (Ettinger and Wittmann, 2014; Specht et al., 2017) to clinically relevant fluorescence

aided surgical tools (Diana, 2018; Nagaya et al., 2017; Zheng et al., 2019). The ability to genetically target with fluorescence a protein of interest has revolutionized modern cell biology. Fluorescence microscopy yields many specific physical attributes from an object that can be used to tag a molecule and to identify them. There are various ways in which fluorescence signal can be utilized to visualize intrinsic cellular biomarker or subcellular structure (Thorn, 2017). One of the ways fluorescence imaging is realized is via genetic tagging fluorescence protein such as GFP. Various labelling technique such as protein labeling, genetic labeling or enzymatic labelling are widely utilized. The fluorophore usually binds to specific region, functional group or target molecule. For example, fluorescent molecule which binds to calcium has allowed studying calcium signaling to understand neuronal activity (Russell, 2011). Autofluorescence imaging of intrinsic autofluorescence co-enzyme such as NADH (reduced nicotinamide adenine dinucleotide) and FAD (flavin adenine dinucleotide) has enabled better understanding of intrinsic cellular microenvironment (Bartolomé and Abramov, 2015; Blacker and Duchen, 2016; Schaefer et al., 2019). Quantitation or quantification has become the key aspect of fluorescence microscopy today; quantification makes the data more functional and the attributes more fathomable in their respective spatial dimensions. Beside fluorescence emission it is now possible to measure fluorescence lifetime (Bastiaens and Squire, 1999; Becker, 2012; Suhling et al., 2015), second harmonic (Chen et al., 2012; Keikhosravi et al., 2014; Moreaux et al., 2000; Stoller et al., 2003), third harmonic (Débarre et al., 2006; Squier et al., 1998; Yelin and Silberberg, 1999), polarization (Lazar et al., 2011; Rizzo and Piston, 2005) and spectral information (Zimmermann et al., 2003) from a single pixel. These properties individually can provide plethora of information about the cellular microenvironment (Imamura et al., 2018; Welf et al., 2016). Using these properties, unique

property of cells such as measuring metabolic and stromal changes can be studied which can be used to better understand cell activity and reaction to external event/stimuli.

1.1 Cellular microenvironment imaging

There has been a growing interest in the imaging the cellular microenvironment because of the abundance of information that can be generated from it and the insight it provides to various biological phenomenon (Chacko and Eliceiri, 2019; Imamura et al., 2018; LeBleu, 2015). Laser scanning microscopy in particular due its high resolution optical sectioning and ability to collect both intrinsic and extrinsic measures has been widely used to characterize the normal and diseased cellular microenvironment. Our lab and others have specialized in developing methodology which can probe the collagen rich extracellular matrix in the cellular microenvironment. This is done by intrinsically imaging collagen fibers and monitoring reorganization utilizing second harmonic generation (SHG) microscopy. The non-centrosymmetric property of collagen allows for intrinsic visualization by SHG (Cox et al., 2003; Zipfel et al., 2003; Zoumi et al., 2002). Using this approach it was established that collagen organization can be a negatively prognostic marker for tumor formation and metastasis (Provenzano et al., 2006, 2008a; Conklin et al., 2011). Cellular metabolism fluxes have always shown to be an important part in normal and diseased processes. For example, one the hallmarks of cancer is the metabolic shift to glycolysis known as the Warburg effect (Heiden et al., 2009). One of the ways to quantify cellular metabolism is fluorescence lifetime imaging (FLIM, discussed later in detail) of intrinsically fluorescent metabolic co-factors such as NADH and FAD. FLIM as a technique has a unique advantage: the lifetime is independent of the other physical parameters of fluorescence such as intensity or spectrum. FLIM can be

deployed readily on laser scanning microscopes and can monitor metabolic events via the autofluorescence of FAD and NADH or specific extrinsic fluorescent sensors. Due its label free, cellular resolution and metabolic sensitivity has

made FLIM a widely used technology for cellular metabolism studies (Bird et al., 2005b; Rehman et al., 2016; Skala et al., 2007). The FLIM based biochemical sensors both intrinsic and extrinsic currently span over many targeted proteins, their activation, binding and aggregation states. These including not only the NADH and FAD based metabolic approaches but also novel FLIM based approaches for oxygen detection (PLIM (Kalinina et al., 2016)) and Forster resonance energy transfer (FRET) measurements (Morton and Parsons, 2011).

1.1.1 FLIM of intrinsic metabolism

FLIM has been demonstrated as an effective tool in the discrimination between free and bound forms of the NAD(P)H (Reduced nicotinamide adenine dinucleotide), providing lifetimes of both states with their relative concentrations(Lakowicz et al., 1992a; Scott et al., 1970). There is extensive literature reports on NADH and FAD (flavin adenine dinucleotide) use as a marker for metabolic imaging (Bird et al., 2005b; Chacko and Eliceiri, 2018; Gómez et al., 2018; Sanchez et al., 2018) and cancer imaging (Ardeshirpour et al., 2014; McGinty et al., 2010a; Peng and Akers, 2016; Skala et al., 2007; Tadrous et al., 2003). For example, a combination of fluorescence lifetime of NADH with fluorescence intensity relative to the emission of tryptophan (an endogenous fluorescent amino acid) as an internal standard was shown to differentiate normal from cervical cancer cells (Galletly et al., 2008; Periasamy et al., 2017). FLIM also has been shown to have clinical implications in skin cancer detection (Dancik et al., 2013). Skin contains a number of

intrinsically fluorescent proteins including elastin, keratin, collagen, FAD, and NADH. These endogenous contrast agents can be used as a marker of homeostasis in *in-vivo* skin imaging when compared against tumor or wound healing models (Krasieva et al., 2012). For example, distinguishing basal cell carcinomas presents a contrast with respect to the surrounding, uninvolved skin in early skin cancer (Galletly et al., 2008). Collagen fiber fluorescence lifetime can also yield contrast for cancer diagnosis; the disruption of collagen by tumor associated matrix metalloproteinases from dermal basal cell carcinoma decreases the lifetime of collagen (Seidenari et al., 2012). Cell types in the skin can also be different in their mean lifetime; melanocytes and keratinocytes present a clear difference between malignant and benign cells (Dimitrow et al., 2009).

FLIM applied to intrinsic tissue autofluorescence generates detectable levels of disparity in lifetime and intensity, in a range of surface tissue tumors, such as colon cancer. With the help of compact, clinically deployable flexible endoscopic instrumentation, FLIM helps to distinguish between cancerous and healthy colon tissue(McGinty et al., 2010b). FLIM has been used to image oral carcinoma(Sun et al., 2009). These endoscopic implementations collect time-resolved images, minimally affected by tissue morphology, endogenous absorbers, and illumination. These results demonstrate the potential of FLIM as an intraoperative diagnostic technique. FLIM techniques for brain tissue characterization can generate optical contrast in underlying tissue structures of normal and malignant brain tissue(Papour et al., 2013) and reveal cerebral metabolism in live cells(Trinh et al., 2017; Yaseen et al., 2013a). Genetically encoded NADH-NAD^+ fluorescence lifetime sensors like Peredox (Tejwani et al., 2017) have also been used in brain tissue redox imaging.

1.2 Fluorescence lifetime for cellular fingerprint

Our lab and others have previously explored and established relation between changes in metabolism in relation to diseases such as cancer (Bird et al., 2005a) and NADH/FAD lifetime (Bird et al., 2005b). FLIM is the tool of choice for probing cellular metabolism as it can probe image autofluorescent metabolic cofactors in their different binding states (Bird et al., 2005b; Chacko and Eliceiri, 2018; Martin et al., 2018; Niesner et al., 2004; Szaszák et al., 2011; Yaseen et al., 2013b). Due to their autofluorescence properties and change of lifetime with protein binding state, fluorescence lifetime has been shown to be a biomarker in several diseases. But more parameters which can add to the differentiating aspect of a cellular fingerprint can be valuable addition. Beside lifetime, existence of different species having different spectral channels can be attributed as unique feature of a biological entity. In a similar way, adding polarization, would also provide additional differentiating characteristics via fluorescence anisotropy (Suhling et al., 2004). A combination of fluorescence lifetime, spectral differentiation and polarization state- is what we eventually think would help us establishing a more complete biological fingerprint. In the following sections, our effort to develop fluorescence lifetime and spectral technique is discussed while the polarization techniques are discussed in the future direction sections.

Endogenous fluorescent biomarkers can identify various cell types based on specific metabolic markers in live tissue or fresh biopsies, helping researchers to monitor their activities unadulterated by external reagent or antibody. Other traditional options such as antibody labeling, exogenous dyes, or genetic manipulation can directly perturb cellular processes. Multiphoton FLIM can be used to exploit the endogenous fluorescence of reduced nicotinamide adenine dinucleotide (NADH) versus flavin adenine dinucleotide (FAD) already present in tissue to identify changes in

metabolism(Chance, 1976). Szulczewski et al.(Szulczewski et al., 2016) and Garcia et al.(Alfonso-García et al., 2016a; Garcia et al., 2016) used such distinct metabolic signatures to identify macrophages and separate them from the intrinsic fluorescence signature of tumor cells, suggesting a role of metabolic reprogramming in the regulation of the innate inflammatory response(Orihuela et al., 2016). Stringari et al.(Stringari et al., 2012a) and Squirrell et al.(Squirrell et al., 2012) separately identified cellular differentiation states in a cultured cells, as well as small animals, using NADH metabolic signatures. Several notable works on cancer cell metabolism by Skala et al (Skala, 2015), Gratton et al(Pate et al., 2014), and others in the past decade have provided the basis for identification of metastatic states associated with cellular proliferation and differentiation states (Blacker et al., 2014; Hou et al., 2016). There are many phasor fingerprinting based work identifying differences in metabolism and environment like LLS-species for oxidized lipids(Datta et al., 2016a; Rupsa Datta, 2016), bacterial species (Bhattacharjee et al., 2017), etc. These trends have also been extended to tissues, including cell differentiation in kidney tissue (Hato et al., 2017), fat content in liver tissue (Ranjit et al., 2017), and renal fibrosis quantification (Ranjit et al., 2016). Lab on a chip and bioreactor applications in oncogene studies and quantitative tumor live-cell studies using microfluidic devices with FLIM as tool for fast quantification of fluorescent markers(Datta et al., 2016b; Li et al., 2010).

1.3 Tools and techniques towards cellular identity

Despite the many improvements in FLIM acquisition and instrumentation and increased applications in life science in the last decade, there are still many areas of improvement which would make FLIM more accurate and practical for both research and clinical adoption. In the

previous sections, we discussed how FLIM can be used as an optical fingerprint to study metabolic changes in the cellular microenvironment. In this thesis work we aim to address several technical shortcomings of current FLIM imaging such as non-transparent acquisition software, few methods for combined spectral lifetime collection and scarcity of machine learning based approaches for FLIM based characterization. Additionally, as a driving technical use case to illustrate the metabolic monitoring power of FLIM we characterize microglia activity using NADH based FLIM as a label-free biomarker. The methods and applications developed in this thesis are largely divided in three main areas, i) novel application of NADH FLIM in biology, ii) advanced quantitative analysis to improve FLIM based post-processing, iii) develop novel FLIM based instrumentation.

1.3.1 Methods proposed in this thesis

First, we explore NADH FLIM as a potential tool to develop label free probing technique for characterizing microglia in the context of the Central Nervous System (CNS). Using NADH FLIM to compare lifetime of surveillant versus activated microglia (discussed in next section). We also explore test our technique with various dose of external stimuli and observe if they have some degree of correlation with FLIM parameters.

Second, we developed a label free cell resolution technique to identify surveillant microglia in mixed cell culture and brain tissue using FLIM combined with Artificial Neural Network (ANN). Additionally, we developed a convolutional neural network (CNN) (LeCun et al.) to differentiate surveillant microglia vs activated microglia based on fluorescent intensity image.

Third, we developed hardware and software to improve FLIM acquisition which could lead to better FLIM based characterization. For example, we demonstrated that using a sufficiently long

graded index or step index fiber optical fiber to introduce dispersion to existing multiphoton FLIM system can lead to simultaneous spectral/lifetime acquisition capability reducing the need to add additional detection pathways for spectra/lifetime imaging. This add-on spectral implementation requires only a few simple modifications to any existing FLIM system and is considerably more cost-efficient compared to currently available spectral detectors. This invention could lead up to innovative ways to probe biochemical environment having multiple spectral fluorophores and distinct fluorescence lifetimes.

Finally, we overview the open source FLIM acquisition software which was developed as part of this thesis. The acquisition routine can be eventually extended to add runtime FLIM analysis or custom FLIM acquisition. Additionally, we also briefly discuss the additional collaborative projects as part of this thesis related to FLIM application in biology (Kader Sagar, 2015; Kenny et al., 2017; Martin et al., 2018) and fast FLIM imaging quantitation (Lee et al., 2019; Wang et al., 2019). We also collaborated to develop optical window to simultaneously monitor and perturb neural activity in mice brain (Ghanbari et al., 2018).

In the following sections in this chapter, more background is discussed about microglia (section 2) and the specific need to develop FLIM based marker (section 3), approaches to improve FLIM and post processing with machine learning and background of spectral/lifetime acquisition (section 4).

2. Microglia in Central Nervous System

Microglia have prominent roles both in injury/disease responses, as well as neuroprotection in the CNS. They are critical nervous system-specific immune cells serving as tissue-resident macrophages which influence brain development, maintain the neural environment, respond to injury, and perform repair functions (Jin and Yamashita, 2016; Michell-Robinson et al., 2015). It is widely accepted that microglia not only act as sensors of damage/injury, but they also play a key role in virtually all pathologies of the CNS including injury, neurodegenerative disease, ischemia, and infection (Charles et al., 2011; Garden and Möller, 2006; Tambuyzer et al., 2009; Watters et al., 2005) often exacerbating neuronal damage as a result of their production of inflammatory molecules that are toxic to neurons. Microglial cell density varies by CNS region, comprising 5-15% of all cells in the rodent and human brain, and 20% of all glial cells (Smith et al., 2012; Tambuyzer et al., 2009).

Microglia form the brain's first line of defense against injury and infection (Nimmerjahn et al., 2005). They are highly sensitive to even slight perturbations in their cellular environment. These disturbances in CNS homeostasis lead to rapid changes in microglial morphology (Raivich et al., 1999a; Ransohoff and Perry, 2009) including their transition from a "ramified" phenotype characteristic of their sentinel and surveillance activities, to the more amoeboid phenotype that they acquire upon immune activation. Their "ramified" morphology involves continual extension and retraction of specialized processes, enabling them to sample the local environment and monitor synaptic transmission. In a healthy brain, microglia have a ramified morphology, and their cell numbers remain constant throughout life. Following injury or disease, surveillant microglia retract their processes and enlarge their cell bodies to morphologically transform into microglia with an

amoeboid phenotype. Concomitant with these microglia in the affected area also proliferate. Thus, studying normal microglial physiology *in vitro* has been challenging, since the disturbances caused by cell isolation and tissue slicing can change their activities.

Microglia have protective functions that involve phagocytosis, removing the toxic accumulation of β-amyloid and secretion of proteases (Qiu et al., 1998), preventing development AD(Hansen et al., 2017). But once activated, microglia can also contribute to AD progression. The inflammatory response in AD is thought to be secondary to the formation of neuritic β-amyloid plaques and neurofibrillary tangles and they serve as stable irritants for microglial inflammatory activities, leading to a self-sustained inflammatory cycle that hastens disease progression (Giulian et al., 1995; Tambuyzer et al., 2009). Activated microglia are also found in MS lesions and their production of inflammatory molecules contributes to the CNS inflammation and death of myelinating oligodendrocytes (Gudi et al., 2014; Wang et al., 2011). Neuronal axons are preserved in MS pathology, although demyelinated plaques are found both in the white and gray matter (Luo et al., 2017). Likewise, microglial activation seems to play an early role in PD since they gradually phagocytose dopaminergic neurons residing in the substantia nigra (Kim and Joh, 2006).

In contrast to neurodegenerative disease where microglial inflammatory activities exacerbate disease progression, their lack of inflammatory activities are important for brain tumor growth and metastases. Indeed, one-third of all cells in glioma biopsies are microglia/macrophages, and some studies suggest a direct correlation between a worsened glioma grade and the number of microglia/macrophages. Glioma cells actively recruit microglia/macrophages (Roggendorf et al., 1996), and in return, microglia/macrophages produce factors that allow tumor cell proliferation and metastasis(Wu and Watabe, 2017). Tumor cells also produce anti-inflammatory cytokines (IL-

6 and TGF- β) which potently downregulate microglia/macrophage inflammatory activities (Hao et al., 2002). Tumor-associated microglia/macrophages also produce the potent anti-inflammatory cytokine IL-10 (Wagner et al., 1999), further dampening their own inflammatory activities. Due to the highly immunosuppressive glioma environment, microglia/macrophages are unable to mount an effective anti-tumor cell T cell response, unlike macrophages in peripheral tumors. Accordingly, tumor-associated microglia/macrophages fail to express MHC II upon stimulation (Schartner et al., 2005), a necessary co-stimulatory molecule for T cell activation.

Thus, although microglia play significant roles in multiple neural disorders, a major obstacle to studying them has been the difficulty with their distinction from other related cell types (i.e. macrophages) in disorders in which peripheral immune cells can infiltrate the CNS. For example, CNS infiltrating monocytes/macrophages acquire a morphology that is indistinguishable from microglia, and all markers used to study microglia are also expressed in macrophages. To make matters more complicated, activated microglia have the same immune functions as CNS-infiltrated macrophages, so it is equally difficult to distinguish them based on function. Therefore, a method allowing for a clear distinction between these populations is indispensable to identify initiators and/or contributors to CNS dysfunction of different etiologies.

2.1 Existing techniques for microglia labeling

Various techniques, including bioluminescence imaging, magnetic resonance imaging, positron emission tomography, and two-photon microscopy now enable the minimally invasive study of microglia in the intact brain (Lalancette-Hébert et al., 2009; Ransohoff and Perry, 2009; Wiart et

al., 2007). Recently, genes uniquely expressed by and regulated in microglia, but not other macrophage populations, have been identified by transcriptomic analyses (Butovsky et al., 2014; Chiu et al., 2013; Gautier et al., 2012; Gosselin et al., 2014). These genes are useful for classifying and distinguishing microglia from other related myeloid cell types, as well as microglia that are activated. However, transcriptomic analyses are not always feasible. Apart from their physical location, the only available means to distinguish microglia from other CNS myeloid populations (CNS-associated macrophages/dendritic cells) and circulating monocytes is by the reduced expression of the common leukocyte antigen CD45, in mice (Sedgwick et al., 1991), most often detected using flow cytometry as it enables the differences in antigen expression levels to be reliably quantified. Accordingly, ramified parenchymal microglia have the phenotype $CD11b^{+}/CD45^{low}$ (Becher and Antel, 1996; Ford et al., 1995), whilst other CNS macrophages and infiltrating peripheral myeloid cells exhibit the phenotype $CD11b^{+}/CD45^{high}$, although activated microglia can also acquire the $CD11b^{+}$, $CD45^{high}$ phenotype, making the expression of even CD45 less useful. Adult myeloid cells and microglia constitutively express high levels of the fractalkine receptor CX3CR1, although the only cell type to express CX3CR1 in the CNS parenchyma is microglia (Yona et al., 2013). Pioneering imaging work has taken advantage of this expression and created CX3CR1-GFP mice which harbor a targeted replacement of one copy of the CX3CR1 gene with the enhanced green fluorescent protein gene (Jung et al., 2000). This mouse is now widely used for visualizing microglia(Wolf et al., 2013). However, again, the downside is that microglia and macrophages still cannot be distinguished even with CX3CR1-GFP. More recently, the transmembrane protein 119 (Tmem119) has been demonstrated to be robustly expressed in microglia (not macrophages) in both mouse and human (Bennett et al., 2016). Tmem119 is a transmembrane orphan receptor that is one of the most highly expressed microglia-specific genes

based on RNA sequencing analyses. The existing microglia labeling scheme works in individual cases as described earlier, however, as evident from all the studies, the preparation time, complexity, inefficient diffusion and unspecific binding can sometimes be a limiting factor for the actual experiment. Further, for microglial analyses to be clinically viable, any label-free technique would have an edge over other staining based techniques because of simplicity. Label-free imaging techniques have the advantage that they are simple, can directly measure intrinsic cellular properties, and can be extended to observing cell activity *in vivo.*

2.2 Limitation of existing staining-based techniques

With regard to the experimental use of fluorescent proteins, it is possible that expression of the fluorescent protein could perturb cellular processes, as their fusion to target proteins can disrupt the native function of the target protein (Gahlmann and Moerner, 2014). Thus, label-free imaging is gaining increasing popularity in the biomedical imaging field as it is free from the drawbacks of dye-based methods including heterogeneous cell type delivery, the potential for nonspecific staining, and FDA approval limitations. Endogenous cellular fluorescence has been used to identify “fluorescent fingerprints” of specific cell types in body fluids such as blood plasma, serum, urine, etc. (Sarkar et al., 2016). However, they have not yet been applied to distinguishing microglial activation state or differences from other CNS glia or closely related cell types (i.e. peripheral myeloid cells).

2.3 Microglia activation detection challenge

Besides characterizing quiescent microglia, activation of microglia can be characterized in different ways and there is not a single parameter that can uniquely characterize activation (Béchade et al., 2013). The process of activation is gradual and most likely involves many intermediate states on the way from quiescence to activation (Raivich et al., 1999b). Various parameters such as cell density, morphology or protein expression can be used to describe activation after inflammatory stimulus exposure. Rapid alterations in neuronal activity by microglia occur upon treatment with lipopolysaccharide (LPS)(Pascual et al., 2012), suggesting that microglial inflammatory activities can alter neurotransmission. LPS is a ligand of the pattern recognition receptor TLR4 that mimics bacterial infection and activates inflammatory signaling pathways in microglia that lead to the production and release of inflammatory cytokines including IL-1β and TNFα. Microglia are also activated during the aging process (Streit and Sparks, 1997) and sleep deprivation (Bellesi et al., 2017). The primary method of observing microglial activation is by using antibody staining to assess morphology and marker expression. However, the problems with using markers for detecting microglial activation are twofold. First, most antibodies cannot distinguish between the resting and activated states of microglia. Second, they also cannot distinguish microglia from macrophages. For example, $CD68^{high}$ detects both activated microglia and macrophages. And while the combination of $CD11b^{+}$ and $CD45^{low}$ is widely used to distinguish microglia from macrophages in mice, it cannot distinguish between an activated microglial cell and a macrophage. Recently, a novel morphology-based image analysis technique was developed to identify microglial activation based on the cell body to size ratio (Hovens et al., 2014). Other studies have tried to characterize microglia activation statistically using changes in

soma size and roundness (Davis et al., 2017). However, this method is largely dependent on the quality of immunohistochemical staining, and this study did not investigate neuroinflammation in the context of CNS injury.

3. Autofluorescence and FLIM for cellular microenvironment imaging

An alternative to antibody-based staining method would ideally be a label-free method which could take advantage of the intrinsic signal inherent to a biological specimen. Fluorescence microscopy technique can illuminate intrinsic autofluorescent metabolic cofactors such as NADH (Bonuccelli et al., 2017), FAD(Lagarto et al., 2018) and tryptophan(Vivian and Callis, 2001). By extension, laser scanning confocal and two-photon microscopes can visualize these co-enzymes with better precision, sensitivity and deeper penetration. As a result, the more quantitative fluorescence parameters are extracted per pixel or a field of view, the more unique differentiable parameters can be ascribed to a biological unit. One of the parameters that are inherent to fluorescence imaging is fluorescent lifetime. Fluorescence lifetime is the time taken for an excited molecule to return to the ground state before emitting a photon upon illumination. FLIM is a microscopy imaging technique which creates a contrast image based on the fluorescence lifetime of the individual fluorophores. FLIM can augment imaging techniques such as confocal, two-photon or multiphoton microscopy. Figure 1a shows the fluorescence lifetime in a Jablonski diagram. In time-domain measurement, a short-pulsed laser is used to excite fluorophore and the emission is measured as a function of intensity decay over time(2006). The fluorescent decay is

modeled as an exponential decay. If there is more than one fluorophore, it can be modeled as a combination of multiple exponential decays

$$F(t) = a_1 e^{-\frac{t}{\tau_1}} + a_2 e^{-\frac{t}{\tau_2}} + a_3 e^{-\frac{t}{\tau_3}} \quad \ldots\ldots\ldots\ldots \quad (1)$$

Here F(t) is the measured fluorescence intensity as a function of time t; τ_i is the individual exponential components, and a_i are the coefficients of each exponential term. Figure 1b shows a fluorescence decay with a single component

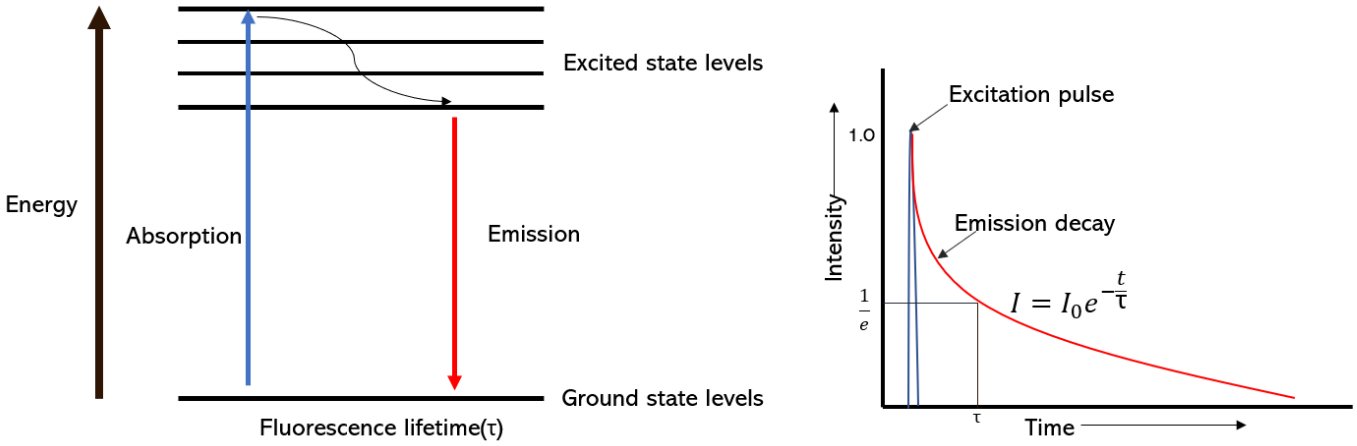

Figure 1: (left)Jablonski diagram showing energy absorption and emission for a fluorophore. (Right) Time domain excitation-emission pair. The blue curve is an excitation signal which excites a fluorophore and the red curve depicts fluorescence emission in time domain. The excitation is instantaneous, and the emission is longer and can vary. The x-axis is time and y-

axis is intensity(normalized). The time taken for the intensity to reach 1/e times the initial intensity is the fluorescence lifetime.

Fluorescence lifetime measurements are dependent on local environment parameters such as pH, oxygen saturation and binding state and hence yield direct information about the cellular microenvironment and the binding state of the fluorophore (Berezin and Achilefu, 2010; Provenzano et al., 2008b; Suhling et al., 2005, 2015; Wang et al., 1992). Imaging endogenous fluorophores also has an inherent advantage because it can be used for label-free imaging, opening up new possible applications. Use of fluorescence lifetime-based intrinsic contrast has especially been shown to be promising for the metabolic coenzyme NADH and FAD. FAD and NADH are the primary electron acceptor and donor respectively in oxidative phosphorylation. Metabolic imaging of NADH and FAD can give insight into the metabolic changes in the microenvironment. Both NADH and FAD are autofluorescent and can be monitored nondestructively without exogenous labels. NADH is fluorescent in its reduced form and FAD is fluorescent when oxidized, loses fluorescence when oxidized. The redox ratio which is defined as the intensity ratio of NADH and FAD, therefore, changes with the redox state of the issue (Chance et al., 1979). Normal cells have an oxidative and cancer cells have reductive metabolism, viz. measurement of Warburg effect (Heiden et al., 2009). The fluorescence lifetime of NADH and FAD depend on the binding state to the proteins (Lakowicz et al., 1992b, 2006). Unbound NADH has a lifetime of about 0.4ns and bound NADH has lifetime that can range from 1.2ns to 4 ns. For FAD the effect is opposite, as bound FAD has lifetime of few hundred picoseconds and free FAD has lifetime of few nanoseconds. In steady-state intensity image of NADH the bound to free ratio is not measurable but fluorescence lifetime imaging and analysis with two-component decay can clearly differentiate

between bound and free NADH. The ratio of the amplitude of the decay component, a1/a2 directly represents the concentration ratio of unbound to bound NADH, the same principle applies for FAD a1/a2 ratio. This ratio of NADH bound to free is the indicator of the metabolic state which is not available from the fluorescent spectra or the fluorescent intensity image. Two-photon excited autofluorescence FLIM has been imaged in normal and pre-cancerous epithelia and it was found that in the precancerous tissue the bound component of the NADH lifetime decreases (Skala et al., 2005, 2007). A significant decrease in the lifetime of the bound FAD was also detected in high-grade pre-cancer(Skala et al., 2007). Another similar approach was used to derive functional maps of intracellular redox ratio in vivo using FLIM of NADH and ratio of bound to free component amplitude(Bird et al., 2005b). It was observed that there is a statistically significant change in both bound and free NADH lifetime. NADH FLIM measurement has also been applied to wound healing and monitor change in the corneal epithelial cell to differentiate between healing and non-healing cell (Gehlsen et al., 2012). Other studies have shown that metabolic rate increase after injury and then gradually decrease(Deka et al., 2013). Additionally, NADH FLIM has been used in different comparative studies like comparing lifetime of glioma and the surrounding tissue (Kantelhardt et al., 2007), stem cell differentiation (Guo et al., 2008; Stringari et al., 2012b), response of tumor cell to various drugs (Walsh et al., 2013, 2014), changes in pH (Ogikubo et al., 2011) or macrophage FLIM signature (Alfonso-García et al., 2016b; Szulczewski et al., 2016).

3.1 Time correlated single photon counting (TCSPC) for multiphoton FLIM acquisition

There are many methods for measuring fluorescence lifetime in a confocal or two photon microscopes. For most of the current methods, fluorescence lifetime is measured from the decay in the intensity, (I(t)), after an excitation with a short pulse of light, where the duration of the excitation pulse is ideally much shorter than the lifetime to be measured. A pulsed excitation produces a fluorescence emission, which decreases the intensity exponentially with time that can be read with photodetector and time-resolving electronics. For a sample containing a single species, the fluorescence lifetime is given by the time over which the intensity of the fluorescent drops to about 1/e, or 37%, of its initial value. Two major instrumentation schemes exist for the calculation of the exponential decay from *pulsed excitation*: 1) *Time Correlated Time Domain Photon Histogram* (example: used in TCSPC(O'Connor, 2012) electronics, Fig 3B), and 2) *Phase Correlated Frequency Domain Histogram* (example: used in FLIM Box(Colyer et al., 2008) electronics, Fig 3B)(Gratton, 2016). Both schemes use fast, programmable electronics, such as Field Programmable Gate Array (FPGA) logic, to tabulate a photon timing histogram with high time resolution and calculates the representative lifetime values. For pulsed systems, there are three instrumentation architectures to determine the decay histogram. The time-digital conversion (TDC) architecture, Time Amplitude Converter - Analog Digital converter (TAC-ADC) architecture, and the phase cross-correlation(pCC) measurement architecture(Becker and Bergmann, 2003; Gratton and Barbieri, 1993; Kalisz, 2004; Spencer and Weber, 1969; Tamborini et al., 2013; Wahl, 2014; Wahl et al., 2013). The frequency domain collection has the advantage of working without a deconvolution routine provides faster component separation with a lower

cost of calculation. Time domain measurements have the advantage of straightforward fitting analysis routines done at a high temporal resolution data(Becker et al., 2003). A comparison of these two collection domains be found in literature(Gratton et al., 2003, 2015), as well as comparisons of same lifetime standards in both domain (Elder et al., 2008, 2006, 2009; Schlachter et al., 2009). The TCSPC histogram creation is demonstrated in figure 2a. Figure 2b shows a traditional laser scanning system employing TCSPC acquisition.

a)

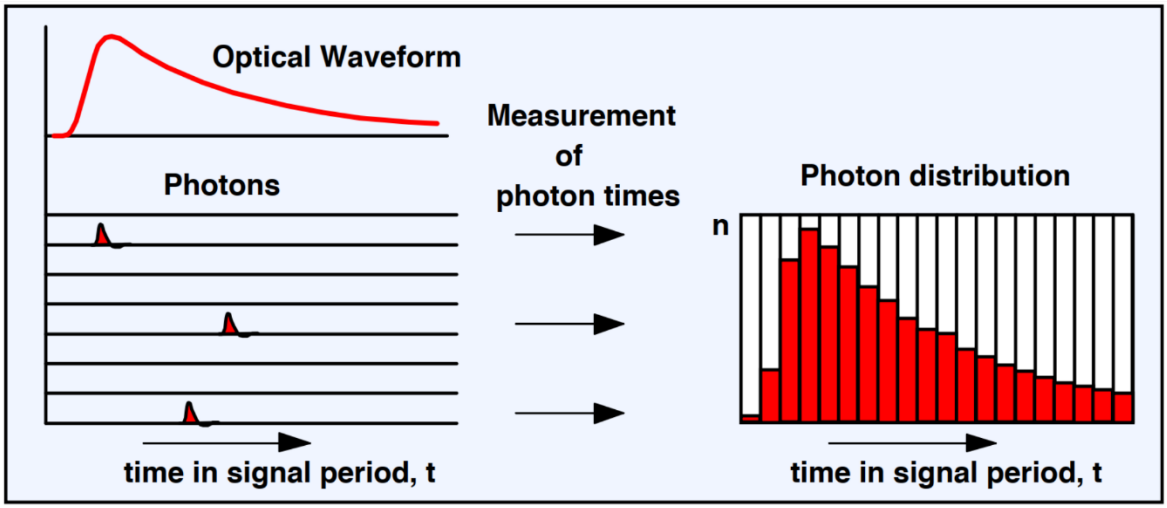

b)

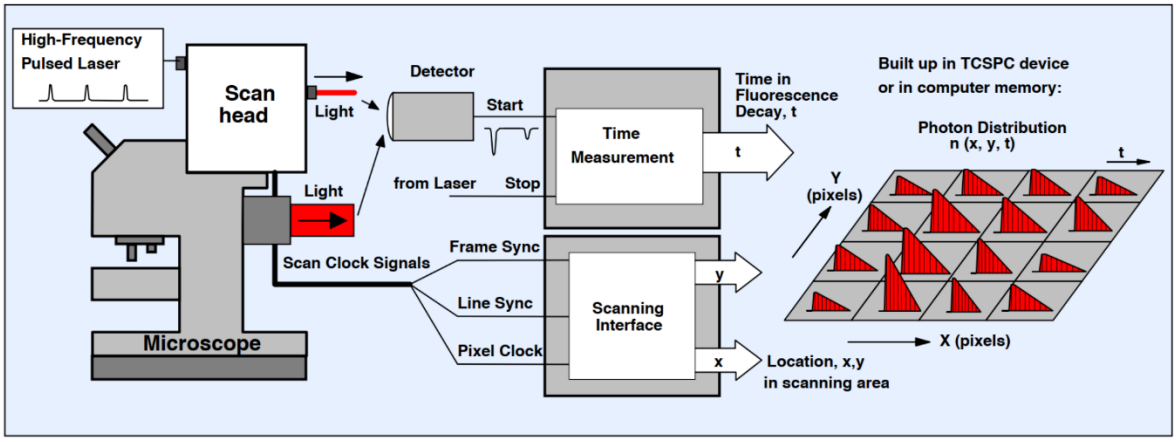

Figure 2: The Primary form of time domain FLIM acquisition is realized using time correlated single photon counting (TCSPC). Figure a and b shows the principle and instrumentation of TCSPC FLIM acquisition a) FLIM histogram building using TCSPC acquisition, a distribution created from multiple photon timing information. Multiple laser excitation is used to excite the fluorophore and the timing information of the emitted photons are recorded. For a sufficient number of photons, a histogram can be created for a single pixel b) An overall depiction of TCSPC system coupled to a laser scanning system (Becker, W., 2014)(Image courtesy: Becker and Hickl TCSPC handbook)

3.1.1 FLIM acquisition software

Most commercial laser scanning microscopes which support time-domain FLIM acquisition are bundled with acquisition software for FLIM and intensity data. In most of the cases, the software is a completely black box and the end-user does not have any control over changing the code/algorithm or even modification of scanning waveform. This inherently limits the available options to perform laser scanning. An open-source software, OpenScan (Dai et al.) is being developed by our lab that works as an add-on to the popular microscope control software, μManager (Edelstein et al., 2014). μManager is an open-source, cross-platform desktop application, to control a wide variety of motorized microscopes, scientific cameras, stages, illuminators, and other microscope accessories. An open-source laser scanning add-on to already available and cross-platform software can enable researchers to have a wide variety of acquisition options hence offering flexibility and reducing the total cost of the system. The system supporting FLIM comes with FLIM acquisition module when bundled. Open-source laser scanning software like ScanImage does not support FLIM acquisition. Software like SymPhoTime 64 (PicoQuant

Photonics) offers both acquisition and analysis functionality but an additional purchase is required and tied to the vendor-specific hardware.

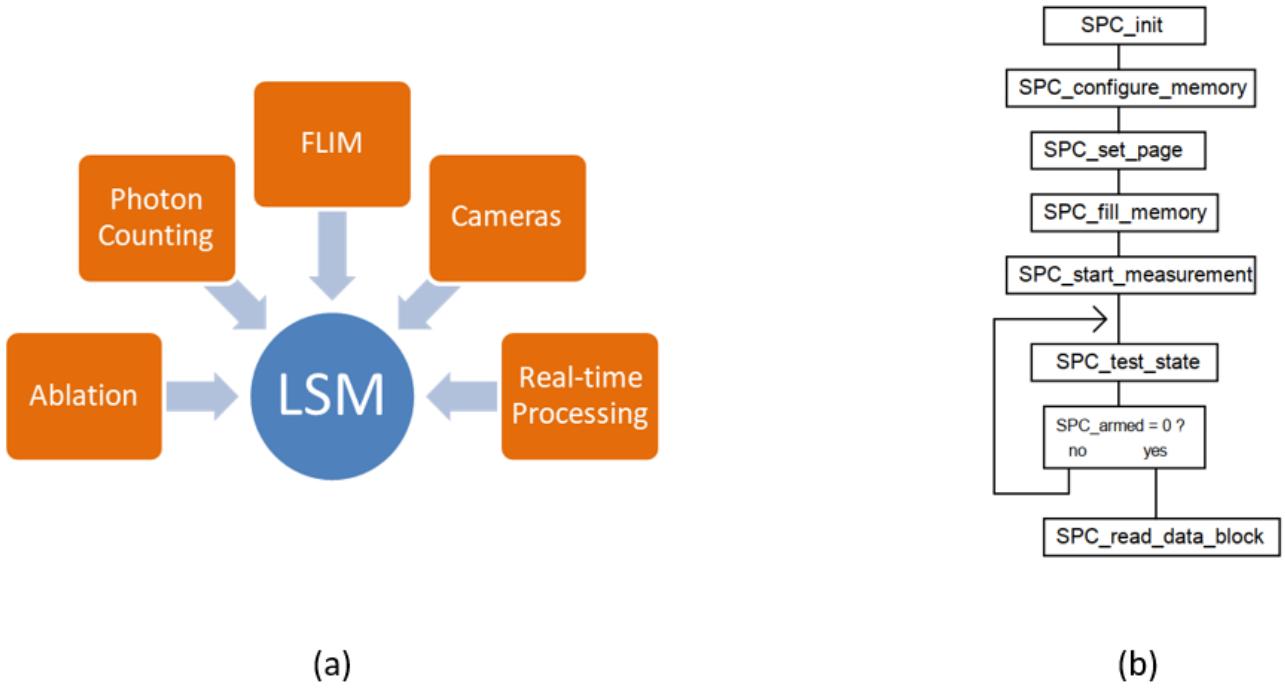

Figure 3: An open source laser scanning software provides the platform for open source lifetime acquisition. OpenScan- an open source device adapter for laser scanning microscopy for a parent image acquisition software for optical microscope (micro-Manager) a) OpenScan's different module that is supported by laser scanning b) Becker and Hickl FIFO acquisition workflow will be the main lifetime acquisition flow for OpenFLIM

3.2 Simultaneous Spectral FLIM acquisition

Beside fluorescence lifetime, every photon that is emitted due to fluorescence emission has a spectral signature that belongs to the emission spectra of the fluorophore. The analysis of the

fluorophore alongside the lifetime carries valuable information about the state of the cellular microenvironment and can provide novel insight into the biophysical properties of a sample (Dickinson et al., 2003; Tadrous et al., 2003; Wagnières et al., 1998). Fluorescence spectroscopy of tissues can be a powerful tool to realize early detection, diagnosis, and monitoring of pathological condition which might result in better treatment of critical diseases. There are several ways to collect both spectral and lifetime information from a sample. One simple approach would be simply collecting the emission several times with different required filter. The problem with this approach is the sample being exposed to excitation several times which could result in damage to the sample and photobleaching. Another classic way is to use multiple channels and detector setup. In this setup, each emission channel has a dichroic beamsplitter, a bandpass filter for the desired spectral range coupled with a detector and each channel builds its own histogram from fluorescence lifetime. Figure 4 shows a conceptual diagram of multi-channel spectral lifetime system having multiple lifetime or single TCSPC hardware for building the histograms for each channel. Roberts et al implemented a 4 channel TCSPC system where each channel has individual PMT (Roberts et al., 2011). Another option is to simultaneously measure all of the spectrum using a spatially dispersive optical element such as a prism (Hanley et al., 2002) or a grating (Bird et al., 2004; Yan et al., 2006) and directing the emission on to multiple timing detectors. Sun et al(Sun et al., 2008) demonstrated a novel fiber optics-based method for simultaneous time and wavelength-resolved fluorescence spectroscopy by combining 3 sets of bandpass filters and dichroic mirrors in a single acquisition. Three channels were coupled by optical fibers to introduce temporal delays. This approach was extended by Shrestha et al(Shrestha et al., 2010) to integrate the scheme in a scanning multispectral FLIM system. The dichroic mirror and filters were chosen such that it can separate emission spectra of three fluorophores to three channels. Optical fibers of

different lengths were used to introduce distinct temporal delays for each channel, thus allowing for multi-channel spectral FLIM with a single detector, a significant step up from the multi-detector approach. Nevertheless, this approach relies on the combination of filters, dichroic mirrors, and optical fibers to achieve spectral-FLIM thus requires a considerate amount of modification to a conventional multiphoton microscope.

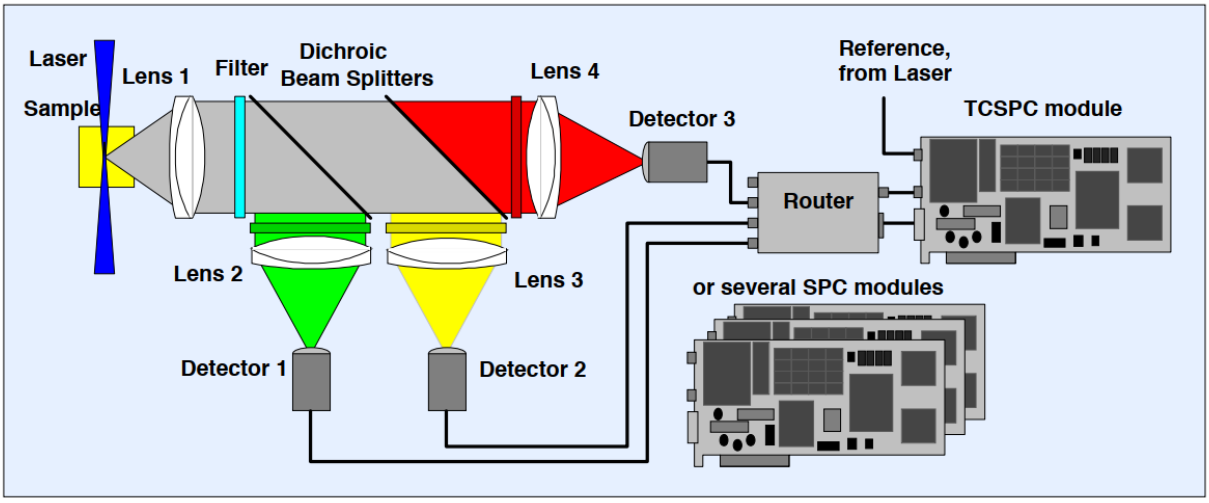

Figure 4: A traditional spectral lifetime system. Traditionally the spectral detection system is set up with dichroic beamsplitter and detector(s). All the channels create their separate histogram and based on their intensity for different channel and lifetime, a spectral lifetime signature can be developed. (image courtesy, Becker and Hickl GmBH TCSPC handbook)

Spectral information beside the fluorescence lifetime and intensity can provide valuable information about the state of cell. Presence or absence of certain fluorophore which have a

substantial change in emission peak can also be a relevant factor in characterizing cell types. There can also be change in emission peak for the same fluorophore based on the cell type or its functional state. For example, there have been studies showing NADH emission peak shifts by as much as 30nm for stem cell differentiation (König et al., 2011). Multispectral FLIM is implemented currently using one of the following strategies. Samples can be imaged multiple times, each time using a different optical band pass filter. However, acquiring multiple images is generally undesirable, as it is time-consuming, and multiple exposures increase the risk of photobleaching or otherwise damaging the sample. This approach can also be implemented as simultaneous imaging of two or more channels by splitting the emission spectra into multiple fixed spectral bandwidth channels by dichroic mirrors and filters, with each channel sharing the timing electronics by intelligent routing. Roberts et al implemented a 4 channel TCSPC system where each channel has an individual PMT (Roberts et al., 2011). Another option is to simultaneously measure all of the spectrum using a spatially dispersive optical element such as a prism (Hanley et al., 2002) or a grating (Bird et al., 2004; Yan et al., 2006) and directing the emission on to multiple timing detectors. The dispersive element and multiple detectors however make this a technically complicated and expensive solution. Following the line of reasoning to use dispersive elements in the optical path for spectral separation: instead of using an optical prism or optical grating to introduce dispersion, one could use an optical fiber to achieve chromatic dispersion. Effective utilization of dispersive properties of optical fibers has been demonstrated in various optical communication applications such as wavelength division optical multiplexing (WDM) (Liew et al., 2016) and optical time domain reflectance characterization (OTDR)(Personick). By specifying the length and choosing the right material, the optical fiber can introduce appropriate dispersion to

allow the separation of the fluorescence emission spectrum to the desired resolution. This approach forms the basis of our study.

4. Software, hardware and techniques development for enhancing FLIM

Despite the recent advancement in electronics and software-based technique to automate the acquisition, there is still limitation in the respective areas. For example, there is no open-source TCSPC FLIM acquisition code. As a result, any technique that depends on running custom routine during runtime helpful for detection label-free signature from samples, could not be implemented. Another limitation is the lack of open source FLIM analysis software packages. An open-source analysis platform can significantly enhance FLIM imaging capability by allow for custom and more transparent routines for analysis. Here software-based techniques to characterize microglia and activation are discussed building on our previous instrumentation efforts (Kader Sagar, 2015) which will ultimately lead to improved FLIM acquisition/analysis. In the following three sections, the primary areas that are addressed in this thesis are discussed along with their limitation and the areas where improvements need to be done.

4.1 Software development for FLIM acquisition

FLIM is acquired primarily in two ways, in the frequency and time domain. Both domains have their advantages and disadvantages. In frequency domain FLIM, a modulated light source and modulated detector is used. The excitation light is modulated or pulsed in intensity at a certain frequency and the fluorescence emission will mirror the modulation pattern. Because of the fluorescence emission, a delay is introduced in the form of phase shift and the signal is demodulated. The lifetime can be calculated from modulation ratio. Frequency domain lifetime is faster and computationally less intensive but can suffer from aliasing, photobleaching induced artifact, low signal-to-noise-ratio and limited dynamic range. In time domain FLIM, an ultrashort pulse is used to excite the sample and the emission is detected via single photon counting. The time from the excitation and photon detection are calculated by electronics that have a temporal resolution in the picoseconds range. This is called Time-Correlated Single Photon Counting (TCSPC)(Becker, W., 2014). Laser scanning multiphoton or confocal microscopes can be upgraded to have TCSPC FLIM capability by adding TCSPC hardware with a pulsed laser. Although TCSPC has many advantages over frequency domain such as its ability to provide pixel-wise statistics and better SNR. However, the time taken to acquire a single image limits its ability to collect data for real-time acquisition for moving subjects. For example, one single image acquisition might take 1-2 minutes, or even 3 minutes in some cases (low intensity image). The post processing involves tuning curve fitting initialization parameters and estimating lifetime using curve fitting routines which would take close to a minute. As a result, imaging a large section which would have several hundred field-of-views, would take days to finish. This is often a limiting factor of Time domain FLIM based study in general.

To optimize these limitations, there are several ways to improve FLIM imaging but those all require ability to modify FLIM acquisition software preferably with an open source acquisition software to ease development and adoption and assure transparency. Unfortunately, there is no open source acquisition software which supports FLIM acquisition. Most commercial vendors making turn-key TCSPC hardware provide their own acquisition software which lacks the ability to add custom routine. Additionally, the currently available commercial software programs do not provide a way of visualizing FLIM parameters during acquisition, only the intensity data are shown during acquisition. As a result, the users end up imaging a lot more regions that could be optimized if there was a way to estimate the parameters during runtime. For example, some parts of the brain is more microglia-dense the other parts (Mittelbronn et al., 2001) and microglia activation level might also differ based on region. It would only make sense to image some parts of the brain than the others given the time constraints of TCSPC FLIM acquisition. Runtime estimation of the lifetime can be helpful assistance in minimizing labor and time for large section imaging.

The current FLIM acquisition platforms are limited in their capability and does not offer the flexibility to customize the acquisition routine or add additional feature. Given the nature of microglia and its distribution in central nervous system, microglia study with FLIM necessitates the development of custom open source acquisition software. To overcome the limitation of existing FLIM platforms, we propose an open source software for TCSPC FLIM acquisition which is based on lab developed open source laser scanning control software that we call OpenScan.

4.2 Hardware development for combined spectral/FLIM imaging

In the previous sections, the need for NADH FLIM for microglia signature development and improving existing FLIM acquisition techniques were discussed. NADH FLIM based signature development are promising and has been explored for other immune cell like macrophages (Alfonso-García et al., 2016b; Szulczewski et al., 2016). But these approaches only consider lifetime as the marker to differentiate cell type. Presence or absence of certain fluorophore which have a substantial change in emission peak can also be a relevant factor in characterizing cell types. There can also be change in emission peak for the same fluorophore based on the cell type or its functional state. For example, there have been studies showing NADH emission peak shifts by as much as 30nm for stem cell differentiation(König et al., 2011). If there is a similar trend for microglia, the combination of lifetime and spectral signature can be used to develop a unique signature which could more reliably identify microglia among other cells and/or differentiate between quiescent/active microglia cell.

To investigate this phenomenon, lifetime imaging system with spectral discrimination capability is needed which can separate emission peak of the desired fluorophore(s). For example, if we are to develop a lifetime-spectral discrimination system able to differentiate between the stem cell differentiation described earlier, the spectral resolution should be less than 30nm. Spectral FLIM has been exploited in some biological studies, such as imaging and identifying the single molecule in a living cell (Knemeyer et al., 2003), super-resolution STED imaging with spectral FLIM (Niehörster et al., 2016). Multispectral FLIM is implemented currently using one of the following strategies. Samples can be imaged multiple times, each time using a different optical band pass filter. However, acquiring multiple images is generally undesirable, as it is time-consuming, and

multiple exposures increase the risk of photobleaching or otherwise damaging the sample. This approach can also be implemented as simultaneous imaging of two or more channels by splitting the emission spectra into multiple fixed spectral bandwidth channels by dichroic mirrors and filters, with each channel sharing the timing electronics by intelligent routing. Roberts et al implemented a 4 channel TCSPC system where each channel has individual PMT (Roberts et al., 2011). Another option is to simultaneously measure all of the spectrums using a spatially dispersive optical element such as a prism (Hanley et al., 2002) or a grating (Bird et al., 2004; Yan et al., 2006) and directing the emission on to multiple timing detectors. The dispersive element and multiple detectors, however, make this a technically complicated and expensive solution. Following the line of reasoning to use dispersive elements in the optical path for spectral separation: instead of using an optical prism or optical grating to introduce dispersion, one could use an optical fiber to achieve chromatic dispersion. Effective utilization of dispersive properties of optical fibers has been demonstrated in various optical communication applications such as wavelength division optical multiplexing (WDM)(Liew et al., 2016) and optical time domain reflectance characterization (OTDR)(Personick). By calibrating the length and choosing the right material, the optical fiber can introduce appropriate dispersion and separate the fluorescence emission spectrum with the desired resolution. Using an optical fiber of appropriate length, diameter and material, we are going to develop an add-on device for a TCSPC FLIM system which is easy to upgrade compared to other multi detector approach and can differentiate between at least 10nm emission peaks. The fiber-based setup is more suitable for investigating spectral shifts in any part of the emission spectra which are separated by the spectral resolution of the system. On the contrary, traditional multi detector based would be cumbersome as those would be limited by the bandpass filters already used in the system.

4.3 Machine learning approaches to differentiate microglia

Machine learning is a class of computational learning techniques where a system learns based on several instances with label. Machine learning based computational prediction models predicts the label of an unknown instance. There are two primary classes of machine learning techniques, supervised and unsupervised techniques. In unsupervised machine learning techniques, the algorithm tries to group a set of data and two or more groups based on the training parameters only without any label. In supervised machine learning, the algorithm learns about the training sets based on the labels and the training parameters provided and predicts the label of a new instance for which the label is unknown. Based on the types of data and the number of instances provided, there can be different machine learning techniques which can be useful. One of the popular machine learning technique is Artificial Neural Network (ANN). ANN emulates the behavior of neuron where several layers of nodes are interconnected with one input and output layer. The nodes between the "input" and output layers are called hidden layer which contains an activation function which works as a switch for a given input value (Abraham, 2005; Hopfield, 1988; Wang, 2003). The interconnection between the nodes is assigned a weight which is adjusted to improve accuracy. In forward propagation, a set of input data is applied to the weights and output is calculated. In the backpropagation stage, the weight of each connection starting from the output layer to input layer is adjusted by measuring the error of the output (Hecht-nielsen, 1992).

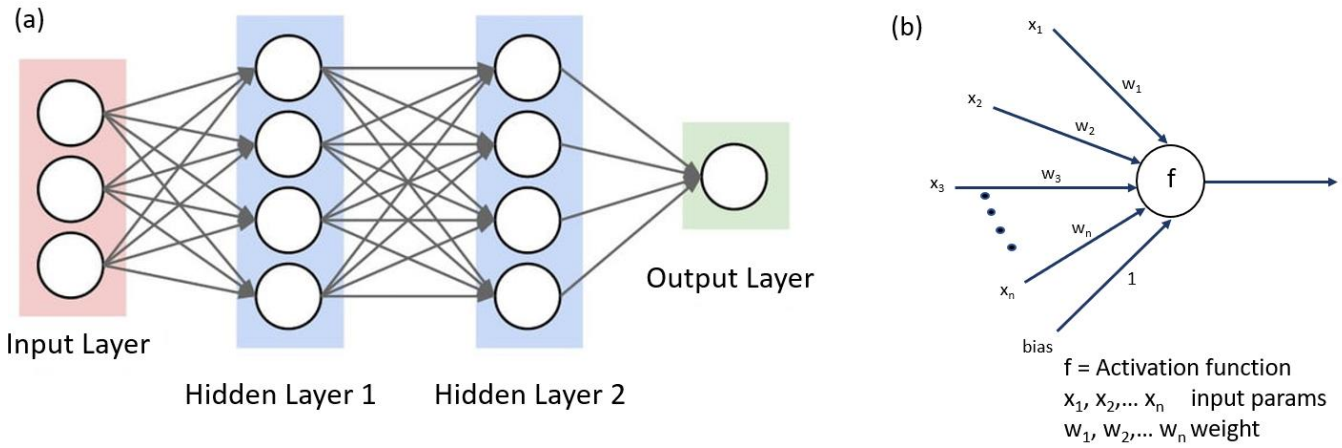

Figure 5: Artificial neural network a) Overall ANN with 2 hidden layer b) One hidden node using n input with n weights

To identify and exploit the distinct features of resting microglia that differentiate them from other glial cells, we are working on developing a machine learning classification system which can be readily used to identify unlabeled microglia. The NADH-FLIM produces six different parameters for each pixel. If there are different trends between microglia and other CNS cells, these parameters can be used to develop robust classifiers which can readily identify microglia based solely on FLIM data. The application of FLIM data to identify cell types is new to our knowledge, and we aim to extend the system based on the results obtained in these studies. We expect that artificial neural network-based classification systems will have tremendous accuracy even when the training dataset is relatively small.

5. Conclusion

In this thesis, we are demonstrating methods for label-free FLIM based technique to characterize microglia activation, machine learning technique to differentiate microglia using FLIM data, enhancing label-free imaging by developing open source FLIM acquisition software and develop optical technique for simultaneous spectral/FLIM imaging. All these methods collectively can help understand role of microglia in neurodegenerative disease better. Some of the methods developed as part of this thesis can help scientists beyond microglia microenvironment imaging. The open source FLIM acquisition software will help researchers develop custom acquisition routine and enable runtime analysis. The simultaneous spectral/FLIM acquisition technique can serve as an easy add-on to existing confocal/multiphoton scope to characterize multiple fluorophores which will eventually lead to developing new application for label-free biomarker identification.

The thesis is divided in four chapters following the introduction. The second chapter describes method to characterize microglia activation using FLIM of NADH as a biomarker. The third chapter builds on the technique developed in the previous chapter and uses FLIM along with computational technique to differentiate microglia in relation to other glial cell and brain tissue. Additionally, Artificial Neural Network based machine learning application was developed which utilizes NADH FLIM data for predicting microglia location. This method is one of the first application of ML on FLIM data for a biological application. In the fourth chapter, software and hardware techniques are discussed which are developed as part of this thesis which would make FLIM more flexible and lead to better FLIM based label-free visualization. In this chapter, first, a novel fiber-based flexible add-on is discussed which enables simultaneous spectral and lifetime acquisition and show some application of this approach. Additionally, an open source FLIM

acquisition module is demonstrated which runs as a plugin of a micromanager (Edelstein et al., 2014) based scanning module. In the final chapter, I discuss my collaborations with other research groups applying FLIM in measuring metabolism and improving FLIM analysis technique. In the biological collaboration projects, I utilized my expertise in multiphoton microscopy/FLIM to better interpret a biological phenomenon (Ghanbari et al., 2018; Kenny et al., 2017; Martin et al., 2018). For example, in one collaboration, I confirmed and validated the use of PET FLIM to be used as cranial window for simultaneous monitoring and perturbation of neural activity from multiple cortical region in mice skull (Ghanbari et al., 2018). In the instrumentation collaboration projects, I worked with other groups to develop fast FLIM techniques such as coding scheme for fast FLIM (Lee et al., 2019).

References

Abraham, A. (2005). Artificial Neural Networks. In Handbook of Measuring System Design, (American Cancer Society), p.

Alfonso-García, A., Smith, T.D., Datta, R., Luu, T.U., Gratton, E., Potma, E.O., and Liu, W.F. (2016a). Label-free identification of macrophage phenotype by fluorescence lifetime imaging microscopy. J. Biomed. Opt *21*, 046005–046005.

Alfonso-García, A., Smith, T.D., Datta, R., Luu, T.U., Gratton, E., Potma, E.O., and Liu, W.F. (2016b). Label-free identification of macrophage phenotype by fluorescence lifetime imaging microscopy. JBO *21*, 046005.

Ardeshirpour, Y., Chernomordik, V., Hassan, M., Zielinski, R., Capala, J., and Gandjbakhche, A. (2014). In Vivo Fluorescence Lifetime Imaging for Monitoring the Efficacy of the Cancer Treatment. Clin Cancer Res *20*, 3531–3539.

Bartolomé, F., and Abramov, A.Y. (2015). Measurement of mitochondrial NADH and FAD autofluorescence in live cells. Methods Mol. Biol. *1264*, 263–270.

Bastiaens, P.I.H., and Squire, A. (1999). Fluorescence lifetime imaging microscopy: spatial resolution of biochemical processes in the cell. Trends in Cell Biology *9*, 48–52.

Béchade, C., Cantaut-Belarif, Y., and Bessis, A. (2013). Microglial control of neuronal activity. Front Cell Neurosci *7*.

Becher, B., and Antel, J.P. (1996). Comparison of phenotypic and functional properties of immediately ex vivo and cultured human adult microglia. Glia *18*, 1–10.

Becker, W. (2012). Fluorescence lifetime imaging – techniques and applications. Journal of Microscopy *247*, 119–136.

Becker, W., and Bergmann, A. (2003). Lifetime imaging techniques for optical microscopy. Tech-Nical Report, Becker & Hickl GmbH.

Becker, W., Bergmann, A., Biskup, C., Kelbauskas, L., Zimmer, T., Klocker, N., and Benndorf, K. (2003). High resolution TCSPC lifetime imaging. In Biomedical Optics 2003, (International Society for Optics and Photonics), pp. 175–184.

Becker, W. (2014). The bh TCSPC Handbook (Becker & Hickl Gmbh).

Bellesi, M., de Vivo, L., Chini, M., Gilli, F., Tononi, G., and Cirelli, C. (2017). Sleep Loss Promotes Astrocytic Phagocytosis and Microglial Activation in Mouse Cerebral Cortex. J. Neurosci. *37*, 5263–5273.

Bennett, M.L., Bennett, F.C., Liddelow, S.A., Ajami, B., Zamanian, J.L., Fernhoff, N.B., Mulinyawe, S.B., Bohlen, C.J., Adil, A., Tucker, A., et al. (2016). New tools for studying microglia in the mouse and human CNS. Proc. Natl. Acad. Sci. U.S.A. *113*, E1738-1746.

Berezin, M.Y., and Achilefu, S. (2010). Fluorescence Lifetime Measurements and Biological Imaging. Chem Rev *110*, 2641–2684.

Bhattacharjee, A., Datta, R., Gratton, E., and Hochbaum, A.I. (2017). Metabolic fingerprinting of bacteria by fluorescence lifetime imaging microscopy. Scientific Reports *7*.

Bird, D.K., Eliceiri, K.W., Fan, C.-H., and White, J.G. (2004). Simultaneous two-photon spectral and lifetime fluorescence microscopy. Appl. Opt., AO *43*, 5173–5182.

Bird, D.K., Yan, L., Vrotsos, K.M., Eliceiri, K.W., Vaughan, E.M., Keely, P.J., White, J.G., and Ramanujam, N. (2005a). Metabolic mapping of MCF10A human breast cells via multiphoton fluorescence lifetime imaging of the coenzyme NADH. Cancer Res. *65*, 8766–8773.

Bird, D.K., Yan, L., Vrotsos, K.M., Eliceiri, K.W., Vaughan, E.M., Keely, P.J., White, J.G., and Ramanujam, N. (2005b). Metabolic Mapping of MCF10A Human Breast Cells via Multiphoton Fluorescence Lifetime Imaging of the Coenzyme NADH. Cancer Res *65*, 8766–8773.

Blacker, T.S., and Duchen, M.R. (2016). Investigating mitochondrial redox state using NADH and NADPH autofluorescence. Free Radic Biol Med *100*, 53–65.

Blacker, T.S., Mann, Z.F., Gale, J.E., Ziegler, M., Bain, A.J., Szabadkai, G., and Duchen, M.R. (2014). Separating NADH and NADPH fluorescence in live cells and tissues using FLIM. Nat Commun *5*, 3936.

Bonuccelli, G., De Francesco, E.M., de Boer, R., Tanowitz, H.B., and Lisanti, M.P. (2017). NADH autofluorescence, a new metabolic biomarker for cancer stem cells: Identification of Vitamin C and CAPE as natural products targeting "stemness." Oncotarget *8*, 20667–20678.

Butovsky, O., Jedrychowski, M.P., Moore, C.S., Cialic, R., Lanser, A.J., Gabriely, G., Koeglsperger, T., Dake, B., Wu, P.M., Doykan, C.E., et al. (2014). Identification of a unique TGF-β–dependent molecular and functional signature in microglia. Nature Neuroscience *17*, 131–143.

Chacko, J.V., and Eliceiri, K.W. (2018). Autofluorescence lifetime imaging of cellular metabolism: Sensitivity toward cell density, pH, intracellular, and intercellular heterogeneity. Cytometry A.

Chacko, J.V., and Eliceiri, K.W. (2019). NAD(P)H fluorescence lifetime measurements in fixed biological tissues. Methods Appl. Fluoresc.

Chance, B. (1976). Pyridine nucleotide as an indicator of the oxygen requirements for energy-linked functions of mitochondria. Circ. Res. *38*, I31-38.

Chance, B., Schoener, B., Oshino, R., Itshak, F., and Nakase, Y. (1979). Oxidation-reduction ratio studies of mitochondria in freeze-trapped samples. NADH and flavoprotein fluorescence signals. J. Biol. Chem. *254*, 4764–4771.

Charles, N.A., Holland, E.C., Gilbertson, R., Glass, R., and Kettenmann, H. (2011). The brain tumor microenvironment. Glia *59*, 1169–1180.

Chen, X., Nadiarynkh, O., Plotnikov, S., and Campagnola, P.J. (2012). Second harmonic generation microscopy for quantitative analysis of collagen fibrillar structure. Nprot *7*, 654–669.

Chiu, I.M., Morimoto, E.T.A., Goodarzi, H., Liao, J.T., O'Keeffe, S., Phatnani, H.P., Muratet, M., Carroll, M.C., Levy, S., Tavazoie, S., et al. (2013). A neurodegeneration-specific gene-expression signature of acutely isolated microglia from an amyotrophic lateral sclerosis mouse model. Cell Rep *4*, 385–401.

Colyer, R.A., Lee, C., and Gratton, E. (2008). A novel fluorescence lifetime imaging system that optimizes photon efficiency. Microscopy Research and Technique *71*, 201–213.

Conklin, M.W., Eickhoff, J.C., Riching, K.M., Pehlke, C.A., Eliceiri, K.W., Provenzano, P.P., Friedl, A., and Keely, P.J. (2011). Aligned collagen is a prognostic signature for survival in human breast carcinoma. Am. J. Pathol. *178*, 1221–1232.

Cox, G., Kable, E., Jones, A., Fraser, I., Manconi, F., and Gorrell, M.D. (2003). 3-Dimensional imaging of collagen using second harmonic generation. Journal of Structural Biology *141*, 53–62.

Dai, B., Li, B., Xu, R., Sagar, M.A.K., Gong, X., Keikhosravi, A., Pinkert, M., Chacko, J.V., Tsuchida, M.A., and Eliceiri, K. OpenScan draft: Extensible Laser Scanning Microscopy in Micro-Manager. Manuscript in Preparation.

Dancik, Y., Favre, A., Loy, C.J., Zvyagin, A.V., and Roberts, M.S. (2013). Use of multiphoton tomography and fluorescence lifetime imaging to investigate skin pigmentation in vivo. J. Biomed. Opt *18*, 026022–026022.

Datta, R., Heylman, C., George, S.C., and Gratton, E. (2016a). Label-free imaging of metabolism and oxidative stress in human induced pluripotent stem cell-derived cardiomyocytes. Biomed. Opt. Express, BOE *7*, 1690–1701.

Datta, R., Sobrino, A., Hughes, C., and Gratton, E. (2016b). Fluorescence Lifetime Imaging Microscopy to study Metabolism in a Microfluidic Device based Tumor Microenvironment. In Optical Tomography and Spectroscopy, (Optical Society of America), pp. JW4A–2.

Davis, B.M., Salinas-Navarro, M., Cordeiro, M.F., Moons, L., and Groef, L.D. (2017). Characterizing microglia activation: a spatial statistics approach to maximize information extraction. Scientific Reports *7*, 1576.

Débarre, D., Supatto, W., Pena, A.-M., Fabre, A., Tordjmann, T., Combettes, L., Schanne-Klein, M.-C., and Beaurepaire, E. (2006). Imaging lipid bodies in cells and tissues using third-harmonic generation microscopy. Nat Methods *3*, 47–53.

Deka, G., Wu, W.-W., and Kao, F.-J. (2013). In vivo wound healing diagnosis with second harmonic and fluorescence lifetime imaging. J Biomed Opt *18*, 061222.

Denk, W., Strickler, J.H., and Webb, W.W. (1990a). Two-photon laser scanning fluorescence microscopy. Science *248*, 73–76.

Denk, W., Strickler, J.H., and Webb, W.W. (1990b). Two-photon laser scanning fluorescence microscopy. Science *248*, 73–76.

Diana, M. (2018). Fluorescence-guided surgery applied to the digestive system: the cybernetic eye to see the invisible. Cir Esp *96*, 65–68.

Dickinson, M.E., Simbuerger, E., Zimmermann, B., Waters, C.W., and Fraser, S.E. (2003). Multiphoton excitation spectra in biological samples. Journal of Biomedical Optics *8*, 329–338.

Dimitrow, E., Riemann, I., Ehlers, A., Koehler, M.J., Norgauer, J., Elsner, P., König, K., and Kaatz, M. (2009). Spectral fluorescence lifetime detection and selective melanin imaging by multiphoton laser tomography for melanoma diagnosis. Exp. Dermatol. *18*, 509–515.

Durr, N.J., Weisspfennig, C.T., Holfeld, B.A., and Ben-Yakar, A. (2011). Maximum imaging depth of two-photon autofluorescence microscopy in epithelial tissues. J Biomed Opt *16*.

Edelstein, A.D., Tsuchida, M.A., Amodaj, N., Pinkard, H., Vale, R.D., and Stuurman, N. (2014). Advanced methods of microscope control using μManager software. J Biol Methods *1*.

Elder, A., Schlachter, S., and Kaminski, C.F. (2008). Theoretical investigation of the photon efficiency in frequency-domain fluorescence lifetime imaging microscopy. J. Opt. Soc. Am. A, JOSAA *25*, 452–462.

Elder, A.D., Frank, J.H., Swartling, J., Dai, X., and Kaminski, C.F. (2006). Calibration of a wide-field frequency-domain fluorescence lifetime microscopy system using light emitting diodes as light sources. Journal of Microscopy *224*, 166–180.

Elder, A.D., Kaminski, C.F., and Frank, J.H. (2009). ϕ^2FLIM: a technique for alias-free frequency domain fluorescence lifetime imaging. Opt. Express, OE *17*, 23181–23203.

Ettinger, A., and Wittmann, T. (2014). Fluorescence live cell imaging. Methods Cell Biol. *123*, 77–94.

Ford, A.L., Goodsall, A.L., Hickey, W.F., and Sedgwick, J.D. (1995). Normal adult ramified microglia separated from other central nervous system macrophages by flow cytometric sorting. Phenotypic differences defined and direct ex vivo antigen presentation to myelin basic protein-reactive CD4+ T cells compared. J. Immunol. *154*, 4309–4321.

Gahlmann, A., and Moerner, W.E. (2014). Exploring bacterial cell biology with single-molecule tracking and super-resolution imaging. Nat Rev Micro *12*, 9–22.

Galletly, N.P., McGinty, J., Dunsby, C., Teixeira, F., Requejo-Isidro, J., Munro, I., Elson, D.S., Neil, M. a. A., Chu, A.C., French, P.M.W., et al. (2008). Fluorescence lifetime imaging distinguishes basal cell carcinoma from surrounding uninvolved skin. Br. J. Dermatol. *159*, 152–161.

Garcia, A.A., Smith, T., Datta, R., Gratton, E., Potma, E.O., and Liu, W. (2016). Visualizing Cellular Metabolic Processes With Combined Nonlinear Optical Microscopy. In Biomedical Optics 2016 (2016), Paper OTh4C.7, (Optical Society of America), p. OTh4C.7.

Garden, G.A., and Möller, T. (2006). Microglia Biology in Health and Disease. Jrnl NeuroImmune Pharm *1*, 127–137.

Gautier, E.L., Shay, T., Miller, J., Greter, M., Jakubzick, C., Ivanov, S., Helft, J., Chow, A., Elpek, K.G., Gordonov, S., et al. (2012). Gene-expression profiles and transcriptional regulatory

pathways that underlie the identity and diversity of mouse tissue macrophages. Nat. Immunol. *13*, 1118–1128.

Gehlsen, U., Oetke, A., Szaszák, M., Koop, N., Paulsen, F., Gebert, A., Huettmann, G., and Steven, P. (2012). Two-photon fluorescence lifetime imaging monitors metabolic changes during wound healing of corneal epithelial cells in vitro. Graefes Arch. Clin. Exp. Ophthalmol. *250*, 1293–1302.

Ghanbari, L., Carter, R.E., Rynes, M.L., Dominguez, J., Chen, G., Naik, A., Hu, J., Sagar, M.A.K., Haltom, L., Mossazghi, N., et al. (2018). Cortex-wide neural interfacing via transparent polymer skulls. BioRxiv 387142.

Giulian, D., Li, J., Bartel, S., Broker, J., Li, X., and Kirkpatrick, J.B. (1995). Cell surface morphology identifies microglia as a distinct class of mononuclear phagocyte. J. Neurosci. *15*, 7712–7726.

Gómez, C.A., Fu, B., Sakadžic, S., and Yaseen, M.A. (2018). Cerebral metabolism in a mouse model of Alzheimer's disease characterized by two-photon fluorescence lifetime microscopy of intrinsic NADH. NPh *5*, 045008.

Göppert-Mayer, M. (1931). Über Elementarakte mit zwei Quantensprüngen. Annalen Der Physik *401*, 273–294.

Gosselin, D., Link, V.M., Romanoski, C.E., Fonseca, G.J., Eichenfield, D.Z., Spann, N.J., Stender, J.D., Chun, H.B., Garner, H., Geissmann, F., et al. (2014). Environment drives selection and function of enhancers controlling tissue-specific macrophage identities. Cell *159*, 1327–1340.

Gratton, E. (2016). Measurements of Fluorescence Decay Time by the Frequency Domain Method. In Perspectives on Fluorescence, D.M. Jameson, ed. (Cham: Springer International Publishing), pp. 67–80.

Gratton, E., and Barbieri, B. (1993). High speed cross-correlation frequency domain fluorometry-phosphorimetry.

Gratton, E., Breusegem, S., Sutin, J., Ruan, Q., and Barry, N. (2003). Fluorescence lifetime imaging for the two-photon microscope: time-domain and frequency-domain methods. J. Biomed. Opt *8*, 381–390.

Gudi, V., Gingele, S., Skripuletz, T., and Stangel, M. (2014). Glial response during cuprizone-induced de- and remyelination in the CNS: lessons learned. Front Cell Neurosci *8*, 73.

Guo, H.-W., Chen, C.-T., Wei, Y.-H., Lee, O.K., Gukassyan, V., Kao, F.-J., and Wang, H.-W. (2008). Reduced nicotinamide adenine dinucleotide fluorescence lifetime separates human mesenchymal stem cells from differentiated progenies. J Biomed Opt *13*, 050505.

Hanley, Q.S., Arndt-Jovin, D.J., and Jovin, T.M. (2002). Spectrally Resolved Fluorescence Lifetime Imaging Microscopy. Appl Spectrosc *56*, 155–166.

Hansen, D.V., Hanson, J.E., and Sheng, M. (2017). Microglia in Alzheimer's disease. J Cell Biol jcb.201709069.

Hao, C., Parney, I.F., Roa, W.H., Turner, J., Petruk, K.C., and Ramsay, D.A. (2002). Cytokine and cytokine receptor mRNA expression in human glioblastomas: evidence of Th1, Th2 and Th3 cytokine dysregulation. Acta Neuropathol. *103*, 171–178.

Hato, T., Winfree, S., Day, R., Sandoval, R.M., Molitoris, B.A., Yoder, M.C., Wiggins, R.C., Zheng, Y., Dunn, K.W., and Dagher, P.C. (2017). Two-Photon Intravital Fluorescence Lifetime Imaging of the Kidney Reveals Cell-Type Specific Metabolic Signatures. Journal of the American Society of Nephrology *28*, 2420–2430.

Hecht-nielsen, R. (1992). III.3 - Theory of the Backpropagation Neural Network**Based on "nonindent" by Robert Hecht-Nielsen, which appeared in Proceedings of the International Joint Conference on Neural Networks 1, 593–611, June 1989. © 1989 IEEE. In Neural Networks for Perception, H. Wechsler, ed. (Academic Press), pp. 65–93.

Heiden, M.G.V., Cantley, L.C., and Thompson, C.B. (2009). Understanding the Warburg Effect: The Metabolic Requirements of Cell Proliferation. Science *324*, 1029–1033.

Hoover, E.E., and Squier, J.A. (2013). Advances in multiphoton microscopy technology. Nat Photon *7*, 93–101.

Hopfield, J.J. (1988). Artificial neural networks. IEEE Circuits and Devices Magazine *4*, 3–10.

Hou, J., Wright, H.J., Chan, N., Tran, R., Razorenova, O.V., Potma, E.O., and Tromberg, B.J. (2016). Correlating two-photon excited fluorescence imaging of breast cancer cellular redox state with seahorse flux analysis of normalized cellular oxygen consumption. J. Biomed. Opt *21*, 060503–060503.

Hovens, I.B., Nyakas, C., and Schoemaker, R.G. (2014). A novel method for evaluating microglial activation using ionized calcium-binding adaptor protein-1 staining: cell body to cell size ratio. Neuroimmunol Neuroinflamm.

Imamura, T., Saitou, T., and Kawakami, R. (2018). In vivo optical imaging of cancer cell function and tumor microenvironment. Cancer Science *109*, 912–918.

Jiang, L., Wang, X., Wu, Z., Du, H., Wang, S., Li, L., Fang, N., Lin, P., Chen, J., Kang, D., et al. (2017). Label-free imaging of brain and brain tumor specimens with combined two-photon excited fluorescence and second harmonic generation microscopy. Laser Phys. Lett. *14*, 105401.

Jin, X., and Yamashita, T. (2016). Microglia in central nervous system repair after injury. J. Biochem. *159*, 491–496.

Jung, S., Aliberti, J., Graemmel, P., Sunshine, M.J., Kreutzberg, G.W., Sher, A., and Littman, D.R. (2000). Analysis of Fractalkine Receptor CX3CR1 Function by Targeted Deletion and Green Fluorescent Protein Reporter Gene Insertion. Mol Cell Biol *20*, 4106–4114.

Kader Sagar, M.A. (2015). Automated acquisition approaches for multidimensional multiphoton microscopy.

Kalinina, S., Breymayer, J., Schäfer, P., Calzia, E., Shcheslavskiy, V., Becker, W., and Rück, A. (2016). Correlative NAD(P)H-FLIM and oxygen sensing-PLIM for metabolic mapping. Journal of Biophotonics *9*, 800–811.

Kalisz, J. (2004). Review of methods for time interval measurements with picosecond resolution. Metrologia *41*, 17.

Kantelhardt, S.R., Leppert, J., Krajewski, J., Petkus, N., Reusche, E., Tronnier, V.M., Hüttmann, G., and Giese, A. (2007). Imaging of brain and brain tumor specimens by time-resolved multiphoton excitation microscopy ex vivo. Neuro-Oncol *9*, 103–112.

Keikhosravi, A., Bredfeldt, J.S., Sagar, A.K., and Eliceiri, K.W. (2014). Second-harmonic generation imaging of cancer. Methods Cell Biol *123*, 531–546.

Kenny, T.C., Hart, P., Ragazzi, M., Sersinghe, M., Chipuk, J., Sagar, M. a. K., Eliceiri, K.W., LaFramboise, T., Grandhi, S., Santos, J., et al. (2017). Selected mitochondrial DNA landscapes activate the SIRT3 axis of the UPR^{mt} to promote metastasis. Oncogene *36*, 4393–4404.

Kim, Y.S., and Joh, T.H. (2006). Microglia, major player in the brain inflammation: their roles in the pathogenesis of Parkinson's disease. Experimental & Molecular Medicine *38*, 333–347.

Knemeyer, J.-P., Herten, D.-P., and Sauer, M. (2003). Detection and identification of single molecules in living cells using spectrally resolved fluorescence lifetime imaging microscopy. Anal. Chem. *75*, 2147–2153.

König, K., Uchugonova, A., and Gorjup, E. (2011). Multiphoton fluorescence lifetime imaging of 3D-stem cell spheroids during differentiation. Microsc. Res. Tech. *74*, 9–17.

Krasieva, T.B., Stringari, C., Liu, F., Sun, C.-H., Kong, Y., Balu, M., Meyskens, F.L., Gratton, E., and Tromberg, B.J. (2012). Two-photon excited fluorescence lifetime imaging and spectroscopy of melanins in vitro and in vivo. JBO, JBOPFO *18*, 031107.

Lagarto, J.L., Dyer, B.T., Talbot, C.B., Peters, N.S., French, P.M.W., Lyon, A.R., and Dunsby, C. (2018). Characterization of NAD(P)H and FAD autofluorescence signatures in a Langendorff isolated-perfused rat heart model. Biomed Opt Express *9*, 4961–4978.

Lakowicz, J.R., Szmacinski, H., Nowaczyk, K., and Johnson, M.L. (1992a). Fluorescence Lifetime Imaging of Free and Protein-Bound NADH. Proceedings of the National Academy of Sciences of the United States of America *89*, 1271–1275.

Lakowicz, J.R., Szmacinski, H., Nowaczyk, K., and Johnson, M.L. (1992b). Fluorescence lifetime imaging of free and protein-bound NADH. PNAS *89*, 1271–1275.

Lalancette-Hébert, M., Phaneuf, D., Soucy, G., Weng, Y.C., and Kriz, J. (2009). Live imaging of Toll-like receptor 2 response in cerebral ischaemia reveals a role of olfactory bulb microglia as modulators of inflammation. Brain *132*, 940–954.

Lazar, J., Bondar, A., Timr, S., and Firestein, S.J. (2011). Two-photon polarization microscopy reveals protein structure and function. Nature Methods *8*, 684–690.

LeBleu, V. (2015). Imaging the Tumor Microenvironment. Cancer J *21*, 174–178.

LeCun, Y., Bengio, Y., and Laboratories, T.B. Convolutional Networks for Images, Speech, and Time-Series. 15.

Lee, J., Chacko, J.V., Dai, B., Reza, S.A., Sagar, A.K., Eliceiri, K.W., Velten, A., and Gupta, M. (2019). Coding Scheme Optimization for Fast Fluorescence Lifetime Imaging. ACM Trans. Graph. *38*, 26:1–26:16.

Li, D.-U., Arlt, J., Richardson, J., Walker, R., Buts, A., Stoppa, D., Charbon, E., and Henderson, R. (2010). Real-time fluorescence lifetime imaging system with a 32 × 32 013μm CMOS low dark-count single-photon avalanche diode array. Optics Express *18*, 10257.

Liew, S.F., Redding, B., Choma, M.A., Tagare, H.D., and Cao, H. (2016). Broadband multimode fiber spectrometer. Opt. Lett., OL *41*, 2029–2032.

Luo, C., Jian, C., Liao, Y., Huang, Q., Wu, Y., Liu, X., Zou, D., and Wu, Y. (2017). The role of microglia in multiple sclerosis. Neuropsychiatr Dis Treat *13*, 1661–1667.

Martin, S.A., Souder, D.C., Miller, K.N., Clark, J.P., Sagar, A.K., Eliceiri, K.W., Puglielli, L., Beasley, T.M., and Anderson, R.M. (2018). GSK3β Regulates Brain Energy Metabolism. Cell Rep *23*, 1922-1931.e4.

McGinty, J., Galletly, N.P., Dunsby, C., Munro, I., Elson, D.S., Requejo-Isidro, J., Cohen, P., Ahmad, R., Forsyth, A., Thillainayagam, A.V., et al. (2010a). Wide-field fluorescence lifetime imaging of cancer. Biomed Opt Express *1*, 627–640.

McGinty, J., Galletly, N.P., Dunsby, C., Munro, I., Elson, D.S., Requejo-Isidro, J., Cohen, P., Ahmad, R., Forsyth, A., Thillainayagam, A.V., et al. (2010b). Wide-field fluorescence lifetime imaging of cancer. Biomed. Opt. Express, BOE *1*, 627–640.

Michell-Robinson, M.A., Touil, H., Healy, L.M., Owen, D.R., Durafourt, B.A., Bar-Or, A., Antel, J.P., and Moore, C.S. (2015). Roles of microglia in brain development, tissue maintenance and repair. Brain *138*, 1138–1159.

Mittelbronn, M., Dietz, K., Schluesener, H.J., and Meyermann, R. (2001). Local distribution of microglia in the normal adult human central nervous system differs by up to one order of magnitude. Acta Neuropathol *101*, 249–255.

Moreaux, L., Sandre, O., and Mertz, J. (2000). Membrane imaging by second-harmonic generation microscopy. J. Opt. Soc. Am. B, JOSAB *17*, 1685–1694.

Morton, P.E., and Parsons, M. (2011). Measuring FRET using time-resolved FLIM. Methods Mol. Biol. *769*, 403–413.

Nagaya, T., Nakamura, Y.A., Choyke, P.L., and Kobayashi, H. (2017). Fluorescence-Guided Surgery. Front Oncol *7*.

Niehörster, T., Löschberger, A., Gregor, I., Krämer, B., Rahn, H.-J., Patting, M., Koberling, F., Enderlein, J., and Sauer, M. (2016). Multi-target spectrally resolved fluorescence lifetime imaging microscopy. Nature Methods *13*, 257–262.

Niesner, R., Peker, B., Schlüsche, P., and Gericke, K.-H. (2004). Noniterative Biexponential Fluorescence Lifetime Imaging in the Investigation of Cellular Metabolism by Means of NAD(P)H Autofluorescence. ChemPhysChem *5*, 1141–1149.

Nimmerjahn, A., Kirchhoff, F., and Helmchen, F. (2005). Resting microglial cells are highly dynamic surveillants of brain parenchyma in vivo. Science *308*, 1314–1318.

O'Connor, D. (2012). Time-correlated single photon counting (Burlington: Elsevier Science).

Ogikubo, S., Nakabayashi, T., Adachi, T., Islam, Md.S., Yoshizawa, T., Kinjo, M., and Ohta, N. (2011). Intracellular pH Sensing Using Autofluorescence Lifetime Microscopy. J. Phys. Chem. B *115*, 10385–10390.

Orihuela, R., McPherson, C.A., and Harry, G.J. (2016). Microglial M1/M2 polarization and metabolic states. Br J Pharmacol *173*, 649–665.

Papour, A., Taylor, Z.D., Sherman, A.J., Sanchez, D., Lucey, G., Liau, L., Stafsudd, O.M., Yong, W.H., and Grundfest, W.S. (2013). Optical imaging for brain tissue characterization using relative fluorescence lifetime imaging. JBO, JBOPFO *18*, 060504.

Pascual, O., Achour, S.B., Rostaing, P., Triller, A., and Bessis, A. (2012). Microglia activation triggers astrocyte-mediated modulation of excitatory neurotransmission. PNAS *109*, E197–E205.

Pate, K.T., Stringari, C., Sprowl-Tanio, S., Wang, K., TeSlaa, T., Hoverter, N.P., McQuade, M.M., Garner, C., Digman, M.A., Teitell, M.A., et al. (2014). Wnt signaling directs a metabolic program of glycolysis and angiogenesis in colon cancer. The EMBO Journal *33*, 1454–1473.

Peng, O., and Akers, W.J. (2016). Fluorescence Lifetime Imaging of Cancer In Vivo. Methods Mol. Biol. *1444*, 55–66.

Periasamy, A., Alam, S.R., Svindrych, Z., and Wallrabe, H. (2017). FLIM-FRET image analysis of tryptophan in prostate cancer cells. pp. 1041402-1041402–1041405.

Personick, S.D. Photon Probe—An Optical-Fiber Time-Domain Reflectometer. Bell System Technical Journal *56*, 355–366.

Provenzano, P.P., Eliceiri, K.W., Campbell, J.M., Inman, D.R., White, J.G., and Keely, P.J. (2006). Collagen reorganization at the tumor-stromal interface facilitates local invasion. BMC Medicine *4*, 38.

Provenzano, P.P., Inman, D.R., Eliceiri, K.W., Knittel, J.G., Yan, L., Rueden, C.T., White, J.G., and Keely, P.J. (2008a). Collagen density promotes mammary tumor initiation and progression. BMC Medicine *6*, 11.

Provenzano, P.P., Eliceiri, K.W., and Keely, P.J. (2008b). Multiphoton microscopy and fluorescence lifetime imaging microscopy (FLIM) to monitor metastasis and the tumor microenvironment. Clin Exp Metastasis *26*, 357–370.

Qiu, W.Q., Walsh, D.M., Ye, Z., Vekrellis, K., Zhang, J., Podlisny, M.B., Rosner, M.R., Safavi, A., Hersh, L.B., and Selkoe, D.J. (1998). Insulin-degrading Enzyme Regulates Extracellular Levels of Amyloid β-Protein by Degradation. J. Biol. Chem. *273*, 32730–32738.

Raivich, G., Bohatschek, M., Kloss, C.U., Werner, A., Jones, L.L., and Kreutzberg, G.W. (1999a). Neuroglial activation repertoire in the injured brain: graded response, molecular mechanisms and cues to physiological function. Brain Res. Brain Res. Rev. *30*, 77–105.

Raivich, G., Bohatschek, M., Kloss, C.U., Werner, A., Jones, L.L., and Kreutzberg, G.W. (1999b). Neuroglial activation repertoire in the injured brain: graded response, molecular mechanisms and cues to physiological function. Brain Res. Brain Res. Rev. *30*, 77–105.

Ranjit, S., Dobrinskikh, E., Montford, J., Dvornikov, A., Lehman, A., Orlicky, D.J., Nemenoff, R., Gratton, E., Levi, M., and Furgeson, S. (2016). Label-free fluorescence lifetime and second harmonic generation imaging microscopy improves quantification of experimental renal fibrosis. Kidney International *90*, 1123–1128.

Ranjit, S., Dvornikov, A., Dobrinskikh, E., Wang, X., Luo, Y., Levi, M., and Gratton, E. (2017). Measuring the effect of Western diet on liver tissue architecture by FLIM autofluorescence and harmonic generation microscopy: erratum. Biomedical Optics Express *8*, 3501.

Ransohoff, R.M., and Perry, V.H. (2009). Microglial physiology: unique stimuli, specialized responses. Annu. Rev. Immunol. *27*, 119–145.

Rehman, S., O'Melia, M.J., Wallrabe, H., Svindrych, Z., Chandra, D., and Periasamy, A. (2016). Investigation of prostate cancer cells using NADH and Tryptophan as biomarker: multiphoton FLIM-FRET microscopy. In Multiphoton Microscopy in the Biomedical Sciences XVI, (International Society for Optics and Photonics), p. 97120Q.

Rizzo, M.A., and Piston, D.W. (2005). High-Contrast Imaging of Fluorescent Protein FRET by Fluorescence Polarization Microscopy. Biophysical Journal *88*, L14–L16.

Roberts, M.S., Dancik, Y., Prow, T.W., Thorling, C.A., Lin, L.L., Grice, J.E., Robertson, T.A., König, K., and Becker, W. (2011). Non-invasive imaging of skin physiology and percutaneous penetration using fluorescence spectral and lifetime imaging with multiphoton and confocal microscopy. European Journal of Pharmaceutics and Biopharmaceutics *77*, 469–488.

Roggendorf, W., Strupp, S., and Paulus, W. (1996). Distribution and characterization of microglia/macrophages in human brain tumors. Acta Neuropathol *92*, 288–293.

Rupsa Datta (2016). Label-free fluorescence lifetime imaging microscopy (FLIM) to study metabolism and oxidative stress in biological systems. Ph.D. University of California, Irvine.

Russell, J.T. (2011). Imaging calcium signals in vivo: a powerful tool in physiology and pharmacology. Br J Pharmacol *163*, 1605–1625.

Sanchez, T., Wang, T., Pedro, M.V., Zhang, M., Esencan, E., Sakkas, D., Needleman, D., and Seli, E. (2018). Metabolic imaging with the use of fluorescence lifetime imaging microscopy (FLIM) accurately detects mitochondrial dysfunction in mouse oocytes. Fertil. Steril. *110*, 1387–1397.

Sarkar, A., Barui, A., Ghosh, B., Mukherjee, A., Sarkar, R., Sengupta, S., and Chatterjee, J. (2016). Autofluorescence signatures for classifying lung cells during epithelial mesenchymal transition. RSC Advances *6*, 77953–77962.

Schaefer, P.M., Kalinina, S., Rueck, A., Arnim, C.A.F. von, and Einem, B. von (2019). NADH Autofluorescence—A Marker on its Way to Boost Bioenergetic Research. Cytometry Part A *95*, 34–46.

Schartner, J.M., Hagar, A.R., Van Handel, M., Zhang, L., Nadkarni, N., and Badie, B. (2005). Impaired capacity for upregulation of MHC class II in tumor-associated microglia. Glia *51*, 279–285.

Schlachter, S., Elder, A.D., Esposito, A., Kaminski, G.S., Frank, J.H., Geest, L.K. van, and Kaminski, C.F. (2009). mhFLIM: Resolution of heterogeneous fluorescence decays in widefield lifetime microscopy. Opt. Express, OE *17*, 1557–1570.

Scott, T.G., Spencer, R.D., Leonard, N.J., and Weber, G. (1970). Synthetic spectroscopic models related to coenzymes and base pairs. V. Emission properties of NADH. Studies of fluorescence lifetimes and quantum efficiencies of NADH, AcPyADH, [reduced acetylpyridineadenine dinucleotide] and simplified synthetic models. J. Am. Chem. Soc. *92*, 687–695.

Sedgwick, J.D., Schwender, S., Imrich, H., Dörries, R., Butcher, G.W., and ter Meulen, V. (1991). Isolation and direct characterization of resident microglial cells from the normal and inflamed central nervous system. Proc. Natl. Acad. Sci. U.S.A. *88*, 7438–7442.

Seidenari, S., Arginelli, F., Dunsby, C., French, P., König, K., Magnoni, C., Manfredini, M., Talbot, C., and Ponti, G. (2012). Multiphoton laser tomography and fluorescence lifetime imaging of basal cell carcinoma: morphologic features for non-invasive diagnostics. Experimental Dermatology *21*, 831–836.

Shrestha, S., Applegate, B.E., Park, J., Xiao, X., Pande, P., and Jo, J.A. (2010). High-speed multispectral fluorescence lifetime imaging implementation for in vivo applications. Opt Lett *35*, 2558–2560.

Skala, M. (2015). Nonlinear Microscopy and Population Density Modeling of Tumor Cell Metabolism. In Novel Techniques in Microscopy, (Optical Society of America), pp. NT4C–2.

Skala, M.C., Squirrell, J.M., Vrotsos, K.M., Eickhoff, J.C., Gendron-Fitzpatrick, A., Eliceiri, K.W., and Ramanujam, N. (2005). Multiphoton Microscopy of Endogenous Fluorescence Differentiates Normal, Precancerous, and Cancerous Squamous Epithelial Tissues. Cancer Res *65*, 1180–1186.

Skala, M.C., Riching, K.M., Bird, D.K., Gendron-Fitzpatrick, A., Eickhoff, J., Eliceiri, K.W., Keely, P.J., and Ramanujam, N. (2007). In vivo multiphoton fluorescence lifetime imaging of protein-bound and free nicotinamide adenine dinucleotide in normal and precancerous epithelia. JBO, JBOPFO *12*, 024014.

Smith, J.A., Das, A., Ray, S.K., and Banik, N.L. (2012). Role of pro-inflammatory cytokines released from microglia in neurodegenerative diseases. Brain Res. Bull. *87*, 10–20.

Specht, E.A., Braselmann, E., and Palmer, A.E. (2017). A Critical and Comparative Review of Fluorescent Tools for Live-Cell Imaging. Annu. Rev. Physiol. *79*, 93–117.

Spencer, R.D., and Weber, G. (1969). Measurements of Subnanosecond Fluorescence Lifetimes with a Cross-Correlation Phase Fluorometer*. Annals of the New York Academy of Sciences *158*, 361–376.

Squier, J.A., Müller, M., Brakenhoff, G.J., and Wilson, K.R. (1998). Third harmonic generation microscopy. Opt. Express, OE *3*, 315–324.

Squirrell, J.M., Fong, J.J., Ariza, C.A., Mael, A., Meyer, K., Shevde, N.K., Roopra, A., Lyons, G.E., Kamp, T.J., Eliceiri, K.W., et al. (2012). Endogenous fluorescence signatures in living pluripotent stem cells change with loss of potency. PloS One *7*, e43708.

Stoller, P., Celliers, P.M., Reiser, K.M., and Rubenchik, A.M. (2003). Quantitative second-harmonic generation microscopy in collagen. Appl. Opt., AO *42*, 5209–5219.

Streit, W.J., and Sparks, D.L. (1997). Activation of microglia in the brains of humans with heart disease and hypercholesterolemic rabbits. J. Mol. Med. *75*, 130–138.

Stringari, C., Edwards, R.A., Pate, K.T., Waterman, M.L., Donovan, P.J., and Gratton, E. (2012a). Metabolic trajectory of cellular differentiation in small intestine by Phasor Fluorescence Lifetime Microscopy of NADH. Scientific Reports *2*, srep00568.

Stringari, C., Sierra, R., Donovan, P.J., and Gratton, E. (2012b). Label-free separation of human embryonic stem cells and their differentiating progenies by phasor fluorescence lifetime microscopy. JBO, JBOPFO *17*, 046012.

Suhling, K., Siegel, J., Lanigan, P.M.P., Lévêque-Fort, S., Webb, S.E.D., Phillips, D., Davis, D.M., and French, P.M.W. (2004). Time-resolved fluorescence anisotropy imaging applied to live cells. Opt. Lett., OL *29*, 584–586.

Suhling, K., French, P.M.W., and Phillips, D. (2005). Time-resolved fluorescence microscopy. Photochem. Photobiol. Sci. *4*, 13–22.

Suhling, K., Hirvonen, L.M., Levitt, J.A., Chung, P.-H., Tregidgo, C., Le Marois, A., Rusakov, D.A., Zheng, K., Ameer-Beg, S., Poland, S., et al. (2015). Fluorescence lifetime imaging (FLIM): Basic concepts and some recent developments. Medical Photonics *27*, 3–40.

Sun, Y., Liu, R., Elson, D.S., Hollars, C.W., Jo, J.A., Park, J., Sun, Y., and Marcu, L. (2008). Simultaneous time- and wavelength-resolved fluorescence spectroscopy for near real-time tissue diagnosis. Opt. Lett., OL *33*, 630–632.

Sun, Y., Phipps, J., Elson, D.S., Stoy, H., Tinling, S., Meier, J., Poirier, B., Chuang, F.S., Farwell, D.G., and Marcu, L. (2009). Fluorescence lifetime imaging microscopy: in vivo application to diagnosis of oral carcinoma. Opt Lett *34*, 2081–2083.

Szaszák, M., Steven, P., Shima, K., Orzekowsky-Schröder, R., Hüttmann, G., König, I.R., Solbach, W., and Rupp, J. (2011). Fluorescence Lifetime Imaging Unravels C. trachomatis Metabolism and Its Crosstalk with the Host Cell. PLOS Pathogens *7*, e1002108.

Szulczewski, J.M., Inman, D.R., Entenberg, D., Ponik, S.M., Aguirre-Ghiso, J., Castracane, J., Condeelis, J., Eliceiri, K.W., and Keely, P.J. (2016). *In Vivo* Visualization of Stromal Macrophages via label-free FLIM-based metabolite imaging. Scientific Reports *6*, srep25086.

Tadrous, P.J., Siegel, J., French, P.M.W., Shousha, S., Lalani, E.-N., and Stamp, G.W.H. (2003). Fluorescence lifetime imaging of unstained tissues: early results in human breast cancer. J. Pathol. *199*, 309–317.

Tamborini, D., Markovic, B., Tisa, S., Villa, F.A., and Tosi, A. (2013). TDC with 1.5% DNL based on a single-stage vernier delay-loop fine interpolation. In 2013 IEEE Nordic-Mediterranean Workshop on Time-to-Digital Converters (NoMe TDC), pp. 1–6.

Tambuyzer, B.R., Ponsaerts, P., and Nouwen, E.J. (2009). Microglia: gatekeepers of central nervous system immunology. Journal of Leukocyte Biology *85*, 352–370.

Tejwani, V., Schmitt, F.-J., Wilkening, S., Zebger, I., Horch, M., Lenz, O., and Friedrich, T. (2017). Investigation of the NADH/NAD+ ratio in Ralstonia eutropha using the fluorescence reporter protein Peredox. Biochimica et Biophysica Acta (BBA) - Bioenergetics *1858*, 86–94.

Thorn, K. (2017). Genetically encoded fluorescent tags. Mol Biol Cell *28*, 848–857.

Trinh, A.L., Chen, H., Chen, Y., Hu, Y., Li, Z., Siegel, E.R., Linskey, M.E., Wang, P.H., Digman, M.A., and Zhou, Y.-H. (2017). Tracking Functional Tumor Cell Subpopulations of Malignant Glioma by Phasor Fluorescence Lifetime Imaging Microscopy of NADH. Cancers *9*, 168.

Vivian, J.T., and Callis, P.R. (2001). Mechanisms of Tryptophan Fluorescence Shifts in Proteins. Biophysical Journal *80*, 2093–2109.

Wagner, S., Czub, S., Greif, M., Vince, G.H., Süss, N., Kerkau, S., Rieckmann, P., Roggendorf, W., Roosen, K., and Tonn, J.C. (1999). Microglial/macrophage expression of interleukin 10 in human glioblastomas. Int. J. Cancer *82*, 12–16.

Wagnières, G.A., Star, W.M., and Wilson, B.C. (1998). In vivo fluorescence spectroscopy and imaging for oncological applications. Photochem. Photobiol. *68*, 603–632.

Wahl, M. (2014). Modern TCSPC Electronics: Principles and Acquisition Modes. In Advanced Photon Counting, P. Kapusta, M. Wahl, and R. Erdmann, eds. (Springer International Publishing), pp. 1–21.

Wahl, M., Röhlicke, T., Rahn, H.-J., Erdmann, R., Kell, G., Ahlrichs, A., Kernbach, M., Schell, A.W., and Benson, O. (2013). Integrated multichannel photon timing instrument with very short dead time and high throughput. Rev Sci Instrum *84*, 043102.

Walsh, A.J., Cook, R.S., Manning, H.C., Hicks, D.J., Lafontant, A., Arteaga, C.L., and Skala, M.C. (2013). Optical metabolic imaging identifies glycolytic levels, subtypes, and early-treatment response in breast cancer. Cancer Res. *73*, 6164–6174.

Walsh, A.J., Cook, R.S., Sanders, M.E., Aurisicchio, L., Ciliberto, G., Arteaga, C.L., and Skala, M.C. (2014). Quantitative optical imaging of primary tumor organoid metabolism predicts drug response in breast cancer. Cancer Res *74*, 5184–5194.

Wang, S.-C. (2003). Artificial Neural Network. In Interdisciplinary Computing in Java Programming, S.-C. Wang, ed. (Boston, MA: Springer US), pp. 81–100.

Wang, B.-G., König, K., and Halbhuber, K.-J. (2010). Two-photon microscopy of deep intravital tissues and its merits in clinical research. Journal of Microscopy *238*, 1–20.

Wang, S., Wang, S., Chacko, J.V., Sagar, A.K., Eliceiri, K.W., Eliceiri, K.W., Yuan, M., and Yuan, M. (2019). Nonparametric empirical Bayesian framework for fluorescence-lifetime imaging microscopy. Biomed. Opt. Express, BOE *10*, 5497–5517.

Wang, X.F., Periasamy, A., Herman, B., and Coleman, D.M. (1992). Fluorescence Lifetime Imaging Microscopy (FLIM): Instrumentation and Applications. Critical Reviews in Analytical Chemistry *23*, 369–395.

Wang, Y., Wang, Q., Haldar, J.P., Yeh, F.-C., Xie, M., Sun, P., Tu, T.-W., Trinkaus, K., Klein, R.S., Cross, A.H., et al. (2011). Quantification of increased cellularity during inflammatory demyelination. Brain *134*, 3590–3601.

Watters, J.J., Schartner, J.M., and Badie, B. (2005). Microglia function in brain tumors. Journal of Neuroscience Research *81*, 447–455.

Welf, E.S., Driscoll, M.K., Dean, K.M., Schäfer, C., Chu, J., Davidson, M.W., Lin, M.Z., Danuser, G., and Fiolka, R. (2016). Quantitative Multiscale Cell Imaging in Controlled 3D Microenvironments. Dev Cell *36*, 462–475.

Wiart, M., Davoust, N., Pialat, J.-B., Desestret, V., Moucharrafie, S., Moucharaffie, S., Cho, T.-H., Mutin, M., Langlois, J.-B., Beuf, O., et al. (2007). MRI monitoring of neuroinflammation in mouse focal ischemia. Stroke *38*, 131–137.

Wolf, Y., Yona, S., Kim, K.-W., and Jung, S. (2013). Microglia, seen from the CX3CR1 angle. Front Cell Neurosci *7*, 26.

Wu, S.-Y., and Watabe, K. (2017). The roles of microglia/macrophages in tumor progression of brain cancer and metastatic disease. Front Biosci (Landmark Ed) *22*, 1805–1829.

Yamada, M., Lin, L.L., and Prow, T.W. (2014). Chapter 13 - Multiphoton Microscopy Applications in Biology. In Fluorescence Microscopy, A. Cornea, and P.M. Conn, eds. (Boston: Academic Press), pp. 185–197.

Yan, L., Rueden, C.T., White, J.G., and Eliceiri, K.W. (2006). Applications of combined spectral lifetime microscopy for biology. Biotechniques *41*, 249.

Yaseen, M.A., Sakadžić, S., Wu, W., Becker, W., Kasischke, K.A., and Boas, D.A. (2013a). In vivo imaging of cerebral energy metabolism with two-photon fluorescence lifetime microscopy of NADH. Biomedical Optics Express *4*, 307.

Yaseen, M.A., Sakadžić, S., Wu, W., Becker, W., Kasischke, K.A., and Boas, D.A. (2013b). In vivo imaging of cerebral energy metabolism with two-photon fluorescence lifetime microscopy of NADH. Biomed Opt Express *4*, 307–321.

Yelin, D., and Silberberg, Y. (1999). Laser scanning third-harmonic-generation microscopy in biology. Opt. Express, OE *5*, 169–175.

Yona, S., Kim, K.-W., Wolf, Y., Mildner, A., Varol, D., Breker, M., Strauss-Ayali, D., Viukov, S., Guilliams, M., Misharin, A., et al. (2013). Fate mapping reveals origins and dynamics of monocytes and tissue macrophages under homeostasis. Immunity *38*, 79–91.

Zheng, Y., Yang, H., Wang, H., Kang, K., Zhang, W., Ma, G., and Du, S. (2019). Fluorescence-guided surgery in cancer treatment: current status and future perspectives. Ann Transl Med *7*.

Zimmermann, T., Rietdorf, J., and Pepperkok, R. (2003). Spectral imaging and its applications in live cell microscopy. FEBS Letters *546*, 87–92.

Zipfel, W.R., Williams, R.M., Christie, R., Nikitin, A.Y., Hyman, B.T., and Webb, W.W. (2003). Live tissue intrinsic emission microscopy using multiphoton-excited native fluorescence and second harmonic generation. Proc. Natl. Acad. Sci. U.S.A. *100*, 7075–7080.

Zoumi, A., Yeh, A., and Tromberg, B.J. (2002). Imaging cells and extracellular matrix in vivo by using second-harmonic generation and two-photon excited fluorescence. PNAS *99*, 11014–11019.

(2006). Principles of Fluorescence Spectroscopy (Boston, MA: Springer US).

(2014). Quantitative Imaging in Cell Biology (Academic Press).

(2015). Advanced Time-Correlated Single Photon Counting Applications (Cham: Springer International Publishing).

Chapter 2

Microglia activation visualization via NADH FLIM

Adapted from "Microglia activation visualization via Fluorescence lifetime Imaging microscopy of intrinsically fluorescent metabolic cofactors" Md Abdul Kader Sagar, Jonathan N Ouellette, Kevin P Cheng, Justin C Williams, Jyoti J Watters, Kevin W Eliceiri, Neurophotonics

Summary. A major obstacle to studying resident microglia has been their similarity to infiltrating immune cell types and the lack of unique protein markers for identifying functional state. Given the role of microglia in all neural diseases and insults, accurate tools for detecting microglial function beyond morphologic alterations are necessary. Here, we investigate the use of the label-free method of Fluorescence Lifetime Imaging Microscopy (FLIM)-based detection of the endogenous metabolic cofactor nicotinamide adenine dinucleotide (NADH) to identify microglia and characterize their activation status. We hypothesized that microglia would have unique metabolic fluxes in NADH that would be detectable by relative change in FLIM parameters, allowing for identification of their activation status. To test whether microglial activation would also confer a unique NADH lifetime signature, murine primary microglial cultures and adult mice were treated with lipopolysaccharide (LPS). We found that there is LPS dose dependent change with reactive microglia lifetime alteration which is also replicated with LPS treatment-time variation. Together, these data indicate that NADH FLIM microscopy can be used as a method to identify microglia and characterize their activation state, both *in vitro* and *ex vivo*.

Keywords: microglia, activation, lipopolysaccharide, non-invasive, NADH, FLIM

1 Introduction

Microglia have prominent roles both in CNS injury/disease responses, as well as in protection of the central nervous system (CNS)[1–4]. Major obstacles in studying microglia have been the lack of specific protein markers that indicate their activation status in the absence of concomitant morphological changes and the difficulty in distinguishing them from related infiltrating myeloid cells. Microglial activation can be characterized in many different ways,

but currently there is no single parameter that can uniquely characterize their activation [5] likely because the process of activation is gradual and involves many intermediate states on the spectrum between surveillance and activation [6]. While proteins such as ionized calcium binding protein 1 (Iba1), the integrin receptor CD11b, the purinergic receptor P2Y12 and the fractalkine receptor CX3CR1 are uniquely expressed in microglia in the healthy CNS [7,8], they are also expressed in macrophages, preventing accurate distinction between resident microglia and infiltrating peripheral cells. The current primary method of observing microglial activation depends on antibody staining to assess morphology and marker expression. For example, $CD68^{high}$ immunoreactivity detects both activated microglia and macrophages. While the combination of $CD11b^{+}$ and $CD45^{low}$ staining is widely used to distinguish microglia from macrophages, it cannot distinguish between activated microglia and macrophages. More recently, other proteins like the orphan receptor TMEM119[9] and the lysosomal hexosaminidase enzyme B (HexB)[10] have been identified by transcriptomic analyses as unique to microglia, and not expressed in macrophages [11–14], but these cannot distinguish activation states either. Thus, a method allowing for a clear distinction in microglial activation states would be indispensable for identifying initiators of and/or contributors to CNS dysfunction in different disease etiologies. To study microglial activity *ex vivo,* methods such as immunomagnetic separation can efficiently isolate microglia without altering their functional state.[15] However, a method that does not require isolation from the rest of the CNS environment that can enable analysis of microglial activation status in intact tissue or whole brain would be more powerful. Recently, novel morphology-based image analysis techniques have been developed to characterize microglial activation based on the ratio of cell body to cell size[16], or morphological categorization based on Hierarchical Cluster and Principal Components Analysis[17]. Other studies have tried to characterize microglial activation using statistical changes in soma size and roundness [18].

To address the limitations of current antibody-based microglial characterization techniques, we hypothesized that Fluorescence Lifetime Imaging Microscopy (FLIM) based monitoring of microglial metabolic alterations could be used to both differentiate surveillant microglia from activated microglia, as well as distinguish them from other CNS cell-types. Fluorescence lifetime is the measure of the average time a molecule remains in its excited state before returning to its ground state; a photon is emitted upon the return to ground state. FLIM measures the lifetime of each individual photon and creates a pixel contrast map based on the calculated exponential decay of each pixel[19]. Importantly, fluorescence lifetime does not depend on concentration, absorption, excitation intensity or sample thickness, and is therefore, more robust than fluorescence intensity-based methods[20–22]. Multiple physiologic parameters can change fluorescence lifetime including the local pH, ion and oxygen concentrations, making FLIM an ideal method with which to image the cellular microenvironment. FLIM monitors metabolism by taking advantage of the intrinsic fluorescence of the ubiquitous metabolic coenzyme NADH (Nicotinamide Adenine Dinucleotide) and flavin adenine dinucleotide (FAD). The fluorescence lifetime of protein-bound NADH changes depending on the enzyme to which it is bound[23]. Recent evidence suggests that immune cells can switch from oxidative phosphorylation to aerobic glycolysis during inflammatory activation; much like the Warburg effect observed in tumor cells[24–28].

Given the known metabolic changes that take place during microglial activation[29] and the ability of FLIM to image free- and enzyme-bound NADH, we hypothesized that NADH lifetime and the fractional contribution of free NADH could be used to first distinguish microglia from other glial cell types, and then identify microglial activation status in the absence of additional fluorophore tagging. Previous efforts have exploited FLIM to examine the metabolic state of the cellular microenvironment and develop label-free signatures for different cell types ranging from bacteria to stem cells[30,31]. A novel strategy reported by our

group[32] used FLIM as a means to non-invasively identify mammary tumor-associated macrophages in live mouse models. Another study[33] also exploited the metabolic shift in macrophages to identify their phenotype label-free in cell culture[33].

Here, we show that a new FLIM-based technique can be used to observe metabolic changes in microglial cells using NADH-based FLIM signatures. We demonstrate the capability of FLIM to differentiate between surveillant and activated states of microglia both in primary mixed glial cultures and in tissue slices from adult mice treated with LPS. First, we tested different doses of LPS to examine changes in microglial FLIM signatures, then we tested the effect of different treatment times of a single LPS dose. We found that FLIM can be readily used to discriminate the activation status of microglia in tissue by quantifying NADH lifetime.

2 Materials and methods

2.1 Animals

All animals were maintained in an AAALAC-accredited animal facility with a 12 hr light/dark cycle regime and access to food and water ad libitum. All experiments were performed in accordance with protocols approved by the University of Wisconsin-Madison Institutional Animal Care and Use Committee and with the Guide to Care and Use of Laboratory Animals.

For FLIM imaging, 100µm thick coronal slices were prepared from the fixed brains of 8 week-old, young adult C57BL/6J (WT) mice (Jackson Labs, Bar Harbor, ME), N=5 each. Mice were either given no treatment (control) or 5mg/kg lipopolysaccharide (LPS, i.p. from *E. coli* O111:B4, Sigma) dissolved in sterile Hank's balanced salt solution (HBSS). 3 hrs after LPS injection, animals were euthanized by isoflurane overdose and transcardially perfused with ice-cold PBS, followed by a second perfusion with an ice-cold solution of 4% paraformaldehyde

(PFA) in phosphate-buffered saline (PBS). Brains were dissected, post fixed for 24 hrs in a solution of 4% PFA in PBS, and then moved to HBSS (all performed at 4°C and protected from light).

2.2 Preparation of primary neonatal mixed glial cultures

Mixed primary glial cultures were prepared from 3-7 day old, CX3CR1-GFP mouse pups as previously described [34]. Briefly, brains were dissected immediately after decapitation, and the brain stem, cerebellum, olfactory bulbs, meninges, and visible blood vessels were removed. The remaining tissue was finely minced, thoroughly triturated with a serological pipette in 0.25% trypsin–ethylenediaminetetraacetic acid (EDTA) containing 0.1mg/ml deoxyribonuclease I, and then incubated at 37°C for 20 mins. The reaction was immediately stopped by the addition of an equal volume of heat-inactivated horse serum. Dissociated cells were resuspended in Dulbecco's modified Eagle's medium (DMEM) supplemented with 10% fetal bovine serum (FBS) and 100 units/ml penicillin/streptomycin. Brains were processed individually for each pup, and the resulting cell suspension was divided equally and plated in 35mm dishes (1 brain per 4-6 dishes). The plated cells were cultured for 7-14 days in a 37°C incubator supplemented with 5% CO2; the culture medium was replaced every 3-4 days.

2.3 Cell culture treatments

Mixed CX3CR1-GFP glial cultures were treated with HBSS (vehicle), 1ng/ml, 10ng/ml, or 100ng/ml of LPS for 3, 8 or 24 hours as indicated in the figure legends (N=5 independent biological replicates each treatment. LPS is a ligand of the pattern recognition receptor TLR4 that mimics bacterial infection and activates inflammatory signaling pathways in microglia that lead to the production and release of inflammatory cytokines including IL-1β and TNFα. Preliminary experiments demonstrated no significant difference in mean NADH lifetimes in HBSS-treated cells between 3 and 24 hrs (data not shown). Following treatment, the culture

medium was aspirated, and the cells were washed with cold HBSS before fixing with 4% PFA for 5 mins, after which time the cells were washed again with cold HBSS and stored at 4°C protected from light.

2.4 Immunohistochemistry

100 µm thick coronal sections were prepared from the midbrain region of WT mouse brains (N=5 for each treatment group) using a Leica vibratome. Two slices from each animal were used for immunohistochemical staining. Briefly, slices were washed at room temperature with 0.3% TritonX-100 in PBS, before incubating in blocking buffer (1% bovine serum albumin (BSA), 0.3% TritonX-100/PBS) for 2 hrs at room temperature. To identify microglia, tissue slices were incubated with anti-Iba1 antibodies (1:1000; Wako Catalog No. 019-19741) in blocking buffer in the dark at 4°C overnight. Slices were washed again at room temperature with 0.3% TritonX-100 in PBS followed by incubation in the dark for 2 hrs with AlexaFlour594 anti-rabbit IgG antibodies (1:200; Thermo Fisher Scientific, Waltham, MA) in blocking buffer, at room temperature. Slices were washed with 0.3% TritonX-100 in PBS and mounted on 1mm slides using Cytoseal 60 (Richard-Allan Scientific, Kalamazoo, MI) mounting medium. Mounted sections were stored at room temperature, protected from light until imaging.

2.5 Multiphoton lifetime imaging

Multiphoton lifetime [35] and intensity imaging were performed on a custom multiphoton laser scanning system built around an inverted Nikon Eclipse TE2000U at the UW-Madison Laboratory for Optical and Computational Instrumentation [36]. A 20x air objective (Nikon Plan Apo VC, 0.75 NA) (Melville, NY, USA) was used for all imaging. For NADH imaging, data were collected using an excitation wavelength of 740 nm, and emission was filtered with a 457 ± 50 nm bandpass filter (Semrock, Rochester, NY), corresponding to the spectral peak for NADH/NADPH. For GFP intensity imaging, excitation was set at 890 nm and a 520 ± 35 nm

bandpass emission filter was used (Semrock). For AlexaFluor594 imaging excitation was set at 810 nm and a 615/20 bandpass emission filter (Semrock) was used. For FAD imaging, excitation was set at 890nm and a 520/35 bandpass emission filter was used (Semrock). FLIM images were collected at a 256x256 pixel resolution for 120 seconds using SPC-150 Photon Counting Electronics (Becker & Hickl GbmH, Berlin, Germany) and a Hamamatsu H7422P-40 GaAsP photomultiplier tube (Hamamatsu Photonics, Bridgewater, NJ). Urea crystals were used to determine the Instrumentation Response Function (IRF) using a 370/10 bandpass emission filter (Semrock). For each sample, ~20 neighboring field of views (FOVs) consisting of several hundred cells were randomly selected, and the mean signal was calculated based on the masking described in section 2.6 below. The optical system IRF was calibrated for each imaging session. Autofluorescence intensity and fluorescence lifetime data were analyzed in SPCImage (Becker & Hickl GmbH); a Levenberg–Marquardt routine for nonlinear fitting was used to fit the fluorescence decay curve collected for each decay after binning. Data were assessed by the minimized chi-squared value generated during the fit so that the analysis was unbiased. To eliminate background fluorescence, a threshold was applied based on photon counts. The use of a multiphoton laser scanning microscope modality for FLIM offers several advantages over confocal microscopy including deeper sample penetration, improved signal to noise ratios, enhanced sample viability (although all samples in the present studies were fixed), and it is tunable to multiple excitation wavelengths to image NADH, FAD and GFP, A594. Figure 1 shows the experimental set up and image analysis

2.6 Data analysis

The lifetime fitted data from SPCImage, and all other parameters were exported into MATLAB (MathWorks Inc, Natick, MA) for calculating the means of custom regions and performing statistical analyses. The mean lifetimes and free/bound ratios were calculated for each sample. ANOVA, paired sample t-tests were performed to determine the statistical significance in tissue

culture experiments. A student's t-test was performed for determining the significance in the tissue slice experiments from mice treated with LPS. Statistical significance was set at $p<0.05$.

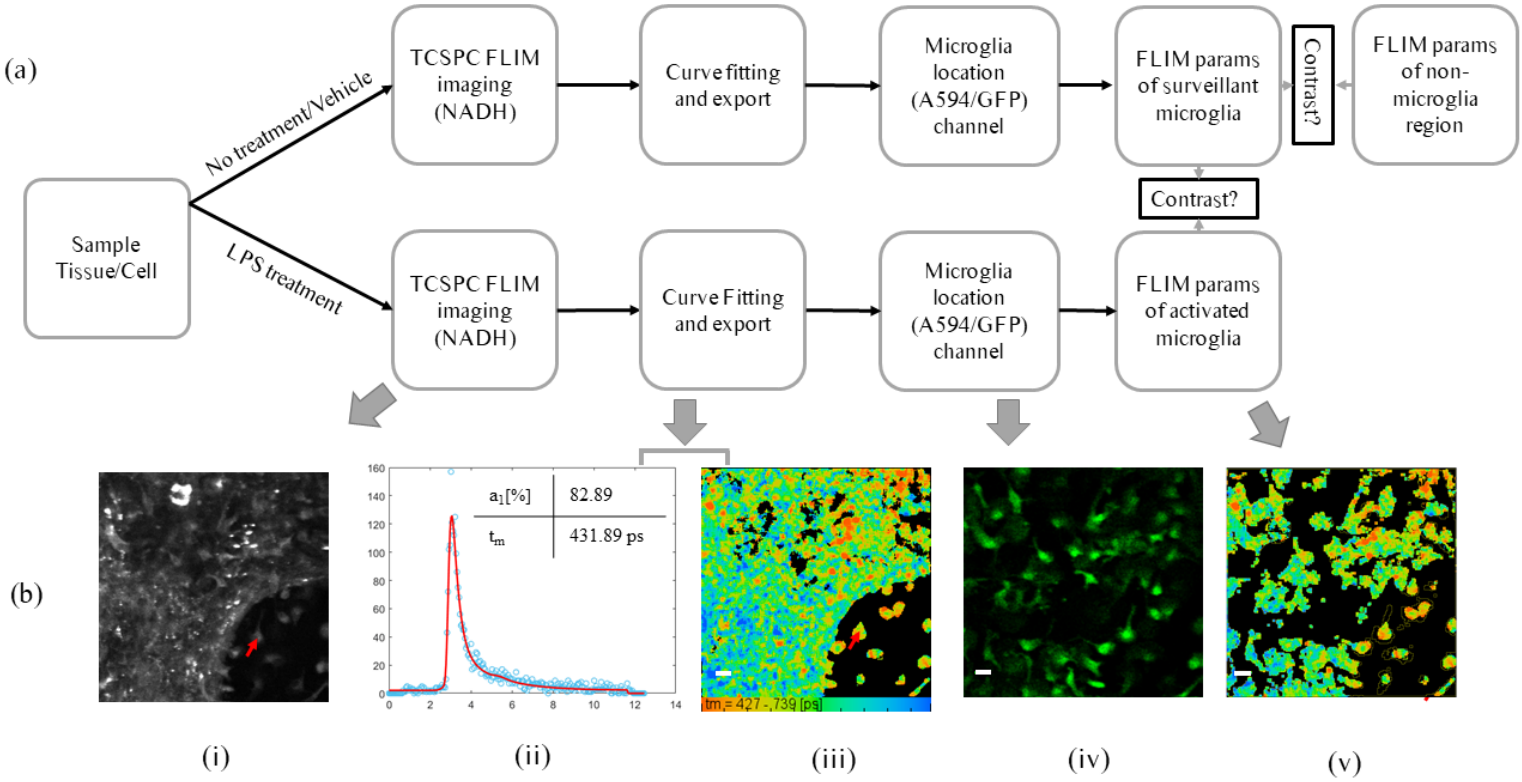

Fig. 1 Methods to image and quantify microglia lifetime upon activation. Top panel (a) shows the steps for the imaging, data processing and final comparison. A fluorescence intensity image was used to identify microglia in mixed glial cultures or brain tissue section. NADH FLIM parameters were extracted from both microglia and non-microglial regions. For activation experiments, only microglial FLIM parameters were compared. The example shown in panel (b) is a use case from a mixed glial culture representing each step outlined in panel (a). An NADH intensity image of a field-of-view (FOV) containing microglia (i) NADH intensity image (ii) The lifetime decay curve of a single microglial pixel marked by the red arrow in (i). The table inset (ii) shows the mean lifetime (t_m) decay from two components (free and bound NADH) and the fractional contribution from free NADH (a1[%]).(iii) The fitted lifetime image for the FOV, and the color bar shows the range of lifetime in ps (iv) The fluorescence (GFP or A594) intensity image was used to identify microglia and calculate average FLIM parameters. (iv). Microglial lifetime image (v). (Scale bar 20 µm).

3 Results

3.1 Microglial NADH fluorescence can distinguish reactive microglia following LPS treatment

According to previous FLIM studies, a lower mean lifetime and a higher fractional contribution implies greater free (and less bound) NADH [37,38]. To study FLIM parameters in activated microglia, we investigated the relative change in NADH FLIM parameters in microglia stimulated with LPS [39–42]. The underlying hypothesis of this experiment was that LPS treatment would initiate an inflammatory response resulting in a change in microglial metabolism, causing alterations in the metabolic co-factor NADH that could be assessed by FLIM. We treated mixed glial cultures with LPS (10ng/mL) for 1 hr. The mean NADH lifetime and fractional contribution of free NADH were compared between the vehicle- and LPS-treated groups. Representative images of microglial NADH lifetime (Fig. 2a, 2b) and the fractional contribution of free NADH (Fig. 2c, 2d) from vehicle- and LPS-treated samples, respectively, show that LPS treatment significantly increased NADH lifetime (vehicle treatment 548.7 ± 19.4 ps and LPS treatment 566.6 ± 28.8 ps) in microglia (Fig. 2e). In contrast, the free NADH fractional contribution (Fig. 2f) was significantly decreased (vehicle treatment 80.3% ± 0.85 and LPS treatment 79.5% ± 1.1). These data suggest that 1 hr of LPS treatment can induce a rapid change in NADH lifetime, indicating that FLIM may be useful to monitor the status of microglial activation prior to a visible change in morphology. To confirm that microglia could still be distinguished from other glia in the context of LPS treatment, the FLIM parameters of microglia and non-microglial cells were compared. Microglial NADH lifetime was significantly lower (566.6 ± 28.8 ps) than non-microglia (603.1 ± 27.4 ps) (Fig. 2g), whereas

the fractional free NADH contribution in microglia was significantly higher (79.5% ±1.1) than non-microglia (76.3% ± 1.5) (Fig. 2h).

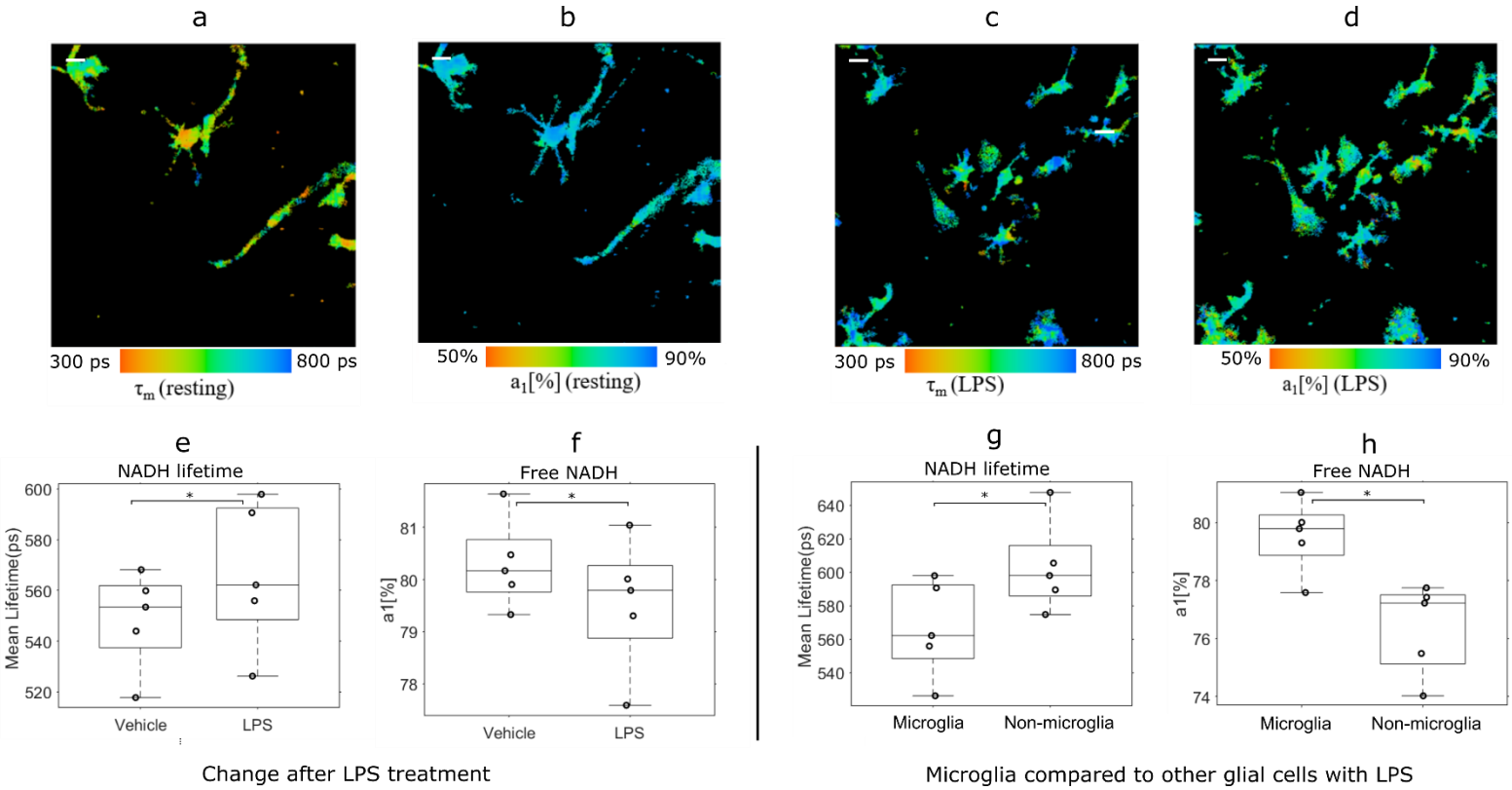

Fig. 2 Relative change in microglia lifetime upon LPS treatment**.** Mixed glial cell cultures were treated with vehicle or LPS (10 ng/mL) for 1 hr. Representative image of NADH lifetime (a) and fractional free NADH (b) from vehicle-treated microglia. Representative image of NADH lifetime (c) and fractional free NADH (d) from LPS-treated microglia. Quantification of NADH lifetime (e) and free NADH levels (f) in vehicle-treated microglia. Quantification of NADH lifetime (g) and free NADH levels (h) in LPS-treated microglia. LPS-stimulated microglia have a significantly higher mean lifetime and a lower free NADH contribution (n=5). Compared to non-microglia, microglia retain their lower lifetimes and higher free NADH levels even when exposed to LPS. T-test *p<0.05. (Scale bar 20 µm).

Additionally, we compared the FLIM parameters of surveillant microglia with other cells in the mixed glial cultures. We looked at 10 different samples consisting of over a thousand cells

from ~20 different FOVs for each sample (Fig. 3). The mean lifetime for microglial cells was 558.8 ± 25.4 picoseconds (ps) and the mean lifetime for non-microglia cells was 594.0 ± 23.3 ps (Fig. 3a) whereas the fractional contribution from free NADH for microglia was 81.1% ± 1.8 and 78.4% ± 1.4 for non-microglia (Fig. 3b). Together, these results indicate that microglia have a significantly lower mean NADH lifetime and a higher free NADH component compared to non-microglial cells.

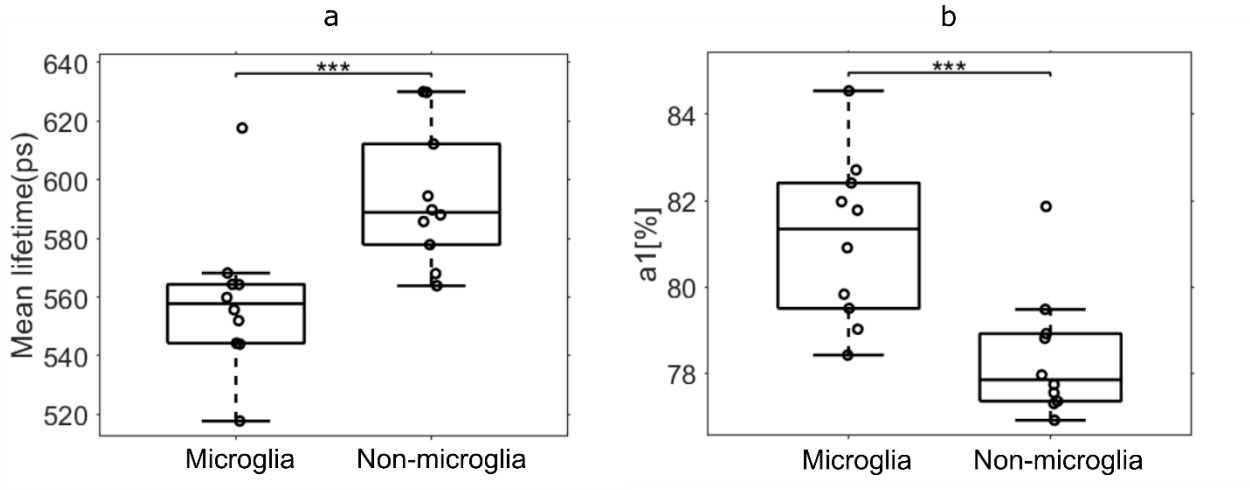

Fig. 3 Comparison of microglia lifetime in mixed glial culture. Microglia have a lower mean NADH lifetime (a), and higher free NADH levels (b) than other cells in mixed glial cultures (n=10). T-test, ***p<0.005.

3.2 FLIM can be used to characterize microglia in brain tissue

After establishing that FLIM parameters can be used to characterize microglia in mixed glial cell cultures, and that FLIM can distinguish activated microglia, we next extended our observations to test whether this trend holds in intact brain tissue. Brain tissue was sectioned for *ex vivo* multiphoton FLIM imaging from WT mice that were either given no treatment, or treated *in vivo* with LPS (5mg/kg) for 3 hrs. The goals of this experiment were twofold: 1) to

investigate whether microglia have a unique lifetime signature in relation to other brain cell types in tissue, 2) to determine if microglial activation causes alterations in FLIM NADH lifetime and free NADH level parameters in tissue. Microglia were labeled with anti-Iba1 antibodies, followed by an AlexaFluor594 secondary antibody. Representative NADH lifetime images of microglia from untreated (Fig. 4a) and LPS-treated (Fig. 4b) mice show a statistically significant reduction in microglial NADH lifetime (751.6 ± 46.58 ps) compared to non-microglial cells (778.6 ± 28.2 ps) in the tissue (Fig. 4c). As we had observed in mixed glial cultures, we found that microglia had a higher mean NADH lifetime (811.8 ± 23.7 ps) in tissue slices from LPS-treated mice compared to microglia from untreated mice (751.6 ± 46.58 ps) (Fig. 4d). We found that LPS treatment increased lifetime from 668.42 ± 34.48 ps to 683.16 ± 41.35 ps. In addition, we observed similar LPS-induced shifts in lifetime values in WT tissue slices stained with Iba1 (not shown) suggesting that GFP expression does not interfere with relative lifetime changes.

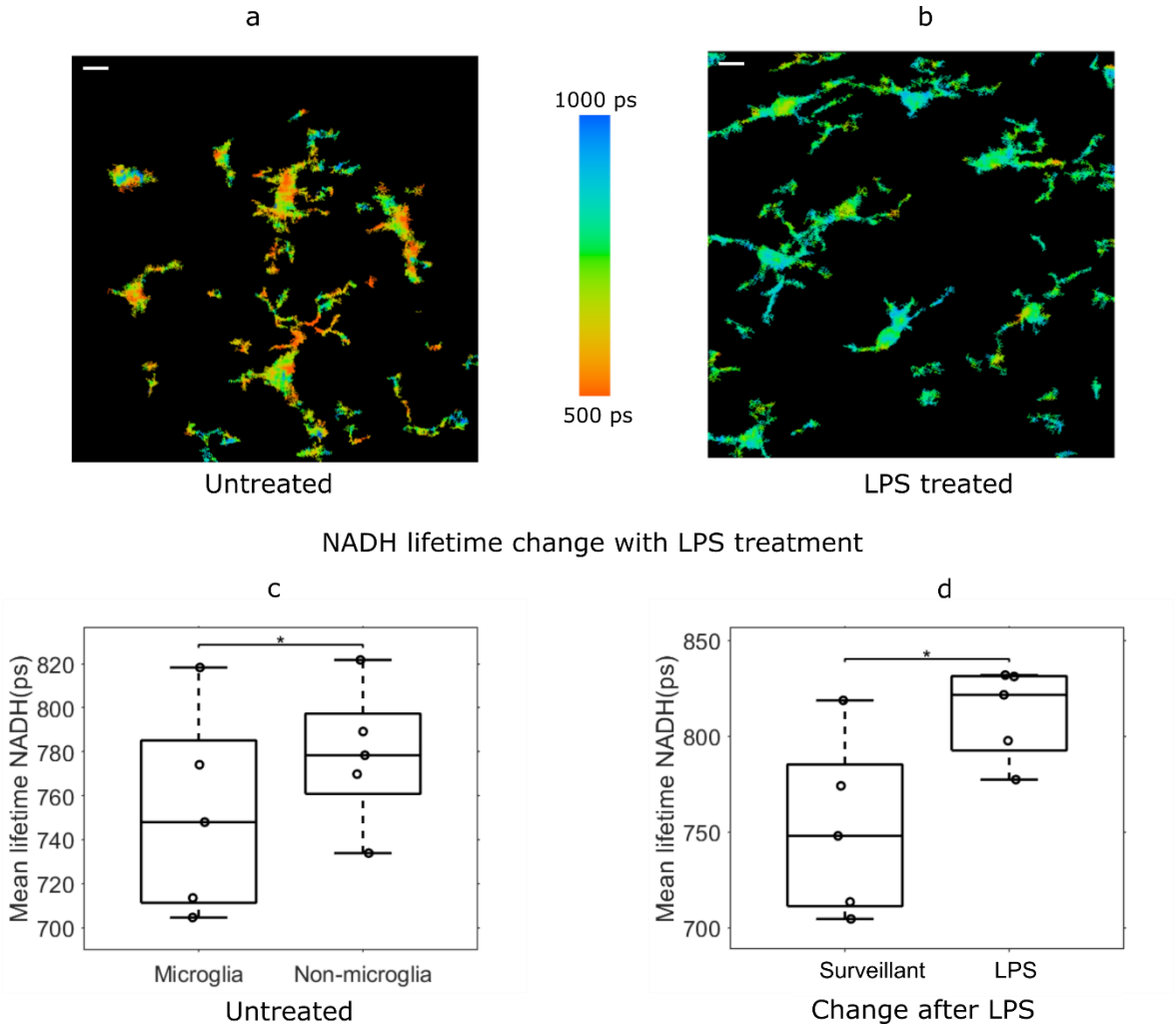

Fig. 4 NADH lifetime can be used to distinguish microglia from non-microglia and characterize microglial activation status in brain tissue. A microglial mask was created using the AlexaFluor594 intensity image from Iba1-labeled brain tissue slices from WT mice that were untreated or treated with LPS (5mg/kg). Representative image of microglial NADH lifetime in tissue slices from vehicle- (a) or LPS-treated (b) mice (n=5). Microglia had a significantly lower NADH lifetime than non-microglial cells in tissues from both vehicle (c) and LPS-treated (d) mice. T-test, $p<0.05$. (Scale bar 10 µm).

3.3 LPS dose-dependently alters NADH lifetime and free NADH ratio

We next sought to determine whether LPS treatment could dose-dependently alter microglial NADH lifetime and free NADH levels. To test this, we treated mixed glial cultures with 1, 10 and 100 ng/mL LPS. We found that NADH lifetimes were indeed dose-dependently increased by LPS treatment (Fig. 5). While the NADH lifetime of cells treated with vehicle (548.4 ± 19.1

ps) did not differ from 1 ng/mL LPS (540.2 ± 34.3 ps), microglial lifetimes in 10ng/mL (568.4 ± 28.5 ps) and 100 ng/mL (578.4 ± 23.5 ps) LPS were significantly increased over control treatment, as expected (Fig. 5a). The fractional NADH contribution in contrast, dose-dependently decreased with increasing LPS concentrations (Fig. 5b). Again, whereas free NADH levels between vehicle (80.3% ± 0.9) and 1 ng/mL LPS (80.2% ± 1.1) did not differ, they were significantly decreased in the 10 ng/mL (79.2% ± 1.2) and 100 ng/mL (79.8% ± 1.1) LPS doses.

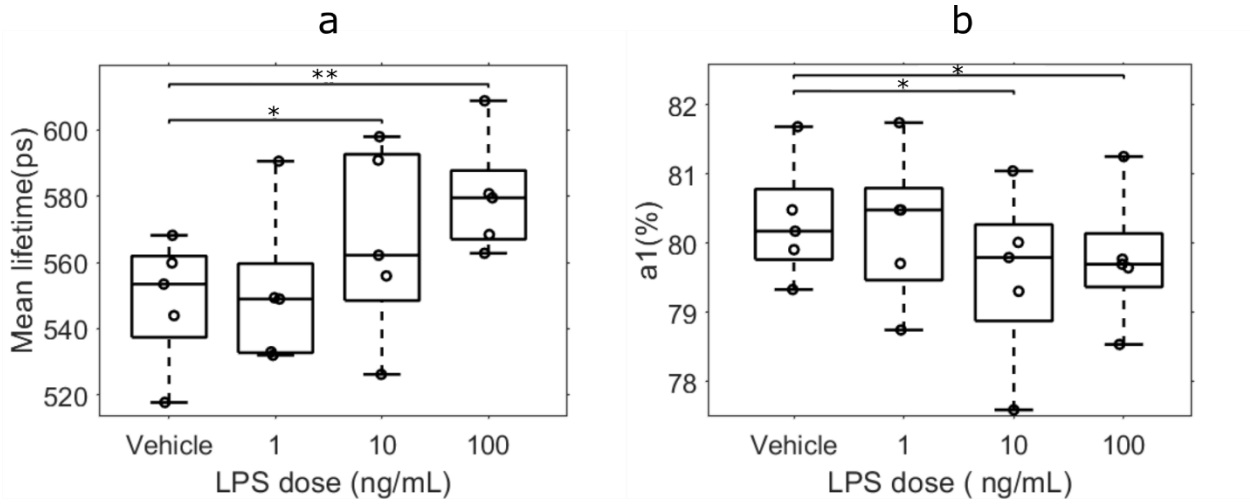

Fig. 5 Microglia FLIM parameters vary with LPS dose. LPS dose-dependently alters NADH lifetime and free NADH ratio. Mixed glial cell cultures from CX3CR1-GFP mice were treated with vehicle, 1ng/mL, 10 ng/mL or 100 ng/mL of LPS for 1 hr. NADH lifetime (a) and free NADH levels (b) were measured in GFP^+ cells. Compared to vehicle treatment, the 10 and 100 ng/mL doses significantly increased NADH lifetime and decreased free NADH levels. One-way ANOVA, *p<0.05, **p<0.01.

3.4 LPS treatment time-dependently increases microglial NADH lifetime

To determine whether the observed differences in FLIM parameters changed with time post-LPS treatment, mixed glial cultures were treated with 10 ng/mL LPS for 3, 8 and 24 hrs. We chose the 10ng/mL dose of LPS because it was the lowest dose tested that had statistically

significant effects on FLIM parameters. Representative images of the mean microglial NADH lifetime (Fig. 6a) and the fractional contribution from free NADH (Fig. 6b) are shown. LPS significantly increased the NADH lifetime of microglia at 3 hrs (599.5 ± 10.2 ps), 8 hrs (616.4 ± 14.7 ps), and 24 hrs (628 ± 8 ps) compared to vehicle-treated cells (570.5 ± 11.3) ps (Fig. 6c). The fractional free NADH components significantly decreased from vehicle treatment (80.9% ± 1.3) at both 8 hrs (79.01% ± 0.4) and 24 hrs (78.7% ± 0.2) but not at 3 hrs (79.5% ± 0.2) (Fig. 6d).

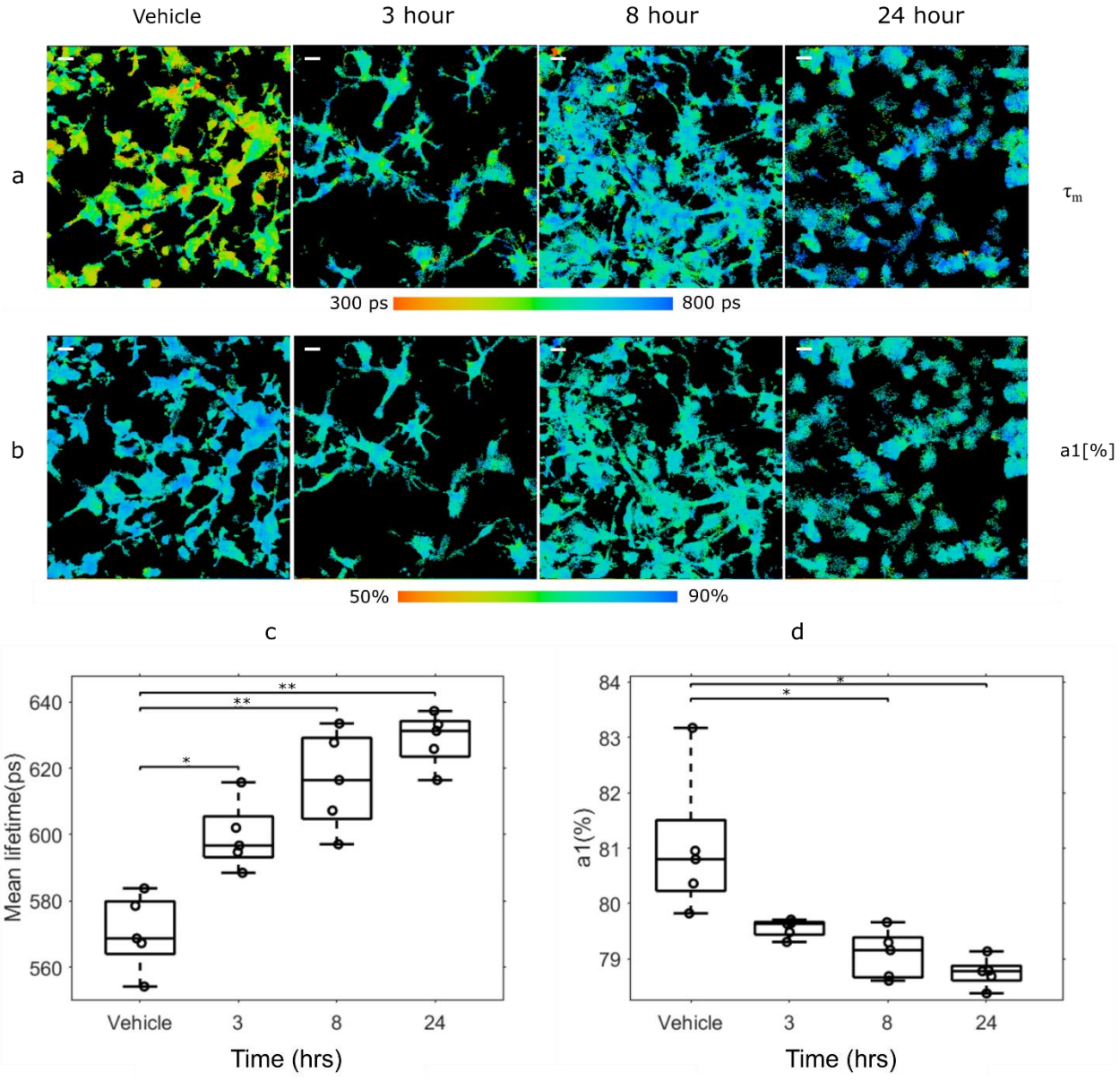

Fig. 6 NADH lifetime dose-dependently increases with time post-LPS treatment. Mixed glial cultures from CX3CR1-GFP mice were treated with vehicle or 10 ng/mL LPS for 3, 8 or 24 hrs (n=5). Representative NADH lifetime (a) and fractional free NADH levels (b) images from microglia are shown. Quantification of NADH lifetime (c) and free NADH levels (d) in LPS-treated microglia show time-dependent changes in FLIM parameters. The mean microglial NADH lifetime increases as early as 3 hrs after LPS exposure ;free NADH levels significantly decrease within 8 hrs of LPS exposure. One-way ANOVA *p<0.05, **p<0.01. (Scale bar 20 μm).

4 Discussion

Here we report a novel method of differentiating microglial activation in relation to surveillant microglia using FLIM measurements of the intrinsically fluorescent metabolic cofactor NADH. We show that NADH FLIM can be used to characterize the activation state of microglia both *in vitro* and *ex vivo* in brain tissue, and that LPS dose and treatment time directly impact FLIM parameters. Additionally, we found that microglia have different FLIM parameter values in relation to other glial cells in mixed glial cultures and in brain tissue sections. Based on previous studies, a relative change in NADH lifetime reflects a change in metabolic state of the intracellular microenvironment such that a lower mean lifetime implies greater free NADH[37,38]. We found that microglia in their surveillant or unactivated state had a lower NADH mean lifetime compared to other glial cells, and that they had a greater fractional contribution from free NADH. In contrast, LPS treatment increased their mean NADH lifetime and decreased the fractional contribution of free NADH (compared to vehicle treatment) To our knowledge, this is the first study to characterize microglia and to study the glial response to an inflammatory stimulus using fluorescence lifetime imaging.

In brain tissue slices, we found that microglia had a lower mean NADH lifetime than other cells in the tissue, and that LPS-treatment increased their mean lifetime for NADH, supporting

our contention that NADH lifetime can be used as a signature to differentiate between surveillant and activated microglia in the brain. While there was a decrease in the fractional contribution from NADH in tissue after 3 hrs of LPS treatment, it did not quite reach statistical significance ($p= 0.058$). Similarly, we observed no statistical difference between 3 hrs LPS treatment and vehicle treatment in the mixed glial cultures. There was, however, a statistically significant increase in the NADH mean lifetime. Differences in microglial NADH FLIM were observed within 1 hr of LPS treatment even before visible morphological changes appeared. Based on these observations, we postulate that mean NADH lifetime is well-suited for identifying a microglial fingerprint upon activation. FAD lifetime may also be useful as an additional parameter to NADH lifetime. In tissue slices, we chose Alexa594 as the fluorophore to identify microglia. This freed the FAD emission channel allowing us to test the efficacy of the FLIM technique with a microglial marker-independent of GFP fluorescence. We found that FAD lifetime had similar changes to NADH lifetime both when compared to non-microglial cells and microglial activation status (Supplementary Fig. 1). Future studies may exploit both NADH and FAD lifetime changes simultaneously to provide better quantification of the microglial redox state and indicate their activation status.

Our observation that NADH lifetime increases upon LPS treatment suggests that microglia become more oxidative upon inflammatory activation. Although there is evidence that reparative macrophages tend to be more oxidative rather than glycolytic[33,43–45], the metabolic status of LPS-stimulated microglia needs to be verified in a separate experiment. It is important to note that the lifetime changes observed here following LPS activation may not necessarily be the same as microglial inflammatory activation by other stimuli such as aging, neurodegenerative disease, or sleep deprivation/fragmentation disorders. Additional studies are needed to quantify FLIM parameters in the context of these scenarios since FLIM may be

extended to study the behavior of microglia in aging[34], multiple sclerosis and neurodegenerative diseases such as Alzheimer's and Parkinson's diseases.

One caveat to note in these studies is that FLIM parameters may be altered in mixed glial cell cultures due to the extraction and culture process. However, since we noted similar changes in brain tissue after *in vivo* LPS treatment, it is unlikely that the altered FLIM signals we have noted are an artifact of the *in vitro* culture system. There may also be concern about lifetime shifts due simply to the fixation process. In this regard, our lab recently demonstrated that fixation does not change the metabolic contrast[46]. Although the absolute lifetime values may be shifted by fixation, the treatment-induced alterations should be relative. Lastly, it is important to note that recent work [47] showed possible overlap between GFP and NADH spectra, which may confound interpretation of FLIM results. While this will require further investigation, when we compared lifetime pattern shifts in WT and CX3CR1-GFP brain tissue slices, we found that NADH lifetime was still increased upon LPS treatment, regardless of the presence of GFP (data not shown). Likewise, we saw similar FLIM signature and activation trends in brain tissue using A594, which is well-separated from the NADH spectra. The increase in NADH lifetime as a result of LPS-induced activation would suggest a more oxidative nature of active microglia compared to surveillant; however, further experiments would need to be done to confirm their metabolic state and the resulting shift in lifetime. Finally, although there may be variability among FLIM systems based on the optics and electronics used, the trends and relative changes in lifetime should be comparable. FLIM can also be used to measure the variability within a specific system.

In the future, NADH and FAD FLIM parameters may be used to determine whether microglia and infiltrating macrophages can be distinguished using novel cell-specific markers and advanced computational techniques (such as machine learning). Another important direction

for future studies would be to utilize FLIM to differentiate microglial phenotypes[48] to better understand their transition between different immune activities, and test the effectiveness of therapeutic drugs[49]. A major limitation for using FLIM assessments in tissues or *in vivo* is the complexity of distinguishing microglial signatures in the context of multiple cell populations and tissue environments. While work is ongoing to improve the speed and accuracy of FLIM for complex multicomponent measurements, FLIM by itself may be insufficient in some cases. Accordingly, we are exploring machine learning-based approaches to exploit the NADH/FAD lifetime differences in microglia compared to the surrounding tissue in metabolically active situations, such as *in vivo*.

5 Conclusion

Using a multiphoton FLIM-based technique, we have characterized microglia and their activation status. Our results demonstrate that, LPS-activated microglia have a higher NADH lifetime than surveillant microglia. We found that the change in NADH FLIM parameters of activated microglia was both LPS dose- and treatment time-dependent, which may be indicative of their activation state. In the future, the relative increase in NADH lifetime may be used to characterize cell activation in various neurodegenerative disorders in the CNS. We conclude that FLIM can be a powerful tool with which to monitor changes in microglial activation states or metabolic changes, perhaps in the absence of additional immunostaining.

References

1. N. A. Charles et al., “The brain tumor microenvironment,” Glia **59**(8), 1169–1180 (2011) [doi:10.1002/glia.21136].

2. G. A. Garden and T. Möller, “Microglia Biology in Health and Disease,” Jrnl NeuroImmune Pharm **1**(2), 127–137 (2006) [doi:10.1007/s11481-006-9015-5].

3. B. R. Tambuyzer, P. Ponsaerts, and E. J. Nouwen, “Microglia: gatekeepers of central nervous system immunology,” Journal of Leukocyte Biology **85**(3), 352–370 (2009) [doi:10.1189/jlb.0608385].

4. J. J. Watters, J. M. Schartner, and B. Badie, “Microglia function in brain tumors,” Journal of Neuroscience Research **81**(3), 447–455 (2005) [doi:10.1002/jnr.20485].

5. C. Béchade, Y. Cantaut-Belarif, and A. Bessis, “Microglial control of neuronal activity,” Front Cell Neurosci **7** (2013) [doi:10.3389/fncel.2013.00032].

6. G. Raivich et al., “Neuroglial activation repertoire in the injured brain: graded response, molecular mechanisms and cues to physiological function,” Brain Res. Brain Res. Rev. **30**(1), 77–105 (1999).

7. A. Mildner et al., “P2Y12 receptor is expressed on human microglia under physiological conditions throughout development and is sensitive to neuroinflammatory diseases,” Glia **65**(2), 375–387 (2017) [doi:10.1002/glia.23097].

8. S. Yona et al., “Fate mapping reveals origins and dynamics of monocytes and tissue macrophages under homeostasis,” Immunity **38**(1), 79–91 (2013) [doi:10.1016/j.immuni.2012.12.001].

9. J. Satoh et al., “TMEM119 marks a subset of microglia in the human brain,” Neuropathology **36**(1), 39–49 (2016) [doi:10.1111/neup.12235].

10. M. L. Dubbelaar et al., “The Kaleidoscope of Microglial Phenotypes,” Front Immunol **9** (2018) [doi:10.3389/fimmu.2018.01753].

11. O. Butovsky et al., “Identification of a unique TGF-β–dependent molecular and functional signature in microglia,” Nature Neuroscience **17**(1), 131–143 (2014) [doi:10.1038/nn.3599].

12. I. M. Chiu et al., “A neurodegeneration-specific gene-expression signature of acutely isolated microglia from an amyotrophic lateral sclerosis mouse model,” Cell Rep **4**(2), 385–401 (2013) [doi:10.1016/j.celrep.2013.06.018].

13. E. L. Gautier et al., “Gene-expression profiles and transcriptional regulatory pathways that underlie the identity and diversity of mouse tissue macrophages,” Nat. Immunol. **13**(11), 1118–1128 (2012) [doi:10.1038/ni.2419].

14. D. Gosselin et al., “Environment drives selection and function of enhancers controlling tissue-specific macrophage identities,” Cell **159**(6), 1327–1340 (2014) [doi:10.1016/j.cell.2014.11.023].

15. M. Nikodemova and J. J. Watters, “Efficient isolation of live microglia with preserved phenotypes from adult mouse brain,” Journal of Neuroinflammation **9**(1), 147 (2012) [doi:10.1186/1742-2094-9-147].

16. I. B. Hovens, C. Nyakas, and R. G. Schoemaker, “A novel method for evaluating microglial activation using ionized calcium-binding adaptor protein-1 staining: cell body to cell size ratio,” Neuroimmunol Neuroinflamm (2014) [doi:10.4103/2347-8659.139719].

17. M. del M. Fernández-Arjona et al., “Microglia Morphological Categorization in a Rat Model of Neuroinflammation by Hierarchical Cluster and Principal Components Analysis,” Front. Cell. Neurosci. **11** (2017) [doi:10.3389/fncel.2017.00235].

18. B. M. Davis et al., “Characterizing microglia activation: a spatial statistics approach to maximize information extraction,” Scientific Reports **7**(1), 1576 (2017) [doi:10.1038/s41598-017-01747-8].

19. W. Becker, “Fluorescence lifetime imaging--techniques and applications,” J Microsc **247**(2), 119–136 (2012) [doi:10.1111/j.1365-2818.2012.03618.x].

20. J. R. Lakowicz, Ed., *Principles of Fluorescence Spectroscopy*, Springer US, Boston, MA (2006).

21. M. Y. Berezin and S. Achilefu, “Fluorescence Lifetime Measurements and Biological Imaging,” Chem Rev **110**(5), 2641–2684 (2010) [doi:10.1021/cr900343z].

22. K. Suhling et al., “Fluorescence lifetime imaging (FLIM): Basic concepts and some recent developments,” Medical Photonics **27**, 3–40 (2015) [doi:10.1016/j.medpho.2014.12.001].

23. I. Iweibo, “Protein fluorescence and electronic energy transfer in the determination of molecular dimensions and rotational relaxation times of native and coenzyme-bound horse liver alcohol dehydrogenase,” Biochimica et Biophysica Acta (BBA) - Protein Structure **446**(1), 192–205 (1976) [doi:10.1016/0005-2795(76)90110-0].

24. O. Warburg, “On the Origin of Cancer Cells,” Science **123**(3191), 309–314 (1956).

25. M. G. V. Heiden, L. C. Cantley, and C. B. Thompson, “Understanding the Warburg Effect: The Metabolic Requirements of Cell Proliferation,” Science **324**(5930), 1029–1033 (2009) [doi:10.1126/science.1160809].

26. L. A. Volobоueva et al., “Inflammatory response of microglial BV-2 cells includes a glycolytic shift and is modulated by mitochondrial glucose-regulated protein 75/mortalin,” FEBS Lett. **587**(6), 756–762 (2013) [doi:10.1016/j.febslet.2013.01.067].

27. J. Gimeno-Bayón et al., “Glucose pathways adaptation supports acquisition of activated microglia phenotype,” J. Neurosci. Res. **92**(6), 723–731 (2014) [doi:10.1002/jnr.23356].

28. B. Kelly and L. A. O’Neill, “Metabolic reprogramming in macrophages and dendritic cells in innate immunity,” Cell Research **25**(7), 771–784 (2015) [doi:10.1038/cr.2015.68].

29. S. Nair et al., “Lipopolysaccharide-induced alteration of mitochondrial morphology induces a metabolic shift in microglia modulating the inflammatory response in vitro and in vivo,” Glia **67**(6), 1047–1061 (2019) [doi:10.1002/glia.23587].

30. C. Stringari et al., “Phasor Fluorescence Lifetime Microscopy of Free and Protein-Bound NADH Reveals Neural Stem Cell Differentiation Potential,” PLOS ONE **7**(11), e48014 (2012) [doi:10.1371/journal.pone.0048014].

31. A. Bhattacharjee et al., “Metabolic fingerprinting of bacteria by fluorescence lifetime imaging microscopy,” Scientific Reports **7**(1), 3743 (2017) [doi:10.1038/s41598-017-04032-w].

32. J. M. Szulczewski et al., “*In Vivo* Visualization of Stromal Macrophages via label-free FLIM-based metabolite imaging,” Scientific Reports **6**, srep25086 (2016) [doi:10.1038/srep25086].

33. A. Alfonso-García et al., “Label-free identification of macrophage phenotype by fluorescence lifetime imaging microscopy,” JBO **21**(4), 046005 (2016) [doi:10.1117/1.JBO.21.4.046005].

34. J. M. Crain, M. Nikodemova, and J. J. Watters, “Microglia express distinct M1 and M2 phenotypic markers in the postnatal and adult central nervous system in male and female mice,” Journal of Neuroscience Research **91**(9), 1143–1151 (2013) [doi:10.1002/jnr.23242].

35. W. Denk, J. H. Strickler, and W. W. Webb, “Two-photon laser scanning fluorescence microscopy,” Science **248**(4951), 73–76 (1990) [doi:10.1126/science.2321027].

36. L. Yan et al., “Applications of combined spectral lifetime microscopy for biology,” Biotechniques **41**(3), 249 (2006).

37. D. K. Bird et al., “Metabolic Mapping of MCF10A Human Breast Cells via Multiphoton Fluorescence Lifetime Imaging of the Coenzyme NADH,” Cancer Res **65**(19), 8766–8773 (2005) [doi:10.1158/0008-5472.CAN-04-3922].

38. M. C. Skala et al., “Multiphoton Microscopy of Endogenous Fluorescence Differentiates Normal, Precancerous, and Cancerous Squamous Epithelial Tissues,” Cancer Res **65**(4), 1180–1186 (2005) [doi:10.1158/0008-5472.CAN-04-3031].

39. J. C. M. Schlachetzki and M. Hüll, “Microglial activation in Alzheimer’s disease,” Curr Alzheimer Res **6**(6), 554–563 (2009).

40. M. E. Lull and M. L. Block, “Microglial activation and chronic neurodegeneration,” Neurotherapeutics **7**(4), 354–365 (2010) [doi:10.1016/j.nurt.2010.05.014].

41. V. H. Perry, J. A. R. Nicoll, and C. Holmes, “Microglia in neurodegenerative disease,” Nature Reviews Neurology **6**(4), 193–201 (2010) [doi:10.1038/nrneurol.2010.17].

42. D. M. Norden and J. P. Godbout, “Microglia of the Aged Brain: Primed to be Activated and Resistant to Regulation,” Neuropathol Appl Neurobiol **39**(1), 19–34 (2013) [doi:10.1111/j.1365-2990.2012.01306.x].

43. S. K. Biswas and A. Mantovani, “Orchestration of Metabolism by Macrophages,” Cell Metabolism **15**(4), 432–437 (2012) [doi:10.1016/j.cmet.2011.11.013].

44. S. Galván-Peña and L. A. J. O'Neill, "Metabolic Reprograming in Macrophage Polarization," Front Immunol **5** (2014) [doi:10.3389/fimmu.2014.00420].

45. D. Vats et al., "Oxidative metabolism and PGC-1beta attenuate macrophage-mediated inflammation," Cell Metab. **4**(1), 13–24 (2006) [doi:10.1016/j.cmet.2006.05.011].

46. J. V. Chacko and K. W. Eliceiri, "NAD(P)H fluorescence lifetime measurements in fixed biological tissues," Methods Appl. Fluoresc. (2019) [doi:10.1088/2050-6120/ab47e5].

47. E. M. York et al., "Green fluorescent protein emission obscures metabolic fluorescent lifetime imaging of NAD(P)H," Biomed. Opt. Express, BOE **10**(9), 4381–4394 (2019) [doi:10.1364/BOE.10.004381].

48. R. M. Ransohoff, "A polarizing question: do M1 and M2 microglia exist?," Nat Neurosci **19**(8), 987–991 (2016) [doi:10.1038/nn.4338].

49. "Neuroinflammation in Alzheimer's disease," The Lancet Neurology **14**(4), 388–405 (2015) [doi:10.1016/S1474-4422(15)70016-5].

Caption list

Fig. 1 Methods to image and quantify microglia lifetime upon activation. Top panel (a) shows the steps for the imaging, data processing and final comparison. A fluorescence intensity image was used to identify microglia in mixed glial cultures or brain tissue section. NADH FLIM parameters were extracted from both microglia and non-microglial regions. For activation experiments, only microglial FLIM parameters were compared. The example shown in panel (b) is a use case from a mixed glial culture representing each step outlined in panel (a). An NADH intensity image of a field-of-view (FOV) containing microglia (i) NADH intensity image (ii) The lifetime decay curve of a single microglial pixel marked by the red arrow in (i). The table inset (ii) shows the mean lifetime (t_m) decay from two components (free and bound NADH) and the fractional contribution from free NADH (a1[%]).(iii) The fitted lifetime image for the FOV, and the color bar shows the range of lifetime in ps (iv) The fluorescence (GFP or A594) intensity image was used to identify microglia and calculate average FLIM parameters. (iv). Microglial lifetime image (v). (Scale bar 20 µm).

Fig. 2 Relative change in microglia lifetime upon LPS treatment**.** Mixed glial cell cultures were treated with vehicle or LPS (10 ng/mL) for 1 hr. Representative image of NADH lifetime (a) and fractional free NADH (b) from vehicle-treated microglia. Representative image of NADH lifetime (c) and fractional free NADH (d) from

LPS-treated microglia. Quantification of NADH lifetime (e) and free NADH levels (f) in vehicle-treated microglia. Quantification of NADH lifetime (g) and free NADH levels (h) in LPS-treated microglia. LPS-stimulated microglia have a significantly higher mean lifetime and a lower free NADH contribution (n=5). Compared to non-microglia, microglia retain their lower lifetimes and higher free NADH levels even when exposed to LPS. T-test *p<0.05. (Scale bar 20 μm).

Fig. 3 Comparison of microglia lifetime in mixed glial culture. Microglia have a lower mean NADH lifetime (a), and higher free NADH levels (b) than other cells in mixed glial cultures (n=10). T-test, ***p<0.005.

Fig. 4 NADH lifetime can be used to distinguish microglia from non-microglia and characterize microglial activation status in brain tissue. A microglial mask was created using the AlexaFluor594 intensity image from Iba1-labeled brain tissue slices from WT mice that were untreated or treated with LPS (5mg/kg). Representative image of microglial NADH lifetime in tissue slices from vehicle- (a) or LPS-treated (b) mice (n=5). Microglia had a significantly lower NADH lifetime than non-microglial cells in tissues from both vehicle (c) and LPS-treated (d) mice. T-test, p<0.05. (Scale bar 10 μm).

Fig. 5 Microglia FLIM parameters vary with LPS dose. LPS dose-dependently alters NADH lifetime and free NADH ratio. Mixed glial cell cultures from CX3CR1-GFP mice were treated with vehicle, 1ng/mL, 10 ng/mL or 100 ng/mL of LPS for 1 hr. NADH lifetime (a) and free NADH levels (b) were measured in GFP^+ cells. Compared to vehicle treatment, the 10 and 100 ng/mL doses significantly increased NADH lifetime and decreased free NADH levels. One-way ANOVA, *p<0.05, **p<0.01.

Fig. 6 NADH lifetime dose-dependently increases with time post-LPS treatment. Mixed glial cultures from CX3CR1-GFP mice were treated with vehicle or 10 ng/mL LPS for 3, 8 or 24 hrs (n=5). Representative NADH lifetime (a) and fractional free NADH levels (b) images from microglia are shown. Quantification of NADH lifetime (c) and free NADH levels (d) in LPS-treated microglia show time-dependent changes in FLIM parameters. The mean microglial NADH lifetime increases as early as 3 hrs after LPSexposure ;free NADH levels significantly decrease within 8 hrs of LPS exposure. One-way ANOVA *p<0.05, **p<0.01. (Scale bar 20 μm).

Chapter 3

Machine learning techniques for label free detection of microglia

This chapter was adapted from: “Machine learning methods for fluorescence lifetime imaging (FLIM) based label-free detection of microglia” Md Abdul Kader Sagar, Kevin P. Cheng, Jonathan N. Ouellette, Justin C. Williams, Jyoti J. Watters, Kevin W. Eliceiri, Frontiers in neuroscience.

Keywords: FLIM, Fluorescence lifetime imaging, CNS, ANN, Machine learning, Brain metabolism, neural networks, microglia, NADH

Abstract

Automated computational analysis techniques utilizing machine learning have been demonstrated to be able to extract more data from different imaging modalities compared to traditional analysis techniques. One new approach is to use machine learning techniques with existing multiphoton imaging modalities to better interpret intrinsically fluorescent cellular signals to characterize different cell types. Fluorescence Lifetime Imaging Microscopy (FLIM) is a high resolution quantitative imaging tool that can detect metabolic cellular signatures based on the lifetime variations of intrinsically fluorescent metabolic co-factors such as nicotinamide adenine dinucleotide (NADH). NADH lifetime-based discrimination techniques have previously been used to develop metabolic cell signatures for diverse cell types including immune cells such as macrophages. However, FLIM could be even more effective in characterizing cell types if machine learning was used to classify cells by utilizing FLIM parameters for classification. Here, we demonstrate the potential for FLIM-based, label-free NADH imaging to distinguish different cell types using Artificial Neural Network (ANN)-based machine learning. For our biological use case, we used the challenge of differentiating microglia from other glia cell types in the brain. Microglia are the resident macrophages of the brain and spinal cord and play a critical role in maintaining the neural environment and responding to injury. Microglia are challenging to identify as most fluorescent labeling approaches cross-react with other immune cell types, are often insensitive to

activation state, and require the use of multiple specialized antibody labels. Furthermore, the use of these extrinsic antibody labels prevents application in *in vivo* animal models and possible future clinical adaptations such as neurodegenerative pathologies. With the ANN based NADH FLIM analysis approach, we found that microglia in cell culture mixed with other glial cells can be identified with more than 0.9 True Positive Rate (TPR). We also extended our approach to identify microglia in fixed brain tissue with a TPR of 0.79. This method can be further extended to potentially study and better understand microglia's role in neurodegenerative disease with improved detection accuracy.

1 Introduction

Unlike external fluorescent labeling approaches, label-free microscopic identification methods can provide equally useful information while leaving the cellular microenvironment unperturbed. Identification of unique metabolic fingerprints based on quantitative data obtained from endogenous cellular properties has been recently explored to develop biomarkers of different cell types and/or disease states. These techniques take advantage of different optical imaging modalities and the intrinsic properties revealed by them followed by quantification techniques to identify different biomarkers. Examples include: diffused optical tomography for breast cancer (Flexman et al., 2013), collagen signature (Kirkpatrick et al., 2006), Stimulated Raman Scattering (SRS) based label-free chemical contrast (Freudiger et al., 2008), and fluorescence lifetime based macrophage signature (Szulczewski et al., 2016).

Fluorescence Lifetime Imaging Microscopy (FLIM) is a well-suited modality for identifying candidate biomarkers as it can be used to assess intrinsic cellular metabolism. Fluorescence

lifetime depends on physiological parameters such as pH and ion/oxygen concentrations; it is also independent of intensity, concentration, sample absorption, and sample thickness (Berezin and Achilefu, 2010; Suhling et al., 2015). FLIM can monitor metabolism by taking advantage of the intrinsic fluorescence of the ubiquitous metabolic coenzyme NADH (Nicotinamide Adenine Dinucleotide). NADH is a key electron donor/acceptor involved in many metabolic processes, especially redox reactions (Lakowicz et al., 1992; Mongeon et al., 2016; Skala et al., 2007). FLIM can quantify the ratio between free and bound NADH, and calculate the mean fluorescence lifetime based on the relative quantity of free:bound components and the individual component's lifetime (Bird et al., 2005; Lakowicz et al., 1992; Provenzano et al., 2008; Skala et al., 2005). The mean lifetime, long lifetime component, or free:bound ratios of NADH are indicative of whether a cell's metabolism is in a more glycolytic or oxidative state. For example, more free NADH measured via FLIM can be used to show a shift towards glycolysis in cancer per the Warburg theory. As a result, FLIM is gaining widespread acceptance as a way to probe the cellular microenvironment (Berezin and Achilefu, 2010; Provenzano et al., 2008; Suhling et al., 2005, 2015; Wang et al., 1992). FLIM is also increasingly used to probe brain metabolism and neuronal function *in vivo.* For instance, quantitative FLIM data has been used by researchers to: 1) find contrast between glioblastoma and normal brain tissue (Kantelhardt et al., 2016; Leppert et al., 2006; Sun et al., 2010), 2) map alterations in cerebral metabolism based on NADH binding (Chia et al., 2008; Yaseen et al., 2017), 3) non-invasively, optically image Alzheimer's Disease (Das et al., 2018), 4) visualize redox activities in the brain (Mongeon et al., 2016), and 5) quantify neuronal dysfunction in neuroinflammation using FLIM instrumentation (Rinnenthal et al., 2013).

There is a need in central nervous system (CNS) studies for non-invasive ways to image and quantify metabolism and identify functional alterations in specific cell types which could lead to better understanding of the role of different cell's in neurodegenerative disease. In particular, one cell type of specific imaging interest are microglia. Microglia are a critical cell type in the nervous system whose activities are implicated in virtually all neuropathologies including traumatic injury, neurodegenerative disease, ischemia, and infection (Charles et al., 2011; Garden and Möller, 2006; Tambuyzer et al., 2009; Watters et al., 2005). These CNS tissue-resident macrophages influence brain development, maintain the neural environment, respond to injury and infection, and orchestrate repair processes among other important functions. Their production of neurotoxic inflammatory molecules often exacerbates neuronal damage. For this reason, we chose microglia as our biological use case for developing a non-invasive label free imaging workflow that combines Fluorescence lifetime Imaging with Machine learning.

The goal of this study was to develop a FLIM-based fingerprint for microglia, as has been done for macrophages (Alfonso-García et al., 2016) and bacteria (Bhattacharjee et al., 2017). Our lab previously demonstrated that FLIM-based, label-free imaging could be used to distinguish unique glycolytic type FLIM signatures between tumor-associated macrophages and mouse mammary tumors cells (Szulczewski et al., 2016). However, this has not been done in the context of the CNS and microglia. Previous studies have used FLIM to show neural stem cell differentiation(Stringari et al., 2012) or characterize metabolic response of astrocytes (Stuntz et al., 2017), but not to identify microglia identity. In order to optimally exploit differences in metabolism-induced lifetime changes for microglia identification, a fast, quantitative approach that can identify their

unique metabolic signature would be ideal. Accordingly, we have coupled FLIM with a machine learning-based solution to detect microglia based on their FLIM parameters.

One of the most common ways FLIM acquisition is performed is Time Correlated Single Photon Counting (TCSPC) connected to multiphoton laser scanning microscopes. TCSPC offers picosecond level time resolution, which is arranged in histograms based on timing information of the detection photon. In a typical time domain FLIM analysis workflow, the lifetime decay curve is subject to one- or two-component exponential curve fitting to estimate the lifetime parameters such as free: bound NADH lifetime, the amplitude of their decay curve, and goodness of fit (chi-squared error). If a machine learning (ML) algorithm has raw unfitted decay data, it could be possible to estimate lifetime accurately and subsequently characterize cell types. This approach would be advantageous in two ways: i) it will reduce time for calculating lifetime from a decay curve (the only remaining bottleneck would then be collection time; the lifetime can be estimated instantly without the time-consuming exponential curve fitting); and ii) possibly identify an optical/metabolic fingerprint which would otherwise not be apparent with regular analysis. This approach of calculating lifetime directly from the decay curve is relatively new, to our knowledge, there is one previous published report that has estimated lifetimes using artificial neural networks (Wu et al., 2016). Another approach of possible utility would be to use the estimated lifetime parameters calculated using standard curve fitting approaches and train where the label is created by antibody staining.

In this study, we have used both approaches to train an Artificial Neural Network (ANN) to identify the location of microglia i.e. i) a fitting based method (FBM) where the fitted data are exported from standard curve fitting routines, and ii) an experimental decay based method (DBM)

training with the exponential decay curve consisting of 256 time-bins directly. To our knowledge, this is the first application of a FLIM-based machine learning application for intrinsic fluorescence signature development.

2 Material and Methods

2.1 Animals

All animals were maintained in an AALAC-accredited animal facility with a 12-hr light/dark cycle regime and had access to food and water ad libitum. All experiments were performed in accordance with the University of Wisconsin-Madison Institutional Animal Care and Use Committee.

For FLIM imaging, 100um thick coronal slices were prepared from the fixed brains of young adult C57BL/6J and CX3CR1-GFP mice (Jackson Labs), aged 6-8 weeks. Animals were euthanized by isoflurane overdose and transcardially perfused with ~30ml of ice-cold PBS, followed by a second perfusion with an ice-cold solution of 4% PFA in PBS. Brains were then dissected, post fixed for 24hrs in a solution of 4% PFA in PBS, and then moved to HBSS (all performed at 4C and protected from light).

2.2 Preparation of primary neonatal mixed glial cultures

Mixed primary glial cultures were prepared from 3-7 day old, CX3CR1-GFP mouse pups as previously described (Crain et al., 2013). Briefly, brains were dissected immediately after decapitation, and the brain stem, olfactory bulbs, meninges, and visible blood vessels were removed. The remaining tissue was finely minced, thoroughly triturated with a serological pipette in 0.25% trypsin-EDTA containing 0.1mg/ml deoxyribonuclease I, and then incubated at 37C for

20 minutes. The reaction was immediately stopped by the addition of an equal volume of heat-inactivated horse serum. The dissociated cells were resuspended in DMEM supplemented with 10% FBS and 100 units/ml penicillin/streptomycin. Brains were processed individually for each pup, and the resulting cell suspension was divided equally and plated in 35mm dishes (4-6 plates/brain). The plated cells were cultured for 7-14 days in a 37C incubator supplemented with 5% CO2; the culture medium was replaced every 3-4 days.

2.3 Immunohistochemistry

100um thick coronal sections were prepared from the midbrain region of each brain using a Leica Vibratome. Two slices from each animal were used for immunohistochemical staining. Briefly, slices were washed at room temperature with 0.3% TritonX-100 in PBS, before incubating in blocking buffer (1 % BSA, 0.3 % TritonX-100/PBS) for 2 hours at room temperature. Slices were then incubated with anti-Iba1 antibodies (1:1000; Wako Catalog No. 019-19741) in blocking buffer in the dark at 4C overnight. Slices were washed again at room temperature with 0.3% TritonX-100 in PBS followed by incubation in the dark for 2 hours with AlexaFlour594 anti-rabbit IgG antibodies (1:200) in blocking buffer, at room temperature. Slices were washed with 0.3% TritonX-100 in PBS and mounted on 1mm slides using Cytoseal60 mounting medium. Mounted sections were stored at room temperature, protected from light until they could be imaged.

2.4 Multiphoton lifetime imaging

The multiphoton based (Denk et al., 1990) lifetime and intensity imaging was performed on a custom multiphoton laser scanning system built around an inverted Nikon Eclipse TE2000U at the Laboratory for Optical and Computational Instrumentation(Yan et al., 2006). A 20x air immersion

objective (Nikon Plan Apo VC, 0.75 NA) (Melville, NY, USA) was used for all imaging. For NADH imaging, data was collected using an excitation wavelength of 740 nm, and the emission was filtered at 457 ± 50 nm (Semrock, Rochester, NY) for the spectral peak for NADH/NADPH. For GFP intensity imaging, the excitation was set at 890 nm, and an emission 520 ± 35 filter was used (Semrock, Rochester, NY). For AlexaFluor594 imaging, excitation was set at 810 nm, and a 615/20 (Semrock, Rochester, NY) bandpass emission filter was used for emission. We used time domain FLIM imaging where the FLIM decays curves were built with TCSPC(Time Correlated Single Photon Counting) electronics. FLIM images were collected at 256x256 resolution with 120 second collection using SPC-150 Photon Counting Electronics (Becker & Hickl GmbH, Berlin, Germany) and Hamamatsu H7422P-40 GaAsP photomultiplier tube (Hamamatsu Photonics, Bridgewater, NJ). Urea crystals were used to determine the Instrumentation Response Function (IRF) with a 370/10 bandpass emission filter (Semrock, Rochester. NY). For each sample, around 20 neighboring FOVs were randomly selected, and the average value of lifetime and free NADH ratio were calculated based on masking described in the Data Analysis section. The instrument response function of the optical system was calibrated during each imaging session. Autofluorescence intensity and fluorescence lifetime data were analyzed in SPCImage (Becker & Hickl GmbH, Berlin, Germany) where a Levenberg–Marquardt routine for nonlinear fitting was used to fit the fluorescence decay curve collected for each decay after binning. Data was assessed by the minimized chi-square value generated during the fit so that the analyses were unbiased. To eliminate background fluorescence, a threshold for analysis was applied based on photon counts.

2.5 Data analysis

The cell cultures used for experiments were CX3CR1-GFP positive, and the GFP intensity image was used to create the mask for identifying microglia. For the brain tissue imaging, anti-Iba1 antibodies visualized with AlexaFluor594 was used to identify microglia (figure 1A). The lifetime fitted data from SPCImage (Becker & Hickl GmbH, Berlin, Germany) and all the parameters were exported for more custom operations. Figure 1B shows the NADH intensity image created from the lifetime image. Figure 1C shows the lifetime image (mean lifetime) created by curve fitting. Mean lifetime is one of the parameters exported for ANN training. The exported data were imported in MATLAB (MathWorks Inc, Natick, MA) for calculating the means of custom regions and statistical analyses. The masks were created from intensity images in MATLAB. The time-resolved Becker and Hickl SDT data was read using Bio-Formats (Linkert et al., 2010) MATLAB support package.

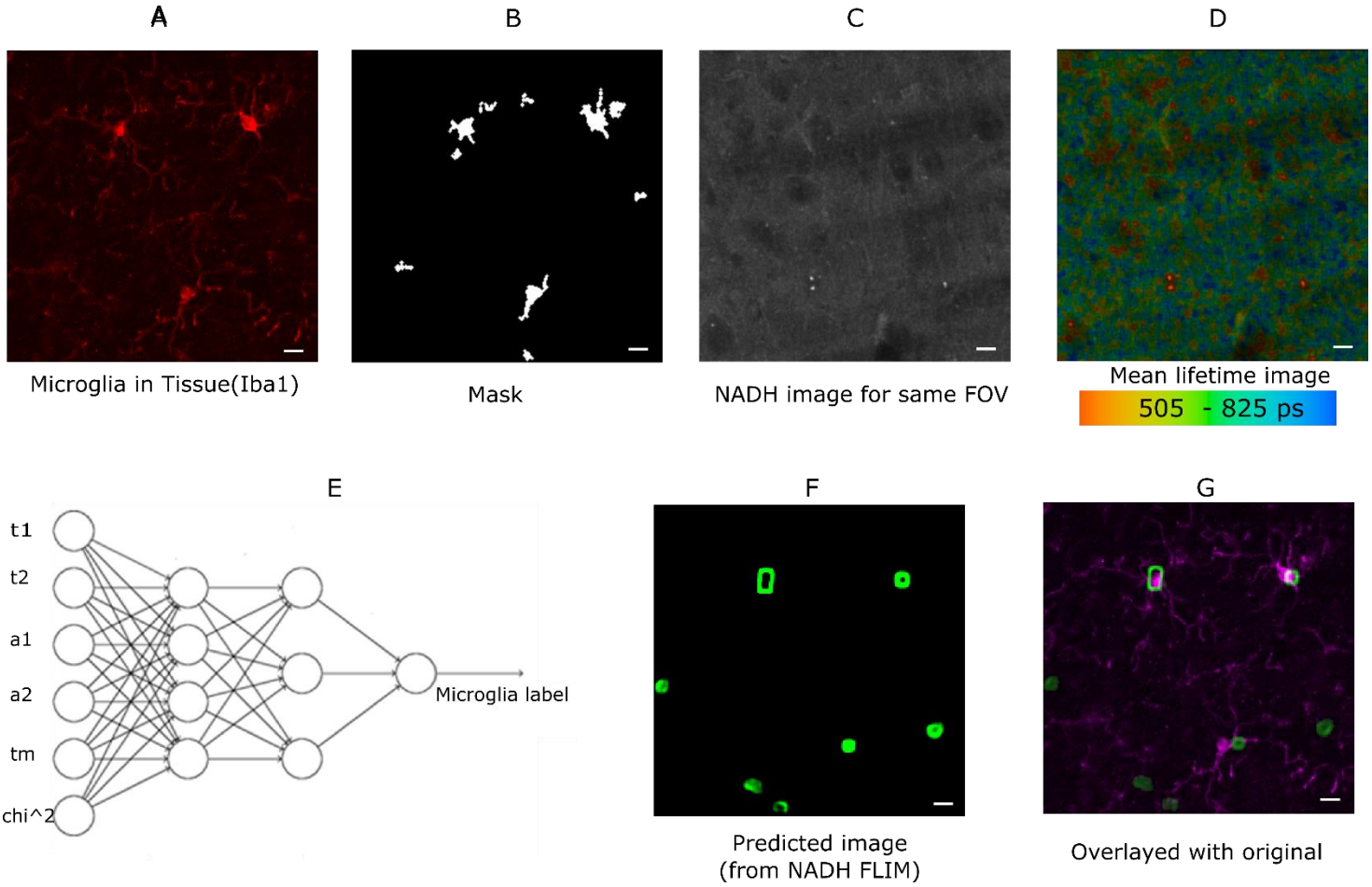

Figure 1: Method demonstrating microglia prediction using ANN. **(A)**Microglia image using Iba1. **(B)**Mask created from Iba1 image **(C)** NADH intensity image from the same FOV. **(D)** Lifetime image of the same FOV created from SPCImage (Becker and Hickl GmbH, Berlin, Germany) **(E)** ANN showing the inputs used for training instances and output **(F)** predicted microglia image. **(G)** Composite image showing fusion of predicted microglia image and actual microglia image created from Iba1(scale bar *10* µm).

2.5.1 ANN implementation, fitting-based method (FBM)

In this approach, the fitted data for NADH lifetime was exported in *.asc format from SPCImage and read in MATLAB for post-processing and training. The exported data were mean free/bound/mean NADH lifetimes (τ_1, τ_2, $\tau_{m)}$, amplitude of their decay curve and free bound ratio (a_1, a_2, $a_1[\%]_)$, goodness of fit (chi-squared error, $\chi 2$). All exported images were exported from 256 x 256 size lifetime images, and smaller overlapping blocks of 8x8 size were taken from each dataset for training instances; the average of each block was calculated for each parameter. In this way, 8,494,137 labeled training datasets were created for cells, and 5,456,088 training dataset were created for tissue training. Subsequently, the data was used for training using MATLAB's neural fitting toolbox. 70% of the dataset was used for training, and 15% was set aside for validation and testing. Bayesian regularization(Foresee and Hagan, 1997) backpropagation was used as a network training function, that updates the values according to Levenberg-Marquardt optimization. We used a feed-forward network with 10 hidden layers. As a cost function, we used mean squared error. The performance with 10 hidden layers and Bayesian Regularization was 0.0202 for mixed glial cell culture and 0.013 for tissue; increasing the number of hidden layers further did not improve performance. The accuracy for microglia detection was determined by first exporting the FLIM parameters from NADH lifetime from a separate testing dataset. The input data for feeding the ANN was created the same way as the training process. Following this step, the label for each block was predicted using the trained model, and the label for that block was created. Repeating this step for all pixels generated a 2D image with microglia detection probabilities. Pixels with lower probability was discarded and smaller detected regions were also discarded. The calibration was done on training images to ensure overlap. Then, these thresholds were used to create a

probability image. Figure 1E shows such a mask which has 7 microglia in the FOV. The predicted image was compared with antibody-labeled (figure 1A) images to locate microglia positions. The composite image (figure 1F) shows the overlap between predicted microglia region and antibody detected microglia region. We calculated the sensitivity (True Positive Rate), Positive Predictive Rate(PPV), False Negative Rate (FNR), and False Discovery Rate(FDR) (2017) from the detected microglia after prediction and post processing. We did not calculate the rest of the parameters of the confusion matrix as we do not have the true negatives with our current approach of imaging. We do not have labelled data for non-microglia cells and it was out of the scope of this paper.

2.5.2 ANN implementation, decay-based method (DBM)

This approach exports the decay directly, which has 256 times bins in the histogram. The data were directly read from time resolved SDT file using the Bio-Formats file reader library (Linkert et al., 2010) in MATLAB. Instead of using the fitted parameters as input to the ANN, we used an ANN with 10 hidden layers and 256 input layers. The rest of the training and testing was the same as the previous method. The performance with these settings for cells was 0.0227.

3 Results

3.1 ANN-FLIM can detect microglia in mixed glial cell cultures

In this section, we demonstrate the ability of ANN-based techniques to identify microglia in mixed glial cell cultures. ANN is applied on exported data after curve fitting from SPCImage software. NADH lifetime fitted data are exported from SPCImage (see methods), and exported parameters are used to compute training instances for individual blocks. The training is performed on training

sets and tested on a separate testing dataset. Figure 2A shows the GFP intensity image created from GFP positive microglia. The predicted microglia image from a sample field of view is shown in Figure 2B. Figure 2C shows the fused image of the original microglia image and predicted image from the same FOV. It is evident from the fused image that, most of the microglia are properly detected when compared with actual microglia image created from GFP. There are some microglia which are not predicted and some false positive in the lower left corner where microglia are falsely identified. Figure 2D shows the error obtained by prediction of individual instances created from FLIM parameters of the testing dataset. The total number of microglia in all (testing) FOVs were 348 and of them 313 were correctly identified, 35 microglia was missed by the prediction algorithm, but 138 additional microglia was falsely identified. Figure 2E shows the result for microglia detection for 5 different dishes; we got TPR 0.9044 ± 0.0311, PPV 0.672 ± 0.1015, FNR 0.0956 ± 0.0311, FDR 0.3298 ± 0.1015.

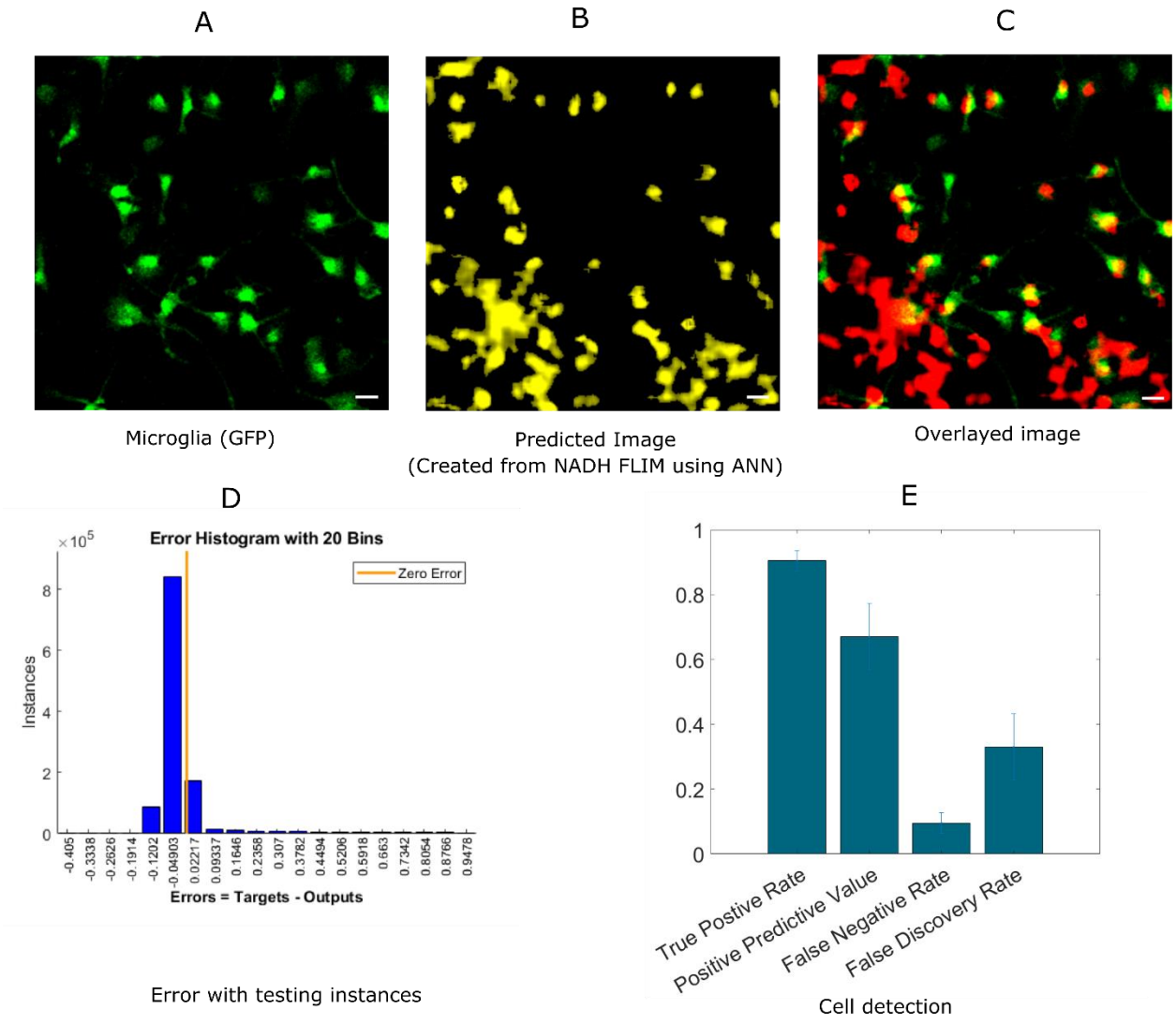

Figure 2*: Prediction of microglia from NADH lifetime data in mixed glial cell cultures where microglia cells are GFP-labeled. In this approach, ANN is applied on exported lifetime parameters of the endogenous fluorophore NADH.* ***(A)*** *Original fluorescence intensity image of microglia created from GFP channel* ***(B)*** *Predicted microglia image from NADH lifetime data from the same field-of-view.* ***(C)*** *Composite image of predicted microglia image and original intensity image. Most of the microglia are accurately predicted as seen from the composite image. But there are a few microglia not detected and some false positive in the lower left corner* ***(D)*** *Error rate from*

testing instances, created from the testing microglia dataset ***(E)*** *TPR, PPV, FNV and FDR from 5 different dishes (Scale bar 20* μm) .

3.2 ANN-FLIM can detect microglia in brain tissue

Next, we extended our approach to identifying microglia in fixed mouse brain tissue slices. Imaging brain tissue is more challenging than imaging cell cultures because of greater heterogenous spatial structures, and a wider degree of variation in microglia lifetimes. The algorithm implementation was the same as in the *in vitro* cell culture experiments, where ANN was applied to the exported lifetime data from curve fitting software, SPCImage. An anti-Iba1 antibody with an AlexaFluor594 secondary antibody was used to visualize and create a microglial intensity image (figure 3A). Figure 3B shows the predicted microglia image created from NADH lifetimes of the same field of view as in Figure 3A, in which the microglia are stained with Iba1. Figure 3C shows the fused image of the original microglia image (from tissue)- and predicted image from the same FOV. It is evident from the fused image that all of the microglia from this FOV are properly detected when compared with the Iba1 intensity positive microglia. Figure 3D shows the error obtained by while predicting using individual instances created from FLIM parameters of the testing dataset. The total number of microglia in the testing FOVs are 170 and 137 were correctly identified, but 76 microglia were falsely identified. Figure 3E shows the result for 5 different tissues where we got TPR 0.79 ± 0.0775, PPV 0.638 ± 0.09, FNR 0.2 ± 0.0775, FDR 0.3641 ± 0.09. The TPR is reduced for microglia in tissue and FNR is increased as the heterogeneity and complexity of the structure complicates the prediction.

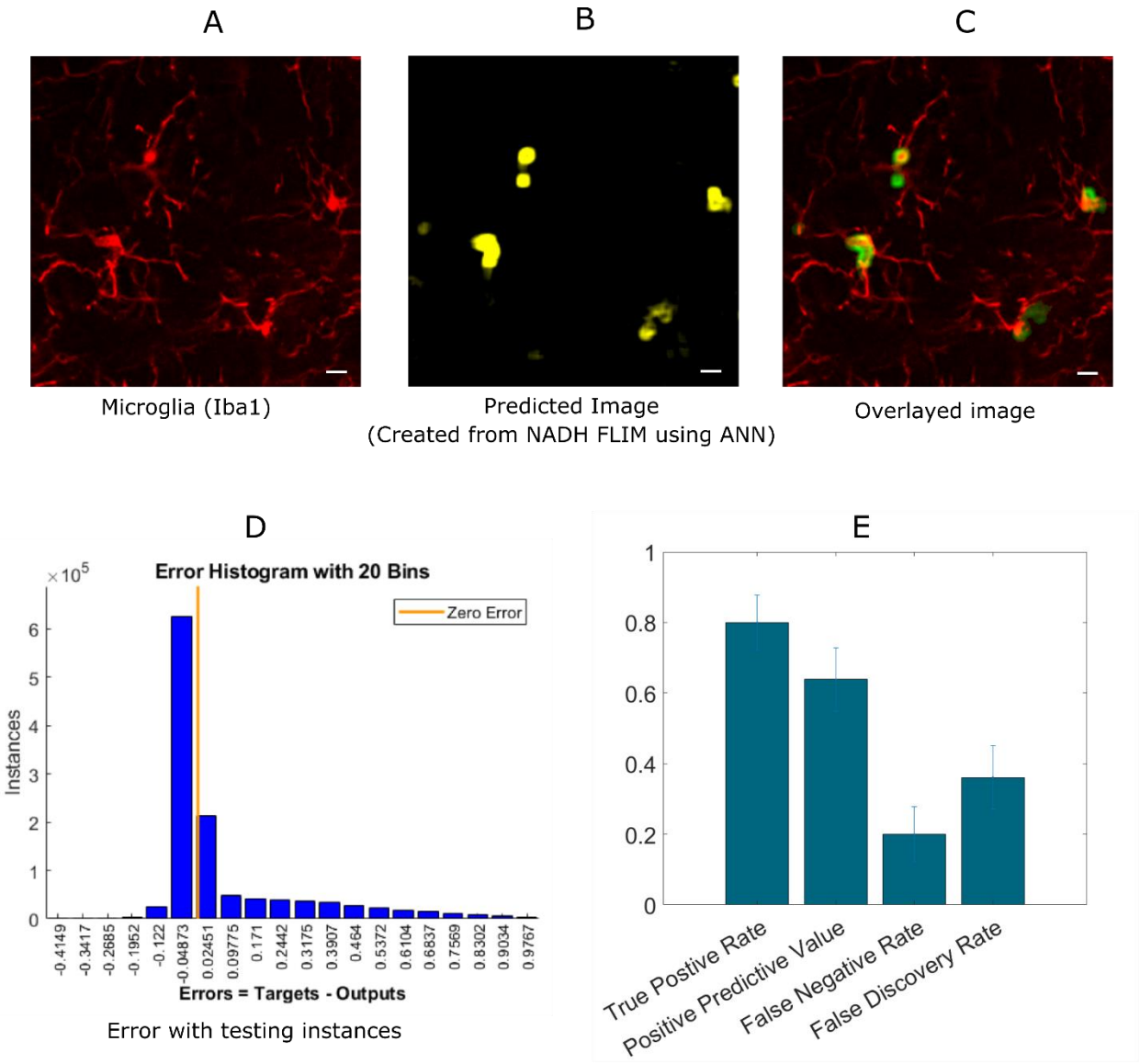

Figure 3 *Prediction of microglia from NADH lifetime data in mouse brain tissue. In this approach, ANN is applied on exported lifetime parameters of the endogenous fluorophore NADH.* ***(A)*** *Original intensity image of microglia location created from the anti-Iba1 antibody AlexaFluor594 channel* ***(B)*** *Predicted microglia image from NADH lifetime data from same field-of-view. Composite image of predicted microglia image and original intensity image.* ***(C)***

Composite image of predicted microglia image and original intensity image. ***(D)*** *Error rate from training and* ***(E)*** *TPR, PPV, FNV and FDR from 5 different dishes (Scale bar 10 µm).*

3.3 ANN directly on exponential decay can detect microglia in mixed cell cultures

Finally, we implemented an experimental approach, where instead of exporting the lifetime fitted data, we used the decay data having 256-time bins as a training instance. A recent study showed the effectiveness of using ANN to calculate lifetime directly from decay (Wu et al., 2016). Instead of calculating lifetime, we directly used microglia locations as labels. This approach is simpler because it bypasses the steps involving exponential curve fitting routines and exporting the fitted lifetime parameters. Figure 4A shows the intensity image of microglia created from the GFP channel in the mixed glial cultures. Figure 4B shows the recreated image from ANN-predicted microglia from the exponential decay. Figure 4C shows the fused image of the original microglia image (from mixed glial culture)- and predicted image from the same FOV. Figure 4D and 4E show the error bar from training and testing instances respectively.

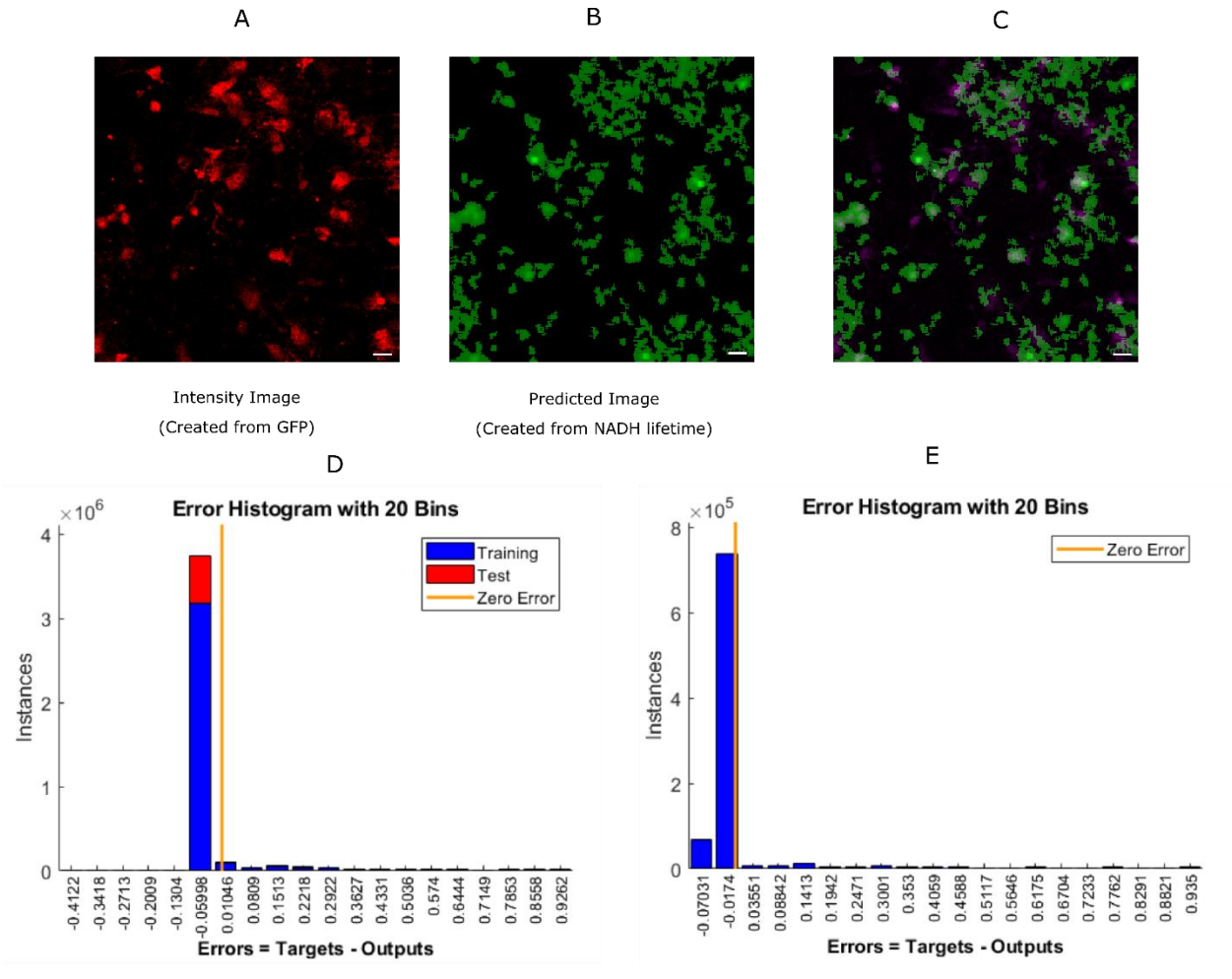

Figure 4: *Prediction of microglia from NADH lifetime data in mixed glial cell cultures where microglia cells are GFP-labelled. In this approach, ANN is applied directly on exponential decay curves of the endogenous fluorophore NADH.* ***(A)*** *Original intensity image of microglia location created from the GFP channel* ***(B)*** *Predicted microglia image from NADH lifetime data only. Both images are from the same field-of-view.* ***(C)*** *Composite image of predicted microglia image and original intensity image.* ***(D)*** *Error bar from training and* ***(E)*** *testing instances (Scale bar 20 µm).*

4 Discussion

In this paper, we have used ML and fluorescence lifetime to identify microglia in both mixed cell cultures and in brain tissue sections. To our knowledge, this is one of the first studies to apply ML algorithm to FLIM data to identify intrinsic cellular metabolic signatures. Moreover, applying ML methods directly on exponential decay data can be potentially augmented to calculate lifetime without curve fitting to help understand underlying trends in biological samples. The techniques applied in this paper can be extended in various ways in studies related to brain metabolism. Although there has been some FLIM studies to visualize brain metabolism but previously, but ML-FLIM used not to characterize cell types previously. This technique can be potentially extended to identify other CNS glial cells such as astrocytes, oligodendrocytes, and neurons. For *in vivo* brain studies, a ML-based, label-free technique can be used in the future where FLIM for different spectral channels can be used in conjunction with trained ML networks to identify and study specific cell types. Here, we used the lifetime information generated by exponential curve fitting from each pixel as training instances, and antibody-stained microglia locations are used as positive microglia pixels. The goal was to be able to identify microglia using the NADH lifetime information alone. We have used two different approaches for training, 1) the calculated lifetime parameters created from curve fitting software SPCImage, FBM, and 2) ML directly on time-resolved data, DBM . The second approach bypasses the time-consuming curve fitting process and reduces the overall number of processing steps. We first implemented our ANN-based approach on microglia in mixed glial cell culture, and then extended this to testing tissue samples. In future, the tissue-based identification can easily be converted for *in vivo* identification of microglia.

Microglia are normally visualized with antibody-based methods, using antibodies such as anti-TMEM119 (Bennett et al., 2016), anti-Iba1, and the combination of anti-CD11b and anti-CD45, among others. These standard labeling techniques have several limitations, including the extended sample preparation time and associated complexity, inefficient antibody penetration, and the potential for non-specific antibody binding. A FLIM based, label-free imaging technique is advantageous because it is simple, free from exogenous labeling, provides the ability to directly measure intrinsic cellular properties, and its potential for extending its use to observe cell activity *in vivo*. NADH-FLIM based endogenous biomarker visualization is an effective way to image intrinsic metabolism as NADH lifetimes and free:bound ratios change with alterations in metabolic state. The metabolic state of immune cells like microglia can be different from other non-immune cells and the surrounding tissue, and these differences are reflected by the alternations in their lifetime signature.

For fitting-based methods (FBM), where the fitted parameters were exported from SPCImage, we were able to achieve TPR of 0.9044 ± 0.0311 for 5 different microglia mixed culture group (Figure 2). However, we got some false positives with FNR being 0.0956 ± 0.0311 and FDR being 0.3298 ± 0.1015. For clinical application the false positive need to be reduced in future studies. This number can be decreased by increasing number of training samples. This approach would require a significant amount of data acquisition and processing time as each FLIM image takes 1-2 minute to acquire. This FBM approach was also applied to brain tissue sections, which achieved a lower accuracy than cell culture which we expected. The tissue is much more heterogenous and different fluorescent signature add to the variation in lifetime alternations. Still, we managed to achieve TPR of 0.79 ± 0.0775 and PPV of 0.638 ± 0.09 but increased false positive resulted in FNR of 0.2

± 0.0775 and FDR of 0.3641 ± 0.09 (figure 3). The reduction in TPR for tissue can be attributed to several factors. In the mixed glial cell, there were primarily glial cell of which majority of non-microglia cells were astrocyte. The lifetime variation is much smaller in this environment compared to an actual brain tissue where lots of different factors contribute to the NADH lifetime variation. We also had fewer number of microglia cell for training for the same number of FOVs, which can also contribute to the reduction in accuracy to some extent. Combination of these factors can contribute to the reduction in TPR and increase in FDR.

The second approach, DBM used the decay curve directly as the input training parameter. However, there is shortfall in the accuracy possibly introduced by curve shift between successive imaging, afterpulsing of the detectors that requires taking into account Instrument Response Function (IRF). When the testing instances (from mixed glial culture) were reorganized to form image after classification, we could detect 60-65% of the original microglia compared to ~90% we achieved using FBM. Moreover, about half of the detected cells were false positives. This method did not yield an acceptable result in tissue as the heterogeneity in the tissue might add to the variation. To make this method more accurate and clinically viable, we need more training datasets as well as take into account the FLIM instrumentation originated variation such as shift in decay and IRF. Moreover, surface-based markers such as CD11b for microglia could result in a better classification compared to Iba1 as they are able to properly identify all of cell body and processes which would reduce false negatives for training. We intend to explore this further in future work, as well as combining advanced deep learning tools such as Convolutional Neural Networks (Krizhevsky et al., 2012) to better predict microglia location using lifetime information and morphological features.

One limitation of our approach is inherent to the TCSPC method itself, as TCSPC acquisition takes several minutes to finish a single frame depending on the sample fluorescence intensity. For *in vivo* live acquisitions, the TCSPC approach might be less useful if real-time visualization is required. Frequency domain FLIM (Gratton et al., 2003) acquisition followed by ML could be another approach to overcome acquisition time limitation. Another limitation is the variability of relative shift in the exponential decay, although this can be overcome with the fitting-based method. The FBM already deals with shifts during the fitting process by the fitting software. It could be an issue with the decay-based method where the shift is not taken into account. It might be one of the reasons why the decay-based method did not yield good results with tissue sections. We plan to address the issue with the decay-based approach in tissue sections by using more training data in the future, incorporating the IRF and adding more classification features that consider morphology and/or the intensity of different spectral channels. One major limitation of our experiment was that we did not identify True Negative (TN) and as a result all the components of confusion matrix and accuracy can't be determined. For the mixed glial culture the TNs would be the non-microglia glial cell. But it is more complicated in brain tissue to define TN as the brain tissue is heterogenous and consist of components that are challenging to define in terms of TN. One final limitation would be the variability of NADH lifetimes from sample to sample. Based on the microenvironment, the NADH lifetime can vary even though the cells/tissues are treated similarly. One way to overcome this limitation would be to train with larger datasets with similar treatments.

5 Conclusion

We have demonstrated a novel machine learning based approach that can use FLIM data to identify microglia based on NADH lifetime parameters. We have successfully shown the effectiveness of the method in both cells and tissue slices, and achieved close to 90% True Positive Rate with relatively low False Discovery Rate. Additionally, we have shown that the decay can be used to directly identify microglia using ANN without exponential curve fitting. This approach can be further enhanced to calculate lifetimes and other parameters from lifetime decay data directly using machine learning.

6 Reference

Alfonso-García, A., Smith, T.D., Datta, R., Luu, T.U., Gratton, E., Potma, E.O., and Liu, W.F. (2016). Label-free identification of macrophage phenotype by fluorescence lifetime imaging microscopy. JBO *21*, 046005.

Bennett, M.L., Bennett, F.C., Liddelow, S.A., Ajami, B., Zamanian, J.L., Fernhoff, N.B., Mulinyawe, S.B., Bohlen, C.J., Adil, A., Tucker, A., et al. (2016). New tools for studying microglia in the mouse and human CNS. Proc. Natl. Acad. Sci. U.S.A. *113*, E1738-1746.

Berezin, M.Y., and Achilefu, S. (2010). Fluorescence Lifetime Measurements and Biological Imaging. Chem Rev *110*, 2641–2684.

Bhattacharjee, A., Datta, R., Gratton, E., and Hochbaum, A.I. (2017). Metabolic fingerprinting of bacteria by fluorescence lifetime imaging microscopy. Scientific Reports *7*, 3743.

Bird, D.K., Yan, L., Vrotsos, K.M., Eliceiri, K.W., Vaughan, E.M., Keely, P.J., White, J.G., and Ramanujam, N. (2005). Metabolic Mapping of MCF10A Human Breast Cells via Multiphoton Fluorescence Lifetime Imaging of the Coenzyme NADH. Cancer Res *65*, 8766–8773.

Charles, N.A., Holland, E.C., Gilbertson, R., Glass, R., and Kettenmann, H. (2011). The brain tumor microenvironment. Glia *59*, 1169–1180.

Chia, T.H., Williamson, A., Spencer, D.D., and Levene, M.J. (2008). Multiphoton fluorescence lifetime imaging of intrinsic fluorescence in human and rat brain tissue reveals spatially distinct NADH binding. Opt. Express, OE *16*, 4237–4249.

Crain, J.M., Nikodemova, M., and Watters, J.J. (2013). Microglia express distinct M1 and M2 phenotypic markers in the postnatal and adult central nervous system in male and female mice. Journal of Neuroscience Research *91*, 1143–1151.

Das, B., Shi, L., Budansky, Y., Rodriguez-Contreras, A., and Alfano, R. (2018). Alzheimer mouse brain tissue measured by time resolved fluorescence spectroscopy using single- and multi-photon excitation of label free native molecules. Journal of Biophotonics *11*, e201600318.

Denk, W., Strickler, J.H., and Webb, W.W. (1990). Two-photon laser scanning fluorescence microscopy. Science *248*, 73–76.

Flexman, M.L., Kim, H.K., Gunther, J.E., Lim, E.A., Alvarez, M.C., Desperito, E., Kalinsky, K., Hershman, D.L., and Hielscher, A.H. (2013). Optical biomarkers for breast cancer derived from dynamic diffuse optical tomography. J Biomed Opt *18*, 096012.

Foresee, F.D., and Hagan, M.T. (1997). Gauss-Newton approximation to Bayesian learning. In Proceedings of International Conference on Neural Networks (ICNN'97), pp. 1930–1935 vol.3.

Freudiger, C.W., Min, W., Saar, B.G., Lu, S., Holtom, G.R., He, C., Tsai, J.C., Kang, J.X., and Xie, X.S. (2008). Label-Free Biomedical Imaging with High Sensitivity by Stimulated Raman Scattering Microscopy. Science *322*, 1857–1861.

Garden, G.A., and Möller, T. (2006). Microglia Biology in Health and Disease. Jrnl NeuroImmune Pharm *1*, 127–137.

Gratton, E., Breusegem, S., Sutin, J., Ruan, Q., and Barry, N. (2003). Fluorescence lifetime imaging for the two-photon microscope: time-domain and frequency-domain methods. J. Biomed. Opt *8*, 381–390.

Kantelhardt, S.R., Kalasauskas, D., König, K., Kim, E., Weinigel, M., Uchugonova, A., and Giese, A. (2016). In vivo multiphoton tomography and fluorescence lifetime imaging of human brain tumor tissue. J Neurooncol *127*, 473–482.

Kirkpatrick, N.D., Hoying, J.B., Botting, S.K., Weiss, J.A., and Utzinger, U. (2006). In vitro model for endogenous optical signatures of collagen. JBO *11*, 054021.

Krizhevsky, A., Sutskever, I., and Hinton, G.E. (2012). ImageNet Classification with Deep Convolutional Neural Networks. In Advances in Neural Information Processing Systems 25, F. Pereira, C.J.C. Burges, L. Bottou, and K.Q. Weinberger, eds. (Curran Associates, Inc.), pp. 1097–1105.

Lakowicz, J.R., Szmacinski, H., Nowaczyk, K., and Johnson, M.L. (1992). Fluorescence lifetime imaging of free and protein-bound NADH. PNAS *89*, 1271–1275.

Leppert, J., Krajewski, J., Kantelhardt, S.R., Schlaffer, S., Petkus, N., Reusche, E., Hüttmann, G., and Giese, A. (2006). Multiphoton Excitation of Autofluorescence for Microscopy of Glioma Tissue. Neurosurgery *58*, 759–767.

Linkert, M., Rueden, C.T., Allan, C., Burel, J.-M., Moore, W., Patterson, A., Loranger, B., Moore, J., Neves, C., MacDonald, D., et al. (2010). Metadata matters: access to image data in the real world. J Cell Biol *189*, 777–782.

Mongeon, R., Venkatachalam, V., and Yellen, G. (2016). Cytosolic NADH-NAD+ Redox Visualized in Brain Slices by Two-Photon Fluorescence Lifetime Biosensor Imaging. Antioxidants & Redox Signaling *25*, 553–563.

Provenzano, P.P., Eliceiri, K.W., and Keely, P.J. (2008). Multiphoton microscopy and fluorescence lifetime imaging microscopy (FLIM) to monitor metastasis and the tumor microenvironment. Clin Exp Metastasis *26*, 357–370.

Rinnenthal, J.L., Börnchen, C., Radbruch, H., Andresen, V., Mossakowski, A., Siffrin, V., Seelemann, T., Spiecker, H., Moll, I., Herz, J., et al. (2013). Parallelized TCSPC for Dynamic Intravital Fluorescence Lifetime Imaging: Quantifying Neuronal Dysfunction in Neuroinflammation. PLOS ONE *8*, e60100.

Skala, M.C., Squirrell, J.M., Vrotsos, K.M., Eickhoff, J.C., Gendron-Fitzpatrick, A., Eliceiri, K.W., and Ramanujam, N. (2005). Multiphoton Microscopy of Endogenous Fluorescence Differentiates Normal, Precancerous, and Cancerous Squamous Epithelial Tissues. Cancer Res *65*, 1180–1186.

Skala, M.C., Riching, K.M., Bird, D.K., Gendron-Fitzpatrick, A., Eickhoff, J., Eliceiri, K.W., Keely, P.J., and Ramanujam, N. (2007). In vivo multiphoton fluorescence lifetime imaging of protein-bound and free nicotinamide adenine dinucleotide in normal and precancerous epithelia. JBO, JBOPFO *12*, 024014.

Stringari, C., Nourse, J.L., Flanagan, L.A., and Gratton, E. (2012). Phasor Fluorescence Lifetime Microscopy of Free and Protein-Bound NADH Reveals Neural Stem Cell Differentiation Potential. PLOS ONE *7*, e48014.

Stuntz, E., Gong, Y., Sood, D., Liaudanskaya, V., Pouli, D., Quinn, K.P., Alonzo, C., Liu, Z., Kaplan, D.L., and Georgakoudi, I. (2017). Endogenous Two-Photon Excited Fluorescence Imaging Characterizes Neuron and Astrocyte Metabolic Responses to Manganese Toxicity. Sci Rep *7*, 1041.

Suhling, K., French, P.M.W., and Phillips, D. (2005). Time-resolved fluorescence microscopy. Photochem. Photobiol. Sci. *4*, 13–22.

Suhling, K., Hirvonen, L.M., Levitt, J.A., Chung, P.-H., Tregidgo, C., Le Marois, A., Rusakov, D.A., Zheng, K., Ameer-Beg, S., Poland, S., et al. (2015). Fluorescence lifetime imaging (FLIM): Basic concepts and some recent developments. Medical Photonics *27*, 3–40.

Sun, Y.H., Hatami, N., Yee, M., Phipps, J.E., Elson, D.S., Gorin, F., Schrot, R.J., and Marcu, L. (2010). Fluorescence lifetime imaging microscopy for brain tumor image-guided surgery. JBO *15*, 056022.

Szulczewski, J.M., Inman, D.R., Entenberg, D., Ponik, S.M., Aguirre-Ghiso, J., Castracane, J., Condeelis, J., Eliceiri, K.W., and Keely, P.J. (2016). *In Vivo* Visualization of Stromal Macrophages via label-free FLIM-based metabolite imaging. Scientific Reports *6*, srep25086.

Tambuyzer, B.R., Ponsaerts, P., and Nouwen, E.J. (2009). Microglia: gatekeepers of central nervous system immunology. Journal of Leukocyte Biology *85*, 352–370.

Wang, X.F., Periasamy, A., Herman, B., and Coleman, D.M. (1992). Fluorescence Lifetime Imaging Microscopy (FLIM): Instrumentation and Applications. Critical Reviews in Analytical Chemistry *23*, 369–395.

Watters, J.J., Schartner, J.M., and Badie, B. (2005). Microglia function in brain tumors. Journal of Neuroscience Research *81*, 447–455.

Wu, G., Nowotny, T., Zhang, Y., Yu, H.-Q., and Li, D.D.-U. (2016). Artificial neural network approaches for fluorescence lifetime imaging techniques. Opt. Lett., OL *41*, 2561–2564.

Yan, L., Rueden, C.T., White, J.G., and Eliceiri, K.W. (2006). Applications of combined spectral lifetime microscopy for biology. Biotechniques *41*, 249.

Yaseen, M.A., Sutin, J., Wu, W., Fu, B., Uhlirova, H., Devor, A., Boas, D.A., and Sakadžić, S. (2017). Fluorescence lifetime microscopy of NADH distinguishes alterations in cerebral metabolism in vivo. Biomed. Opt. Express, BOE *8*, 2368–2385.

(2017). Encyclopedia of Machine Learning and Data Mining (Springer US).

Chapter 4

Optical fiber-based dispersion for spectral discrimination in FLIM

This chapter was adapted from

"Optical fiber-based dispersion for spectral discrimination in fluorescence lifetime imaging systems", Md Abdul Kader Sagar, Bing Dai, Jenu V. Chacko, Joshua J. Weber, Andreas Velten, Scott T Sanders, John G White, Kevin W Eliceiri, Journal of Biomedical Optics

Summary. The excited state lifetime of a fluorophore together with its fluorescence emission spectrum provide information that can yield valuable insights into the nature of a fluorophore and its microenvironment. However, it is difficult to obtain both channels of information in a conventional scheme as detectors are typically configured either for spectral or lifetime detection. In this work, we present a fiber-based method to obtain spectral information from a multiphoton fluorescence lifetime imaging (FLIM) system. This is made possible by using the time delay introduced in the fluorescence emission path by a dispersive optical fiber coupled to a detector operating in time-correlated single photon counting (TCSPC) mode. This add-on spectral implementation requires only a few simple modifications to any existing FLIM system and is considerably more cost-efficient compared to currently available spectral detectors.

Keywords: Hyperspectral Imaging, Multiphoton Microscopy, Fiber-based dispersion, time-correlated single photon counting, FLIM, fluorescence lifetime

1 Introduction

Fluorescence lifetime imaging microscopy (FLIM) is a microscopy technique that maps the fluorescence lifetime values at each voxel (the average time spent by the molecule in the excited state) into image contrast. FLIM can reveal spatial variations in the microenvironment of a sample by the virtue of the molecule's available electronic states and the relaxation times from those levels to its ground state(Strickler and Berg, 1962). The technique of molecular probing using fluorescence lifetime has enabled the development of optical methods that reveal a wide range of properties including molecular binding activity, and autofluorescence based diagnostics(Suhling et al., 2017). Another fluorescence methodology which can provide information on the identity and microenvironment of a molecule is spectral or, when implemented across a broader sensing range, as hyperspectral imaging (HSI)(Chang, 2003).

FLIM measures the fluorescence intensity as a function of time between excitation and fluorescence emission. Time domain FLIM acquisition methods use high time resolution electronics to measure the arrival time of the emission photon relative to the time of excitation photon pulse. Fluorescence is a stochastic process; many individual photon events must be measured to characterize the lifetime of a fluorophore. The minimum number of events needed to accurately determine the fluorescence lifetime limits the speed of fluorescence lifetime imaging. Hyperspectral imaging is an imaging technique that maps the fluorescence emission spectrum as a false color image(Haraguchi et al., 2002). These techniques are well-established and are currently used in a wide range of applications from food and dietary sciences(Qiao et al., 2007) to semiconductor nanocrystals studies and quantum dots(Michalet et al., 2005). The simultaneous detection of spectral and lifetime information provides extra dimensions of data from fluorescence signals which can be used to facilitate the identification of a fluorophore. These environmentally sensitive fluorescence parameters can determine aspects of the molecule's physical and chemical association with other molecules.

With a combined FLIM-HSI correlative microscopy scheme, each dimension (spectrum and lifetime) is simultaneously acquired. However, when multiple fluorophores are present in the sample, the resulting histogram of emission events is no longer a simple exponential decay or a single emission spectrum. The events from multiple fluorophores are combined (both spectrally and temporally). In order to separate different species of fluorescence emission, spectral methods like *linear un-mixing*(Fereidouni et al., 2012) or *deconvolution*(Griffiths and Pariente, 1986) can be used for HSI and *phasor analysis*(Digman and Gratton, 2014) and *multi-exponential fitting* can be used for FLIM. However, these deconvolution approaches grow more complicated with increasing numbers of fluorophores (*i.e.*, with an increasing number of contributions from different

exponentials), and thus the approach is limited to a small number of spectral components. However, these methods have been successful in computationally deconvolving the overlapping curves to separate up to seven independent species(Becker et al., 2007; Cranfill et al., 2016; Cutrale et al., 2017; Meagher et al., 1998). Recently, correlative species identification schemes that use both spectral and lifetime information have been introduced(Beule et al., 2007; Campos-Delgado et al., 2015).

Multispectral FLIM is implemented currently using one of the following strategies. Samples can be imaged multiple times, each time using a different optical band pass filter. However, acquiring multiple images is generally undesirable, as it is time-consuming, and multiple exposures increase the risk of photobleaching or otherwise damaging the sample. This approach can also be implemented as simultaneous imaging of two or more channels by splitting the emission spectra into multiple fixed spectral bandwidth channels by dichroic mirrors and filters, with each channel sharing the timing electronics by intelligent routing. Roberts et al implemented a 4 channel TCSPC system where each channel has an individual PMT(Roberts et al., 2011). Another option is to simultaneously measure all of the spectrum using a spatially dispersive optical element such as a prism(Hanley et al., 2002) or a grating(Bird et al., 2004; Yan et al., 2006) and directing the emission on to multiple timing detectors. The dispersive element and multiple detectors however make this a technically complicated and expensive solution. Following the line of reasoning to use dispersive elements in the optical path for spectral separation: instead of using an optical prism or optical grating to introduce dispersion, one could use an optical fiber to achieve chromatic dispersion. Effective utilization of dispersive properties of optical fibers has been demonstrated in various optical communication applications such as wavelength division optical multiplexing (WDM) (Liew et al., 2016) and optical time domain reflectance characterization

(OTDR)(Personick). By specifying the length and choosing the right material, the optical fiber can introduce appropriate dispersion to allow the separation of the fluorescence emission spectrum to the desired resolution. This approach forms the basis of this study.

Prior studies demonstrating spectral imaging using optical fibers as the dispersive element have been reported in the literature. Sun et al(Sun et al., 2008) demonstrated a novel fiber optics-based method for simultaneous time and wavelength resolved fluorescence spectroscopy by combining 3 sets of bandpass filters and dichroic mirrors in a single acquisition. Three channels were coupled by optical fibers to introduce temporal delays. This approach was extended by Shestha et al(Shrestha et al., 2010) to integrate the scheme in a scanning multispectral FLIM system. The dichroic mirror and filters were chosen such that it can separate emission spectra of three fluorophores to three channels. Optical fibers of different lengths were used to introduce distinct temporal delays for each channel, thus allowing for multi-channel spectral FLIM with a single detector, a significant step up from the multi-detector approach [17]. Nevertheless, this approach replies on the combination of filters, dichroic mirrors, and optical fibers to achieve spectral-FLIM thus requiring considerable modifications to a conventional multiphoton microscope. Also, in these systems the optical fibers were used to route the signal rather than for their dispersive properties. However, a fiber based multi-channel that used this setup was used to detect glycosaminoglycan (GAG) loss in articular cartilage(Zhou et al., 2018). The utilization of dispersive property of optical fiber has been used to generate a rapid excitation scan. Rapid wavelength scan of laser-induced fluorescence was demonstrated by transmitting broadband excitation light through a mile-long optical fiber which introduced group-velocity (*i.e.*, spectral) dispersion(Walewski and Sanders, 2005). Goda *et al*.(Goda et al., 2009) used a STEAM (serial time-encoded amplified microscopy) camera along with an optical fiber to effectively map a 2D

spatial image into a serial time-domain data stream for ultra-fast real time optical imaging. However, this does not work with low intensity signals such as fluorescence emission and gives no spectral information on the specimen. Redding(Redding and Cao, 2012; Redding et al., 2013) demonstrated a high-resolution spectrometer by reconstructing an arbitrary spectrum from the output intensity profile recorded by a 2D camera, based on pre-calibrated wavelength-dependent speckle patterns produced by interference between the guided modes of a multimode optical fiber. The idea was extended by integrating a wavelength division multiplexer with seven multimode fibers to increase the spectral bandwidth(Liew et al., 2016). While the sub-nanometer resolution was achieved along with 100-nm bandwidth, this technique lacks lifetime imaging capability. One study(Petrov et al., 2011) has demonstrated utilizing dispersive property of optical fiber to perform Raman spectroscopy without spectrometer. This fiber based approach was extended(Toussaint et al., 2015) using superconducting nanowire single-photon detector for higher temporal accuracy.

In this paper, we propose a simple, cost-efficient method that, by the addition of an optical fiber to a conventional single detector multiphoton FLIM microscope, we are able to obtain spectral information of emission signals which is otherwise unavailable without the fiber in addition to the lifetime information. This method will work with any multiphoton or confocal microscope with a pulsed excitation scheme and a time-correlated single photon counting electronics (TCSPC). While it is demonstrated using time-domain single photon counting, this method is extendable to other systems capable of measuring lifetime. The method proposed here produces additional spectral information together with the lifetime distribution within the field of view. We first present the theory and rationale, then describe the experiment setup and report the optimizations obtained with an appropriate choice of commercially available optical fibers. The measurements are validated and data analysis techniques to map spectral separation are provided to enable the

extension of the imaging capabilities of a FLIM system to combined HSI-FLIM. Proof of principle experiments are demonstrated where spectral and lifetime information is extracted from signals from fluorescent beads and fluorescently labeled cells. The impact of the technique and its potential are finally discussed.

2 Theory

Generally, optical chromatic dispersion is used to separate different wavelengths in spectrally resolved lifetime imaging systems. However, instead of relying on spatial dispersion to send different wavelengths of light to different detectors (such as with a prism or grating), temporal chromatic dispersion introduced by an optical fiber is used to separate all the wavelengths and send them to a single detector in sequence (refer figure 1).

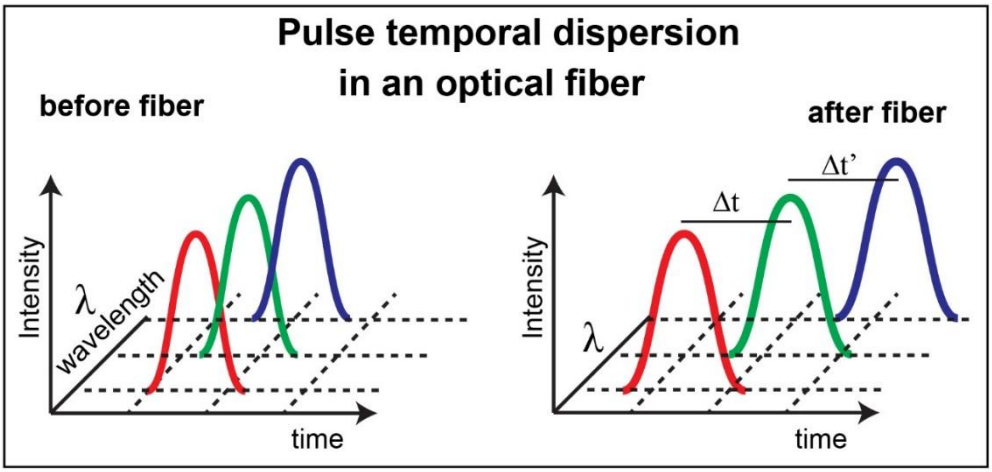

Fig. 1 Spectral separation achieved by virtue of the temporal chromatic dispersion of an optical fiber.

Spectral dispersion is achieved by guiding the emission fluorescence signal through a multimode optical fiber, which introduces different travel times for different wavelengths of light that travel

through the fiber, *i.e.*, chromatic dispersion. The red (longer wavelength) components of the fluorescence, which see a lower index of refraction, travel faster through the fiber than the blue (shorter wavelength). Thus, the spectral information of the fluorescence is encoded into the timing of the photon arrival at the detector. Once the decay curves of fluorophores at each pixel are recorded by a TCSPC, computational deconvolution of the decay curves allow one to separate individual decay curves from different colored fluorophores. This deconvolution is practically limited by the finite instrument response function (IRF) of the photon detector (Commercial TCSPC systems vary from 100 to 350 ps IRF with a time resolution of ~40 ps). The spectral information content per pixel is convolved with the lifetime histogram which in turn is convolved with the shape of the IRF. Hence, the average spectral information can be deduced as the average relative time delay (or shift) of the leading edge of each fluorescence decay curve. In this manner, with knowledge of the dispersion characteristics of the fiber such as the Sellmeier coefficients of the material of the fiber, attenuation, and bandwidth, it is possible to determine the mean wavelength of a photon distribution encoded in the transit delay through the fiber without deconvoluting the decay curves.

If the spectral dispersion in the fiber is sufficient, there is enough time difference between the arrival times of the different colors of light at the detector that the fluorescence decay curves for the individual fluorophores can be separated. The temporal dispersion experienced by the emission light in the optical fiber is a consequence of the wavelength-dependent index of refraction. The time delay for a light pulse (assuming plane wave) propagating through an optical fiber of length L is $L(n - \lambda dn/d\lambda)/c$, where c is the speed of light in vacuum. The speed of light in a medium, v, is then approximated as $v=c/n_\lambda$, where n_λ is the wavelength-dependent group refractive index.

Therefore, the transit time difference through an optical fiber for light of two different wavelengths can be written as

$\Delta t = L/v_{\lambda 1} - L/v_{\lambda 2}$

$\Delta t = L(n_{\lambda 1} - n_{\lambda 2})/c$

$$\Delta t = L\,\Delta n_{\lambda}/c \quad (1)$$

For common optical glasses, the index of refraction variation over the visible region of the spectrum is small, generally less than 1%(Bansal and Doremus, 2013). For example, for fused silica (a commonly used material for glass optical fiber fabrication), group refractive indices of n = 1.4623 at 500 nm and 1.4618 at 510 nm are reported. With fast detectors and timing electronics with a resolution of 50 ps, in order to achieve 10 nm spectral resolution, we will need a fiber length of 30 m. In our proposed experiment, we, therefore, adopt optical fibers of at least 10 m long for the sake of sufficient spectral separation. More detailed analysis is presented in Section 4.1.

3 Methods

3.1 Experimental setup

A schematic of our experimental setup is shown in Figure 2. This instrumentation is implemented on a custom-built multiphoton microscope built around an inverted Nikon microscope frame (Nikon Eclipse TE2000). The excitation source is a tunable ultrafast Titanium: Sapphire laser (Coherent Chameleon Ultra II) with a pulse repetition rate of 80 MHz. The imaging was carried out using a 20x air objective (Nikon, Plan Apo VC, NA = 0.75) and a 60x oil objective (Nikon, Plan Apo VC, NA = 1.4). The emission beam splitters in the microscope frame allow one to direct

the fluorescence emission into a custom-built side arm on a fixed optical cage assembly or to the regular imaging ports. A Uniblitz shutter (not shown in the schematic), which only opens during active image acquisition, is employed on the side port before the 50 mm lens to protect the detector from unintentional over-exposure of light. The emission light is demagnified in beam diameter by a telescopic lens combination of plano-convex lenses (f = 50 mm Φ = 1" and f = 20 mm Φ = 1/2", respectively, Thorlabs N-BK7). This smaller beam diameter allows a better optical coupling to the fiber coupler (Thorlabs CFC-11X-A) with a built-in aspheric collimating lens (f = 11 mm, NA = 0.3, clear aperture Φ = 6.6 mm).

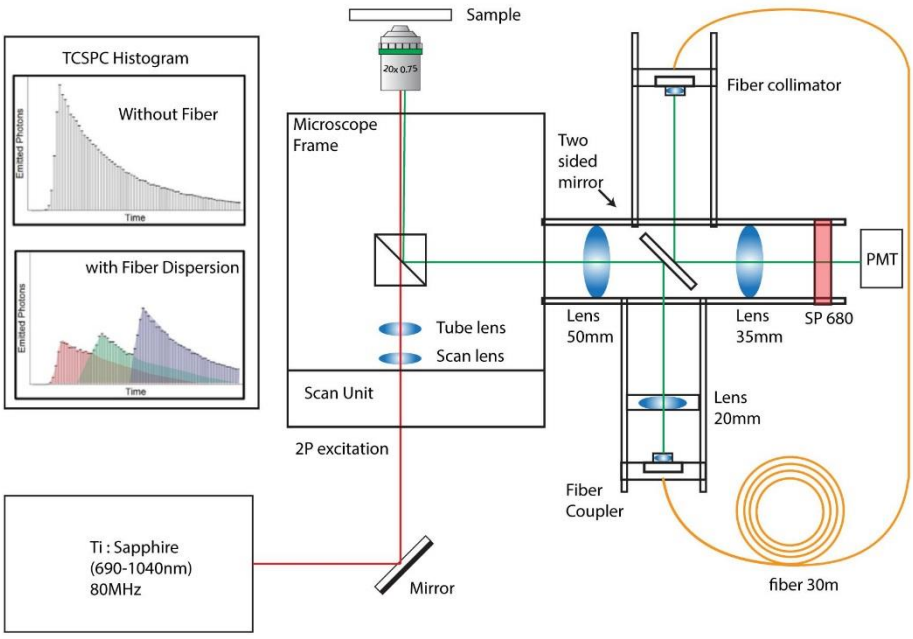

Fig. 2 Schematic of the fiber based spectral lifetime experimental setup. (PMT: Photo multiplier tube, SP680: 680 nm short pass filter). The figure inset TCSPC histograms show representative temporal spread in RGB wavelengths. Without the fiber, i.e., in conventional TCSPC setup, fluorescent decay curves for three separate fluorophores overlap and the contribution from the individual fluorophores are not evident (top). With the spectral separation

introduced by the fiber, the different colored fluorophores are easier to distinguish, even without deconvolution (bottom).

The fiber coupler is mounted on a tiltable cage plate (Thorlabs KC1-S X/Y/Tilting cage plate) with adjustable axial distance and angle between the fiber tip and the collimating lens to aid in optical coupling. On the output end of the fiber, a fiber collimator (Thorlabs F810C-543) is used with a doublet lens (f = 35 mm), followed by a condenser lens (f = 35 mm) that focus the emission light onto a GaAsP photon counting photomultiplier tube (PMT) (Hamamatsu H7422P-40, Hamamatsu Photonics, Bridgewater, NJ). From the detector, photon data is time tagged using TCSPC Electronics (SPC-150 Photon Counting Electronics, Becker & Hickl GmBH, Berlin, Germany). The fluorescence decay histogram is created within a 12.5 ns temporal duration defined by laser pulses (for 80 MHz laser). The duration is divided to 256 time-bins by an 8-bit time to digital conversion (TDC). Each time bin is approximately 40 ps and each photon collected during the 12.5 ns acquisition window is placed in one of the time bins based on the arrival time with respect to the laser signal. The distribution of photons in the 256 time-bins essentially creates the fluorescence decay histogram. A 680 nm short pass filter (Semrock FF01-680/SP-25) is placed in front of the PMT to block any residual multiphoton excitation light in the emission path. An additional feature of the experimental setup is the removable back-to-back mirrors (Thorlabs PFR10-P01) on the cage assembly (Thorlabs 30mm). The mirrors can be easily removed, and then the collecting lens focuses the light from the microscope directly on the detector, bypassing the fiber. This allows convenient switching between spectral separation setup (with the mirrors) and conventional single-channel FLIM (without the mirrors). Whilst this mirror is not essential to the experiment, it provides a convenient way to verify the performance of the system by imaging with

and without the fiber. A challenge with this presented spectral lifetime fiber implementation is the efficient coupling of the uncollimated sample emission light into the fiber. Multimode fibers with large core diameters facilitate this coupling. This is discussed later in Section 4.1 on fiber - scan angle dependence.

3.2 Fibers in the experiment

Primarily due to scattering, the propagation of visible light through the core of the optical fiber suffers from intensity loss (attenuation). The fluorescence emission spectra for commonly used fluorophores falls in the wavelength range of 400 nm to 700 nm, so fibers with lower attenuation in this range are required. Glass fibers are preferred over plastic ones owing to their lower attenuation(Acakpovi and Matoumona, 2012). Based on manufacturer's datasheets (Corning([CSL STYLE ERROR: reference with no printed form.]), Fujikura([CSL STYLE ERROR: reference with no printed form.]), Thorlabs([CSL STYLE ERROR: reference with no printed form.])), the attenuation of common off-the-shelf glass fibers are between 30 to 60 dB/km (~66% -81% transmission for 30 meter length) at 445 nm. The transmission of the fibers listed in Table 1 were measured with a 445 nm laser. Modal dispersion was measured by sending a second harmonic generation (SHG) signal through a fiber and measuring the rise time of the transmitted pulse (*i.e.*, instrument response function, IRF) by using Becker & Hickl TCSPC electronics. An SHG signal from a Urea crystal (Sigma-Aldrich) was used rather than a fluorescence signal because it is a quasi-instantaneous process, which allows the IRF to be measured without the effects of fluorescence life-time delays in the sample. The IRF is broadened by the modal dispersion, and is also affected by the finite spectral bandwidth of the SHG radiation, when measured with a fiber.

Nevertheless, in our experiment, the IRF measured with fibers was close to or below the resolution limit of the utilized FLIM system (~200 ps) and thus these data were not included. Due to broadening of the IRF, the accuracy of determining arrival time of photon should be slightly lower. The relative change in the FWHM is ~137% "with fiber" when compared to "without-fiber" case and accuracy should scale accordingly.

Table 1 List of optical fibers used in the Spectral Lifetime experiment. Some data are unavailable from the manufacturers. Values in *italic* are measured by authors.

Fiber Model	**Type**	**Core Material**	**Core diameter (μm)**	**Length (m)**	**NA**	**Attenuation (dB/km) @ 445nm**	**Measured Transmission @ 445nm (%)**
Corning Clear Curve OM4	GRIN	silica	50	30	0.2	-	*71*
Corning InfiniCor300 OM1			62.5	10, 30, 50	0.275	-	*83 / 65 / 53*
Newport F-MLD-C		Unknown*	100	30	0.29	-	*58*
Fujikura G.400/500		GeO2-SiO2/SiO2	400	30	0.21	30	-
Fujikura G.600/750			600	30	0.21	30	-

Fujikura G.800/1000			800	30	0.21	30	-
Thorlabs FP400URT	Step index	silica	400	10	0.5	30	*65*
Thorlabs FP400ERT			400	30	0.5	60	*61*
Thorlabs FP400URT			400	50	0.5	30	*45*

3.3 Sample preparation

3.3.1 Mixed fluorescence beads

The bead samples used in our experiments were mixed fluorescent microspheres (Polysciences, Inc) that have distinct, well-characterized emission spectra. The two kinds of beads were used: Fluoresbrite® 10μm YG carboxylate microspheres (Cat#18142-2([CSL STYLE ERROR: reference with no printed form.]), emission peak 486 nm) and Fluoresbrite® 2.0μm polychromatic Red microspheres (Cat#19508-2([CSL STYLE ERROR: reference with no printed form.]), emission peak 565 nm). The mixture was applied to the surface of a glass microscope slide, dried, and then covered with a #1.5 coverslip, which was then sealed with nail polish. In each mixture, the two kinds of microspheres were chosen so that they share common excitation wavelengths and their distinct emission peaks were ~80 nm apart. The measured lifetime value for YG beads was

2.45 ns and for RED beads was 2.80 ns. Instrument response for TCSPC was measured as the SHG signal from Urea crystals (Sigma-Aldrich).

3.3.2 Cells

Fixed bovine pulmonary artery endothelial cells (BPAEC) purchased from ThermoFisher (Catalog # F36924) were pre-labeled with: MitoTracker® Red CMXRos for mitochondria, Alexa Fluor® 488 phalloidin for F-Actin, and DAPI for nuclei.

3.4 Data Analysis

The spectral information is extracted from the lifetime data by calculating the shift (i.e. delay) of the peak position of the exponential decay curve. Typical lifetime data analysis requires an IRF which is measured using second harmonic generation (SHG) to estimate the excitation laser pulse's position and the instrument timing resolution. Measured lifetime curves are convolved with this system response function. Decay fitting of lifetime curve uses a parameter called 'shift' which is the timing difference of the peak of fluorescence decay to the excitation pulse due to the IRF. In the case of the data taken with the fiber, this shift of lifetime curve with respect to the IRF is dominated by the spectral shift: the wavelength-based delay (i.e. temporal chromatic dispersion) introduced by the fiber (~20 ps/nm) for a 30m long fiber generates ~400ps for 20nm spectral difference. This is significantly larger than the measured IRF of 200ps for the final system presented (a 10 nm spectral shift shifts the IRF by its FWHM). Since the spectral shift produced by the fiber is a linear function of this measured shift in peak position (Figure 6C), the spectral value per pixel may be determined by the shift of the peak of the decay curve measured for each pixel (each lifetime curve yields one wavelength). Practically, TCSPC works at the single photon regime and a spatial binning can be used to aggregate the photons from neighboring pixels to

reduce the error in estimating the peak of the decay curve. A 5x5 pixel binning can improve the accuracy of determining the center of shift by 5 times.

The workflow used to determine both lifetime and spectral distribution has 3 main steps. 1) Calculating shift from decay curve, 2) Determining the fiber calibration factor (ratio of unit shift in wavelength to unit shift in time), 3) Mapping the shift from each pixel to emission spectral peaks based on this calibration factor using output of step 1 and 2. Finally, an additional optional step would be deconvolution of IRF and estimation of lifetime. The lifetime data presented in the study uses the lifetime estimation by mathematical fitting provided by the TCSPC analysis software SPCImage (Becker & Hickl GmbH). SPCImage offers a time-shift estimation along with the lifetime estimation. The shift parameter in SPCImage determines the temporal shift of the rising edge of the decay curve relative to the IRF (taken with fiber) position. Unfortunately, the SPCImage estimation of shift is coupled to the lifetime fitting algorithm and requires significant computational time. We wrote a code-snippet that calculates the location of the peak of the lifetime decay independent of the fitting procedure and all the figures shown in this paper which displays delay measurement are generated using this method. This method is fast and can extract the delay information virtually instantaneously without the exponential curve fitting required by SPCImage to calculate shift. For the data that show lifetime in this paper, the lifetimes were calculated using SPCImage. For Step 2, we measured the shift for a series of second harmonic generation wavelengths with the fiber and the calibration factor was calculated by a linear fitting of wavelength vs shift plot. For example, the calibration factor for converting temporal shift to emission spectrum for 800µm 30m Fujikura fiber was estimated to be 1.90 nm/(40ps time-bin) in a 256 bin TCSPC collection scheme with a pulsed laser of 80 MHz repetition rate. Using these calibration data, the relative wavelengths (difference in the emission peaks with respect to the IRF

position) for a lifetime image can be mapped to each pixel's shift value. The shift image can also be adjusted using a custom calibration factor and/or a custom offset for adjusting the spectrum using a known maximum emission wavelength from a fluorescence dye.

Regions of Interest (ROI) were created by segmenting the intensity images using ImageJ. For the bead images presented, the beads were separated by a common intensity image mask and filtered by a size criterion of beads as YG (diameter>6 μm) and red (diameter< 4 μm) beads. This ROI based separation splits the image visually into two groups and their respective distribution of shift are measured. For calculating relative shift between the two groups, we calculate the difference in mean values for both distributions. For the cell images, the background is filtered out where the photon counts are low, and the colors are separated by visual separation of the morphology.

4 Results

4.1 System Optimization

A longer optical fiber will give a better spectral resolution, but it will also suffer from larger signal attenuation. Fluorescence emission from biological samples has limited signal strength, so it is desirable to obtain a compromise between transmission efficiency and sufficient spectral separation. In this section, various optical-fiber-related factors are studied for their effects on the system performance.

4.1.1 Fiber length

As discussed in Section 2, to achieve sufficient spectral separation in our proposed setup, the optical fiber should be on the order of 10 meters or longer. A variety of 'off-the-shelf' step-index

and graded-index optical fibers of different lengths were evaluated in our system by imaging the same sample: a mixture of 10 μm yellow-green (486nm emission peak) and 2 μm Red (565nm emission peak) fluorescent beads with the same excitation wavelength (980 nm) and at the same region of interest. This was made possible by the modular cage assembly and universal fiber couplers.

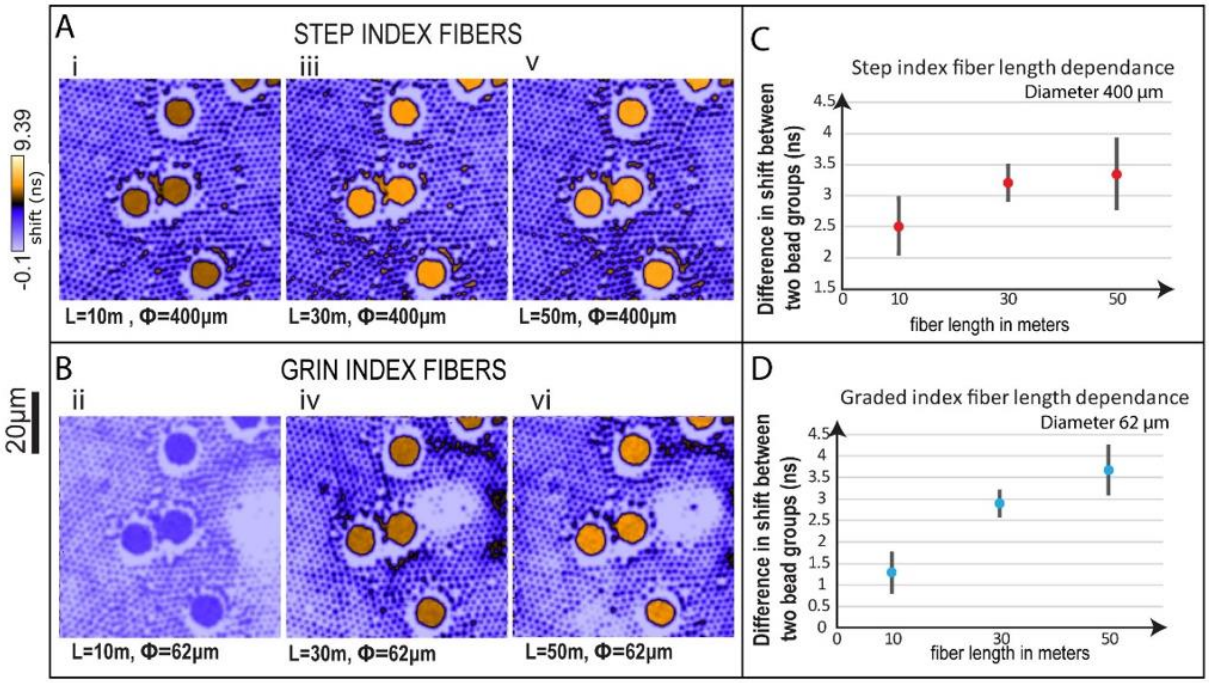

Fig. 3 Spectral separation (represented by relative temporal shift in ns between two bead groups) demonstrated with step-index and graded-index fibers of various lengths. The fibers used are (A) Thorlabs 400/425 μm step index fibers and (B) Corning InfiniCor300 OM1 62.5/125 μm graded index fibers of 10 m, 30 m, and 50 m in length, respectively (refer to Table 1). The fiber length (in meter) and fiber diameter (in um) are marked below each image. The sample is a mixture of 10 μm YG (emission 486 nm) and 2 μm Red fluorescent microspheres (emission 554 nm) excited at 490 nm. (C) and (D): the difference in averaged shift between two bead groups for 400um step index fibers and 62.5um GRIN fibers of 3 lengths. Images were taken with a 20x air objective (NA = 0.75). The acquisition time was 60 seconds for all the images in this paper unless otherwise specified.

At the same region of interest (ROI) on the same sample, FLIM data was recorded with Thorlabs 400/425 μm step index fibers and Corning InfiniCor300 OM1 graded index fibers of 10 m, 30 m, and 50 m in length. The temporal delay (shift) at each pixel introduced by the chromatic dispersion of a fiber is extracted from fluorescence delay curves and plotted as colormap at the same scale for all fibers (Figure 3A&B), using the method described in Section 3.4. The color contrast in the images represents the difference in the spectral distributions of two bead population (~ 80nm apart) translated in shift. In the shift images, higher color contrast between pixels corresponds to a larger relative temporal shift, thus resulting in a better spectral separation for different colored fluorophores in the same sample. The 10 m fibers can separate YG and Red beads whose emission peaks are ~80 nm apart; but longer fibers offer better spectral separations. The two 10m GRIN and STEP index fibers show significant differences between them. Although we have not examined this further, this is possibly due to differences in their composition and doping profiles.

Figure 3(C) and (D) show the difference in averaged shift between two bead ROIs (large YG beads -- small RED beads) for fibers of different lengths. The method was described in the last paragraph in Sec 3.4. For both step-index fiber and GRIN fibers, we observe the same trend, i.e., the delay increases with fiber length. The relationship may not be linear in the experiment possibly due to the nonlinear dependence of the group velocity (also the temporal delay) on the wavelength, the error in spatial segmentation where pixel of the neighboring segment are incorrectly accounted for, and the error in estimating the peak positions of decay curves. However, an underlying linear relationship is possible as this would be within our experimental error bounds.

The collimator lens in front of the fiber has a NA = 0.3. The Thorlabs step-index fibers have NA 0.5 and GRIN fibers 0.275. Therefore, the modes in the GRIN fibers were filled at the fiber input

but not those of the step-index fibers (although these can still be filled at the fiber output through a process called mode mixing or mode scrambling). Fibers were coiled in the same way as when they were shipped from the manufacturers, i.e., larger than the minimal suggested bending curvature.

4.1.2 Fiber diameter and fiber type

Within the field of view (FOV) of a laser scanning microscope, each pixel of the scan pattern in the sample plane represents an incident excitation at a particular galvanometer scan angle of the excitation beam on the back aperture of the objective lens. In our system (Figure 2), the emission signal from all of the pixels (i.e., scan angles) is relayed to the tip of the fiber for photon collection with the help of the additional optics on the side arm (f = 50 mm and f = 20 mm plano-convex lenses and the f = 11 mm collimator lens). The maximum field of view (i.e. at zoom 1) is achieved with a galvanometer scan angle of +/-3 degree. The excitation light is relayed to the objective using a scan lens and a tube, with the scan angle scaled down to ~ +/-1 degree after the tube lens. Therefore, the input scan angle to the side arm of the microscope on the left side of the 50mm lens is +/- 1 degree at zoom 1. The NA is 0.09 at the output of the microscope frame, and 0.3 at the input to the fiber.

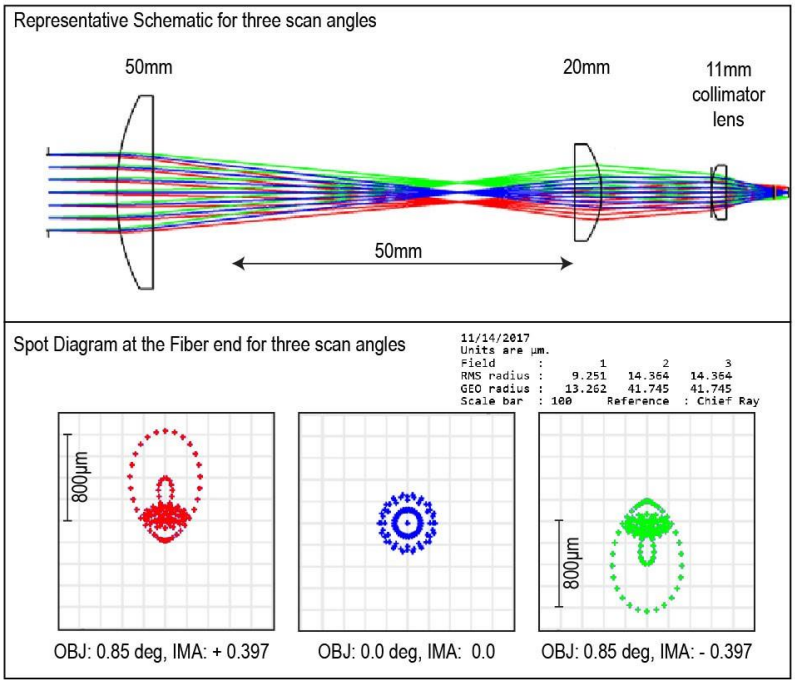

Fig. 4 Zemax simulation of the fiber coupling in the proposed system to study the theoretical limits of the transmission. The combination of f = 50mm (1" diameter) and f = 20mm (1/2" diameter) plano-convex lenses is used to reduce the beam diameter of fluorescent emission light, which is in turn focused to the tip of the fiber which is mounted to Thorlabs CFC-11x-A collimator by a built-in f=11mm aspheric lens (NA = 0.3). At +/- 0.85 degree input scan angle to f=50mm lens, the field of view at the tip of the fiber is 800 μm, matching the core diameter of Fujikura G.800/1000 graded index fiber. Different colors represent different scan angles.

The fiber coupling scheme of our current experimental setup was simulated with Zemax software (Figure 4). Assuming that the emission signal is perfectly focused at the tip of the fiber (i.e., minimizing the RMS radius of the focused beam), it has 930 μm FOV at the back focal plane of the collimator lens at nominal scan angle (+/- 1 degree on the left side of the 50mm lens at zoom 1), leading to 74% $(800um/930um)^2$ transmission coefficient. By reducing the scan angle, i.e., higher zoom, the FOV at the back focal plane of the collimator lens decreases, resulting in improved transmission ratio. The Zemax simulation shows that when the scan angle is <0.85

degree, the FOV at the tip of the fiber will be < 800 um, a size that matches the core diameter of Fujikura G.800/1000 graded index fiber (Table 1), leading to optimal coupling. Therefore, it is evident that the core diameter of the fiber selected should be as large as possible to allow for efficient coupling of emission signals from large scan angles.

Note that in our experiment, we intentionally defocus the incident beam at the tip of the fiber to allow the signal from large scan angles that would otherwise be focused outside the fiber core to be partially collected by the fiber, effectively increasing the FOV of the system, although at the cost of reduced transmission efficiency as well as more vignetting. It is especially helpful when we want to obtain a large FOV with small core fibers.

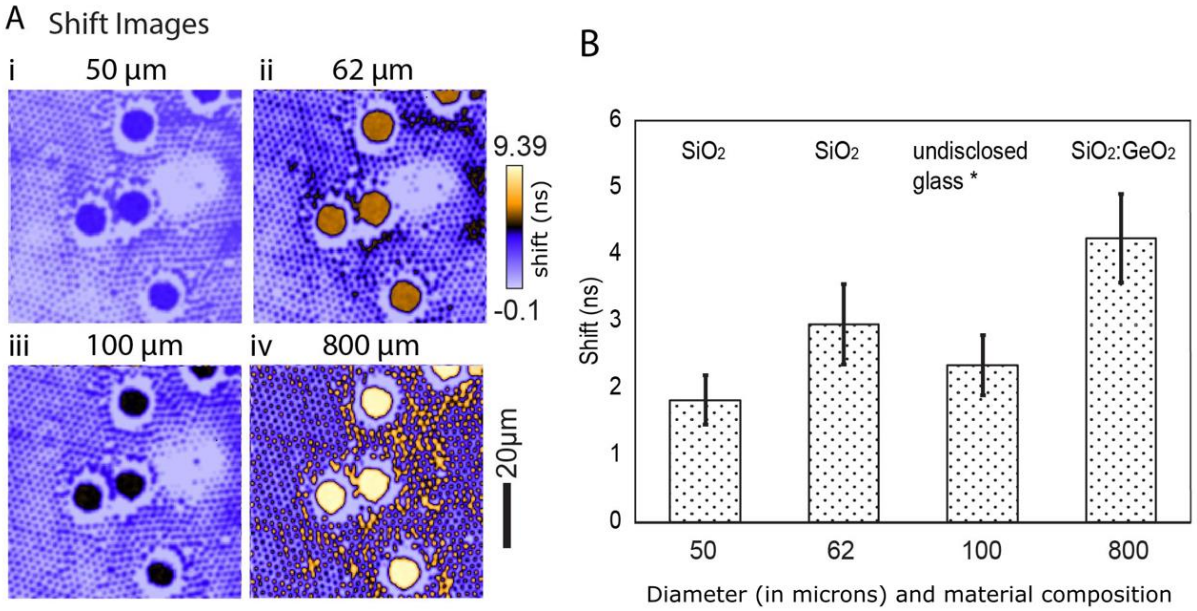

Fig. 5 Spectral separation (translated to relative temporal shift in ns) demonstrated with 30 m long graded-index fibers of various core diameters and material compositions. A-i: Corning ClearCurve OM4, A-ii: Corning InfiniCor300 OM1, A-iii: Newport F-ML-D-C, and A-iv: Fujikura G.800/1000. (A) Shift images are plotted with the

same LUTs for all the fibers. The sample is a mixture of 10 μm YG (emission 486 nm) and 2 μm Red fluorescent microspheres (emission 554 nm) excited at 490 nm. (B) difference in shift between two bead groups for different fibers. Images were taken with a Nikon Plan Apo 20x/0.75 objective. 8x zoom was used in this experiment to achieve the same FOV for all the fibers for a fair comparison.

The impact of fiber diameter and fiber material on spectral separation was also studied (shown in Figure 5) with four types of graded-index fibers: Corning ClearCurve OM4, Corning InfiniCor300 OM1, Newport F-ML-D-C, and Fujikura G.800/1000, with core diameters of 50 um, 62.5 um, 100 um, and 800 um, respectively. From the images of relative temporal delays (the second column in Figure 5 A), clearly Fujikura 800 μm core GRIN fiber performs best in spectral separation, possibly because of its core material and doping profile, with the Corning 62.5 μm GRIN fiber second in place. The same trend can also be revealed quantitatively by the difference in averaged delay between the bead groups (Figure 5 B). We found no scan angle dependence on the shift over the entire FOV for all the fibers. Note that 400 μm and 600 μm core Fujikura fibers generated similar spectral separation as the 800 μm one. Considering that larger core diameter provides better coupling we showed only the 800 μm result in Fig. 5.

Overall, for sufficient spectral separation and maximum transmission efficiency, we chose the 30-meter multimode graded-index glass fiber with the largest possible core diameter (>800 μm) and the largest available numerical aperture (0.21). Thus, out of the fibers that we are in possession (Table 1), the 30 m Fujikura 800μm/1000μm graded index fiber appears to the most practical candidate for the spectral lifetime system.

4.2 Spectral mapping

Experiments with different fibers using the same sample, field of view and similar excitation wavelength revealed the best delay and transmission properties among the fibers (Figure 3 and Figure 5). As expected, longer fibers provide better spectral contrast and fibers with larger core diameter and lower attenuation increase the signal-to-noise ratio. The contrast obtained by the 30 m 800μm graded index fiber was higher than other fibers and was chosen for the setup. With the optimized setup described above, a mixture of YG: RED beads was imaged to characterize the spectral and lifetime differences.

4.2.1 Effect on lifetime estimates because of the fiber

Fluorescence lifetime estimation from TCSPC histograms is a straightforward mathematical parameter estimation under known physical constraints. Estimating the lifetime with the YG: RED mixture is detailed in Data Analysis and the results are shown in Figure 6A. A separation in the lifetime distribution is obtained from YG beads (~2.55 ns) and RED beads (~2.80 ns) without the fiber. The broader distribution of the YG beads can be attributed to the spatial/temporal binning associated with the calculation of the shift near the edges of the beads. However, with the fiber in the emission path, the shift per pixel from the TCSPC photon distribution will be convolved with the sample exponential decay and the estimated lifetime will diverge from its absolute lifetime. Figure 6A shows that the shorter lifetime of YG beads gets shorter and the longer lifetime of RED beads gets longer. This is an effect of convolved spectral information on the lifetime decay curve. We use this increased contrast of the lifetime measurement to distinguish species in a lifetime-spectral domain. However, it should be noted that although the “with fiber” lifetime image produces the shift needed for estimating the spectral emission image, the resultant decay is the result of the TCSPC decay being convolved with the shift per pixel. Because fluorescence emission

exhibits an extended spectrum rather than a single spectral line, there is a resultant shift of the measured mean lifetime value. For optimum result, a “without fiber” image is needed for the real lifetime distribution.

The YG beads and RED beads with the fiber show estimated lifetimes (sFLIM-Spectral FLIM) of 2.2 ns and 3.18 ns, a shift of -0.1ns for YG and +0.30 ns for RED beads. As shown in Figure 6B, the range of the color values shown (contrast) in the fiber FLIM image is higher than that without the fiber. The LUTS are same for both panel Bi and Bii and a visual comparison of two panels shows that the image with fiber spans a larger range of colors.

Note that the absolute lifetime determination does get complicated with conventional TCSPC fitting with the presence of the fiber. A complicated spectral-IRF deconvolution is required to get absolute lifetime values. A deconvolution of the lifetime with its spectral width can be done using spectral width estimation using pixel binning or using a time lapse to generate enough points to build a spectrum and find the spectral width. This approach will be pursued in future studies.

4.2.2 Calibrating spectral separation per delay time bin

As described in Section 3.4 Data Analysis, in order to calibrate the spectral separation obtained per time bin of TCSPC excitation for the 30m fiber, the second harmonic signal for a series of excitation wavelengths was measured and plotted against their corresponding delays to estimate the fiber calibration factor as -1.9nm/(40ps time bin) (or -47.6 nm per ns) (Figure 6C). Based on the calibration factor, temporal shift images can be mapped and colored according to their mean spectral shifts. This color map was applied to the shift image to make spectral image as shown in Figure 6D. Figure 6A shows the estimated distribution of lifetime for both YG and RED beads with and without the fiber. The lifetime for YG beads shifts by -0.1 ns and for RED beads it is

shifted by +0.3ns. These delays can be attributed to the effect of convolution of real lifetime distribution with the spectral distribution. Each pixel has a whole spectral emission distribution which is convolved with the lifetime distribution of the individual fluorophores. This results in the deviation from the real lifetime distribution. Chromatic dispersion in fiber (Fig 6D-i) is illustrated by the color-coded image in which the two bead populations are clearly distinct. The image without fiber (Figure 6D-ii) serves a comparison, showing the relatively small distribution in values that results from fluctuations in the measurement.

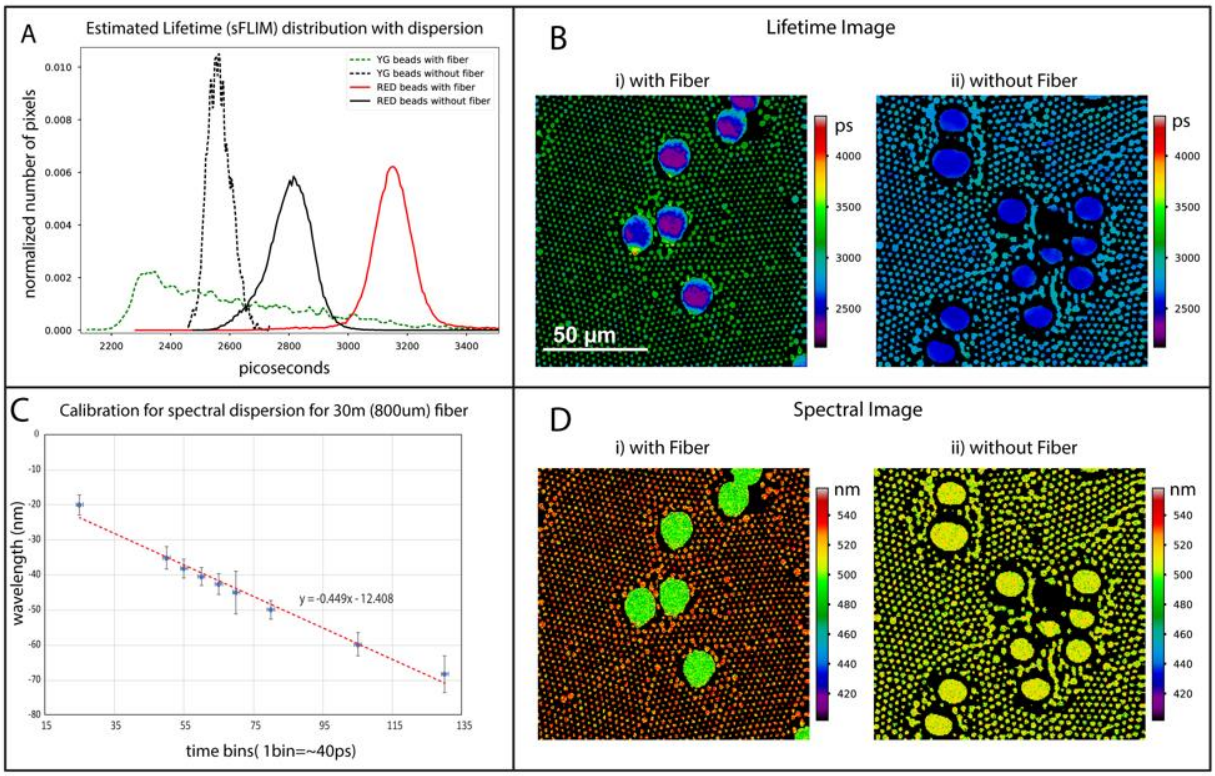

Fig. 6 A) Estimated lifetime distribution with fiber dispersion for YG: RED bead mixture. The averaged estimated lifetime for YG shifts from 2.2 ns to 2.1 ns and for RED shifts from 2.8 ns to 3.18 ns. These delays (-0.1ns) and (+0.3ns) are an effect of the convolved spectral distribution with the real lifetime distribution of the observed photons. The colored curves are separable because of the fiber spectral dispersion. The green dotted line shows the

YG beads and red dotted line shows the Red beads with the fiber. The non-colored curves show the beads without fiber. B) The estimated lifetime images in the same color scheme, with the color scale determined by the range of the estimated lifetime with fiber (2100ps – 4500ps). With the fiber, the dynamic range (thus, the contrast) of the image (B-i) increases compared to the non-fiber case (B-ii). C) Calibration curve for temporal delay due to fiber chromatic dispersion with respect to the change in the emission wavelength. For this calibration, second harmonic signal was measured for a series of wavelengths with the 30m 800 μm GRIN fiber and used to create spectral LUT for the images. D) Spectral images (obtained by mapping shift to spectrum) of the same measurements from (B) shown in the same spectral color scale. Without the fiber, the RED and YG beads can be visually identified by size, but there is no contrast, and no meaningful spectral information is displayed.

4.3 Spectral mapping in cells

The contrast demonstrated in the fiber based spectral FLIM imaging can be used to distinguish different species and can address biologically important heterogeneity in samples. For spectrally separable populations, this approach helps to obtain a lifetime-independent degree of separation derived from the respective shift values.

4.3.1 Spectral Image

In order to study the efficacy of this strategy of spectral separation we procured pre-labeled slices of bovine pulmonary artery endothelial cells (BPAEC, FluoCells, ThermoFisher Scientific, Waltham, MA; Cat #F36924). The slides are labeled with MitoTracker Red CMXRos, Alexa-Fluor-488 phalloidin and DAPI. This will give three channel color images showing red mitochondria, green F-Actin, and blue DAPI. The sample was imaged under 750 nm excitation with the 800 μm 30m GRIN fiber and the results are presented in Figure 7. An intensity- adjusted image is shown in Panel A. The intensity adjustment is necessary because the DAPI is very bright

under a common multiphoton excitation for the three fluorescent probes reported. The shift was calculated with the calibration used for the fiber and a custom offset, so that the DAPI spectrum peaks at the expected value of 450nm. The software supplied has the capability to shift the spectrum measured to any known spectral peak instead of the IRF to offset the spectrum by using a custom shift. For example: we provided a custom shift value 450 nm for DAPI signal instead of the IRF measurement at 890nm (445nm). The value would be different for a different fiber-based setup. The spectrum was split into three based on two spectral thresholds at 460nm and 507 nm to separate three cellular areas visually. The KDE (Kernel Density Estimation) plot for the spectral separation of the entire image (solid black curve) to the three colors is shown in panel D. The calibration curve shown in figure 6C was used to create the distribution by converting the time shift to wavelength. This spectral separation can be used to color the intensity image as seen in panel B. The histogram of lifetime (calculated without the fiber) and the spectrum calculated with the fiber is plotted in panel C as λ(wavelength)-τ(lifetime) plot. This histogram shows the separation of species better than either lifetime or spectrum alone. The colors can be separated as three species in this histogram using cursors or simply by a projection to the λ axis as shown in panel D. Panel E and F show the lifetime images with and without the fiber. For calculating the lifetime for both of the images, SPCImage was used for performing the curve fitting.

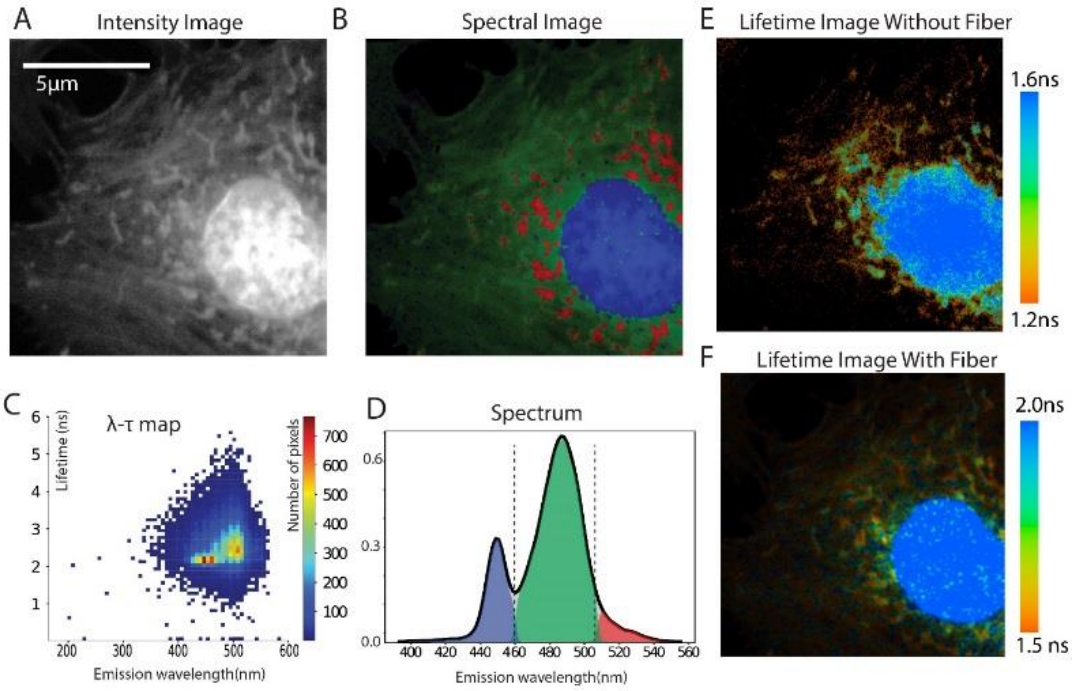

Fig. 7: Hyperspectral Image: Fluocells (ThermoFisher Scientific) prepared slides shows bovine pulmonary cells that are labelled with Mito tracker Red for mitochondria, Alexa Fluor 488 for F actin and DAPI. (A) the intensity image when excited with 750nm multiphoton excitation. (B) the spectral image obtained by thresholding shift into 400-460 nm (blue), 460-507 nm (green), 507 nm -Inf (red). (C) the two-dimensional histogram plotted between wavelength (calculated with fiber) and fluorescence lifetime (calculated without fiber). (D) the experimental result of spectral separation obtained from the spectrum (solid black line) into three colors blue, green and red at the thresholding limits mentioned before (460 nm, 507 nm). Images were taken with a 60x oil objective (NA = 1.4). (E) Lifetime image without fiber (F) lifetime image with fiber (lifetime scale shown in the right).

5 Discussion

In this paper, a low-cost spectral addon to an existing FLIM implementation is demonstrated. Utilizing an optical fiber added to the emission path of a time domain FLIM multiphoton microscope, we achieve spectral discrimination in the FLIM signal. The technique exploits the

fiber induced chromatic dispersion of the fluorescence photon travelling through the fiber to identify its wavelength. Note that this method is not presented as an alternative to multi detector/filter systems(Shrestha et al., 2010), but a fast and cost effective way to induce spectral contrast into an existing FLIM acquisition system. The spectral information will be coded as the rather larger time delay on the lifetime curve (50nm spectral separation codes as 1ns shift of the lifetime curve). Employing a method as demonstrated to acquire lifetime data both with and without fiber allows one to get both average lifetime and average spectral wavelength from a pixel, thence building a FLIM and spectral image.

Chromatic dispersion is a function of the length of the fiber and longer fibers increase the time delay between spectral components enhancing spectral resolution. However, longer fibers also introduce higher attenuation as well as larger modal dispersion, which limits the ability to resolve spectral separation and causes signal loss and reduces the signal-to-noise ratio. To make the system practical for investigating emission spectra of biological samples, the fiber should be long enough to produce separation with minimized modal dispersion, have a diameter large enough to accommodate the scanning light that is focused on the fiber tip, and be made of a material with an acceptable attenuation in the visible spectral range. Based on our experiments with our limited selection of optical fibers, we have found that using a 30m long 800 μm core diameter graded-index (GRIN) fiber from Fujikura Corporation([CSL STYLE ERROR: reference with no printed form.]) gives the best result for spectral separation between species with the optimum transmission. With the current fiber-based spectral lifetime setup, we were able to spectrally separate and map fluorescent microspheres, by using the calibrated 1.9 nm/40ps time-bin (47.6 nm/ns) factor for converting emission spectrum shift into temporal shift measured in our TCSPC collection scheme.

A priori knowledge of lifetime or spectrum could be used to deconvolve the curve to get one or the other. All the data we collected have both lifetime and spectral information collected sequentially, but we have not explored any deconvolution methods in this study. While this system is not a substitute for previously published schemes such as multichannel/multidetector(Roberts et al., 2011) or multichannel/single detector schemes(Shrestha et al., 2010), this method offers an alternative low-cost spectral discrimination scheme to a microscope.

For a simultaneous spectral-lifetime acquisition and analysis, the calculated lifetimes with fibers diverge from the true lifetime values due to the convolution between the lifetime and spectrum distribution. Future developments could be to acquire the ability to quantify the presence of various fluorophores in the same pixel or ROI using mathematical modeling of the temporal distribution of photons traveling through fibers. In the cases where known fluorophores with known spectra are used (which is commonly the case of biological labeling experiments), it should be possible to deconvolve the spectral and lifetime data. For estimating the lifetime faster, alternative methods like rapid lifetime estimation (RLD) can generate the mean lifetime faster from these images than multiparametric fitting. However, even without exploring this, we have demonstrated that the combined temporal/lifetime data can provide better discrimination between fluorescence signals rather than spectra or lifetime alone. Although it should be noted that, to identify multiple fluorophores, a custom offset is needed for a known fluorophore (specific to the fiber) relative to which the other fluorophores are identified.

To improve the resolution of the system, a detector free from afterpulsing and shortened IRF width could be used. Using a hybrid detector(Becker et al.) instead of GaAsP detector should result in a better approximation of the IRF because of its lack of afterpulsing and narrow width resulting in a clean response function. We expect this to result in an improved temporal resolution.

In theory, a longer fiber should give us improved spectral resolution, but modal dispersion and fiber attenuation place practical limits to the use of longer fibers. As many commercially-available fibers are not characterized for refractive index, modal dispersion, and attenuation in the visible spectrum, better characterization of the fibers in appropriate spectral ranges would help us to have a quantitative understanding of the potential performance and limitations of the approach, thus enabling us to optimize the system. The accuracy of the temporal delay calculation is limited by the instrument response function of the system. For current commercial TCSPC system, the photon detection accuracy is in the range of 100-350 ps with a timing resolution of ~40 ps. The fitting routine also needs to be faster with better delay estimation for each pixel to account for the spectral data being convolved with the lifetime data.

The long-term goal of this system is to identify multiple fluorophores accurately with improved resolution from a single acquisition and utilize this new combined lifetime and spectral modality to solve biological challenges. This study provides the foundational work for such a faster multimodal acquisition scheme.

References

Acakpovi, A., and Matoumona, P.L.M.V. (2012). Comparative analysis of plastic optical fiber and glass optical fiber for home networks. In 2012 IEEE 4th International Conference on Adaptive Science Technology (ICAST), pp. 154–157.

Bansal, N.P., and Doremus, R.H. (2013). Handbook of Glass Properties (Elsevier).

Becker, W., Bergmann, A., and Biskup, C. (2007). Multispectral fluorescence lifetime imaging by TCSPC. Microsc. Res. Tech. *70*, 403–409.

Becker, W., Su, B., Holub, O., and Weisshart, K. FLIM and FCS detection in laser-scanning microscopes: Increased efficiency by GaAsP hybrid detectors. Microscopy Research and Technique *74*, 804–811.

Beule, P.D., Owen, D.M., Manning, H.B., Talbot, C.B., Requejo-Isidro, J., Dunsby, C., Mcginty, J., Benninger, R.K.P., Elson, D.S., Munro, I., et al. (2007). Rapid hyperspectral fluorescence lifetime imaging. Microsc. Res. Tech. *70*, 481–484.

Bird, D.K., Eliceiri, K.W., Fan, C.-H., and White, J.G. (2004). Simultaneous two-photon spectral and lifetime fluorescence microscopy. Appl. Opt., AO *43*, 5173–5182.

Campos-Delgado, D.U., Gutierrez-Navarro, O., Arce-Santana, E.R., Skala, M.C., Walsh, A.J., and Jo, J.A. (2015). Blind deconvolution estimation of fluorescence measurements through quadratic programming. Journal of Biomedical Optics *20*, 075010–075010.

Chang, C.-I. (2003). Hyperspectral Imaging: Techniques for Spectral Detection and Classification (Springer Science & Business Media).

Cranfill, P.J., Sell, B.R., Baird, M.A., Allen, J.R., Lavagnino, Z., de Gruiter, H.M., Kremers, G.-J., Davidson, M.W., Ustione, A., and Piston, D.W. (2016). Quantitative assessment of fluorescent proteins. Nat Meth *13*, 557–562.

Cutrale, F., Trivedi, V., Trinh, L.A., Chiu, C.-L., Choi, J.M., Artiga, M.S., and Fraser, S.E. (2017). Hyperspectral phasor analysis enables multiplexed 5D in vivo imaging. Nat Meth *14*, 149–152.

Digman, M., and Gratton, E. (2014). The phasor approach to fluorescence lifetime imaging: Exploiting phasor linear properties. In Fluorescence Lifetime Spectroscopy and Imaging, (CRC Press), pp. 235–248.

Fereidouni, F., Bader, A.N., and Gerritsen, H.C. (2012). Spectral phasor analysis allows rapid and reliable unmixing of fluorescence microscopy spectral images. Optics Express *20*, 12729–12741.

Goda, K., Tsia, K.K., and Jalali, B. (2009). Serial time-encoded amplified imaging for real-time observation of fast dynamic phenomena. Nature *458*, nature07980.

Griffiths, P.R., and Pariente, G.L. (1986). Introduction to spectral deconvolution. TrAC Trends in Analytical Chemistry *5*, 209–215.

Hanley, Q.S., Arndt-Jovin, D.J., and Jovin, T.M. (2002). Spectrally Resolved Fluorescence Lifetime Imaging Microscopy. Appl Spectrosc *56*, 155–166.

Haraguchi, T., Shimi, T., Koujin, T., Hashiguchi, N., and Hiraoka, Y. (2002). Spectral imaging fluorescence microscopy. Genes to Cells *7*, 881–887.

Liew, S.F., Redding, B., Choma, M.A., Tagare, H.D., and Cao, H. (2016). Broadband multimode fiber spectrometer. Opt. Lett., OL *41*, 2029–2032.

Meagher, J.L., Beechem, J.M., Olson, S.T., and Gettins, P.G. (1998). Deconvolution of the fluorescence emission spectrum of human antithrombin and identification of the tryptophan residues that are responsive to heparin binding. J. Biol. Chem. *273*, 23283–23289.

Michalet, X., Pinaud, F.F., Bentolila, L.A., Tsay, J.M., Doose, S., Li, J.J., Sundaresan, G., Wu, A.M., Gambhir, S.S., and Weiss, S. (2005). Quantum Dots for Live Cells, in Vivo Imaging, and Diagnostics. Science *307*, 538–544.

Personick, S.D. Photon Probe—An Optical-Fiber Time-Domain Reflectometer. Bell System Technical Journal *56*, 355–366.

Petrov, G.I., Yakovlev, V.V., and Shcheslavskiy, V.I. (2011). Raman spectroscopy without spectrometer. In CLEO:2011 - Laser Applications to Photonic Applications (2011), Paper PDPB6, (Optical Society of America), p. PDPB6.

Qiao, J., Ngadi, M.O., Wang, N., Gariépy, C., and Prasher, Shiv.O. (2007). Pork quality and marbling level assessment using a hyperspectral imaging system. Journal of Food Engineering *83*, 10–16.

Redding, B., and Cao, H. (2012). Using a multimode fiber as a high-resolution, low-loss spectrometer. Opt. Lett., OL *37*, 3384–3386.

Redding, B., Popoff, S.M., and Cao, H. (2013). All-fiber spectrometer based on speckle pattern reconstruction. Opt. Express, OE *21*, 6584–6600.

Roberts, M.S., Dancik, Y., Prow, T.W., Thorling, C.A., Lin, L.L., Grice, J.E., Robertson, T.A., König, K., and Becker, W. (2011). Non-invasive imaging of skin physiology and percutaneous penetration using fluorescence spectral and lifetime imaging with multiphoton and confocal microscopy. European Journal of Pharmaceutics and Biopharmaceutics *77*, 469–488.

Shrestha, S., Applegate, B.E., Park, J., Xiao, X., Pande, P., and Jo, J.A. (2010). High-speed multispectral fluorescence lifetime imaging implementation for in vivo applications. Opt Lett *35*, 2558–2560.

Strickler, S.J., and Berg, R.A. (1962). Relationship between Absorption Intensity and Fluorescence Lifetime of Molecules. The Journal of Chemical Physics *37*, 814.

Suhling, K., Hirvonen, L.M., Levitt, J.A., Chung, P.-H., Tregidgo, C., Rusakov, D.A., Zheng, K., Ameer-Beg, S., Poland, S.P., Coelho, S., et al. (2017). Fluorescence Lifetime Imaging. In Handbook of Photonics for Biomedical Engineering, A.H.-P. Ho, D. Kim, and M.G. Somekh, eds. (Springer Netherlands), pp. 353–405.

Sun, Y., Liu, R., Elson, D.S., Hollars, C.W., Jo, J.A., Park, J., Sun, Y., and Marcu, L. (2008). Simultaneous time- and wavelength-resolved fluorescence spectroscopy for near real-time tissue diagnosis. Opt. Lett., OL *33*, 630–632.

Toussaint, J., Dochow, S., Latka, I., Lukic, A., May, T., Meyer, H.-G., Il'in, K., Siegel, M., and Popp, J. (2015). Proof of concept of fiber dispersed Raman spectroscopy using superconducting nanowire single-photon detectors. Opt. Express, OE *23*, 5078–5090.

Walewski, J.W., and Sanders, S.T. (2005). Rapid wavelength scans over one octave and application to laser-induced fluorescence. Opt. Lett., OL *30*, 2394–2396.

Yan, L., Rueden, C.T., White, J.G., and Eliceiri, K.W. (2006). Applications of combined spectral lifetime microscopy for biology. Biotechniques *41*, 249.

Zhou, X., Haudenschild, A.K., Sherlock, B.E., Hu, J.C., Leach, J.K., Athanasiou, K.A., and Marcu, L. (2018). Detection of glycosaminoglycan loss in articular cartilage by fluorescence lifetime imaging. JBO *23*, 126002.

ClearCurve® Multimode Optical Fiber Cable | Corning.

Fujikura Ltd. | Products.

0.50 NA Step-Index Multimode Fibers.

Fluoresbrite® YG Carboxylate Microspheres 10.00µm.

Fluoresbrite® Polychromatic Red Microspheres 2.0µm.

Chapter 5

Open source TCSPC FLIM acquisition

Summary

Fluorescence Lifetime Imaging Microscopy (FLIM) in Time-Correlated Single Photon Counting (TCSPC) (Becker, 2012) mode, an imaging technique that can be performed as an extension to either confocal or two-photon LSM. Laser scanning multiphoton or confocal microscope can be upgraded to have TCSPC FLIM capability by adding a proprietary TCSPC electronics module, like the SPC series card from Becker and Hickl GmbH. Commercial turn-key systems can be purchased, which use proprietary software; such software is often limited to a predefined set of acquisition routines and supported equipment, and/or cannot readily be connected to custom image analysis algorithms. A FLIM acquisition package that is (merely) open source would be an improvement in terms of customizability, but by itself of limited applicability, because in many cases FLIM is not used in isolation but in combination with other LSM techniques (e.g. photobleaching), non-LSM techniques (e.g. wide-field imaging with a camera), and data analysis. An ideal software platform for a scientist looking to develop a new FLIM technique would be one that already interfaces with a wide array of LSM and non-LSM microscopy equipment, and supports basic imaging modalities. However, most commercial vendors making turn-key TCSPC hardware provide their own acquisition software, which lacks the ability to add custom acquisition routine or perform custom runtime analysis. To overcome these limitations of current TCSPC acquisition software, there we propose an open source FLIM software which can be customized to ease the development and adoption of FLIM and to integrate with existing FLIM analysis tools.

Introduction

Fluorescence Lifetime Imaging Microscopy (FLIM) has generated significant interest from scientist especially in the last decade due to its ability to probe pH, temperature, ion concentration

while being independent of intensity, concentration, absorption by sample and thickness. As a result, FLIM is gaining widespread acceptance as a way to probe cellular microenvironment (Berezin and Achilefu, 2010; Elson et al., 2004; Provenzano et al., 2008; Suhling et al., 2005, 2015; Wang et al., 1992). FLIM is acquired primarily in two ways, frequency and time domain. Both domains have their own set of advantages/disadvantages and based on the specific application need, both modalities can have their unique advantage. Frequency domain lifetime is faster and computationally less intensive but suffers from aliasing, photobleaching induced artifact, low signal-to-noise-ratio and limited dynamic range. In time domain FLIM, an ultrashort pulse is used to excite the sample and the emission is detected via single photon counting. The time from the excitation and photon detection are calculated by electronics that have a temporal resolution in the picoseconds range. This is called Time-Correlated Single Photon Counting (TCSPC)(Becker, W., 2014). Laser scanning multiphoton or confocal microscope can be upgraded to have TCSPC FLIM capability by adding a TCSPC hardware. Although TCSPC has many advantages like its ability to provide pixel-wise statistics, better SNR but the time taken to acquire a single image limits its ability to collect data for real-time acquisition for moving subjects. For example, one single image acquisition might take 1-2 minutes, or even 3 minutes in some cases (low intensity image). The post processing involves tuning curve fitting initialization parameters and estimating lifetime using curve fitting routines which would take close to a minute. As a result, imaging a large section which would have several hundred field-of-views, would take days to finish. This is often a limiting factor of FLIM based study in general.

There are two primary ways to collect FLIM data using the BH TCSPC hardware. Scan-sync-in and FIFO mode. In the Scan-sync-in mode, the build-up of the histogram is accomplished on board and the timing information from the tagged photons are automatically extracted. Whole FLIM

image is stored onboard during acquisition and transferred to the computer memory after the acquisition is over. This approach has several limitations like the data size is limited by on-board memory capacity runtime photon buildup can't be displayed. The FIFO mode or as the name implies "First-In-First-Out" mode stores a very limited number of photon information on-board and are immediately transferred to computer memory when full. This is possible due to the recent development in the transfer speed via the computer bus. This mode has enabled acquisition of very large dataset and live display. Additionally, as the photon information are available on-the-fly, they can be processed during runtime. As a result, it would be possible to implement runtime lifetime analysis routine on the lifetime histogram.

To realize the goal of having an open source software for FLIM acquisition we need to first have an open source laser scanning software for intensity imaging. Currently, we are developing an open source software, OpenScan that works as an add-on to the popular microscope control software, μManager (Edelstein et al., 2014). μManager is an open-source, cross-platform desktop application, to control a wide variety of motorized microscopes, scientific cameras, stages, illuminators, and other microscope accessories. Figure 1 shows the laser scanning module for Micro-manager showing FPGA/DAQ based scanner and a detection module. The SPC 150 TCSPC card from Becker and Hickl will be used for the FLIM acquisition module.

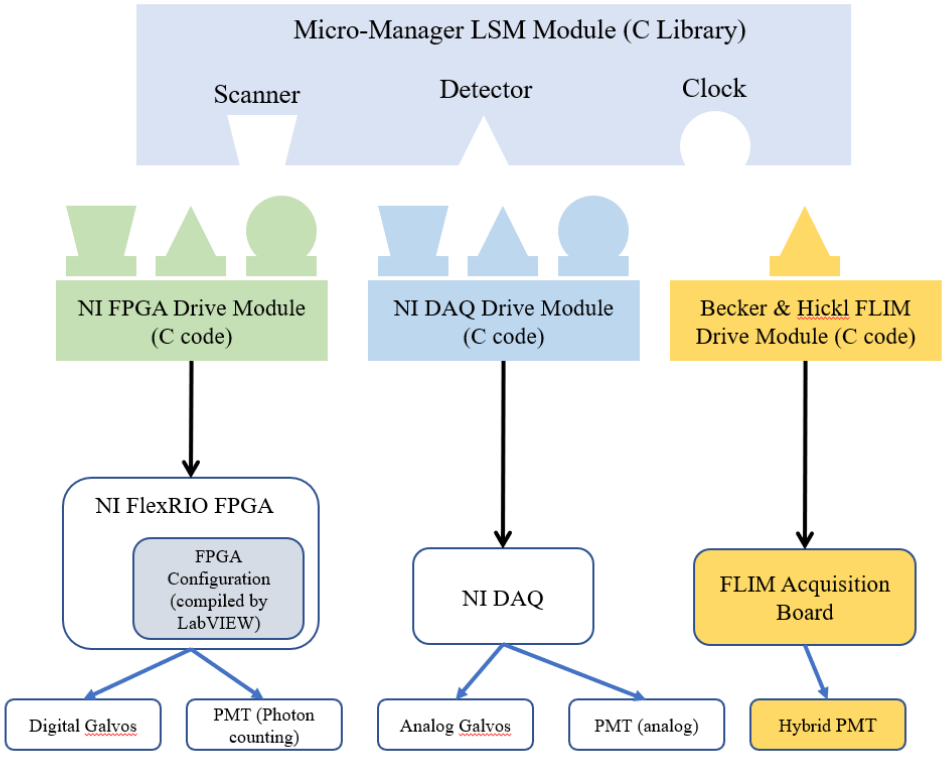

***Figure 1**: The architecture of micromanager Laser Scanning Module. The scanning and detection can be realized using two separate architecture, FPGA and DAQ. The right most section depicts the OpenFLIM module based on Becker & Hickl TCSPC hardware. The development of open source FLIM is the focus of this thesis.*

The B&H SPC 150 FLIM card operates on FIFO which enables us to extract timing information to create the histogram. The way it works is can be largely divided into two main tasks. i) Filling out the FIFO buffer with the time-tagged photon data continuously as long as the acquisition is going on, ii) flushing the buffer to computer memory to free up space for further accumulation. Although it should be noted that, these two steps do not create the exponential decay. They are created after the photons are read from the computer memory. Figure 2a shows the flowchart of FIFO acquisition using the BH SPC library and the *SPC_read_FIFO( )* library function. Figure 2b shows the structure of a typical time-tagged photon. The macro time field refers to the time from the start of the acquisition having a typical resolution of 25 to 50 ns. This can be used to directly

find the location of a photon in x-y location and help build the photon counting histogram image. The microtime is the time in the signal period and this information is used to the time bin referred to by the time. Other bits like identifier bits contains info about various events like if there is an overflow or a frame/line clock has arrived. The 'Channel' identifier will not be used for a single detector case.

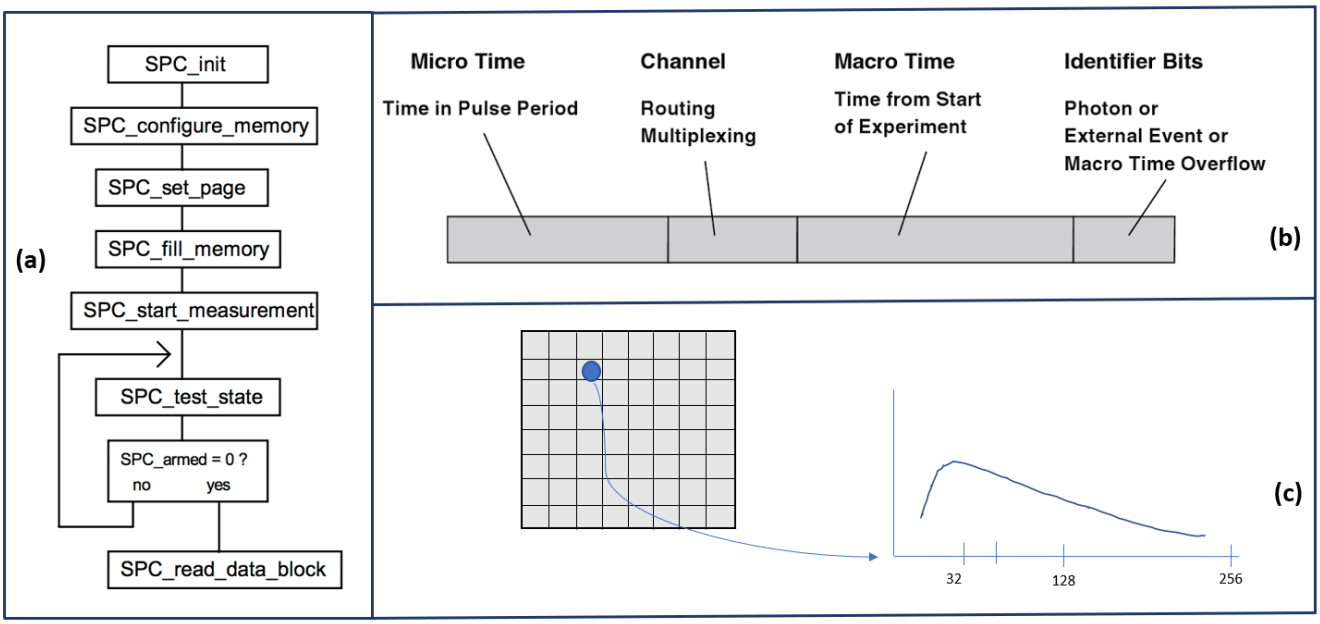

***Figure 2**: In FIFO(First-in-First-Out) mode, the time tagged photons are continuously stored in a buffer and transferred to computer memory once the buffer is full. From the parameter tagged photon data the macro-time and micro-time is calculated which are used to create the intensity and exponential data histogram is created a) The flowchart of library functions used for FIFO acquisition b) Structure of each time-tagged photon, each photon contains macro and micro time information c) Locating a photon using macro time and micro time is used for finding the location of a photon in x-y grid and the micro-time is used to find the location in exponential decay in a pixel*

It should be noted here that, the library provided by the Becker and Hickl starts the acquisition process by starting the put the parameter tagged photon in the buffer, but the buffer management, transfer from PC and creating the histogram from the saved photon needs to be handled by the

acquisition software. Figure 3 shows the flowchart with the overall process that needs to be running beside a laser scanning module. After the laser scanning is started with the laser scanning module the FIFO acquisition also starts concurrently with the initial set of parameters like resolution, collection time, buffer size. As soon as the FIFO acquisition is started, the photons go through the TCSPC process CFD->TAC-> ADC and a full parameter tagged photon is generated as shown in figure 7b. These photons are continuously filled in the buffer. Throughout this process, the buffer size needs to be checked continuously and if the buffer becomes full, the photon data is transferred to computer memory and the buffer is freed up. If the buffer is not freed up it will show an overload signal and further photon will not be collected. This process goes on as long as the collection time is not over, or the user does not stop manually.

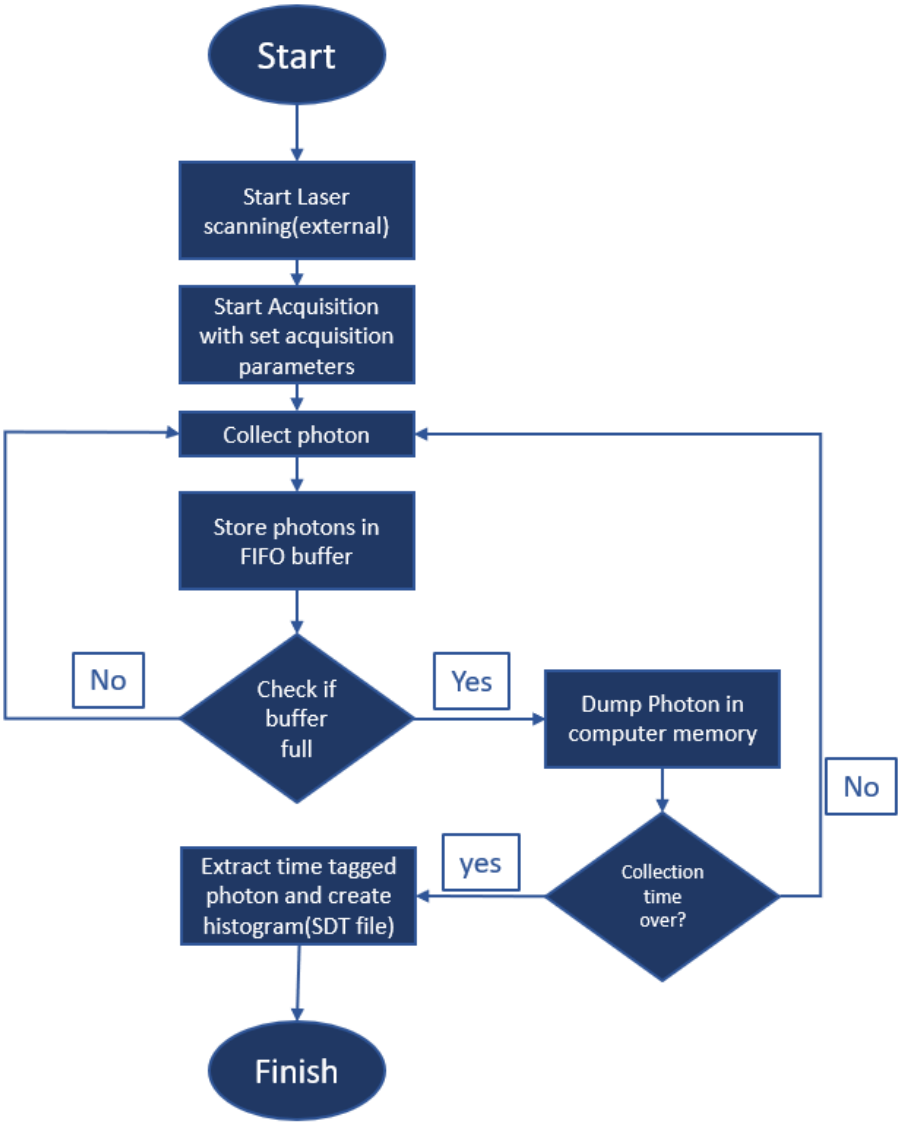

***Figure 3**: Flowchart depicting the FIFO acquisition process from the start of scanning to saving the lifetime histogram. FIFO acquisition is a continuous process for a given amount of time. The FIFO buffer is filled with photon received the TCSPC system which time tags each photon. Once the buffer is full, the data is dumped in computer memory to free the buffer. This goes on until the collection time is over.*

Results

WiscScan Implementation

The method described here is already implemented in a closed source laser scanning software WiscScan (Kader Sagar, 2015) that I early developed and fully functional. It is being regularly used in our lab (Ghanbari et al., 2018; Kenny et al., 2017; Martin et al., 2018). Figure 4 shows the lifetime acquisition window, currently being used in WiscScan which utilizes the FIFO architecture for acquisition. Currently that code is being converted to be accommodated by OpenScan's acquisition architecture and concurrently debugging is being carried out that it performs in a similar fashion to WiscScan. The Open source FLIM architecture is being developed to make sure it can support other TCSPC board other than Becker and Hickl in future.

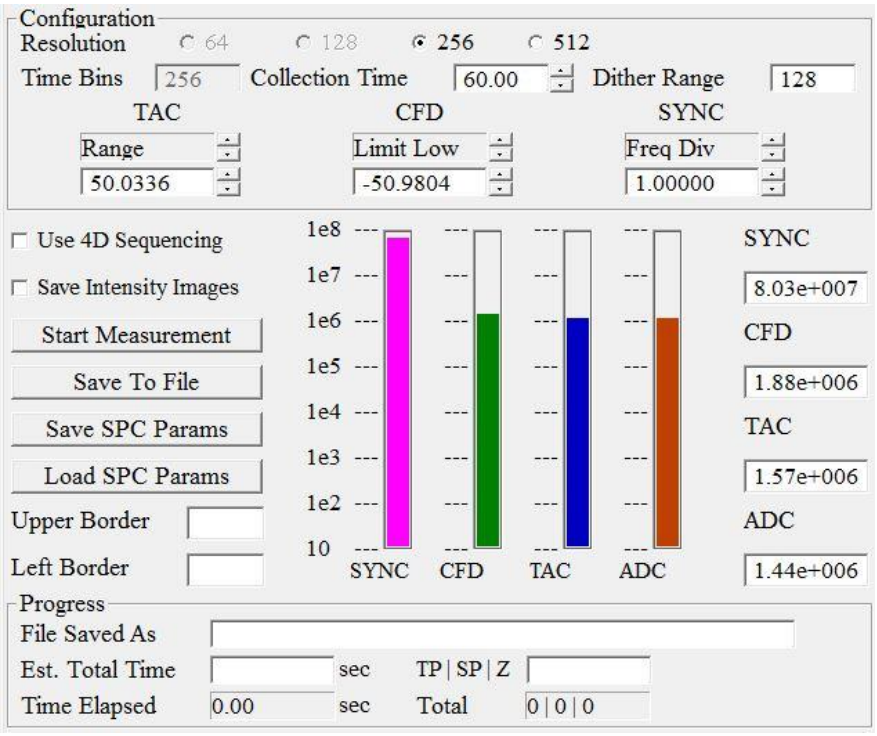

***Figure 4**: Lifetime FIFO acquisition based on the architecture described earlier is implemented in LOCI homebuilt scanning software WiscScan. This software can control all the necessary parameters (collection time, excitation intensity, TAC, CFD, ADC parameters) for acquisition.*

OpenScan implementation

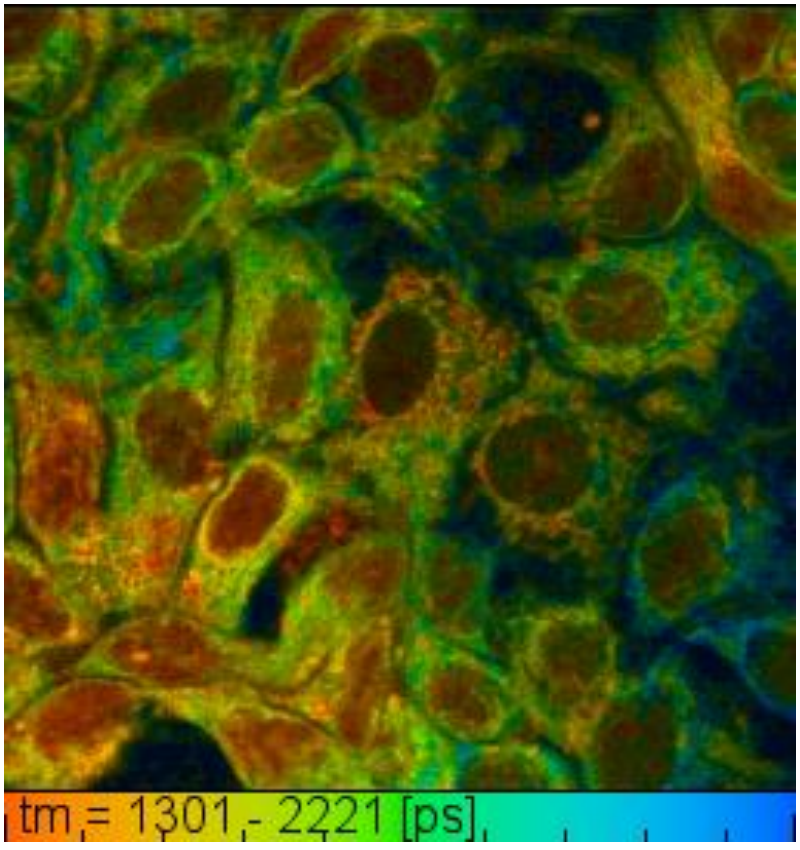

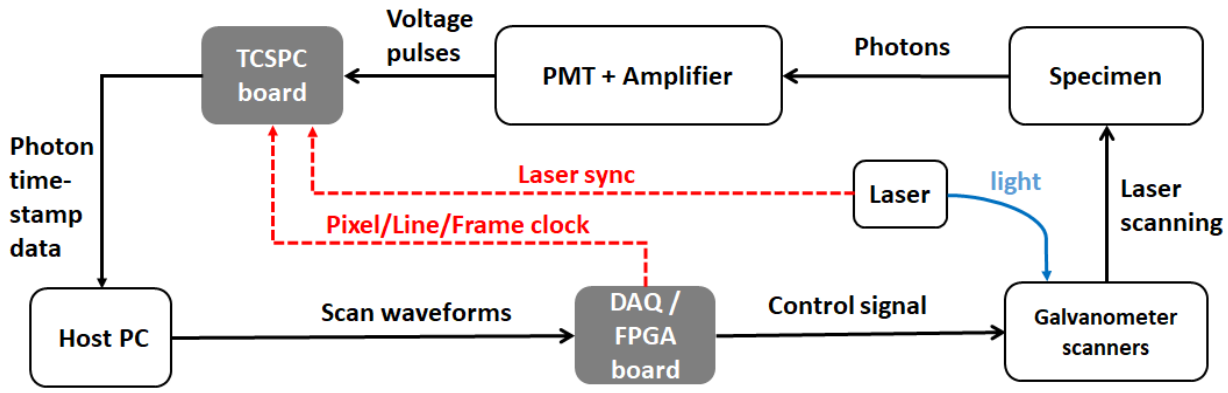

Figure 5: *NADH FLIM images of MCf10a human breast cells acquired with OpenScan FLIM implementation. FPGA was used to perform the scanning and SPC-150 FLIM board (Becker and Hickl GmbH, Berlin, Germany) as TCSPC (Time-Correlated single photon Counting) electronics to collect time-tagged photon data. The FIFO (First In First Out) mode of photon acquisition is implemented in the acquisition framework and exponential decay is created from time-tagged photon data. The analysis using exponential curve fitting was performed using SPCImage (Becker and Hickl GmbH, Berlin, Germany).*

As previously mentioned, in OpenScan either DAQ or FPGA can be configured as a scanner to generate scan waveforms as well as clock signals (particularly for FPGA, it is possible to generate pixel clocks of nanosecond precision) to trigger the acquisition of other detectors. In this section, we demonstrate an OpenScan FLIM (*OpenFLIM* for short) implementation by coupling a NI FPGA (PXIe-7972) and a TCSPC FLIM board (SPC-150 from Becker and Hickl GmbH, Berlin, Germany).

Becker and Hickl with its SPC series of cards is one of the TCSPC electronics manufacturers and provides external software library support for the basic FLIM acquisition routine. Although different SPC boards have different strengths, the software library for acquisition is supported by most of the boards. Thus, the code development on the SPC-150 board, which our lab possess, will be supported by most of the boards sold by BH. As shown in Figure 1, a BH SPC150 FLIM driver

module was developed on top of the BH library to abstract the FLIM board as a *detector* in OpenScan. A DAQ or an FPGA can be selected as a *scanner* to pair with it to realize FLIM acquisition.

The FLIM acquisition runs in “FIFO mode”, in which raw photon timestamp data is continuously streamed to the computer, in contrast to more conventional modes of operation in which time histograms were accumulated in the TCSPC board before transfer to the computer. This is possible due to the recent improvements in the transfer speed via the computer bus. This mode has enabled the acquisition of very large datasets and live display. Operating the TCSPC board in FIFO mode allows us to perform the creation of TCSPC histograms in software. The way it works can be largely divided into two main tasks. i) Filling out the FIFO buffer with the time-tagged photon data continuously as long as the acquisition is going on, ii) flushing the buffer to computer memory to free up space for further accumulation.

Although it should be noted that, these two steps do not create the exponential decay. They are created after the photons are read from the computer memory. The library provided by the Becker and Hickl takes care the former task implicitly, while the latter, i.e., managing the buffer by transferring data to the computer and creating the histogram from the saved photons, is handled by the OpenFLIM driver. Note that the OpenFLIM driver is designed to be able to support other vendors’ TCSPC boards with minimal efforts by replacing the BH library and making some minor modifications to the code involving buffer management.

OpenFLIM module initiates the TCSPC FLIM board, which starts the acquisition of photon arrival times and markers. Image markers like frame/line/pixel clock are generated by OpenScan (either

DAQ or FPGA). This photon-marker stream is dumped into a FIFO file, which is saved by OpenFLIM to the hard drive and can be analyzed by BH proprietary software or other open source counterparts such as SLIM Curve [https://imagej.net/SLIM_Curve], PIE [https://gitlab.com/PAM-PIE], Photon-hdf5 [https://github.com/Photon-HDF5], etc. In addition to the photon stream file, a real-time readout of SPC hardware parameters including total photon counts per second, time-tagged photons per second is also possible through OpenFLIM. It should be noted that the image marker outputs like pixel, line, frame markers allow OpenScan not to be limited to BH hardware, but open to being used with any other commercial FLIM acquisition hardware such as ISS-FLIMBox, Picoquant-TimeHarp, Swabian-Timetagger and others.

Figure 5 shows the NADH lifetime images of MCF10A human breast cells at two locations captured with OpenFLIM and analyzed with commercial software SPCImage (Becker and Hickl GmbH). A H7422-40 (Hamamatsu, Hamamatsu City, Japan) PMT was coupled with an HFAC-26 preamplifier (Becker and Hickl GmbH, Berlin, Germany) to collect emission photons and send the output to the FLIM board. A Nikon Plan Apo 20x/0.75 air objective was used with 750 nm excitation coupled with 450/70-nm band-pass emission filter (Semrock, Rochester. NY) to selectively collect NADH fluorescence emission signal. The acquisition time was 180 seconds and the resolution was 256 x 256.

Method

This implementation was realized by pairing either a NI DAQ (PXIe-6356) or a NI FPGA (FlexRIO PXI3-7972R) with a TCSPC FLIM board (Becker and Hickl GmbH, Berlin, Germany). The instrumentation was implemented on a functional custom-built multiphoton microscope built

around a Nikon inverted microscope base (Eclipse Ti-U, Nikon, Tyoto, Japan) with a Coherent Mira 900 Ti:Sapphire pulsed laser (Coherent, Santa Clara, California, USA), a motorized XY-Z stage (ASI MS-2000, Applied Scientific Instruments, Eugene, OR, USA). Either a Hamamatsu H7422P-40 PMT (Hamamatsu, Hamamatsu City, Japan) coupled with HFAC-26 preamplifier (Becker and Hickl GmbH, Berlin, Germany) or a Becker-Hickl HPM-100-40 hybrid PMT (Becker and Hickl GmbH, Berlin, Germany) was used for light collection. Refer to Figure 6(A) for the schematic of the experimental setup.

References

Becker, W. (2012). Fluorescence lifetime imaging--techniques and applications. J. Microsc. *247*, 119–136.

Becker, W. (2014). The bh TCSPC Handbook (Becker & Hickl Gmbh).

Berezin, M.Y., and Achilefu, S. (2010). Fluorescence Lifetime Measurements and Biological Imaging. Chem. Rev. *110*, 2641–2684.

Edelstein, A.D., Tsuchida, M.A., Amodaj, N., Pinkard, H., Vale, R.D., and Stuurman, N. (2014). Advanced methods of microscope control using μManager software. J. Biol. Methods *1*.

Elson, D., Requejo-Isidro, J., Munro, I., Reavell, F., Siegel, J., Suhling, K., Tadrous, P., Benninger, R., Lanigan, P., McGinty, J., et al. (2004). Time-domain fluorescence lifetime imaging applied to biological tissue. Photochem. Photobiol. Sci. *3*, 795–801.

Ghanbari, L., Carter, R.E., Rynes, M.L., Dominguez, J., Chen, G., Naik, A., Hu, J., Sagar, M.A.K., Haltom, L., Mossazghi, N., et al. (2018). Cortex-wide neural interfacing via transparent polymer skulls. BioRxiv 387142.

Kader Sagar, M.A. (2015). Automated acquisition approaches for multidimensional multiphoton microscopy.

Kenny, T.C., Hart, P., Ragazzi, M., Sersinghe, M., Chipuk, J., Sagar, M. a. K., Eliceiri, K.W., LaFramboise, T., Grandhi, S., Santos, J., et al. (2017). Selected mitochondrial DNA landscapes activate the SIRT3 axis of the UPR^{mt} to promote metastasis. Oncogene *36*, 4393–4404.

Martin, S.A., Souder, D.C., Miller, K.N., Clark, J.P., Sagar, A.K., Eliceiri, K.W., Puglielli, L., Beasley, T.M., and Anderson, R.M. (2018). GSK3β Regulates Brain Energy Metabolism. Cell Rep. *23*, 1922-1931.e4.

Provenzano, P.P., Eliceiri, K.W., and Keely, P.J. (2008). Multiphoton microscopy and fluorescence lifetime imaging microscopy (FLIM) to monitor metastasis and the tumor microenvironment. Clin. Exp. Metastasis *26*, 357–370.

Suhling, K., French, P.M.W., and Phillips, D. (2005). Time-resolved fluorescence microscopy. Photochem. Photobiol. Sci. *4*, 13–22.

Suhling, K., Hirvonen, L.M., Levitt, J.A., Chung, P.-H., Tregidgo, C., Le Marois, A., Rusakov, D.A., Zheng, K., Ameer-Beg, S., Poland, S., et al. (2015). Fluorescence lifetime imaging (FLIM): Basic concepts and some recent developments. Med. Photonics *27*, 3–40.

Wang, X.F., Periasamy, A., Herman, B., and Coleman, D.M. (1992). Fluorescence Lifetime Imaging Microscopy (FLIM): Instrumentation and Applications. Crit. Rev. Anal. Chem. *23*, 369–395.

Chapter 6

Future directions

In this thesis, we have demonstrated the capability of FLIM as a non-invasive tool to investigate microglia activation status, and showed how it can be used to characterize various activation states in response to external stimuli (Sagar et al., 2019a). We believe that this approach can be used in the future *in vivo* to study functional state changes of microglia in various neurodegenerative diseases, perhaps even in early stages (Sagar et al, 2019b). This may help create better therapeutic approaches and better screening techniques for pre-clinical application. To move towards this in vivo detection direction, lifetime of microglia in well characterized disease models needs to be measured. If there is a correlation, a follow-up study could be used to find the effectiveness of therapeutic technique based on changes on lifetime. This was beyond the scope of the presented project but will be explored in future studies. There are also have been clearly established relationships between microglia activation as biomarker in relation to injury (Hernadez-Ontiveros et al., 2013; Watanabe et al., 1999; Zhang et al., 2012). In future, we want to examine how injury can affect microglia metabolism by utilizing NADH/FAD lifetime information.

In chapter 3, we demonstrated the machine learning approach to visualize microglia label free using intrinsic fluorescence lifetime data. With limited amount of data, we are able to use fluorescence lifetime data to identify microglia cell without using any external labels. This approach can in the future be potentially extended to identifying other cell types in CNS and differentiate resident CNS cells and infiltrating cell types. An important follow-up study would be differentiation of microglia and macrophages as they have similar phenotype and morphological appearance. It is important to be able to differentiate between them as it will be relevant in differentiating how microglia and macrophage affect CNS diseases. After we finished working on the results presented here, a new study came out demonstrating deep learning approaches to calculate lifetime without fitting (Smith et al., 2019). In our next step, we envisioned something

similar, but instead of calculating lifetime, we want to directly characterize cell type using FLIM data. This is one of the areas we will be working on in future. Additionally, we demonstrated some preliminary result by using convolutional neural network (CNN) to classify microglia in tissue using just the fluorescence intensity image and achieved over 95% accuracy. Very recently, a similar method has been applied for classification of T-cell (Wang et al., 2019). But in future we want to build combine deep learning approaches to use morphology and lifetime together to classify different stages of microglia activation and phenotype. It can be further improved with the inclusion of FLIM data to improve training accuracy. This hybrid approach has the potential to be very helpful in discriminating microglia and macrophages. A therapeutic technique aimed at CNS diseases which aims to understand the role of macrophage and microglia, would likely benefit from this approach.

For the proposed spectral-lifetime technique in Chapter X (and Sagar et al., 2019b), improvement is required to increase temporal resolution of our proposed fiber-based spectral lifetime system. First, better optical fiber is needed to reduce modal dispersion and increase transmission. But that likely will require custom fiber design which was beyond the scope of this thesis. As well a hybrid detector-based (Becker et al., 2011) detection electronic setup can improve the temporal resolution significantly. Moreover, for a given optical fiber and an optical system, the modal dispersion needs to be properly modelled so that the emission spectra can be more accurately calculated. Furthermore, the spectral-temporal map we designed for this project, can be used as an additional optical biomarker for cellular state change. In future, more experiments need to be done to investigate cellular state change.

Building on the OpenScan FLIM acquisition, and combining the FLIMJ (https://imagej.net/FLIMJ) lifetime analysis approaches, a potentially open source tool can be

developed which can do runtime analysis and provide lifetime estimation at various stages of acquisition. Combining this approach with the deep learning methods, we can build a computational robust, open source FLIM acquisition and analysis tool which can enhance FLIM

based biological study more robust, fast and transparent. The following figure summarizes the achievements/findings as a result of this thesis and the future direction.

Figure: Summary of achievement and future direction

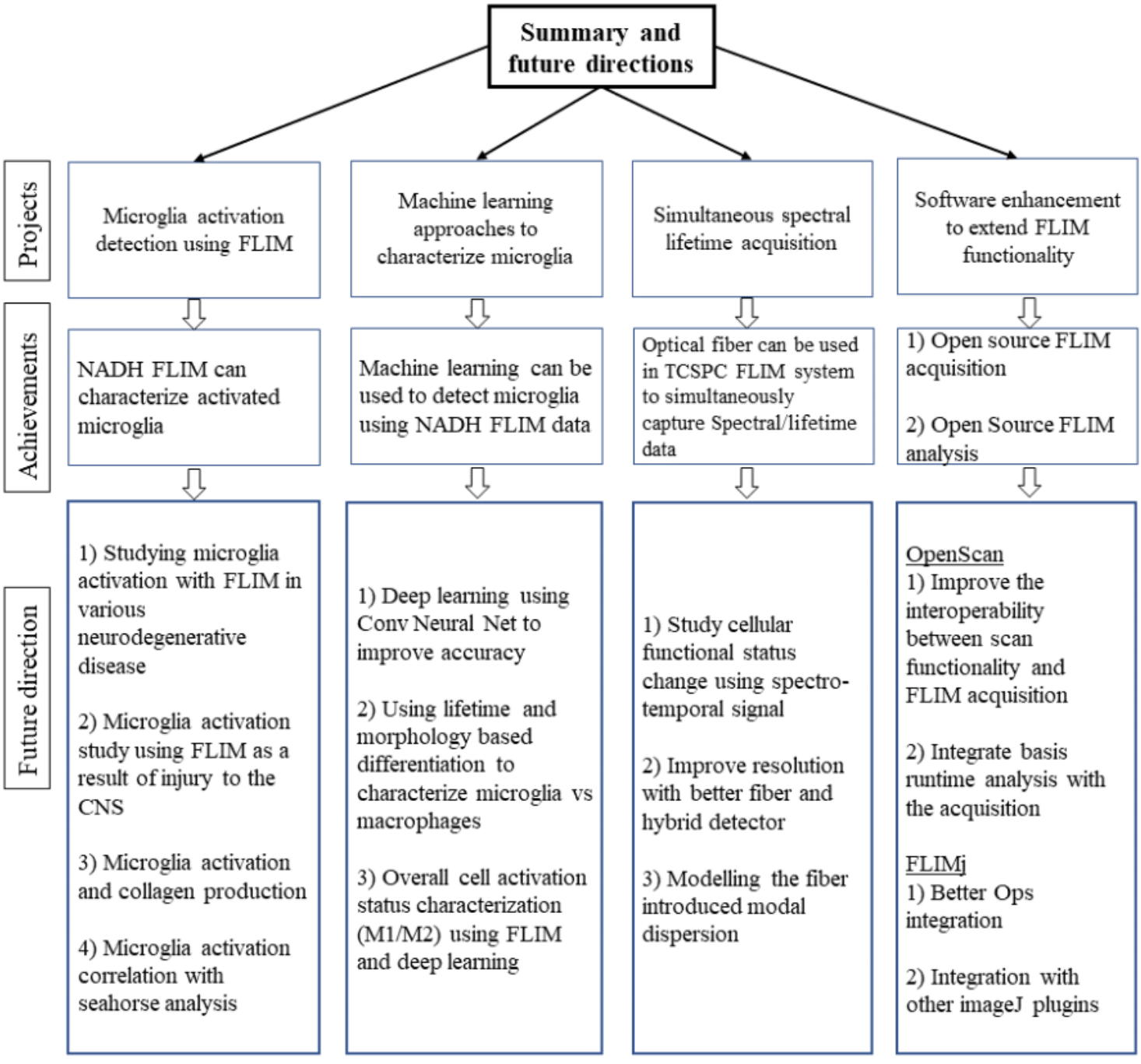

References

Becker, W., Su, B., Holub, O., and Weisshart, K. (2011). FLIM and FCS detection in laser-scanning microscopes: Increased efficiency by GaAsP hybrid detectors. Microsc. Res. Tech. *74*, 804–811.

Hernadez-Ontiveros, D.G., Tajiri, N., Acosta, S., Giunta, B., Tan, J., and Borlongan, C.V. (2013). Microglia Activation as a Biomarker for Traumatic Brain Injury. Front. Neurol. *4*.

Sagar, M.A.K., Cheng, K.P., Ouellette, J., Williams, J.C., Watters, J.J., and Eliceiri, K. (2019a). Fluorescence lifetime-based intrinsic metabolic signatures of microglia cell (Conference Presentation). In Light in Nature VII, (International Society for Optics and Photonics), p. 110990C.

Sagar, M.A.K., Dai, B., Chacko, J.V., Weber, J.J., Velten, A., Sanders, S.T., White, J.G., and Eliceiri, K.W. (2019b). Optical fiber-based dispersion for spectral discrimination in fluorescence lifetime imaging systems. J. Biomed. Opt. *25*, 014506.

Sagar, M.A.K., Ouellette, J., Cheng, K.P., Williams, J.C., Watters, J.J., and Eliceiri, K. Microglia activation visualization via Fluorescence lifetime Imaging microscopy of intrinsically fluorescent metabolic cofactors. (Under review).

Smith, J.T., Yao, R., Sinsuebphon, N., Rudkouskaya, A., Un, N., Mazurkiewicz, J., Barroso, M., Yan, P., and Intes, X. (2019). Fast fit-free analysis of fluorescence lifetime imaging via deep learning. Proc. Natl. Acad. Sci. *116*, 24019–24030.

Wang, Z.J., Walsh, A.J., Skala, M.C., and Gitter, A. (2019). Classifying T cell activity in autofluorescence intensity images with convolutional neural networks. J. Biophotonics.

Watanabe, T., Yamamoto, T., Abe, Y., Saito, N., Kumagai, T., and Kayama, H. (1999). Differential Activation of Microglia After Experimental Spinal Cord Injury. J. Neurotrauma *16*, 255–265.

Zhang, Q.-G., Laird, M.D., Han, D., Nguyen, K., Scott, E., Dong, Y., Dhandapani, K.M., and Brann, D.W. (2012). Critical Role of NADPH Oxidase in Neuronal Oxidative Damage and Microglia Activation following Traumatic Brain Injury. PLOS ONE *7*, e34504.

Appendix

In the course of the development of the projects described in the previous chapters, there were several collaborations which implemented the knowledge/expertise gained from the projects. Several of the resulted in peer reviewed article which are briefly described in the following sections. The papers can be broadly divided in two areas, 1) Application of microscopy in life science, 2) Technical development to enhance microscopy

Application of microscopy in life science

FLIM (Fluorescence Lifetime Imaging Microscopy) can quantify time-resolved imaging data from laser scanning microscope. Due to recent advancements in Time-Correlated Single Photon Counting (TCSPC) electronics, we are able to image picoseconds level timing resolution from intrinsic/extrinsic fluorophore. With FLIM, we are able to probe intrinsic metabolic cofactors such as NADH and FAD both of which are autofluorescent. The binding status of the metabolic cofactors changes with alterations in the cellular microenvironment and FLIM based quantification helps us understand the intrinsic microenvironment. In this project, we aim to better understand metabolism and its relation to biochemical changes with NADH/FAD based FLIM imaging. With fluorescence microscopy, we can illuminate a sample with particular wavelength and detect the emission at particular wavelength. But with FLIM, we can additionally calculate how much time a fluorophore stays at excited state. A number of previous studies have found that, with FLIM imaging we can measure various intrinsic cellular properties such as pH, temperature, oxygen sensing etc. To simplify, FLIM can help us image cell properties which is otherwise very difficult to image or quantify. NADH is enzyme that is present in all living cell and is very important part of cellular ATP production process i.e. metabolism. Our lab has previously shown that, FLIM

imaging of NADH can reveal cell metabolism state and can also differentiate between cancer and non cancerous cell. But NADH FLIM can achieve this without adding any external dyes because all living cell has NADH intrinsically.

In the first study (Kenny et al., 2017) , we collaborated to find out that activation of SIRT3 axis of unfolded protein response of mitochondria is linked to cancer metastasis. With our understanding of NADH FLIM, we helped confirm the observation in primary breast cancer. In this project, we collaborated to find out ability of selected mtDNA species to activate the UPRmt is a process that is exploited by cancer cells to maintain mitochondrial fitness and facilitate metastasis. With our FLIM imaging of NADH/NAD+ and interpretation of the result, we found that SOD2 is significantly enriched in metastatic lesions compared with primary tumors, and that areas of SOD2 positivity correlate with NAD+ rather than NADH by FLIM.

In a separate study (Martin et al., 2018), we studied the role of GSK3β in regulating mitochondrial energy metabolism in neurons and in glia. GSK3β is an enzyme implicated in the progression of Alzheimer's disease. The role of GSK3β in metabolic response is not little known and studying them would help us better understand its role in aging and neurodegenerative disease. Here, we show that GSK3β regulates mitochondrial energy metabolism in human H4 neuroglioma cells and rat PC12-derived neuronal cells and that inhibition of GSK3β in mice in vivo alters metabolism in the hippocampus in a region-specific manner. We demonstrate that GSK3β inhibition increases mitochondrial respiration and membrane potential and alters NAD(P)H metabolism. With our understanding of NADH FLIM we confirmed the metabolic changes as a result of GSK3β regulation.

One other aspect of multiphoton microscopy is its ability to image collagen via SHG microscopy and quantify the alignment with cancer grade. We wrote a book chapter reviewing the current techniques to image and quantify cancer with SHG microscopy (Keikhosravi et al., 2014).

Techniques summary

The collaboration projects in this subsection are methods and technical approaches to improve Fluorescence lifetime imaging and multiphoton imaging. The techniques to improve FLIM are aimed at improving FLIM coding technique to improve speed or propose novel non-parametric Bayesian approach to calculate lifetime with low photon count.

In the first project (Ghanbari et al., 2019), we collaborated with researchers in University of Minnesota to develop digitally designed, morphologically realistic transparent polymer skulls that allow long term(>300 days) optical access to dorsal cerebral cortex in the mouse. This allowed two photon imaging of neural structures up to 600 μm deep allowing calcium imaging from multiple non-contiguous region across the cortex. For our part in the collaboration, we hypothesized that polyethylene terephthalate (PET) film can be used as alternative to glass offering. PET has several advantages over glass such as flexibility, can be 3D printed. We performed the optical characterization and biological viability of PET to make sure glass and PET flim perform similarly optically and does not introduce toxicity. For optical characterization we compared Point Spread Function(PSF) of 3 different PET films with PSF of glass and found there is no significant difference between the PSFs. We additionally performed optical transmission efficiency comparison at different biologically relevant wavelengths and found there is statistically no significant different between glass and PET flim. Finally, to make sure the PET film does not introduce toxicity, we cultured MCF10a cells for over 17 days and found that there is no toxicity induces cell deaths.

In another project (Lee et al., 2019), we developed theory and algorithms for designing high-performance FD-FLIM coding schemes that can achieve high SNR and short acquisition time, given a fixed source power budget. In frequency-domain FLIM (FD-FLIM), the object of interest is illuminated with a temporally modulated light source. The fluorescence lifetime is measured by computing the correlations of the emitted light with a demodulation function at the sensor. The signal-to-noise ratio (SNR) and the acquisition time of a FD-FLIM system is determined by the coding scheme (modulation and demodulation functions). Based on a geometric analysis of the image formation and noise model, we propose a novel surrogate objective for the performance of a given coding scheme. The surrogate objective is extremely fast to compute, and can be used to efficiently explore the entire space of coding schemes. Based on this objective, we design novel, high-performance coding schemes that achieve up to an order of magnitude shorter acquisition time as compared to existing approaches.

To improve time domain FLIM analysis speed, in a separate study (Wang et al., 2019), we introduce a new nonparametric empirical Bayesian framework for FLIM data analysis (NEB-FLIM), leading to both improved pixel-wise lifetime estimation and a more robust and computationally efficient integral property inference. This framework is developed based on a newly proposed hierarchical statistical model for FLIM data and adopts a novel nonparametric maximum likelihood estimator to estimate the prior distribution.

References

Ghanbari, L., Carter, R.E., Rynes, M.L., Dominguez, J., Chen, G., Naik, A., Hu, J., Sagar, M.A.K., Haltom, L., Mossazghi, N., et al. (2019). Cortex-wide neural interfacing via transparent polymer skulls. Nat. Commun. *10*, 1–13.

Keikhosravi, A., Bredfeldt, J.S., Sagar, A.K., and Eliceiri, K.W. (2014). Second-harmonic generation imaging of cancer. Methods Cell Biol. *123*, 531–546.

Kenny, T.C., Hart, P., Ragazzi, M., Sersinghe, M., Chipuk, J., Sagar, M. a. K., Eliceiri, K.W., LaFramboise, T., Grandhi, S., Santos, J., et al. (2017). Selected mitochondrial DNA landscapes activate the SIRT3 axis of the UPR^{mt} to promote metastasis. Oncogene *36*, 4393–4404.

Lee, J., Chacko, J.V., Dai, B., Reza, S.A., Sagar, A.K., Eliceiri, K.W., Velten, A., and Gupta, M. (2019). Coding Scheme Optimization for Fast Fluorescence Lifetime Imaging. ACM Trans Graph *38*, 26:1–26:16.

Martin, S.A., Souder, D.C., Miller, K.N., Clark, J.P., Sagar, A.K., Eliceiri, K.W., Puglielli, L., Beasley, T.M., and Anderson, R.M. (2018). GSK3β Regulates Brain Energy Metabolism. Cell Rep. *23*, 1922-1931.e4.

Wang, S., Wang, S., Chacko, J.V., Sagar, A.K., Eliceiri, K.W., Eliceiri, K.W., Yuan, M., and Yuan, M. (2019). Nonparametric empirical Bayesian framework for fluorescence-lifetime imaging microscopy. Biomed. Opt. Express *10*, 5497–5517.

Kenny, T. C., Peter Hart, Moira Ragazzi, Madhavika Sersinghe, Jerry Chipuk, Md Abdul Kader Sagar, Kevin W. Eliceiri et al. "**Selected mitochondrial DNA landscapes activate the SIRT3 axis of the UPR mt to promote metastasis**." Oncogene 36, no. 31 (2017): 4393.

Summary:

By causing mitochondria DNA (mtDNA) mutations and oxidation of mitochondrial proteins, reactive oxygen species (ROS) leads to perturbations in mitochondrial proteostasis. Several studies have linked mtDNA mutations to metastasis of cancer cells but the nature of the mtDNA species involved remain unclear. Our data suggests that no common mtDNA mutation identifies metastatic cells; rather the metastatic potential of several ROS-generating mutations is largely determined by their mtDNA genomic landscapes, which can act either as an enhancer or repressor of metastasis. However, mtDNA landscapes of all metastatic cells are characterized by activation of the SIRT/FOXO/SOD2-axis of the mitochondrial unfolded protein response (UPRmt). The UPRmt promotes a complex transcription program ultimately increasing mitochondrial integrity and fitness in response to oxidative proteotoxic stress. Using SOD2 as a surrogate marker of the UPRmt, we found that in primary breast cancers, SOD2 is significantly increased in metastatic lesions. We propose that the ability of selected mtDNA species to activate the UPRmt is a process that is exploited by cancer cells to maintain mitochondrial fitness and facilitate metastasis.

OPEN

Oncogene (2017) **36**, 4393–4404

www.nature.com/onc

ORIGINAL ARTICLE

Selected mitochondrial DNA landscapes activate the SIRT3 axis of the UPR^{mt} to promote metastasis

TC Kenny[1], P Hart[2], M Ragazzi[3], M Sersinghe[4], J Chipuk[4], MAK Sagar[5], KW Eliceiri[5], T LaFramboise[6], S Grandhi[6], J Santos[7], AK Riar[1], L Papa[1], M D'Aurello[8], G Manfredi[8], MG Bonini[2] and D Germain[1]

By causing mitochondrial DNA (mtDNA) mutations and oxidation of mitochondrial proteins, reactive oxygen species (ROS) leads to perturbations in mitochondrial proteostasis. Several studies have linked mtDNA mutations to metastasis of cancer cells but the nature of the mtDNA species involved remains unclear. Our data suggests that no common mtDNA mutation identifies metastatic cells; rather the metastatic potential of several ROS-generating mutations is largely determined by their mtDNA genomic landscapes, which can act either as an enhancer or repressor of metastasis. However, mtDNA landscapes of all metastatic cells are characterized by activation of the SIRT/FOXO/SOD2 axis of the mitochondrial unfolded protein response (UPR^{mt}). The UPR^{mt} promotes a complex transcription program ultimately increasing mitochondrial integrity and fitness in response to oxidative proteotoxic stress. Using SOD2 as a surrogate marker of the UPR^{mt}, we found that in primary breast cancers, SOD2 is significantly increased in metastatic lesions. We propose that the ability of selected mtDNA species to activate the UPR^{mt} is a process that is exploited by cancer cells to maintain mitochondrial fitness and facilitate metastasis.

Oncogene (2017) **36,** 4393–4404; doi:10.1038/onc.2017.52; published online 3 April 2017

INTRODUCTION

Cancer is lethal due to the ability of cancer cells to enter the circulation and recur as metastatic disease. Recent reports have suggested that changes in mitochondrial biology are associated with this process. A study by Draetta and colleagues[1] in pancreatic cancer indicated that oxidative phosphorylation, autophagy and mitochondrial biogenesis are upregulated in recurrent pancreatic tumors. Likewise, Depinho and colleagues[2] found that tumors, which recurred after surviving the telomere-shortening crisis by activating the alternative lengthening of telomeres pathway, are characterized by an upregulation of mitochondrial biogenesis, oxidative phosphorylation and anti-oxidant machinery. Interestingly, these tumors were also found to upregulate SOD2 and to be drastically sensitive to SOD2 inhibition, suggesting that SOD2 is essential for their survival. In addition, analysis of circulating cancer cells showed a specific upregulation of mitochondrial biogenesis and oxidative phosphorylation through PGC-1α.[3] Notably, this study also found a strong positive correlation between PGC-1α expression and distant metastasis.[3] Therefore, although the switch from oxidative phosphorylation to glycolysis characterizes primary tumors, recent data suggest that disseminated cells, circulating cancer cells and metastatic cells are characterized by elevated oxidative phosphorylation and appear to be highly dependent on the anti-oxidant enzyme, Mn-superoxide dismutase (SOD2). The discovery of oxidative tumors has led to the concept of metabolic flexibility,[4] where tumors able to use both glycolysis and oxidative phosphorylation may represent a more aggressive sub-population due to their ability to adapt to stress. The mechanism coordinating these changes remains unknown.

Another important link between mitochondrial biology and metastasis has arisen from the observation that introduction of mitochondrial DNA (mtDNA) from a metastatic cell line into a non-metastatic cell line using cybrid technology, was sufficient to confer metastatic capacity to the non-metastatic cells.[5] Following this initial report, several others have described similar findings.[6–12] Further, the nuclear gene expression profiles of cybrids, sharing the same nuclear genome but having different mitochondrial genomes, were found to differ suggesting that mitochondrial stress affects nuclear gene expression.[13] Mutations in mtDNA can lead to a defect in oxidative phosphorylation and accumulation of reactive oxygen species (ROS), which can in turn lead to the oxidation of proteins and their misfolding. Cancer cells, therefore, are predicted to rely on the mitochondrial unfolded protein response (UPR^{mt}) to survive such stress.

The original identification of the UPR^{mt} was made in mammalian cells using the overexpression of misfolded OTCΔ in the mitochondrial matrix.[14,15] These studies led to the identification of CCAAT-enhancer-binding protein homologous protein (CHOP) as the transcription factor responsible for the activation of the chaperone hsp60 and proteases such as a ClpP in response to mitochondrial proteotoxic stress.[14,15] Subsequently, the promoter of hsp60 was used extensively as a marker of the UPR^{mt} in *Caenorhabditis elegans*.[16–24] However, the impressive expansion of the study of the UPR^{mt} using mainly *C. elegans* and has also lead to the misconception that the UPR^{mt} does not exist in mammals. Further, it is now clear that the UPR^{mt}

[1]Division of Hematology/Oncology, Department of Medicine, Tisch Cancer Institute, Icahn School of Medicine at Mount Sinai, New York, NY, USA; [2]Department of Medicine, University of Illinois at Chicago, Chicago, IL, USA; [3]Pathology Unit, Arcispedale Santa Maria Nuova - IRCCS, Reggio Emilia, Italy; [4]Department of Oncological Sciences, Icahn School of Medicine at Mount Sinai, New York, NY, USA; [5]Department of Biomedical Engineering, Laboratory for Optical and Computational Instrumentation, University of Wisconsin, Madison, WI, USA; [6]Department of Genetics, School of Medicine, Case Western Reserve University, Cleveland, OH, USA; [7]National Institute of Environmental Health Sciences, Durham, NC, USA and [8]Brain and Mind Research Institute, Weill Cornell Medicine, New York, NY, USA. Correspondence: Dr D Germain, Division of Hematology/Oncology, Department of Medicine, Tisch Cancer Institute, Icahn School of Medicine at Mount Sinai One Gustave L. Levy Place Box 1079, New York, NY 10029, USA.
E-mail: doris.germain@mssm.edu

Received 19 September 2016; revised 13 January 2017; accepted 20 January 2017; published online 3 April 2017

activates much more than proteases and chaperones, and is a complex transcriptional program,[25] which places this pathway as a prime candidate to explain the changes in nuclear gene expression profile of cybrids. In mammalian cells, we and others have used the expression of misfolded proteins in the mitochondria to identify factors of the UPR^{mt}.[14,15,26,27] Namely, we reported a SIRT3/FOXO3a/SOD2 axis of the UPR^{mt}, which is activated independently of the CHOP/hsp60 axis.[27] Considering the regulation of PCG1α by SIRT3,[28–30] the SIRT3 axis of the UPR^{mt} appears favorably placed to explain the upregulation of mitochondrial biogenesis and increased mitochondrial anti-oxidant machinery seen in aggressive disease. Interestingly, a SIRT1/FOXO axis of the UPR^{mt} leading to the activation of SOD2 has also been reported in *C. elegans*.[31] As FOXO transcription factors are regulated by both SIRT3 and SIRT1,[32,33] these observations suggest that this axis of the UPR^{mt} is conserved and may have an important role in both aging and cancer. We therefore initiated the current study to investigate whether the SIRT3 axis of the UPR^{mt} may be associated with specific ROS-generating mtDNA mutations and metastasis. We found that the context in which a mutation is found influences its effect on invasion. As the term landscape is now widely used when referring to variations in the nuclear genome, we propose to use the same concept but in relation to the mitochondrial genome. Therefore, our results suggest that specific combinatorial genomic landscapes of mtDNA, rather than individual missense mutations, are able to activate the SIRT3 axis of the UPR^{mt} and facilitate metastasis. In the context of mitochondrial diseases, it was recently shown that the UPR^{mt} inadvertently maintains deleterious mtDNA species.[19] In the context of cancer, instead, we propose that the UPR^{mt} is exploited to maintain deleterious mtDNA mutations that allow them to advantageously adapt during the metastatic process.

RESULTS

Metastasis of breast cancer cells correlates with mtDNA heteroplasmy

Invasion capacity of cancer cells has been associated with specific mtDNA mutations.[6–12] To determine whether common mutations can be found in multiple invasive breast cancer cells but not in non-invasive cells, we first selected a panel of six breast cancer cells lines and tested their invasion capacity. We found that three cell lines (MCF-7, MCF7R and ZR-75.1) show significantly less invasion than the other three cell lines (MDA-MB361, MDA-MB-231 and MDA-MB-157; Figure 1a). However, MCF-7R cells, which are a clone selected for resistance to endocrine therapy,[34] were more invasive than their parental cell line MCF-7 (Figure 1a). We then performed mtDNA sequencing on all cell lines and compared their

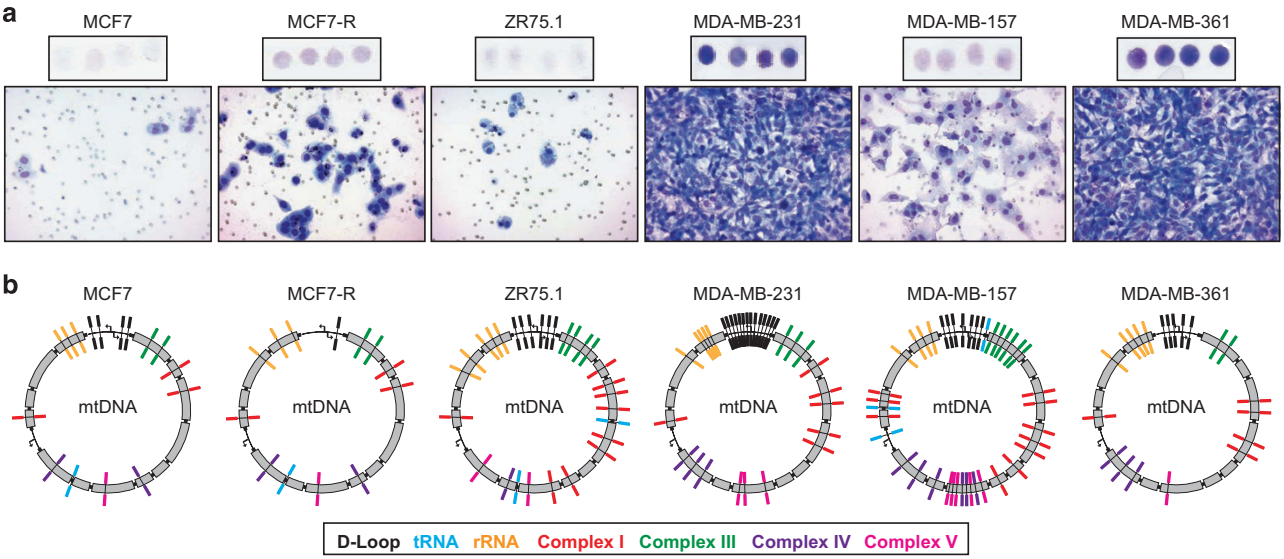

c

mRNA	# of Variants	Heteroplasmy	# of Variants	Heteroplasmy	# of Variants	Heteroplasmy	# of Variants	Heteroplasmy	# of Variants	Heteroplasmy	# of Variants	Heteroplasmy
Missense	5		5		9		5	1 Low	7	4 Low	5	
Frameshift	0		0		0		0		2	2 High	0	
Stop Codon	0		0		1	1 Low	0		0		0	
Modifiers												
D-Loop	4		1		6	2 Low	14	1 Low, 1 High	7	3 Low	5	2 Low
tRNA	0		0		2		0		3	1 Low, 1 High	0	
rRNA	3		3	1 High	5		5		3	1 Low	5	1 High
Synonymous	4		4		6		10	1 High	16	7 Low, 2 High	6	2 Low
	MCF7		**MCF7-R**		**ZR75.1**		**MDA-MB-231**		**MDA-MB-157**		**MDA-MB-361**	

Figure 1. Invasion capacity correlates with mtDNA heteroplasmy. (**a**) Invasion assays were performed on the indicated cell lines and filters collected at 24 h. Top panel show the overall intensity of 4 independent filters, whereas bottom panels show a magnification of a representative area of one filter. (**b**) Schematic representation of the mtDNA map of the indicated cell lines. Variants and mutations at specific locations along mtDNA are indicated by a line across the map and are color coded according to the area/ gene affected. (**c**) Summary table of number of variants and the level of heteroplasmy in either area encoding mRNA or modifiers. High levels of heteroplasmy are indicated in red. Details of each variant are found in Supplementary Figures 1–4.

sequence with the revised Cambridge reference sequence[35] as the cell lines are derived from different patients and no other internal controls are available. Variants with no known functional consequences that were found in all cell lines were interpreted as background variation related to the difference in the tissue of origin. All remaining variants were classified in three groups as follows: (1) mutations affecting mRNA sequence; (2) modifier variants affecting the sequence in the D-loop, rRNA or tRNA; and (3) synonymous variants representing sequence polymorphisms. Interestingly, the mutations in the ND6 gene (G13997A and 13885insC) previously linked to metastasis were not present in any of the invasive cell lines.[5] In contrast, missense mutations in ATP8 (A8860G) and CYB (A15380G) were present in all cell lines and were homoplasmic (Figures 1b and c, and Supplementary Figures 1–4). However, as these mutations did not distinguish the invasive from the non-invasive cell lines, they alone cannot explain the role of mtDNA mutations in metastasis. Instead, a common characteristic of invasive cells compared with non-invasive cells, including the MCF7R cells, was the presence of at least one variant with significant levels of heteroplasmy (Figures 1b and c, and Supplementary Figures1–4). These observations raise the possibility that the ability of missense mutations in major subunits of the electron transport chain to promote invasiveness may be context dependent and defined by their overall mitochondrial genomic landscapes. In this setting, heteroplasmy may offer the option for the selection of the optimal pro-metastatic mtDNA genomic landscape. Further, the number of lesions per kilobase of mtDNA was higher in invasive cells compared with non-invasive cells (Supplementary Figure 5), which is in agreement with the recent report that low mtDNA repair facilitates invasion.[36]

mtDNA heteroplasmy correlates with heterogeneity in mitochondrial morphology in cancer cells

In theory, the presence of homoplasmic mutations in the context of other heteroplasmic variants allows for the combinatorial diversity of mtDNA and the generation of a pool of different mtDNA species within a given cell. If this were the case, we reasoned that such mtDNA diversity could be reflected in a heterogeneous mitochondrial population. To test this possibility, we performed transmission electron microscopy on all cell lines. We found a remarkable heterogeneity in the morphology of the mitochondrial networks among cell lines. The morphology of the mitochondria in MCF-7 cells showed the largest organelles of all cell lines with homogeneous morphology (Figure 2a). The ZR-75.1 cells showed smaller organelles compared with the MCF-7 cells, which were also of homogeneous morphology (Figure 2b). In contrast, all invasive cells showed intra-cellular (MDA-MB-231, Figure 2c) or inter-cellular (MDA-MB-361, MDA-MB 157 and MCF7R; Figures 2d–f) differences in mitochondrial morphology.

This analysis, therefore, is consistent with the hypothesis that heteroplasmy not only generates diverse mtDNA species but may contribute to heterogeneous mitochondrial morphologies.

Mitochondrial heterogeneity correlates with metabolic flexibility and the activation of the UPR^{mt}

To further investigate the heterogeneity of the mitochondrial population, we next determined the level of oxidative phosphorylation (oxygen consumption rate, OCR) and glycolysis (extracellular acidification rate, ECAR) using the Seahorse XF Analyzer. In three separate experiments including eight replicates in each experiment, we found that the OCR/ECAR ratio was consistent in MCF-7, MCF7R and ZR75.1 cells, and was >1, indicating a

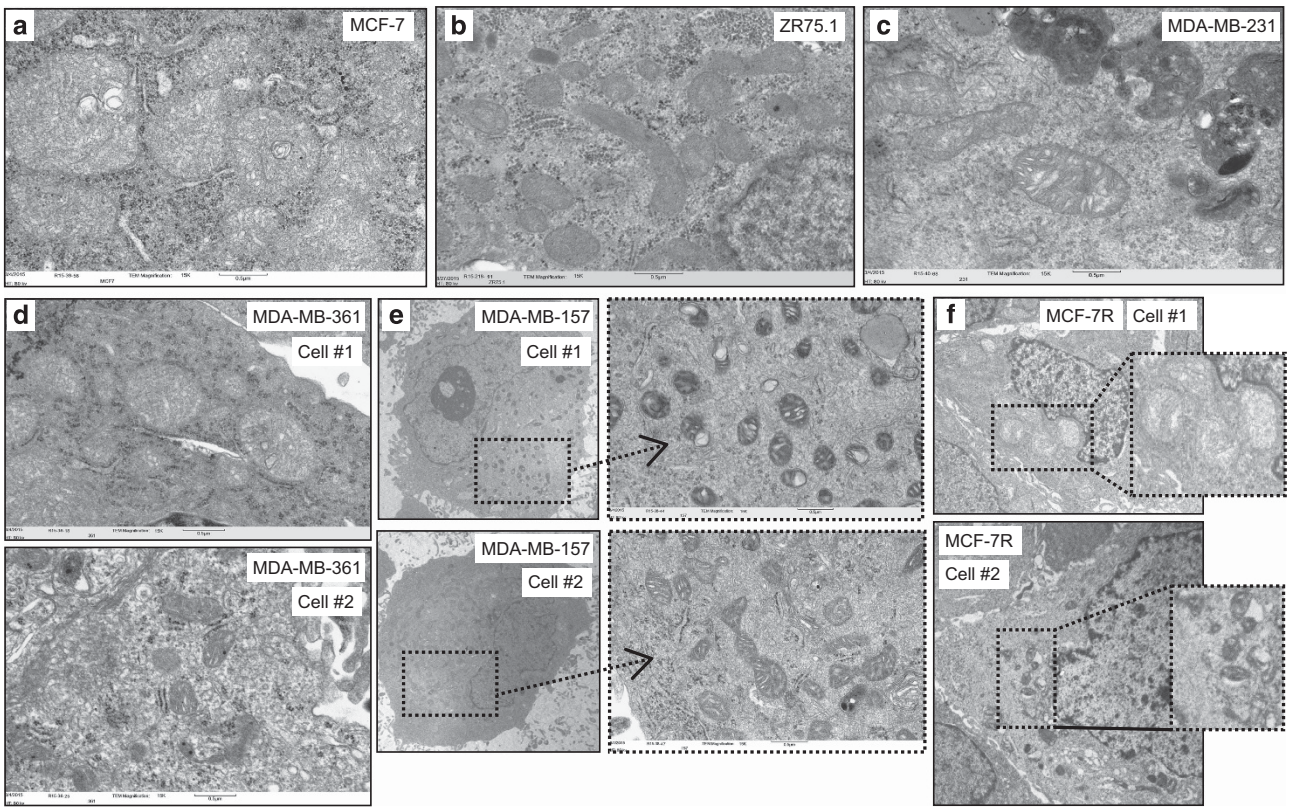

Figure 2. Mitochondrial morphology varies widely among cell lines and correlates with heterogeneity in invasive cell lines. Electron microscopy at a magnification of 15 K in MCF-7 cells (**a**), ZR-75.1 (**b**), MDA-MB231 (**c**), MDA-MD-361 (**d**), MDA-MB-157 (**e**) and MCF-fulvestrant at magnification of 7K (**f**). In **d**–**f**, images from two independent cells from the same field are shown.

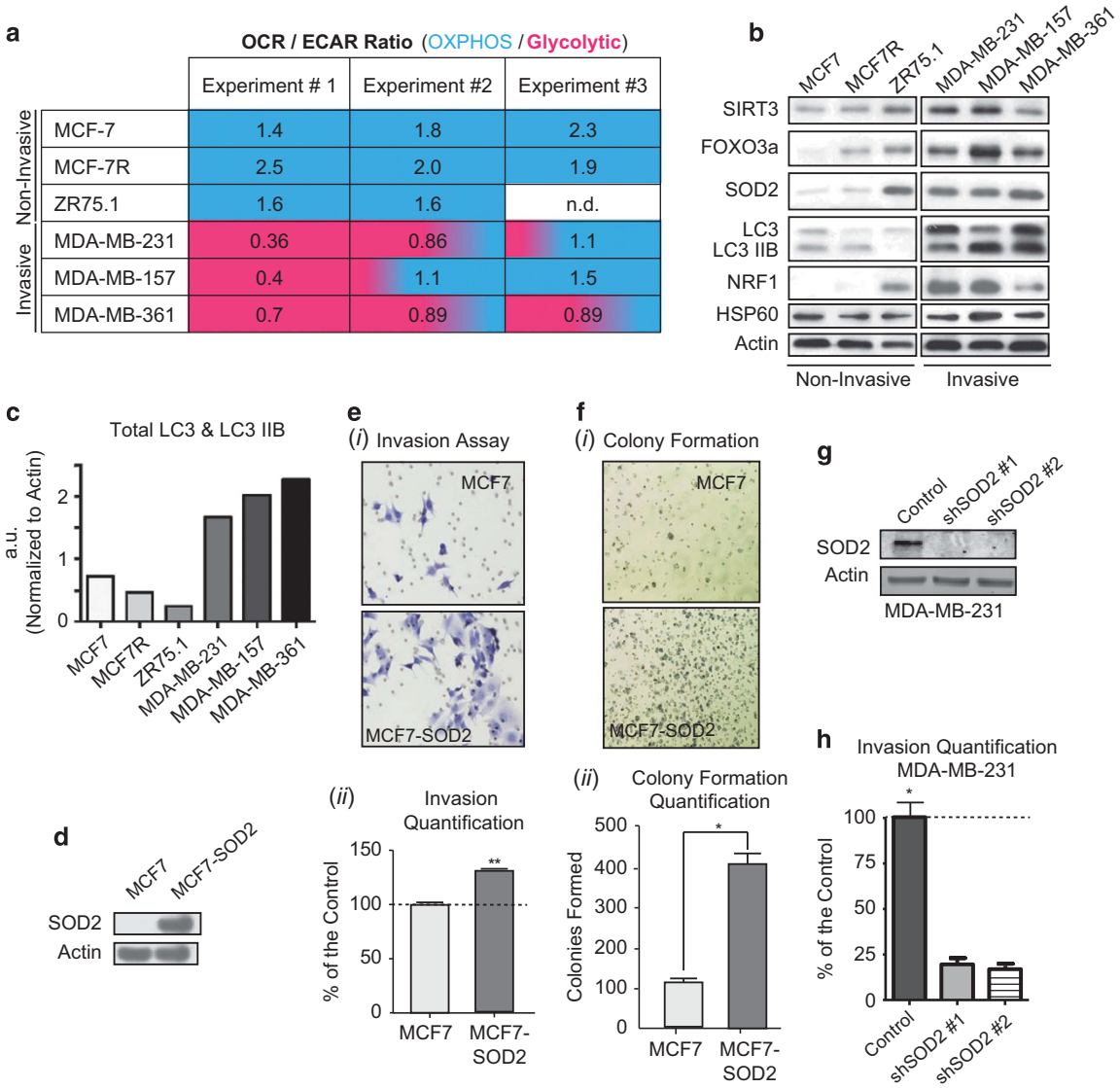

Figure 3. Metabolic flexibility, activation of the SIRT3 axis of the UPR^{mt} characterizes invasive cell lines and modulation of SOD2 levels alone alters the invasion capacity. (**a**) OCR/ECAR ratio obtained by Seahorse analysis of the indicated cell lines in three separate experiments; blue indicates a higher use of oxidative phosphorylation over glycolysis and pink indicates a higher use of glycolysis over oxidative phosphorylation; gradient indicates equal use of both. (**b**) Western blot analysis of markers of the UPR^{mt} in the indicated breast cancer cell lines. (**c**) Quantification of LC3 and LC3IIB in non-invasive and invasive cell lines. (**d**) Western blotting of SOD2 levels in a stable clone overexpressing SOD2. (**e**) (i) Invasion assay at 24 h in MCF-7 and MCF7-SOD2 cells, (ii) a quantification of the invasion. (**f**) (i) Colony formation assay in MCF-7 and MCF-7-SOD2 cells, and (ii) quantification of colonies. (**g**) Western blotting of SOD2 in MDA-MB-231 cells where SOD2 was inhibited by two independent shRNA. (**h**) A quantification of the invasion with and without shRNA against SOD2 is shown. $^{*}P < 0.05$ calculated by analysis of variance and $^{**}P < 0.01$.

preferential use of oxidative phosphorylation over glycolysis, in these cells (Figure 3a). In contrast, the OCR/ECAR ratio varied widely from one experiment to the other in invasive cell lines, despite identical experimental conditions. One interpretation of this finding is that at any given time, the percentage of cells within the population showing preferential use of oxidative phosphorylation or glycolysis may vary (Figure 3a).

Recently, the presence of deleterious mtDNA mutations has been reported to activate the mitochondrial UPR (UPR^{mt}) via the transcription factor ATFS-1 using the hsp60 promoter reporter in *C. elegans*.[19] The functional homolog of ATFS1 was identified as ATF5 in mammals[17] and acts downstream of CHOP, the original transcription factor identified in mammals for the regulation of hsp60 and matrix proteases.[14,15] In addition to the CHOP axis of the UPR^{mt}, a SIRT/FOXO/SOD2 axis of the UPR^{mt} has been reported and is conserved between *C. elegans* and mammals.[27,31] In contrast to the CHOP axis, which regulates chaperones and proteases,[14,15] the SIRT3 axis regulates anti-oxidant machinery (SOD2) via FOXO3a, mitophagy (LC3IIB) and mitochondrial biogenesis via NRF1.[27] Further, SOD2 has been shown to be functionally linked to the activation of glycolysis.[37] We therefore screened the panel of cell lines for markers of the UPR^{mt}. No differences in hsp60 were observed between cell lines, suggesting that the CHOP axis of the UPR^{mt} does not mediate the differences observed. As hsp60 is the best-characterized marker of the UPR^{mt}, this result was surprising. We reasoned that as hsp60 is upregulated early in cancer progression in human cancer,[38,39] and that our analysis was performed in established cancer cell lines, hsp60 may also be activated early during transformation in cell lines. To test this possibility, we analyzed the level of hsp60

following induction of the oncogene ras in the non-transformed cell line MCF10A. We found that hsp60 is indeed upregulated within hours (Supplementary Figure 6a). However, we found that MDA-MB-231, MDA-MB-157 and MDA-MB-361 cells were positive for all five markers of the SIRT/FOXO/SOD2 axis of the UPR^{mt} (Figure 3b). However, this was not simply due to differences in mitochondrial mass since other mitochondrial markers such ATP5O, COX1 and cytochrome *c* did not distinguished the invasive from the non-invasive cell lines (Supplementary Figure 6b). Interestingly MCF7R cells show an increase in the level of four of these markers relative to the MCF-7 parental cell line (Figure 3b). The non-invasive ZR75.1 cells, however, showed four out of the five UPR^{mt} markers to be elevated but failed to activate autophagy. Given that these cells carry several missense mutations and one stop codon mutation (Supplementary Figure 2), this result suggests that their inability to eliminate irreversibly damaged mitochondria from the network by autophagy may limit their ability to survive invasion. In support of this possibility, the MDA-MB157 cells also carry several missense mutations and one stop codon mutation (Supplementary Figure 3) but show elevated levels of autophagy and are invasive. Overall, the quantification of autophagy was higher in the invasive cell lines (Figure 3c).

As SOD2 has been shown to promote metabolic flexibility,[37] we next tested whether SOD2 alone is able to increase invasion and created MCF-7 stable clones expressing SOD2 (Figure 3d). We found that expression of SOD2 did in fact increase the invasion capacity of these cells (Figure 3ei, ii), as well as their ability to form colonies on soft agar (Figure 3fi, ii). Further, inhibition of SOD2 by shRNA in MDA-MB-231 cells significantly decreased their invasion capacity (Figures 3g and h). Despite increasing relative invasion, SOD2 overexpression alone in the MCF-7 cells was not sufficient to increase the invasion to the same level as in the metastatic cell lines such as MDA-MB-231. Our interpretation of these results is that SOD2 is important, but the other downstream effectors of the $UPR^{mt\text{-}SIRT3}$ are also required.

Metastatic potential of ROS-generating mtDNA mutation is context dependent

Our data suggest that the metastatic potential of missense mutations in major subunits of the electron transport chain is dependent on its surrounding mtDNA landscape and the activation of the SIRT3 axis of the UPR^{mt}. However, as the nuclear genomic landscape of the cell lines in our panel is also widely different, a significant contribution of the nuclear genome to the activation of the UPR^{mt} remains a distinct possibility.

Therefore, to further interrogate the role of the mtDNA landscape on the activation of the UPR^{mt}, we took advantage of a collection of cybrids derived from the 143B/206 osteosarcoma cells lacking mtDNA.[40] Given that we found a missense mutation in cytochrome *B* (CyB) present in all breast cancer cell lines in our panel, we first focused on one cybrid line where the mtDNA was repopulated with mtDNA from a patient carrying a frame-shift mutation in CyB and is therefore referred to as CyB.[40] As in the breast cancer cell lines, the CyB line is homoplasmic for this mutation. In addition to this cybrid, a hybrid called Hybrid B, between the CyB line and another cybrid was generated, leading to a variant of the CyB carrying a mixed mtDNA landscape.[40] A schematic representation of the various lines is shown in Figure 4a. First, the expression of the markers of the UPR^{mt} was analyzed by western blotting. We found that both the cybrid CyB and the Hybrid B show elevated expression of all markers of the SIRT/FOXO/SOD2 axis of the UPR^{mt} compared with the parental cell line (wild type (WT)), with the exception of SOD2, which was not significantly elevated in Hybrid B cells compared with the WT cell line (Figures 4b and c). Further, hsp60, ATP5O, COX1 and cytochrome *c* were not significantly different between invasive and non-invasive cell lines (Figures 4b and c, and Supplementary Figure 6c). We next determined the invasion capacity of each cell line. Remarkably, we found that both CyB and Hybrid B were significantly more invasive compared with the parental cell line at both 24 and 48 h (Figures 4d and e). However, the invasiveness of Hybrid B was lower than CyB most noticeably at 24 h supporting our observation that levels of SOD2 impact invasion in MCF7 cells (Figure 3e). However, as Hybrid B remains much more invasive than WT cells, whereas SOD2 does seem to have an important role, it is clearly not the only factor and the additional factors of the UPR^{mt} impact invasion.

We then sequenced the mtDNA in CyB, Hybrid B and the WT parental cell line. We found that CyB and Hybrid B were remarkably similar with only a few differences in heteroplasmy (Figures 4f and g, and Supplementary Figures 7 and 8). Given that both lines carry the same missense mutation in CyB and share the same nuclear DNA, this result indicates that the effect of a ROS-generating mutation on invasion is context-dependent and the presence of even small differences in the mtDNA landscape affects the extent of the activation of the SIRT3 axis of the UPR^{mt} and invasion.

To expand our analysis, we also performed the same analysis on a separate cybrid of the same recipient 143B/206 osteosarcoma cells lacking mtDNA that was repopulated with mtDNA from a patient harboring a stop codon in COX1 and is therefore referred as COX1 line.[40] The COX1 cybrid was also used to construct another hybrid called Hybrid E (Figure 5a). Interestingly, in this pair we found a similar trend in the elevation of the UPR^{mt} markers (Figures 5b and d) and did not show difference in other mitochondrial markers (Supplementary Figure 6d). In contrast to the CyB and Hybrid B cells, the overall difference in the levels of FOXO3a was not as pronounced; however, the molecular weight of FOXO3a was slightly lower in COX1 and HybridE, which is consistent with the deacetylation of FOXO3a. Importantly, deacetylation of FOXO3a is required for its nuclear localization and transcription of SOD2. To test this possibility, the presence of acetylated FOXO3a was tested and we found that in both COX 1 and Hybrid E, the levels of acetylated FOXO3a are decreased (Figures 5c and d). Further, although both cell lines were more invasive than the parental cell line, (Figures 5e and f), Hybrid E was also less invasive than COX1 cells at 24 h (Figure 5e). Sequencing of both cells and the WT parental clone showed that these cells are remarkably similar with only a few minor differences in the heteroplasmy of variants (Figures 5g and h, and Supplementary Figures 7 and 9). Therefore, as was seen in the CyB mutation, the invasive effect of the COX1 mutation is sensitive to its mtDNA landscape and correlates with the extent of the activation of the UPR^{mt}.

Elevated expression of SOD2 is associated with oncocytic tumors with poor prognosis, NAD+ staining and metastasis

Having established that activation of the SIRT3/FOXO3a/SOD2 axis of the UPR^{mt} is associated with invasion, we aimed at validating this axis in primary breast cancers. We reasoned that, if the UPR^{mt} promotes mitochondrial biogenesis, tumors showing increased mitochondrial mass, such as oncocytic tumors, might be characterized by the activation of the UPR^{mt}. Oncocytic tumors of the thyroid and other endocrine tissues are usually benign. However, in the breast, oncocytic tumors and mitochondria-rich tumors were found to have a worse prognosis.[41] This observation suggests that the amount of mitochondria alone is not sufficient to predict outcome but rather the quality and fitness of the mitochondrial network may be most relevant. If so, we hypothesize that oncocytic breast cancers may not only upregulate mitochondrial biogenesis but also oxidative phosphorylation and the anti-oxidant machinery simultaneously through activation of the UPR^{mt}. To test this possibility, we used a unique collection

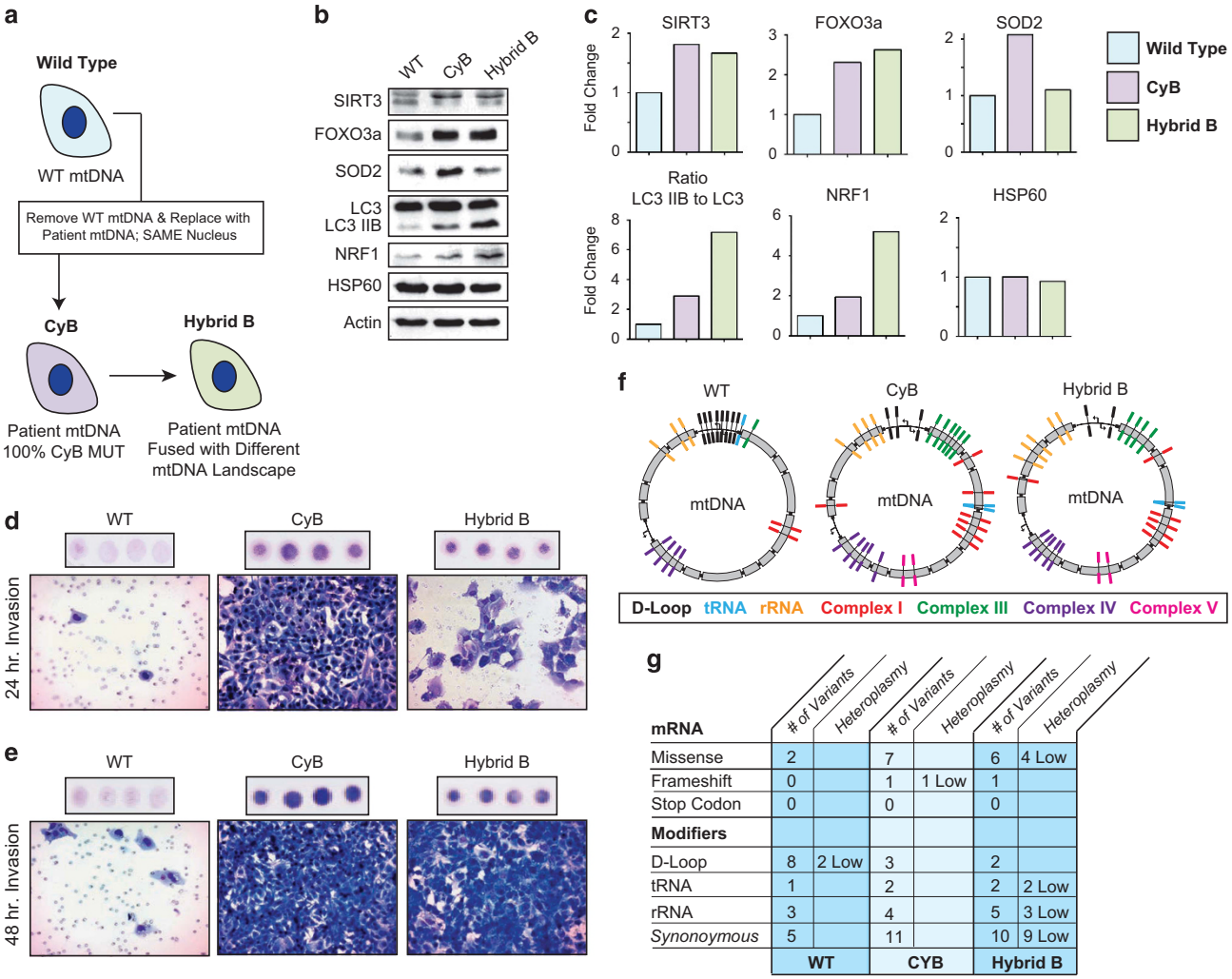

g

mRNA	# of Variants	Heteroplasmy	# of Variants	Heteroplasmy	# of Variants	Heteroplasmy
Missense	2		7		6	4 Low
Frameshift	0		1	1 Low	1	
Stop Codon	0		0		0	
Modifiers						
D-Loop	8	2 Low	3		2	
tRNA	1		2		2	2 Low
rRNA	3		4		5	3 Low
Synonymous	5		11		10	9 Low
	WT		**CYB**		**Hybrid B**	

Figure 4. Increased invasion capacity and activation of the UPR^{mt} of cybrids. (**a**) Schematic representation of the generation of the CyB cybrid and their fusion resulting in hybrid B. (**b**) Western blotting of the markers of the UPR^{mt} in the indicated cell lines. (**c**) Quantification of the levels of the UPR^{mt} shown in **b**. (**d**) Invasion assays of the indicated cell lines after 24 h. Top panel represents an overall view of four independent filters. Bottom panel represent a magnification of a representative area of a single filter. (**e**) Invasion assays of the indicated cell lines after 48 h. Top panel represents an overall view of four independent filters. Bottom panel represent a magnification of a representative area of a single filter. (**f**) Schematic representation of the mtDNA map of the indicated cell lines. Variants and mutations at specific locations along mtDNA are indicated by a line across the map and are color code according to the area/ gene affected. (**g**) Summary table of number of variants and the level of heteroplasmy in either area encoding mRNA or modifiers. Details of each variant are found in Supplementary Figures 7 and 8.

of oncocytic, mito-rich and mito-poor breast cancers, and performed SOD2 staining as a marker of the SIRT3 axis of the UPR^{mt}. We found a statistically significant increase in SOD2 staining in the oncocytic tumors compared to the mito-rich and mito-poor samples (Figures 6a and b). This observation was not simply due to the increase in mitochondrial mass in this subpopulation, because SOD2 staining in normal ducts, which show low number of mitochondria, also had elevated SOD2 staining (Figures 6a and b). This analysis also revealed the presence of strongly positive SOD2 foci within tumors that are otherwise negative for SOD2 (Figure 6a). This pattern raised the possibility that SOD2 may identify heterogeneity within the cancer cell population of a primary tumor. Further, as SOD2 staining was found to be upregulated in recurrent cancers,[2] the expression of SOD2 may allow for the survival of cells through the metastatic process. Therefore, we aimed at evaluating whether SOD2 positivity predicts overall survival. SOD2 staining was scored for extent (percentage of positive cells) and intensity (1+, 2+ or 3+), and patients were classified in two groups. The first group was classified as high SOD2 expressers (SOD2^{high}) based on the presence of any extent of 3+ staining or intensity × extent score of >100. The second group was classified as low SOD2 expressers (SOD2^{Low}) based on an intensity × extent score of less than 100. This classification revealed a statistically significant worse outcome of patients with SOD2^{High} staining (Figure 6c). Importantly, the presence of small foci of intense SOD2 staining within otherwise largely negative tumors is sufficient to predict worse clinical outcome.

SOD2 requires deacetylation by SIRT3[42] in order to be active. Sirtuins require NAD+ for their activity. In their analysis of the SIRT1/FOXO axis of the UPR^{mt}, Auwerx and colleagues[31] showed that modulating the NAD+/NADH ratio affects longevity by activating the UPR^{mt}. In cancer biology, elevated NADH level is used as a surrogate marker of glycolysis, whereas NAD+ correlates with an increased oxidative state.[43] Therefore, we further reasoned that areas of the tumors that are positive for SOD2 could also be positive for NAD+ rather than NADH for two reasons. First, NAD+ is required for SIRT3 to deacetylate SOD2 and, second, NAD+

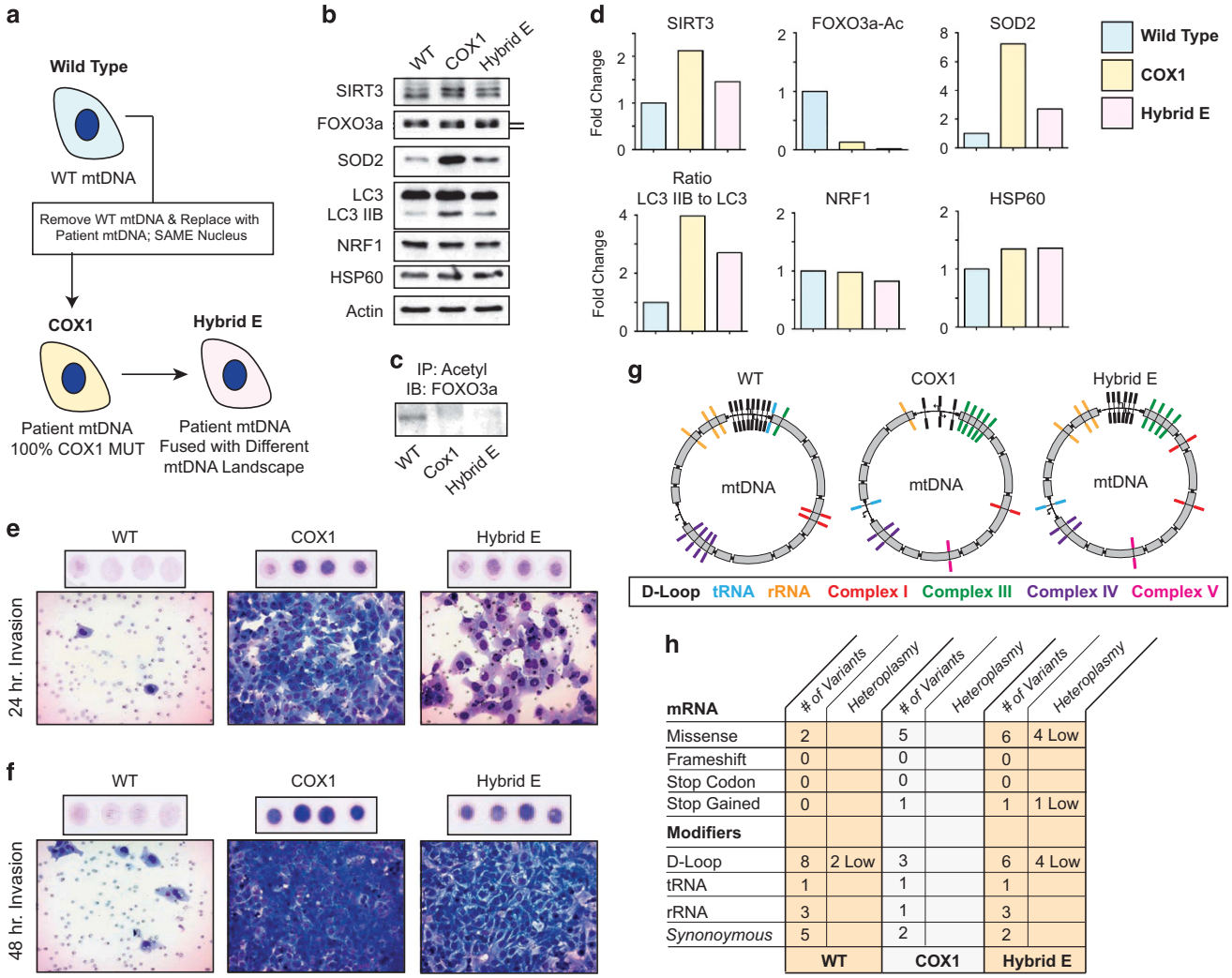

h

mRNA	# of Variants	Heteroplasmy	# of Variants	Heteroplasmy	# of Variants	Heteroplasmy
Missense	2		5		6	4 Low
Frameshift	0		0		0	
Stop Codon	0		0		0	
Stop Gained	0		1		1	1 Low
Modifiers						
D-Loop	8	2 Low	3		6	4 Low
tRNA	1		1		1	
rRNA	3		1		3	
Synonoymous	5		2		2	
	WT		**COX1**		**Hybrid E**	

Figure 5. Increased invasion capacity and activation of the UPR^{mt} of cybrids. (**a**) Schematic representation of the generation of the COX1 cybrid and their fusion resulting in hybrid E. (**b**) Western blotting of the markers of the UPR^{mt} in the indicated cell lines. (**c**) Immunoprecipitation of pan-acetylated proteins followed by western of FOXO3a. (**d**) Quantification of the levels of the UPR^{mt} shown in **b** and **c**. (**e**) Invasion assays of the indicated cell lines after 24 h. Top panel represents an overall view of four independent filters. Bottom panel represent a magnification of a representative area of a single filter. (**f**) Invasion assays of the indicated cell lines after 48 h. Top panel represents an overall view of four independent filters. Bottom panel represent a magnification of a representative area of a single filter. (**g**) Schematic representation of the mtDNA map of the indicated cell lines. Variants and mutations at specific locations along mtDNA are indicated by a line across the map and are color code according to the area/ gene affected. (**h**) Summary table of number of variants and the level of heteroplasmy in either area encoding mRNA or modifiers. Details of each variant are found in Supplementary Figures 7 and 9.

would indicate area of the tumor that activates oxidative phosphorylation. If so, NAD+ may be used as a surrogate marker of the activation of the UPR^{mt} along with SOD2. Fluorescent lifetime imaging microscopy (FLIM) can produce an image based on the differences in the exponential decay rate of the fluorescence from a fluorescent sample including that of endogenous fluorophores such as NADH.[43] The detection of free and bound NADH by FLIM has been used to measure for a number of metabolic profiling experiments including measuring glycolysis in cancer sections. In this study, the oncocytic, mito-rich and mito-poor breast cancers were tested by FLIM. We found an impressive overlapping between areas that are positive for SOD2 by immunohistochemistry (IHC) and NAD+ by FLIM (Figure 6d). These results suggest that the activation of the SIRT/FOXO/SOD2 axis of the UPR^{mt} can be detected in primary breast cancers.

As our hypothesis is that the SOD2^{High} population will survive the metastatic process, we next aimed at testing whether SOD2 staining is indeed enriched in metastatic lesions compared with the primary tumors of the same patient. We tested 50 such matched samples (100 cores) and found a statistically significant increase in SOD2 staining in the metastatic lesions compared with the primary tumors (Figures 6e and f). Further, we found that SOD2 staining of the primary tumors correlated with lymph node status (Figure 6g). This analysis strongly supports our hypothesis of the clonal selection of SOD2^{High} sub-populations, which activate the UPR^{mt}, during metastasis.

DISCUSSION

The first report that transfer of mtDNA from metastatic cell line to a non-metastatic cell line was able to modify invasion capacity linked this effect to a specific ROS-generating mtDNA mutation in the ND6 gene (*G13997A* and *13885insC*).[5] Since then, several other groups have reported similar findings although using different mtDNA mutations.[6–12] Of interest, one group reported that mild mtDNA mutations were actually more potent at generating

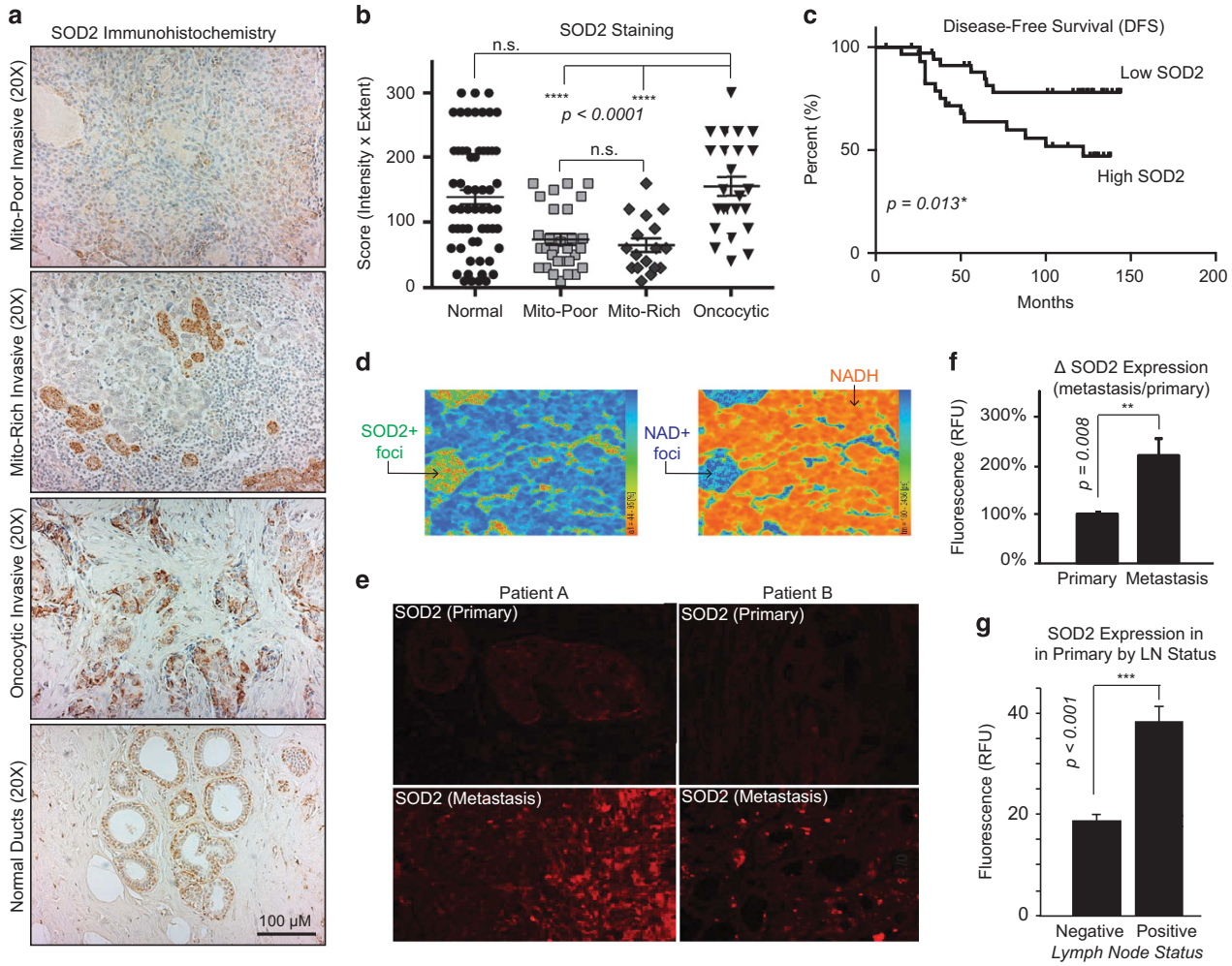

Figure 6. SOD2 staining is associated with worse prognosis and is enriched specifically in metastases. (**a**) IHC of SOD2 in mito-poor, mito-rich, oncocytic breast cancers and in normal ducts. (**b**) Quantification of SOD2 staining of individual patients and adjacent normal ducts. (**c**) Disease free survival rate of patients with high SOD2 (any extent of 3+ staining of SOD2 or a intensity x extent score of more than 100) versus SOD 2 (intensity × extent score of < 100). (**d**) FLIM analysis of mito-rich tumors show overlapping between SOD2-positive foci and NAD+ area, whereas the remainder of the tumors is negative for both. (**e**) Immunofluorescence staining of SOD2 in matched primary/metastatic breast tumors from the same patients. (**f**) Quantification of the ratio of SOD2 expression in metastatic/primary tumor tissue ($n = 50$ patients, 100 matches pairs). (**g**) Graph of SOD2 expression in primary tumors according to nodal status.

aggressive tumors compared to cells carrying mutations causing severe defect in OXPHOS.[11] Although in most studies the mechanism remained unclear, some have suggested that mtDNA mutations affecting OXPHOS act on invasion via a cross-talk between cancer cell mitochondria and the extracellular matrix.[12] More recently, it was suggested that synonymous mtDNA variants found in different mouse strains also affects the metastatic potential of tumors.[44,45] Although it is now recognized that mtDNA can influence metastasis, the nature of the type of mtDNA mutations involved and the mechanism as to how these effects are exerted remains controversial.

Data presented here offer an alternative model that may reconcile these various observations. Our data show that the ability of strong or mild missense mutations such as those in CyB to promote invasion is highly dependent on its surrounding mtDNA landscape. This conclusion is based on the fact that CyB cells and Hybrid B cells share the same mutation in CyB and the same nuclear genomes but differ in their invasion capacity (most visible at 24 h), which is associated with subtle differences in mtDNA. Our results suggest that some mtDNA landscapes act as enhancers of the missense mutations, whereas others act as repressors. Therefore, our data suggest that rather than being associated with specific mutations alone, metastasis may require specific mtDNA combinatorial landscapes. The common denominator of these landscapes is their ability to activate the SIRT3/FOXO3A/SOD2 axis of the UPR^{mt}.

Recently, the mtDNA repair machinery was reported to be reduced during disease progression and forced expression of mtDNA repair enzymes in mice delayed metastasis.[36] Therefore, defects in mtDNA repair, as suggested by the increased steady-state level of mtDNA lesions in the UPR^{mt}-positive cell lines (Supplementary Figure 5), may be a critical partner in the generation of heteroplasmy and pro-metastatic mtDNA landscapes. Our data suggest that in this context, heteroplasmy even at very low frequency can have significant effects on the invasion capacity. Interestingly, analysis of both Hybrids E and B initially revealed heteroplasmy at the COX1 and CyB mutations.[40] However, complete sequencing of the mtDNA genomes of these clones was not performed. Our data revealed homoplasmy at the COX1 and CyB mutations, and a remarkable similarity between the COX1 cybrid and hybrid E, and the CyB cybrid and hybrid B, respectively, suggesting mtDNA heteroplasmic drift toward higher mutation levels. This observation raises the possibility that mtDNA drifting and heteroplasmy work hand in hand toward the selection

of the optimal mtDNA landscape favoring metastasis. This is in agreement with a more recent study indicating a wide range of heteroplasmy in breast cancer.[46] Our data are also in line with the observation that mtDNA polymorphisms affect the risk of breast cancer.[47,48]

Based on our results and the observations by others, we propose the following model: homoplasmic mtDNA landscapes unable to activate the SIRT3 axis of the UPR^{mt} have little capacity to adapt to mitochondrial stress and as a result do not survive metastasis (Figure 7, sub-population 1). However, homoplasmic mtDNA landscapes able to lead to the activation of the SIRT3 axis of the UPR^{mt} have increased mitochondrial fitness and can adapt to stress and survive metastasis (Figure 7, sub-population 2). As mtDNA repair capacity has been linked to metastasis,[36] the prediction is that the number of mtDNA mutations will increase leading to heteroplasmy (Figure 7, sub-population 2). Heteroplasmy may lead to generation of mtDNA landscapes that fail to activate the SIRT3 axis of the UPR^{mt} and others that do (Figure 7, sub-population 2). We propose that those that do not are eliminated from the population as the disease progresses, while the others survive. Within the surviving cells, mtDNA drifting may underlie a selection mechanism toward the optimal mtDNA landscape.

Although some studies have suggested that mtDNA may directly lead to the activation of nuclear encoded genes involved in metastasis,[12,49] we propose an additional possibility; by activating the SIRT3 axis of the UPR^{mt}, the pro-invasive mtDNA landscapes promote increased mitochondrial fitness, which indirectly supports cells through the metastatic process. This possibility will be tested in the future.

We found that the levels of SOD2 appear to be an important, but not the only, determinant of invasion capacity. We previously described that SIRT3 acts upstream of FOXO3a, and that the transcription of SOD2 is dependent on FOXO3a.[27] In some cells however, SOD2 does not correlate with FOXO3A. One potential explanation is that the regulation of sub-cellular localization of FOXO3a by Akt may alter its effect on SOD2. Further the regulation of SOD2 by the UPR^{mt} may not be restricted to FOXO3a. These possibilities will be addressed further in the future.

Although others have also implicated the sirtuins, the transcription factors FOXO3a and SOD2 in the UPR^{mt}, the validation of this pathway in human cancer was lacking.[27,31] The present study supports the notion that the activation of the SIRT3 axis of the UPR^{mt} is associated with increased mitochondrial heterogeneity, metabolic flexibility and metastasis.

We found that SOD2 is significantly enriched in metastatic lesions compared with primary tumors, and that areas of SOD2 positivity correlate with NAD+ rather than NADH by FLIM. This finding is in agreement with the observation that affecting the NAD+/NADH balance using NAD+ precursors inhibits metastasis.[9]

The DePinho group reported that elevated SOD2 protein levels are found in recurring tumors but are low in primary tumors in mouse models, and that these recurring lesions are extremely sensitive to inhibition of SOD2.[2] We found that elevated SOD2 correlates with worse prognosis, even if the expression of SOD2 is limited to small foci in the primary tumors and the bulk of the tumor is negative for SOD2. These findings are also consistent with our observation that metastatic tumors have higher SOD2 protein levels in metastatic lesions when compared with the primary tumor of the same patient (Figures 6e and f). Therefore, we hypothesize that SOD2 may be important to support the survival of metastatic and recurrent cancer cells.

This leads to the question of how this model can reconcile with the findings by Haigis and colleagues[50] and our own pervious report that SIRT3 and SOD2 are downregulated in the vast majority of breast cancers.[51] We propose a model whereby, although a decrease in SIRT3 and SOD2 may be required to increase superoxide and facilitate the switch to glycolysis early during disease progression as suggested by Haigis and colleagues,[50] SOD2 expression is re-activated later to allow for metabolic flexibility. In support of this hypothesis, Bonini and colleagues[37] recently reported the ability of SOD2 to promote glycolysis. In this study, modulation of SOD2 levels was shown to allow metabolic flexibility.[37] Further, Haigis and colleagues[52] have also reported recently that SIRT3 is activated upon depolarization of the mitochondria, a result that is consistent with the role of SIRT3 in the UPR^{mt}. Therefore, we propose that the mitochondria heterogeneity within the same cell population may provide a

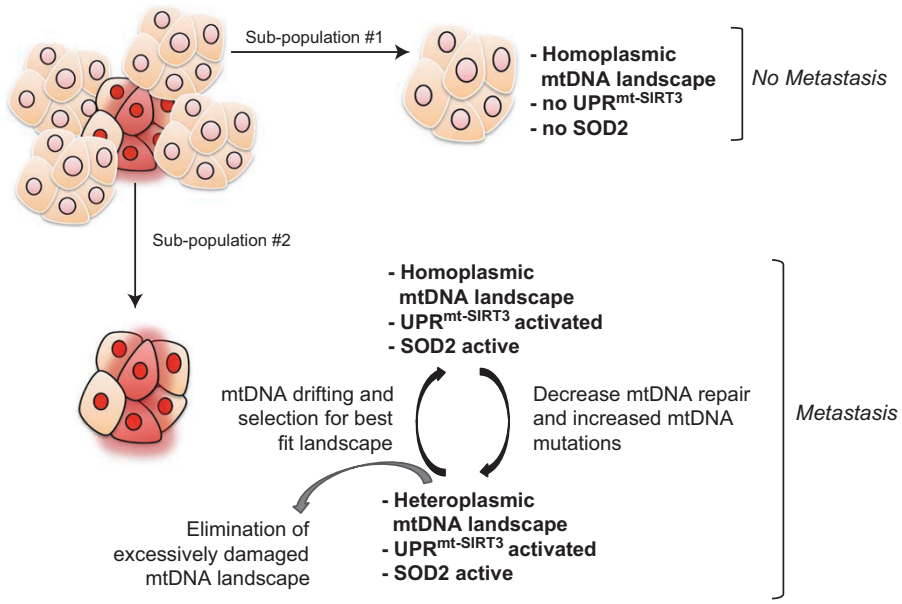

Figure 7. Model of mitochondrial heterogeneity in cancer based on mtDNA status. In this model, sub-population 1 carries homoplasmic mtDNA and do not activate the SIRT3 axis of the UPR^{mt} or SOD2. This sub-population is more sensitive to therapy. In sub-population 2, mtDNA is heteroplasmic leading to the generation of different mtDNA species. Some of these combinations lead to the activation of the SIRT3 axis of the UPR^{mt} and metabolic flexibility, which facilitates metastasis.

larger 'tool-box' that facilitates adaptation to stress and metabolic flexibility.

Recently, the UPR^{mt} has been proposed to maintain deleterious mutations in the context of mitochondrial diseases.[19] Our data suggest that cancer cells may utilize a similar mechanism toward the selection of cells with increased metastatic potential. Importantly, although the UPR^{mt} was initially identified as a result of the accumulation of misfolded proteins in the matrix and the activation of chaperone and proteases,[15] we and others have now established that the UPR^{mt} activates several genes other than chaperones and proteases.[25–27] An important role of the matrix protease ClpxP in metastasis has been reported recently.[53] Although we did not find changes in hsp60, which is expected to be in the same axis of as ClpxP, it is important to note that in breast cancer cells, the main difference in ClpxP was observed between MCF10A and MCF7 cells.[53] Therefore, it is possible that changes in the hsp60/ClpxP axis of the UPR^{mt} are an early event, a possibility supported by our observation that hsp60 is activated a few hours after activation of ras (Supplementary Figure 6). This possibility will be investigated further in the future. Collectively, it is becoming clear that the UPR^{mt} is a complex transcriptional program encompassing several parallel axes fulfilling different aspects of this large program.

Collectively, the results presented in the current study indicate that the activation of the SIRT3 axis of the UPR^{mt} is linked to metastasis. Therefore, agents able to target the UPR^{mt} could represent promising candidates for therapy.

MATERIALS AND METHODS

Reagents, cell culture and western blotting

Breast cancer cell lines were cultured in either Dulbecco's modified Eagle's medium (DMEM; MDA-MB-231, MDA-MB-361, MDA-MB-157, MCF7 and MCF7R) or RPMI medium (ZR75.1) supplemented with 10% fetal bovine serum and 100 units/ml penicillin and 100 μg/ml streptomycin. WT osteosarcoma cell lines and cybrids COX1 and CyB, and Hybrids B and E cultured in DMEM supplemented with 10%, 100 units/ml penicillin, 100 μg/ml streptomycin and 50 μg/ml uridine. Western blot analyses were performed as described previously,[26] using the following antibodies: SIRT3 (Cell Signaling, Danvers, MA, USA), LC3B (MBL International, Woburn, MA, USA), FOXO3A (Cell Signaling), SOD2 (Millipore, Billerica, MA, USA), Hsp60 (BD Transduction Laboratories, San Jose, CA, USA), NRF1 (Abcam, Cambridge, MA, USA), and Actin (Millipore).

Invasion assay

A transwell *in vitro* invasion assay was used to characterize invasion. Growth factor-reduced matrigel basement membrane matrix (BD Biosciences) was diluted 1:100 in cold PBS and 200 μl was added to the top of the cell permeable membrane (0.3 μm pore size) inside cell culture inserts for 24-well plates (Falcon). These inserts were incubated at for 2 h at room temperature, to allow polymerization of the artificial extracellular matrix. Following incubation, excess matrigel solution was removed by pipette. Cells split the day prior were then trypsinized and collected in serum-free DMEM supplemented with 100 units/ml Penicillin/Streptomycin (Gibco, Carlsbad, CA, USA) and then spun at 2000 r.p.m. for 5 min. Media was aspirated and cells were resuspended in DMEM supplemented with only 100 units/ml Penicillin/Streptomycin and counted using a hemocytometer and tryphan blue (Invitrogen). Fifty-thousand cells in 0.5 ml of serum-free DMEM were plated inside cell culture insert atop polymerized matrigel solution. Five-hundred microliters of 10% fetal bovine serum in DMEM supplemented with 100 units/ml Penicillin/Streptomycin was added to the 24-well plate outside cell culture inserts and invasion assay was incubated at 37 °C and 5% CO_2 for 12, 24 or 48 h. (For invasion assays using WT osteosarcoma cells, Cybrids CyB or COX1 and Hybrids B or E culture medium was supplemented with 50 μg/ml uridine).

Histology and IHC staining

Histological slides were obtained from the Department of Anatomic Pathology at Bellaria Hospital, University of Bologna (Italy). For immunostaining of paraffin-embedded sections with SOD2 (Millipore 06-984), samples were deparaffinized in xylene and rehydrated in water, and antigen retrieval was performed in citrate buffer. Endogenous peroxidase activity was blocked with 3% hydrogen peroxide for 10 min. All washes were performed using 50 mM Tris-HCl, pH 7.6, three times for 2 min. Blocking solution was applied for 30 min before the incubation with SOD2 antibody at a dilution of 1/100 for 2 h at room temperature. Secondary antibody was incubated for 1 h and the sections developed using the LSAB + kit peroxidase (DAKO, Glostrup, Denmark; catalogue number K0690) for 10 min. Sections were then counterstained in hematoxylin and mounted with Permount (Fischer Scientific, Waltham, MA, USA; catalogue number SP15-100).

Scoring of IHC staining

Immunostain for antimitochondrion antibody was scored as previously described.[41] To score SOD2 immunostaining, the intensity and percentage of IHC staining were recorded. The intensity was scored from 0 to 3+ and defined as follows: 0, no staining; 1+, weak staining; 2+, moderate staining; 3+, strong staining based on the granular cytoplasmic staining evaluation. In addition, the quickscore (*Q* score) based on estimating the percentage (*P*) of tumor cells showing characteristic staining (0–100%) and by estimating the intensity (*I*) of staining was adopted for IHC semi-quantification. The slides were scored by multiplying the percentage of positive cells by the intensity ($Q = P \times I$; maximum = 300). Multiplying staining intensity per percentage of stained cells we obtained a score 0–300. SOD2 expression was recorded as high, based on the presence of any extent of 3+ staining or a *Q* score >100. SOD2 expression was recorded as low, when *Q* score <100.

Fluorescent lifetime imaging microscopy

FLIM analysis was performed on slides stained for SOD2 by IHC as to identify the area of interest. All FLIM images were collected in a multiphoton optical workstation at the Laboratory of Optical and Computational Instrumentation at University of Wisconsin–Madison. The excitation source was a Ti:Sapphire laser (Spectra Physics; Maitai) tuned to wavelength of 740 nm. The excitation and emission were coupled through an inverted microscope (Nikon, Shinagawa, Japan; Eclipse TE300) with a $\times 40$ water-immersion objective (Nikon; Apo, Lambda S, numerical aperture 1.25). A 470/50 nm bandpass emission filter (Chroma, Burlington, VT, USA) was also used to selectively collect NADH fluorescence. FLIM images were collected at 256×256 resolution with 150 s collection using SPC-830 Photon Counting Electronics (Becker and Hickl GmbH, Berlin, Germany) and Hamamatsu H7422P-40 GaAsP photomultiplier tube (Hamamatsu Photonics, Bridgewater, NJ, USA). Urea crystals were used to determine the Instrumentation Response Function with a 370/10 bandpass emission filter (Semrock, Rochester. NY, USA).

SPCImage software (Becker & Hickl GmbH) was used to analyze the fluorescence lifetime decay curves. The lifetime decay of each pixel was fit with a double exponential decay, which resulted in a tau-mean of 1.3 with s.d. of 0.2. The two component of the double exponential decay refers to short and long lifetime component (1and 2, respectively). Unnecessary pixels were excluded using thresholding and the nearest 3×3 pixel were used with a binning of 2 for the analysis. An incomplete exponential model was used for the analyzing the FLIM data.

Seahorse analysis

Cells were seeded in 200 μl of complete media (RPMI for ZR75.1, DMEM for all other cell lines) in XF96 plates (Seahorse Bioscience, Santa Clara, CA, USA). Cells were seeded 24 h before assay to obtain ~50–60% confluency on day of assay; seeding densities: HBL-100 4.5×10^3, MCF7 4×10^3, MCF7-R 4.5×1^3, ZR75.1 7×10^3, MDA-MB-231 4×10^3, MDA-MB-361 3.5×10^3, MDA-MB-157 3.5×10^3 and MDA-MB-453 3.5×10^3. OCR and ECAR were measured using the XF96 Extracellular Flux Analyzer and the XF Cell Mito Stress Test Kit (Agilent/Seahorse Bioscience, Chicopee, MA, USA) according to manufacturer's instructions with optimized concentrations of metabolic inhibitors: Oligomycin 2 μM, carbonilcyanide p-triflouromethoxyphenylhydrazone (FCCP) 2 μM, Rotenone/Antimycin A 0.5 μM (Seahorse Bioscience). Following the assay, cell density was calculated as previously described.[54] OCR and ECAR measurements were normalized to calculated cell densities. Reported OCR/ECAR ratios represent the ratio between basal OCR rate and basal ECAR (before addition of any metabolic inhibitors). All experiments were performed with cell line-specific measurements done in eight replicates.

mtDNA sequencing and analysis

For each sample, 1 ng of DNA was indexed using the Nextera XT library preparation kit (Illumina, San Diego, CA, USA). During the Nextera procedure, after the tagmentation, amplification and PCR cleanup steps, fragment size distribution was assessed using the Bioanalyzer (Agilent, Santa Clara, CA, USA) and total DNA concentration was determined using the PicoGreen assay. Inputs were normalized accordingly. The remainder of the library preparation was performed as per the manufacturer's protocols. DNA sequencing was performed on the Illumina MiSeq, generating paired-end 150 bp reads. From the.fastq files output by the MiSeq machine, reads were sorted into individual files based on their adapter sequences. Adapter sequences were automatically removed and quality trimming performed by the Illumina software, followed by alignment to the GRCh38 human genome build using Burrows-Wheeler Aligner (BWA) (PMID: 20080505). The Picard software (Broad Institute, Cambridge, MA, USA) was used to remove PCR duplicates and the resulting files were processed using GATK's BaseRecalibrator (Broad Institute) and INDELRealigner tools (Broad Institute) (PMID: 25431634). GATK's haplotypecaller algorithm was used to call mtDNA variants and their heteroplasmy levels were inferred by allelic read depths from the.vcf files.

Transmission electron microscopy

For transmission electron microscopy, cells were fixed at 4 °C overnight, in 2.5% glutaraldehyde/4.0% paraformaldehyde in 0.1 M phosphate buffer and were processed by the electron microscopy facility at Mount Sinai.

Statistical analysis

Disease-specific survival was obtained from patients' medical records and survival analysis was performed using GraphPad Prism software (La Jolla, CA, USA). Reported *P*-value for survival analysis was calculated using the Log-rank test. Unpaired *t*-test, Mann–Whitney test or analysis of variance with *post-hoc* comparisons were used to compare groups, where appropriate. Error bars represent s.e.m.

CONFLICT OF INTEREST

The authors declare no conflict of interest.

ACKNOWLEDGEMENTS

We thank the electron microscopy facility at Mount Sinai and the sequencing core facility at Case Western. We thank Maria Gomez for her help in generating the Supplementary Tables, Elizabeth Slocum for her contribution to the analysis by electron microscopy and Yukie Takabatake for her contribution to the graphical illustration of the model in Figure 7. This work was funded by an NIH RO1 number CA1722046 to DG.

AUTHOR CONTRIBUTIONS

TK contributed to the design and interpretation of the data, and has performed the majority of the analysis including western blotting, invasion assays, analysis of mtDNA sequencing data for presentation, preparation of samples for electron microscopy, Seahorse XF Flux Assays and SOD2 scoring statistical analysis. MR has scored the SOD2 slides, established the association with the mitochondria phenotypes and performed the chart review of patients' survival. MS and JC assisted in the Seahorse analysis and the interpretation of the results. AKS and KF have performed the FLIM analysis of tumor sections and guided the interpretation of the results. TL and SG have performed the analysis of the mtDNA sequencing. JS performed the mtDNA repair assay. PH and MB established the stable cell lines overexpressing and inhibiting SOD2 and their characterization, and the analysis of SOD2 staining in metastatic lesions in human samples. AR performed western blot analysis on the cybrids and hybrids. L performed the IHC on SOD2. MDA and GM generated the cybrids and hybrids. DG is the PI and has designed the experiments, interpreted the data and wrote the manuscript.

REFERENCES

1 Viale A, Pettazzoni P, Lyssiotis CA, Ying H, Sanchez N, Marchesini M *et al.* Oncogene ablation-resistant pancreatic cancer cells depend on mitochondrial function. *Nature* 2014; **514**: 628–632.
2 Hu J, Hwang SS, Liesa M, Gan B, Sahin E, Jaskelioff M *et al.* Antitelomerase therapy provokes ALT and mitochondrial adaptive mechanisms in cancer. *Cell* 2012; **148**: 651–663.
3 LeBleu VS, O'Connell JT, Gonzalez Herrera KN, Wikman H, Pantel K, Haigis MC *et al.* PGC-1alpha mediates mitochondrial biogenesis and oxidative phosphorylation in cancer cells to promote metastasis. *Nat Cell Biol* 2014; **16**: 992-1003 1–15.
4 Obre E, Rossignol R. Emerging concepts in bioenergetics and cancer research: metabolic flexibility, coupling, symbiosis, switch, oxidative tumors, metabolic remodeling, signaling and bioenergetic therapy. *Int J Biochem Cell Biol* 2015; **59**: 167–181.
5 Ishikawa K, Takenaga K, Akimoto M, Koshikawa N, Yamaguchi A, Imanishi H *et al.* ROS-generating mitochondrial DNA mutations can regulate tumor cell metastasis. *Science* 2008; **320**: 661–664.
6 Imanishi H, Hattori K, Wada R, Ishikawa K, Fukuda S, Takenaga K *et al.* Mitochondrial DNA mutations regulate metastasis of human breast cancer cells. *PLoS One* 2011; **6**: e23401.
7 Hashizume O, Shimizu A, Yokota M, Sugiyama A, Nakada K, Miyoshi H *et al.* Specific mitochondrial DNA mutation in mice regulates diabetes and lymphoma development. *Proc Natl Acad Sci USA* 2012; **109**: 10528–10533.
8 Ishikawa K, Imanishi H, Takenaga K, Hayashi J. Regulation of metastasis; mitochondrial DNA mutations have appeared on stage. *J Bioenerg Biomembr* 2012; **44**: 639–644.
9 Santidrian AF, Matsuno-Yagi A, Ritland M, Seo BB, LeBoeuf SE, Gay LJ *et al.* Mitochondrial complex I activity and NAD+/NADH balance regulate breast cancer progression. *J Clin Invest* 2013; **123**: 1068–1081.
10 Yuan Y, Wang W, Li H, Yu Y, Tao J, Huang S *et al.* Nonsense and missense mutation of mitochondrial ND6 gene promotes cell migration and invasion in human lung adenocarcinoma. *BMC Cancer* 2015; **15**: 346.
11 Cruz-Bermudez A, Vallejo CG, Vicente-Blanco RJ, Gallardo ME, Fernandez-Moreno MA, Quintanilla M *et al.* Enhanced tumorigenicity by mitochondrial DNA mild mutations. *Oncotarget* 2015; **6**: 13628–13643.
12 Nunes JB, Peixoto J, Soares P, Maximo V, Carvalho S, Pinho SS *et al.* OXPHOS dysfunction regulates integrin-beta1 modifications and enhances cell motility and migration. *Hum Mol Genet* 2015; **24**: 1977–1990.
13 Jandova J, Janda J, Sligh JE. Changes in mitochondrial DNA alter expression of nuclear encoded genes associated with tumorigenesis. *Exp Cell Res* 2012; **318**: 2215–2225.
14 Martinus RD, Garth GP, Webster TL, Cartwright P, Naylor DJ, Hoj PB *et al.* Selective induction of mitochondrial chaperones in response to loss of the mitochondrial genome. *Eur J Biochem* 1996; **240**: 98–103.
15 Zhao Q, Wang J, Levichkin IV, Stasinopoulos S, Ryan MT, Hoogenraad NJ. A mitochondrial specific stress response in mammalian cells. *EMBO J* 2002; **21**: 4411–4419.
16 Benedetti C, Haynes CM, Yang Y, Harding HP, Ron D. Ubiquitin-like protein 5 positively regulates chaperone gene expression in the mitochondrial unfolded protein response. *Genetics* 2006; **174**: 229–239.
17 Fiorese CJ, Schulz AM, Lin YF, Rosin N, Pellegrino MW, Haynes CM. The transcription factor ATF5 mediates a mammalian mitochondrial UPR. *Curr Biol* 2016; **26**: 2037–2043.
18 Haynes CM, Petrova K, Benedetti C, Yang Y, Ron D. ClpP mediates activation of a mitochondrial unfolded protein response in *C. elegans*. *Dev Cell* 2007; **13**: 467–480.
19 Lin YF, Schulz AM, Pellegrino MW, Lu Y, Shaham S, Haynes CM. Maintenance and propagation of a deleterious mitochondrial genome by the mitochondrial unfolded protein response. *Nature* 2016; **533**: 416–419.
20 Mohrin M, Shin J, Liu Y, Brown K, Luo H, Xi Y *et al.* Stem cell aging. A mitochondrial UPR-mediated metabolic checkpoint regulates hematopoietic stem cell aging. *Science* 2015; **347**: 1374–1377.
21 Nargund AM, Fiorese CJ, Pellegrino MW, Deng P, Haynes CM. Mitochondrial and nuclear accumulation of the transcription factor ATFS-1 promotes OXPHOS recovery during the UPR(mt). *Mol Cell* 2015; **58**: 123–133.
22 Nargund AM, Pellegrino MW, Fiorese CJ, Baker BM, Haynes CM. Mitochondrial import efficiency of ATFS-1 regulates mitochondrial UPR activation. *Science* 2012; **337**: 587–590.
23 Durieux J, Wolff S, Dillin A. The cell-non-autonomous nature of electron transport chain-mediated longevity. *Cell* 2011; **144**: 79–91.
24 Tian Y, Merkwirth C, Dillin A, Mitochondrial UPR, Double-Edged Sword. A. *Trends Cell Biol* 2016; **26**: 563–565.
25 Munch C, Harper JW. Mitochondrial unfolded protein response controls matrix pre-RNA processing and translation. *Nature* 2016; **534**: 710–713.

26 Papa L, Germain D. Estrogen receptor mediates a distinct mitochondrial unfolded protein response. *J Cell Sci* 2011; **124**(Pt 9): 1396–1402.
27 Papa L, Germain D. SirT3 regulates the mitochondrial unfolded protein response. *Mol Cell Biol* 2014; **34**: 699–710.
28 Palacios OM, Carmona JJ, Michan S, Chen KY, Manabe Y, Ward JL 3rd *et al.* Diet and exercise signals regulate SIRT3 and activate AMPK and PGC-1alpha in skeletal muscle. *Aging* 2009; **1**: 771–783.
29 Pillai VB, Sundaresan NR, Kim G, Gupta M, Rajamohan SB, Pillai JB *et al.* Exogenous NAD blocks cardiac hypertrophic response via activation of the SIRT3-LKB1-AMP-activated kinase pathway. *J Biol Chem* 2010; **285**: 3133–3144.
30 Shi T, Fan GQ, Xiao SD. SIRT3 reduces lipid accumulation via AMPK activation in human hepatic cells. *J Dig Dis* 2010; **11**: 55–62.
31 Mouchiroud L, Houtkooper RH, Moullan N, Katsyuba E, Ryu D, Canto C *et al.* The NAD(+)/Sirtuin pathway modulates longevity through activation of mitochondrial UPR and FOXO signaling. *Cell* 2013; **154**: 430–441.
32 Houtkooper RH, Pirinen E, Auwerx J. Sirtuins as regulators of metabolism and healthspan. *Nat Rev Mol Cell Biol* 2012; **13**: 225–238.
33 Lombard DB, Tishkoff DX, Bao J. Mitochondrial sirtuins in the regulation of mitochondrial activity and metabolic adaptation. *Handb Exp Pharmacol* 2011; **206**: 163–188.
34 Riggins RB, Zwart A, Nehra R, Clarke R. The nuclear factor kappa B inhibitor parthenolide restores ICI 182,780 (Faslodex; fulvestrant)-induced apoptosis in antiestrogen-resistant breast cancer cells. *Mol Cancer Ther* 2005; **4**: 33–41.
35 Andrews RM, Kubacka I, Chinnery PF, Lightowlers RN, Turnbull DM, Howell N. Reanalysis and revision of the Cambridge reference sequence for human mitochondrial DNA. *Nat Genet* 1999; **23**: 147.
36 Yuzefovych LV, Kahn AG, Schuler MA, Eide L, Arora R, Wilson GL *et al.* Mitochondrial DNA repair through OGG1 activity attenuates breast cancer progression and metastasis. *Cancer Res* 2016; **76**: 30–34.
37 Hart PC, Mao M, de Abreu AL, Ansenberger-Fricano K, Ekoue DN, Ganini D *et al.* MnSOD upregulation sustains the Warburg effect via mitochondrial ROS and AMPK-dependent signalling in cancer. *Nat Commun* 2015; **6**: 6053.
38 Desmetz C, Bibeau F, Boissiere F, Bellet V, Rouanet P, Maudelonde T *et al.* Proteomics-based identification of HSP60 as a tumor-associated antigen in early stage breast cancer and ductal carcinoma in situ. *J Proteome Res* 2008; **7**: 3830–3837.
39 Rappa F, Pitruzzella A, Marino Gammazza A, Barone R, Mocciaro E, Tomasello G *et al.* Quantitative patterns of Hsps in tubular adenoma compared with normal and tumor tissues reveal the value of Hsp10 and Hsp60 in early diagnosis of large bowel cancer. *Cell Stress Chaperones* 2016; **21**: 927–933.
40 D'Aurelio M, Gajewski CD, Lin MT, Mauck WM, Shao LZ, Lenaz G *et al.* Heterologous mitochondrial DNA recombination in human cells. *Hum Mol Genet* 2004; **13**: 3171–3179.
41 Ragazzi M, de Biase D, Betts CM, Farnedi A, Ramadan SS, Tallini G *et al.* Oncocytic carcinoma of the breast: frequency, morphology and follow-up. *Hum Pathol* 2011; **42**: 166–175.
42 Tao R, Coleman MC, Pennington JD, Ozden O, Park SH, Jiang H *et al.* Sirt3-mediated deacetylation of evolutionarily conserved lysine 122 regulates MnSOD activity in response to stress. *Mol Cell* 2010; **40**: 893–904.
43 Conklin MW, Provenzano PP, Eliceiri KW, Sullivan R, Keely PJ. Fluorescence lifetime imaging of endogenous fluorophores in histopathology sections reveals differences between normal and tumor epithelium in carcinoma *in situ* of the breast. *Cell Biochem Biophys* 2009; **53**: 145–157.
44 Feeley KP, Bray AW, Westbrook DG, Johnson LW, Kesterson RA, Ballinger SW *et al.* Mitochondrial genetics regulate breast cancer tumorigenicity and metastatic potential. *Cancer Res* 2015; **75**: 4429–4436.
45 Takibuchi G, Imanishi H, Morimoto M, Ishikawa K, Nakada K, Toyama-Sorimachi N *et al.* Polymorphic mutations in mouse mitochondrial DNA regulate a tumor phenotype. *Mitochondrion* 2013; **13**: 881–887.
46 McMahon S, LaFramboise T. Mutational patterns in the breast cancer mitochondrial genome, with clinical correlates. *Carcinogenesis* 2014; **35**: 1046–1054.
47 Bai RK, Leal SM, Covarrubias D, Liu A, Wong LJ. Mitochondrial genetic background modifies breast cancer risk. *Cancer Res* 2007; **67**: 4687–4694.
48 Covarrubias D, Bai RK, Wong LJ, Leal SM. Mitochondrial DNA variant interactions modify breast cancer risk. *J Hum Genet.* 2008; **53**: 924–928.
49 van Waveren C, Sun Y, Cheung HS, Moraes CT. Oxidative phosphorylation dysfunction modulates expression of extracellular matrix--remodeling genes and invasion. *Carcinogenesis* 2006; **27**: 409–418.
50 Finley LW, Carracedo A, Lee J, Souza A, Egia A, Zhang J *et al.* SIRT3 opposes reprogramming of cancer cell metabolism through HIF1alpha destabilization. *Cancer Cell* 2011; **19**: 416–428.
51 Papa L, Hahn M, Marsh EL, Evans BS, Germain D. SOD2 to SOD1 switch in breast cancer. *J Biol Chem* 2014; **289**: 5412–5416.
52 Yang W, Nagasawa K, Munch C, Xu Y, Satterstrom K, Jeong S *et al.* Mitochondrial sirtuin network reveals dynamic SIRT3-dependent deacetylation in response to membrane depolarization. *Cell* 2016; **167**: 985–1000 e21.
53 Seo JH, Rivadeneira DB, Caino MC, Chae YC, Speicher DW, Tang HY *et al.* The mitochondrial unfoldase-peptidase complex ClpXP controls bioenergetics stress and metastasis. *PLoS Biol* 2016; **14**: e1002507.
54 Serasinghe MN, Wieder SY, Renault TT, Elkholi R, Asciolla JJ, Yao JL *et al.* Mitochondrial division is requisite to RAS-induced transformation and targeted by oncogenic MAPK pathway inhibitors. *Mol Cell* 2015; **57**: 521–536.

Supplementary Information accompanies this paper on the Oncogene website (http://www.nature.com/onc)

Martin, Stephen A., Dylan C. Souder, Karl N. Miller, Josef P. Clark, Abdul Kader Sagar, Kevin W. Eliceiri, Luigi Puglielli, T. Mark Beasley, and Rozalyn M. Anderson. "GSK3β Regulates Brain Energy Metabolism." *Cell reports* 23, no. 7 (2018): 1922-1931.

Summary

There are 4 key finding of this article-

1) GSK3β regulates mitochondrial energy metabolism in neurons and in glia

2) Metabolic regulation by GSK3β extends to cellular NAD metabolism

3) Inhibition of GSK3β alters PGC-1α protein stability, localization, and activity

4) GSK3β inhibition alters hippocampal energy metabolism

Report

Cell Reports

GSK3β Regulates Brain Energy Metabolism

Graphical Abstract

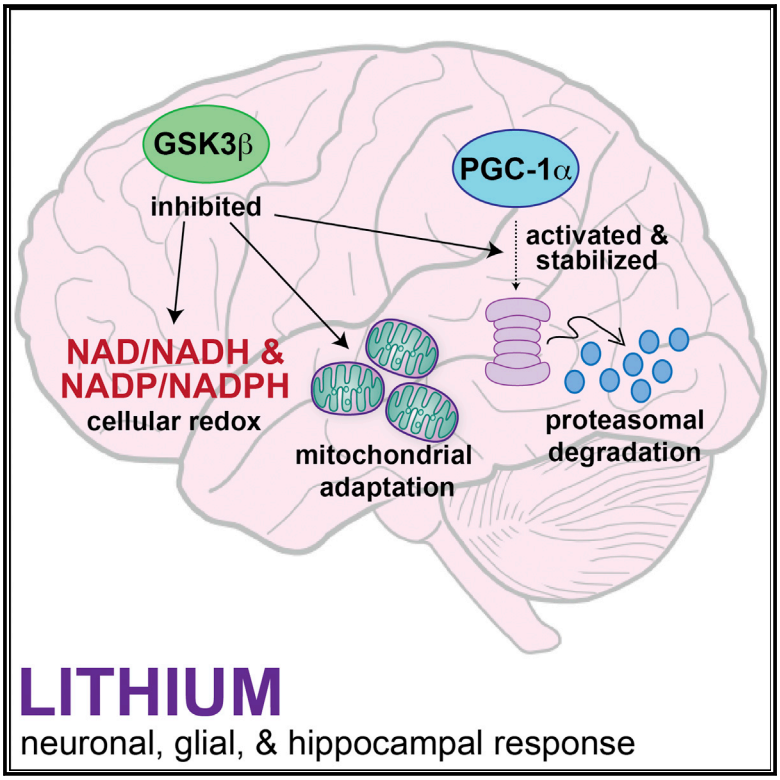

Highlights

- GSK3β regulates mitochondrial energy metabolism in neurons and in glia
- Metabolic regulation by GSK3β extends to cellular NAD metabolism
- Inhibition of GSK3β alters PGC-1α protein stability, localization, and activity
- GSK3β inhibition alters hippocampal energy metabolism

Authors

Stephen A. Martin, Dylan C. Souder, Karl N. Miller, ..., Luigi Puglielli, T. Mark Beasley, Rozalyn M. Anderson

Correspondence

rozalyn.anderson@wisc.edu

In Brief

Martin et al. demonstrate that GSK3β is a regulator of energy metabolism in the brain. They show that GSK3β inhibition stimulates mitochondrial regulator PGC-1α and leads to activation of mitochondrial and redox pathways in glia, in neurons in culture, and in the hippocampus in mice *in vivo*.

Martin et al., 2018, Cell Reports *23*, 1922–1931
May 15, 2018
https://doi.org/10.1016/j.celrep.2018.04.045

GSK3β Regulates Brain Energy Metabolism

Stephen A. Martin,[1,6,7] Dylan C. Souder,[1,6] Karl N. Miller,[1] Josef P. Clark,[1] Abdul Kader Sagar,[2] Kevin W. Eliceiri,[2] Luigi Puglielli,[1,5] T. Mark Beasley,[3,4] and Rozalyn M. Anderson[1,5,8,*]

[1]Division of Geriatrics, Department of Medicine, SMPH, University of Wisconsin-Madison, Madison, WI, USA
[2]Laboratory for Optical and Computational Instrumentation, University of Wisconsin-Madison, Madison, WI, USA
[3]Department of Biostatistics, University of Alabama, Birmingham, AL, USA
[4]GRECC, Birmingham/Atlanta Veterans Administration Hospital, Birmingham, AL, USA
[5]GRECC William S. Middleton Memorial Veterans Hospital, Madison, WI, USA
[6]These authors contributed equally
[7]Present address: Oregon State University, Corvallis, OR, USA
[8]Lead Contact
*Correspondence: rozalyn.anderson@wisc.edu
https://doi.org/10.1016/j.celrep.2018.04.045

SUMMARY

GSK3β is a serine threonine kinase implicated in the progression of Alzheimer's disease. Although the role of GSK3β in growth and pathology has been extensively studied, little is known about the metabolic consequences of GSK3β manipulation, particularly in the brain. Here, we show that GSK3β regulates mitochondrial energy metabolism in human H4 neuroglioma cells and rat PC12-derived neuronal cells and that inhibition of GSK3β in mice *in vivo* alters metabolism in the hippocampus in a region-specific manner. We demonstrate that GSK3β inhibition increases mitochondrial respiration and membrane potential and alters NAD(P)H metabolism. These metabolic effects are associated with increased PGC-1α protein stabilization, enhanced nuclear localization, and increased transcriptional co-activation. In mice treated with the GSK3β inhibitor lithium carbonate, changes in hippocampal energy metabolism are linked to increased PGC-1α. These data highlight a metabolic role for brain GSK3β and suggest that the GSK3β/PGC-1α axis may be important in neuronal metabolic integrity.

INTRODUCTION

Many of the most common neurodegenerative disorders share a phenotype of protein aggregation and proteostatic crisis that ultimately lead to neuronal loss (Hetz and Mollereau, 2014); however, these disorders also exhibit a common phenotype of mitochondrial dysfunction (Schon and Przedborski, 2011). Mitochondrial efficiency is critical in maintaining neuronal function and plasticity (Yin et al., 2014), and mitochondrial integrity is an essential component in learning/memory (Pei et al., 2015). GSK3β (glycogen synthase kinase 3 beta) is a growth-signaling-sensitive kinase negatively regulated by inhibitory phosphorylation downstream of the insulin receptor, Wnt, and mTOR growth signaling pathways (Patel and Woodgett, 2017). Genetic studies demonstrate a mechanistic role for GSK3β in memory, behavior, and neuronal fate determination (Beurel et al., 2015; Kaidanovich-Beilin and Woodgett, 2011). GSK3β has also been implicated in Alzheimer's disease (AD), where activation of GSK3β can promote tau hyperphosphorylation, neurofibrillary tangles, and amyloid plaques (DaRocha-Souto et al., 2012; Serenó et al., 2009). In contrast, levels of GSK3β are lower in the brains of monkeys that are protected from age-related brain atrophy by the dietary intervention of caloric restriction (CR) (Colman et al., 2009; Martin et al., 2016).

GSK3 was originally identified as an insulin sensitive kinase involved in the activation of glycogen synthesis (Parker et al., 1983). Two isoforms of GSK3, GSK3α and GSK3β, have been identified (Woodgett, 1990) that have distinct non-redundant functions: global knockout of GSK3α is phenotypically silent (Patel et al., 2011), whereas global knockout of GSK3β is embryonic lethal (Hoeflich et al., 2000). We and others have identified a role for GSK3β in regulating the stability and activity of PGC-1α (peroxisome proliferator-activated receptor gamma coactivator 1-alpha), a key regulator of mitochondrial function (Anderson et al., 2008; Olson et al., 2008); however, the involvement of GSK3β specifically in energy metabolism is not well defined. In this study, we utilize lithium, a robust GSK3β inhibitor (Klein and Melton, 1996; Stambolic et al., 1996) and common psychiatric drug used in the treatment of schizophrenia and bipolar disorder (Geddes et al., 2004), to determine the role of GSK3β brain cell energy metabolism.

RESULTS

GSK3β Inhibition Stimulates Glial Mitochondrial Energy Metabolism

Human H4 neuroglioma cells were treated with lithium chloride (15 mM), a direct inhibitor of GSK3β (Zhang et al., 2003). Consistent with a growth regulatory role of GSK3, GSK3β inhibition by lithium negatively affected cellular growth in the absence of a difference in cell viability (Figures S1A and S1B). An increase in mitochondrial membrane potential was induced by 24 hr of lithium treatment (Figure 1A) in a dose-dependent manner (Figure S1C). Inhibitor VIII (15 μM), a selective non-competitive inhibitor of GSK3β, also induced an increase in mitochondrial

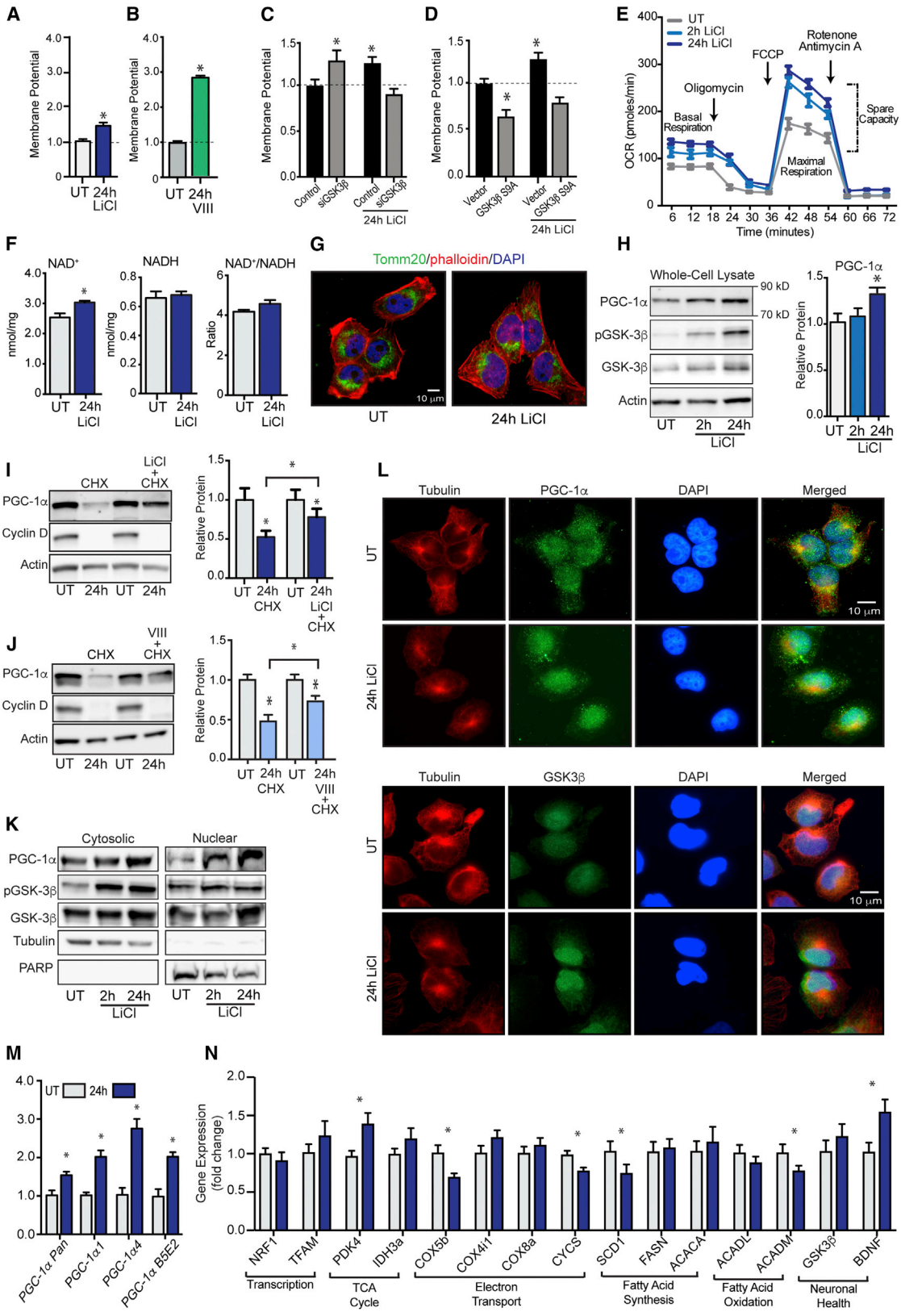

(legend on next page)

membrane potential in H4 glioma (Figure 1B). To determine if the metabolic effects of lithium were GSK3β dependent, we used small interfering RNA (siRNA) to knockdown GSK3β at the RNA and protein levels (Figure S1D). GSK3β knockdown significantly increased mitochondrial membrane potential, phenocopying the effect of lithium, but abrogated the increase in membrane potential induced by lithium treatment confirming the requirement for GSK3β in lithium's metabolic effects (Figure 1C). The metabolic impact of inhibitor VIII was similarly disrupted by knockdown of GSK3β (Figure S1E). Furthermore, expression of constitutively active GSK3β with the phosphorylation site serine 9 mutated to alanine (Figure S1F), significantly decreased mitochondrial membrane potential in H4 glioma, and abrogated lithium's ability to increase mitochondrial membrane potential (Figure 1D). Lithium induced an increase in mitochondrial respiration (Figure 1E), with basal respiration, maximal respiration, and spare capacity significantly higher in treated cells (Table S1). Despite subtle differences in the impact of lithium and inhibitor VIII on membrane potential, the effect of GSK3β inhibition by either modality on respiration was equivalent and non-additive (Figure S1G) and was phenocopied by siRNA against GSK3β (Figure S1H). In terms of the broader metabolic effects, lithium induced an increase in free intracellular levels of co-factor NAD^+ as detected by biochemical assay, although redox ratios were not significantly different (Figures 1F and S1I). These metabolic changes occurred in the absence of overt differences in mitochondrial abundance: mitochondrial content, as assessed by staining for the outer membrane protein Tomm20 (translocase of outer mitochondrial membrane 20) was not different (Figures 1G and S1J), and levels of proteins involved in the electron transport system (ETS) were unchanged (Figure S1K). These data indicate that mitochondria were activated but biogenesis was not induced. At the protein level, lithium-induced inhibitory phosphorylation of GSK3β at serine 9, confirming efficacy of lithium-induced GSK3β inhibition (Figures 1H and S1L). Coincident with this, a 1.3-fold significant increase in PGC-1α protein levels was detected in lithium-treated cells, and although the impact of inhibitor VIII on PGC-1α levels was more modest, treatment with both GSK3β inhibitors was not additive (Figure S1M). A difference in PGC-1α cellular distribution was evident upon knockdown of GSK3β with an apparent increase in nuclear PGC-1α (Figure S1N).

To investigate PGC-1α protein turnover, we exposed H4 glioma to the ribosomal inhibitor cycloheximide (100 μM) resulting in significant depletion of PGC-1α after 24 hr. Cycloheximide-induced depletion of PGC-1α levels was blocked by concomitant treatment with lithium (Figure 1I) or GSK3β inhibitor VIII (Figure 1J), confirming the role of GSK3β in regulating PGC-1α protein stability. Next, we investigated PGC-1α subcellular distribution and detected increased nuclear accumulation of PGC-1α in lithium-treated cells by subcellular fractionation (Figure 1K) and confirmed by immunofluorescent detection (Figure 1L). GSK3β was also enriched in the nuclei of lithium-treated cells consistent with the increase in the phosphorylated form, which is almost exclusively nuclear in H4 glioma (Figure S1O) and increased upon treatment with lithium. Next, we investigated the regulation of PGC-1α at the transcript level. Lithium resulted in increased expression of PGC-1α isoforms α1 and α4 and a subset of brain-specific isoforms (Martinez-Redondo et al., 2016) (Figure 1M). Gene targets of PGC-1α were also differentially expressed, including the glycolytic regulator PDK4 (pyruvate dehydrogenase kinase 4), BDNF (brain-derived neurotrophic factor), SCD1 (stearoyl coenzyme A [CoA] desaturase 1), and COX5b (cytochrome *c* oxidase subunit 5b) (Figure 1N). As before, siRNA knockdown of GSK3β partially mimicked the effect of lithium (Figure 1SP). These data demonstrate that GSK3β regulation of mitochondrial activity in H4 glioma is associated with changes in PGC-1α activity, stability, and subcellular localization.

GSK3β Inhibition Stimulates Neuronal Mitochondrial Energy Metabolism

The rat PC12 neuroblastic cell line can be induced to differentiate into electrically excitable neuron-like cells upon treatment with nerve growth factor (NGF) (Fujita et al., 1989). Treatment of PC12-derived neurons with lithium chloride (15 mM) for 24 hr resulted in a 1.5-fold increase in PGC-1α protein levels and increased phosphorylation of GSK3β, recapitulating the outcomes observed in H4 glioma (Figures 2A and S2A). At the transcript level, lithium induced expression of the PGC-1α4 isoform, but a significant impact on other isoforms, including a novel rat-specific isoform (Figures 2B and S2B), was not detected. Lithium affected the expression of PGC-1α targets, with induction of both BDNF and PDK4 (Figure 2C); however, the impact of lithium on expression of genes encoding subunits of complex IV of ETS was not equivalent to that observed in H4 glioma, suggesting that there are differences in PGC-1α gene target specificity between these cell types. Similar to H4 glioma, lithium induced an increase in intracellular levels of NAD^+ (Figure 2D). These effects were not explained by a difference in mitochondrial content; Tomm20 staining intensity was equivalent in untreated and lithium-treated PC12-derived neurons (Figure 2E), and protein levels of components of ETS complexes I–V were equivalent (Figure S2C). Unlike the case for H4 glioma, PGC-1α was almost entirely nuclear in PC12-derived neurons and subcellular localization was not changed in response to lithium. GSK3β was

Figure 1. GSK3β Regulates Mitochondrial Metabolism and PGC-1α Stability, Localization, and Activity in H4 Glioma

(A–D) JC-1 measurement of mitochondrial membrane potential following (A) LiCl (15 mM) or (B) inhibitor VIII (15 μM) treatment and following LiCl treatment (15 mM) in cells transfected with GSK3β siRNA (C) or GSK3β-S9A (D).

(E–J) Basal and maximal cellular respiration (E); NAD^+, NADH, and NAD^+/NADH ratio (F); immunodetection of mitochondrial Tomm20 (G); PGC-1α, GSK3β, GSK3β, and actin protein levels following 2- or 24-hr LiCl treatment (H); PGC-1α, cyclin D, and actin protein detection in cells treated with cyclohexamide (100 μM) in the absence or presence of LiCl (15 mM) (I); or inhibitor VIII (15 μM) (J).

(K–N) Protein levels of PGC-1α, pGSK3β, GSK3β, tubulin, and PARP protein in cytoplasmic and nuclear fractions following 24-hr LiCl treatment (K); immunodetection of tubulin, PGC-1α, and GSK3β (L); RT-PCR detection of PGC-1α (M); and the indicated transcripts following LiCl treatment (N).

n = 3–6 biological replicates per assay; data are shown as an average ± SEM; *$p < 0.05$ ANOVA.

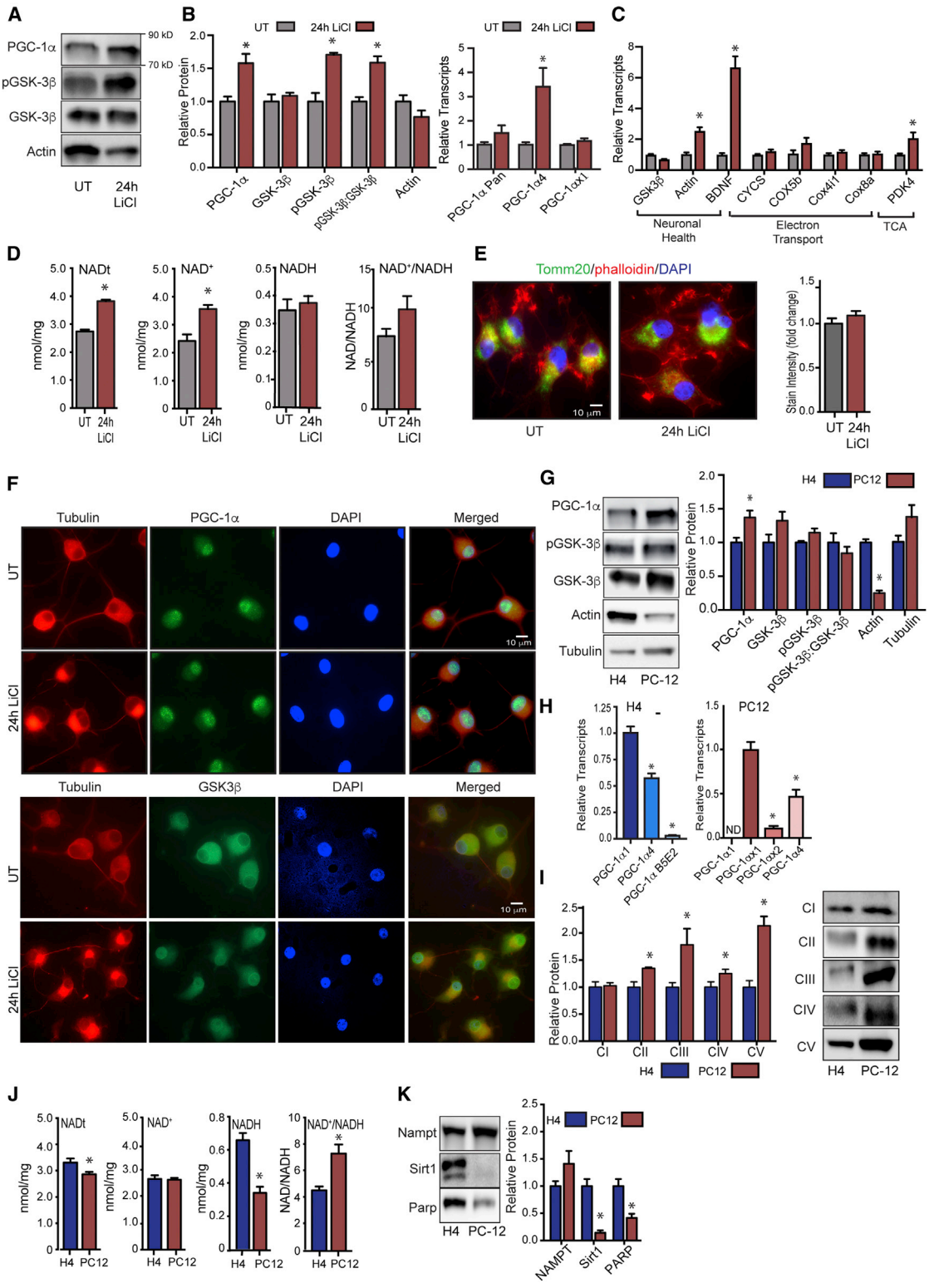

Figure 2. GSK3β Regulation of PGC-1α Activity in PC12-Derived Neuron-like Cells

(A) Detection of PGC-1α, pGSK3β, GSK3β, and actin proteins following LiCl treatment (15 mM).

(B and C) RT-PCR detection of PGC-1α (B) and indicated transcripts following 24-hr LiCl treatment (C).

(D) Total NAD (NADt), NAD^+, NADH, and NAD^+/NADH ratio following 24-hr LiCl treatment.

(legend continued on next page)

predominantly cytosolic in untreated PC12-derived neurons and a clear shift to nuclear localization was detected following lithium treatment (Figure 2F). Phospho-GSK3β was predominantly cytosolic and treatment with lithium resulted in the formation of discrete puncta of phospho-GSK3β in the perinuclear region (Figure S2D); however, the significance of this change in localization is currently unclear. These data show that the effects of GSK3β inhibition on cellular NAD metabolism and PGC-1α protein levels are common to H4 glioma and PC12-derived neurons.

The above experiments suggested that metabolic status might differ at baseline between H4 glioma and PC12-derived neurons. Although levels of GSK3β were not significantly different between cell types, protein levels of PGC-1α were significantly higher in PC12-derived neurons than in H4 glioma (Figures 2G and S2E). PGC-1α transcript isoform distribution was also different between the two cell types. The predominant isoform in glia was PGC-1α1 that was expressed at twice the level of PGC-1α4, with a lesser contribution from the brain-specific isoform (Figure 2H). PGC-1α2 and PGC-1α3 were not detected in H4 glioma. In PC12-derived neurons, PGC-1αx1 was the predominant isoform expressed, with PGC-1α4 expressed at ~30% of that level and PGC-1αx2 lower again. The αx1 and αx2 isoforms are previously unreported but predicted variants of rat PGC-1α closest in equivalence to murine PGC-1α1. Next, we looked at metabolic parameters and identified significantly higher levels of proteins from mitochondrial ETS complexes II through V in PC12-derived neurons (Figure 2I), and significant differences in basal redox state between the cell types (Figure 2J). Abundance of NAMPT (nicotinamide phosphoribosyltransferase), the rate-limiting enzyme of the NAD salvage pathway, was not significantly different between cell types; however, NAD-dependent enzymes, including the deacetylase SIRT1 and the DNA repair enzyme PARP1 (poly-ADP-ribose polymerase 1), were significantly lower in PC12-derived neurons, pointing to potential differences in NAD consumption between these cell types (Figure 2K).

NAD Metabolism Is Responsive to GSK3β Inhibition

Multi-photon laser-scanning microscopy (MPLSM) is a high-resolution imaging-based technique that allows for quantitation of differences in cellular metabolism among cells or as a function of treatment. This technology takes advantage of the autofluorescence of reduced forms of NAD and NADP (Denk et al., 1990). Kinetic properties of photon release can be quantified by fluorescence lifetime imaging microscopy (FLIM), informing of the cellular environment of the fluorophores (Lakowicz et al., 1992). Mean fluorescence lifetime (τ_m) summarizes a first order decay curve including a fast component (τ_1) and a slow component (τ_2) that correspond to free and protein-bound pools of NAD(P)H, respectively. The relative contribution of τ_1 to τ_m is indexed by the a_1 coefficient where $\tau_m = a_1 \cdot \tau_1 + a_2 \cdot \tau_2$. Decay curves were generated over multiple pulses, repeated for each pixel in the image capture field, and were quantified on a by-pixel basis and color-coded by picoseconds of decay (Figures 3A and 3B). Remarkably, the mean fluorescence lifetime was completely different in nuclear and cytosolic compartments for both cell types (Figures 3C, 3D, and S3), with significantly shorter τ_m detected for nuclear pools. This difference is primarily explained by the significantly higher values of a_1 in the nuclei, indicating that most of the nuclear co-factor pool is in the unbound state.

In general, factors influencing the decay values (τ_1 and τ_2) include the immediate local environment, including hypoxia, pH, redox, and, in the case of τ_2, the proteins to which the fluorophores are bound. Changes in a_1 values are indicative of a shift in the balance of free and bound NAD(P)H, where lower a_1 values are associated with greater reliance on oxidative metabolism (Bird et al., 2005). Lithium treatment increased the τ_m in H4 glioma (Figure 3C), with main effects of treatment, cellular compartment, and a treatment by compartment interaction (Table S2). These differences extended to all parameters of the decay curve including higher τ_1 (free pool), a more modest increase in τ_2 (bound pool), and a substantial decrease in a_1 that was most evident in the cytosolic pool. These outcomes are consistent with the respiratory measures described earlier.

Larger magnitude changes in FLIM were detected in lithium-treated PC12-derived neurons, with an increase in τ_m and main effects of treatment, cellular compartment, and a treatment by compartment interaction detected (Table S2). The impact of lithium extended to main effects and interaction for all parameters of the decay curve with significant increases detected for τ_1 and τ_2, and a substantial decrease in a_1, again suggesting a shift toward increased proportion of bound co-factors in cellular NAD(P)H pools (Figure 3D).

Next, we investigated the impact of lithium on fluorescence intensity of NAD(P)H. Fluorescence intensity reflects total fluorophore pools and can be influenced by changes in abundance of the total NAD(P)H pool and also by changes in the bound proteome within that pool. Here, the outcomes differed between H4 glioma and PC12-derived neurons where lithium had no impact on fluorescence intensity in H4 glioma (Figure 3E) but significantly increased fluorescence intensity in PC12-derived neurons (Figure 3F). Taken together, these data demonstrate that GSK3β inhibition affects cellular NAD metabolism and the metabolic environment in both PC12-derived neurons and H4 glioma.

Inhibition of GSK3β Affects Brain Energy Metabolism

To determine the impact of GSK3β inhibition on PGC-1α processing *in vivo*, male C3B6-F1 hybrid mice were treated with

(E) Immunodetection of mitochondrial Tomm20.
(F) Immunodetection of PGC-1α, GSK3β, and tubulin.
(G) Protein levels of PGC-1α, pGSK3β, GSK3β, actin, and tubulin in H4 glioma and PC12-derived neuronal cells.
(H) RT-PCR detection PGC-1α isoforms in H4 glioma and PC12.
(I) Protein levels of subunits of complexes I–V of the electron transport system.
(J) Total NAD (NADt), NAD^+, NADH, and NAD^+/NADH ratio in H4 glioma and PC12-derived neuronal cells.
(K) Protein levels of NAMPT, Sirt1, and PARP proteins in H4 glioma and PC12-derived neuronal cells.
n = 3–6 biological replicates per assay; data are shown as an average ± SEM; *$p < 0.05$ Student's t test.

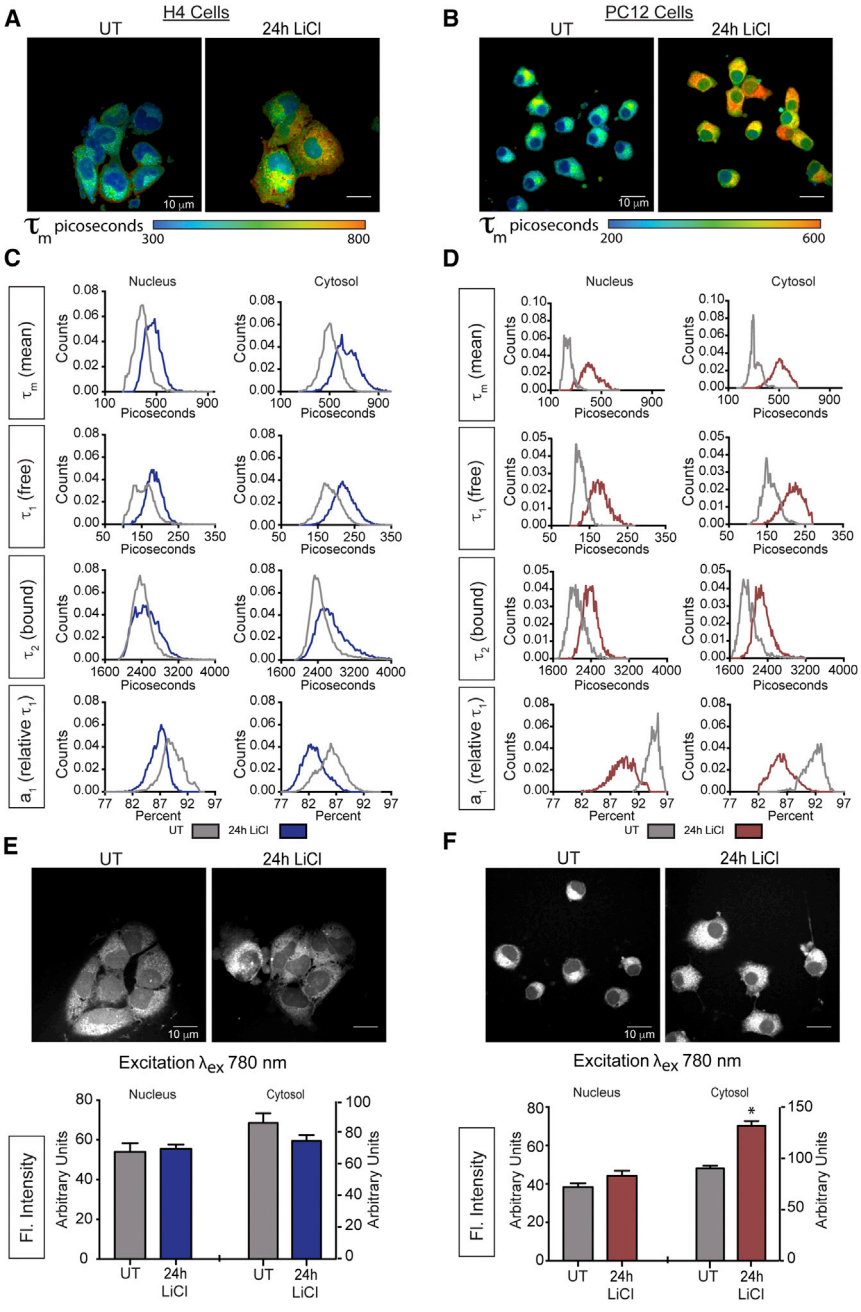

Figure 3. GSK3β Affects Cellular NAD(P)H Metabolism

(A and B) Representative image showing mean fluorescence lifetime (τ_m) in picoseconds ($_{ex}\lambda_{780}$) in the absence or presence of LiCl (15 mM) for H4 glioma (A) and PC12-derived neurons (B).

(C and D) Distributions of mean fluorescence lifetime τ_m (top rows), short component τ_1 (upper middle rows), long component τ_2 (lower middle rows), a_1, the relative contribution of τ_1 to τ_m (bottom row) before and after 24 hr LiCl treatment for H4 glioma (C) and PC12-derived neurons (D).

(E and F) NAD(P)H fluorescent intensity within the nucleus and cytoplasm following 24-hr LiCl treatment (15 mM) for H4 glioma (E) and PC12-derived neurons (F).

n = 6–8 biological replicates per measure; data are shown as a distribution or as an average ± SEM; *p < 0.05, linear mixed model.

lithium carbonate (0.6–2.4 mg/g in the diet) for 4 months from 2 months of age. At higher doses lithium had an impact on body weight even though food intake was identical among all animals of the cohort (Table S3). PGC-1α4 isoform was detected in whole-brain extracts by RT-PCR, with PGC-1α1 expression at about two-thirds that level and PGC-1α2 lower again (Figure 4A). Investigation of PGC-1α expression in *ex-vivo*-isolated cells indicated that PGC-1α1 isoform expression was significantly higher in glia than in neurons while PGC-1α4 isoform was the major isoform detected in neurons (Figure 4B). Lithium-induced increases in PGC-1α1 and PGC-1α4 transcripts in neurons, and PGC-1α4, but not PGC-1α1 in glia (Figure 4C), although the effect was dose specific. Histochemical measures of mitochondrial cytochrome *c* oxidase activity (complex IV of the ETS) revealed cell type and regional differences within the hippocampus, consistent with prior reports (Martin et al., 2016) (Figure 4D). Activity stain intensity was quantified by region, including the dentate gyrus granular layer (GL), the neurons of the polymorphic layer (PL), the molecular layer (ML), and the outer hippocampal CA1 and CA3 regions, where cell bodies and neuropil were separately quantified (Figure S4A). Main effects of region and treatment as well as an interaction of region and treatment were detected (Table S4). The impact of lithium was region and dose dependent: the GL and cell bodies of the CA1 and CA3 were refractory to treatment; activity stain intensity was increased in the PL and ML, but the response was non-linear; and the CA1 neuropil exhibited a linear dose-dependent impact of lithium to increase cytochrome *c* oxidase activity. These data show a hippocampal region and cell-type-specific mitochondrial response to lithium treatment *in vivo*.

Hippocampal protein levels of GSK3β (Figure 4E) and PGC-1α (Figure 4F) were highly region and cell type specific (Figures S4B and S4C). A main effect of region was detected for both proteins (Table S4), and a region by dose interaction was detected. Dose-dependent effects of lithium were non-linear within responsive regions, where PGC-1α levels were increased in neurons of the PL, GL, and cell bodies of the CA1 and CA3 at lower doses (1.2 and 1.8 mg/kg). The impact of lithium on phospho-GSK3β showed a similar dose response (Figure S4D), where increased

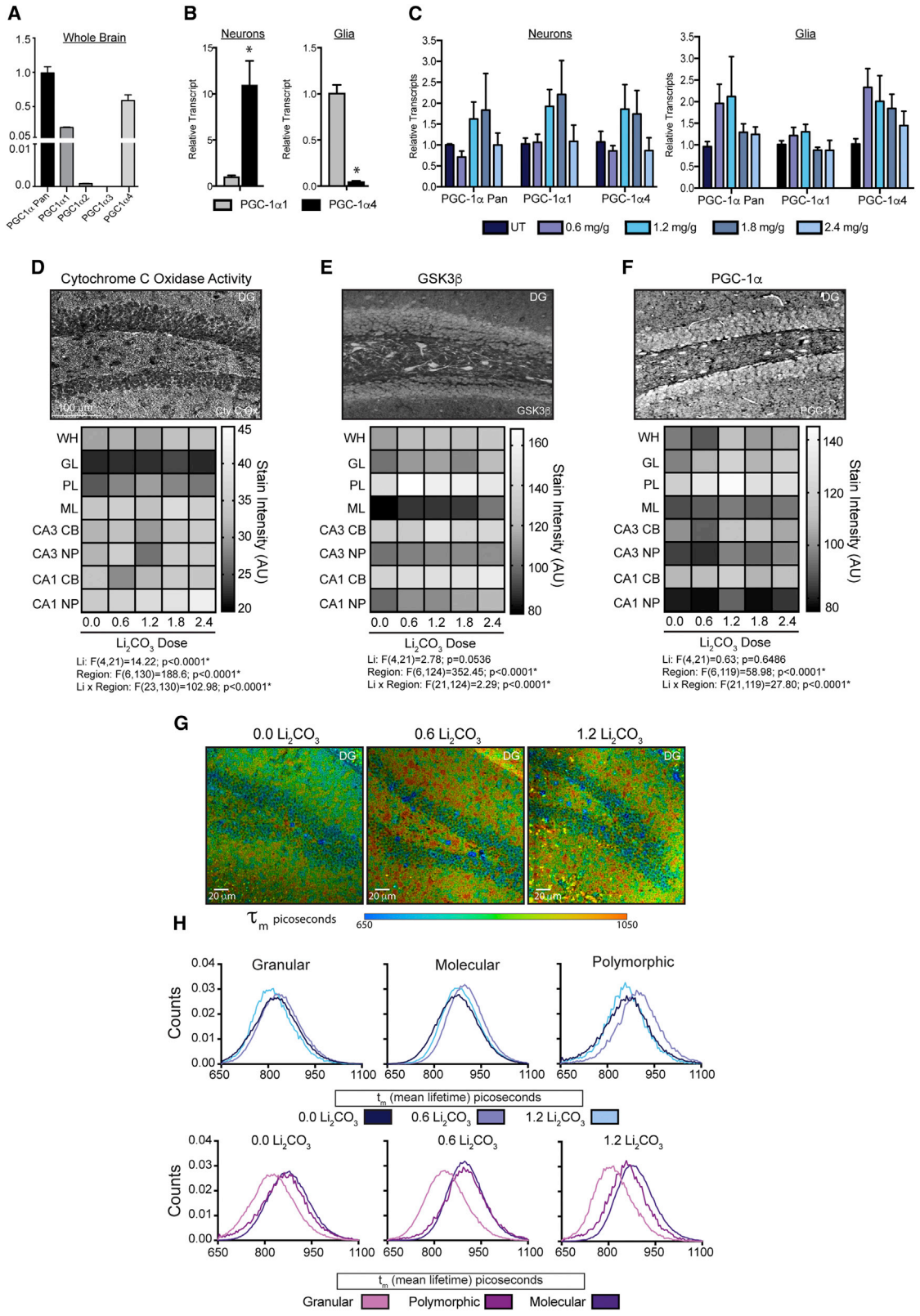

(legend on next page)

levels detected at lower doses in neurons of the GL, PL, and the cell bodies of CA1 were not observed at the higher dose (2.4 mg/kg). Multi-photon imaging of hippocampal sections from lithium-treated mice revealed no difference in fluorescence intensity, but main effects of region, treatment, and an interaction of region by treatment were detected by FLIM in the GL, PL, and ML (Figures 4G and S5; Table S5). Lithium increased τ_m at 0.6 mg/kg for all three regions, similar to what was observed in lithium-treated cultured cells (Figure 4H). Unexpectedly, values returned to those of untreated at 1.2 mg/kg; however, this dynamic was explained by differences in components contributing to τ_m, where τ_1, τ_1, and a_1 values each differed between lithium treatment and no treatment. These data demonstrate a clear NAD-associated metabolic response to hippocampal GSK3β inhibition *in vivo*.

DISCUSSION

Several lines of evidence presented here are indicative of a role for GSK3β in the regulation brain energy metabolism. In cultured cells, inhibition of GSK3β by treatment with either lithium or Inhibitor VIII stimulated mitochondrial energy metabolism, including increases in the mitochondrial proton motive force and concomitant increases in mitochondrial respiration. Genetic approaches confirm the role of GSK3β in cellular metabolic regulation, where lithium's effects were diminished when levels of GSK3β were lowered by RNA interference and were abrogated by expression of a GSK3β mutant (GSK3β-S9A) that is resistant to the effects of inhibitory phosphorylation. This GSK3β-associated change in mitochondrial function was accompanied by a lengthening of NAD(P)H fluorescence lifetime, an adaptation that is also consistent with a shift toward an oxidative phenotype. The metabolic response to GSK3β inhibition was largely conserved between cell culture models of glia and neurons despite critical differences in the underlying biology of these cell types including differences in innate oxidative metabolic capacity and differences in levels of proteins associated with the GSK3β/PGC-1α axis. Lithium's effects on metabolism in mice *in vivo* were consistent with those observed in cultured cells. GSK3β inhibition increased mitochondrial activity the hippocampus and lengthened NAD(P)H fluorescent lifetime. A role for PGC-1a is implied in the metabolic response to GSK3b inhibition, where stability of PGC-1α protein was increased by either lithium or inhibitor VIII treatment in cultured cells, and expression of PGC-1α target genes was altered in both H4 glioma and PC12-derived neurons. In mice treated *in vivo*, hippocampal levels of PGC-1α protein were increased in response to lithium and PGC-1α transcripts were increased in isolated glia and neurons. Minor differences between the cell culture and *in vivo* responses to lithium might be explained by crosstalk among cell types in the brain (Bélanger et al., 2011). Co-culturing and 3D growth experiments with neurons and glia together may shed light on secondary signaling, metabolic coupling, and adaptive mechanisms involved in the brain metabolic response to GSK3β inhibition that are not captured in homogeneous culture models.

The role of metabolism in age-related disease has become a major focus in aging research, and NAD specifically, due to its central role in intermediate metabolism and as a regulator of sirtuin activity, has moved to the fore in this arena (Chini et al., 2017; Verdin, 2015; Yoshino et al., 2017). In peripheral tissues, PGC1α activity is stimulated by the actions of the NAD-dependent deacetylase SIRT1 (Nemoto et al., 2005; Rodgers et al., 2005) and studies in cultured neurons have implicated SIRT1 in neuroprotection (Qin et al., 2006). Genetic studies have independently revealed parallel roles for GSK3β and PGC-1α in vital brain processes. GSK3β has a long established role in cytoskeletal regulation, including dendritic spine stability (Ochs et al., 2015), as well as regulation of neurogenesis and memory consolidation, while PGC-1α has been shown regulate dendritic arborization (Cheng et al., 2012). An imbalance in GSK3β impedes neuroregenerative processes in mice (Kondratiuk et al., 2013) and disruptions in PGC-1α produce a neurodegenerative phenotype (St-Pierre et al., 2006). GSK3β and PGC-1α are both influenced by aging within the hippocampus. Aged rats exhibit significantly elevated levels of GSK3β in the dentate gyrus and CA regions of the hippocampus, while aged mice exhibit decreased hippocampal PGC-1α protein (Lee et al., 2006; Martin et al., 2016). In the context of Alzheimer's disease, GSK3β inhibition has been previously demonstrated to ameliorate disease pathology and improve cognitive function (Forlenza et al., 2012; Ly et al., 2013), while hippocampal PGC-1α gene delivery protects against neurodegeneration and cognitive impairment (Katsouri et al., 2016). A number of studies place mitochondrial dysfunction downstream of aging-related neurodegeneration and Alzheimer's pathology (Reddy, 2013; Rhein et al., 2009), but it is possible that in normal disease progression metabolic dysfunction and pathology arise concomitantly. Indeed, recent studies suggest that mitochondrial dysfunction may be a driver of cognitive decline (Grimm and Eckert, 2017). The ability of GSK3β to regulate brain mitochondrial function and NAD metabolism brings a new aspect to its role in aging and neurodegenerative disease, with implications for neurotransmitters and neurotrophic signaling pathways

Figure 4. Inhibition of GSK3β Regulates Hippocampal Energy Metabolism in Mice

(A and B) RT-PCR detection of PGC-1α isoforms in the whole-mouse brain (A) or in isolated neurons and glia (B).

(C) RT-PCR detection of PGC-1α isoforms in neurons and glia isolated from the whole brain of mice fed the indicated doses of dietary lithium carbonate (Li_2CO_3) for 4 months.

(D–F) Representative images and quantification of cytochrome C oxidase mitochondrial activity stain (D), GSK3β immunodetection (E), and PGC-1α immunodetection in the indicated hippocampal regions from Li_2CO_3 fed mice (F).

(G and H) Representative images of mean fluorescence lifetime (τ_m) in picoseconds ($_{ex}\lambda_{780}$) in the dentate gyrus from Li_2CO_3 fed mice (G) and τ_m distributions separated by region (top panel) and by dose (bottom panel) (H).

n = 4–6 mice per Li_2CO_3 dosage; data shown as an average ± SEM or distributions; *p < 0.05, linear mixed models. WH, whole hippocampus; DG, dentate gyrus; GL, granular layer; PL, polymorphic layer; ML, molecular layer; CB, cell bodies; and NP, neuropil.

that impinge on GSK3β as part of normal inter- and intracellular communication.

STAR★METHODS

Detailed methods are provided in the online version of this paper and include the following:

- KEY RESOURCES TABLE
- CONTACT FOR REAGENT AND RESOURCE SHARING
- EXPERIMENTAL MODEL AND SUBJECT DETAILS
  - Animals
  - Cell Culture
- METHOD DETAILS
  - PC-12 cell differentiation
  - Lithium Treatment
  - Lipofectamine Transfection
  - Metabolic Assays
  - Immunoblotting and qRT-PCR
  - Microscopy
- QUANTIFICATION AND STATISTICAL ANALYSES

SUPPLEMENTAL INFORMATION

Supplemental Information includes five figures and six tables and can be found with this article online at https://doi.org/10.1016/j.celrep.2018.04.045.

ACKNOWLEDGMENTS

This work was supported by The Glenn Foundation for Medical Research, the American Federation for Aging Research, and the UW-ADRC: NIH/NIA (AG033514). S.A.M., D.C.S., and J.P.C. were supported by fellowships from NIH/NIA (T32 AG000213). K.N.M. was supported by a fellowship from NIH/NIDDK (T32 DK007665). This work was conducted with the use of resources and facilities at the William S. Middleton Memorial Veterans Hospital (Madison, WI).

AUTHOR CONTRIBUTIONS

S.A.M., D.C.S., and R.M.A. designed the study; S.A.M., D.C.S., K.N.M., and J.P.C. conducted the experiments; A.K.S. and K.W.E. consulted on the multiphoton imaging; L.P. provided reagents and expertise; S.A.M. and T.M.B. conducted the statistical analyses; and S.A.M., D.C.S., and R.M.A. wrote the manuscript.

DECLARATION OF INTERESTS

The authors declare no competing interests.

Received: June 15, 2017
Revised: January 8, 2018
Accepted: April 11, 2018
Published: May 15, 2018

REFERENCES

Anderson, R.M., Barger, J.L., Edwards, M.G., Braun, K.H., O'Connor, C.E., Prolla, T.A., and Weindruch, R. (2008). Dynamic regulation of PGC-1alpha localization and turnover implicates mitochondrial adaptation in calorie restriction and the stress response. Aging Cell *7*, 101–111.

Bélanger, M., Allaman, I., and Magistretti, P.J. (2011). Brain energy metabolism: focus on astrocyte-neuron metabolic cooperation. Cell Metab. *14*, 724–738.

Beurel, E., Grieco, S.F., and Jope, R.S. (2015). Glycogen synthase kinase-3 (GSK3): regulation, actions, and diseases. Pharmacol. Ther. *148*, 114–131.

Bird, D.K., Yan, L., Vrotsos, K.M., Eliceiri, K.W., Vaughan, E.M., Keely, P.J., White, J.G., and Ramanujam, N. (2005). Metabolic mapping of MCF10A human breast cells via multiphoton fluorescence lifetime imaging of the coenzyme NADH. Cancer Res. *65*, 8766–8773.

Cheng, A., Wan, R., Yang, J.L., Kamimura, N., Son, T.G., Ouyang, X., Luo, Y., Okun, E., and Mattson, M.P. (2012). Involvement of PGC-1α in the formation and maintenance of neuronal dendritic spines. Nat. Commun. *3*, 1250.

Chini, C.C.S., Tarragó, M.G., and Chini, E.N. (2017). NAD and the aging process: role in life, death and everything in between. Mol. Cell. Endocrinol. *455*, 62–74.

Colman, R.J., Anderson, R.M., Johnson, S.C., Kastman, E.K., Kosmatka, K.J., Beasley, T.M., Allison, D.B., Cruzen, C., Simmons, H.A., Kemnitz, J.W., and Weindruch, R. (2009). Caloric restriction delays disease onset and mortality in rhesus monkeys. Science *325*, 201–204.

DaRocha-Souto, B., Coma, M., Pérez-Nievas, B.G., Scotton, T.C., Siao, M., Sánchez-Ferrer, P., Hashimoto, T., Fan, Z., Hudry, E., Barroeta, I., et al. (2012). Activation of glycogen synthase kinase-3 beta mediates β-amyloid induced neuritic damage in Alzheimer's disease. Neurobiol. Dis. *45*, 425–437.

Denk, W., Strickler, J.H., and Webb, W.W. (1990). Two-photon laser scanning fluorescence microscopy. Science *248*, 73–76.

Forlenza, O.V., de Paula, V.J., Machado-Vieira, R., Diniz, B.S., and Gattaz, W.F. (2012). Does lithium prevent Alzheimer's disease? Drugs Aging *29*, 335–342.

Fujita, K., Lazarovici, P., and Guroff, G. (1989). Regulation of the differentiation of PC12 pheochromocytoma cells. Environ. Health Perspect. *80*, 127–142.

Geddes, J.R., Burgess, S., Hawton, K., Jamison, K., and Goodwin, G.M. (2004). Long-term lithium therapy for bipolar disorder: systematic review and meta-analysis of randomized controlled trials. Am. J. Psychiatry *161*, 217–222.

Grimm, A., and Eckert, A. (2017). Brain aging and neurodegeneration: from a mitochondrial point of view. J. Neurochem. *143*, 418–431.

Hetz, C., and Mollereau, B. (2014). Disturbance of endoplasmic reticulum proteostasis in neurodegenerative diseases. Nat. Rev. Neurosci. *15*, 233–249.

Hoeflich, K.P., Luo, J., Rubie, E.A., Tsao, M.S., Jin, O., and Woodgett, J.R. (2000). Requirement for glycogen synthase kinase-3beta in cell survival and NF-kappaB activation. Nature *406*, 86–90.

Kaidanovich-Beilin, O., and Woodgett, J.R. (2011). GSK-3: Functional Insights from Cell Biology and Animal Models. Front. Mol. Neurosci. *4*, 40.

Katsouri, L., Lim, Y.M., Blondrath, K., Eleftheriadou, I., Lombardero, L., Birch, A.M., Mirzaei, N., Irvine, E.E., Mazarakis, N.D., and Sastre, M. (2016). PPARγ-coactivator-1α gene transfer reduces neuronal loss and amyloid-β generation by reducing β-secretase in an Alzheimer's disease model. Proc. Natl. Acad. Sci. USA *113*, 12292–12297.

Klein, P.S., and Melton, D.A. (1996). A molecular mechanism for the effect of lithium on development. Proc. Natl. Acad. Sci. USA *93*, 8455–8459.

Kondratiuk, I., Devijver, H., Lechat, B., Van Leuven, F., Kaczmarek, L., and Filipkowski, R.K. (2013). Glycogen synthase kinase-3beta affects size of dentate gyrus and species-typical behavioral tasks in transgenic and knockout mice. Behav. Brain Res. *248*, 46–50.

Lakowicz, J.R., Szmacinski, H., Nowaczyk, K., and Johnson, M.L. (1992). Fluorescence lifetime imaging of free and protein-bound NADH. Proc. Natl. Acad. Sci. USA *89*, 1271–1275.

Lee, S.J., Chung, Y.H., Joo, K.M., Lim, H.C., Jeon, G.S., Kim, D., Lee, W.B., Kim, Y.S., and Cha, C.I. (2006). Age-related changes in glycogen synthase kinase 3beta (GSK3beta) immunoreactivity in the central nervous system of rats. Neurosci. Lett. *409*, 134–139.

Littell, R., Milliken, G., Stroup, W., Wolfinger, R., and Schabenberger, O. (2006). SAS System for Mixed Models (SAS Institute).

Ly, P.T., Wu, Y., Zou, H., Wang, R., Zhou, W., Kinoshita, A., Zhang, M., Yang, Y., Cai, F., Woodgett, J., and Song, W. (2013). Inhibition of GSK3β-mediated

BACE1 expression reduces Alzheimer-associated phenotypes. J. Clin. Invest. *123*, 224–235.

Martin, S.A., DeMuth, T.M., Miller, K.N., Pugh, T.D., Polewski, M.A., Colman, R.J., Eliceiri, K.W., Beasley, T.M., Johnson, S.C., and Anderson, R.M. (2016). Regional metabolic heterogeneity of the hippocampus is nonuniformly impacted by age and caloric restriction. Aging Cell *15*, 100–110.

Martínez-Redondo, V., Jannig, P.R., Correia, J.C., Ferreira, D.M., Cervenka, I., Lindvall, J.M., Sinha, I., Izadi, M., Pettersson-Klein, A.T., Agudelo, L.Z., et al. (2016). Peroxisome proliferator-activated receptor γ coactivator-1 α isoforms selectively regulate multiple splicing events on target genes. J. Biol. Chem. *291*, 15169–15184.

Nemoto, S., Fergusson, M.M., and Finkel, T. (2005). SIRT1 functionally interacts with the metabolic regulator and transcriptional coactivator PGC-1alpha. J. Biol. Chem. *280*, 16456–16460.

Ochs, S.M., Dorostkar, M.M., Aramuni, G., Schön, C., Filser, S., Pöschl, J., Kremer, A., Van Leuven, F., Ovsepian, S.V., and Herms, J. (2015). Loss of neuronal GSK3β reduces dendritic spine stability and attenuates excitatory synaptic transmission via β-catenin. Mol. Psychiatry *20*, 482–489.

Olson, B.L., Hock, M.B., Ekholm-Reed, S., Wohlschlegel, J.A., Dev, K.K., Kralli, A., and Reed, S.I. (2008). SCFCdc4 acts antagonistically to the PGC-1alpha transcriptional coactivator by targeting it for ubiquitin-mediated proteolysis. Genes Dev. *22*, 252–264.

Parker, P.J., Caudwell, F.B., and Cohen, P. (1983). Glycogen synthase from rabbit skeletal muscle; effect of insulin on the state of phosphorylation of the seven phosphoserine residues in vivo. Eur. J. Biochem. *130*, 227–234.

Patel, P., and Woodgett, J.R. (2017). Glycogen synthase kinase 3: a kinase for all pathways? Curr. Top. Dev. Biol. *123*, 277–302.

Patel, S., Macaulay, K., and Woodgett, J.R. (2011). Tissue-specific analysis of glycogen synthase kinase-3α (GSK-3α) in glucose metabolism: effect of strain variation. PLoS ONE *6*, e15845.

Pei, L., Mu, Y., Leblanc, M., Alaynick, W., Barish, G.D., Pankratz, M., Tseng, T.W., Kaufman, S., Liddle, C., Yu, R.T., et al. (2015). Dependence of hippocampal function on ERRγ-regulated mitochondrial metabolism. Cell Metab. *21*, 628–636.

Qin, W., Yang, T., Ho, L., Zhao, Z., Wang, J., Chen, L., Zhao, W., Thiyagarajan, M., MacGrogan, D., Rodgers, J.T., et al. (2006). Neuronal SIRT1 activation as a novel mechanism underlying the prevention of Alzheimer disease amyloid neuropathology by calorie restriction. J. Biol. Chem. *281*, 21745–21754.

Reddy, P.H. (2013). Amyloid beta-induced glycogen synthase kinase 3β phosphorylated VDAC1 in Alzheimer's disease: implications for synaptic dysfunction and neuronal damage. Biochim. Biophys. Acta *1832*, 1913–1921.

Rhein, V., Song, X., Wiesner, A., Ittner, L.M., Baysang, G., Meier, F., Ozmen, L., Bluethmann, H., Dröse, S., Brandt, U., et al. (2009). Amyloid-beta and tau synergistically impair the oxidative phosphorylation system in triple transgenic Alzheimer's disease mice. Proc. Natl. Acad. Sci. USA *106*, 20057–20062.

Rodgers, J.T., Lerin, C., Haas, W., Gygi, S.P., Spiegelman, B.M., and Puigserver, P. (2005). Nutrient control of glucose homeostasis through a complex of PGC-1alpha and SIRT1. Nature *434*, 113–118.

Saville, D.J. (1990). Multiple comparison procedures–the practical solution. Am. Stat. *44*, 174–180.

Schon, E.A., and Przedborski, S. (2011). Mitochondria: the next (neurode)generation. Neuron *70*, 1033–1053.

Serenó, L., Coma, M., Rodríguez, M., Sánchez-Ferrer, P., Sánchez, M.B., Gich, I., Agulló, J.M., Pérez, M., Avila, J., Guardia-Laguarta, C., et al. (2009). A novel GSK-3beta inhibitor reduces Alzheimer's pathology and rescues neuronal loss in vivo. Neurobiol. Dis. *35*, 359–367.

St-Pierre, J., Drori, S., Uldry, M., Silvaggi, J.M., Rhee, J., Jäger, S., Handschin, C., Zheng, K., Lin, J., Yang, W., et al. (2006). Suppression of reactive oxygen species and neurodegeneration by the PGC-1 transcriptional coactivators. Cell *127*, 397–408.

Stambolic, V., Ruel, L., and Woodgett, J.R. (1996). Lithium inhibits glycogen synthase kinase-3 activity and mimics wingless signalling in intact cells. Curr. Biol. *6*, 1664–1668.

Verdin, E. (2015). NAD^+ in aging, metabolism, and neurodegeneration. Science *350*, 1208–1213.

Woodgett, J.R. (1990). Molecular cloning and expression of glycogen synthase kinase-3/factor A. EMBO J. *9*, 2431–2438.

Yin, F., Boveris, A., and Cadenas, E. (2014). Mitochondrial energy metabolism and redox signaling in brain aging and neurodegeneration. Antioxid. Redox Signal. *20*, 353–371.

Yoshino, J., Baur, J.A., and Imai, S.I. (2017). NAD(+) intermediates: the biology and therapeutic potential of NMN and NR. Cell Metab. *27*, 513–528.

Zhang, F., Phiel, C.J., Spece, L., Gurvich, N., and Klein, P.S. (2003). Inhibitory phosphorylation of glycogen synthase kinase-3 (GSK-3) in response to lithium. Evidence for autoregulation of GSK-3. J. Biol. Chem. *278*, 33067–33077.

STAR★METHODS

KEY RESOURCES TABLE

REAGENT or RESOURCE	SOURCE	IDENTIFIER
Antibodies		
Rabbit anti-PGC-1α	Santa Cruz	sc-13067
Rabbit anti-GSK3β	Cell Signaling Tech.	9315S
Rabbit anti-pGSK3β	Cell Signaling Tech.	9336
Mouse anti-β−actin	Sigma Aldrich	A1978
Mouse anti-α−tubulin	Sigma Aldrich	T6199
Mouse anti-OxPhos Cocktail	AbCam	ab110413
Mouse anti-Sirt1	Santa Cruz	sc-74504
Rabbit anti-NAMPT	Sigma Aldrich	V9139
Rabbit anti-PARP	Cell Signaling Tech.	9542
Rabbit anti-cyclin d1	AbCam	ab7958
Biotinylated anti-mouse Ig	Vector Labs	BA-9200
Biotinylated anti-mouse Ig	Vector Labs	BA-1000
Chemicals, Peptides, and Recombinant Proteins		
Lithium Chloride (8M)	Sigma Aldrich	L7026
Cycloheximide	Sigma Aldrich	C7698
GSK3β Inhibitor VIII	Millipore	361549-5mg
ABC Solution	Vector Labs	PK-6200
NovaRed Reagent	Vector Labs	SK-4850
Critical Commercial Assays		
JC-1 Reagent	Invitrogen	T3168
Cell Mito Stress Test Kit	Agilent	103015-100
NAD+/NADH Quantification Kit	Biovision	K337-100
Oxoplate	Presens	OP96U
Nuclear/Cytosol Fractionation Kit	BioVision	K266-100
Neuronal Isolation Kit	Miltenyi Biotec	130-098-754
LIVE/DEAD Viability/Cytotoxicity Kit	Molecular Probes	L3224
Experimental Models: Cell Lines		
H4	ATCC	HTB-148
PC12	ATCC	CRL-1721
Experimental Models: Organisms/Strains		
B6C3F1	Harlan	N/A
Oligonucleotides		
See Table S6	N/A	N/A
Other		
Custom Mouse Diet w/ Lithium Carbonate	Bio-Serv	AIN-93M
GSK3b siRNA	ThermoFisher	S6239
Negative Control siRNA	ThermoFisher	AM4615
HA-GSK3b S9A pcDNA3	Addgene	14754
Lipofectamine 2000	ThermoFisher	11668019

CONTACT FOR REAGENT AND RESOURCE SHARING

Further information and requests for resources and reagents should be directed to and will be fulfilled by the Lead Contact Rozalyn Anderson (rozalyn.anderson@wisc.edu).

EXPERIMENTAL MODEL AND SUBJECT DETAILS

Animals

Six-week-old male B6C3F1 hybrid mice were obtained from Harlan Laboratories (Madison, WI, USA) and housed under controlled pathogen-free conditions in accordance with the recommendations of the University of Wisconsin Institutional Animal Care and Use Committee. Mice were fed 87 kcal week^{-1} of control diet (F05312; Bio-Serv, Flemington, NJ, USA) and were individually housed with *ad libitum* access to water. This level of food intake is ~95% *ad libitum* for the B6C3F1 strain so all food was consumed. Following two weeks of facility acclimation, mice were randomized into five treatment groups fed the control diet supplemented with increasing concentrations of dietary lithium carbonate (2 months old; n = 10/group): Group 1) 0.0 g/kg/day Li_2CO_3; Group 2) 0.6 g/kg/day Li_2CO_3; Group 3) 1.2 g/kg/day Li_2CO_3; Group 4) 1.8 g/kg/day Li_2CO_3; Group 5) 2.4 g/kg/day Li_2CO_3. Li_2CO_3 supplemented mice were administered an additional drinking bottle containing saline (0.45% NaCl) to offset polyuria, a common side effect of lithium treatment. Mice consumed dietary lithium for 4 months, and were euthanized at 6 months of age. Brains were isolated, bisected, embedded in OCT, frozen in liquid nitrogen, and stored at −80°C until further processing.

Cell Culture

H4 cells were obtained from ATCC (HTB-148; Manassas, VA, USA) and cultured in DMEM containing 10% fetal bovine serum and 1% penicillin/streptomycin. PC-12 cells were obtained from ATCC (CRL-1721) and cultured in Dulbecco's modified Eagle's medium (DMEM) with 10% horse serum, 5% fetal bovine serum, and 1% penicillin/streptomycin.

METHOD DETAILS

PC-12 cell differentiation

All PC-12 experiments were conducted on fully differentiated PC-12 cells (7 days of differentiation). For differentiation, PC-12 cells were plated on collagen coated plates and cultured for 7 days in DMEM containing 0.1% horse serum, 100 ng/ml 2.5S nerve growth factor (N-100; Alomone Labs, Jerusalem, Israel), and 1% penicillin/streptomycin. Media was changed every 2 days.

Lithium Treatment

Lithium time-course experiments were carried out using cell culture media supplemented with 15mM lithium chloride (LiCl). Media change was carried out 2 or 24 hours prior to collection as indicated. For PGC-1α protein stability experiments, cells were pretreated for 1 hour with media containing 15mM LiCl or control media, followed by the direct addition of cycloheximide (100nM) or eqivolume DMSO to the plates for the indicated time.

Lipofectamine Transfection

H4 cells were seeded in 6-well plates 24 hours prior to lipofectamine transfection (6ul/well). HA-GSK3b[S9A] and pcDNA3.1 control vectors were transfected at 3ug/well and media change was carried out 4 hours after transfection and prior to lithium treatment. GSK3b siRNA was transfected at 30nM for 24h and media was changed prior to lithium treatment.

Metabolic Assays

Mitochondrial membrane potential

Mitochondrial membrane potential was determined using the JC-1 assay (T-3168; Thermo Fisher Scientific) in accordance with the manufacturer's instructions. Cells were incubated in 1 μg/mL JC-1 dye for 15-minutes prior to counting and re-suspension in D-PBS for assay. Fluorescent emission was measured at 590nm and 530nm with excitation at 535nm and 485nm respectively.

Mitochondrial Respiration (Seahorse Assay)

Basal and maximal respiration of H4 cells was determined using a Seahorse extracellular flux (XF) Cell Mito Stress Test Kit (103015-100; Agilent Technologies, Santa Clara, CA, USA). Cells were plated at 4.0x10^4/well in a 96-well microplate using growth media in the presence or absence of 15mM LiCl and incubated overnight. One hour prior to assay, cells were switched into assay media in accordance with the manufacturer's instructions and incubated at 37 C in a non-CO_2 incubator. At the time of assay, cells were loaded into the XF analyzer along with a loaded sensor cartridge containing the following ETS inhibitors: Oligomycin (100 uM), FCCP (100uM), and Rotenone/antimycin A (50 uM). Inhibitors were sequentially injected into the assay media and basal respiration, ATP production, maximal respiration, and non-mitochondrial respiration were measured as a function of cellular oxygen consumption.

Cellular Respiration (OxoPlate Assay)

Oxygen consumption of H4 cells was determined using an Oxoplate (OP96U; Presens) oxygen monitoring system. Cells were suspended in respiration buffer (pH 7.4) containing D-Mannitol, Potassium Chloride (KCL), Magnesium Chloride ($MgCl_2$), and Monopotassium Phosphate (KH_2PO_4) at 4.0x10^5/well in quadruplicate. Fluorescent emission was measured at 650nm and 590nm with excitation at 540nm at 10-minute intervals at 37 C.

Biochemical NAD(H) Assays

NAD/NADH quantification was determined using the Biovision NAD/NADH quantification colorimetric assay kit (K337-100; Biovision) per manufacturer's instructions.

Cell Proliferation Analysis

Cellular proliferation was quantified using a CyQUANT direct cell proliferation assay (C35011; Thermo Fisher Scientific) per manufacturer's instructions.

Live/Dead Assay

Cellular viability in response to lithium and GSK3b inhibitor VIII treatment was determined using a Molecular Probes LIVE/DEAD Viability/Cytotoxicity Kit (L3224; Thermo Fisher Scientific).

Immunoblotting and qRT-PCR

Western Blotting and Antibodies

Cells were lysed and protein was extracted in modified RIPA buffer containing protease and phosphatase inhibitors (P8340 and 524624, respectively; Sigma Aldrich, St. Louis, MO, USA). Proteins were detected by immunoblotting using standard techniques. Antibodies used were PGC-1α (sc-13067; Santa Cruz Biotechnology, Santa Cruz, CA, USA) GSK3β (9315; Cell Signaling Technologies, Boston, MA), serine 9 phospho-GSK3β (9336; Cell Signaling Technology), Total OXPHOS (ab110413; Abcam, Cambridge, MA, USA), Cyclin-d1 (ab7958; Abcam) beta-actin (A1978; Sigma Aldrich) and Sirt1 ((sc-74504, Santa Cruz), PARP (9542S; Cell Signaling). Subcellular fractionation was performed using nuclear/cytoplasmic fractionation kit (K266-100; Biovision, Milpitas, CA, USA) per manufacturer's instructions. Equivalent protein amounts were loaded for both the nucleus and cytoplasm.

RNA Analysis

Cells were lysed in Trizol (15596018; Thermo Fisher Scientific, Waltham, MA, USA) and RNA was isolated using Direct-zol RNA Miniprep kit (R2072; Zymo Research, Irvine, CA, USA) in accordance with manufacturers instructions. cDNA was synthesized using a High Capacity reverse transcription cDNA kit (4368813; Thermo Fisher Scientific). Quantitive real-time reverse transcription PCR was performed on an Applied Biosystems Prism 7900 using TaqMan and SYBR Green gene expression assays (Thermo Fisher Scientific)

Microscopy

Immunofluorescence Microscopy

Cellular localization was analyzed by immunofluorescence using standard techniques. H4 cells were cultured on glass coverslips and PC-12 cells were cultured on Nunc Lab-Tek CC2 chamber slides (154917; Thermo Fisher Scientific). Following 24h LiCl treatment, cells were fixed in 3.7% formaldehyde for 10 minutes. Cells were incubated overnight in primary antibodies (sc-13067; Santa Cruz Biotechnology, Santa Cruz, CA, USA) GSK3β (9315; Cell Signaling Technologies, Boston, MA), serine 9 phospho-GSK3β (9336; Cell Signaling Technology), alpha-tubulin (T6199; Sigma Aldrich)), and Tomm20 (ab 56783; Abcam). Cellular distribution of proteins was visualized using fluorescent-tagged secondary antibodies (FI-2000, FI-1000; Vector Laboratories) USA. F-actin was visualized using Rhodamine Phalloidin (PDHR1; Cytoskeleton Inc, Denver, CO, USA). Nuclei were visualized using Hoechst Solution (62249; Thermo Fisher Scientific). All images were captured using uniform exposure settings on a Leica DM4000B microscope (Leica Microsystems, Wetzlar, Germany) and photographed with a Retiga 4000R digital camera (QImaging Systems, Surrey, BC, Canada)

Multiphoton laser scanning Microscopy

Immediately prior to multiphoton imaging, cells were fixed for 10 minutes with formalin and mounted onto glass coverslips using Vectashield (Vector Labs) hard-mount mounting solution. Cryostat sections were dried onto glass coverslips and mounted using Clearmount mounting solution (Thermo Fisher Scientific). The instrument response function of the optical system was calibrated before each imaging session. A Nikon CFI Plan Apo 60x lens (Melville, NY, USA) was used for all imaging. Data were collected using an excitation wavelength of 780 nm, and emission was filtered at 457 ± 50 nm, the spectral peak for NADH/NADPH. The data collection time was 120 s using a pixel frame size of 256 × 256. The system has multiple detectors including a 16 channel combined spectral lifetime detector (utilizes a Hamamatsu PML-16 PMT), detection range 350 to 720 nm, and a H7422P GaAsP photon counting PMT (Hamamatsu) for intensity and lifetime imaging. Acquisition was performed with WiscScan, a LOCI developed acquisition package software. Autofluorescence intensity and fluorescence lifetime data were analyzed in SPCImage (Becker & Hickl, v.3.9.7, Berlin, Germany) where a Levenberg–Marquardt routine for nonlinear fitting was used to fit the fluorescence decay curve collected for each pixel in the 256 × 256 frame to a model multi-exponential decay function. Data were assessed by the minimized chi-square value generated during the fit so that analysis was unbiased. To eliminate background fluorescence a threshold for analysis was applied based on photon counts. Additionally, pixels were assigned a bin of 2 for optimal fitting of the data. For NAD(P)H autofluorescent intensity, data were analyzed in ImageJ (NIH, Wayne Rasband; https://imagej.nih.gov/ij/) and regions were defined by cellular compartment or hippocampal region. For fluorescence lifetime, regions of interest were defined by the same criteria using the inclusion tool in SPC image.

Histochemistry and Immunodetection

Serial cryostat sections 10 μm in thickness were cut at _14°C with a Leica Cryostat, defrosted and air-dried, and stained for cytochrome *c* oxidase enzymatic activity as previously described (Martin et al., 2016). For each experiment, tissues were sliced, batches were processed, and data were captured start to finish within 24 h. Immunodetection of PGC-1α and GSK3β was conducted as previously described (Martin et al., 2016) following antigen retrieval on 10-μm cryosections (mouse) tissues. Antibodies and reagents used are as follows: biotinylated anti-mouse Ig (BA-9200; Vector Labs, Burlingame, CA, USA) or biotinylated anti-rabbit IgG (BA-1000; Vector Labs), peroxidase-labeled avidin biotin complex (ABC) solution (PK-6200; Vector Labs), ImmPACT NovaRED reagent

(SK-4805; Vector Labs), PGC-1α (sc-13067; Santa Cruz Biotechnology), total GSK3b (9315; Cell Signaling Technology), serine 9 phospho-GSK3β (9336; Cell Signaling Technology). With the exception of the multiphoton imaging, stained slides were imaged with a Leica Microsystems DM4000B microscope and photographed with a Retiga 4000R digital camera (QImaging Systems, Surrey, BC, Canada). Camera settings were optimized for each stain; for uniformity, all images for a given stain were taken on the same day with identical settings, fixed light levels, and fixed shutter speed optimized at each magnification. Digital images were converted from color to monochrome and inverted, so that greater stain intensity is shown as brighter pixels. All image analysis was performed using Adobe Photoshop (Adobe Systems, San Jose, CA, USA). Stain intensity was measured using either the rectangular marquee tool or the lasso outline tool in the hippocampal region of interest. Within each region for each stain, the size of the capture box was uniform with an average inclusion of ~30K pixels.

Neuron Isolation

Mouse neurons and non-neuronal cells were isolated from whole brain suspensions using the Neuron Isolation Kit (130-098-754; Miltenyi Biotec, San Diego, CA, USA) per manufacturer's instructions. Briefly, brain tissue was enzymatically dissociated and debris was removed through centrifugation at 4°C. Non-neuronal cells were labeled using the Non-Neuronal Cells Biotin-Antibody Cocktail and depleted using magnetic separation. Isolated cell populations were lysed in Trizol and RNA analysis was conducted as previously described.

QUANTIFICATION AND STATISTICAL ANALYSES

Independent Student's t test and ANOVA with post hoc analyses were used to evaluate statistical significance in all cell culture studies. Statistical analyses for the hippocampal immunohistochemistry and MPLSM-FLIM was conducted as previously described (Martin et al., 2016). Briefly, to account for the dependence among observations due to multiple measurements per animal, we performed linear mixed models (LMM) assuming a compound symmetric covariance structure using SAS PROC MIXED (Littell et al., 2006). The LMMs included full factorial with Type 3 tests of the main effects and interactions. To explore the lithium carbonate dosage-by-region interaction, simple main effects were investigated to determine whether there were dosage effects within each region. We employed no formal multiple testing correction. Instead, consistent with published guidelines for statistical reporting (Saville, 1990), exact p values are reported. All data are reported as mean ± SEM.

Publication: Keikhosravi, Adib, Jeremy S. Bredfeldt, Abdul Kader Sagar, and Kevin W. Eliceiri. "Second-harmonic generation imaging of cancer." In *Methods in cell biology*, vol. 123, pp. 531-546. Academic Press, 2014.

Second-harmonic generation imaging of cancer

Adib Keikhosravi, Jeremy S. Bredfeldt, Md Abdul Kader Sagar, and Kevin W. Eliceiri
Laboratory for Optical and Computational Instrumentation
University of Wisconsin at Madison

Abstract

The last thirty years have seen great advances in optical microscopy with the introduction of sophisticated fluorescence based imaging methods such as confocal and multiphoton laser scanning microscopy. There is increasing interest in using these methods to quantitatively examine sources of intrinsic biological contrast including autofluorescent endogenous proteins and light interactions such as Second Harmonic Generation (SHG) in collagen. In particular, SHG based microscopy has become a widely used quantitative modality for imaging non-centrosymmetric proteins such as collagen in a diverse range of tissues. Due to the underlying physical origin of the SHG signal, it is highly sensitive to collagen fibril/fiber structure, and, importantly, to collagen associated changes that occur in diseases such as cancer, fibrosis and

connective tissue disorders. An overview of SHG physics background and technologies is presented with a focused review on applications of SHG primarily as applied to cancer.

Keywords: Cancer, cells, tumor, second harmonic generation, imaging, imaging biomarkers

1. Introduction

Over the past decade, second harmonic generation microscopy (SHG) has been widely used for biology and tissue engineering research (Campagnola, 2011; Campagnola and Dong, 2011; Campagnola and Loew, 2003; Cox et al., 2003; Zipfel et al., 2003). Increasingly, SHG has been applied to solve biomedical problems and has been used to study a wide spectrum of diseases, from different kinds of cancer to fibrosis and atherosclerosis, by providing quantitative features about disease related collagen changes (Ajeti et al., 2011; Conklin et al., 2011; Han et al., 2005; Kirkpatrick et al., 2007; Kwon et al., 2008; Lacomb et al., 2008; Le et al., 2007; Lin et al., 2005; Lo et al., 2006; Nadiarnykh et al., 2010; Provenzano et al., 2006; Sahai et al., 2005; Schenke-Layland et al., 2008; Strupler et al., 2007; Sun et al., 2008).

In 1961, Franken et al. discovered SHG as an optical nonlinear effect in quartz samples (Franken et al., 1961). Fine and Hansen later found that tissues with collagen were able to intrinsically produce SHG when excited with the appropriate laser source (Fine and Hansen, 1971). Nearly three decades later, Campagnola et al. demonstrated the practicality of using SHG in the laser scanning microscope for cellular and tissue imaging (Campagnola et al., 1999).

In this chapter, we review SHG theory, instrumentation and techniques. We then discuss the many kinds of cancer that have been investigated using SHG focusing on breast, ovarian, and skin cancer. We also present emerging research on other cancers such as lung adenocarcinoma, colonic, and pancreatic cancer.

2. SHG physical and chemical background

Two photon excited fluorescence (TPEF) rises from the inelastic absorption of two photons. After a slight energy loss, one photon is emitted with less than twice the initial photon frequency. SHG, on the other hand, is a coherent, non-absorptive process, which produces an emission photon at exactly twice the frequency of the excitation photon. Generally, the nonlinear polarization for a material can be expressed as

$$P = \chi^{(1)}E^1 + \chi^{(2)}E^2 + \chi^{(3)}E^3 + \cdots, \quad (1)$$

where P is the total induced polarization, $\chi^{(n)}$ is the *n*th order nonlinear susceptibility, and E is the electric field vector of incident light (Shen, 2003). The first term ($\chi^{(1)}E^1$) describes linear absorption, scattering and reflection; the second term describes SHG, sum and difference frequency generation; and the third term describes two-and three-photon absorption, third harmonic generation (THG), stimulated Raman processes and coherent anti-Stokes Raman scattering (CARS). Considering the second term in Eq. (1):

$$P = \chi^{(2)}EE, \quad (2)$$

we see that the second order non-linear polarization depends on the quantity $\chi^{(2)}$ and the field strength E squared. $\chi^{(2)}$ is the second order non-linear optical susceptibility and is measured experimentally in bulk samples. This quantity is non-zero only in non-centrosymmetric materials. The notable materials of biological relevance where this is the case are collagen, microtubules and myosin, with collagen fibrils giving the strongest SHG signal and thus the focus of most SHG studies.

The expression for SHG signal strength is described in Eq. (3) below,

$$I(2\omega) \propto \left[\chi^{(2)} \frac{P}{\tau}(\omega)\right]^2 \tau, \quad (3)$$

where P is the pulse energy, τ is the laser pulse width, and ω is the angular frequency of the excitation light (Campagnola et al., 2001). A notable point here is that the SHG signal is only available during the excitation laser pulse width.

3. SHG instrumentation

The schematic diagram for a typical SHG microscope is shown in Fig. 1 (Campagnola, 2011). In SHG, the wavelength of the excitation laser is not critical since SHG is not a resonant process (Chen et al., 2012). Modern SHG instrumentation typically has two primary components: 1) a mode locked femtosecond laser such as a Titanium Sapphire, and 2) a laser scanning microscope. As shown in Fig. 1, a complete SHG microscope that takes advantage of the full directionality of the SHG signal needs both forward and backward detection paths. This corresponds to transmission and reflection respectively, and they need to be well aligned and calibrated in terms of detection efficiency to perform quantitative assessment (Pavone and Campagnola, 2013). The backward signal is collected using the epi-illumination path of the microscope, where the signal is first isolated using a dichroic mirror, then travels through a bandpass filter with approximately 10 nm bandwidth and is finally detected with a photomultiplier tube. For the forward direction, the detection of the signal is performed by a high numerical aperture condenser or objective and filtered similar to the backward direction. Half and quarter waveplates are used to control the linear and circular polarization of the laser at the focal point of the microscope (Campagnola, 2011).

4. Collagen structure as a biomarker

Collagen, the most abundant protein in vertebrates, forms the structural network of the extracellular matrix (ECM) in tissue and can vary in structure depending on type. For example, fibrillar collagen type I is composed of triple helical macromolecules that are self-assembled into fibrils and fibers. The molecular organization, amount, and distribution of fibrillar collagen is important for the structural and mechanical properties of tissue and plays an important role in several diseases including cancer. Although there are many opportunities for using collagen as a biomarker in a diversity of disease types including wound healing, aging, atherosclerosis, and diabetes (Kim et al., 2000; Lilledahl et al., 2007; Odetti et al., 1994; Tanaka et al., 1988), we will focus here on reviewing cancer applications.

5. SHG in cancer research

I. Breast cancer

Breast cancer is one of the most common cancers among American women, second only to skin cancers (American Cancer Society, 2013). Mammographic density is an emerging risk factor that has shown a large correlation with breast cancer risk (Brower, 2010). Since mammographic density is correlated with collagen density (Alowami et al., 2003), many studies have focused on the collagen's role in tumorigenesis and metastasis.

Differentiation between healthy and malignant tumors and prediction of survival rate has been investigated by Falzon et al. with respect to morphological collagen changes such as fibrillar collagen shape (Falzon et al., 2008). Keely et al. quantified the arrangement of collagen fibers in murine tumor models to investigate if collagen organization can be an early diagnostic factor for breast cancer. They characterized three reproducible “Tumor-associated Collagen

Signature (TACS)" during defined levels of tumor progression (Provenzano et al., 2006). TACS-1 describes the dense collagen surrounding early stage, pre-palpable tumors where collagen fibers have no specific alignment. As tumors develop, the TACS-2 phenotype emerges and we observe collagen fibers begin to wrap around the developing tumor such that fibers are oriented parallel to the tumor-stromal boundary. Finally, in later stage tumors, the TACS-3 pattern can be observed where collagen fibers are oriented perpendicular to the tumor-stromal boundary. Also, in TACS-3, collagen fibers are often observed to be aligned in the direction of cell invasion. Although these observations were first made in breast cancer tumor models, in 2011, a study was performed on a cohort of human breast cancer patients and it was shown that the presence of the TACS-3 phenotype was highly correlated with patient survival (Conklin et al., 2011). Figure 2 illustrates the general TACS stages and gives examples of each observed in human breast biopsy tissue.

More recently, Ambekar et al. used Fourier Transform SHG and Polarization resolved-SHG (P-SHG) to investigate collagen structural changes at the cellular and molecular scale to evaluate the percentage of abnormal collagen fibrils from different pathologic conditions: normal, hyperplasia, dysplasia, and malignant (Ambekar et al., 2012). Their FT-SHG technique estimated the number of areas with aligned or randomly oriented collagen fibers and differentiated malignant from other breast pathologies based on collagen fiber organization. P-SHG was used to investigate structural changes at the molecular scale by estimating the normalized tensor elements of the second-order susceptibility.

Quantitative evaluations of forward and backward SHG (F/B SHG) signals have proven useful to differentiate invasive breast cancer and to monitor the progress of collagen changes during breast carcinogenesis (Burke et al., 2013). This study captured F/B SHG images

throughout breast tumor progression in order to understand how this optical signature, which is influenced by fibrillar collagen microstructural properties, evolved alongside the tumor size and cell morphology that determine the grade and stage of the tumor. Although many research studies have been conducted using SHG for breast cancer research, it is not yet established as a formal clinical method for diagnostic or prognostic use.

II. Ovarian cancer

Every year there are more than 20,000 new cases of ovarian cancer in the US, and more than 15,000 deaths each year. There is currently no effective way to screen for ovarian cancer, thus only 15% of ovarian cancers are diagnosed before metastasis has occurred. Early diagnostic tests that can detect premalignant changes could save many lives (American Cancer society, 2011). SHG holds promise to augment existing techniques and potentially help fill this great diagnostic need. Kirkpatrick et al. used SHG to observe a uniform epithelial layer with highly structured collagen in ovarian stroma versus varied epithelium with large cells and substantial quantifiable changes to the collagen structure in abnormal tissues (Kirkpatrick et al., 2007). Furthermore, the collagen structure of normal low-risk and normal high-risk postmenopausal ovaries is slightly different (Nadiarnykh et al., 2010).

Nadiarnykh et al. proposed a method to use characteristic anisotropy of SHG to quantify alignment of collagen molecules in fibers. They used Eq. 4 to calculate anisotropy:

$$\beta = \frac{I_{par} - I_{perp}}{I_{par} + 2I_{perp}} \quad (4)$$

Where I_{par} is the polarized SHG intensity parallel to the laser polarization, and I_{perp} is the polarized SHG intensity prependicular to the laser polarization (Nadiarnykh et al., 2010). β lies between 0 to 1 for biological tissues. Where 0 represents completely random organization and 1

implies completely ordered fiber organization. They calculate β as 0.88 for malignant ovary and 0.76 for normal ovary, showing that higher β for malignant tissues indicates more ordered structure. These observations are consistent with previous ovarian cancer stroma studies (Fig. 3).

Recently, Watson et al. used SHG imaging to study ex-vivo mouse ovarian tissues of four different types: normal, benign abnormality, dysplasia, and carcinoma (Watson et al., 2012). In this research they used the Fourier transform and gray-level co-occurrence matrix (GLCM) techniques to extract features for classification. They then used a support vector machine (SVM) to classify the images. Using this approach they reached 81.2% sensitivity for separating cancer from non-cancer samples and 77.8% sensitivity for cancer versus normal tissue classification.

III. Skin cancer

Basal cell carcinoma is the most prevalent skin cancer and accounts for 800,000 cases per year in the United States, with an annual incidence rate of nearly 200 for every 100,000 women and 400 for every 100,000 men (Rubin et al., 2005).

The combination of TPEF and SHG is particularly useful when imaging dermis tissue because the two main components of dermis (collagen and elastin) can be imaged with SHG and TPEF microscopy, respectively. Combined TPEF-SHG microscopy was applied to skin physiology and pathology, and specifically to the study of normal skin (König et al., 2005; Konig and Riemann, 2003; Malone et al., 2002; Masters and So, 2001; Masters et al., 1998; So et al., 1998), cutaneous photoaging (Koehler et al., 2006), psoriasis (Konig and Riemann, 2003), selected skin tumors, including basal cell carcinoma (BCC) (Cicchi et al., 2007; Lin et al., 2006; Paoli et al., 2008), and malignant melanoma (MM) (Dimitrow et al., 2009; Menon et al., 2009).

Lin et al. used combined TPEF and SHG to identify the margin of human basal cell carcinoma (Lin et al., 2006). To help in the determination of this margin, a quantitative index is used that is multiphoton fluorescence (MF) to SHG (MFSI). After selection of the region of interest of the image, they defined this TPEF to SHG index as $MFSI = (a - b)/(a + b)$, where a is the number of thresholded TPEF pixels and b is the number of thresholded SHG pixels in the image. The MFSI index ranges from -1 to 1, corresponding to pure SHG and on TPEF images respectively. The highest MFSI is within the tumor masses, where the contribution of the fluorescent signal comes from the cytoplasm. In the normal dermal stroma, the MFSI is the lowest, indicating the relatively high content of intact collagen molecules. In the cancer stroma, the MFSI is significantly higher than that of normal dermal stroma. Cicchi et al. used the combination of TPEF and SHG for the ex-vivo investigation of healthy dermis, normal scar, and keloid tissues (Cicchi et al., 2010).

Later (Chen et al., 2010), proposed higher harmonic generation microscopy (HHGM), which is a combination of SHG and third harmonic generation microscopy (THG), for in-vivo virtual biopsy. They used this technique for inspecting melanoma and a benign cellular proliferation called a compound nevi. Their results suggest that strong epi-THG enhancement is observable in melanoma, suggesting the possible molecular resonance enhancement through melanin. Also, they found that the absorption of melanin to the generated epi-THG light at 410 nm might cause relatively limited penetrability in dark melanoma samples. These results suggested HHGM biopsy could be ideal for diagnosing early dysplasia melanoma and for distinguishing benign nevi and other pigmented diseases.

SHG has also shown the capability to define borders of melanoma. Thrasivoulou et al. (2011) showed that borders of skin melanoma can be delineated quickly and accurately using

SHG. In summary these studies indicate that SHG has the potential to augment current excisional biopsy protocols for melanoma diagnosis and treatment.

IV. SHG research in other types of cancer

Lung cancer is the second most common cancer in both men and women (not counting skin cancer; American Cancer society, 2013b). Wang et al. (2009) used three groups of human lung tissue composed of non-cancerous (NC), lung adenocarcinoma (LC), and lung squamous cell carcinoma (SCC). Their results indicated a significant decrease in SHG signal in both LC and SCC, due to a lack of fibrillar collagen in these groups.

SHG microscopy may also be useful for probing changes in the basement membrane of colonic mucosa that are not accessible by other imaging modalities. In the first SHG study of colonic cancer, 72 colonic biopsy specimens from thirty two patients showed a significant difference between the circle length and population density of the basement membrane (Zhuo et al., 2012). Later, Liu et al. (2013) used SHG/TPEF images to quantify differences between normal and cancerous mucosa and showed that SHG/TPEF ratio of normal tissue was higher than that for cancerous tissue at both mucosa and submucosa. Both results showed the power of SHG for label-free imaging in cancer diagnosis.

In another study, Zhuo et al. (2009a) performed multiple analyses of SHG and TPEF signals and found several significant differences between normal and neoplastic human esophageal stroma. In comparison with normal esophageal stroma, neoplastic stroma displayed: 1) less defined and more diffuse collagen fibril structure, 2) loss of collagen, which is shown by reduced SHG pixel area, 3) reduced spacing between elastin fibers, 4) increased elastin area, and 5) reduced ratio of collagen to elastin (i.e., SHG/TPEF) signals. A similar study also showed a

reduced collagen area (i.e., ratio of SHG pixels to total pixels) in cancerous compared to normal gastric tissues (Chen et al., 2011).

Cervical cancer has also been studied by Zhuo et al. (2009a) through measurement of the size of epithelial cell nuclei and collagen quantity in stroma using TPEF and SHG. Recently, a study of mouse prostate tissue was conducted using different SHG excitation wavelengths producing three main results. First, the maximum SHG intensity occurred at 830 nm. Second, the cell nucleus was found to be larger in cancerous tissue compared to benign prostatic hyperplasia (BPH). Third, DNA level and arrangement might have changed, since DNA is perceived as one of the important sources of SHG in the nucleus (Huang and Zhuang, 2013; Zheng-Fei et al., 2010). Kidney tissue was imaged by non-linear multimodal optical microscopy (i.e. combination of coherent anti-Stokes Raman scattering, TPEF, and SHG) for differentiating normal kidney tissue, tumor and necrosis (Galli et al., 2014).

For Pancreatic cancer Hu et al. (2012) showed the density of the collagen fibers increased, which resembles the intensive stromal fibrosis manifest in pancreatic cancer patients (Chu et al., 2007). Drifka et al. (2013) showed with SHG that there were detectable changes in collagen organization (Fig. 4) surrounding normal versus ductal adenocarcinoma.

6. Quantitative analysis of SHG images

From the time that collagen was first used as a target for SHG imaging (Fine and Hansen, 1971), researchers have tried to find quantitative parameters to help differentiate normal and diseased tissue. Although interesting features such as collagen density and alignment have been proposed by groups such as Provenzano et al., (2006, 2008), tools have not been readily available for automating density and alignment analysis of the collagen fibers in SHG images. Recently,

Fourier transform, co-occurrence matrix, and characteristic anisotropy have been proposed to monitor the alignment and density of the collagen (Burke et al., 2013; Malone et al., 2002; Nadiarnykh et al., 2010). Bredfeldt et al. (2014) implemented four algorithms for extraction of quantitative information from collagen fibers. They used Gaussian, SPIRAL-TV (Harmany et al., 2012), Tubeness (Sato et al., 1998), and curvelet-denoising (Candès et al., 2006; Starck et al., 2002) filters combined with a fiber tracking algorithm (Stein et al., 2008) to extract the number, length, and curvature of collagen fibers in SHG images of breast cancer tissue. They showed that the curvelet denoising filter accompanied by the FIRE algorithm (Stein et al., 2008), which when combined is called CT-FIRE, gives the best results compared to manual fiber extraction. Further, tools for SHG quantitation are needed not only to improve the direct measurement of collagen parameters but just as importantly to measure these in association with cell changes in the microenvironment. There is great interest in the tumor microenvironment and together advanced imaging and quantitation of cell and collagen-rich extracellular matrix interactions could reveal new information on the processes surrounding tumor invasion and progression.

7. Conclusion

Second-harmonic generation (SHG) microscopy has become a powerful modality for imaging fibrillar collagen in a diverse range of tissues. Because of its underlying physical origin, it is highly sensitive to the collagen fibril/fiber structure, and, importantly, to changes that occur in diseases such as cancer, fibrosis and connective tissue disorders. Although it has not been utilized yet as a clinical modality, SHG has shown its ability to reveal important biological information about extracellular matrix alterations that accompany cancer progression and metastasis. As a research tool it has great power in examining cell-matrix associations and can be

used to quantitatively examine a number of collagen attributes that may be affected by cell signaling or direction force interactions.

Figure 1. Overview of SHG photophysics, representative images, and instrumentation. A) The Jablonski diagram for non-resonant SHG. Typical laser and SHG wavelengths are 900 and 450 nm, respectively. The images are representative single optical sections (field size = 170 **μ** m) of the collagen fibers in normal human ovary (left) and malignant ovary (right), in which striking differences in collagen morphology are revealed by SHG. B) Schematic of a typical SHG microscope optimized for forward and backward detection. Polarization optics in the excitation and signal paths (omitted from the backward path for figure clarity) allow detailed structural analysis of collagen organization. The forward and backward detectors are identical, and the paths are calibrated for collection and detection efficiency. PMT=photomultiplier, GLP=Glan-Laser Polarizer, **λ** /2 and **λ** /4=half and quarter wave plates, respectively (Campagnola, 2011).

Figure 2. Illustration of the TACS stages 1-3 (A) with corresponding real examples of TACS-1, 2, and 3 (B-D) from the region within and surrounding a human invasive ductal carcinoma tumor. Fresh biopsy tissue was vibratome sectioned at 300 microns thick, in-situ hybridization stained for E-Cadherin, and imaged with 780 nm excitation light. TPEF captured the epithelium (red) and SHG captured the collagen (green) signals. In the TACS-1 example, a region of locally dense collagen surrounds a relatively normal looking duct (B). The TACS-2 example (C) shows straightened (taut) collagen fibers stretched around and constraining a duct which has been filled with epithelial cells. In the example of TACS-3 (D), we observe tumor cells, which have lost most of their E-Cadherin receptors, invading into a region of aligned collagen fibers. Scale bar = 50 microns.

Figure 3. Representative SHG and TPEF images from normal (a) and malignant (b) ovarian biopsies. The left panels are en face SHG images of single optical sections where the tissue thickness was ~100 microns; the center and right images are SHG and TPEF images respectively from H&E optical sections from the same tissue as used for the en face images. Scale bar = 25 microns (Nadiarnykh et al., 2010).

Figure 4. Top left: H&E image of a normal pancreatic ductal structure. Top right: Merged SHG (orange)/multiphoton-excited eosin florescence (green) image of corresponding tissue. Scale bar = 100 microns. Bottom left: H&E image of pancreatic ductal adenocarcinoma (grade 2).
Bottom right: Merged SHG (orange)/multiphoton-excited eosin florescence (green) image of corresponding tissue. Scale bar = 100 microns. Image courtesy of LOCI, UW-Madison.

References

Ajeti, V., Nadiarnykh, O., Ponik, S.M., Keely, P.J., Eliceiri, K.W., and Campagnola, P.J. (2011). Structural changes in mixed Col I/Col V collagen gels probed by SHG microscopy: implications for probing stromal alterations in human breast cancer. Biomed Opt Express *2*, 2307–2316.

Alowami, S., Troup, S., Al-Haddad, S., Kirkpatrick, I., and Watson, P.H. (2003). Mammographic density is related to stroma and stromal proteoglycan expression. Breast Cancer Res. *5*, R129–135.

Ambekar, R., Lau, T.-Y., Walsh, M., Bhargava, R., and Toussaint, K.C., Jr (2012). Quantifying collagen structure in breast biopsies using second-harmonic generation imaging. Biomed Opt Express *3*, 2021–2035.

Brower, V. (2010). Breast Density Gains Acceptance As Breast Cancer Risk Factor. JNCI J Natl Cancer Inst *102*, 374–375.

Burke, K., Tang, P., and Brown, E. (2013). Second harmonic generation reveals matrix alterations during breast tumor progression. J Biomed Opt *18*, 31106.

Campagnola, P. (2011). Second Harmonic Generation Imaging Microscopy: Applications to Diseases Diagnostics. Anal Chem *83*, 3224–3231.

Campagnola, P. j., and Dong, C.-Y. (2011). Second harmonic generation microscopy: principles and applications to disease diagnosis. Laser & Photonics Reviews *5*, 13–26.

Campagnola, P.J., and Loew, L.M. (2003). Second-harmonic imaging microscopy for visualizing biomolecular arrays in cells, tissues and organisms. Nat Biotech *21*, 1356–1360.

Campagnola, P.J., Wei, M.D., Lewis, A., and Loew, L.M. (1999). High-resolution nonlinear optical imaging of live cells by second harmonic generation. Biophys J *77*, 3341–3349.

Campagnola, P.J., Clark, H.A., Mohler, W.A., Lewis, A., and Loew, L.M. (2001). Second-harmonic imaging microscopy of living cells. J Biomed Opt *6*, 277–286.

Candès, E., Demanet, L., Donoho, D., and Ying, L. (2006). Fast Discrete Curvelet Transforms. Multiscale Modeling & Simulation *5*, 861–899.

Chen, J., Zhuo, S., Chen, G., Yan, J., Yang, H., Liu, N., Zheng, L., Jiang, X., and Xie, S. (2011). Establishing diagnostic features for identifying the mucosa and submucosa of normal and cancerous gastric tissues by multiphoton microscopy. Gastrointest. Endosc. *73*, 802–807.

Chen, S.-Y., Chen, S.-U., Wu, H.-Y., Lee, W.-J., Liao, Y.-H., and Sun, C.-K. (2010). In Vivo Virtual Biopsy of Human Skin by Using Noninvasive Higher Harmonic Generation Microscopy. IEEE Journal of Selected Topics in Quantum Electronics *16*, 478–492.

Chen, X., Nadiarynkh, O., Plotnikov, S., and Campagnola, P.J. (2012). Second harmonic generation microscopy for quantitative analysis of collagen fibrillar structure. Nat. Protocols *7*, 654–669.

Chu, G.C., Kimmelman, A.C., Hezel, A.F., and DePinho, R.A. (2007). Stromal biology of pancreatic cancer. J. Cell. Biochem. *101*, 887–907.

Cicchi, R., Massi, D., Sestini, S., Carli, P., De Giorgi, V., Lotti, T., and Pavone, F.S. (2007). Multidimensional non-linear laser imaging of Basal Cell Carcinoma. Opt Express *15*, 10135–10148.

Cicchi, R., Kapsokalyvas, D., De Giorgi, V., Maio, V., Van Wiechen, A., Massi, D., Lotti, T., and Pavone, F.S. (2010). Scoring of collagen organization in healthy and diseased human dermis by multiphoton microscopy. J Biophotonics *3*, 34–43.

Conklin, M.W., Eickhoff, J.C., Riching, K.M., Pehlke, C.A., Eliceiri, K.W., Provenzano, P.P., Friedl, A., and Keely, P.J. (2011). Aligned collagen is a prognostic signature for survival in human breast carcinoma.

Am. J. Pathol. *178*, 1221–1232.

Cox, G., Kable, E., Jones, A., Fraser, I., Manconi, F., and Gorrell, M.D. (2003). 3-dimensional imaging of collagen using second harmonic generation. J. Struct. Biol. *141*, 53–62.

Dimitrow, E., Riemann, I., Ehlers, A., Koehler, M.J., Norgauer, J., Elsner, P., König, K., and Kaatz, M. (2009). Spectral fluorescence lifetime detection and selective melanin imaging by multiphoton laser tomography for melanoma diagnosis. Exp. Dermatol. *18*, 509–515.

Drifka, C.R., Eliceiri, K.W., Weber, S.M., and Kao, W.J. (2013). A bioengineered heterotypic stroma-cancer microenvironment model to study pancreatic ductal adenocarcinoma. Lab Chip *13*, 3965–3975.

Falzon, G., Pearson, S., and Murison, R. (2008). Analysis of collagen fibre shape changes in breast cancer. Phys. Med. Biol. *53*, 6641.

Fine, S., and Hansen, W.P. (1971). Optical Second Harmonic Generation in Biological Systems. Appl. Opt. *10*, 2350–2353.

Franken, P.A., Hill, A.E., Peters, C.W., and Weinreich, G. (1961). Generation of Optical Harmonics. Phys. Rev. Lett. *7*, 118–119.

Galli, R., Sablinskas, V., Dasevicius, D., Laurinavicius, A., Jankevicius, F., Koch, E., and Steiner, G. (2014). Non-linear optical microscopy of kidney tumours. J Biophotonics *7*, 23–27.

Han, M., Giese, G., and Bille, J. (2005). Second harmonic generation imaging of collagen fibrils in cornea and sclera. Opt. Express *13*, 5791–5797.

Harmany, Z.T., Marcia, R.F., and Willett, R.M. (2012). This is SPIRAL-TAP: Sparse Poisson Intensity Reconstruction ALgorithms—Theory and Practice. Trans. Img. Proc. *21*, 1084–1096.

Huang, Y., and Zhuang, Z. (2013). Second harmonic microscopic imaging and spectroscopic characterization in prostate pathological tissue. Scanning.

Kim, B.-M., Eichler, J., Reiser, K.M., Rubenchik, A.M., and Da Silva, L.B. (2000). Collagen structure and nonlinear susceptibility: Effects of heat, glycation, and enzymatic cleavage on second harmonic signal intensity. Lasers in Surgery and Medicine *27*, 329–335.

Kirkpatrick, N.D., Brewer, M.A., and Utzinger, U. (2007). Endogenous optical biomarkers of ovarian cancer evaluated with multiphoton microscopy. Cancer Epidemiol. Biomarkers Prev. *16*, 2048–2057.

Koehler, M.J., König, K., Elsner, P., Bückle, R., and Kaatz, M. (2006). In vivo assessment of human skin aging by multiphoton laser scanning tomography. Opt Lett *31*, 2879–2881.

Konig, K., and Riemann, I. (2003). High-resolution multiphoton tomography of human skin with subcellular spatial resolution and picosecond time resolution. J Biomed Opt *8*, 432–439.

König, K., Schenke-Layland, K., Riemann, I., and Stock, U.A. (2005). Multiphoton autofluorescence imaging of intratissue elastic fibers. Biomaterials *26*, 495–500.

Kwon, G.P., Schroeder, J.L., Amar, M.J., Remaley, A.T., and Balaban, R.S. (2008). Contribution of macromolecular structure to the retention of low-density lipoprotein at arterial branch points. Circulation

117, 2919–2927.

Lacomb, R., Nadiarnykh, O., and Campagnola, P.J. (2008). Quantitative second harmonic generation imaging of the diseased state osteogenesis imperfecta: experiment and simulation. Biophys. J. *94*, 4504–4514.

Le, T.T., Langohr, I.M., Locker, M.J., Sturek, M., and Cheng, J.-X. (2007). Label-free molecular imaging of atherosclerotic lesions using multimodal nonlinear optical microscopy. J Biomed Opt *12*, 054007.

Lilledahl, M.B., Haugen, O.A., de Lange Davies, C., and Svaasand, L.O. (2007). Characterization of vulnerable plaques by multiphoton microscopy. J Biomed Opt *12*, 044005.

Lin, S.-J., Wu, R.-, Jr, Tan, H.-Y., Lo, W., Lin, W.-C., Young, T.-H., Hsu, C.-J., Chen, J.-S., Jee, S.-H., and Dong, C.-Y. (2005). Evaluating cutaneous photoaging by use of multiphoton fluorescence and second-harmonic generation microscopy. Opt Lett *30*, 2275–2277.

Lin, S.-J., Jee, S.-H., Kuo, C.-J., Wu, R.-J., Lin, W.-C., Chen, J.-S., Liao, Y.-H., Hsu, C.-J., Tsai, T.-F., Chen, Y.-F., et al. (2006). Discrimination of basal cell carcinoma from normal dermal stroma by quantitative multiphoton imaging. Opt Lett *31*, 2756–2758.

Lo, W., Teng, S.-W., Tan, H.-Y., Kim, K.H., Chen, H.-C., Lee, H.-S., Chen, Y.-F., So, P.T.C., and Dong, C.-Y. (2006). Intact corneal stroma visualization of GFP mouse revealed by multiphoton imaging. Microscopy Research and Technique *69*, 973–975.

Malone, J.C., Hood, A.F., Conley, T., Nürnberger, J., Baldridge, L.A., Clendenon, J.L., Dunn, K.W., and Phillips, C.L. (2002). Three-dimensional imaging of human skin and mucosa by two-photon laser scanning microscopy. Journal of Cutaneous Pathology *29*, 453–458.

Masters, B., and So, P. (2001). Confocal microscopy and multi-photon excitation microscopy of human skin in vivo. Opt. Express *8*, 2–10.

Masters, B.R., So, P.T.C., and Gratton, E. (1998). Optical Biopsy of In Vivo Human Skin: Multi-photon Excitation Microscopy. Lasers Med Sci *13*, 196–203.

Menon, U., Gentry-Maharaj, A., Hallett, R., Ryan, A., Burnell, M., Sharma, A., Lewis, S., Davies, S., Philpott, S., Lopes, A., et al. (2009). Sensitivity and specificity of multimodal and ultrasound screening for ovarian cancer, and stage distribution of detected cancers: results of the prevalence screen of the UK Collaborative Trial of Ovarian Cancer Screening (UKCTOCS). Lancet Oncol. *10*, 327–340.

Nadiarnykh, O., LaComb, R.B., Brewer, M.A., and Campagnola, P.J. (2010). Alterations of the extracellular matrix in ovarian cancer studied by Second Harmonic Generation imaging microscopy. BMC Cancer *10*, 94.

Odetti, P., Pronzato, M.A., Noberasco, G., Cosso, L., Traverso, N., Cottalasso, D., and Marinari, U.M. (1994). Relationships between glycation and oxidation related fluorescences in rat collagen during aging. An in vivo and in vitro study. Lab. Invest. *70*, 61–67.

Paoli, J., Smedh, M., Wennberg, A.-M., and Ericson, M.B. (2008). Multiphoton laser scanning microscopy on non-melanoma skin cancer: morphologic features for future non-invasive diagnostics. J. Invest. Dermatol. *128*, 1248–1255.

Pavone, F.S., and Campagnola, P.J. (2013). Second Harmonic Generation Imaging (CRC Press).

Provenzano, P.P., Eliceiri, K.W., Campbell, J.M., Inman, D.R., White, J.G., and Keely, P.J. (2006). Collagen reorganization at the tumor-stromal interface facilitates local invasion. BMC Medicine *4*, 38.

Provenzano, P.P., Inman, D.R., Eliceiri, K.W., Knittel, J.G., Yan, L., Rueden, C.T., White, J.G., and Keely, P.J. (2008). Collagen density promotes mammary tumor initiation and progression. BMC Medicine *6*, 11.

Rubin, A.I., Chen, E.H., and Ratner, D. (2005). Basal-Cell Carcinoma. New England Journal of Medicine *353*, 2262–2269.

Sahai, E., Wyckoff, J., Philippar, U., Segall, J.E., Gertler, F., and Condeelis, J. (2005). Simultaneous imaging of GFP, CFP and collagen in tumors in vivo using multiphoton microscopy. BMC Biotechnology *5*, 14.

Sato, Y., Nakajima, S., Shiraga, N., Atsumi, H., Yoshida, S., Koller, T., Gerig, G., and Kikinis, R. (1998). Three-dimensional multi-scale line filter for segmentation and visualization of curvilinear structures in medical images. Medical Image Analysis *2*, 143–168.

Schenke-Layland, K., Xie, J., Angelis, E., Starcher, B., Wu, K., Riemann, I., MacLellan, W.R., and Hamm-Alvarez, S.F. (2008). Increased degradation of extracellular matrix structures of lacrimal glands implicated in the pathogenesis of Sjögren's syndrome. Matrix Biol. *27*, 53–66.

Shen, Y.R. (2003). The principles of nonlinear optics (Hoboken, N.J.: Wiley-Interscience).

So, P., Kim, H., and Kochevar, I. (1998). Two-Photon deep tissue ex vivo imaging of mouse dermal and subcutaneous structures. Opt Express *3*, 339–350.

Starck, J.-L., Candes, E.J., and Donoho, D.L. (2002). The curvelet transform for image denoising. IEEE Transactions on Image Processing *11*, 670–684.

Stein, A.M., Vader, D.A., Jawerth, L.M., Weitz, D.A., and Sander, L.M. (2008). An algorithm for extracting the network geometry of three-dimensional collagen gels. Journal of Microscopy *232*, 463–475.

Strupler, M., Pena, A.-M., Hernest, M., Tharaux, P.-L., Martin, J.-L., Beaurepaire, E., and Schanne-Klein, M.-C. (2007). Second harmonic imaging and scoring of collagen in fibrotic tissues. Opt Express *15*, 4054–4065.

Sun, W., Chang, S., Tai, D.C.S., Tan, N., Xiao, G., Tang, H., and Yu, H. (2008). Nonlinear optical microscopy: use of second harmonic generation and two-photon microscopy for automated quantitative liver fibrosis studies. J. Biomed. Opt *13*, 064010–064010–7.

Tanaka, S., Avigad, G., Brodsky, B., and Eikenberry, E.F. (1988). Glycation induces expansion of the molecular packing of collagen. J. Mol. Biol. *203*, 495–505.

Watson, J.M., Rice, P.F., Marion, S.L., Brewer, M.A., Davis, J.R., Rodriguez, J.J., Utzinger, U., Hoyer, P.B., and Barton, J.K. (2012). Analysis of second-harmonic-generation microscopy in a mouse model of ovarian carcinoma. J Biomed Opt *17*, 076002.

Zheng-Fei, Z., Han-Ping, L., Zhou-Yi, G., Shuang-Mu, Z., Bi-Ying, Y., and Xiao-Yuan, D. (2010). Second-harmonic generation as a DNA malignancy indicator of prostate glandular epithelial cells. Chinese Phys. B *19*, 049501.

Zhuo, S., Yan, J., Chen, G., Shi, H., Zhu, X., Lu, J., Chen, J., and Xie, S. (2012). Label-Free Imaging of Basement Membranes Differentiates Normal, Precancerous, and Cancerous Colonic Tissues by Second-Harmonic Generation Microscopy. PLoS ONE *7*, e38655.

Zipfel, W.R., Williams, R.M., Christie, R., Nikitin, A.Y., Hyman, B.T., and Webb, W.W. (2003). Live tissue intrinsic emission microscopy using multiphoton-excited native fluorescence and second harmonic generation. Proc. Natl. Acad. Sci. U.S.A. *100*, 7075–7080.

American Cancer society. (2011). What are the key statistics about breast cancer? Website:http://www.cancer.org/acs/groups/content/@epidemiologysurveilance/documents/document/acspc-029771.pdf

American Cancer society. (2013, Sep. 13). What are the key statistics about breast cancer? Website: http://www.cancer.org/cancer/breastcancer/detailedguide/breast-cancer-key-statistics

American Cancer society. (2013b, May. 22). What are the key statistics about lung cancer? http://www.cancer.org/cancer/lungcancer-non-smallcell/detailedguide/non-small-cell-lung-cancer-key-statistics

Ghanbari, L., Carter, R.E., Rynes, M.L., Dominguez, J., Chen, G., Naik, A., Hu, J., Sagar, M.A.K., Haltom, L., Mossazghi, N. and Gray, M.M., 2019. **Cortex-wide neural interfacing via transparent polymer skulls**. Nature communications, 10(1), p.1500.

Summary

There is a lack of tool that allows simultaneous monitoring and perturbation of neural activity in multiple cortical regions. A method allowing such would help us understand neural computation simultaneously in cortex. 'See-Shells'—a digitally designed; morphologically realistic, transparent polymer skulls was developed in this projects that allow long-term (>300 days) optical access to 45 mm^2 of the dorsal cerebral cortex in the mouse. The ability to perform mesoscopic imaging, as well as cellular and subcellular resolution two-photon imaging of neural structures up to 600 µm deep was demonstrated. See-Shells allow calcium imaging from multiple, non-contiguous regions across the cortex. Perforated See-Shells enable introducing penetrating neural probes to perturb or record neural activity simultaneously with whole cortex imaging. See-Shells are constructed using common desktop fabrication tools, providing a powerful tool for investigating brain structure and function.

nature COMMUNICATIONS

ARTICLE

https://doi.org/10.1038/s41467-019-09488-0 OPEN

Cortex-wide neural interfacing via transparent polymer skulls

Leila Ghanbari [1], Russell E. Carter[2], Mathew L. Rynes [3], Judith Dominguez[1], Gang Chen[2], Anant Naik[3], Jia Hu[3], Md Abdul Kader Sagar[4], Lenora Haltom[1], Nahom Mossazghi[2], Madelyn M. Gray[2], Sarah L. West[2], Kevin W. Eliceiri[4], Timothy J. Ebner [2] & Suhasa B. Kodandaramaiah[1,3]

Neural computations occurring simultaneously in multiple cerebral cortical regions are critical for mediating behaviors. Progress has been made in understanding how neural activity in specific cortical regions contributes to behavior. However, there is a lack of tools that allow simultaneous monitoring and perturbing neural activity from multiple cortical regions. We engineered 'See-Shells'—digitally designed, morphologically realistic, transparent polymer skulls that allow long-term (>300 days) optical access to 45 mm^2 of the dorsal cerebral cortex in the mouse. We demonstrate the ability to perform mesoscopic imaging, as well as cellular and subcellular resolution two-photon imaging of neural structures up to 600 μm deep. See-Shells allow calcium imaging from multiple, non-contiguous regions across the cortex. Perforated See-Shells enable introducing penetrating neural probes to perturb or record neural activity simultaneously with whole cortex imaging. See-Shells are constructed using common desktop fabrication tools, providing a powerful tool for investigating brain structure and function.

[1] Department of Mechanical Engineering, University of Minnesota, Twin Cities, MN, USA. [2] Department of Neuroscience, University of Minnesota, Twin Cities, MN, USA. [3] Department of Biomedical Engineering, University of Minnesota, Twin Cities, MN, USA. [4] Department of Biomedical Engineering, University of Wisconsin, Madison, WI, USA. Correspondence and requests for materials should be addressed to S.B.K. (email: suhasabk@umn.edu)

The mammalian cerebral cortex mediates learned and adaptive forms of sensory–motor behaviors and the evolutionary expansion of the cortex underlies many advanced cognitive capabilities in humans and non-human primates. Neuroscientists have taken advantage of the modular organization and segregation of the cortex into anatomically and functionally distinct regions and have made enormous progress understanding how computations performed in specific cortical regions engage in behavior. However, operation of the brain cannot be understood only by analysis of its components in isolation. Yet, the mechanisms by which neural activity is coordinated across the cerebral cortex to produce a unitary behavioral output are not well understood. Even simple sensory or motor tasks involve processing of information in multiple cortical areas. For example, deflection of a single whisker results in activation distributed across the sensorimotor cortices[1], locomotion modulates the neural responses in the primary visual cortex with cell-type specificity[2], and arousal exerts markedly different effects across the cerebral cortex, both spatially and temporally[3]. Further, such long-range information flow is dependent on the internal brain state as well as information learned from past experiences.

Understanding these large-scale computations requires the ability to monitor and perturb neural activity across large regions of the cortex. Until recently, the study of mesoscopic and macroscopic brain networks has been limited to functional magnetic resonance imaging (fMRI) and magnetoencephalography (MEG). However, fMRI and MEG are limited by their spatial and temporal resolution. Two-photon (2P) imaging has rapidly emerged as a tool of choice for in vivo imaging in rodent models due to improved deep imaging over one-photon (1P) imaging methods[4]. The development of optical sensing tools in recent years allows 2P-based cellular resolution monitoring of neural activities in local circuits. Genetically encoded Ca^{2+} indicators (such as GCaMP6) have enabled in vivo high-resolution monitoring of activities of hundreds to thousands of neurons[5]. The development of red-shifted variants of Ca^{2+} indicators and optogenetic tools open deep cortical regions for optical sensing and perturbation[6,7]. The advent of streamlined strategies to rapidly generate transgenic mice expressing optical reporters has been matched by the recent development of wide-field 2P imaging approaches[8–10].

Deploying these new optical tools and instrumentation for chronic imaging of large areas of the cerebral cortex requires replacing the overlying opaque skull with a transparent substrate. A widely used method to achieve chronic optical access to the brain surface involves implanting optical windows or cranial windows in which sections of the skull are excised and replaced with glass coverslips[11]. To image even larger regions, strategies for refractive index matching[12] and thinned skull preparations[13] have been used. These techniques, however, do not reliably allow cellular resolution imaging as image quality is dependent on the surgical preparation and is susceptible to bone regrowth over time. Recently, curved glass windows and associated surgical implantation methodology were introduced that allow chronic optical access to the whole dorsal cortex for cellular resolution imaging[14]. While each of these approaches has advanced the field, each has limitations. Ideally, wide-field optical imaging would be combined with modalities that allow simultaneous perturbation of neural activities to reveal the effect of various brain regions on global cortical activity. Further, combining wide-field optical imaging with simultaneous electrophysiological recordings from different brain regions will provide a better understanding of how global activity patterns modulate activity in local circuits[15]. Therefore, large optical windows with excellent optical properties, long-term functionality, design flexibility, easy fabrication and surgical implantation, and accommodation of other modalities are needed.

Here we introduce See-Shells, digitally designed and morphologically realistic transparent polymer skulls that can be chronically implanted for long durations (>300 days) and allow optical access to 45 mm^2 of the dorsal cerebral cortex. See-Shells can be customized to fit a variety of skull morphologies and allow for subcellular resolution structural imaging. Further, Ca^{2+} imaging can be performed at both mesoscale and cellular resolution from populations of neurons spread across millimeters of the cortex during awake, head-fixed behavior. See-Shells are easily adapted to include perforations for penetrating stimulation or recording probes. We also demonstrate the ability to perform wide-field Ca^{2+} imaging simultaneously with intracortical microstimulation and extracellular recordings. See-Shells can be inexpensively fabricated using desktop prototyping tools and can be implanted using methodologies adapted from standard cranial window implantation procedures.

Results

Device design and fabrication. The overall design of the See-Shells is shown in Fig. 1a. A motorized stereotaxic instrument was used to profile the skull surface covering the dorsal cortex of an 8-week-old C57BL/6 mouse at 85 points (see Methods). These 85 coordinates provided a point cloud representation of the skull surface used to interpolate a three-dimensional (3D) surface that accurately mimicked the skull morphology (Supplementary Figs. 1 and 2). Previous cranial morphometry studies of commonly used inbred laboratory mouse strains have shown that intra-species variations in cranial bone shape and size are minimal[16]. Further, postnatal size and shape of the skull are established within the first 3 weeks and change minimally after reaching adulthood[17]. Thus the interpolated surface from a single mouse skull served as a template to digitally design generalized transparent skulls (See-Shells) using computer-aided design (CAD) software. The frame was 3D-printed out of polymethylmethacrylate (PMMA) onto which a thin, flexible and transparent polyethylene terephthalate (PET) film was bonded (Fig. 1a and Supplementary Fig. 3). The 3D-printed frame also incorporated screw holes for fastening a custom-designed titanium head-plate for head-fixing the animal during experiments.

PET was chosen for the transparent element as this polymer has excellent optical properties[18] and is biocompatible[19]. The optical properties of the PET film were compared to the current gold standard, 170 µm thick glass coverslips (#1.5) used for a variety of microscopic imaging experiments. Sub-diffraction limit 200 nm fluorescent beads were imaged using a high magnification (×40) objective through glass coverslip and PET film to construct the lateral and axial point spread functions (PSFs, Fig. 1b, c). For beads imaged through PET, the full width at half maximum (FWHM) of the lateral PSF (Fig. 1b) was 425 ± 26.2 nm (mean ± standard deviation, $n = 15$) and was 409.3 ± 13.7 nm ($n = 5$) for beads imaged through glass coverslip. No significant difference was observed between PET and coverslip glass (Fig. 1d top, $p = 0.35$, Welch's t-test). For beads imaged through PET, the FWHM for the axial PSF (Fig. 1c) was 2.88 ± 0.08 µm ($n = 15$) and was 3.01 ± 0.10 µm ($n = 5$) for beads imaged through glass coverslip. Again, no significant difference was observed (Fig. 1d bottom, $p = 0.34$, Welch's t-test). Additional experiments characterized the light transmittance of three PET samples using a widely tunable laser at common wavelengths used for 2P imaging. All three PET samples yielded light transmittance of >90% (Supplementary Table 1). On average, across all wavelengths, light transmittance was 91.17 ± 0.94, 90.85 ± 1.1 and 91.71 ± 0.78% in the three samples tested, compared to 92.79 ± 0.82% in a standard glass coverslip.

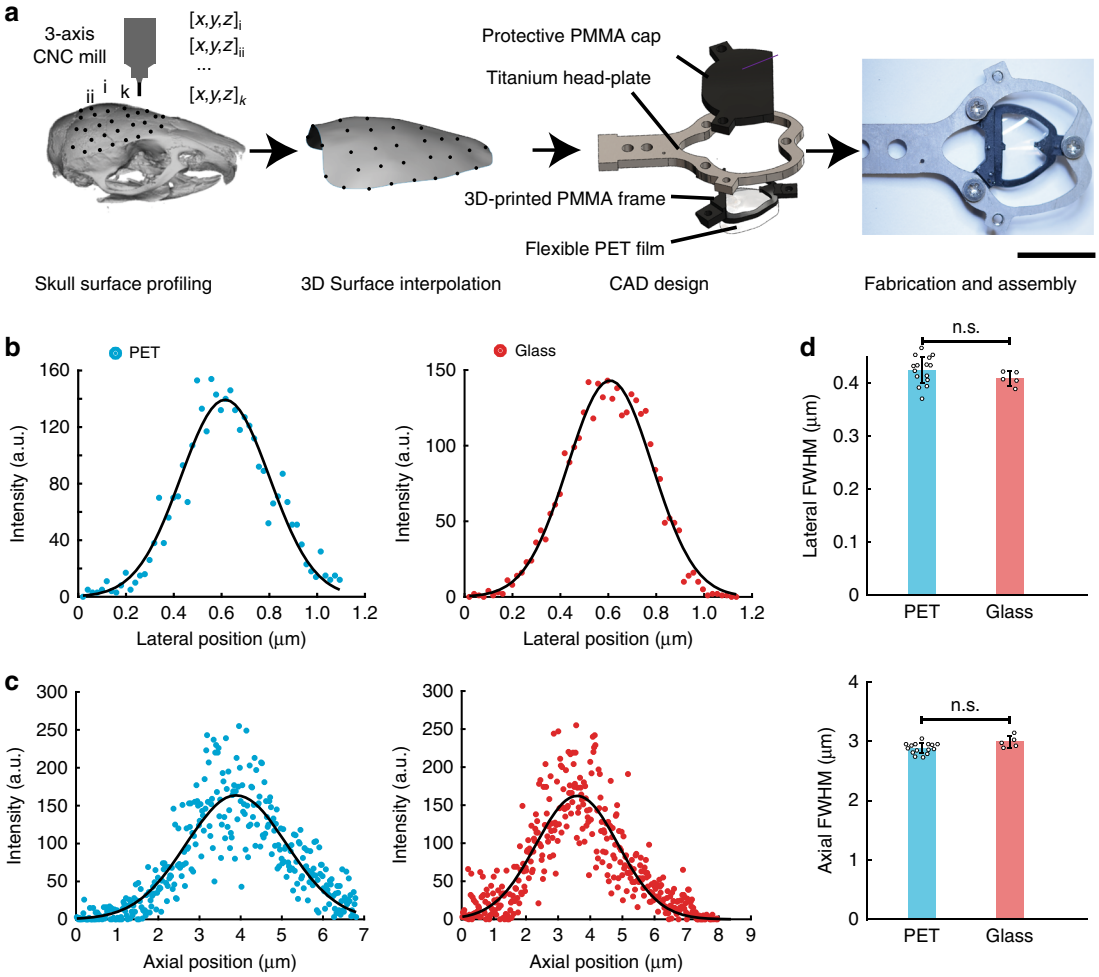

Fig. 1 Digitally generating See-Shells. **a** The dorsal surface of the mouse skull is profiled using a computer numerical controlled mill integrated into the stereotaxic instrument. This skull surface profile is used to interpolate a three-dimensional (3D) surface. The 3D surface is used as a template to design morphologically conformant transparent implants (See-Shells), consisting of a 3D-printed polymethylmethacrylate (PMMA) frame, onto which a thin, optically clear and flexible polyethylene terephthalate (PET) film is bonded. A titanium head-plate fastened to the frame provides mechanical support for head-fixation and a 3D-printed cap protects the implant and underlying brain tissue. Photograph of a fully fabricated and assembled See-Shell is illustrated on the right. Scale bar indicates 1 cm. **b** Lateral point spread functions (PSFs) of 200 nm yellow green (YG) fluorescent beads imaged with a ×40 (1.15 NA) objective through the PET film (left) and glass coverslip (right). Black curved line indicates Gaussian fit to the intensity measurements. **c** Axial PSFs of 200 nm YG fluorescent beads imaged with the same objective as in **b**, through the PET film (left) and glass coverslip (right). Black curved line indicates Gaussian fit to the intensity measurements. **d** Bar plots overlaid with the dot plots of lateral (top) and axial (bottom) full width at half maximum (FWHM) of the PSF measured through the PET film and #1.5 glass coverslip ($n = 15$ measurements in each of three PET films, and $n = 5$ measurements in glass coverslip). a.u. arbitrary unit, n.s. not significant. Error bars indicate s.d.

Multi-photon and time-correlated single-photon counting (TCSPC) based fluorescence-lifetime imaging microscopy (FLIM) of fluorescent yellow-green (YG) beads was performed to assess whether the PET film introduces changes in light intensity or fluorescence lifetime, respectively. While the present application for See-Shells is fluorescence intensity measurements, FLIM has an additional utility due its sensitivity to changes in the tissue microenvironment and sample conditions without being affected by changes in fluorophore concentration. Concerning light intensity, 2P imaging of YG beads through the PET film required 1–2% higher gain settings on the photomultiplier tube (PMT) compared to glass coverslips. This was expected, as PET film has a slightly lower light transmission efficiency. Given that the imaging was performed well within the PMT specifications, the reduction in light transmission can be easily overcome by increased laser power or PMT gain settings or a combination of both. Next FLIM imaging was performed using the same 2P instrument. Mean fluorescence lifetime of three PET film samples were 2.13 ± 0.01, 2.16 ± 0.07, and 2.15 ± 0.02 ns ($n = 3$ measurements in each substrate), comparable to the mean fluorescence ifetime of #1.5 glass coverslips (2.15 ± 0.01 ns, $n = 3$ measurements, Supplementary Fig. 4). The mean lifetimes are within the resolution limit of this 2P-based FLIM system. Therefore, PET has negligible effects on both 2P and FLIM imaging.

Chronic implantation of See-Shells. See-Shells were chronically implanted on wild-type C57BL/6 ($n = 9$), Thy1-GCaMP6f ($n = 31$), Thy1-YFP mice ($n = 3$), and Thy1-GFPm mice ($n = 3$) after a craniotomy was performed to remove the skull over the dorsal cortex (Fig. 2a, see Methods). The median duration of the implantation was 92 days, with durations ranging from 7 to 337 days. Of these, some procedures failed because the dental cement used to seal the implants (see Methods) had not sufficiently adhered to the skull. These experiments were terminated within 10 days of surgery. Thus the overall surgery success rate was 93.5% (3 surgeons, $n = 43/46$ mice). A subset of the mice was

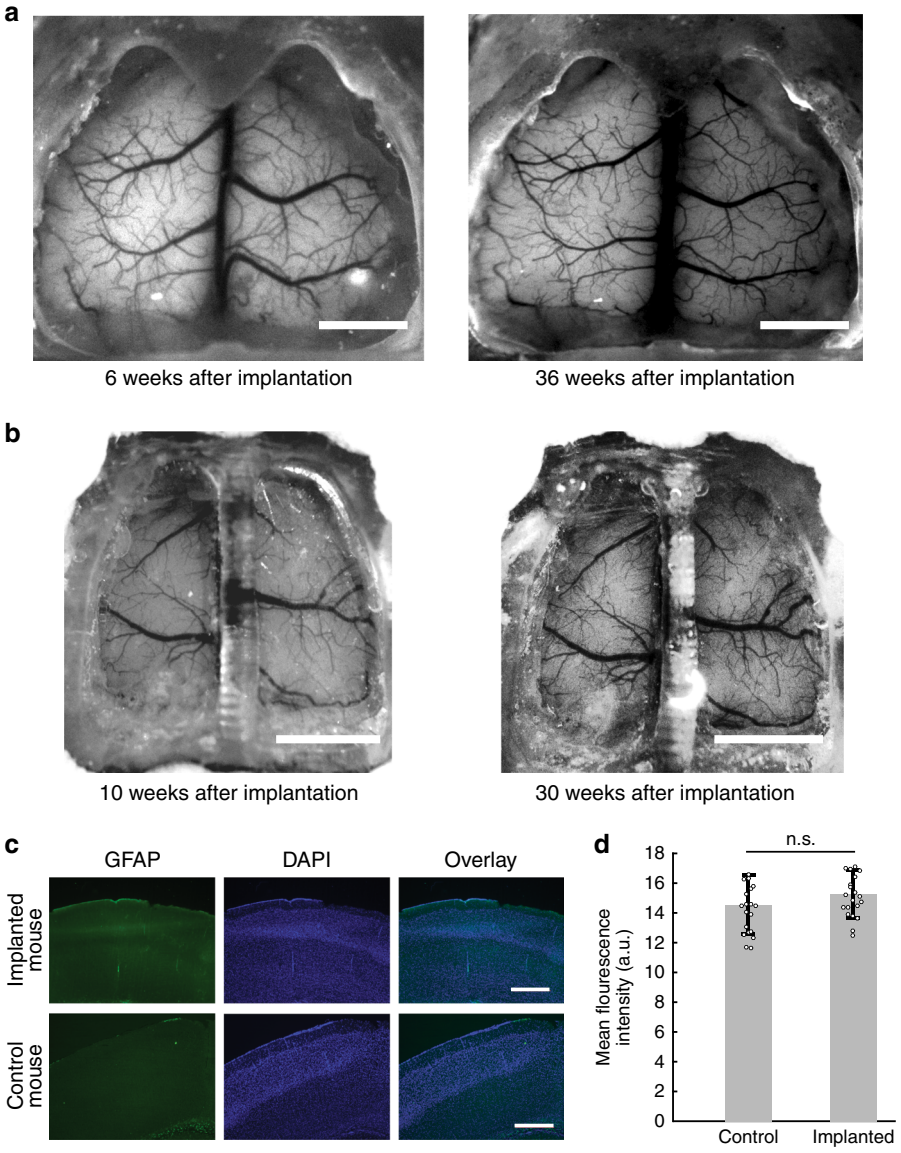

Fig. 2 Chronic implantation of See-Shells. **a** Photographs of a Thy1-GCaMP6f mouse 6 and 36 weeks after implantation with See-Shells. Scale bars indicate 2 mm. **b** The design can be modified to fit different skull morphologies. Photographs of a *tg/tg* mouse 10 and 30 weeks after implantation. Scale bar indicates 2 mm. **c** Immunohistology analysis of mice chronically implanted with See-Shells for 5 weeks compared to age-matched non-surgical control mice at ~2.0 mm posterior to bregma and 1.5 mm lateral to the midline. Coronal slices were immunolabeled with anti-glial fibrillary acidic protein (anti-GFAP) and DAPI. No activated astrocytes were observed in any of the mice assessed. Scale bar indicates 500 µm. **d** Bar plots overlaid with the dot plots of mean GFAP fluorescence measured in 21 regions of interest (ROIs) in See-Shell implanted and non-surgical control mice. Error bars indicate s.d.

observed under a high magnification (×6) stereo-zoom microscope after implantation to assess implant opacity or bone regrowth. In 75% of the mice ($n = 18/24$), no opacity of the windows or bone regrowth was observed in any part of the field of view (FOV). In 3 mice, significant opacity (10–30% of the FOV) was observed within 60 days. In 3 mice, opacity blocking optical access to <10% of the FOV along the midline suture was observed after >100 days of implantation, with 48 weeks being the longest duration assessed.

As Thy1-GCaMP6f and Thy1-YFP mice are derived from C57BL/6 lines, implants based on the surface profile from the C57BL/6 mouse readily fit these transgenic mice. The digital design methodology used to generate the See-Shells allows easy modifications to fit skull morphologies different from commonly used wild-type mouse strains. As an example, See-Shells were custom designed for the tottering (*tg/tg*) mouse, a strain that has a mutation in the *Cacna1a* gene[20] and has a narrower skull than C57BL/6 mice of the same age (Supplementary Fig. 2). Similar to chronic implantations on C57BL/6 and derivative mouse strains, the modified See-Shells on *tg/tg* mice ($n = 5$) remain optically clear for up to 30 weeks (Fig. 2b).

In a subset of mice ($n = 3$), the inflammatory effect of chronic implantation was assessed after 5 weeks of implantation by immunostaining for expression of glial fibrillary acidic protein (GFAP), a marker for chronic inflammation. No activated astrocytes were observed in the cortex of the implanted and control mice consistent with previous studies[21]. To assess whether there is any increased expression of GFAP, the fluorescent intensity was measured in multiple cortical areas using the methodology described previously[22]. GFAP fluorescence intensity in arbitrary units (a.u.), in the areas assessed, was 15.26 ± 1.64 a.u. in the implanted mice. In comparison, GFAP fluorescence intensity was 14.55 ± 1.99 a.u. in naive control mice ($n = 21$ measurements from 3 mice each,Student's *t*-test,

$p = 0.2971$, Fig. 2c, d). Thus the See-Shells can be implanted on mice for long durations of time and allow longitudinal imaging of the dorsal cortex.

Sub-cellular resolution structural imaging across the cortex. Chronically implanted cranial glass windows have been used for high-resolution imaging of neural structure in vivo over extended periods of time[11]. Several of these studies have revealed key cellular and structural mechanisms underlying experience-dependent plasticity[23–25]. Therefore, we assessed the structural imaging capability of See-Shells across the large FOV with spatial resolution and imaging depths comparable with glass cranial windows. See-Shells were implanted on Thy1-YFP mice ($n = 3$) that express the yellow fluorescent protein (YFP) in layer 2/3 and layer 5 pyramidal neurons of the cortex[26]. Figure 3a, top left shows a mesoscale image obtained using a wide-field epi-fluorescence microscope at ×1 magnification. Multiple locations distributed across the cortex of the same mouse were then imaged at high-resolution with a 2P microscope. Whole cortical columns ($360 \times 360\ \mu m^2$) were reconstructed up to depths of 600 µm (Fig. 3a, inset #1). Capturing multiple z-stacks from adjacent tiles allowed reconstruction of large contiguous volumes of tissue spread across millimeters of the cortex (Fig. 3a, inset #2 and #3). At an optical zoom of ×4.4 using a ×25 objective, individual neurons and their processes were imaged at depths of ~300 µm from the pial surface (Fig. 3a, inset #4). At a zoom of ×7, finer sub-cellular structures including dendrites and dendritic spines were clearly visible (Fig. 3a, inset #5 and #6). In Thy1-GFPm mice[26], the same dendrites and dendritic spines can be imaged across multiple days and imaged at multiple locations throughout

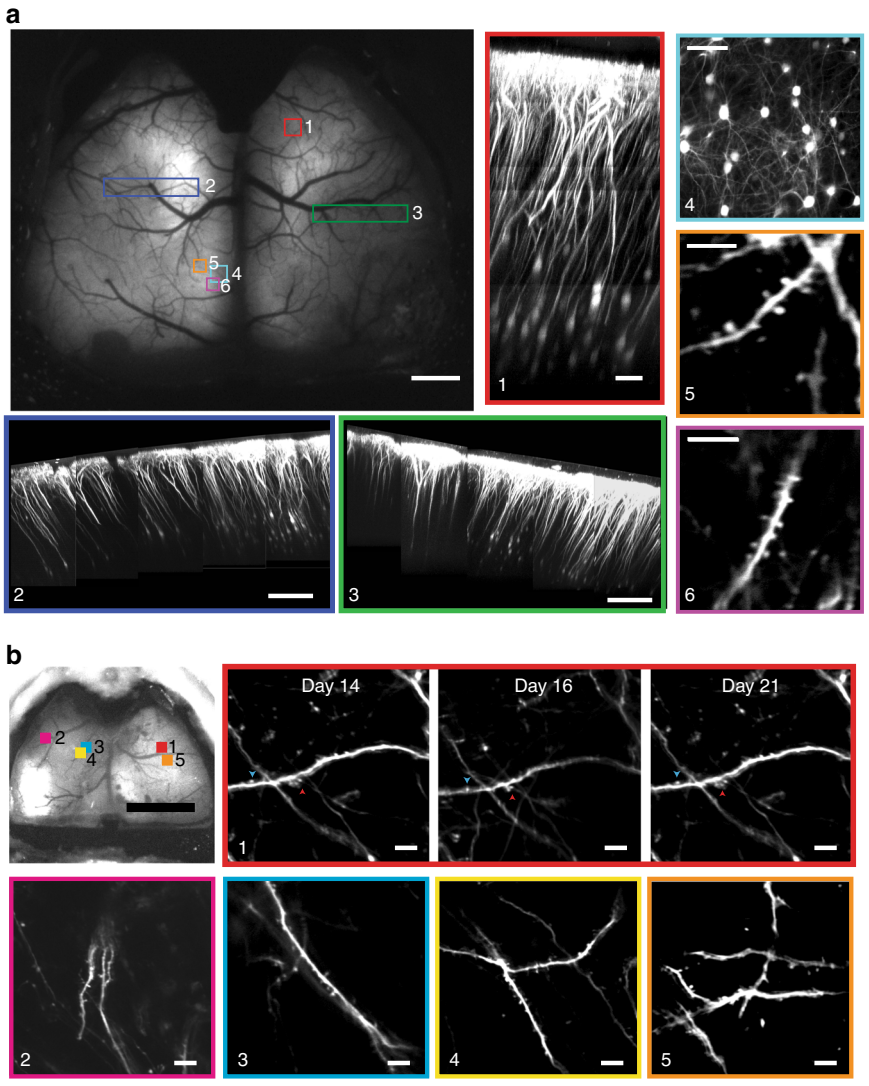

Fig. 3 See-Shells allow structural imaging from mesoscale to microscale. **a** Wide-field image of a Thy1-YFP mouse implanted with a See-Shell taken 2 weeks after implantation. Locations marked with colored blocks were targeted for two-photon (2P) imaging. Scale bar indicates 1 mm. Inset #1: Imaging of a whole cortical column at the location marked by red block in the wide-field image. Scale bar indicates 80 µm. Inset #2 and #3: Composite images of cortical columns imaged from large contiguous areas denoted by the blue and green blocks in the wide-field image. Scale bar indicates 200 µm. Inset #4: High-resolution image of layer 2/3 pyramidal neurons imaged from the cyan block denoted in the wide-field image. Scale bar indicates 80 µm. Inset #5 and #6: Dendrites with dendritic spines of layer 2/3 neurons imaged at ~245 µm depth from the orange and magenta blocks shown in the wide-field image. Scale bars indicate 10 µm. **b** Wide-field image of a Thy1-GFPm mouse implanted with a See-Shell obtained 2 weeks after implantation. Locations marked with colored blocks were targeted for 2P imaging. Scale bar indicates 2 mm. Inset #1: Longitudinal 2P structural imaging of dendritic structures within the red block outlined on the wide-field image on the left taken in multiple experiments over 1 week. Scale bar indicates 10 µm. Insets #2–#5: Multi-site 2P imaging of dendritic structures at locations indicated by blocks 2–5 in the wide-field image. Scale bar indicates 10 µm

the cerebral cortex (Fig. 3b). Thus See-Shells allow the study of fine sub-cellular structures of neurons across the cerebral cortex.

Ca^{2+} imaging at multiple spatial scales across the cortex. To assess the capabilities to monitor cortical neural activity, See-Shells were implanted on Thy1-GCaMP6f mice that express the Ca^{2+} indicator GCaMP6f in layer 2/3 and layer 5 pyramidal neurons[27]. Wide-field imaging using a standard epi-fluorescence microscope captured mesoscale activity across the entire FOV (Supplementary Fig. 5, Supplementary Movie 1). Robust activation of the entire cortex was observed during locomotion, with spontaneous activity observed even at rest. In the mouse shown in Fig. 4a, four random areas highlighted by the colored blocks were targeted for 2P imaging. At each area, *z*-stacks of 365 × 365 μm^2 were captured when the mouse was fully awake and head-fixed on a custom-built disk treadmill (Fig. 4b). Two-dimensional (2D) maximum intensity projections of the *z*-stacks revealed macroscopic anatomical features such as blood vessels that could be matched with wide-field images to determine the imaging locations post hoc. In each tile, time series of Ca^{2+} activity were acquired in planes at 200–300 μm from the pial surface. Individual cells were readily visualized in the average intensity projections of the time series (Fig. 4c). Spontaneous Ca^{2+} activity traces from a small subset of the detected neurons in each tile during awake head-fixation are shown in Fig. 4d.

To evaluate See-Shells' capability to monitor Ca^{2+} signals in the same neurons over time, multiple imaging sessions were performed in the same FOV over a month starting 44 weeks after implantation on a Thy1-GCaMP6f mouse (Fig. 4e). Average intensity projections from a set of high-resolution images qualitatively indicated that the same neurons could be identified over time. Robust Ca^{2+} signals were obtained with the peak $\Delta F/F$ of randomly selected individual neurons ranging between 128.7 to 240.4% across all imaging sessions. Linear regression analysis of peak $\Delta F/F$ measured over imaging sessions indicated that Ca^{2+} signals were diminished slightly across duration evaluated ($R^2 = 0.378$, average slope of trend-line = −1.23% per day, $n = 5$ neurons, Supplementary Fig. 6). Further, 2P imaging was performed at multiple sites distributed across the cortex in a late-stage implanted mouse (Day 335, Supplementary Fig. 7). Similar to the data shown in Fig. 4, robust Ca^{2+} signals were acquired from each region with peak $\Delta F/F$ of individual neurons ranging between 61.51 to 191.84%.

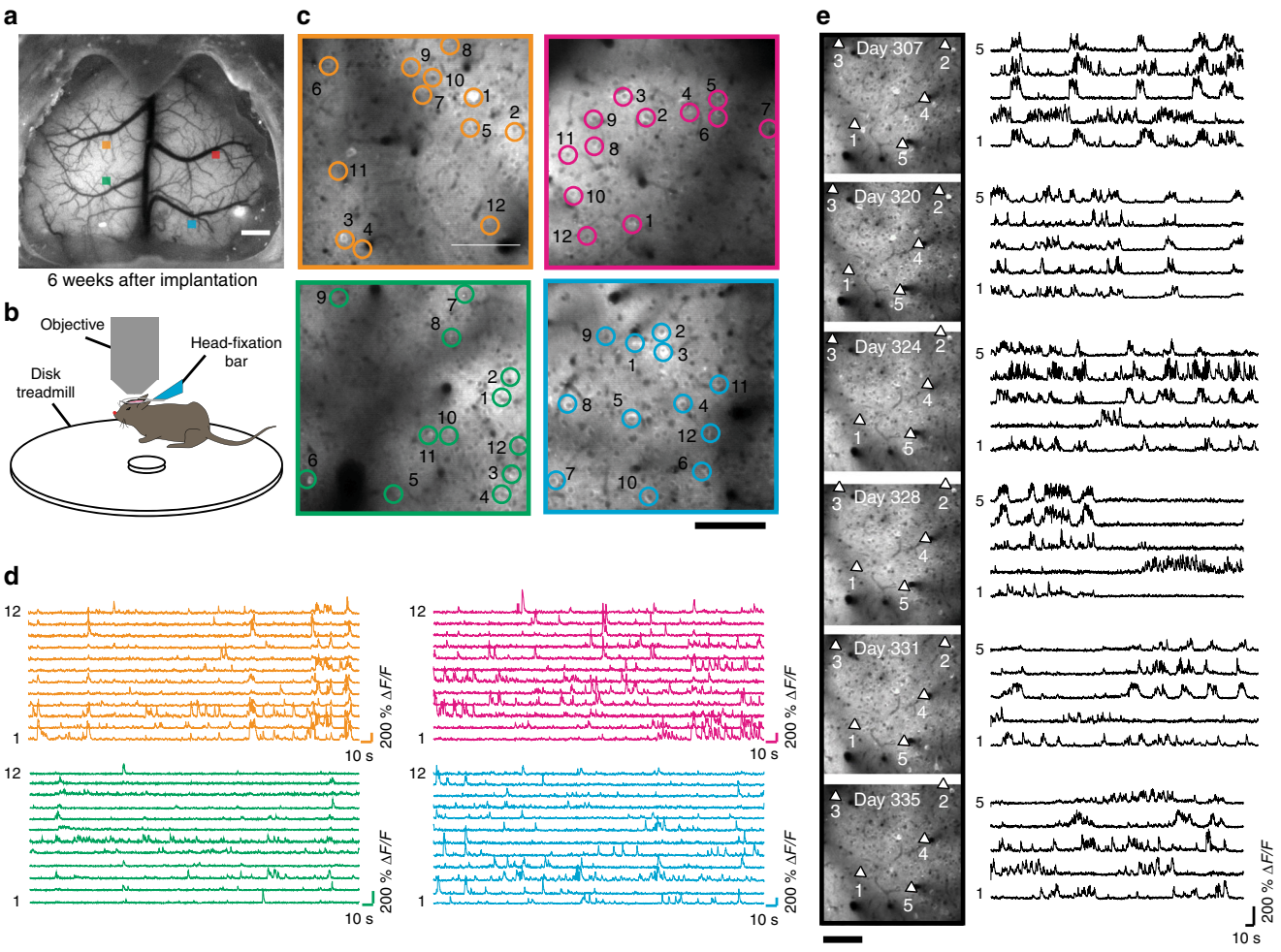

Fig. 4 Monitoring Ca^{2+} activities in awake head-fixed mice. **a** Wide-field image of a Thy1-GCaMP6f mouse implanted with a See-Shell taken 6 weeks after implantation. Four locations indicated by the colored blocks were imaged using a 2P microscope. Scale bar indicates 1 mm. **b** Schematic of the mouse on the custom-designed disk treadmill used for 2P imaging. **c** Average intensity images calculated from 5-min time series acquired 200–300 μm deep from pial surface. Scale bar indicates 100 μm. **d** Color-coded time series of Ca^{2+} activities of neurons identified and annotated by open circles in the respective average intensity images in **c**. **e** Time lapse Ca^{2+} imaging: Left: Average intensity images calculated from 5 min time series acquired from the same field of view in a See-Shell-implanted Thy1-GCaMP6f mouse in six separate imaging sessions. Activities of individual neurons, indicated by arrows, are shown in the right. Scale bar indicates 100 μm

Further, Ca^{2+} activities were tracked in Thy1-GCaMP6f mice using 2P imaging in the hindlimb area of the primary motor cortex along with high-speed video monitoring. Mice implanted with See-Shells readily performed a variety of behaviors including walking and grooming during head-fixation. In the recording highlighted in Supplementary Movie 2, increased Ca^{2+} activity occurred during walking as tracked by movements of the hindlimb, forelimb, and disk treadmill but the modulation was absent during grooming, indicated by forelimb movement (Supplementary Fig. 8).

Thus See-Shells allow multi-scale imaging over long durations in the mouse cerebral cortex during a wide range of head-fixed behaviors. The capability to image in the same animal structurally at subcellular resolution as well as Ca^{2+} activity at the cell and mesoscale level will provide new insights between factors, such as physical structure and neural state.

Multi-modal and bidirectional neural interfacing. Another advantage of the See-Shell design and PET film is incorporation of additional modalities to record and/or perturb neural structures. For example, combining wide-field Ca^{2+} activity monitoring while simultaneously recording neural firing from localized circuits will enable determination of how global cortical activity relates to local circuit activity[15]. See-Shells were engineered with a ~1.5 mm perforation over the primary somatosensory cortex to introduce a 32-channel, silicon-based recording probe (Fig. 5a). The perforations were made prior to implantation and sealed with quick setting silicone sealant that could be removed during experiments ($n = 3$ Thy1-GCaMP6f, Fig. 5b).

Mesoscale Ca^{2+} imaging was performed simultaneously with the single cell recordings in left primary somatosensory cortex and high-speed behavioral recording during awake head-fixation (Fig. 5c). Ca^{2+} activity from six regions of interest (ROIs) in the bilateral motor (M1), somatosensory (S1), and visual cortices (V1) show robust co-activation of multiple homotopic regions. Single-cell electrophysiology recordings revealed a subset of neurons with increased firing rates correlated with mesoscale Ca^{2+} activity in the ipsilateral primary somatosensory cortex (I-S1) (Fig. 5c, d). To assess the relation between the Ca^{2+} activity and activity of individual neurons, the Ca^{2+} signal in I-S1 was cross-correlated with the spike firing rate of each recorded neuron and compared

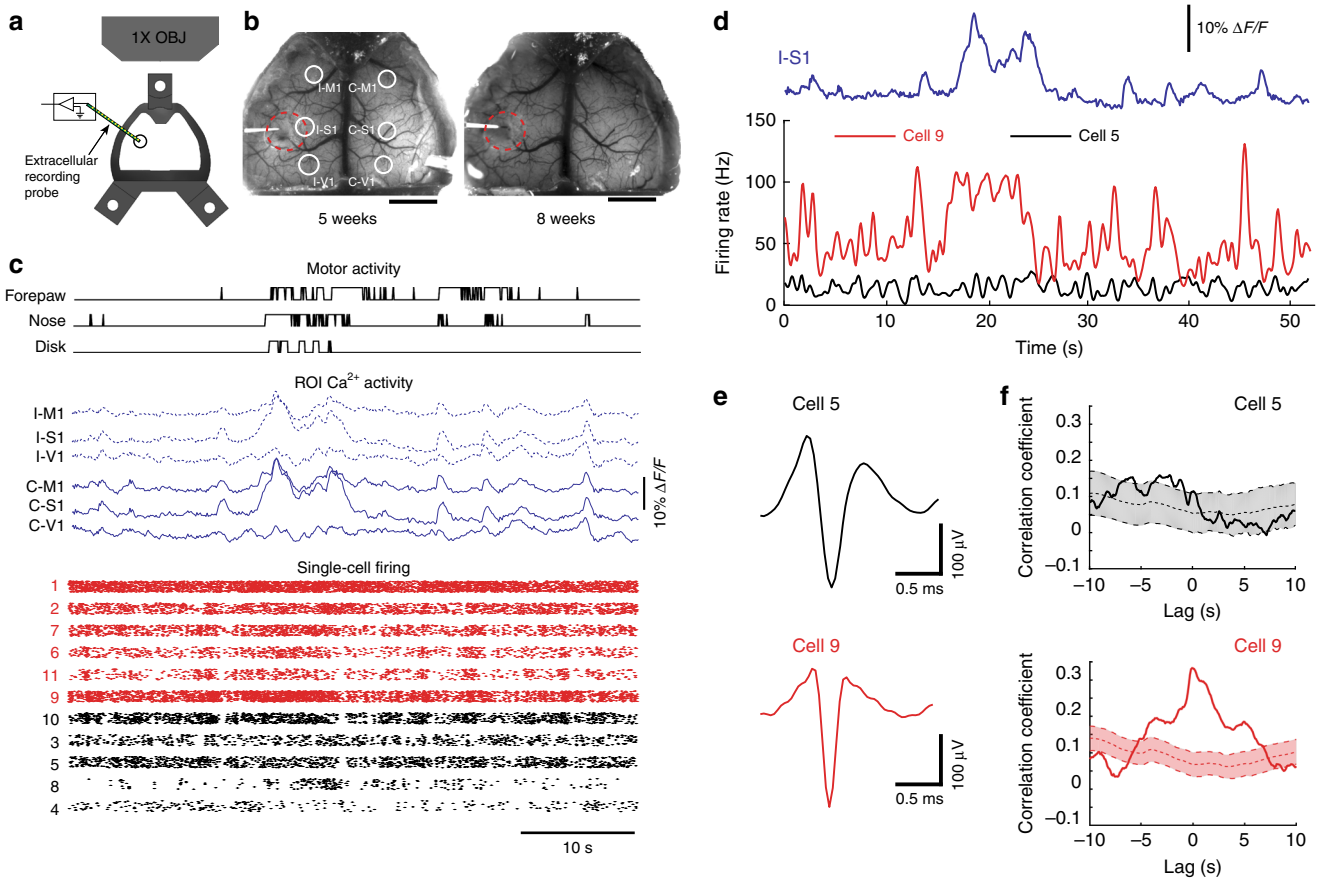

Fig. 5 Simultaneous extracellular recordings with wide-field Ca^{2+} imaging and behavioral tracking. **a** Schematic of implanted See-Shells with perforation over the primary somatosensory cortex allowing insertion of a multi-channel silicon-based neural probe. **b** Photographs of a Thy1-GCaMP6f mouse implanted with a perforated See-Shell taken during two experimental sessions. Red dashed lines indicate the outline of perforation. White circles indicate regions of interest (ROIs) analyzed for extracting Ca^{2+} traces. I-M1 ipsilateral primary motor cortex, I-S1 ipsilateral primary somatosensory cortex, I-V1 ipsilateral primary visual cortex, C-M1 contralateral primary motor cortex, C-S1 contralateral primary somatosensory cortex, C-V1 contralateral primary visual cortex. Scale bars indicate 2 mm. **c** Simultaneously recorded disk, nose, and forelimb movements, aligned with Ca^{2+} activity traces in the ROIs indicated in **b**, and single unit spike raster plots recorded from the multi-channel silicon-based neural probe. Red raster plots indicate neurons with spike firing rates correlated with Ca^{2+} activity in I-S1. Individual points from each cell were slightly shifted in a randomized fashion in the *y* axis for ease of visualization. **d** Spike firing rates of two representative cells, with one that was correlated with Ca^{2+} activity in I-S1 (cell 9) and one that did not show correlation (cell 5). **e** Average action potential waveforms of the two cells shown in **d**. **f** Cross-correlation of firing rates of representative cells in **d** and Ca^{2+} activity in I-S1 with 95% confidence interval of cross-correlations with 1000 bootstrapped shuffled trials of the firing rate to determine significance

to the 1000 randomly shuffled spike firing rate of each cell (See Methods)[28]. As shown for two representative cells, one has spike firing rate correlated with the Ca^{2+} signals in I-S1 (cell 9) and one that did not (cell 5, Fig. 5e, f). At zero lag, 6 of the 11 neurons had significant correlation with the Ca^{2+} signals in I-S1 (correlation coefficient > mean + 1.98 s.d. of the shuffled traces). These experiments suggest that activities of individual neurons are diverse in terms of their correlation with mesoscale activity. See-Shells thus allow us to observe cortical activity at multiple scales and understand their significance to behavior.

Finally, we demonstrate that perforations in See-Shells introduced after chronic implantation can be used to perturb neural circuits with intracortical microstimulation, which has been widely used to assess cortical connectivity and function including effects on downstream targets. In a subset of Thy1-GCaMP6f mice ($n = 3$, Fig. 6a), the PET film was carefully punctured with a sterile syringe needle to introduce microstimulation electrodes. Stimulation resulted in robust activation of both hemispheres in the awake and anesthetized states (Fig. 6b, c) with significantly prolonged responses in the anesthetized mouse compared to responses in the mouse when awake. Traces shown in Fig. 6c represent the average trace of ≥10 trials for the awake state, and ≥4 trials for anesthetized state in each mouse (Mouse #1: 10 awake, 5 anesthetized, Mouse #2: 15 awake, 6 anesthetized, and Mouse #3: 11 awake, 4 anesthetized). The FWHM of the post-stimulus Ca^{2+} fluorescence response was significantly longer in all ROIs examined during isoflurane anesthesia (Fig. 6d, Student's *t*-test, $p < 0.001$). These results with See-Shells in the awake animal extend previous flavoprotein imaging observations in anesthetized mice showing that microstimulation of the primary motor cortex co-activates homotopic regions via the corpus callosum[29]. Therefore, See-Shells can be used to study the effects of perturbing localized regions and suggest that the arousal state alters cortical dynamics. While the present study employed intracortical microstimulation, the methodology could be easily compatible with optogenetic or chemical stimulation of cortical or sub-cortical brain regions.

Discussion

We developed See-Shells, transparent, morphologically conformant polymer skulls that allow optical access to a large part of the dorsal cerebral cortex for high-resolution structural and functional imaging. These windows can be implanted for long periods and remain functional for over 300 days. In line with estimates from recent studies using curved glass windows[14], See-Shells provide optical access to ~1 million neurons from the cortical surface. In addition, optical imaging with See-Shells can be combined with other modalities. Perforation of the PET film allows access to the brain underneath the implant and here we demonstrated wide-field Ca^{2+} imaging with simultaneous intracortical microstimulation and electrophysiological recordings.

The optical properties of PET compare favorably with glass coverslips when evaluated by 2P or FLIM imaging. The latter opens up the possibility for FLIM intra-vital brain imaging of auto-fluorescence using PET windows[30,31]. For example, the

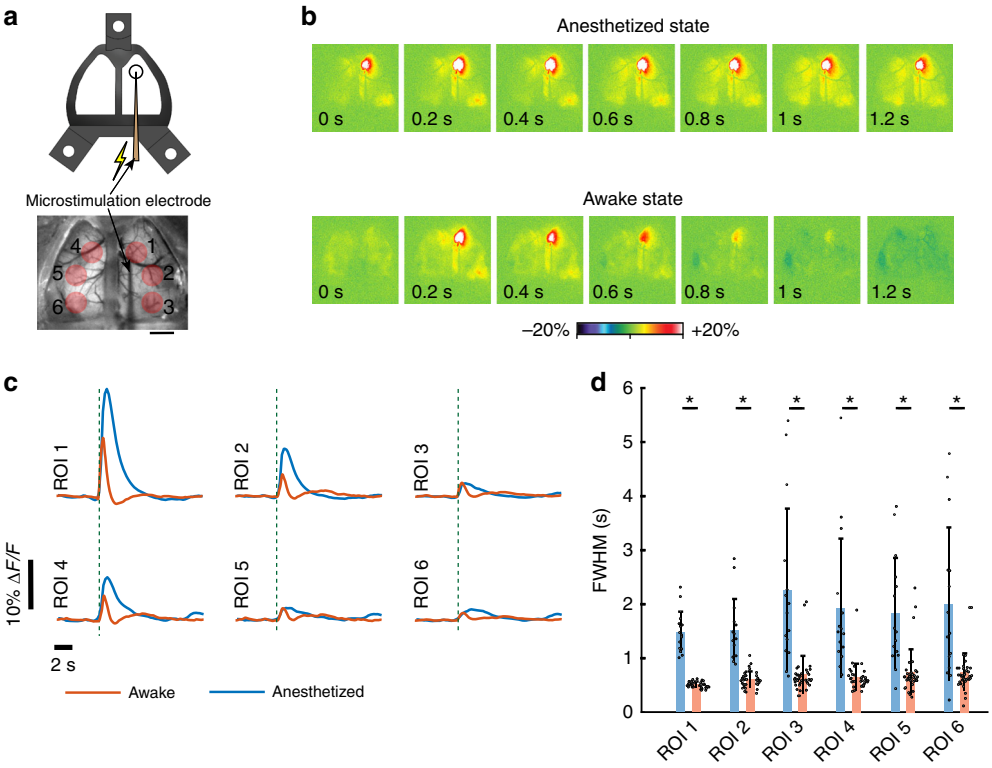

Fig. 6 Cortical microstimulation during wide-field Ca^{2+} imaging. **a** Top: Cartoon schematic of a microstimulation electrode inserted through a perforated See-Shell. Bottom: a wide-field image showing microstimulation electrode inserted at the primary motor cortex. Red circles indicate regions of interest (ROIs) analyzed. Scale bar indicates 2 mm. **b** Pseudocolor plots of normalized change in fluorescent intensity in response to primary motor cortex microstimulation. Top: under isoflurane anesthesia, bottom: awake. Post-stimulation time stamps are indicated at the bottom of each image. **c** Average normalized Ca^{2+} activity traces in response to microstimulation of primary motor cortex for different ROIs indicated in **a**. ROI 1: primary motor cortex and stimulation site; ROI 2: ipsilateral somatosensory cortex; ROI 3: ipsilateral visual cortex; ROI 4: contralateral motor cortex; ROI 5: contralateral somatosensory cortex; and ROI 6: contralateral visual cortex. Dashed lines indicate the time of stimulus. **d** Bar plots overlaid with the dot plots of full width at half maximum in the different ROIs under anesthetized and awake conditions. Error bars indicate s.d.; Student's *t*-test, *indicates $p < 0.001$

intrinsically fluorescent metabolites nicotinamide adenine dinucleotide hydrogen and flavin adenine dinucleotide are widely used in vivo to record label-free cellular activity based on their oxidation state[32–34]. Changes in the lifetime of both coenzymes are used to monitor the biological microenvironment[32], including in intra-vital studies[35]. Thus, while the current goal is to use PET to realize transparent skulls for cortex-wide imaging, the flexibility, optical clarity, and biocompatibility demonstrate the feasibility of engineering anatomically realistic windows for intra-vital imaging in a wide variety of organs, such as mammary gland[36] and lung[37].

See-Shells can be implanted using simple modifications to well-established chronic cranial window implantation procedures[38,39], with the major change being the removal of large sections of the skull above the dorsal cerebral cortex. In this study, we utilized a robot that uses surface profiling to guide a computer numerical controlled (CNC) mill to perform the craniotomy[40]. Automation enabled reliable removal of the bone without damage to the underlying dura and brain and also allowed precise positioning of the implant relative to bregma. We also performed manual craniotomies for See-Shells implantations on *tg/tg* mice, demonstrating that automation of the craniotomy is not a pre-requisite for successful implantation, although it could help investigators quickly adapt these tools for their research.

High-quality mesoscopic Ca^{2+} imaging in the awake animal has been performed in mice implanted with See-Shells for 48 weeks, the longest period tested to date. Chronic imaging over this duration provides the opportunity for very long-term studies of brain development, plasticity and learning, disease processes, and evaluation of new therapies. For developmental studies, the primary limitation will be skull growth in the postnatal period. Mouse skull sutures that fuse do so by ~45 days of age, and most cranial expansion is complete by 6 weeks[17,41]. However, the majority of skull growth is complete earlier (~2–3 weeks of age), suggesting that the windows could be implanted in younger animals.

Several aspects of the design and fabrication of the See-Shells are widely adoptable and highly flexible. See-Shells can be fabricated using desktop tools and are inexpensive (<$20 each). Once the individual components are fabricated (or procured from commercial fabrication services), the implant can be assembled in <15 min. Therefore, this is a tool that can be readily adopted by most laboratories. Although the cranial implants were developed for the dorsal cerebral cortex with its fairly regular convex surface, the design can be modified for a variety of skull morphologies. Future versions can be designed to cover not only the dorsal cerebral cortex but also other regions including the olfactory bulb, cerebellum, and more lateral cortical regions such as the auditory cortex.

See-Shells could also be engineered for optical interfacing with complex and mobile anatomical structures such as the spine. The 3D-printed frame can be modified to incorporate mounting features to precisely attach miniaturized microscopes[42] and wirelessly controlled devices for infusing pharmacological agents or performing optogenetic stimulations[43]. Recently, ultra-miniaturized lens-less fluorescence microscopes <1 mm in size have been developed[44]. Engineering See-Shells embedded with these miniaturized lens-less imaging systems offers the possibility of monitoring the activity of the whole cortex during freely moving behaviors.

The ability to simultaneously monitor local microcircuit activity using extracellular recordings combined with wide-field Ca^{2+} imaging offers the potential to integrate the contribution of local microcircuits to mesoscale activities. We show that both mesoscale and single unit activities correlated with motor activity. Additional information about the cortical state is likely represented in the complex spatio-temporal patterns of activity observed with mesoscale imaging. See-Shells would allow systematic multi-scale studies tying activity at microcircuits to large scale network activity. Using See-Shells to combine wide-field Ca^{2+} imaging with in vivo patch clamping methodologies to record from single[45] and multiple neurons[46] will help us to better understand how mesoscale network activity influences sub-threshold membrane potential dynamics in individual neurons.

We have used perforated See-Shells to perform intracortical microstimulation. In addition to stimulating electrodes, this methodology can be used to introduce probes for optogenetic or chemical perturbation of cortical and sub-cortical brain regions. These perturbation strategies will be particularly useful to study how activation or inhibition of localized brain regions or circuits affect global cerebral cortical activity. This includes both specific pathways such as the cerebello-thalamo-cortical[47,48] and basal ganglia-thalamo-cortical projections[49,50] or the more diffuse neuromodulatory projections such as noradrenergic inputs from the brain stem[51,52] or cholinergic inputs from the basal forebrain[53].

With their similar genetics, anatomy, physiology, and behavioral repertoire, non-human primates (NHPs) provide the closest animal model to humans for understanding both normal functions as well as disease[54–56]. Emerging genetic modification techniques, including CRISPR, make generating transgenic NHPs with broad expression of Ca^{2+} reporters a possibility[57]. Further, techniques for long-term 2P imaging in NHPs are also emerging[58]. The See-Shells methodology can be adapted to build customized implants derived from computed-tomographic (CT) scans of the skull, enabling imaging of neural activities across centimeters of the NHP cortex.

While the See-Shells allow sub-cellular resolution imaging across the cortex, imaging across the whole FOV simultaneously at high resolution is currently not possible. Recently developed wide-field 2P imaging systems[8–10] allow simultaneous imaging of nearly an entire hemisphere. Extending such optical systems to simultaneously image the whole dorsal cortex at cellular resolution would be very powerful. We have performed mesoscale imaging while simultaneously inserting neural probes for extracellular recordings and microstimulation. It is difficult to do such experiments with 2P microscopes, given the short working distance of high NA and high-magnification objectives. In the future, it may be possible to perform random access 2P imaging across the whole FOV using customized long working distance high-resolution objectives or by using optical relays between the PET surface and the objectives to allow more room for the introduction of recording probes[59]. Neural probes that are specifically designed to be compatible with 2P imaging could also be engineered, or flexible neural probes that can be reconfigured after implantation to provide unimpeded optical access could be used[60,61].

Methods

See-Shell design and fabrication. All of the animal studies were approved by and conducted in conformity with the Institutional Animal Care and Use Committee of the University of Minnesota. An adult C57BL/6 male mouse (8 weeks, #000664, Jackson Laboratories) and a *tg/tg* male mouse (16 weeks) were used for skull surface profiling. In each experiment, the mouse was anesthetized using isoflurane in oxygen (4–5% induction, 0.8–1.5% maintenance). The scalp was shaved and sterilized using standard aseptic procedures, after which the mouse was head-fixed in a stereotaxic instrument (David Kopf Instruments Inc.) which was modified to have CNC milling capabilities by incorporating a programmatically controlled three-axis motorized manipulator (MTS25-Z8, Thorlabs)[40]. A handheld mill (Rampower, Ram Products Inc.) fitted with a 200-µm diameter end mill (Harvey tools Inc.) was mounted on the three-axis manipulator using a custom adaptor plate. A custom computer program was written in LabVIEW (National Instruments Inc.) to control the position of the manipulator.

The scalp covering the dorsal skull surface was excised and fascia removed using a micro-curette to prepare the skull for surface profiling. The end mill mounted on a motorized stage was carefully lowered until the end mill tip made contact with

the skull surface at bregma. This process was visualized at the highest magnification setting of the stereo-zoom microscope (×6, M60, Leica) to ensure that the tip did not exert a force large enough to deform the skull surface before registering the coordinates in the LabVIEW program. This served as the origin of a Cartesian coordinate system. The LabVIEW program then raised the end mill 0.5 mm above bregma and moved it laterally to the first profiling point (Supplementary Figs. 1a and 2a). The end mill was carefully lowered until it made contact with the skull surface and the *z*-coordinate was registered. The program then raised the end mill by 0.5 mm and moved it laterally to the next profiling point. The process of registering the *z*-coordinate was repeated at 85 profiling points on the dorsal skull surface of the C57BL/6 mouse and 134 points on the *tg/tg* mouse. These data were used to construct 3D point clouds to define the skull surfaces (Supplementary Figs. 1b and 2b).

The point cloud was imported into a CAD software (Solidworks, Dassault Systèmes). Points along the medial–lateral direction were used to define 3D curves and to interpolate a 3D surface mimicking the skull surface (Supplementary Figs. 1c and 2c). This 3D surface was then extruded to 0.6–0.8 mm thickness to create a solid surface, which was then used as a template for defining the structural frame of the See-Shell (Fig. 1a, Supplementary Figs. 1d and 2d). The CAD files used for 3D printing of the frame are available for download (Supplementary Data 1).

See-Shells were fabricated in a multistep process illustrated in detail in Supplementary Fig. 3. First, the See-Shell structural frame and two molds to assist with bonding the PET to the See-Shell frame were 3D-printed out of PMMA (RS-F2-GPBK-04, RS-F2-GPCL-04, Formlabs Inc.) using a desktop stereolithography (SLA) printer (Form 2, Formlabs Inc., Supplementary Fig. 3a, b). The three holes in the frame were tapped using a 0–80 hand tap (# 15J611, Grainger). A desktop laser jet printer (HP210w, Hewlett Packard Inc.) was used to print an outline matching the See-Shell frame on a 50 µm thick PET film (MELINEX 462, Dupont Inc.). The PET film was cleaned using ethanol and low-lint cleaning tissue (KimWipes, Kimtech Inc.). A pair of scissors was used to cut the PET film using the printed outline as a reference. This PET film was then aligned to the PMMA frame and bonded using a clear, two-part quick setting epoxy adhesive (Scotch-Weld™ DP100 Plus Clear, 3 M Inc.) (Supplementary Fig. 3c–f). A head-plate was fabricated from a 0.016 inch sheet of titanium using a water jet cutter (Omax Inc., see Supplementary Data 1 for CAD drawing). The titanium head-plate was designed such that a ×25 objective, with 3 mm long working distance could access the whole FOV provided by the See-Shells while also providing adequate mechanical support for the head-fixed experiments.

PET optical characterization. An inverted 2P laser scanning microscope was used to image 200 nm YG beads (Polysciences Inc., Warrington, PA, cat#18142-2) using a ×40 magnification, 1.15 numerical aperture (NA) objective (Nikon Apo LWD) through three PET film samples and compared to imaging through a #1.5 glass bottom dish. A Gaussian curve was fit using a standard curve fitting toolbox (MATLAB, Mathworks Inc.). The Gaussian profile was used to estimate the PSFs as illustrated in Fig. 1b, c. YG beads were imaged at 500 sections over 13 µm along the *z*-axis to construct the axial PSF (Fig. 1c). In these characterizations, identical gain settings and analyses were used for the PET and glass coverslip measurements.

Time domain FLIM was performed using TCSPC with Becker and Hickl SPC-150 board to determine the fluorescent lifetime of YG beads imaged through PET. An 80 MHz Ti:Sapphire laser (Spectra Physics; Maitai) tuned to the wavelength of 890 nm was used as the excitation source. The excitation and emission were coupled through an inverted microscope (Nikon; Eclipse TE300) with a ×20 air immersion objective (Nikon, Plan Fluor, N.A. 0.75). A 520/30 nm band-pass emission filter (Semrock, Rochester NY) was also used to selectively collect YG beads fluorescence. FLIM images were collected at 256 × 256 pixel resolution with 30 s acquisition using SPC-830 Photon Counting Electronics (Becker & Hickl GbmH, Berlin, Germany) and Hamamatsu H742MP-40 GaAsP photomultiplier tube (Hamamatsu Photonics, Bridgewater, NJ). To compare light intensity attenuation of PET with glass, the laser power was kept at a fixed value using the calibrated power control on a custom-built 2P microscope and the gain on the PMT was recorded to reach saturation. Urea crystals were used to determine the Instrumentation Response Function with a 445/20 bandpass emission filter (Semrock, Rochester, NY). SPCImage software (Becker & Hickl GbmH, Berlin, Germany) was used to analyze the fluorescence-lifetime decay curves. The lifetime decay of each pixel was fit with a single exponential decay that resulted in a χ^2 error of 1.05 ± 0.12 ($n = 3$). Image analyses to estimate FWHM of fluorescent intensities were performed in Fiji[62].

In vivo surgical implantation. The procedure for implantation of the See-Shells was adapted from previously reported chronic glass window implantation protocols[39]. Mice were anesthetized using 1–3% isoflurane in pure oxygen (0.6 mL min^{-1}). The scalp was shaved and cleaned using standard aseptic surgical procedures. Eyes were covered with ophthalmic eye ointment (Puralube, Dechra Veterinary Products). Buprenorphine (0.1 mg kg^{-1}) and Meloxicam (1–2 mg kg^{-1}) were administered subcutaneously for analgesia and managing inflammation, respectively. Mice were then head-fixed using ear bars and a nose cone in the stereotaxic instrument equipped with the CNC milling machine. A feedback regulated heating pad was used to maintain the body temperature at 37 °C throughout the procedure. Anesthetic depth was assessed every 15 min via toe pinch stimulus and anesthesia dosage adjusted as needed. Warm lactated Ringer's solution was administered subcutaneously every 2 h to prevent dehydration. A local anesthetic (1% Lidocaine) was administered subcutaneously at the incision sites. The scalp was then removed to expose the skull covering the dorsal and cerebellar cortices. A micro curette was used to scrape the skull surface to remove fascia.

The CNC milling machine[40] incorporated in the stereotaxic instrument was used to perform automated craniotomies on C57BL/6, Thy1-YFP (#003709, Jackson Laboratories), Thy1-GFPm (#007788, Jackson Laboratories), and Thy1-GCaMP6f mice (#024276, Jackson Laboratories) (Supplementary Fig. 1a). Briefly, the CNC end mill was lowered to the skull surface at pilot points along a predefined path slightly smaller than the perimeter of the See-Shell. Once the contact was confirmed visually through a stereomicroscope, the *z*-coordinate at that point was registered. This process was repeated at multiple points along the desired craniotomy path. The registered coordinates were then used to interpolate a 3D cutting path for milling the skull in the LabVIEW program. For each craniotomy, the initial milling depth was 50 µm, which was well within the thickness of the skull. In each subsequent milling pass, the depth was incremented in 10 µm steps until reaching the soft part of the bone or trabeculae in a section of the craniotomy path. This was sufficient to pry open the bone for excision across the whole craniotomy. Of the surgeries assessed, the milling was stopped at depths of 107.85 ± 16.79 µm in C57BL/6 ($n = 7$ mice), 57.14 ± 16.25 µm in Thy1-GCaMP6f ($n = 14$ mice), and 70 µm in three Thy1-YFP mice. Craniotomies in *tg/tg* mice were performed manually.

Prior to removing the milled skull, one or two self-tapping screws (F000CE094, Morris Precision Screws and Parts) were implanted 2–3 mm posterior and 3 mm mediolateral to lambda to assist in anchoring the See-Shell to the skull. The skull was removed using surgical forceps taking care to ensure the dura was intact over the entire exposed brain. The brain was covered with sterilized surgical gauze pad soaked in 0.9% saline. The See-Shell was sterilized by soaking in 70% ethanol for 2–3 min followed by rinsing in sterile saline. The gauze pad was removed and the See-Shell was gently placed on top of the exposed brain and aligned to the craniotomy (Supplementary Fig. 3g). The edge of the See-Shell was attached to the skull around the craniotomy by applying a few drops of cyanoacrylate glue (VetBond, 3 M Inc.) using a 29-gauge syringe needle. Dental cement (S380, C&B Metabond, Parkell Inc.) was applied to the periphery of the See-Shell to cement it to the skull surface. Care was taken to ensure the screw holes for fastening the titanium head-plates were not filled in with the uncured dental cement. The dental cement was allowed to fully cure. The titanium head-plate was attached to the frame using 3/32 inch flat head 0–80 screws on the day of implantation. This was followed by a second round of dental cement application to ensure that three fastening locations were fully enclosed in the cement to make it a structurally rigid implant. To protect the implant and underlying brain from light and physical impacts, an opaque 3D-printed PMMA cap was fastened to the titanium head-plate using 3/16 inch flat head 0–80 screws.

In a subset of Thy1-GCaMP6f mice implanted ($n = 3$), the See-Shells had ~1.5 mm diameter perforations above the primary somatosensory cortex (centered −0.76 mm, −2.47 mm AL to bregma). The perforation was sealed using quick setting silicone sealant (KWIK-SIL, World Precision Instruments) on the day of the surgery. The brain could be accessed in multiple experimental sessions across weeks by removing and replacing the silicone seal.

After implantation, mice were allowed to recover on a heating pad until ambulatory and then returned to a clean home cage. All mice were administered Buprenorphine and Meloxicam post-operatively on the day of the surgery as well as the 3 succeeding days to assist with full recovery.

2P imaging. All mice were allowed to recover from surgery for ≥7 days before imaging experiments were attempted. A 2P microscope (Leica SP5II) with a ×25 (0.95 NA) water immersion objective was used for high-resolution imaging experiments in vivo. A Mai: Tai Deepsee (Spectra-Physics) laser was tuned to 940 nm wavelength for excitation. Mice were head-fixed under the 2P microscope in a custom-designed disk treadmill (Fig. 4b). Locations in the FOV were targeted at random locations as illustrated in Figs. 3a and 4a.

For structural imaging in Thy1-YFP mice, each *z*-stack had a FOV of 365 × 365 µm^2 (512 × 512 pixels), starting ~100 µm above the top surface of the PET film, with images acquired every 2 µm down to 800 µm below the starting plane. In two instances, *z*-stacks were acquired from 5 adjacent tiles by moving the objective in the medial–lateral direction by 340 µm such that one edge has an overlap of 25 µm.

Ca^{2+} imaging was performed in Thy1-GCaMP6f using the same head-fixation set-up in fully awake mice. *Z*-stacks were acquired every 10 µm from adjacent 365 × 365 µm^2 tiles with a 15 µm overlap along one edge. Maximum intensity projects of these *z*-stacks were constructed and macroscopic feature in these projects were used to determine their coordinates in the corresponding wide-field epifluorescence image. Time series were acquired at 20 Hz (256 × 256 pixels) for 5 min at one plane in each tile at depths ranging between 200 and 300 µm.

Intracortical microstimulation during wide-field imaging. Mice were head-fixed in the custom-designed disk treadmill placed under a stereo-zoom microscope under light (0.5–1%) isoflurane anesthesia. A feedback regulated heating pad was used to regulate the body temperature at 37 °C. The PET film was carefully perforated (+1 mm, +1 mm, AL to bregma) using a 29-gauge needle for introduction

of an intracortical stimulation electrode. The treadmill was then placed under an epifluorescence microscope (QUANTEM: 5125 C, Nikon). A 250-µm diameter tungsten micro-electrode (Lot # 217037, FHC) was introduced into the brain at an angle of 45° (anterior–posterior direction) using a micromanipulator. Imaging was performed using a ×1 objective when the animal was anesthetized (0.5–1% isoflurane). Each trial lasted a total duration of 2 min sampled at 20 Hz using Metamorph (Molecular Devices Inc.). Stimulation train of 20 pulses (200 µA at 100 Hz) was delivered to the primary motor cortex ~5 s after initiation of each trial. Anesthesia was turned off and mouse was allowed to recover for 1 h before recording during awake state. Behavior was recorded during awake trials using a high-speed camera (FL3-U3-13Y3M-C, FLIR Inc.) at 20 frames per second to monitor whisker or limb movements. At the end of the experiment, the perforations were covered with silicone sealant and the animals were returned to the home cage.

Simultaneous extracellular recordings and wide-field imaging. Simultaneous extracellular recording and wide-field imaging were performed on Thy1-GCaMP6f mice that had perforations created in the See-Shells prior to implantation. The implants were fully assembled and the PET film perforated by gently touching the film with a hot solder iron tip at 550–600 °F. This resulted in ~1.5 mm diameter perforation over the primary somatosensory cortex. On the day of the experiment, mice were head-fixed in a custom treadmill under a stereo-zoom microscope under light (0.5–1%) isoflurane anesthesia. The silicone seal covering the perforation was carefully removed and the treadmill was placed under the epifluorescence microscope. A 32-channel probe (Neuronexus, A1x32-Edge-5mm-100-177-A32) was mounted on a motorized stage (MPC 385, Sutter Instruments Inc.) and guided to the center of the perforation to touch the dura at ~2.47 mm lateral and ~0.76 mm caudal from bregma. Then the See-Shell was covered with a conductive gel bath of 1% agarose and the ground electrode was placed in a corner of the gel bath. The recording probe was inserted into the brain in 10 µm steps up to a depth of 1 mm from the pial surface into the cortex using a high precision DC motor (MTS25-Z8, Thorlabs) mounted on the Sutter manipulator at a 45° entry angle.

Recordings from the neural probe were first pre-amplified (RA16PA Medusa PreAmps, Tucker Davis Technologies), then transmitted to a second amplifier and digitizer (RZ2 system, Tucker Davis Technologies). Neural data was sampled at 24 kHz and band passed at 700-5000 Hz to visualize extracellular single units or between 0 and 200 Hz to visualize local field potentials. Simultaneous mesoscale optical imaging was performed at 10 Hz. Behavior was recorded during awake trials using a high-speed camera (FL3-U3-13Y3M-C, FLIR Inc.) at 20 frames per second. At the end of the experiment, the perforation was covered with the silicone sealant.

Data analyses. For wide-field 1P imaging data analyses, six ROIs covering the bilateral motor, somatosensory, and visual cortices were defined. Data analyses were performed in Fiji. Average fluorescent intensity was measured for each ROI in each image. A custom MATLAB script was used to calculate the normalized change in fluorescent intensity over the time series of images. Baseline average fluorescence was obtained by averaging fluorescent intensity over the first 4 s of the time series. After normalization, the time series were filtered (2-pole Butterworth low-pass filter: 0.3 Hz)[63].

2P Ca^{2+} imaging data were analyzed with Fiji and MATLAB. Briefly, for each time series, the moco (Motion Correction) plugin[64] in Fiji was used to correct for motion artifacts. Maximum intensity and standard deviation images were used to identify cells and place ROIs over each cell in the FOV. For each ROI, the average of the pixel intensity was extracted and imported into a custom MATLAB code. Differential fluorescence intensity ($\Delta F/F_0$) was calculated for each ROI, where F_0 was equal to the lowest 20% of the average pixel value in the ROI over the complete time series.

Behavioral image sequences were imported and analyzed in Fiji. Each image sequence was binned at 3 × 3. ROIs were placed over the nose, forelimb, hindlimb, and the disk. Changes in average pixel intensity across the ROIs in sequential frames when there was movement detected or when there was no movement detected were given a value of 1 or 0, respectively. This allowed for various types of behavior to be quantified. Walking was classified as changes in all ROIs; grooming was classified as changes in only the forepaw and nose ROIs.

All extracellular recording data were post-processed using custom MATLAB scripts. The raw voltage traces from multiple channels were filtered using a 150th order finite impulse response filter with bounds of 800–5000 Hz. The filtered signals were thresholded to detect action potentials using previously described methods[65]. Cells were sorted using linear discriminant analyses and wavelet decomposition[65–67]. Firing rate for each cell was computed using kernel density estimation and smoothing[68]. To determine the relationship between Ca^{2+} signals and firing rates, we generated 1000 bootstrapped shuffled trials of the spike firing rate of each cell[65] and computed the cross-correlations with the Ca^{2+} activity in I-S1. The cells were categorize as modulated if their correlation coefficient at zero-lag was greater than mean + 1.96 times the standard deviation of the bootstrapped trials.

Histology. A subset of mice ($n = 3$ control mice and $n = 3$ mice implanted with See-Shells for 5 weeks) were fully anesthetized in 5% isoflurane and transcardially perfused with phosphate-buffered saline (PBS; CAT# P5493-1L, Sigma Aldrich) followed by 4% paraformaldehyde (PFA; CAT# P6148-500G, Sigma Aldrich). The brains were extracted and stored overnight in 4% PFA for fixation. The brain was sliced into 50 µm slices and then kept in PBS solution containing 100 mM glycine (50046-50 G, Sigma Aldrich) for 30 min to quench excess PFA. This was followed by keeping the slices in PBS solution containing 100 mM glycine and 2% Triton X-100 (93443-100 ML, Sigma Aldrich) to permeabilize the tissue. Slices were then kept in PBS solution containing Triton X-100 and blocking agent (Goat Serum, CAT# 927502, Biolegend) for 2 h after which they were incubated in the solution containing 1:1500 primary antibody–Monoclonal Anti-GFAP antibody produced in mouse (G3893-.2 ML, Sigma Aldrich) for 24 h at 4 °C. Slices were washed and incubated in solution containing the secondary antibody conjugated with fluorophores (anti-mouse Alexa 488, ab150117, abcam). Next, the slices were thoroughly washed to clear any excess antibody and mounted on glass slides in VECTASHEILD (H-1200, Vector Labs), a mounting medium containing 4′,6-diamidino-2-phenylindole (DAPI). Mounted slices were imaged under an upright confocal microscope (FV1000 BX2, Olympus FluoView). GFAP expression was quantified using a previously established protocol[22]. In each slice, average fluorescent intensity was measured using the "measure" function in Fiji at 7 ROIs ($500 \times 500\ \mu m^2$) distributed in the image, with 4 ROIs at the pial surface and 3 ROIs in layer 2/3. This analysis was repeated in slices from three implanted and three non-surgical control mice.

Data availability

The source data underlying Figs. 1b–d, 2c, 4d, e, 5c–e, and 6c, d and Supplementary Figs. 1, 2, 4, 6, 7, and 8 are provided as a Source Data file. All other data supporting the findings of this study are available from the corresponding author on request.

Received: 30 August 2018 Accepted: 12 March 2019
Published online: 02 April 2019

References

1. Ferezou, I. et al. Spatiotemporal dynamics of cortical sensorimotor integration in behaving mice. *Neuron* **56**, 907–923 (2007).
2. Dipoppa, M. et al. Vision and locomotion shape the interactions between neuron types in mouse visual cortex. *Neuron* **98**, 602–615.e8 (2018).
3. Shimaoka, D., Harris, K. D. & Carandini, M. Effects of arousal on mouse sensory cortex depend on modality. *Cell Rep.* **22**, 3160–3167 (2018).
4. Centonze, V. E. & White, J. G. Multiphoton excitation provides optical sections from deeper within scattering specimens than confocal imaging. *Biophys. J.* **75**, 2015–2024 (1998).
5. Chen, T.-W. et al. Ultrasensitive fluorescent proteins for imaging neuronal activity. *Nature* **499**, 295–300 (2013).
6. Akerboom, J. et al. Genetically encoded calcium indicators for multi-color neural activity imaging and combination with optogenetics. *Front. Mol. Neurosci.* **6**, 2 (2013).
7. Chuong, A. S. et al. Noninvasive optical inhibition with a red-shifted microbial rhodopsin. *Nat. Neurosci.* **17**, 1123–1129 (2014).
8. Stirman, J. N., Smith, I. T., Kudenov, M. W. & Smith, S. L. Wide field-of-view, multi-region, two-photon imaging of neuronal activity in the mammalian brain. *Nat. Biotechnol.* **34**, 857–862 (2016).
9. Tsai, P. S. et al. Ultra-large field-of-view two-photon microscopy. *Opt. Express* **23**, 13833–13847 (2015).
10. Sofroniew, N. J., Flickinger, D., King, J. & Svoboda, K. A large field of view two-photon mesoscope with subcellular resolution for in vivo imaging. *eLife* **5**, e14472 (2016).
11. Holtmaat, A. et al. Imaging neocortical neurons through a chronic cranial window. *Cold Spring Harb. Protoc.* **7**, 694–701 (2012).
12. Silasi, G., Xiao, D., Vanni, M. P., Chen, A. C. N. & Murphy, T. H. Intact skull chronic windows for mesoscopic wide-field imaging in awake mice. *J. Neurosci. Methods* **267**, 141–149 (2016).
13. Drew, P. J. et al. Chronic optical access through a polished and reinforced thinned skull. *Nat. Methods* **7**, 981–984 (2010).
14. Kim, T. H. et al. Long-term optical access to an estimated one million neurons in the live mouse cortex. *Cell Rep.* **17**, 3385–3394 (2016).
15. Xiao, D. et al. Mapping cortical mesoscopic networks of single spiking cortical or sub-cortical neurons. *eLife* **6**, e19976 (2017).
16. Kawakami, M. & Yamamura, K. I. Cranial bone morphometric study among mouse strains. *BMC Evol. Biol.* https://doi.org/10.1186/1471-2148-8-73 (2008).
17. Vora, S. R., Camci, E. D. & Cox, T. C. Postnatal ontogeny of the cranial base and craniofacial skeleton in male C57BL/6J mice: a reference standard for quantitative analysis. *Front. Physiol.* https://doi.org/10.3389/fphys.2015.00417 (2016).

18. Faraj, M. G., Ibrahim, K. & Ali, M. K. M. PET as a plastic substrate for the flexible optoelectronic applications. *Optoelectron. Adv. Mater. Rapid Commun.* **5**, 879–882 (2011).
19. Khan, W., Muntimadugu, E., Jaffe, M. & Domb, A. J. in *Focal Controlled Drug Delivery, Advances in Delivery Science and Technology* (eds Domb, A. J. & Khan, W.) 33–59 (2014).
20. Fletcher, C. F. et al. Absence epilepsy in tottering mutant mice is associated with calcium channel defects. *Cell* **87**, 607–617 (1996).
21. Gong, S. et al. A gene expression atlas of the central nervous system based on bacterial artificial chromosomes. *Nature* https://doi.org/10.1038/nature02033 (2003).
22. Cvetanovic, M., Ingram, M., Orr, H. & Opal, P. Early activation of microglia and astrocytes in mouse models of spinocerebellar ataxia type 1. *Neuroscience* https://doi.org/10.1016/j.neuroscience.2015.01.003 (2015).
23. Holtmaat, A. & Svoboda, K. Experience-dependent structural synaptic plasticity in the mammalian brain. *Nat. Rev. Neurosci.* **10**, 647–658 (2009).
24. Yang, G., Pan, F. & Gan, W. B. Stably maintained dendritic spines are associated with lifelong memories. *Nature* **462**, 920–924 (2009).
25. Roberts, T. F., Tschida, K. A., Klein, M. E. & Mooney, R. Rapid spine stabilization and synaptic enhancement at the onset of behavioural learning. *Nature* **463**, 948–952 (2010).
26. Feng, G. et al. Imaging neuronal subsets in transgenic mice expressing multiple spectral variants of GFP. *Neuron* **28**, 41–51 (2000).
27. Dana, H. et al. Thy1-GCaMP6 transgenic mice for neuronal population imaging in vivo. *PLoS ONE* **9**, e108697 (2014).
28. Popa, L. S., Streng, M. L. & Ebner, T. J. Long-term predictive and feedback encoding of motor signals in the simple spike discharge of Purkinje cells. *eNeuro* https://doi.org/10.1523/ENEURO.0036-17.2017 (2017).
29. Chen, G. et al. Altered levels of the splicing factor muscleblind modifies cerebral cortical function in mouse models of myotonic dystrophy. *Neurobiol. Dis.* **112**, 35–48 (2018).
30. Papour, A. et al. Optical imaging for brain tissue characterization using relative fluorescence lifetime imaging. *J. Biomed. Opt.* **18**, 60504 (2013).
31. Yaseen, M. A. et al. In vivo imaging of cerebral energy metabolism with two-photon fluorescence lifetime microscopy of NADH. *Biomed. Opt. Express* **4**, 307–321 (2013).
32. Skala, M. C. et al. In vivo multiphoton microscopy of NADH and FAD redox states, fluorescence lifetimes, and cellular morphology in precancerous epithelia. *Proc. Natl Acad. Sci.* **104**, 19494–19499 (2007).
33. Shibuki, K. et al. Dynamic imaging of somatosensory cortical activity in the rat visualized by flavoprotein autofluorescence. *J. Physiol.* **549**, 919–927 (2003).
34. Reinert, K. C. et al. Cellular and metabolic origins of flavoprotein autofluorescence in the cerebellar cortex in vivo. *Cerebellum* **10**, 585–599 (2011).
35. Cheng, S. et al. Flexible endoscope for continuous in vivo multispectral fluorescence lifetime imaging. *Opt. Lett.* **38**, 1515 (2013).
36. Szulczewski, J. M. et al. In vivo visualization of stromal macrophages via label-free FLIM-based metabolite imaging. *Sci. Rep.* **6**, 25086 (2016).
37. Entenberg, D. et al. In vivo subcellular resolution optical imaging in the lung reveals early metastatic proliferation and motility. *Intravital* **4**, 1–11 (2015).
38. Roome, C. J. & Kuhn, B. Chronic cranial window with access port for repeated cellular manipulations, drug application, and electrophysiology. *Front. Cell. Neurosci.* **8**, 379 (2014).
39. Holtmaat, A. et al. Long-term, high-resolution imaging in the mouse neocortex through a chronic cranial window. *Nat. Protoc.* **4**, 1128–1144 (2009).
40. Ghanbari, L. et al. Craniobot: a computer numerical controlled robot for cranial microsurgeries. *Sci. Rep.* **9**, 1023 (2019).
41. Bradley, J. P., Levine, J. P., Roth, D. A., McCarthy, J. G. & Longaker, M. T. Studies in cranial suture biology: IV. Temporal sequence of posterior frontal cranial suture fusion in the mouse. *Plast. Reconstr. Surg.* **98**, 1039–1345 (1996).
42. Ghosh, K. K. et al. Miniaturized integration of a fluorescence microscope. *Nat. Methods* **8**, 871–878 (2011).
43. Jeong, J. W. et al. Wireless optofluidic systems for programmable in vivo pharmacology and optogenetics. *Cell* **162**, 662–674 (2015).
44. Adams, J. K. et al. Single-frame 3D fluorescence microscopy with ultraminiature lensless FlatScope. *Sci. Adv.* **3**, e1701548 (2017).
45. Kodandaramaiah, S. B., Talei Franzesi, G., Chow, B. Y., Boyden, E. S. & Forest, C. R. Automated whole-cell patch-clamp electrophysiology of neurons in vivo. *Nat. Methods* https://doi.org/10.1038/nMeth.1993 (2012).
46. Kodandaramaiah, S. B. et al. Multi-neuron intracellular recording in vivo via interacting autopatching robots. *eLife* **7**, e24656 (2018).
47. Chaumont, J. et al. Clusters of cerebellar Purkinje cells control their afferent climbing fiber discharge. *Proc. Natl Acad. Sci.* **110**, 16223–16228 (2013).
48. Evarts, E. V. & Thach, W. T. Motor mechanisms of the CNS: cerebrocerebellar interrelations. *Annu. Rev. Physiol.* **31**, 451–498 (1969).
49. Shipp, S. The functional logic of corticostriatal connections. *Brain Struct. Funct.* **222**, 669–706 (2017).
50. Marchand, W. R. Cortico-basal ganglia circuitry: a review of key research and implications for functional connectivity studies of mood and anxiety disorders. *Brain Struct. Funct.* **215**, 73–96 (2010).
51. Borodovitsyna, O., Flamini, M. & Chandler, D. Noradrenergic modulation of cognition in health and disease. *Neural Plast.* **2017**, 6031478 (2017).
52. Szabadi, E. Functional neuroanatomy of the central noradrenergic system. *J. Psychopharmacol.* **27**, 659–693 (2013).
53. Ballinger, E. C., Ananth, M., Talmage, D. A. & Role, L. W. Basal forebrain cholinergic circuits and signaling in cognition and cognitive decline. *Neuron* **91**, 1199–1218 (2016).
54. Huang, L., Merson, T. D. & Bourne, J. A. In vivo whole brain, cellular and molecular imaging in nonhuman primate models of neuropathology. *Neurosci. Biobehav. Rev.* **66**, 104–118 (2016).
55. Camus, S., Ko, W. K. D., Pioli, E. & Bezard, E. Why bother using non-human primate models of cognitive disorders in translational research? *Neurobiol. Learn. Mem.* **124**, 123–129 (2015).
56. Dettmer, A. M. & Suomi, S. J. Nonhuman primate models of neuropsychiatric disorders: Influences of early rearing, genetics, and epigenetics. *ILAR J.* **55**, 361–370 (2014).
57. Park, J. E. et al. Generation of transgenic marmosets expressing genetically encoded calcium indicators. *Sci. Rep.* **6**, 34931 (2016).
58. Li, M., Liu, F., Jiang, H., Lee, T. S. & Tang, S. Long-term two-photon imaging in awake macaque monkey. *Neuron* **93**, 1049–1057.e3 (2017).
59. Lecoq, J. et al. Visualizing mammalian brain area interactions by dual-axis two-photon calcium imaging. *Nat. Neurosci.* **17**, 1825–1829 (2014).
60. Luan, L. et al. Ultraflexible nanoelectronic probes form reliable, glial scar–free neural integration. *Sci. Adv.* https://doi.org/10.1126/sciadv.1601966 (2017).
61. Luan, L. et al. Nanoelectronics enabled chronic multimodal neural platform in a mouse ischemic model. *J. Neurosci. Methods* **295**, 68–76 (2018).
62. Schindelin, J. et al. Fiji: an open-source platform for biological-image analysis. *Nat. Methods* **9**, 676–682 (2012).
63. Cai, D. J. et al. A shared neural ensemble links distinct contextual memories encoded close in time. *Nature* **534**, 115–118 (2016).
64. Dubbs, A., Guevara, J. & Yuste, R. moco: fast motion correction for calcium imaging. *Front. Neuroinform.* **10**, 6 (2016).
65. Quiroga, R. Q., Nadasdy, Z. & Ben-Shaul, Y. Unsupervised spike detection and sorting with wavelets and superparamagnetic clustering. *Neural Comput.* **16**, 1661–1687 (2004).
66. Keshtkaran, M.R. and Yang, Z. J., Noise-robust unsupervised spike sorting based on discriminative subspace learning with outlier handling *J Neural Eng.* **14**, 036003 (2017). https://doi.org/10.1088/1741-2552/aa6089. Epub 2017 Feb 15
67. Yang, Z., Zhao, Q. & Liu, W. Spike feature extraction using informative samples. Spotlight presentation, Advances in Neural Information Processing Systems (NIPS21) 1865–1872 (2009).
68. Fujisawa, S., Amarasingham, A., Harrison, M. T. & Buzsáki, G. Behavior-dependent short-term assembly dynamics in the medial prefrontal cortex. *Nat. Neurosci.* **11**, 823–833 (2008).

Acknowledgements

S.B.K. acknowledges funds from the Mechanical Engineering department, College of Science and Engineering, MnDRIVE RSAM initiative of the University of Minnesota, McGovern Institute Neurotechnology (MINT) fund, National Institutes of Health (NIH) 1R21NS103098-01, and the Minnesota Department of Higher Education. M.L.R. was supported by 3R21 NS103098-01S1. L.G. was supported by the University of Minnesota Informatics Institute (UMII) Graduate Research fellowship. T.J.E. was supported, in part, from NIH grants RO1 NS18338 and R37 NS040389. K.W.E. acknowledges funding from DARPA grant N66001-17-2-4010. We would like to thank Bonita Van Heel at Minnesota Dental Research Center for Biomaterials and Biomechanics for help with micro-CT scanning experiments. We would also like to acknowledge Dr. Mark Sanders and Jason Mitchell at the UMN University Imaging Center where all 2P intensity imaging experiments were conducted. We also acknowledge Dr. Jenu Chacko and Dr. Jayne Squirrell of the UW-Madison who assisted with cell culture and viability experiments for FLIM.

Author contributions

L.G. and S.B.K. conceptualized the technology. L.G., R.E.C, T.J.E., K.W.E., and S.B.K. designed experiments. L.G., R.E.C., M.L.R., J.D., G.C., J.H., M.A.K.S., L.H., N.M., M.M.G., S.L.W., and S.B.K. conducted the experiments. L.G., R.E.C., G.C., M.A.K.S., A.N., T.J.E., and S.B.K. analyzed the data. L.G., R.E.C., M.A.K.S., T.J.E., K.W.E., and S.B.K. wrote the paper.

Additional information

Supplementary Information accompanies this paper at https://doi.org/10.1038/s41467-019-09488-0.

Competing interests: The authors declare no competing interests.

Reprints and permission information is available online at http://npg.nature.com/reprintsandpermissions/

Journal peer review information: *Nature Communications* thanks the anonymous reviewers for their contribution to the peer review of this work. Peer reviewer reports are available.

Publisher's note: Springer Nature remains neutral with regard to jurisdictional claims in published maps and institutional affiliations.

Wang, Shulei, Jenu V. Chacko, Abdul K. Sagar, Kevin W. Eliceiri, and Ming Yuan. "Nonparametric empirical Bayesian framework for fluorescence-lifetime imaging microscopy." Biomedical Optics Express 10, no. 11 (2019): 5497-5517.

Summary:

Fluorescence lifetime imaging microscopy (FLIM) is a powerful imaging tool used to study the molecular environment of flurophores. In time domain FLIM, extracting lifetime from fluorophores signals entails fitting data to a decaying exponential distribution function. However, most existing techniques for this purpose need large amounts of photons at each pixel and a long computation time, thus making it difficult to obtain reliable inference in applications requiring either short acquisition or minimal computation time. In this work, we introduce a new nonparametric empirical Bayesian framework for FLIM data analysis (NEB-FLIM), leading to both improved pixel-wise lifetime estimation and a more robust and computationally efficient integral property inference. This framework is developed based on a newly proposed hierarchical statistical model for FLIM data and adopts a novel nonparametric maximum likelihood estimator to estimate the prior distribution. To demonstrate the merit of the proposed framework, we applied it on both simulated and real biological datasets and compared it with previous classical methods on these datasets

Research Article | Vol. 10, No. 11 / 1 November 2019 / Biomedical Optics Express 5497
Biomedical Optics EXPRESS

Nonparametric empirical Bayesian framework for fluorescence-lifetime imaging microscopy

SHULEI WANG,[1,5] JENU V. CHACKO,[2] ABDUL K. SAGAR,[2] KEVIN W. ELICEIRI,[2,3] AND MING YUAN[4,6]

[1]Department of Biostatistics, Epidemiology and Informatics, Perelman School of Medicine, University of Pennsylvania, Philadelphia, PA 19104, USA
[2]Laboratory for Optical and Computational Instrumentation, University of Wisconsin at Madison, Madison, WI 53706, USA
[3]Morgridge Institute for Research, Madison, WI 53706, USA
[4]Department of Statistics, Columbia University, New York, NY 10027, USA
[5]Shulei.Wang@pennmedicine.upenn.edu
[6]ming.yuan@columbia.edu

Abstract: Fluorescence lifetime imaging microscopy (FLIM) is a powerful imaging tool used to study the molecular environment of flurophores. In time domain FLIM, extracting lifetime from fluorophores signals entails fitting data to a decaying exponential distribution function. However, most existing techniques for this purpose need large amounts of photons at each pixel and a long computation time, thus making it difficult to obtain reliable inference in applications requiring either short acquisition or minimal computation time. In this work, we introduce a new nonparametric empirical Bayesian framework for FLIM data analysis (NEB-FLIM), leading to both improved pixel-wise lifetime estimation and a more robust and computationally efficient integral property inference. This framework is developed based on a newly proposed hierarchical statistical model for FLIM data and adopts a novel nonparametric maximum likelihood estimator to estimate the prior distribution. To demonstrate the merit of the proposed framework, we applied it on both simulated and real biological datasets and compared it with previous classical methods on these datasets.

1. Introduction

Fluorescence lifetime imaging microscopy (FLIM) is a widely used technique to reveal the changes in fluorophores' local environments by measuring fluorophores' lifetime [1,2]. The application of FLIM includes, but is not limited to, measuring local environmental parameters within cells such as pH or oxygenation state, studying protein interactions by quantifying Förster resonance energy transfer (FRET), and investigating the metabolic state of cells [2]. In particular, due to noninvasiveness and high-resolution, FLIM has been used to monitor the dynamic change in metabolic state of living cells by measuring lifetime of auto-fluorescent properties of reduced nicotinamide adenine dinucleotide (NADH) and flavin adenine dinucleotide (FAD) in cancer research [2–4].

To investigate and compare different types of cells/tissues, the typical analysis workflow for FLIM data follows a two-step procedure [3–5]: 1) pixel-wise lifetime recovery at each pixel: the lifetime of each component and component contribution are extracted from fluorescence signal by fitting data to a single/double decaying exponential distribution function [6–9]; 2) integral property inference: one or several summary statistics of each sample are calculated from all pixel-wise estimations of the previous step, e.g. the mean or standard deviation of lifetime or component contribution. The pixel-wise fitted lifetime and these summary statistics are then used to investigate the spatial change within each sample and the difference across groups of samples, respectively.

#372067 https://doi.org/10.1364/BOE.10.005497
Journal © 2019 Received 8 Jul 2019; revised 31 Aug 2019; accepted 29 Sep 2019; published 3 Oct 2019

Research Article Vol. 10, No. 11 / 1 November 2019 / Biomedical Optics Express 5498
Biomedical Optics EXPRESS

To infer pixel-wise lifetime, numerous exponential curve fitting approaches have been proposed [6–18]. Due to easy implementation, pixel-wise analysis has been arguably the most widely used strategy for pixel-wise lifetime recovery, including least-squares fitting and maximum likelihood estimation (MLE) approaches [8–10]. One main obstacle for pixel-wise analysis is that it requires a large number of photons per pixel [19], resulting in long photon collection time, usually more than tens of seconds for the whole image. This time requirement for photon collection prohibits FLIM to be used for acquisition at higher speeds [20]. Despite the recent improvement in fast detector [21], one of the most commonly used computation strategies to alleviate this issue is global analysis, which estimates global fluorescence lifetime by using photons across all pixels and then calculates pixel-wise component contribution [7,12,13]. Although global analysis might provide more robust estimation in low-photon regime, it brings irreversible bias for pixel-wise lifetime estimation due to neglect of spatial change in fluorescence lifetime. Therefore, there is a need for more robust pixel-wise lifetime fitting algorithms that work for low-photon regimes.

On the other hand, the goal of integral property inference in the classical workflow is different from pixel-wise lifetime recovery because only summary information is needed in this step. As described above, the most common way is direct calculation from pixel-wise recovered lifetime. However, this way requires reliable estimation of pixel-wise lifetime, which usually needs many photons at each pixel as we previously discussed. Moreover, it usually takes long computation time, which brings difficulty to analysis in real time monitoring [4] and large scale experiments, especially when there are thousands of datasets to compare in high-throughput screenings [7,22]. The main difficulty lies in the pixel-wise fitting step, as pixel-wise lifetime recovery needs a large number of photons per pixel and thousands of iterative instrumental response function deconvolutions. Therefore, a natural question arises: can we just conduct integral property inference directly and bypass the pixel-wise lifetime recovery step? In this paper, we show this is feasible.

Motivated by these two needs, we introduce a new Nonparametric Empirical Bayesian framework for analyzing FLIM data, referred as NEB-FLIM, to improve both pixel-wise lifetime recovery and integral property inference in the classical workflow. Specifically, we introduce a hierarchical statistical model for FLIM data by assuming that the fluorescence lifetime at each pixel is drawn from some prior distribution. Under this hierarchical model, NEB-FLIM first adopts a non-parametric maximum likelihood estimator (NPMLE) to estimate the prior distribution by using all photons of the image. This estimated prior distribution is then incorporated into subsequent bayesian analysis for pixel-wise lifetime recovery. Through this, NEB-FLIM provides a more accurate and pixel-dependent estimation of fluorescence lifetime. NEB-FLIM uses a plugin estimator of previously estimated prior distribution to conduct integral property inference directly, instead of summarizing from pixel-wise recovered lifetime. In doing so, summary statistics can be computed in a much more computationally efficient and more robust fashion. Thus, it allows its use in applications when low acquisition or computation time is required.

2. Methods

In this section, we introduce a hierarchical statistical model for FLIM data in Section 2.1, the nonparametrical estimator of prior distribution in Section 2.2, the pixel-wise bayesian estimator in Section 2.3, and the method for integral property inference in Section 2.4.

2.1. Statistical model for photon-counting FLIM data

In this section, we introduce a statistical model for photon-counting time-domain FLIM data, which is collected by a time-correlated single photon counting system (TCSPC) [1,2]. The form of this statistical model is different from commonly-used physical exponential decay models for fluorophores [1,2], but they are equivalent in terms of data analysis. We adopt this model because

Research Article Vol. 10, No. 11 / 1 November 2019 / Biomedical Optics Express 5499
Biomedical Optics EXPRESS

it is more convenient for statistical analysis. In the end of this section, we compare these two equivalent models and point out their connections.

In light of fluorophores' properties [1,2], the decay of the fluorescence intensity follows an exponential decay law $F(t) = F_0 e^{-t/\tau}$, where $F(t)$ is fluorescence intensity at time t, F_0 is fluorescence intensity at time $t = 0$, and τ is defined as lifetime of fluorescence, the main parameter of interest in this article. Thus, our statistical model assumes each photon emitted by fluorophores obeys the following exponential distribution $\tau^{-1}e^{-t/\tau}$ when $t>0$. To measure τ by TCSPC, a pulsed laser is used to excite the sample repeatedly with time period T_p, and only the first photon within every period is recorded. Thus, if the photons emitted from previous periods are taken into account, the probability distribution can be expressed as

$$g(t) := \sum_{n=0}^{\infty} \frac{1}{\tau} e^{-\frac{t+nT_p}{\tau}} = \frac{1}{\tau(1-e^{-T_p/\tau})} e^{-\frac{t}{\tau}}, \qquad \text{when } 0 < t < T_p.$$

Due to instrumental responding delay and dispersion of the laser, we need to consider the extra error brought on by the instruments themselves, i.e the distribution of observed fluorescence lifetime is expressed as the circular convolution form $(g \otimes h)(t)$, when $0 < t < T_p$, where $g(t)$ can be seen as a periodic function with period T_p, and $h(t)$ is instrumental response function (IRF), which can be assumed known in advance or estimated accurately in separate experiment. Besides the error brought by IRF, another corruption comes from the background light. Suppose the ratio of background photons is α, then the distribution function of arriving photon times can be written as

$$f(t) := \frac{\alpha}{T_p}\mathbb{I}_{(0<t<T_p)} + (1-\alpha)(g \otimes h)(t), \qquad \text{when } 0 < t < T_p. \tag{1}$$

The design of the TCSPC technique only allows us to know a rough interval of each arriving photon. More specifically, suppose the detection range $(0, T_p]$ is divided into m bins equally $B_j = \big((j-1)T_p/m, jT_p/m\big], j = 1, \ldots, m$. When the fluorescence lifetime is τ, the probability of a photon arriving at bin B_j is

$$P_j^{(\tau)} = \int_{B_j} f(t)dt. \tag{2}$$

Write $\mathbf{P}_{(\tau)} = (P_1^{(\tau)}, \ldots, P_m^{(\tau)})$ as the probability of mono-exponential model defined in (2) when fluorescence lifetime is τ. The observational data read from TCSPC are the numbers of photons in each bin, $N_j, j = 1, \ldots, m$, which can be assumed to be drawn from multinomial distribution $\text{Multi}(\sum_{j=1}^m N_j, \mathbf{P}_{(\tau)})$. The goal of fluorescence lifetime analysis is to estimate τ based on histogram $N_1, \ldots, N_m$.

In the above statistical model, we focus on the situation where all fluorescence distribution have the same lifetime, i.e. mono-exponential component model. In a lot of applications, the fluorescence distribution shows the status of the fluorophore, its confirmations and interactions with its local micro-environment [2]. For example, NADH has different fluorescence lifetime when it is bound and unbound to proteins [23]. In such situations, the decay of the fluorescence intensity follows a double exponential decay law $F(t) = F_0\left(A_1 e^{-t/\tau_1} + A_2 e^{-t/\tau_2}\right)$, where A_k is the fraction of the kth component, also called component contribution, such that $A_1 + A_2 = 1$ and τ_k is lifetime of the kth component. For convenience of statistical analysis, our statistical model assumes each photon follows a mixture of exponential distributions, i.e.

$$a\frac{1}{\tau_1}e^{-\frac{t}{\tau_1}} + (1-a)\frac{1}{\tau_2}e^{-\frac{t}{\tau_2}}, \qquad \text{when } t>0.$$

This representation is a bit different from multiple exponential decay law, and we have different interpretations for a and A_1 and A_2. To distinguish them, we call a the statistical component contribution and A_1 and A_2 the physical component contribution. This representation is actually

Research Article Vol. 10, No. 11 / 1 November 2019 / Biomedical Optics Express 5500
Biomedical Optics EXPRESS

equivalent to multiple exponential decay law, so estimation of a and estimation of A_1 and A_2 can naturally lead to one another. In most of this article, we adopt the mixture model representation (i.e. adopting a) for convenience of statistical analysis and discuss how the estimation of a can be transformed to the estimation of A_1 and A_2 in later sections.

Following the same conduction in setting of a single type of fluorescence, the distribution function of arriving photon times is thus a mixture distribution $f(t) = af_{\tau_1}(t) + (1-a)f_{\tau_2}(t)$, where $f_{\tau_k}(t)$ has the same form of distribution in Eq. (1). Besides $\boldsymbol{\tau} := (\tau_1, \tau_2)$, the contribution of each component a is of more interest in many applications. Hence, the lifetime analysis of double exponential components model aims to recover a and $\boldsymbol{\tau}$ from observations $\mathbf{N} = (N_1, \ldots, N_m)$, which is drawn from Multi$(\sum_{j=1}^m N_j, a\mathbf{P}_{(\tau_1)} + (1-a)\mathbf{P}_{(\tau_2)})$.

To reflect the spatial trend of fluorescence lifetime, the arrival time of photons are recorded at each pixel $i \in \mathbb{I}$ through microscopy scanning techniques. More specifically, the observed data at each pixel $i \in \mathbb{I}$ is a histogram of photon counts $\mathbf{N}_i = (N_{i1}, \ldots, N_{im})$, and the goal is to study the pixel-wise fluorescence lifetime $\boldsymbol{\tau}_i = (\tau_{i1}, \tau_{i2})$ and pixel-wise statistical component contribution a_i of each pixel from the pixel-wise observations $\mathbf{N}_i$s. In other words, the FLIM data can be seen generated from thousands of parallel double exponential models. Figure 1 illustrates the data structure of fluorescence-lifetime imaging microscopy (FLIM). In order to analyze data from all pixels jointly, we further assume τ_{i1} and τ_{i2} are independently drawn from two prior distributions: $\pi_1(t)$ and $\pi_2(t)$. The prior distribution $\pi_1(t)$ and $\pi_2(t)$ can be also seen as empirical distribution of $\boldsymbol{\tau}_i$

$$\pi_1(t) = \frac{1}{|\mathbb{I}|}\sum_{i\in\mathbb{I}} \delta_{\tau_{i1}} \qquad \text{and} \qquad \pi_2(t) = \frac{1}{|\mathbb{I}|}\sum_{i\in\mathbb{I}} \delta_{\tau_{i2}},$$

where δ_x is delta function at x, and $|\mathbb{I}|$ is the number of pixels in FLIM image. By the definition of prior distributions, the FLIM data can be seen generated from the following hierarchical model

$$\begin{aligned} \tau_{i1} \sim \pi_1(t) \quad \text{and} \quad \tau_{i2} \sim \pi_2(t) \\ \mathbf{N}_i \sim \text{Multi}\left(n_i, a_i\mathbf{P}_{(\tau_{i1})} + (1-a_i)\mathbf{P}_{(\tau_{i2})}\right) \end{aligned}$$

where $n_i = \sum_{j=1}^m N_{ij}$ is the number of photons observed at pixel i. Based on this model, we propose our nonparametric empirical bayesian framework for FLIM data.

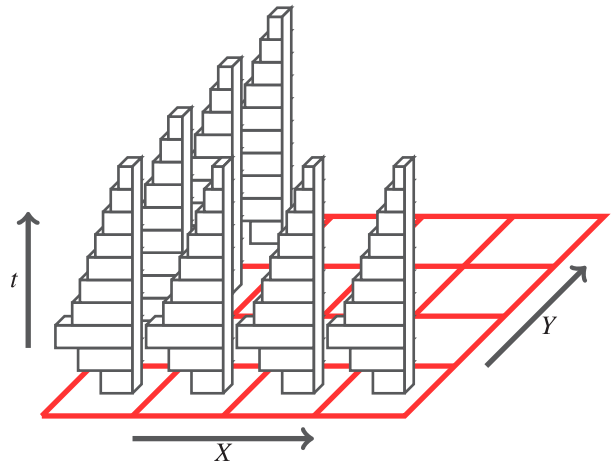

Fig. 1. The data structure of fluorescence-lifetime imaging microscopy photon counting data.

Research Article | Vol. 10, No. 11 / 1 November 2019 / Biomedical Optics Express 5501
Biomedical Optics EXPRESS

2.2. Estimation of prior distribution

In most traditional bayesian FLIM analysis methods, the prior distribution of lifetime is usually a predetermined distribution, which is either manually input or uninformative prior [14,15,17,18]. These subjective prior distribution leads to unavoidable bias when misspecified. Thus, we opt to estimate prior distributions by maximizing marginal likelihood distribution.

The model of FLIM data defined in Section 2.1 suggests that, if we pool all photons across pixels of images together, these photons can be seen drawn from a single mixture model

$$\begin{aligned} &\tau_l \sim \pi^*(t) \\ &j_l \sim \text{Multi}(1, \mathbf{P}_{(\tau_l)}), \qquad l = 1, \ldots, n^* := \sum_{i\in\mathbb{I}} n_i. \end{aligned} \tag{3}$$

Here, j_l represents the j_lth bin from m bins, n^* is total number of photons of all pixel of the FLIM image, and $\pi^*(t)$ can be written as

$$\pi^*(t) = \frac{1}{n^*} \sum_{i\in\mathbb{I}} \left[n_i a_i \delta_{\tau_i} + n_i(1-a_i)\delta_{\tau_{i2}} \right].$$

One main advantage of FLIM is that fluorescence lifetime is not dependent on intensity values, which is defined as the number of photons at each pixel [1,2]. Thus, it is natural to assume the number of photons at each pixel, the statistical component contribution, and lifetime are independent from each other

$$\frac{1}{|\mathbb{I}|}\sum_{i\in\mathbb{I}} f_1(n_i) f_2(a_i) f_3(\tau_{ik}) = \left(\frac{1}{|\mathbb{I}|}\sum_{i\in\mathbb{I}} f_1(n_i)\right)\left(\frac{1}{|\mathbb{I}|}\sum_{i\in\mathbb{I}} f_2(a_i)\right)\left(\frac{1}{|\mathbb{I}|}\sum_{i\in\mathbb{I}} f_3(\tau_{ik})\right) \tag{4}$$

for any measurable function f_1, f_2, and f_3, and $k = 1$ or 2. With this independence assumption (4), the combined prior distribution $\pi^*(t)$ can be rewritten as a linear combination of prior distributions $\pi_1(t)$ and $\pi_2(t)$

$$\pi^*(t) = a^*\pi_1(t) + (1-a^*)\pi_2(t),$$

where $a^* = \sum_{i\in\mathbb{I}} a_i/|\mathbb{I}|$. This motivates us to firstly estimate $\pi^*(t)$ by pooling all photons together and then segment estimated $\pi^*(t)$ into $\pi_1(t)$ and $\pi_2(t)$.

The model in (3) can be written in its equivalent form

$$\mathbf{M} := (M_1, \ldots, M_m) \sim \text{Multi}\left(n^*, \int \mathbf{P}_{(t)} d\pi^*(t)\right), \tag{5}$$

where M_j is the total number of photons in bin j across the pixels of image, i.e. $M_j = \sum_{i\in\mathbb{I}} N_{ij}$. The form in (5) suggests that recovering $\pi^*(t)$ from count data $\mathbf{M}$ is a deconvolution problem. To solve this deconvolution problem, we consider nonparametric maximum likelihood estimator (NPMLE), as we do not put any shape or parametric form assumptions for the distribution $\pi^*(t)$. NPMLE for mixture model is firstly introduced in [24] and then developed by [25–27] and so on.

To be specific, we assume the support of distribution $\pi^*(t)$ belongs to some known interval $[T_L, T_U]$ and divide $[T_L, T_U]$ into L equal-spaced interval with $L+1$ points $T_L = h_0 < \ldots < h_L = T_U$. This bounded support assumption is suitable in most applications, as the knowledge of an roughly lifetime is available in advance. With this grid $h_0, \ldots, h_L$, we can discretize the distribution $\pi^*(t)$

Research Article | Vol. 10, No. 11 / 1 November 2019 / Biomedical Optics Express 5502
Biomedical Optics EXPRESS

as a L dimension discrete distribution

$$\pi^*_\Delta(t) = \sum_{l=1}^{L} p^*_l \delta_{h_l}$$

where $p^*_l = \int_{h_{l-1}}^{h_l} d\pi^*(t)$. To recover $\pi^*_\Delta(t)$, it is sufficient to recover $\boldsymbol{p}^* = (p^*_1, \ldots, p^*_L)$. After discretization, the likelihood function of marginal distribution of $\mathbf{M}$ can be written as

$$f(p_1, \ldots, p_L) := \frac{n^*!}{M_1! \ldots M_m!} \prod_{j=1}^{m} \left(\sum_{l=1}^{L} p_l P_j^{(h_l)} \right)^{M_j},$$

where $P_j^{(t)}$ is the probability defined in (2). The maximum likelihood estimator (MLE) is thus defined as a solution of the following convex optimization problem

$$\begin{aligned} &\min_{(p_1,\ldots,p_L)} -\sum_{j=1}^{m} M_j \log \left(\sum_{l=1}^{L} p_l P_j^{(h_l)} \right) \\ &\text{s.t.} \sum_{l=1}^{L} p_l = 1 \quad \text{and} \quad p_l \geq 0,\ l = 1, \ldots, L. \end{aligned} \tag{6}$$

As suggested in [27], this convex optimization problem can be solved efficiently by modern interior point methods. The estimated prior distribution $\hat{\pi}^*(t)$ thus can be written as

$$\hat{\pi}^*(t) = \sum_{l=1}^{L} \hat{p}_l \delta_{h_l}.$$

A typical example of prior distribution $\hat{\pi}^*(t)$ estimated by the above procedure is shown in Fig. 2.

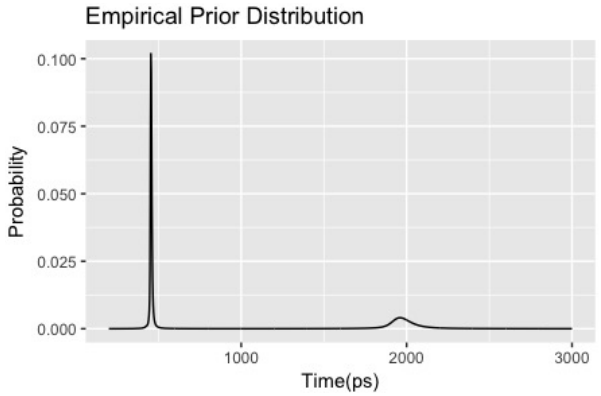

Fig. 2. A typical example of empirical prior distribution estimated from data.

After estimating $\hat{\pi}^*(t)$, we now segment this distribution to recover $\pi_1(t)$ and $\pi_2(t)$. Generally, it is impossible to recover $\pi_1(t)$ and $\pi_2(t)$ by $\hat{\pi}^*(t)$ alone because they are not identifiable if there is overlapping area between them. To address this issue, we appeal to the observation that the two prior distributions can be separated very well in many FLIM applications. For example, the two components of NADH, bound and unbound, have lifetimes of roughly 400 to 500 picosecond(ps) and 2000 to 2500 ps, respectively [3]. Another example in FRET quantification is NowGFP, an

Research Article Vol. 10, No. 11 / 1 November 2019 / Biomedical Optics Express 5503
Biomedical Optics EXPRESS

improved version of green fluorescent protein. Its two components, close to and far away from acceptor such as mRuby2 or tdTomato, have lifetimes of roughly 2000 to 3000 ps and 5000 ps [28]. Thus, we shall assume $\pi_1(t)$ from $\pi_2(t)$ are identifiable in the following sense

$$\sup\{t : \pi_1(t)>0\} < \inf\{t : \pi_2(t)>0\}. \tag{7}$$

Motivated by this identification assumption (7), we segment $\hat{\pi}^*(t)$ by minimizing intra-component variance, equivalently maximizing inter-component variance.

To be specific, the segmentation threshold t_T can be seen as the solution of the below optimization problem

$$t_T = \underset{r\in\{h_1,\ldots,h_{L-1}\}}{\operatorname{argmax}} \hat{a}^*(r)(1-\hat{a}^*(r))\left[\hat{\tau}_1^*(r) - \hat{\tau}_2^*(r)\right]^2 \tag{8}$$

where

$$\hat{a}^*(r) = \sum_{l=1}^{L} \hat{p}_l \mathbf{I}(h_l \le r), \quad \hat{\tau}_1^*(r) = \frac{\sum_{l=1}^{L} h_l \hat{p}_l \mathbf{I}(h_l \le r)}{\hat{a}^*(r)} \quad \text{and} \quad \hat{\tau}_2^*(r) = \frac{\sum_{l=1}^{L} h_l \hat{p}_l \mathbf{I}(h_l > r)}{1-\hat{a}^*(r)}.$$

Here, $\hat{a}^*(r)$ is the contribution of the first component, $\hat{\tau}_1^*(r)$ and $\hat{\tau}_2^*(r)$ are the average lifetimes of the first and second component if we choose the segmentation threshold at r. With segmentation threshold t_T, the estimated $\pi_1(t)$, $\pi_2(t)$, and a^* can be defined as

$$\hat{\pi}_1(t) = \frac{\sum_{l=1}^{L} \hat{p}_l \delta_{h_l} \mathbf{I}(h_l \le t_T)}{\hat{a}^*}, \qquad \hat{\pi}_2(t) = \frac{\sum_{l=1}^{L} \hat{p}_l \delta_{h_l} \mathbf{I}(h_l > t_T)}{1-\hat{a}^*},$$

and

$$\hat{a}^* = \sum_{l=1}^{L} \hat{p}_l \mathbf{I}(h_l \le t_T).$$

Clearly, this segmentation procedure relies on the separation assumption (7). When the distance between two components $\inf\{t : \pi_2(t)>0\} - \sup\{t : \pi_1(t)>0\}$ is larger, the prior distributions $\hat{\pi}_1(t)$ and $\hat{\pi}_2(t)$ can be separated more easily. Due to the fact that the prior distributions are estimated by pooling all photons together, we could expect very accurate estimations and are therefore able to separate two component in a more accurate way than conventional single-pixel fitting procedure. With $\hat{\pi}_1(t)$, $\hat{\pi}_2(t)$, and $\hat{a}^*$, we are in position to conduct pixel-wise lifetime recovery and integral property inference.

2.3. Pixel-wise Bayesian analysis

In this section, we show the pixel-wise lifetime recovery benefits from accurate estimated prior distribution as well. To incorporate the estimated prior distribution, we opt to adopt the empirical bayesian framework [26,29–31] to analyze FLIM photon counting data. Under the hierarchical model defined in Section 2.1, the posterior distribution of $\boldsymbol{\tau}_i, a_i$ can be written as

$$p(\boldsymbol{\tau}_i, a_i|\mathbf{N}_i) \propto \frac{(\sum_{j=1}^{m} N_{ij})!}{N_{i1}!\ldots N_{im}!} \prod_{j=1}^{m} \left(a_i P_j^{(\tau_{i1})} + (1-a_i) P_j^{(\tau_{i2})}\right)^{N_{ij}} \prod_{k=1}^{2} \pi_k(\tau_{ik}).$$

This posterior distribution can be seen as a mixture of local information (likelihood function) and global information (the prior distribution estimated from data across the pixels). The estimation at each pixel could be expectation or mode of the above posterior distribution. It is also worth noting that the expectation and mode of posterior should be similar because Bernstein-von Mises theorem suggests the posterior distribution converges to normal distribution when sample size at each pixel n_i goes to infinity [32].

Research Article | Vol. 10, No. 11 / 1 November 2019 / Biomedical Optics Express 5504
Biomedical Optics EXPRESS

Here, we consider the maximum of posterior distribution as our estimator after plugging in the prior distribution we estimated in Section 2.2. To be specific, the maximum of posterior distribution can be obtained by optimizing the following function

$$\min_{\tau_{i1},\tau_{i2},a_i} -\sum_{j=1}^{m} N_{ij} \log\left(a_i P_j^{(\tau_{i1})} + (1-a_i)P_j^{(\tau_{i2})}\right) - \sum_{k=1}^{2} \log\left(\hat{\pi}_k(\tau_{ik})\right). \tag{9}$$

To solve the above optimization problem, any optimization algorithm could be employed. In particular, we adopt the expectation-maximization (EM) algorithm [33] to solve the above optimization problem because it can provide a relatively stable estimation. At pixel i, a random variable $z_{is} \in \{1, 2\}$ is assigned to indicate which component the sth photon comes from, i.e.

$$j_{is}|z_{is} \sim \text{Multi}(1, \mathbf{P}_{(\tau_{iz_{is}})}) \quad \text{and} \quad P(z_{is}=1) = 1 - P(z_{is}=2) = a_i, \quad l = 1, \ldots, n_i,$$

where j_{is} is a random variable indicating into which bin the sth photon falls. EM algorithm consists of two main steps: expectation (E-step) and maximization (M-step). In the E-step, the posterior probability of z_{is} is evaluated given the estimation in the last step

$$\gamma_{ij}^{(t)} = P(z_{is}=1|j_{is}=j) = \frac{a_i^{(t)} P_j^{\left(\tau_{i1}^{(t)}\right)}}{a_i^{(t)} P_j^{\left(\tau_{i1}^{(t)}\right)} + (1-a_i^{(t)}) P_j^{\left(\tau_{i2}^{(t)}\right)}}.$$

Then, the Q function in EM algorithm can be written as

$$\begin{aligned} &Q(\boldsymbol{\tau}_i, a_i|\boldsymbol{\tau}_i^{(t)}, a_i^{(t)}) \\ &= \sum_{j=1}^{m} N_{ij}\left[\gamma_{ij}^{(t)} \log\left(a_i P_j^{(\tau_{i1})}\right) + (1-\gamma_{ij}^{(t)}) \log\left((1-a_i)P_j^{(\tau_{i2})}\right)\right] + \sum_{k=1}^{2} \log\left(\hat{\pi}_k(\tau_{ik})\right). \end{aligned}$$

In the M-step, we can then maximize a_i, τ_{i1}, and τ_{i2} in $Q(\boldsymbol{\tau}_i, a_i|\boldsymbol{\tau}_i^{(t)}, a_i^{(t)})$ separately

$$a_i^{(t+1)} = \frac{\sum_{j=1}^{m} N_{ij}\gamma_{ij}^{(t)}}{\sum_{j=1}^{m} N_{ij}}, \qquad \tau_{i1}^{(t+1)} = \underset{\tau_{i1}}{\text{argmax}} \sum_{j=1}^{m} N_{ij}\gamma_{ij}^{(t)} \log P_j^{(\tau_{i1})} + \log\left(\hat{\pi}_1(\tau_{i1})\right),$$

and

$$\tau_{i2}^{(t+1)} = \underset{\tau_{i2}}{\text{argmax}} \sum_{j=1}^{m} N_{ij}(1-\gamma_{ij}^{(t)}) \log P_j^{(\tau_{i2})} + \log\left(\hat{\pi}_2(\tau_{i2})\right).$$

These E-step and M-step are repeated until the estimation converges.

One challenge of EM algorithm in practice is the choice of initial values, $\tau_{i1}^{(0)}$, $\tau_{i2}^{(0)}$, and $a_i^{(0)}$, as different initial values might lead to different local optimum points. Fortunately, the estimated prior distribution could provide a good guidance for good choices of initial values because the support of $\hat{\pi}_1(t)$ and $\hat{\pi}_2(t)$ can allow us to narrow the search region down. More specifically, we choose $\tau_{i1}^{(0)}$ as 5% lower quantile of $\hat{\pi}_1(t)$, $\tau_{i2}^{(0)}$ as 5% upper quantile of $\hat{\pi}_2(t)$, and $a_i^{(0)}$ as the estimation $\hat{a}^*$. When the support of prior distribution lies in a small region, the EM algorithm can be accelerated a lot based on the above choices of initial values. Another challenge of the EM algorithm is slow convergence speed in practice. To accelerate the EM algorithm, we also adopt the acceleration scheme in [34].

Research Article | Vol. 10, No. 11 / 1 November 2019 / Biomedical Optics Express 5505
Biomedical Optics EXPRESS

2.4. Integral property inference

Different from pixel-wise lifetime recovery, integral property inference aims to estimate/test a functional of pixel-wise parameters. Under the hierarchical model in Section 2.1, a functional of pixel-wise parameters can be written as a functional of prior distribution. Thus, we consider the estimation of linear functional of prior distribution in this section. To be specific, for any given function $g(t)$ defined on $[T_L, T_U]$, the goal is to estimate the following linear functional

$$F_k(g) = \int_{T_L}^{T_U} g(t) d\pi_k(t), \qquad k = 1, 2. \tag{10}$$

Most summarized statistics of interest in FLIM studies can be written in the combination form of linear functional. For example, the mean and variance of lifetime of the kth component τ_k^* and $v(\tau_k)$ can be written as

$$\tau_k^* := \int t d\pi_k(t) \qquad \text{and} \qquad v(\tau_k) := \int t^2 d\pi_k(t) - \left(\int t d\pi_k(t) \right)^2. \tag{11}$$

Another example is the mean of physical contributions of the first and second components

$$A_1^* := \frac{1}{|\mathbb{I}|} \sum_{i \in \mathbb{I}} A_{i1} = \frac{a^* \int \frac{1}{t} d\pi_1(t)}{a^* \int \frac{1}{t} d\pi_1(t) + (1 - a^*) \int \frac{1}{t} d\pi_2(t)} \qquad \text{and} \qquad A_2^* = 1 - A_1^*.$$

Therefore, we mainly focus on estimation of functional in (10).

To summarize the pixel-wise information, the most commonly used estimator in practice for $F_k(g)$ is plugin estimator of pixel-wise fitted lifetime in the last section

$$\hat{F}_k^{\text{naive}}(g) = \frac{1}{|\mathbb{I}|} \sum_{i \in \mathbb{I}} g(\hat{\tau}_{ik}), \qquad k = 1, 2.$$

If we write the empirical distribution of $\hat{\tau}_{ik}$ as $\widetilde{\pi}_k$, then the above estimator can be rewritten as $\hat{F}_k^{\text{naive}}(g) = \int g(t) d\widetilde{\pi}_k$. This suggests that $\hat{F}_k^{\text{naive}}(g)$ is a plugin estimator of empirical distribution of $\hat{\tau}_{ik}$. Motivated by this observation, we consider a plugin estimator of estimated prior distribution in Section 2.2

$$\hat{F}_k^{\text{NEB}}(g) = \int g(t) d\hat{\pi}_k(t), \qquad k = 1, 2.$$

As we mentioned in the introduction, $\hat{F}_k^{\text{NEB}}(g)$ is a much more accurate and computationally efficient estimator for $F_k(g)$ because NPMLE $\hat{\pi}_k(t)$ is more precise and easy to compute. Later, we discuss its performance in more details in Section 3.

To illustrate the idea of NPMLE plug-in estimator, we show the explicit expression of five commonly used summarized statistics: mean of lifetime τ_1^* and τ_2^*, mean of physical contributions A_1^* and A_2^*, and mean of average lifetime

$$\tau_m^* := \frac{1}{|\mathbb{I}|} \sum_{i \in \mathbb{I}} \left(A_{i1} \tau_{i1} + A_{i2} \tau_{i2} \right).$$

By plugging in $\hat{\pi}_1(t)$ and $\hat{\pi}_2(t)$, the estimator for these summarized statistics are defined as

$$\hat{\tau}_1^* = \int t d\hat{\pi}_1(t) \qquad \text{and} \qquad \hat{\tau}_2^* = \int t d\hat{\pi}_2(t),$$

$$\hat{A}_1^* = \frac{\hat{a}^* \int \frac{1}{t} d\hat{\pi}_1(t)}{\hat{a}^* \int \frac{1}{t} d\hat{\pi}_1(t) + (1 - \hat{a}^*) \int \frac{1}{t} d\hat{\pi}_2(t)} \qquad \text{and} \qquad \hat{A}_2^* = 1 - \hat{A}_1^*,$$

Research Article | Vol. 10, No. 11 / 1 November 2019 / Biomedical Optics Express 5506
Biomedical Optics EXPRESS

and

$$\hat{\tau}_m^* = \hat{A}_1^* \hat{\tau}_1^* + \hat{A}_2^* \hat{\tau}_2^*.$$

All above estimators are transformed from prior distribution estimation $\hat{\pi}^*(t)$ directly, so they are easy to compute.

2.5. Practical considerations

After we combine all components introduced in the previous sections, the new non-parametric empirical bayesian framework for FLIM data (NEB-FLIM) is summarized in Fig. 3. In the step of prior distribution estimation, the core component is the optimization problem in (6). After obtaining data M_j for each bin, the optimization problem in (6) is ready to be solved by 'REBayes' R package [35]. To segment the estimated prior distribution, we calculate the object function (8) at each h_l, $l = 1, \ldots, L$ and take h_l achieving the maximum of them as the cutting threshold t_T.

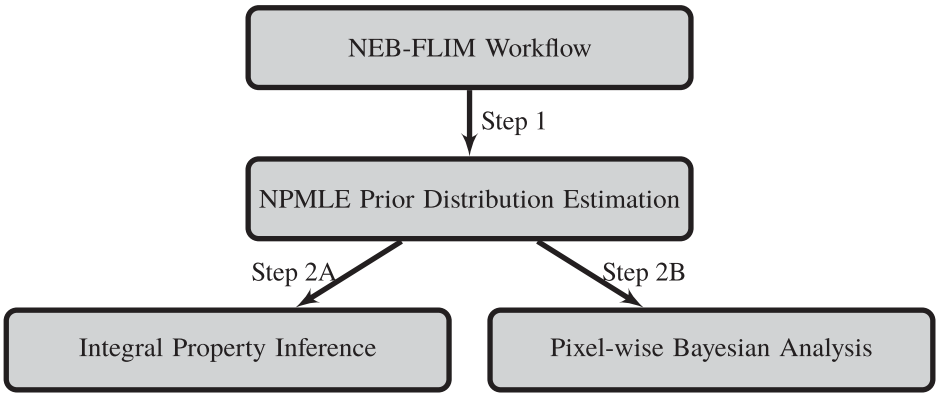

Fig. 3. Flow chart of the non-parametric empirical bayesian framework for FLIM data (NEB-FLIM).

After estimating the prior distribution, the estimated prior distribution can be then used to conduct integral property inference or pixel-wise Bayesian analysis. The integral property inference can be completed by common used numerical integration algorithms. For simplicity, we just take $\sum_{l=1}^{L} g(h_l)p_l$ as $\hat{F}_k^{\mathrm{NEB}}(g)$ for any function g and $k = 1, 2$. Here, p_l is the probability mass of $\hat{\pi}_k(t)$ at lth bin between h_{l-1} and h_l. The pixel-wise Bayesian analysis is implemented by EM algorithm as we described in previous section. We adopt scheme of [34] to accelerate the EM algorithm and stop the iteration when the object function is increased less than 10^{-2} (or any small number) in one iteration or number of iteration reaches some maximum number.

In this NEB-FLIM framework, there are mainly three tuning parameters: the lower bound of lifetime T_L, the upper bound of lifetime T_U and the number of intervals L. T_L and T_U are chosen according to the specific application. The choice of L is very important, as larger L usually implies more accurate estimation of prior distribution, but more computation time as well. We discuss the choice of L in more details in the later section.

3. Results

We now conduct numerical experiments to demonstrate the merits of our nonparametric empirical bayesian FLIM analysis framework (NEB-FLIM) in this section.

3.1. Simulation

The first simulation experiment we consider here is to assess the performance of prior distribution $\pi^*(t)$ estimation. To this end, we simulated FLIM images on a 32×32 square lattice $\mathbb{I}$ according

Research Article | Vol. 10, No. 11 / 1 November 2019 / Biomedical Optics Express 5507
Biomedical Optics EXPRESS

to the model described in Section 2.1. We assumed the period of laser excitation, T_p, was 10000 ps (or 10 ns), ratio of background photons, α, was 0.001, and $[0, T_p]$ was divided into $m = 256$ bins. The IRF h we use in this experiment is gaussian distribution function with mean 1500 ps and standard deviation 100 ps. At each pixel $i \in \mathbb{I}$, we assumed there were two types of fluorescence, and $\mathbf{N}_i$ was randomly generated from the following bi-exponential model

$$a\frac{1}{\tau_1}e^{-\frac{t}{\tau_1}} + (1-a)\frac{1}{\tau_2}e^{-\frac{t}{\tau_2}}.$$

The pixel-wise lifetime of both components (τ_{i1}, τ_{i2}) and the contribution of the first component a_i are shown in Fig. 4. For simplicity, the number of photons at each pixel $i \in \mathbb{I}$ is assumed to be equal, i.e. $n_i = n,\ \forall i \in \mathbb{I}$.

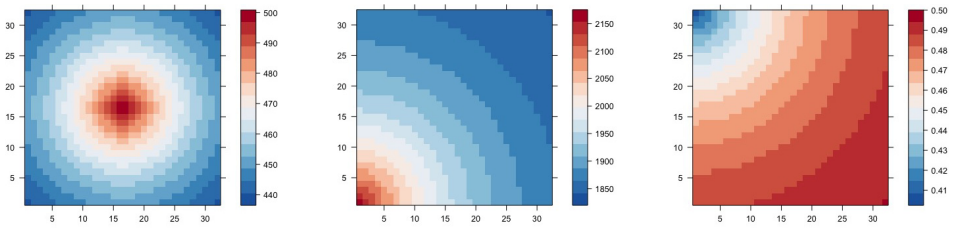

(a) τ_1 truth (b) τ_2 truth (c) a truth

Fig. 4. Ground truth of τ_1, τ_2, and a in simulation. All lifetimes in the figures are shown in picosecond(ps).

In this simulation experiment, we compare the performance of prior distribution estimation at different numbers of photons per pixel n and different numbers of intervals L in NPMLE. To assess the performance, we calculate the L_2 distance between cumulative distribution of the true prior distribution $\pi^*(t)$ and our estimator $\hat{\pi}^*(t)$

$$D(\pi^*(t), \hat{\pi}^*(t)) = \int_{T_L}^{T_U} \left(F_\pi(t) - \hat{F}_\pi(t)\right)^2 dt,$$

where

$$F_\pi(t) = \frac{1}{|\mathbb{I}|}\sum_{i\in\mathbb{I}}[a_i\mathbf{I}(\tau_{i1} \le t) + (1-a_i)\mathbf{I}(\tau_{i2} \le t)] \qquad \text{and} \qquad \hat{F}_\pi(t) = \sum_{l=1}^{L} p_l\mathbf{I}(h_l \le t).$$

We chose $T_L = 200$ ps and $T_U = 3000$ ps in this experiment and assumed they are known. We conducted the experiment when number of photons at each pixel n was 10^1, $10^{1.5}$, 10^2, $10^{2.5}$, 10^3, $10^{3.5}$, and 10^4 and number of intervals L in NPMLE was 400, 600, 800, 1000, and 1200. The experiment was repeated 100 times at each combination of n and L. We summarized the mean error of $D(\pi^*(t), \hat{\pi}^*(t))$ in 100 experiments in Fig. 5. The Fig. 5 suggests that the prior distribution in general is well estimated, even in a low photon regime, e.g. $n = 10$. Through the results in Fig. 5, we can also conclude that increasing L could help reduce the bias when the number of photons is large and small L is relatively robust when there are not many photons at each pixel.

We designed the next two simulation experiments to compare NEB-FLIM and previous methods. In particular, we mainly focus on two of the most popular methods: pixel-wise analysis and global analysis. As mentioned before, pixel-wise analysis methods fit the exponential curve only by photons at each pixel [8–10]. In this simulation experiment, we only focus on likelihood

Research Article | Vol. 10, No. 11 / 1 November 2019 / Biomedical Optics Express 5508
Biomedical Optics EXPRESS

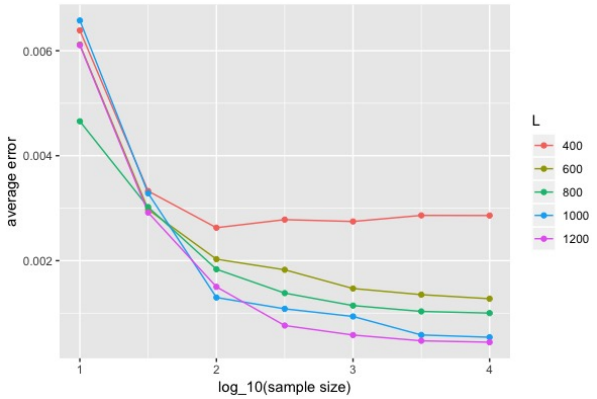

Fig. 5. Performance of lifetime prior distribution estimation at different n and L: the average error $D(\pi^*(t), \hat{\pi}^*(t))$ against logarithm of number of photons per pixel $\log n$. Different colors represent different numbers of intervals L.

based pixel-wise analysis, as it has been shown more efficient than other popular pixel-wise analysis methods [9]. The global analysis estimates lifetime of two components globally and then estimates the components' contribution at each pixel [7,12,13]. The two experiments are designed to compare the performance in terms of pixel-wise lifetime recovery and integral property inference, respectively.

We now compare performance of pixel-wise lifetime recovery. To this end, we still followed the bi-exponential model and chose the same setting with the previous experiment. L was chosen at $L = 1400$. The performance of each method is assessed by the mean square error

$$\frac{1}{|\mathbb{I}|}\sum_{i\in\mathbb{I}}(r(\hat{\boldsymbol{\tau}}_i, \hat{a}_i) - r(\boldsymbol{\tau}_i, a_i))^2,$$

where $r(\boldsymbol{\tau}_i, a_i)$ can be any function of $\boldsymbol{\tau}_i$ and a_i. In particular, we chose $r(\boldsymbol{\tau}_i, a_i) = \tau_{i1}$, τ_{i2} and a_i in this simulation experiment. We conducted the experiment when the number of photons at each pixel n was $10^2, 10^{2.5}, 10^3, 10^{3.5}, 10^4$, and $10^{4.5}$. The results are summarized in Fig. 6. As suggested by Fig. 6, pixel-wise analysis is more reliable than global analysis when there are enough available photons at each pixel, while the latter can provide relatively robust estimations in the low-photon regime. Figure 6 also shows that NEB-FLIM is always able to achieve better performance due to the fact that empirical Bayesian analysis combines both local and global information.

We design the next experiment to assess performance of integral property inference. To be specific, we compare four different methods to estimate the mean of lifetime τ_1^* and τ_2^* defined in (11). The four methods we would like to compare are: direct integral property inference in NEB-FLIM(PI-NEB), mean of pixel-wise lifetime estimated by NEB-FLIM(PBA-NEB), mean of pixel-wise lifetime estimated by pixel-wise analysis(PA), and mean of pixel-wise lifetime estimated by global analysis(GA). To compare these methods, we follow the same settings of previous experiments, but consider different sample sizes per pixel: $n = 50$, 100, and 200. For each n, the experiment was repeated 100 times, and for each time, we applied these four methods on the generated FLIM image. We assessed the performance of estimating τ_1^* and τ_2^* by evaluating square root of mean square error

$$e(\tau_k) := \sqrt{\frac{1}{H}\sum_{h=1}^{H}(\hat{\tau}_{kh}^* - \tau_k^*)^2},$$

Research Article | Vol. 10, No. 11 / 1 November 2019 / Biomedical Optics Express 5509
Biomedical Optics EXPRESS

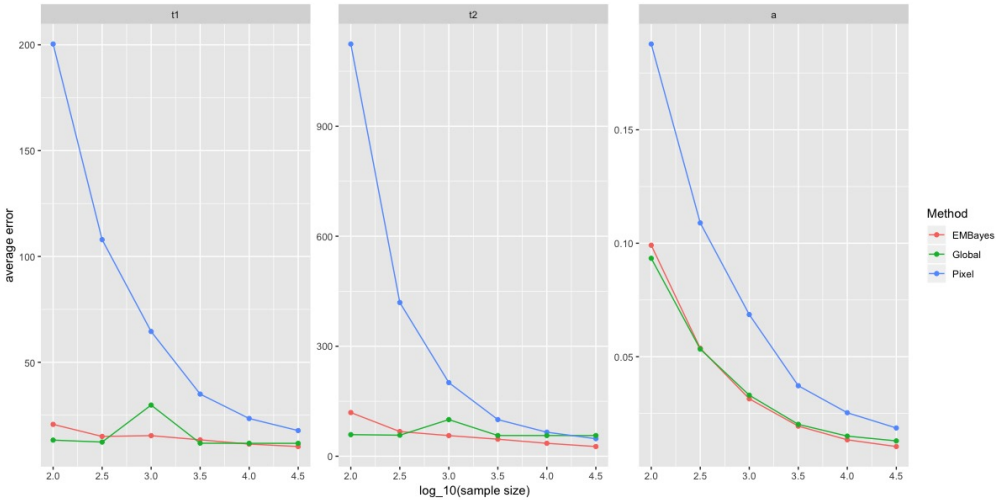

Fig. 6. Pixel-wise recovery performance comparisons between pixel-wise analysis, global analysis, and NEB-FLIM: the plots are of mean square error across the image against the number of photons per pixel. All results of lifetimes in the figures are shown in ps^2. Left is plot of τ_1; middle is plot of τ_2 and right is plot of a.

where H is total number of simulation experiments and $\hat{\tau}^*_{kh}$ is the estimation τ^*_k at the hth simulation experiment. The results are summarized in Table 1. As shown in Table 1, it is clear that direct integral property inference in NEB-FLIM(PI-NEB) has better performance than the other methods.

Table 1. Accuracy comparisons between different integral property inference methods: PI-NEB=direct integral property inference in NEB-FLIM, PBA-NEB=mean of pixel-wise lifetime estimated by NEB-FLIM, PA=mean of pixel-wise lifetime estimated by pixel-wise analysis, and GA=mean of pixel-wise lifetime estimated by global analysis. The error criteria is square root of mean square error $e(\tau_k)$ for $k = 1, 2$. All results in the table are shown in ps.

	$n = 200$		$n = 100$		$n = 50$	
	$e(\tau_1)$	$e(\tau_2)$	$e(\tau_1)$	$e(\tau_2)$	$e(\tau_1)$	$e(\tau_2)$
PI-NEB	10.32	16.47	10.10	20.08	17.36	29.43
PBA-NEB	12.50	26.30	14.53	174.43	65.83	315.41
PA	9.73	114.83	6.68	310.79	14.53	452.99
GA	4.72	13.18	12.70	53.87	34.42	73.13

In the last experiment, we evaluate different methods for integral property inference from computation efficiency angle. In particular, we followed the same bi-exponential model in previous experiments and simulated image on 32×32, 64×64 and 128×128 square lattice. The number of photons at each pixel n is chosen as 10^3. We compare the computation time of 4 different methods to estimate the mean of lifetime τ^*_1 and τ^*_2: direct integral property inference in NEB-FLIM with $L = 400$ and 800 (NEB-400 and NEB-800), plugin estimator of pixel-wise lifetime estimated by pixel-wise analysis(PA), and plugin estimator of pixel-wise lifetime estimated by global analysis(GA). To make comparison fair, all the algorithms are implemented in R and evaluated in the same desktop (Intel Core i5 @3.4 GHz/16GB). The computing times of all algorithms are reported in Table 2, which is based on 10 runs for each image size. It is clear from Table 2 that direct integral property inference in NEB-FLIM is faster than the other two methods. Moreover, the speed of NEB-FLIM mainly relies on the choice of L,

Research Article Vol. 10, No. 11 / 1 November 2019 / Biomedical Optics Express 5510
Biomedical Optics EXPRESS

but not the image size. It is also worth noting that the computation speed may depend on choice the programming language, computing environment and specific implementation, so all these algorithms might be accelerated under other programming languages or implementation.

Table 2. Computation speed comparisons between different integral property inference methods: NEB-400, NEB-800=direct integral property inference in NEB-FLIM with L = 400 and 800, PA=plugin estimator of pixel-wise lifetime estimated by pixel-wise analysis, and GA=plugin estimator of pixel-wise lifetime estimated by global analysis. The computation time in the table is shown in seconds.

Image Size	NEB-400	NEB-800	PA	GA
32×32	0.283	1.184	23.579	0.170
64×64	0.293	1.181	94.650	0.689
128×128	0.331	1.200	375.310	2.581

3.2. Real data example

Finally, we consider a specific biological dataset examining the metabolic state of cancer/normal living cells by measuring lifetime of reduced nicotinamide adenine dinucleotide (NADH). FLIM has been shown to be able to distinguish between free and protein bound state of NADH, as the two states of NADH have different fluorescence lifetimes [3,36]. The first component refers to free NADH, and the second component refers to the protein-bound NADH. Higher contribution of free NADH and hence lower average lifetime value, $A_1\tau_1 + A_2\tau_2$, has been found to correlate with higher glycolytic metabolism. Apart from NADH lifetime imaging, FLIM can also be used to visualize flavin adenine dinucleotide (FAD) lifetime for early detection of cancer and for other micro-environment measurement of viscosity, pH and others [4].

This FLIM data set includes NADH FLIM data of MDA-MB-231 breast cancer cells and MCF10A normal cells. The excitation source was a Ti:Sapphire laser (Spectra Physics; Maitai) tuned to wavelength of 740 nm. The excitation and emission were coupled through an inverted microscope (Nikon; Eclipse TE300) with a 20x objective (Nikon, Plan Fluor, N.A. 0.75). A 450/70-nm band-pass emission filter (Semrock, Rochester. NY) was also used to selectively collect the NADH fluorescence emission signal. For each type of cell, FLIM images were collected at 256x256 resolution at 4 different durations(20, 60, 120, and 240 seconds) using SPC-150 Photon Counting Electronics (Becker & Hickl GmbH, Berlin, Germany) and Hamamatsu H7422P-40 GaAsP photomultiplier tube (Hamamatsu Photonics, Bridgewater, NJ). Urea crystals were used to measure the Instrumental Response Function (IRF) with a 370/10 bandpass emission filter (Semrock, Rochester. NY). Emission intensity was checked by the photon counts after each imaging session to make sure there was no photobleaching or photodamage of the sample. For each duration and sample, the average numbers of photons per pixel, $\bar{n}$, are summarized in Table 3.

We estimated the prior distribution of lifetime $\pi^*(t)$ by setting $T_L = 2$, $T_U = 4000$, and $L = 500$. We applied NEB-FLIM to extract summarized information directly from prior distributions estimated by these 8 FLIM images. In particular, we estimated the mean of statistical component contribution a^*, mean of lifetime of the first component τ_1^*, mean of lifetime of the second component τ_2^*, mean of physical component contribution (after normalization) A_1^*, A_2^* and mean of weighted averaged lifetime τ_m^*. All these results are summarized in Table 3. To assess the potential uncertain brought by different field-of-views, we randomly chose regions of size 128×128 from the original image and applied intergal property inference of NEB-FLIM to estimate mean of weighted averaged lifetime τ_m^* on each chosen region. The estimated weighted averaged lifetime τ_m^* and corresponding standard deviation are reported in Fig. 7, which are based on 100 runs for each combination of duration and cell type. Through Table 3 and Fig. 7, we can conclude that the integral property inference of NEB-FLIM is relatively stable with respect to

Research Article | Vol. 10, No. 11 / 1 November 2019 / Biomedical Optics Express 5511
Biomedical Optics EXPRESS

Table 3. Summarized information of the biological data set estimated by direct integral property inference of NEB-FLIM: the average number of photons per pixel $\bar{n}$, the mean of statistical component contribution a^*, mean of lifetime of the first component τ_1^*, mean of lifetime of the second component τ_2^*, mean of physical component contribution (after normalization) A_1^*, A_2^* and mean of weighted averaged lifetime τ_m^* All results of lifetime in the table are shown in picosecond.

	Time	$\bar{n}$	$\hat{a}^*$	$\hat{\tau}_1^*$	$\hat{\tau}_2^*$	$\hat{A}_1^*$	$\hat{A}_2^*$	$\hat{\tau}_m^*$
MDA-MB-231	20s	32.1	0.212	324.2	2516.7	0.683	0.317	1018.3
	60s	96.4	0.208	321.7	2506.5	0.675	0.325	1032.4
	120s	200.0	0.207	331.1	2514.4	0.668	0.332	1055.2
	240s	411.4	0.204	337.7	2526.1	0.661	0.339	1078.6
MCF10A	20s	27.1	0.162	567.5	2627.1	0.475	0.525	1648.8
	60s	79.0	0.168	567.4	2625.1	0.486	0.514	1625.3
	120s	155.7	0.158	573.4	2639.6	0.466	0.534	1676.0
	240s	401.6	0.155	493.1	2670.1	0.499	0.501	1583.4

the imaging time. In other words, NEB-FLIM provides a robust estimation even in low-photon regime. If we compare these two samples, the results suggest cancer cells MDA-MB-231 have a larger mean of physical component contribution A_1 and smaller weighted averaged lifetime τ_m than normal cell MCF10A cells. This discovery is consistent with results of previous experiments in [4]. The difference between NADH lifetime/cell metabolic state can be easily captured by our new method when the imaging time is 20s (~30 photons per pixel). It is also worth noting that the processing time of integral property inference of NEB-FLIM on each image is less than 1 second on a common desktop (Intel Core i5 @3.4 GHz/16GB).

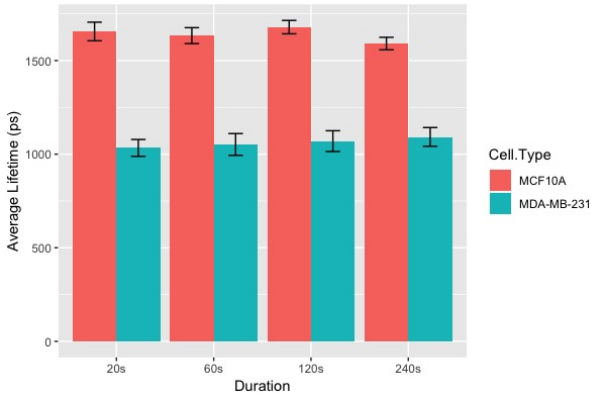

Fig. 7. Average estimated mean of weighted averaged lifetime τ_m^* with error bar of double standard deviation for each imaging duration and cell type. The plot is summarized from results of intergal property inference of NEB-FLIM on 100 randomly chosen regions.

To compare performance of pixel-wise curve fitting, we applied NEB-FLIM, pixel-wise analysis (maximum likelihood estimation based), and global analysis on these 8 FLIM images. In particular, we did 3×3 binning at each pixel to accumulate more photons. To make the comparisons fair, the initial values of pixel-wise analysis and global analysis were also guided by the prior distribution as NEB-FLIM, although this way might improve the accuracy of pixel-wise analysis and global analysis. Due to space limits, we only showed the physical component contribution A_2 and weighted average lifetime τ_m, which are shown in Fig. 8 and Fig. 9 (top right corresponds to MCF10A cells and bottom left corresponds to MDA-MB-231 cells). To summarize the fitting result of estimated lifetime, we also made density plot of pixel-wise

Research Article Vol. 10, No. 11 / 1 November 2019 / Biomedical Optics Express 5512
Biomedical Optics EXPRESS

estimated lifetime of MCF10A Cell in Fig. 10. Through Fig. 8, Fig. 9 and Fig. 10, our proposed NEB-FLIM framework behaves almost the same with pixel-wise analysis when the number of photons is large (imaging time 240s). Furthermore, if we regard the result of imaging time 240s as a benchmark, we could see that the performance of our NEB-FLIM framework is better than the other two methods when the imaging time is short (e.g. 60s).

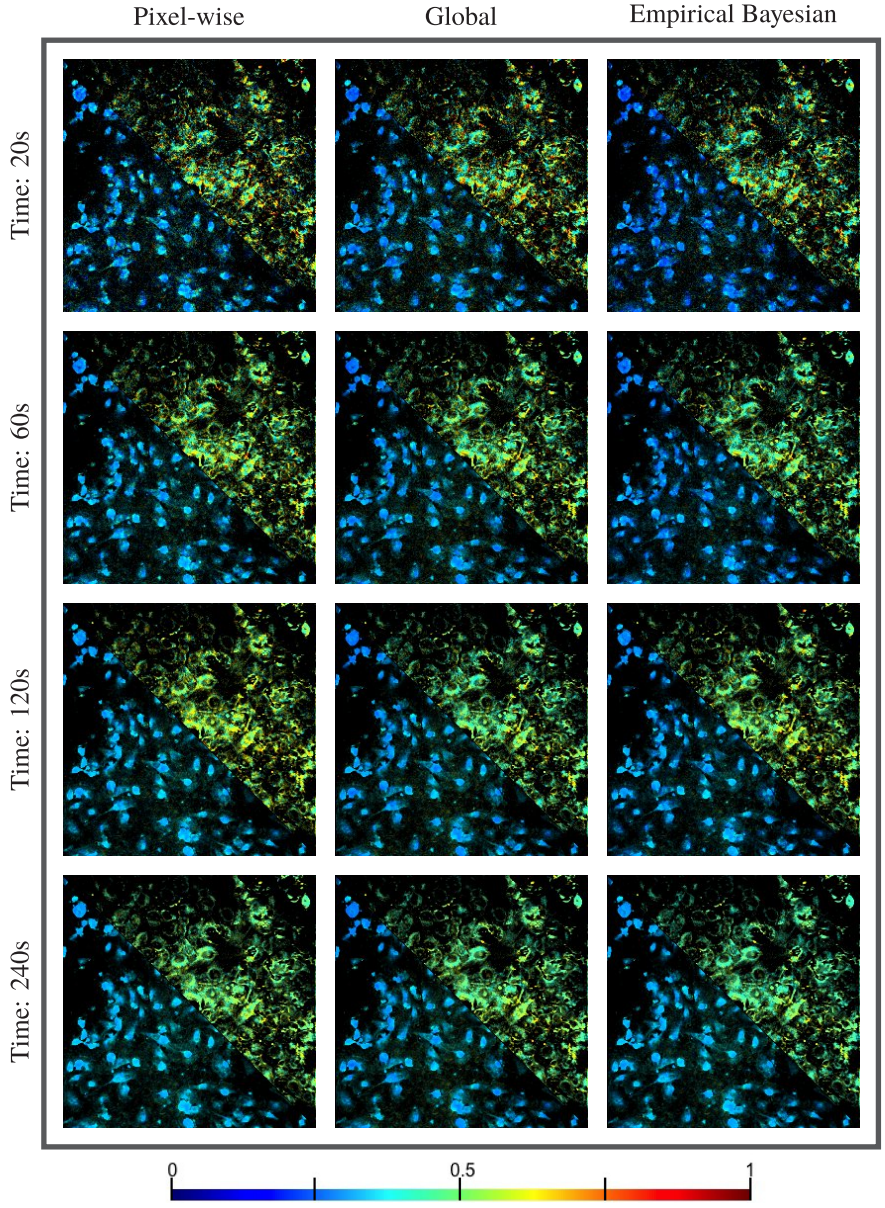

Fig. 8. Comparisons of pixel-wise recovery result by pixel analysis, global analysis, and empirical bayesian analysis on real datasets: pixel-wise physical component contribution A_2. Top right is MCF10A cells and bottom left is MDA-MB-231 cells. The imaging time from top to bottom is 20s, 60s, 120s and 240s.

Research Article Vol. 10, No. 11 / 1 November 2019 / Biomedical Optics Express 5513
Biomedical Optics EXPRESS

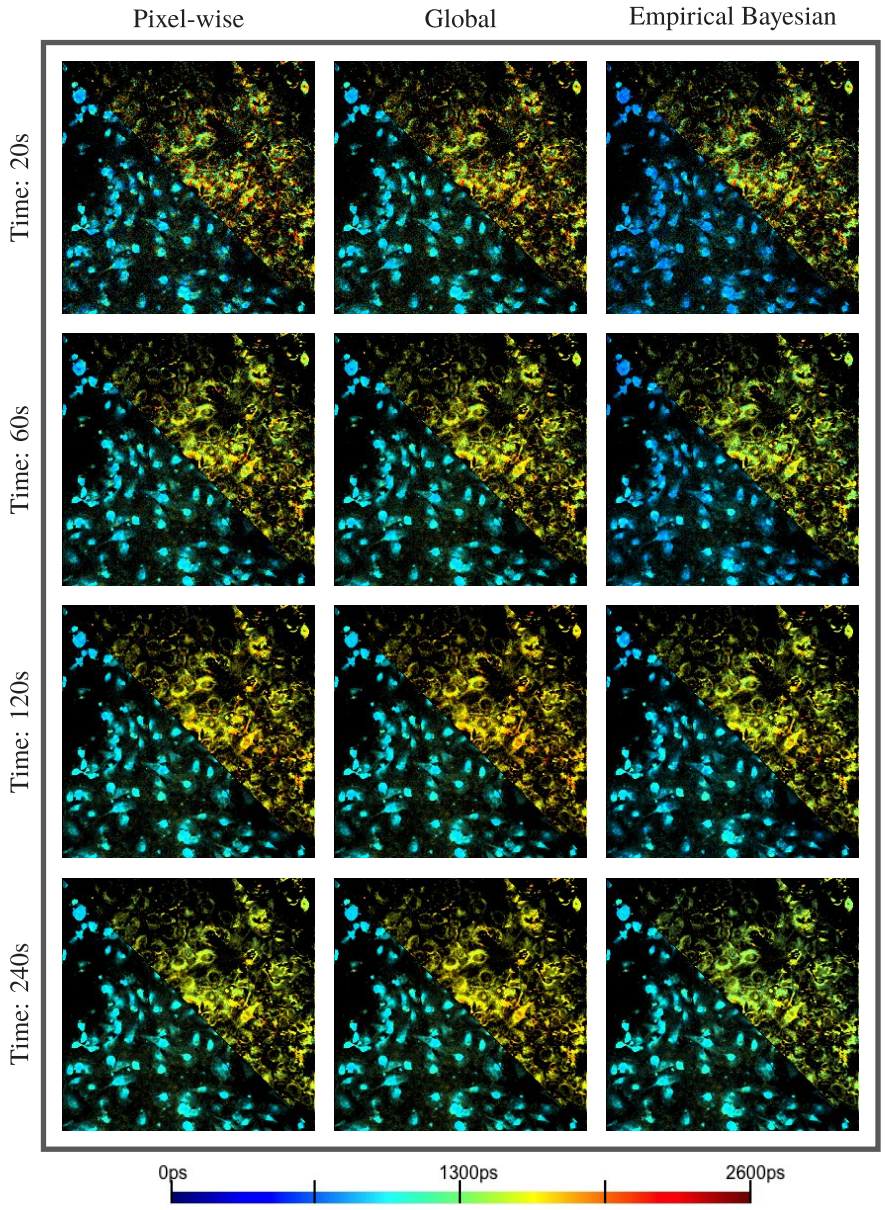

Fig. 9. Comparisons of pixel-wise recovery result by pixel analysis, global analysis, and empirical bayesian analysis on real dataset: pixel-wise weighted average lifetime τ_m in ps. Top right is MCF10A cells and bottom left is MDA-MB-231 cells. The imaging time from top to bottom is 20s, 60s, 120s and 240s.

Research Article | Vol. 10, No. 11 / 1 November 2019 / Biomedical Optics Express 5514
Biomedical Optics EXPRESS

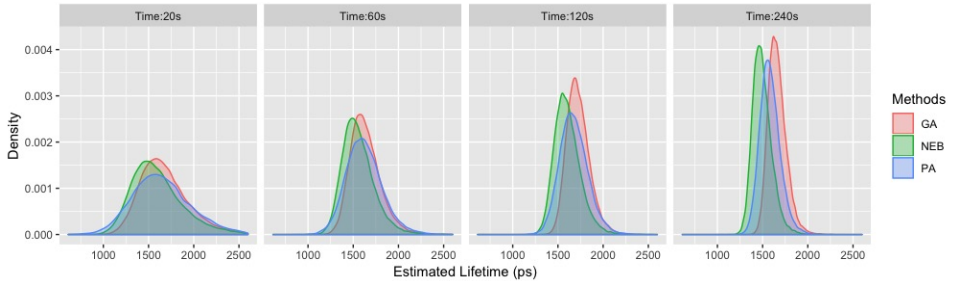

Fig. 10. Density plot of estimated weighted averaged lifetime τ_m^* of MCF10A cell for different pixel-wise lifetime recovery methods and imaging time: NEB=pixel-wise lifetime estimated by NEB-FLIM, PA=pixel-wise lifetime estimated by pixel-wise analysis, and GA=pixel-wise lifetime estimated by global analysis.

Finally, we compare the results of property inference (just as in the third simulation experiment). The lifetimes of images with imaging time 20s and 240s are summarized in Table 4. We followed the same procedure in Fig. 7 to evaluate the potential uncertain arose from choices of field-of-views, which is summarized in Fig. 11. It is clear that all methods can detect the difference of NADH lifetime between two types of cells. However, if we regard the recovery results of pixel-wise analysis (PA) when the imaging time is 240s as the benchmark, the performance of PI-NEB is better than the other methods when the imaging time is 20s (see e.g. MCF10A cell), especially better than pixel-wise analysis, the most popular method. This suggests that NEB-FLIM proposed in this article is able to recover more accurately summarized information and tell subtle differences between cells in both high and low photon regimes.

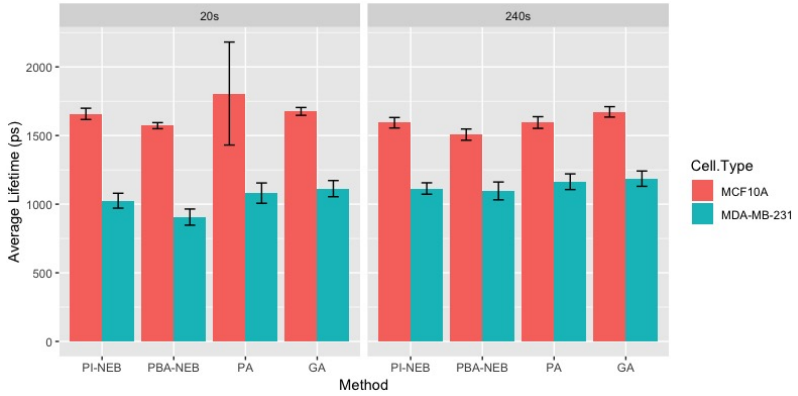

Fig. 11. Average estimated mean of weighted averaged lifetime τ_m^* with error bar of standard deviation for different methods, imaging time and cell types. The results are summarized from estimation results of NEB-FLIM on 100 randomly chosen regions for each combination of method, imaging time and cell type.

Research Article | Vol. 10, No. 11 / 1 November 2019 / Biomedical Optics Express 5515
Biomedical Optics EXPRESS

Table 4. Comparisons between different property inference methods on real data: PI-NEB=direct integral property inference in NEB-FLIM, PBA-NEB=mean of pixel-wise lifetime estimated by NEB-FLIM, PA=mean of pixel-wise lifetime estimated by pixel-wise analysis, and GA=mean of pixel-wise lifetime estimated by global analysis. All results of lifetime in the table are shown in picosecond.

	Method	$\hat{a}^*$	$\hat{\tau}_1^*$	$\hat{\tau}_2^*$	$\hat{A}_1^*$	$\hat{A}_2^*$	$\hat{\tau}_m^*$
MDA-MB-231, 20s	PI-NEB	0.212	324.2	2516.7	0.683	0.317	1018.3
	PBA-NEB	0.142	187.4	2492.7	0.688	0.312	907.5
	PA	0.197	326.6	2585.3	0.666	0.334	1081.5
	GA	0.196	312.6	2534.6	0.639	0.361	1115.4
MDA-MB-231, 240s	PI-NEB	0.204	337.7	2526.1	0.661	0.339	1078.6
	PBA-NEB	0.170	274.2	2517.9	0.648	0.352	1064.9
	PA	0.183	322.3	2551.5	0.636	0.364	1132.9
	GA	0.185	329.5	2547	0.628	0.372	1154.8
MCF10A, 20s	PI-NEB	0.162	567.5	2627.1	0.475	0.525	1648.8
	PBA-NEB	0.121	458.7	2637.4	0.496	0.504	1556.3
	PA	0.153	589.8	2646.5	0.391	0.609	1841.4
	GA	0.173	557.7	2629	0.466	0.534	1664.4
MCF10A, 240s	PI-NEB	0.155	493.1	2670.1	0.499	0.501	1583.4
	PBA-NEB	0.138	394.6	2668.6	0.516	0.484	1495.8
	PA	0.152	485.4	2662.1	0.495	0.505	1584.6
	GA	0.177	586.9	2718.1	0.496	0.504	1661.9

4. Discussion and conclusion

In this paper, we propose a new empirical bayesian framework for fluorescence lifetime imaging microscopy data (NEB-FLIM). Different from previous analysis workflows, our new NEB-FLIM framework first estimates the prior distribution of lifetime non-parametrically by using all photons across the whole image. This empirical prior distribution can either be used to conduct integral property inference directly or be incorporated into bayesian analysis to fit an exponential curve at each pixel. Through this method, the summarized information can be estimated very accurately and efficiently computationally. This leads to its potential usage in applications of FLIM requiring either short acquisition or computation times, such as when previewing the lifetime status of cells/tissues before formal analysis and real-time fluorescence lifetime tracking. Due to incorporation of this empirical distribution, the pixel-wise lifetime recovered by NEB-FLIM combines both global and local information, allowing more robust quantification of lifetime at each pixel.

In this presented paper, we only focus on NEB-FLIM framework within the context of a pixel-wise double exponential lifetime model. However, NEB-FLIM, as a generalized framework, can be extend to multiple exponential lifetime models at each pixel. If we assume there is a large gap between different components of lifetime, we can still apply NEB-FLIM to estimate prior distributions by replacing the binary segmentation method with some clustering method which segments the prior distribution into multiple pieces.

The key component to estimate the prior distribution in NEB-FLIM framework is the deconvolution problem in (5). In NEB-FLIM, we adopt linear programming to solve it after data collection. On the other hand, when data becomes available in a sequential order, this deconvolution problem is still solvable if we adopt some online learning algorithm. In other words, we can estimate the prior distribution at the same time as data acquisition. The prior distribution estimation and integral property inference can be completed just after data collection.

Research Article | Vol. 10, No. 11 / 1 November 2019 / Biomedical Optics Express 5516
Biomedical Optics EXPRESS

Funding

U.S. Department of Energy (DE-SC0019013, Morgridge Institute for Research).

Acknowledgments

We thank Dr. Ellen T. Arena of the University of Wisconsin-Madison for careful reading of an earlier draft that has led to improved presentation.

Disclosures

The authors declare that there are no conflicts of interest related to this article.

References

1. W. Becker, *Advanced Time-correlated Single Photon Counting Techniques*, vol. 81 (Springer, 2005).
2. W. Becker, *Advanced Time-correlated Single Photon Counting Applications*, vol. 111 (Springer, 2015).
3. D. K. Bird, L. Yan, K. M. Vrotsos, K. W. Eliceiri, E. M. Vaughan, P. J. Keely, J. G. White, and N. Ramanujam, "Metabolic mapping of MCF10A human breast cells via multiphoton fluorescence lifetime imaging of the coenzyme NADH," Cancer Res. **65**(19), 8766–8773 (2005).
4. A. J. Walsh, R. S. Cook, H. C. Manning, D. J. Hicks, A. Lafontant, C. L. Arteaga, and M. C. Skala, "Optical metabolic imaging identifies glycolytic levels, subtypes, and early-treatment response in breast cancer," Cancer Res. **73**(20), 6164–6174 (2013).
5. M. C. Skala, K. M. Riching, D. K. Bird, A. Gendron-Fitzpatrick, J. Eickhoff, K. W. Eliceiri, P. J. Keely, and N. Ramanujam, "In vivo multiphoton fluorescence lifetime imaging of protein-bound and free nicotinamide adenine dinucleotide in normal and precancerous epithelia," J. Biomed. Opt. **12**(2), 024014 (2007).
6. S. Pelet, M. Previte, L. Laiho, and P. So, "A fast global fitting algorithm for fluorescence lifetime imaging microscopy based on image segmentation," Biophys. J. **87**(4), 2807–2817 (2004).
7. S. C. Warren, A. Margineanu, D. Alibhai, D. J. Kelly, C. Talbot, Y. Alexandrov, I. Munro, M. Katan, C. Dunsby, and P. French, "Rapid global fitting of large fluorescence lifetime imaging microscopy datasets," PLoS One **8**(8), e70687 (2013).
8. K. Santra, E. A. Smith, J. W. Petrich, and X. Song, "Photon counting data analysis: Application of the maximum likelihood and related methods for the determination of lifetimes in mixtures of rose bengal and rhodamine b," J. Phys. Chem. A **121**(1), 122–132 (2017).
9. K. Santra, J. Zhan, X. Song, E. A. Smith, N. Vaswani, and J. W. Petrich, "What is the best method to fit time-resolved data? a comparison of the residual minimization and the maximum likelihood techniques as applied to experimental time-correlated, single-photon counting data," J. Phys. Chem. B **120**(9), 2484–2490 (2016).
10. M. Maus, M. Cotlet, J. Hofkens, T. Gensch, F. C. De Schryver, J. Schaffer, and C. Seidel, "An experimental comparison of the maximum likelihood estimation and nonlinear least-squares fluorescence lifetime analysis of single molecules," Anal. Chem. **73**(9), 2078–2086 (2001).
11. D. A. Turton, G. D. Reid, and G. S. Beddard, "Accurate analysis of fluorescence decays from single molecules in photon counting experiments," Anal. Chem. **75**(16), 4182–4187 (2003).
12. P. J. Verveer and P. Bastiaens, "Evaluation of global analysis algorithms for single frequency fluorescence lifetime imaging microscopy data," J. Microsc. **209**(1), 1–7 (2003).
13. P. R. Barber, S. M. Ameer-Beg, J. D. Gilbey, R. J. Edens, I. Ezike, and B. Vojnovic, "Global and pixel kinetic data analysis for FRET detection by multi-photon time-domain FLIM," Proc. SPIE **5700**, 171–181 (2005).
14. P. Barber, S. Ameer-Beg, S. Pathmananthan, M. Rowley, and A. Coolen, "A bayesian method for single molecule, fluorescence burst analysis," Biomed. Opt. Express **1**(4), 1148–1158 (2010).
15. M. I. Rowley, P. R. Barber, A. C. Coolen, and B. Vojnovic, "Bayesian analysis of fluorescence lifetime imaging data," Proc. SPIE **7903**, 790325 (2011).
16. J. Kim, J. Seok, H. Lee, and M. Lee, "Penalized maximum likelihood estimation of lifetime and amplitude images from multi-exponentially decaying fluorescence signals," Opt. Express **21**(17), 20240–20253 (2013).
17. M. I. Rowley, A. Coolen, B. Vojnovic, and P. R. Barber, "Robust bayesian fluorescence lifetime estimation, decay model selection and instrument response determination for low-intensity FLIM imaging," PLoS One **11**(6), e0158404 (2016).
18. B. Kaye, P. J. Foster, T. Yoo, and D. J. Needleman, "Developing and testing a bayesian analysis of fluorescence lifetime measurements," PLoS One **12**(1), e0169337 (2017).
19. M. Köllner and J. Wolfrum, "How many photons are necessary for fluorescence-lifetime measurements?" Chem. Phys. Lett. **200**(1-2), 199–204 (1992).
20. M. Raspe, K. M. Kedziora, B. van den Broek, Q. Zhao, S. de Jong, J. Herz, M. Mastop, J. Goedhart, T. W. Gadella, I. T. Young, and K. Jalink, "siFLIM: single-image frequency-domain FLIM provides fast and photon-efficient lifetime data," Nat. Methods **13**(6), 501–504 (2016).

Research Article | Vol. 10, No. 11 / 1 November 2019 / *Biomedical Optics Express* 5517

Biomedical Optics EXPRESS

21. N. Krstajić, S. Poland, J. Levitt, R. Walker, A. Erdogan, S. Ameer-Beg, and R. K. Henderson, "0.5 billion events per second time correlated single photon counting using cmos spad arrays," Opt. Lett. **40**(18), 4305–4308 (2015).
22. C. Guzmán, C. Oetken-Lindholm, and D. Abankwa, "Automated high-throughput fluorescence lifetime imaging microscopy to detect protein–protein interactions," J. Lab. Autom. **21**(2), 238–245 (2016).
23. J. R. Lakowicz, *Principles of Fluorescence Spectroscopy* (Springer, 2006).
24. J. Kiefer and J. Wolfowitz, "Consistency of the maximum likelihood estimator in the presence of infinitely many incidental parameters," Ann. Math. Stat. **27**(4), 887–906 (1956).
25. B. G. Lindsay, "The geometry of mixture likelihoods: a general theory," Ann. Statist. **11**(1), 86–94 (1983).
26. W. Jiang and C. Zhang, "General maximum likelihood empirical bayes estimation of normal means," Ann. Statist. **37**(4), 1647–1684 (2009).
27. R. Koenker and I. Mizera, "Convex optimization, shape constraints, compound decisions, and empirical bayes rules," J. Am. Stat. Assoc. **109**(506), 674–685 (2014).
28. B. G. Abraham, K. S. Sarkisyan, A. S. Mishin, V. Santala, N. V. Tkachenko, and M. Karp, "Fluorescent protein based fret pairs with improved dynamic range for fluorescence lifetime measurements," PLoS One **10**(8), e0134436 (2015).
29. H. Robinns, "Asymptotically subminimax solutions of compound decision problems," in *Proceedings of the Second Berkeley Symposium on Mathematical Statistics and Probability*, vol. 1950, (1951), pp. 131–148.
30. C. Zhang, "Compound decision theory and empirical bayes methods," Ann. Statist. **31**(2), 379–390 (2003).
31. B. Efron, "Two modeling strategies for empirical bayes estimation," Statist. Sci. **29**(2), 285–301 (2014).
32. B. Kleijn and A. Van der Vaart, "The bernstein-von-mises theorem under misspecification," Electron. J. Stat. **6**, 354–381 (2012).
33. A. P. Dempster, N. M. Laird, and D. B. Rubin, "Maximum likelihood from incomplete data via the EM algorithm," J. Royal Stat. Soc. Ser. B (methodological) **39**(1), 1–22 (1977).
34. R. Varadhan and C. Roland, "Simple and globally convergent methods for accelerating the convergence of any EM algorithm," Scand. J. Stat. **35**(2), 335–353 (2008).
35. R. Koenker and J. Gu, "Rebayes: an r package for empirical bayes mixture methods," Tech. Rep., Journal of Statistical Software **82**(8), 1–30 (2017).
36. J. V. Chacko and K. W. Eliceiri, "Autofluorescence lifetime imaging of cellular metabolism: Sensitivity toward cell density, ph, intracellular, and intercellular heterogeneity," Cytometry, Part A **95**(1), 56–69 (2019).

Coding Scheme Optimization for Fast Fluorescence Lifetime Imaging

JONGHO LEE, JENU VARGHESE CHACKO, BING DAI, SYED AZER REZA, ABDUL KADER SAGAR, KEVIN W. ELICEIRI, ANDREAS VELTEN, and MOHIT GUPTA, University of Wisconsin-Madison

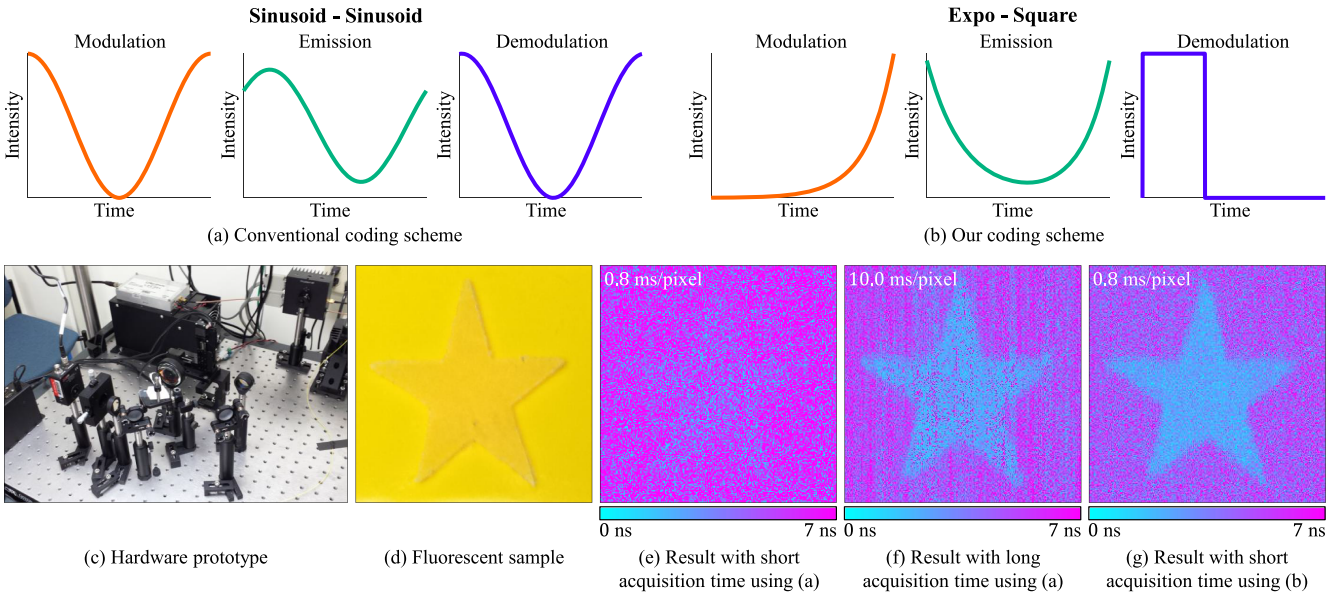

Fig. 1. **Fast frequency domain fluorescence lifetime imaging (FLIM).** (a)-(b) Fluorescence excitations by different modulation functions (orange) lead to different fluorescence emissions (green). The intensities obtained by correlating the emissions with demodulation functions (blue) determine the SNR. We propose a theoretical framework for analysis and design of FD-FLIM coding schemes (modulation and demodulation functions), and use that to design (b) novel coding schemes that achieve considerably higher SNR as compared to conventional methods. (c) We developed a prototype FD-FLIM system to implement various coding schemes. (d) A fluorescent sample with two different fluorescence lifetimes for the foreground and the background is excited by a low power light source. (e) With the conventional coding scheme and 0.8ms/pixel acquisition time, no clear boundary is observed between the foreground and background. (f) A considerably longer (10ms/pixel) acquisition time is required to obtain a clear boundary. (g) With the proposed coding schemes, 0.8ms/pixel acquisition time is sufficient to detect a clear boundary.

Fluorescence lifetime imaging (FLIM) is used for measuring material properties in a wide range of applications, including biology, medical imaging, chemistry, and material science. In frequency-domain FLIM (FD-FLIM), the object of interest is illuminated with a temporally modulated light source. The fluorescence lifetime is measured by computing the correlations of the emitted light with a demodulation function at the sensor. The signal-to-noise ratio (SNR) and the acquisition time of a FD-FLIM system is determined by the coding scheme (modulation and demodulation functions). In this article, we develop theory and algorithms for designing high-performance FD-FLIM coding schemes that can achieve high SNR and short acquisition time, given a fixed source power budget. Based on a geometric analysis of the image formation and noise model, we propose a novel surrogate objective for the performance of a given coding scheme. The surrogate objective is extremely fast to compute, and can be used to efficiently explore the entire space of coding schemes. Based on this objective, we design novel, high-performance coding schemes that achieve up to an order of magnitude shorter acquisition time as compared to existing approaches. We demonstrate the performance advantage of the proposed schemes in a variety of imaging conditions, using a modular hardware prototype that can implement various coding schemes.

CCS Concepts: • **Computing methodologies** → **Computational photography**;

Additional Key Words and Phrases: Fluorescence lifetime, coding optimization, waveform optimization, time-of-flight

This work is supported in part by the DARPA REVEAL program DARPA0, by the ONR ONR0 under Grants No. N000141612995 and No. N000141512652I ONR0, and by the NIH NIH0 under Grant No. R01 CA185251 NIH0.
Authors' addresses: J. Lee and M. Gupta, 1210 W. Dayton Street, Department of Computer Sciences, UW-Madison, Madison, WI 53706; emails: {jongho, mohitg}@cs.wisc.edu; J. V. Chacko, B. Dai, A. K. Sagar, and K. W Eliceiri, 1675 Observatory Drive, Laboratory for Optical and Computational Instrumentation, UW-Madison, Madison, WI 53706; emails: {jenu.chacko, bdai6, msagar, eliceiri}@wisc.edu; S. A. Reza and A. Velten, 1300 University Ave., Medical Sciences Building, UW-Madison, Madison, WI 53706; emails: {sreza2, velten}@wisc.edu.

0730-0301/2019/06-ART26 $15.00
https://doi.org/10.1145/3325136

ACM Reference format:
Jongho Lee, Jenu Varghese Chacko, Bing Dai, Syed Azer Reza, Abdul Kader Sagar, Kevin W. Eliceiri, Andreas Velten, and Mohit Gupta. 2019. Coding Scheme Optimization for Fast Fluorescence Lifetime Imaging. *ACM Trans. Graph.* 38, 3, Article 26 (June 2019), 16 pages.
https://doi.org/10.1145/3325136

1 INTRODUCTION

Fluorescence is the phenomena where a material absorbs light at certain wavelengths, and then emits light at different, typically longer wavelengths. The wavelengths at which light is absorbed and emitted are characteristic of the physical and chemical properties of the material (Hollas 2004). Therefore, the excitation and emission spectra are used as signatures for material recognition in a variety of applications, such as wine classification (Airado-Rodríguez et al. 2009), honey classification (Lenhardt et al. 2015), and oil classification (Sikorska et al. 2005).

Spectrum based fluorescence imaging techniques rely on steady-state measurements, i.e., the measurements are assumed to be constant over time. However, fluorescence also manifests as a transient (high-speed temporal) phenomena. When the molecule of a fluorescent material absorbs a photon, it goes into an excited state. The molecule returns to the ground state after a time delay, when it emits a photon. The delay between absorption and emission of photon is a random variable (due to the stochastic nature of emission), with an exponential distribution (Becker 2014). The mean delay, i.e., the average time the molecule spends in the excited state prior to returning to the ground state, is called fluorescence lifetime. The typical scale of the fluorescent lifetime is from several picoseconds (ps) to several nanoseconds (ns) (Bastiaens and Squire 1999).

Due to the exponential distribution of time delay, if a fluorescent material is illuminated with a short (e.g., few picoseconds duration) light pulse, the intensity of the emitted light decays exponentially over time. The rate of the exponential decay and the fluorescence lifetime provide information about material properties (e.g., temperature, viscosity, pH (Shi et al. 2014), chemical concentration (Sun et al. 2015)) that is often not available in the steady-state fluorescence spectral measurements (Berezin and Achilefu 2010). As a result, fluorescence lifetime imaging (FLIM) has found applications in several domains, including biology, medicine, chemistry, material science, agriculture, and art, where it has been used to distinguish between cancerous and noncancerous tissue (Colasanti et al. 2000; Pradhan et al. 1995), perform fingerprint detection (Seah et al. 2005, 2006), non-destructive fruit quality detection (Kim et al. 2008), non-invasive artwork analysis (Comelli et al. 2004; Nevin et al. 2007), and wood classification (Donaldson and Radotic 2013).

Broadly, FLIM techniques can be classified two ways: time domain (TD) FLIM, and frequency domain (FD) FLIM. In TD-FLIM, the sample of interest is illuminated with a short light pulse. A high-speed sensor (e.g., a single photon avalanche diode (Pancheri et al. 2013)) records the time profile of the emitted light, from which lifetime is extracted by performing an exponential function fit. Although TD-FLIM achieves high precision, it requires expensive components (short-pulse laser, high-speed sensor) (Elson et al. 2004). Furthermore, since the sensor requires capturing the entire time profile of the emitted light, in most cases (e.g., TD-FLIM by time-correlated single photon counting), the sample needs to be scanned one pixel at a time due to bandwidth constraints, making it prohibitively slow, especially for in vivo diagnostic applications where the motion artifacts need to be minimized (Requejo-Isidro et al. 2004).

Our focus is on frequency domain FLIM (FD-FLIM), where the sample is illuminated continuously (instead of with short pulses), with a light source whose brightness is modulated over time. The sensor captures intensity measurements by correlating the emitted light with a demodulation function, over relatively long integration times (e.g., few milliseconds). FD-FLIM requires capturing a small number (as few as three) of correlation intensity measurements in order to recover the lifetime (Elder et al. 2008), with relatively low cost components. The signal-to-noise ratio (SNR), and hence, the acquisition time, of a FD-FLIM system is determined by the coding scheme (modulation and demodulation functions) used. Most existing FD-FLIM systems use sinusoid (Philip and Carlsson 2003) or square waves (Booth and Wilson 2004; Schlachter et al. 2009). For example, an often used FD-FLIM coding scheme is sinusoid coding, where both modulation and demodulation functions are sinusoids of the same frequency (Philip and Carlsson 2003). Unfortunately, the SNR achieved by sinusoid coding remains low, thus often requiring long acquisition times to achieve the desired precision.

We propose a geometric framework for design and analysis of novel, high-performance FD-FLIM coding schemes. We define the mean lifetime error, a measure of coding scheme performance, based on a geometric analysis of the FD-FLIM image formation model. The mean lifetime error is conceptually easy to understand, and can be used to predict the performance of a given coding scheme over a specified range of lifetimes. However, mean lifetime error requires expensive numerical computations. Therefore, a coding scheme optimization procedure that directly uses the mean lifetime error as an objective function, remains prohibitively expensive from a computational standpoint.

Contributions and Implications. Our main theoretical contribution is the derivation of a computationally lightweight surrogate for the mean lifetime error based on the first-order partial derivative of the FD-FLIM image formation equation. The surrogate is considerably faster to compute than the mean lifetime error, and thus, enables us to efficiently explore the large space of FD-FLIM coding functions to find the optimal solution. Based on this surrogate objective, we design FD-FLIM coding schemes that achieve up to an order of magnitude higher acquisition speed (given a fixed source power budget), as compared to conventional schemes. An example is shown in Figure 1. FD-FLIM can be considered a special case (with an exponential impulse scene response) of transient imaging. Due to this relationship, the scope of transient and time-of-flight (ToF) imaging principles developed in graphics and computer vision could be expanded to a broader set of applications involving FLIM (e.g., medical and clinical). Furthermore, the proposed FD-FLIM measurement optimization approaches can be used in transient imaging scenarios where the scene's impulse response can be modeled as an exponential function (e.g., single scattering (Wu et al. 2012)).

Hardware Prototype. We develop a proof-of-concept hardware prototype (Figure 1(c)) capable of implementing a wide range of coding schemes, and demonstrate the performance benefit of the proposed coding schemes, for several materials and a broad range of SNR scenarios. Our current hardware prototype is slow in acquisition because it is based on mechanical scanning. The proposed coding schemes can potentially be implemented on full-frame FLIM systems (Requejo-Isidro et al. 2004) for real-time FLIM measurements (Bhandari et al. 2015a).

2 RELATED WORK

Performance Metric and Code Design for FLIM. There has been surprisingly little work on optimization of coding functions for FLIM. While a few specific functions (e.g., sinusoid, square waves, impulse function) have been evaluated in terms of a figure of merit called F-value (Elder et al. 2008; Esposito et al. 2007; Lin and Gmitro 2010; Philip and Carlsson 2003), there is no general recipe for designing optimal FD-FLIM coding schemes. Our goal is to develop universal, easy to compute, performance metrics for the entire space of coding schemes, which can be used to design and analyze novel, high-performance coding schemes that considerably outperform existing approaches in a broad range of scenarios.

Fluorescence in Computer Vision and Graphics: Fluorescence-based phenomena have been used in computer vision and graphics in various contexts. For example, the observation that fluorescent materials behave approximately like Lambertian surfaces (emits light equally in all directions) was used to reconstruct 3D shape (Sato et al. 2012; Treibitz et al. 2012). Hullin et al. (2008) developed a technique to reconstruct 3D shape of transparent objects by immersing them in fluorescent liquid. Fu et al. (2014) proposed an inter-reflection removal method using reflective and fluorescent components in two channels from the captured image of a fluorescent object. Han et al. (2012) used fluorescence emission for estimating camera spectral sensitivity. Approaches for jointly capturing (Hullin et al. 2010), and using reflectance and fluorescent emission images, e.g., for improved classification of coral reef images (Beijbom et al. 2016), have also been proposed. These approaches are based on steady-state fluorescence spectral measurements. In contrast, this article focuses on the *transient aspects* of fluorescence.

Relationship to Transient Imaging. The goal of transient imaging is to recover the entire time profile of light transport. Wu et al. (2012) decomposed light transport into individual components (direct, indirect, scattering, inter-reflections) for scene analysis applications. Velten et al. (2012) recovered 3D shape around a corner using transient imaging. Heide et al. (2013, 2014) obtained transient images by a correlation-based ToF image sensor.

In general, the structure of transient waveforms depends on scene complexity, and can have arbitrary shapes. Typically, hundreds of measurements, per-pixel, are required to recover the transient waveforms. In contrast, the focus of this article is on FLIM, where the incident waveform can be modeled by an exponentially decaying function with a single parameter (Equation (1)). Therefore, only a few measurements are sufficient to recover the fluorescence lifetime. The proposed approaches can be relevant in transient imaging scenarios where the scene's impulse response can be modeled as a low-dimensional parametric function. For example, subsurface scattering, among various light transport components, can be modeled with an exponentially decaying function where the decay parameter is related with concentration of scattering media (Wu et al. 2012).

Fluorescence Lifetime Estimation with ToF sensors. Recently, approaches based on ToF sensors have been proposed for low-cost fluorescence lifetime estimation. Esposito et al. showed that CCD/CMOS sensors, originally developed for depth sensing, can be used for lifetime estimation (Esposito et al. 2006, 2005). Bhandari et al. also showed that lifetime can be estimated with ToF sensors using codes unifying time domain and and frequency domain approaches (Bhandari et al. 2015b; Bhandari and Raskar 2016). Our goal is different. Instead of analyzing specific hardware implementations and sensors, we develop a general coding theory for FD-FLIM. We envision that the proposed coding schemes and optimization approaches, along with modern transient and ToF sensors, will enable faster and low-cost hardware implementation of FD-FLIM in the future.

3 IMAGE FORMATION MODEL

3.1 Fluorescence Transient Response

The fluorescence transient response $h(t;\tau)$ of a material is defined as the exponentially decaying temporal intensity profile of the emitted light, after the material is illuminated with a light impulse $\delta(t)$. $h(t;\tau)$ is given as

$$h(t;\tau) = \frac{1}{\tau} e^{-\frac{t}{\tau}} \quad (t \geq 0), \tag{1}$$

where τ is the material's fluorescence lifetime; it determines the rate of exponential decay.[1] $h(t;\tau)$ is normalized so that $\int_0^\infty h(t;\tau) = 1$.

3.2 FD-FLIM Imaging Model

A FD-FLIM imaging system consists of a light source (e.g., a laser diode) used to illuminate the sample of interest, and a sensor used to capture the fluorescence emission, as shown in Figure 2. Let the intensity of the source be temporally modulated according to a periodic function $M(t)$ ($M(t) \geq 0$), also called the modulation or the excitation function. Due to absorption of incident light and fluorescence, the sample emits light, which is captured by the sensor. Then, the fluorescence emission $E(t)$,[2] as observed at the sensor, is given as a scaled and offset version of the convolution of $M(t)$

[1] We assume mono-exponential decay, where the fluorescence emission intensity follows a single exponential function. Certain fluorescent materials have multi-exponential decay, where the fluorescence emission profile is a linear combination of multiple exponential functions (Lakowicz 2006). While designing coding schemes for multi-exponential decay is outside the scope of this article, the approaches presented in this article can potentially be extended for multi-exponential lifetime decay estimation. This forms a promising future research direction.

[2] The wavelengths of the emitted light $E(t)$ and incident signal $M(t)$ are different due to fluorescence spectral shift (also called Stokes shift). In this article, for ease of notation, we ignore the wavelength dependence, and consider only the temporal variation of the incident and emitted signals. In practice, a dichroic mirror can be used to reflect the incident light to the sample and to transmit the fluorescence emission to the sensor, based on the wavelength, as shown in Figure 2.

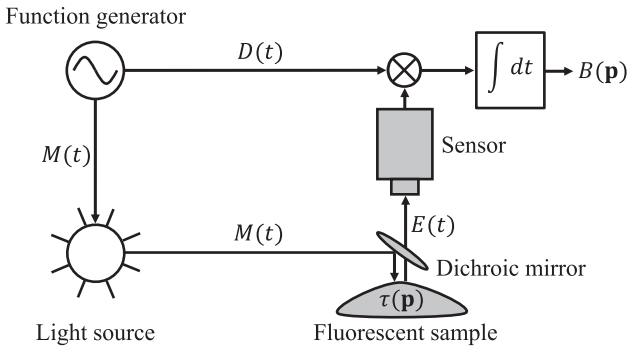

Fig. 2. **Image formation model of FD-FLIM.** A light source with temporally modulated intensity according to function $M(t)$ excites a fluorescent sample. The resulting fluorescence emission $E(t)$ captured by a sensor is correlated with the demodulation function $D(t)$ to get the image intensity B. The lifetime τ is measured from an intensity vector $\mathbf{B} = [B_1, B_2, \ldots, B_K]$ ($K \geq 3$) where each measurement B_i is captured using a different pair of modulation and demodulation functions.

and $h(t;\tau)$:

$$E(t;\tau) = \alpha(M \otimes h)(t;\tau) + \gamma = \alpha \int_{-\infty}^{\infty} M(s;\tau)h(t-s;\tau)\,ds + \gamma, \tag{2}$$

where α is a scale factor depending on system parameters (e.g., system instrumentation) and the sample (e.g., concentration, quantum yield). γ is an offset corresponding to ambient illumination due to external sources and $\otimes$ is a convolution operator. Equation (2) does not account for the temporal shift in $E(t)$ caused by the travel time along the excitation path (light source → sample) and the emission path (sample → sensor). We assume this shift can be computed independently and compensated by a calibration process.

The sensor computes the correlation of the emitted light $E(t;\tau)$ with a demodulation function $D(t)$ ($0 \leq D(t) \leq 1$). We assume that both modulation function $M(t)$ and demodulation function $D(t)$ are periodic functions with the same fundamental frequency f_0, i.e., the same period $T_0 = 1/f_0$ (homodyne detection). The ideal (noise-free) measured intensity B is given as

$$B = \int_T E(t;\tau)\,D(t)\,dt, \tag{3}$$

where $T \gg T_0$ is the sensor integration time. Next, we define $\mathfrak{V}(\tau) = \int_T (M \otimes h)(t;\tau)\,D(t)\,dt$ as the fluorescence correlation function. It is described completely by the modulation and demodulation functions $M(t)$ and $D(t)$, respectively, and is a function only of the fluorescence lifetime τ. Substituting Equation (1) and Equation (2) into Equation (3), the measured image intensity is given as

$$B(\alpha;\beta;\tau) = \alpha\,\mathfrak{V}(\tau) + \beta, \tag{4}$$

where $\beta = \gamma \int_T D(t)\,dt$ is the component of the measured intensity due to ambient light sources (other than the laser source). Equation (4) is the image formation equation of FD-FLIM. It states that the measured intensity is a function of three arguments: α, β, and τ. In general, all three are unknown. Therefore, K ($K \geq 3$) intensity measurements are needed to recover the unknowns, where each measurement B_i ($1 \leq i \leq K$) is taken by using a different pair of modulation and demodulation functions $M_i(t)$ and $D_i(t)$, respectively. For example, one popular FD-FLIM measurement method is sinusoid coding, where both modulation and demodulation functions are sinusoids of the same frequency (Philip and Carlsson 2003). Different intensity measurements are taken by phase-shifting the demodulation function, while the modulation function remains the same.

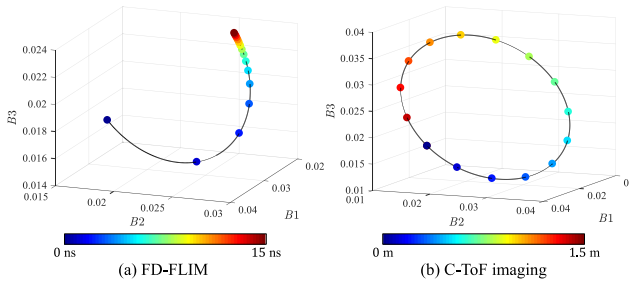

Fig. 3. **The space of captured intensities for FD-FLIM and C-ToF imaging.** (a) In FD-FLIM, the set of intensity points when the lifetime is varied forms an open 1D curve, with a non-uniform inter-point distance. (b) In C-ToF imaging, the set of intensity points when the scene depth is varied form a closed loop with a uniform inter-point distance.

Let the set of measured intensities be represented as a vector $\mathbf{B} = [B_1, B_2, \ldots, B_K]$ in the K-dimensional intensity space. For a given tuple of unknowns α, β, and τ, $\mathbf{B}$ is completely determined by the *coding scheme* C, which is defined as the set of modulation and demodulation functions $C = \{M_i(t), D_i(t)\},\ 1 \leq i \leq K$. The analysis in the article is generally valid for the entire space of modulation and demodulation functions that are physically realizable (i.e., bounded amplitudes of modulation and demodulation functions), given a fixed light source power budget. Please refer to Section 6 for amplitude constraints for C. Further practical constraints can be imposed on C due to the source peak power or system bandwidth. Figure 3(a) shows the set of intensity vectors $\mathbf{B}$ when $K = 3$ and sinusoid is used for both modulation and demodulation functions. The locus of $\mathbf{B}$ is obtained by changing τ while fixing α and β.

Relationship to Phasor Plot Representation: The semi-circle shape in Figure 3(a) looks similar to the phasor plot often used to illustrate fluorescence emission with sinusoid illumination (Digman et al. 2008). However, while a phasor plot is the representation of amplitude attenuation and phase shift of sinusoid fluorescence emission, Figure 3(a) is the set of raw intensity values after integration of fluorescence emission with demodulation functions. In general, for a non-sinusoid coding scheme, the shape of the set of $\mathbf{B}$ is not a semi-circle.

Nomenclature. In the rest of the article, we will use the names of modulation and demodulation functions to denote a coding scheme. For example, "Sinusoid-Square" denotes a coding scheme that uses sinusoid modulation functions, and square demodulation functions.

3.3 FD-FLIM vs. C-ToF Imaging

Conceptually, the image formation model of FD-FLIM shares many aspects with that of continuous wave ToF (C-ToF) imaging (Bhandari et al. 2015a). Both imaging modalities require temporal coding of light intensities, and sinusoid coding is a well-established

Table 1. Comparisons between FD-FLIM and C-ToF Imaging

	C-ToF imaging	FD-FLIM
Functional form of light incident on the sensor	Same as the light emitted by the source	Different functional form
Space of intensity points when the lifetime or scene depth is varied	Closed loop with wrapping	Open curve
Optimal modulation frequency	High frequencies	Function of the lifetime

coding scheme in both modalities. However, beyond these high-level similarities, these two modalities have important differences, with different goals. The *main difference* in the image formation model is the impulse response $h(t)$ of the scene. As stated in Equation (1), the impulse response for FD-FLIM is an exponentially decaying function. In contrast, the impulse response for C-ToF is a shifted delta function $h(t) = \delta(t - \frac{2d}{c})$, where d is the scene depth, and c is the speed of light. This key difference in $h(t)$ leads to several distinctions between FD-FLIM and C-ToF imaging, as discussed below. The main differences are also summarized in Table 1.

Functional Form of Reflected vs. Emitted Light. In C-ToF imaging, the light emitted from the source is time-shifted during travel from source to the scene and back, and thus, retains its functional form (e.g., a square wave remains a square wave). In contrast, in FD-FLIM, due to the exponential response function, the functional form of the fluorescence emission can be different from that of the incident light. As a result, the fluorescence lifetime information is encoded in not just the shift, but other properties of the waveform received at the sensor. For example, with sinusoid modulation functions, fluorescence lifetime information is encoded in *both* the amplitude and the phase shift of the emission signal. In contrast, in C-ToF, depth information is encoded in only the phase shift of the reflected signal. Please see the supplementary technical report for a detailed explanation.

The Space of Intensity Points When Lifetime or Scene Depth is Varied. Consider the locus of intensity points $\mathbf{B}$ for FD-FLIM, as τ is varied. The set of points form a 1D curve. Similarly, the set of intensities captured by a C-ToF imaging system, as scene depth is varied, also form a 1D curve in the intensity space (Gupta et al. 2018). For example, Figure 3(a) and (b) show example sets of intensity points $\mathbf{B}$ for FD-FLIM and C-ToF imaging (for $K = 3$ sinusoid-sinusoid coding), as τ and d are varied, respectively. The *key difference* is that in FD-FLIM, the locus of $\mathbf{B}$ forms an *open curve*, but forms a *closed loop* in C-ToF imaging, which wraps around itself as d is increased further. Therefore, while C-ToF based depth measurements are limited to a specific unambiguous depth range due to phase wrapping (Hansard et al. 2012), an FD-FLIM system, in principle, can recover the *entire range* of lifetimes ($\tau \in [0, \infty)$), without ambiguities, with as few as three measurements.

The Optimal Modulation Frequency. For C-ToF imaging, the distance between intensity points on the curve remains the same if d increases by a constant amount, as shown in Figure 3(b). Also, the spacing between points increases uniformly over the entire curve, as the frequency of the modulation functions increases (Gupta et al. 2018; Lange 2000). On the other hand, in FD-FLIM, the distance between intensity points is non-uniform (exponentially decreasing as τ increases), as shown in Figure 3(a). Furthermore, as the modulation frequencies increase, the inter-point distance increases for relatively short τ's, whereas it becomes shorter for relatively long τ's. Therefore, the optimal frequency (in terms of lifetime recovery precision) in FD-FLIM is actually a function of the lifetime τ. In contrast, in C-ToF imaging, higher modulation frequencies always result in higher depth precision, irrespective of the scene depths. Please see the supplementary technical report for details.

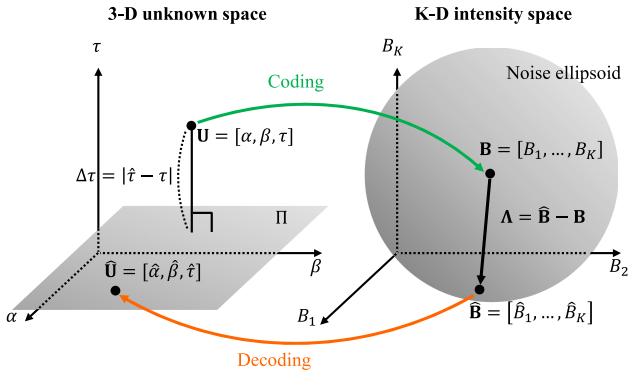

Fig. 4. **Coding space theory of FD-FLIM.** The 3D unknown space is the set of all possible unknown vectors $\{\mathbf{U} = [\alpha, \beta, \tau]\}$, and the K-D intensity space ($K \geq 3$) is the set of corresponding intensity vectors $\{\mathbf{B} = [B_1, B_2, \ldots, B_K]\}$. A coding scheme maps $\mathbf{U}$ to $\mathbf{B}$, and the noise Λ in $\mathbf{B}$ causes the lifetime error $\Delta\tau = |\hat{\tau} - \tau|$.

4 MEAN LIFETIME ERROR

In this section, we define a new measure to evaluate the performance of a given FD-FLIM coding scheme, based on the mean precision of the recovered lifetime. Consider the 3D space consisting of all possible unknown vectors $\{\mathbf{U} = [\alpha, \beta, \tau]\}$, as shown in Figure 4. A given coding scheme maps an unknown vector $\mathbf{U}$ in the unknown space to a *true* (without noise) intensity vector $\mathbf{B} = [B_1, B_2, \ldots, B_K] (K \geq 3)$ in a K-dimensional intensity space. However, due to various sources of measurement noise (e.g., photon noise, sensor read noise, quantization noise), the sensor measures a noisy intensity vector $\hat{\mathbf{B}} = \mathbf{B} + \Lambda$ in the intensity space, where Λ is the noise vector. A decoding algorithm then maps $\hat{\mathbf{B}}$ to an estimated unknown vector $\hat{\mathbf{U}}$, as shown in Figure 4. Consider a plane Π in the unknown space, parallel to the α and β axes, and passing through the estimated unknown vector $\hat{\mathbf{U}}$. Note that all the vectors on plane Π correspond to the same lifetime τ. Therefore, the shortest (perpendicular) distance from the true unknown point $\mathbf{U}$ to Π is the lifetime estimation error $\Delta\tau = |\tau - \hat{\tau}|$, as shown in Figure 4.

Since noise vector Λ, and hence, the measured intensity vector $\hat{\mathbf{B}}$ are random variables, the expected lifetime error for a given

unknown $\mathbf{U} = [\alpha, \beta, \tau]$ and coding scheme C is given as

$$\mathbb{E}[\Delta\tau](C) = \int_{\hat{\mathbf{B}}} |\tau - \hat{\tau}|\, p(\hat{\mathbf{B}}|\mathbf{B}(C))\, d\hat{\mathbf{B}}, \tag{5}$$

where $p(\hat{\mathbf{B}}|\mathbf{B})$ is the probability density function of the measured noisy intensity $\hat{\mathbf{B}}$, given the true intensity $\mathbf{B}$, which is determined by $\mathbf{U}$ and C. $p(\hat{\mathbf{B}}|\mathbf{B})$ follows the K-dimensional normal distribution[3] $\mathcal{N}(\mathbf{B}, \Sigma)$, where Σ is a noise covariance matrix determined by the noise model, including photon noise and read noise (Hasinoff et al. 2010). For the sake of simplicity, we assume Σ is diagonal. Equation (5) provides the expected lifetime error for a specific lifetime, corresponding to the unknown point $\mathbf{U}$. The *mean lifetime error* for a given range of lifetimes $[\tau_1, \tau_2]$ is given as

$$\mathbb{E}_{mean}[\Delta\tau](C; [\tau_1, \tau_2]) = \frac{1}{\tau_2 - \tau_1} \int_{\tau_1}^{\tau_2} \int_{\hat{\mathbf{B}}} |\tau - \hat{\tau}| p(\hat{\mathbf{B}}|\mathbf{B}(C))\, d\hat{\mathbf{B}}\, d\tau. \tag{6}$$

Equation (5) is a special case of Equation (6) when $\tau_1 = \tau_2 = \tau$. The mean lifetime error is a measure of the performance of any given coding scheme, in terms of the precision of the recovered lifetime.

The mean lifetime error is a universal objective: given any coding scheme, the mean lifetime error can be numerically computed using the expression in Equation (6). Figure 6(a) shows the inverse mean lifetime error $\mathbb{E}_{mean}[\Delta\tau]^{-1}$ over the frequency f_0 for several coding schemes. Refer to Table 3 for the functional forms of each coding scheme. Based on the mean lifetime error, we define the *optimal coding scheme* C_{opt} as the coding scheme that minimizes the mean lifetime error, over a specified range of lifetimes $[\tau_1, \tau_2]$:

$$C_{opt} = \arg\min_{C} \mathbb{E}_{mean}[\Delta\tau](C; [\tau_1, \tau_2]), \tag{7}$$

where $\mathbb{E}_{mean}[\Delta\tau](C; [\tau_1, \tau_2])$ is the mean lifetime error achieved by a coding scheme C over the lifetime range $[\tau_1, \tau_2]$.

Computational Considerations for Mean Lifetime Error. The mean lifetime error derived in Equation (6) is generally applicable to the entire space of coding schemes, and thus can be used as a valuable analysis tool for evaluating the performance of different schemes. However, unfortunately, mean lifetime error does not have a closed-form analytical expression, and requires computationally intensive numerical computations, which involve the inverse problem of computing lifetime estimate $\hat{\tau}$ from the measured intensities.

In general, there is no closed-form solution for estimating $\hat{\tau}$, except for a few specific cases (e.g., Sinusoid - Sinusoid). Therefore, for most coding schemes, this *decoding* step requires an expensive iteration-based search procedure. Furthermore, the expression for the mean lifetime error requires high-dimensional numerical integration over the intensity space. As a result, estimating mean lifetime error, while conceptually simple, is prohibitively expensive from a computational standpoint for it to be used as an objective function in an efficient FD-FLIM coding optimization method.

[3]We assume that photon noise follows normal distribution. For a relatively large number of photon counts, Poisson distribution approaches the normal distribution, due to the central limit theorem.

5 FAST SURROGATE FOR MEAN LIFETIME ERROR

In this section, we derive a fast surrogate objective for the mean lifetime error, based on a first-order differential analysis of the FD-FLIM image formation model. The surrogate does not require computationally intensive decoding and integration, and thus, is *significantly* (three to four *orders of magnitude*) *faster* to compute as compared to the mean lifetime error, while *accurately* predicting the relative performance of different FD-FLIM coding schemes. Due to these properties, it can be used to efficiently explore and optimize over the space of coding schemes. In the following, we derive the surrogate.

First-Order Approximation of FD-FLIM Model. The mean lifetime error derived in the previous section (Equation (6)) is based on a relationship between intensity deviation (expressed as noise vector $\Lambda = \hat{\mathbf{B}} - \mathbf{B}$), and the resulting lifetime error $\Delta\tau = |\hat{\tau} - \tau|$. We can approximate the relationship between the intensity deviation and the lifetime error by taking the first-order partial derivative of the measured intensity $\mathbf{B}$ with respect to τ from the image formation model (Equation (4)). Let $\mathbf{B}_\tau = \partial\mathbf{B}/\partial\tau$ be the partial derivative of intensity vector $\mathbf{B}$ with respect to τ. The L_2-norm of the vector $\mathbf{B}_\tau$ is given as $\|\mathbf{B}_\tau\| = \|\partial\mathbf{B}\|/|\partial\tau|$. Rearranging, we get a relationship between differential lifetime error $|\partial\tau|$ and the norm of the differential intensity variation vector $\partial\mathbf{B} = [\partial B_1, \ldots, \partial B_K]$:

$$|\partial\tau| = \frac{\|\partial\mathbf{B}\|}{\|\mathbf{B}_\tau\|}. \tag{8}$$

Consider an intensity variation (noise) vector $\Lambda = [\Lambda_1, \ldots, \Lambda_K]$, where Λ_i is the standard deviation of noise in B_i $(i = 1, \ldots, K)$, the ith intensity measurement. $\Lambda = diag(\Sigma)$, where Σ is the noise covariance matrix that can be computed from the intensity measurements $\mathbf{B}$ using the affine noise model. Λ can be considered a *representative* (root-mean-square) intensity variation vector for the measurements. Then, by using the first-order approximation in the above equation, the first-order lifetime error $\Delta\tau_f$ due to intensity variation vector Λ can be approximated as

$$\Delta\tau_f = \frac{\|\Lambda\|}{\|\mathbf{B}_\tau\|}. \tag{9}$$

With a slight abuse of notation, we define the mean $\Delta\tau_f$, over a range of lifetimes $[\tau_1, \tau_2]$ as

$$\Delta\tau_f = \frac{1}{\tau_1 - \tau_2} \int_{\tau_1}^{\tau_2} \frac{\|\Lambda\|}{\|\mathbf{B}_\tau\|}\, d\tau. \tag{10}$$

The first-order lifetime error $\Delta\tau_f$ can be computed from vectors Λ and $\mathbf{B}_\tau$, both of which can be estimated with minimal computations directly from the image formation equation, without computationally expensive inverse decoding or numerical integration required to estimate the mean lifetime error.[4] However, unfortunately, $\Delta\tau_f$ does not accurately predict the coding scheme performance. Figure 6(a) and (b) compare the mean lifetime error $\mathbb{E}_{mean}[\Delta\tau]$ and the first-order lifetime error $\Delta\tau_f$, as a function of modulation frequency, for several coding schemes. All the values

[4]$\mathbf{B}_\tau$ can be estimated analytically as $\mathbf{B}_\tau = \alpha\mathfrak{V}'(\tau)$ from Equation (4), if $\mathfrak{V}'(\tau)$, the gradient of the fluorescence correlation function, can be expressed in an analytical form. In general, $\mathbf{B}_\tau$ can be computed numerically by finite element approximation as $(\mathbf{B}(\tau + \Delta\tau) - \mathbf{B}(\tau))/\Delta\tau$, with an infinitesimal $\Delta\tau$. In our computations, we used the numerical approach with $\Delta\tau = 0.001$ns.

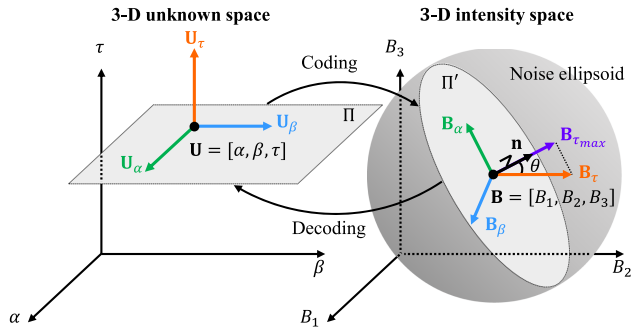

Fig. 5. **Surrogate derivation.** The direction $\mathbf{n}$ along which the variation in $\mathbf{B}$ leads to the maximum variation in decoded lifetime. The maximum differential lifetime error can be approximated by the norm of the noise variance along $\mathbf{n}$ divided by the norm of $\mathbf{B}_{\tau_{max}}$, which is the projection of $\mathbf{B}_\tau = \partial\mathbf{B}/\partial\tau$ onto $\mathbf{n}$. The surrogate is the average of the maximum differential lifetime error over a range of lifetimes.

are computed at a given lifetime range. For ease of visualization, the inverse values $\mathbb{E}_{mean}[\Delta\tau]^{-1}$ and $\Delta\tau_f^{-1}$ are plotted. As can be noticed, there is *no strong correlation* between the values of the two objectives. Thus, while $\Delta\tau_f$ is fast to compute, it cannot be used as a surrogate objective function for coding scheme optimization.

Geometrical Analysis of FD-FLIM Imaging Model. The main reason behind weak correlation between $\mathbb{E}_{mean}[\Delta\tau]$ and $\Delta\tau_f$ is the following. The approximation in Equation (9) implicitly assumes that the noise vector Λ and the intensity derivative vector $\mathbf{B}_\tau$ point in the same direction. In general, this is not true. Therefore, we need to find a *representative direction* in the intensity space, variation along which can be accurately related to the lifetime error.

Consider vectors $\mathbf{B}_\alpha$ and $\mathbf{B}_\beta$, defined as the partial derivatives of the intensity vector $\mathbf{B}$ with respect to the unknowns α and β, respectively:

$$\mathbf{B}_\alpha = \frac{\partial \mathbf{B}}{\partial \alpha} = \mho(\tau) \tag{11}$$

and

$$\mathbf{B}_\beta = \frac{\partial \mathbf{B}}{\partial \beta} = \mathbf{1}, \tag{12}$$

where $\mathbf{1}$ is a vector whose elements are all 1's. Let Π' be the plane defined by vectors $\mathbf{B}_\alpha$ and $\mathbf{B}_\beta$ in the intensity space. The key observation is that any intensity variation (due to noise) within Π' results in *zero lifetime error*. This is because intensity changes along $\mathbf{B}_\alpha$ (or $\mathbf{B}_\beta$) corresponds to change in α (or β) in the unknown space, but τ remains constant. Let $\mathbf{n}$ be the unit vector perpendicular to plane Π', as shown in Figure 5:

$$\mathbf{n} = \frac{\mathbf{B}_\alpha \times \mathbf{B}_\beta}{\|\mathbf{B}_\alpha \times \mathbf{B}_\beta\|}, \tag{13}$$

where $\times$ is the cross product. Since the variation in $\mathbf{B}$ along $\mathbf{n}$ leads to the maximum variation in decoded lifetime $\hat{\tau}$ (thus, maximum lifetime error), we compute the differential lifetime error $|\partial\tau|$ from $\|\partial\mathbf{B}\|$ along $\mathbf{n}$. To this end, we define $\mathbf{B}_{\tau_{max}}$ as the projection of $\mathbf{B}_\tau = \partial\mathbf{B}/\partial\tau$ onto $\mathbf{n}$:

$$\mathbf{B}_{\tau_{max}} = \|\mathbf{B}_\tau\|\mathbf{n}\cos\theta\,, \tag{14}$$

where θ is the angle between $\mathbf{n}$ and $\mathbf{B}_\tau$. Similarly, we define the noise variance along $\mathbf{n}$ as

$$\Lambda_\mathbf{n} = \Lambda \circ \mathbf{n}, \tag{15}$$

where $\circ$ is the element-wise vector multiplication operator. Then, substituting $\mathbf{B}_{\tau_{max}}$ and $\Lambda_\mathbf{n}$ for $\mathbf{B}_\tau$ and Λ, respectively, in Equation (10), we get

$$\Delta\tau_S = \frac{1}{\tau_2 - \tau_1}\int_{\tau_1}^{\tau_2} \frac{\|\Lambda_\mathbf{n}\|}{\|\mathbf{B}_{\tau_{max}}\|}\,d\tau\,. \tag{16}$$

This is an important equation; it provides the expression for the proposed surrogate of mean lifetime error. Figure 6(c) shows the inverse surrogate values $\Delta\tau_S^{-1}$ for the same coding schemes and lifetime ranges as Figure 6(a). As can be noticed, there is a *strong correlation* between the values of the mean lifetime error and surrogate, for all the coding schemes, over the entire range of modulation frequencies. Figure 7 shows that the surrogate can predict the coding scheme performance well even with much larger lifetime ranges. For two lifetime ranges, $[\tau_1, \tau_2] = [0.5\text{ns}, 10\text{ns}]$ and $[\tau_1, \tau_2] = [5\text{ns}, 50\text{ns}]$, the surrogate shows high correlation with mean lifetime error. Note that the surrogate approximates the mean lifetime error only up to a scale factor. Although the surrogate cannot be used to directly predict the mean lifetime error, it can be used to compare relative performance of coding schemes since the scale factor is the same for different coding schemes. Consequently, we use this surrogate as an objective function to find the optimal coding scheme, instead of the computationally intensive mean lifetime error. For more comparison results between the surrogate and the mean lifetime error with other lifetime ranges, please see the supplementary technical report.

Runtime Comparison. The surrogate (Equation (16)) can be computed via a small number of analytic lightweight computations. Specifically, $\mathbf{n}$ can be computed from Equations (11) and (12). The noise vector Λ and gradient $\mathbf{B}_\tau$ can be computed from $\mathbf{B}$, which in turn can be used to compute the projections $\Lambda_\mathbf{n}$ and $\mathbf{B}_{\tau_{max}}$, as given in Equations (14) and (15). There is no computationally expensive high-dimensional integration and lifetime decoding procedures, as required for the mean lifetime error computation. Table 2 shows the runtime comparison between the mean lifetime error and the surrogate for the coding schemes used in Figure 6 when the modulation frequency $f_0 = 1.6$MHz. Computation of the surrogate is three orders of magnitude faster than the mean lifetime error, while maintaining high correlation with the mean lifetime error, as shown in Figure 6.

6 CODING SCHEME OPTIMIZATION

In this section, we demonstrate the capability of the surrogate for FD-FLIM coding scheme optimization. The surrogate is general in its scope, and could be used as an objective function in a broad range of derivative-free optimization approaches, including based on pattern search (Torczon 1997), genetic algorithms (Deb et al. 2002), and Nelder-Mead method (Nelder and Mead 1965). For ease of implementation, we adopt a simple search-based optimization approach as a proof-of-concept.

Search-Based Optimization. In principle, the space of coding functions is infinite dimensional. To keep the optimization

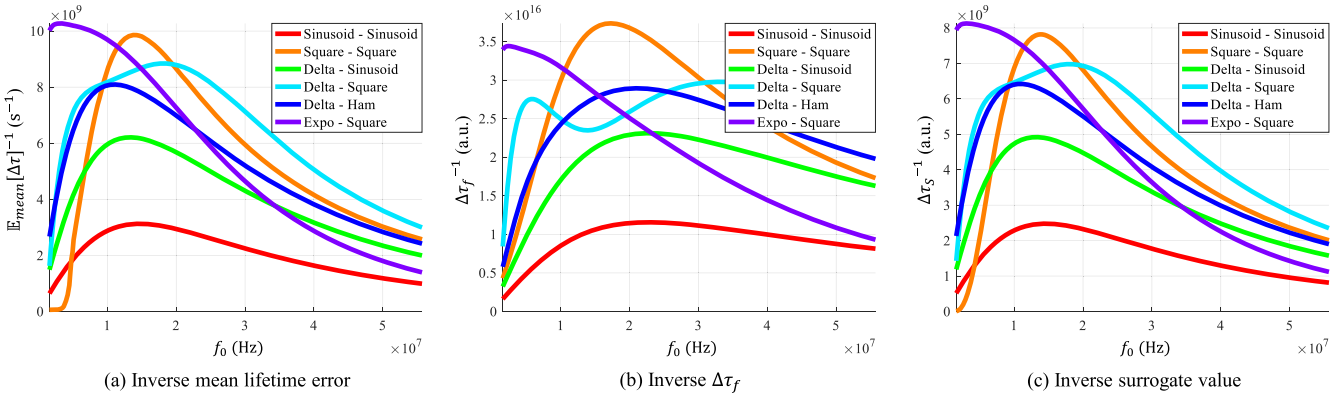

(a) Inverse mean lifetime error (b) Inverse $\Delta\tau_f$ (c) Inverse surrogate value

Fig. 6. **Coding scheme performance comparison according to different objectives.** (a) Inverse mean lifetime errors $\mathbb{E}_{mean}[\Delta\tau]^{-1}$, (b) inverse values of the first-order lifetime error $\Delta\tau_f^{-1}$, and (c) inverse surrogate values $\Delta\tau_S^{-1}$. The performance of several coding schemes is compared as a function of the fundamental modulation frequency f_0, for a given lifetime range $[\tau_1, \tau_2] = [6\text{ns}, 8\text{ns}]$ and $K = 3$. The surrogate values have a strong correlation with the mean lifetime errors across various coding schemes and frequencies, and thus, can be used as a lightweight alternative to the computationally intensive mean lifetime error, in order to find the optimal coding scheme efficiently.

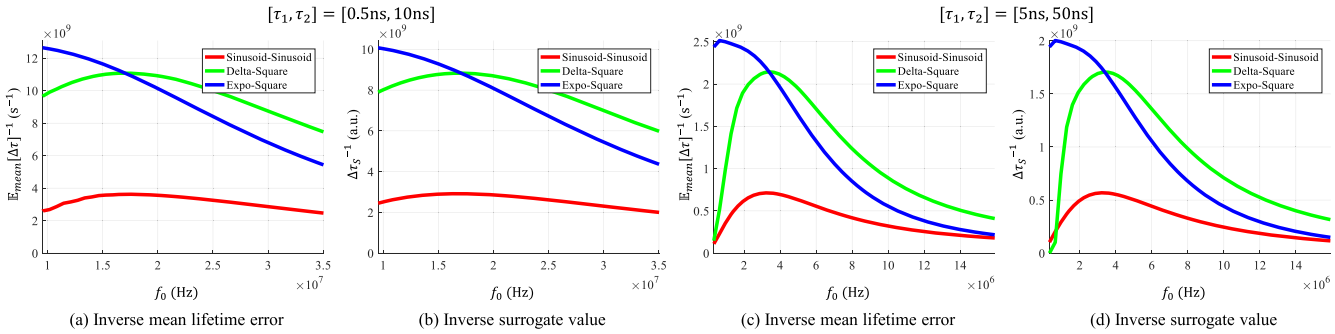

(a) Inverse mean lifetime error (b) Inverse surrogate value (c) Inverse mean lifetime error (d) Inverse surrogate value

Fig. 7. **Coding scheme performance comparison with relatively large lifetime ranges.** Sinusoid-Sinusoid, Delta-Square, and Expo-Square are compared in terms of (a) inverse mean lifetime errors $\mathbb{E}_{mean}[\Delta\tau]^{-1}$, and (b) inverse surrogate values $\Delta\tau_S^{-1}$ when the lifetime range is $[\tau_1, \tau_2] = [0.5\text{ns}, 10\text{ns}]$, and also in terms of (c) inverse mean lifetime errors $\mathbb{E}_{mean}[\Delta\tau]^{-1}$, and (d) inverse surrogate values $\Delta\tau_S^{-1}$ when the lifetime range is $[\tau_1, \tau_2] = [5\text{ns}, 50\text{ns}]$. The surrogate accurately predicts the coding scheme performance even for relatively large lifetime ranges.

Table 2. Runtime Comparison between the Mean Lifetime Error and the Surrogate

Schemes	Runtime (s)	
	Mean lifetime error	Surrogate
Sinusoid-Sinusoid	3.58×10^1	2.60×10^{-2}
Square-Square	0.52×10^1	0.87×10^{-2}
Delta-Sinusoid	3.08×10^1	0.73×10^{-2}
Delta-Square	2.58×10^1	0.54×10^{-2}
Delta-Ham	1.31×10^1	1.21×10^{-2}
Expo-Square	1.57×10^1	0.62×10^{-2}

The surrogate is up to three orders of magnitude faster to compute as compared to the mean lifetime error.

Table 3. Functions Used for Coding Schemes in Optimization

Functions	Equations
Sinusoid	$E_0\,(1 + \cos(2\pi f_0 t))$
Square	$E_0\,(1 + \text{sqr}(2\pi f_0 t, \chi))$
Delta	$E_0 \sum_{n=-\infty}^{\infty} \delta(t - nT_0)$
Expo	$E_0 e^{\kappa t}$, $\kappa > 0$, $0 \le t \le T_0$
Ham	Hamiltonian functions (Gupta et al. 2018)

The modulation frequency f_0, duty cycle χ of the Square function, and the exponent κ of the Expo function are the function parameters that are optimized. The scale factor E_0 is chosen appropriately to satisfy the constraints (constant average source power, non-negativity) on the modulation and the demodulation functions.

tractable, we narrow the space to a finite set of functions. We consider coding schemes created using pairs of modulation and demodulation functions derived from a fixed library of functions, including sinusoid, square waves, impulse train, exponential functions (Aljunid et al. 2013), and trapezoidal Hamiltonian function (Gupta et al. 2018).

Table 3 provides a list of the functional forms and the corresponding mathematical expressions. sqr is the square function whose amplitude is between −1 and 1. χ is the duty cycle of sqr function. The amplitudes E_0 of all functions are scaled appropriately such that the average source power is the same for all the modulation functions, and the amplitudes of the demodulation functions are between 0 and 1. Please refer to

the supplementary technical report for details. Specifically, we consider 12 pairs of modulation and demodulation functions: For modulation functions $M(t)$, we use sinusoidal, square, delta, and exponentially rising functions. For demodulation functions $D(t)$, we use sinusoidal, square, and trapezoidal Hamiltonian functions. We use the notation Sinusoid, Square, Delta, Expo, and Ham for sinusoidal, square, delta, exponentially rising, and Hamiltonian functions, respectively.

Importance of Optimizing Functional Parameters. Each functional form (e.g., sinusoid, square, exponential) is described by a set of parameters, such as modulation frequency f_0 (period T_0), duty cycle χ for the square waves, and exponent κ for the exponential function. The performance (mean lifetime error) of a coding scheme has a strong dependence on the functional parameters. For example, Figure 6(a) shows the mean lifetime error of different schemes varies significantly as the modulation frequency is varied. Furthermore, the optimal modulation frequency (location of the peak of the curves) is different for different coding schemes, and it also depends on the range of lifetimes ($[\tau_1, \tau_2]$) used to compute the errors. Therefore, given an application with a given range of lifetimes to be measured, in order to determine the optimal scheme, it is critical to compute the optimal functional parameters.

Despite limiting the coding schemes to a finite set of functional forms, due to the parameter optimization, the search space is high-dimensional. As a result, developing an efficient optimization procedure that can estimate globally optimal solution remains challenging. One solution is to perform an exhaustive search in the parameter space. Such an exhaustive search, while conceptually simple, is prohibitively expensive from a computational standpoint if the mean lifetime error is used as the objective function. However, since the proposed surrogate is computationally lightweight, we show that it is possible to perform an exhaustive search-based optimization using the surrogate as an objective function, and determine the *globally optimal solution*. It may be possible to use the surrogate to design more efficient optimization procedures. Developing such optimization algorithms based on the proposed surrogate may enable optimization over a larger search space (e.g., more functional forms), and is a promising future research direction.

Our search-based algorithm has two steps. First, the optimal parameter set $\mathcal{P}_{opt}$ for each coding scheme is obtained by minimizing the surrogate:

$$\mathcal{P}_{opt} = \arg\min_{\mathcal{P}} \Delta\tau_{\mathcal{S}}(\mathcal{P}). \tag{17}$$

For example, the optimal parameters for the Expo-Square coding scheme are determined by performing a search over the 3D parameter space $\mathcal{P} = \{f_0, \kappa, \chi\}$; the three parameters are the fundamental modulation frequency f_0, the exponent κ of the exponential function, and duty cycle χ of the square wave. Figure 8(a) shows $\Delta\tau_{\mathcal{S}}^{-1}$ over the 2D parameter space of the Expo-Square coding scheme. The lifetime range is [4ns, 6ns]. Although the search is performed over a 3D space, we show the search results over a 2D space for visualization. As seen from the figure, the surrogate varies significantly over the parameter space, and is a non-convex function of the parameters. Since the surrogate is fast to compute, we can compute the optimal solution via an exhaustive search.

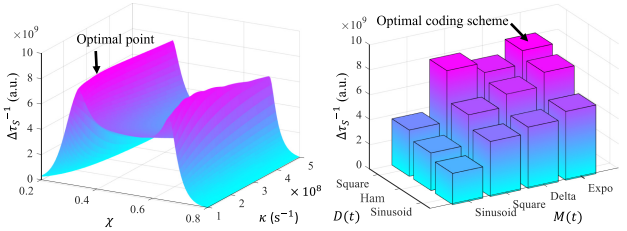

(a) Optimization over Expo - Square (b) Optimization over various coding schemes

Fig. 8. **Optimization.** (a) Inverse surrogate values over two parameters of Expo-Square, the exponent κ, and the duty cycle χ. The optimal parameters can be found by minimizing the surrogate (or maximizing the inverse surrogate). (b) The optimum inverse surrogate values for various coding schemes. The optimum value for each coding scheme is determined by finding its optimal parameters.

In the second step, the optimal coding scheme C_{opt} is determined by simply finding the scheme (with the optimized parameters) that achieves the minimum value of the surrogate:

$$C_{opt} = \arg\min_{C} \Delta\tau_{\mathcal{S}}(C(\mathcal{P}_{opt})). \tag{18}$$

Figure 8(b) shows $\Delta\tau_{\mathcal{S}}^{-1}$ over the search space where each coding scheme's parameters are optimized. Among the 12 coding schemes considered in our search space, the Expo-Square scheme achieves the best performance, with three times higher precision as compared to the conventional Sinusoid-Sinusoid coding scheme. Expo-Square denotes the coding scheme with exponential modulation, and square demodulation function. The explicit forms of these functions are listed in Table 3. The relevant parameters of Expo-Square are κ, the exponent of the modulation function, χ, the duty cycle of the demodulation function, and f_0, the modulation frequency. For detailed equations, please refer to the supplementary technical report.

Dependence of Relative Coding Scheme Performance on Lifetime Range. The relative coding scheme performance depends on the range of lifetimes considered during the optimization. Given the low computational complexity of the proposed surrogate, it is possible to perform such optimization for any set of coding schemes with a different set of parameters, and for *a different range of lifetimes*, depending on the application. For more optimization results with other lifetime ranges, please see the supplementary technical report.

6.1 Unipolar and Bipolar Demodulation Functions

Demodulation functions in FD-FLIM can be unipolar ($0 \le D(t) \le 1$) or bipolar ($-1 \le D(t) \le 1$). For example, a FD-FLIM system using an image intensifier can implement unipolar (positive) demodulation functions, such as a positive sinusoid, $0.5 + 0.5\cos(2\pi f_0 t)$. On the other hand, a lock-in amplifier-based FD-FLIM system can implement bipolar demodulation functions, such as a zero-mean sinusoid, $\cos(2\pi f_0 t)$. Lock-in detection, in general, has better photon efficiency than image intensifiers (Philip and Carlsson 2003), since bipolar functions use the entire incident flux for FLIM estimation.

We compare the performance between unipolar and bipolar demodulation functions for the Sinusoid-Sinusoid and Expo-Square

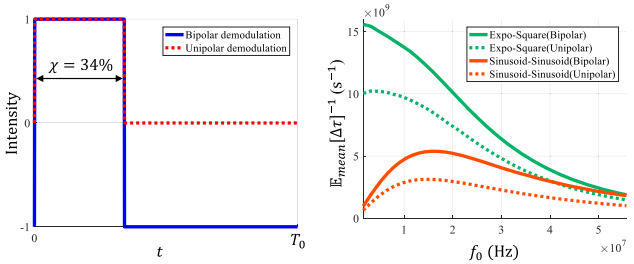

(a) Unipolar and bipolar demodulation functions for Expo-Square

(b) Inverse mean lifetime error with two demodulation functions

Fig. 9. **Performance comparison between unipolar and bipolar demodulation functions.** Coding schemes with Unipolar and bipolar demodulation functions are compared in terms of mean lifetime error ($\mathbb{E}_{mean}[\Delta\tau]$). Sinusoid-Sinusoid and Expo-Square coding schemes are used for comparison, for $\tau = 7$ns. The optimal parameters for Expo-Square with unipolar demodulation function is also used for the bipolar demodulation case for comparison. Figure 9(a) shows unipolar and bipolar demodulation functions used for Expo-Square. As shown in Figure 9(b), coding schemes with bipolar demodulation functions show better performance.

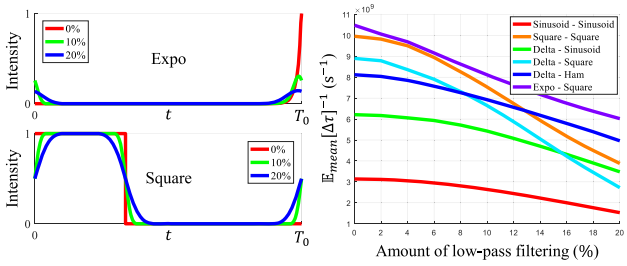

(a) Distorted Expo-Square coding scheme

(b) Inverse mean lifetime error over distortion

Fig. 10. **Robustness of coding schemes to signal distortion.** Coding scheme performance is compared when different amounts of low-pass filtering is applied to either modulation or demodulation function. Photon noise is added to the measurements and a look-up table for decoding lifetime is created by calibration. Inverse mean lifetime error is compared between coding schemes. The performance of every scheme degrades as the distortion level increases.

coding schemes. For Expo-Square with unipolar demodulation function, two parameters, κ and χ are optimized by surrogate, and the same parameters are used for the bipolar demodulation case for comparison. Figure 9(a) shows unipolar and bipolar demodulation functions used for Expo-Square. As shown in Figure 9(b), coding schemes with bipolar demodulation functions achieve better performance than unipolar demodulation functions. This is due to efficient use of photons for both positive and negative lobes as well as increased amplitudes in the case of bipolar demodulation functions. It is interesting to note that Expo-Square with unipolar demodulation performs better as compared to Sinusoid-Sinusoid with bipolar demodulation, at their respective optimal frequencies. For the following analysis, we limit our scope to unipolar demodulation functions for ease of analysis and noise standard deviation computation. The same analysis can be extended to bipolar demodulation functions.

6.2 Robustness of Coding Schemes to Signal Distortions

In practice, it is challenging to create perfect desired signal shapes for coding schemes due to hardware limitations. The distortion in signal shapes for coding schemes degrades coding scheme performance. We tested robustness of coding schemes to signal shape distortion. We model the hardware impulse response causing signal distortion as a low-pass (Gaussian) filter. We distort the modulation and demodulation functions by applying Gaussian filters with different sizes. The size of the Gaussian filter (amount of low-pass filtering) is changed from 0% to 20%, where 20% means that the filter size is 20% of a modulation period of Expo-Square. For each amount of low-pass filtering, the same size of the filter is applied to all coding schemes. The correlation values are obtained with these distorted coding schemes and photon noise is added to the measurements. Figure 10(a) shows distorted modulation and demodulation functions for Expo-Square, with three different amounts of low-pass filtering. For distorted waveforms, we used look-up tables (built by calibrating the system's distorted impulse response) for decoding lifetimes. Figure 10(b) shows the inverse mean lifetime error when the amount of low-pass filtering changes from 0% to 20%. The performance of each coding scheme degrades as the distortion level increases.

Different Types of Signal Distortion and Decoding Without Calibration. In some scenarios, the signal distortion is not modeled as a low-pass filtering. For example, often digital circuits are used for generating demodulation functions in a sinusoid coding scheme. The resulting demodulation function (ideally a square wave) has extra harmonics, resulting in a distorted sinusoid. However, the extra harmonics are canceled out by the sinusoid modulation function in correlation. In this case, the lifetime can be estimated by sinusoid coding scheme without calibration.

7 VALIDATION BY SIMULATIONS

In this section, we use simulations to demonstrate the capability of the proposed surrogate as an analysis and design tool for FD-FLIM coding design. To this end, we evaluated the performance of various FD-FLIM coding schemes via simulations, and compared the results with our surrogate prediction results. As example test cases, we use the fluorescence lifetime data of the brain tissue (Figure 11(a) and (b)) which is used to characterize metabolic changes for Glioblastoma Multiforme (a type of brain cancer) study and another data of cells (Figure 11(c)) where fat cells are differentiated from other cells by lifetime. The ground-truth fluorescence lifetime image was acquired using a TD-FLIM approach. The size of the image is 256×256. Since the lifetime range for Figure 11(a) is relatively short, we artificially increased the lifetime range linearly in Figure 11(b) to evaluate the performance of coding schemes on samples with relatively large lifetime range. For each pixel and each coding scheme, we compute $K = 3$ intensity values as captured by the sensor, based on the the image formation model (Equation (4)) with $\alpha = 48.6$, $\gamma = 5.1$, and $T = 0.1$s. For Figure 11(b), relatively short integration time, $T = 0.005$s, is used to highlight performance difference in longer lifetime range. The values of α and γ depend on imaging system properties, and were computed based on typical FD-FLIM system parameters (Zhao et al. 2011). Finally, we add noise to the computed intensity values,

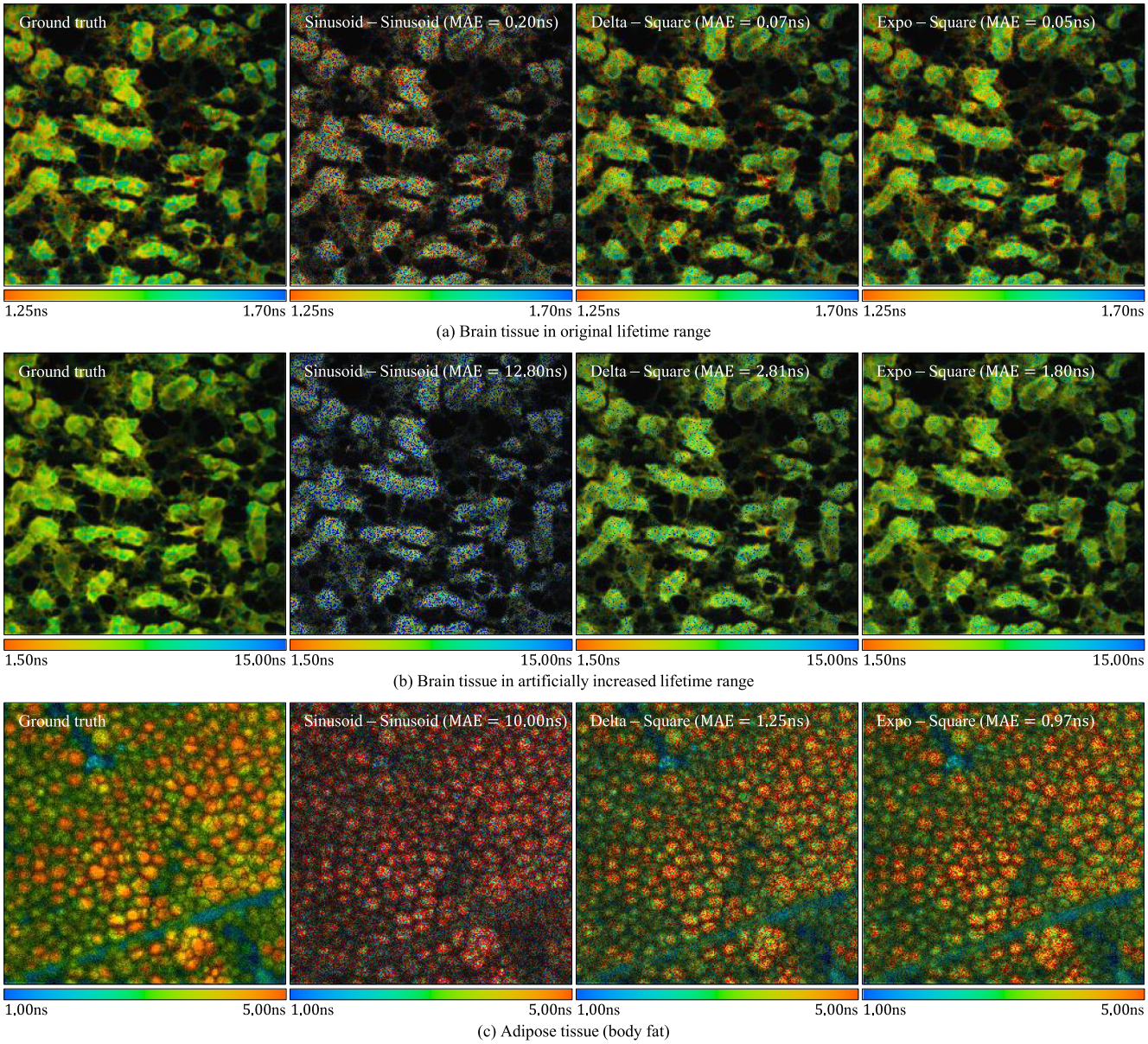

Fig. 11. **Simulation-based comparisons between different coding schemes.** Given ground truth fluorescence lifetime data, fluorescence lifetime images are reconstructed using Sinusoid-Sinusoid, Delta-Square, and Expo-Square from the simulated captured intensities of brain tissue in original lifetime range (a), same tissue in artificially increased lifetime range (b), and adipose tissue (c). In all cases, Expo-Square shows the best performance.

where the noise variance is estimated from the affine noise model, including photon noise and read noise (Hasinoff et al. 2010).

Decoding. In the decoding stage, lifetime is estimated for each pixel from the K noisy intensity values, and shown as a color-coded fluorescence lifetime image. For $K = 3$ measurements, from Equation (4), we can eliminate the unknowns α and β as follows:

$$F(\tau) = \frac{\mathfrak{V}_1(\tau) - \mathfrak{V}_2(\tau)}{\mathfrak{V}_2(\tau) - \mathfrak{V}_3(\tau)} = \frac{B_1 - B_2}{B_2 - B_3}, \tag{19}$$

where $F(\tau)$ is a known function determined by a coding scheme. Given three intensity values B_1, B_2, and B_3, we can estimate τ by solving Equation (19). Refer to the supplementary technical report for details.

We compared three coding schemes, Sinusoid-Sinusoid, perhaps the most widely used FD-FLIM coding scheme (Philip and Carlsson 2003), Delta-Square, a high-performance FD-FLIM coding scheme proposed recently in literature (Schlachter et al. 2009), and Expo-Square, which is the optimal coding scheme according to our surrogate computation. The optimal parameters $\mathcal{P}_{opt}$ for these coding schemes were computed using the surrogate for the given lifetime ranges of the ground truth. The lifetime ranges are $[1.17\text{ns}, 1.82\text{ns}]$, $[0.3\text{ns}, 16\text{ns}]$, and $[1\text{ns}, 5\text{ns}]$ for Figure 11(a),

Table 4. Estimated Optimal Parameter Sets

	Sinusoid-Sinusoid	Delta-Square	Expo-Square
Brain tissue of Figure 11(a)	$\{f_0 = 72.7\text{MHz}\}$	$\{f_0 = 5.1\text{MHz}, \chi = 0.34\}$	$\{f_0 = 8.9\text{MHz}, \kappa = 1.1e9\text{s}^{-1}, \chi = 0.34\}$
Brain tissue of Figure 11(b)	$\{f_0 = 11.1\text{MHz}\}$	$\{f_0 = 10.8\text{MHz}, \chi = 0.36\}$	$\{f_0 = 3.0\text{MHz}, \kappa = 0.19e9\text{s}^{-1}, \chi = 0.35\}$
Adipose tissue	$\{f_0 = 32.9\text{MHz}\}$	$\{f_0 = 27.2\text{MHz}, \chi = 0.39\}$	$\{f_0 = 4.1\text{MHz}, \kappa = 0.52e9\text{s}^{-1}, \chi = 0.34\}$

The optimal parameter sets of three coding schemes, for different tissues, were computed using our surrogate for simulations.

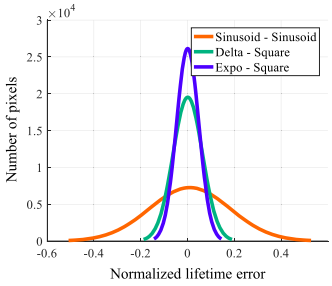

(a) Histograms of the normalized lifetime errors

Coding schemes	$\overline{\text{MAE}}$	$\overline{\Delta\tau_S}$
Sinusoid - Sinusoid	1.000	1.000
Delta - Square	0.365	0.370
Expo - Square	0.278	0.282

(b) Standard deviations of the normalized lifetime errors and the surrogate values

Fig. 12. **Statistical results of the simulation and comparison with the surrogate values.** (a) Histograms of the normalized lifetime errors $((\tau - \hat{\tau})/\tau)$ for different coding schemes. (b) Comparison of the normalized mean absolute errors, $\overline{\text{MAE}}$ with the surrogate values $\overline{\Delta\tau_S}$. The values are normalized such that both values for Sinusoid-Sinusoid are 1. There is a strong correlation between $\overline{\sigma_{\Delta\tau}}$ and $\overline{\Delta\tau_S}$.

(b), and (c), respectively. The optimal parameters for the different schemes and different tissues are listed in Table 4. Note that the optimal parameters for different schemes and different tissues are significantly different.

Figure 11 shows the comparison between the fluorescence lifetime images obtained by three coding schemes. The black pixels in the images denote a region with no lifetime information. The result with the Sinusoid-Sinusoid scheme is noisy, with low SNR. In contrast, the lifetime image achieved by Delta-Square and Expo-Square is closer to ground truth, with lower noise. Figure 12(a) shows the histograms of normalized lifetime errors $(\tau - \hat{\tau})/\tau$ of the three coding schemes for brain tissue in original lifetime range (Figure 11(a)). Expo-Square achieves the best performance in terms of estimated lifetime precision and SNR. Figure 12(b) shows the comparison between the mean absolute errors $\overline{\text{MAE}}$ and the surrogate values $\overline{\Delta\tau_S}$. Both $\overline{\text{MAE}}$ and $\overline{\Delta\tau_S}$ are normalized such that the corresponding values for the Sinusoid-Sinusoid scheme is 1. As shown in the table, $\overline{\text{MAE}}$ and $\overline{\Delta\tau_S}$ show strong correlation, thus suggesting that the proposed surrogate can be used as an easy-to-compute and accurate objective function for coding scheme optimization.

8 HARDWARE PROTOTYPE AND EXPERIMENTS

8.1 Hardware Prototype

We developed a proof-of-concept hardware prototype that can implement various FD-FLIM coding schemes (Figure 13). Since most off-the-shelf FD-FLIM systems use a fixed coding scheme, we develop a single-pixel-based prototype that can admit arbitrary waveforms. A lifetime image of a sample is created by moving the sample on translation stages, or by scanning light beam via

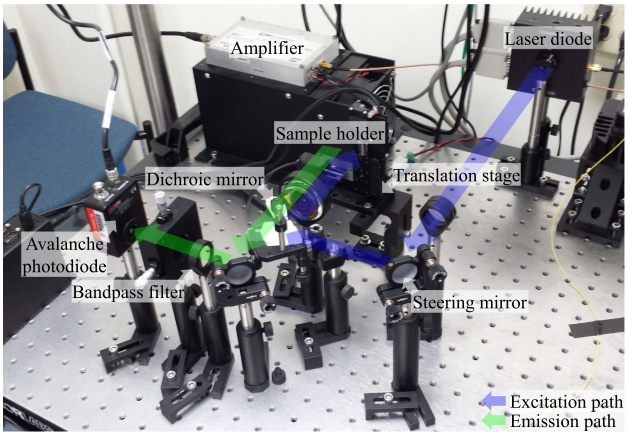

Fig. 13. **Hardware prototype.** Temporally modulated light from the laser diode travels along the excitation path (in blue) and excites the fluorescent sample. The fluorescent emission from the sample travels along the emission path (in green) and is detected by the avalanche photodiode. The final measurements are obtained by correlation of the emission signal with the demodulation signal from the function generator. The fluorescence lifetime is measured from the final measurements.

galvo-mirrors. In this article, we compare different coding schemes in terms of the SNR or acquisition time per pixel. Although the current prototype system results in slow acquisition due to mechanical scanning, it serves as a test-bed for evaluating relative coding scheme performance. An important next step, although outside the scope of this article, is to implement the proposed coding schemes on optimized hardware for faster and low-cost FLIM estimation.

Details of Hardware Setup. Our setup consists of a laser diode (L450P1600MM, Thorlabs) of wavelength 450nm for illuminating the sample of interest. The intensity of the laser diode is modulated by a Siglent SDG 5162 arbitrary function generator for generating arbitrary modulation functions. The function generator has two channels: One is used for generating the modulation functions, and the other for generating the demodulation functions. The modulation signal from the function generator is amplified by the power amplifier with 45dB gain (LZY-22+, Mini-Circuits) before applying to the laser diode. For fair comparisons, we used the same average source power and acquisition time for all coding schemes.

The light emitted by the laser diode is reflected by a dichroic mirror and excites a fluorescent sample. A dichroic mirror, which reflects the light below the cutoff wavelength and transmits the light above it, is used to separate the emission signal from the excitation signal. The fluorescent sample is mounted on a translation stage and can move along x and y directions for scanning purposes. The translation stage is driven by a stepper controller

Table 5. Estimated Optimal Parameter Sets

	Sinusoid-Sinusoid	Delta-Square	Expo-Square
Coumarin 6 in ethanol	$\{f_0 = 41.2\text{MHz}\}$	$\{f_0 = 40.0\text{MHz}, \chi = 0.4\}$	$\{f_0 = 8.6\text{MHz}, \kappa = 0.55e9\text{s}^{-1}, \chi = 0.34\}$
Rhodamine 110 in ethanol	$\{f_0 = 26.4\text{MHz}\}$	$\{f_0 = 33.3\text{MHz}, \chi = 0.4\}$	$\{f_0 = 5.6\text{MHz}, \kappa = 0.35e9\text{s}^{-1}, \chi = 0.34\}$
Fluorescein in ethanol	$\{f_0 = 24.4\text{MHz}\}$	$\{f_0 = 30.4\text{MHz}, \chi = 0.4\}$	$\{f_0 = 5.1\text{MHz}, \kappa = 0.32e9\text{s}^{-1}, \chi = 0.34\}$

The optimal parameter sets of three coding schemes, for three different solutions, were computed using our surrogate.

(MMC-203, Micronix USA). The emission light from the fluorescent sample passes through a bandpass filter (FB550-40, Thorlabs), gets focused by a lens, and then detected by an avalanche photodiode (APD430A2/M, Thorlabs). The bandpass filter is necessary to block the excitation light (wavelength (λ) = 450nm) and to allow only the emission light ($\lambda \approx$ 550nm). The avalanche photodiode has a high responsivity around 600nm.

The emission signal detected at the APD is multiplied by the demodulation signal from the function generator using a frequency mixer (ZX05-1L-S+, Mini-Circuits). The multiplied signal from the frequency mixer is integrated using a low-pass filter with a 1kHz passband (EF110, Thorlabs), digitized by a DAQ (USB-6000, National Instruments) and then recorded by a computer. Note that the demodulation process (computing the correlation of the fluorescence emission with a demodulation signal) is performed electronically in our prototype. In practice, the demodulation can be performed with an image intensifier or lock-in amplifiers (Philip and Carlsson 2003), in full-frame FD-FLIM systems. Figure 13 shows the path taken by light from the source to the sample (the excitation path) and from the sample to the sensor (the emission path).

8.2 Experimental Results

8.2.1 Single Pixel Experiment. We measured the lifetimes of three fluorescent samples: *Coumarin 6 in ethanol, Rhodamine 110 in ethanol, and Fluorescein in ethanol* with the coding schemes used for simulation: Sinusoid-Sinusoid, Delta-Square, and Expo-Square. The concentrations of all three solutions were 0.1mM. The lifetimes of Coumarin 6 in ethanol, Rhodamine 110 in ethanol, and Fluorescein in ethanol are known as 2.5ns, 3.9ns, and 4.25ns, respectively (Magde et al. 1999; Shaner et al. 2013; Wilkerson Jr. et al. 1993).

Computing Optimal Parameters. The optimal parameter sets $\mathcal{P}_{opt}$ of three coding schemes, for each of the three solutions, were computed using our surrogate. We used known lifetime values for the surrogate computation, but, in general, we can use the approximate lifetime range. The computed optimal parameter sets of three coding schemes, for three solutions, are in Table 5. The data acquisition time for each measurement was 10ms, and a 174mA DC signal was used to drive the laser diode for all tested coding schemes for the same average source power constraint. The waveforms were band-limited since the maximum output frequency of the function generator in our setup is limited to 160MHz.

Results: We measured the lifetimes at a single position for each sample 1,000 times, and compared the mean absolute errors of the repeated measurements for the three coding schemes. Figure 14 shows the histograms and the mean absolute errors of the measured lifetimes. For all solutions, Expo-Square achieves approximately three times better performance as compared to Sinusoid-Sinusoid in terms of the mean absolute error of the measured lifetimes, which is consistent with the surrogate prediction.

8.2.2 Scanning Experiments. In order to compare the performance of different schemes over full-frame fluorescence lifetime images, we created six solutions with different lifetimes by mixing Coumarin 6 and Fluorescein in ethanol in different proportions in cuvettes. The concentration of Coumarin 6 varies linearly from 47.8μM to 13.7μM, while that of Fluorescein varies linearly from 0.0μM to 11.9μM. Each solution in a cuvette was scanned with our system to get a 50×50 lifetime image. We compared two coding schemes, Sinusoid-Sinusoid and Expo-Square. $\mathcal{P}_{opt} = \{f_0 =$ 30.6MHz$\}$ and $\mathcal{P}_{opt} = \{f_0 = 6.8\text{MHz}, a = 0.4e9\text{s}^{-1}, \chi = 0.34\}$ for Sinusoid-Sinusoid and Expo-Square, respectively, were computed using the surrogate based on the lifetime range [2.5ns, 3.9ns]. The data acquisition time for each pixel was 12.5ms, and we used the same 168mA DC signal to drive the laser diode for two coding schemes to ensure the same average source power.

Figure 15(a) shows the fluorescence lifetime images obtained by Sinusoid-Sinusoid (upper) and Expo-Square (lower). Six 50×50 lifetime images for the six solutions were combined to form a 300×50 image. Expo-Square shows more uniform lifetime estimation results than Sinusoid-Sinusoid, whose lifetime image suffers from strong noise. Figure 15(b) shows the mean lifetime m_τ and the mean absolute errors, MAE, of the measured lifetimes for six solutions. m_τ increases as the relative proportion of Fluorescein increases and that of Coumarin 6 decreases.

The measurement mean absolute error, MAE, for Sinusoid-Sinusoid is significantly higher than that for Expo-Square. As a result, the error bars for Sinusoid-Sinusoid overlap across cuvettes, thus making it challenging to differentiate materials with similar lifetimes (neighboring images). This is demonstrated by performing an edge detection on the composite lifetime images for both schemes, as shown in Figure 15(c). For Sinusoid-Sinusoid, many spurious edges are detected within each individual sub-image, in addition to the desired boundary between the solutions. This is because the variation in the estimated lifetimes within each image is large, making it difficult to classify the solutions based on the estimated lifetimes. For Expo-Square, no clear edges are found except the boundaries between the solutions. Therefore, the solutions can be classified well according to the estimated lifetimes.

Figure 1(d) and Figure 16(a) show FLIM results on fluorescent objects made with fluorescent tape and a fluorescent slide such that each object has different lifetimes for the foreground (fluorescent tape) and the background (fluorescent slide). The lifetimes were measured by Sinusoid-Sinusoid and Expo-Square. The data acquisition time for each pixel of the star (Figure 1(d)) and the bird (Figure 16(a) upper) samples was 0.8ms, while that for the logo sample (Figure 16(a) lower) was 1ms. We used very

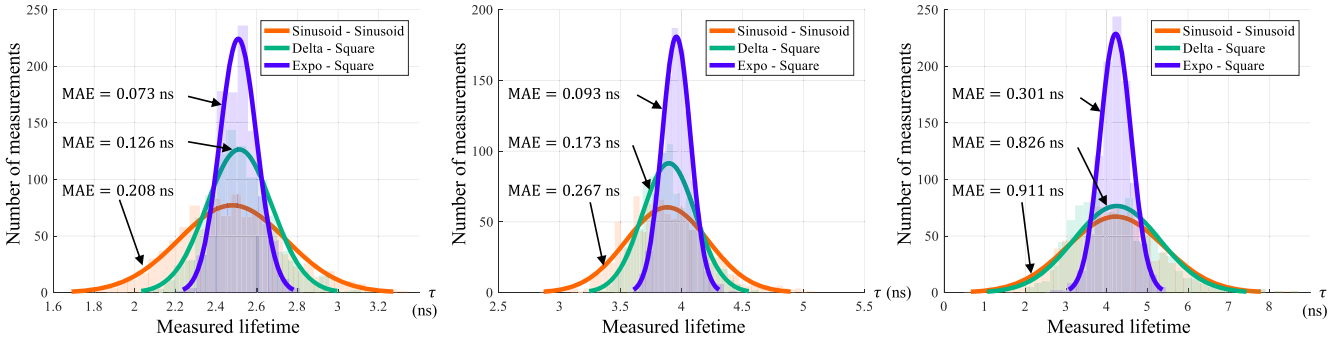

(a) Coumarin 6 in ethanol (b) Rhodamine 110 in ethanol (c) Fluorescein in ethanol

Fig. 14. **Single pixel fluorescence lifetime estimation.** Lifetimes were measured at single positions for three solutions: (a) Coumarin 6 in ethanol, (b) Rhodamin 110 in ethanol, and (c) Fluorescein in ethanol, using three coding schemes, Sinusoid-Sinusoid, Delta-Square, and Expo-Square. For each solution and each coding scheme, lifetimes were measured 1,000 times, and the histogram and the mean absolute error of the repeated measurements were obtained. Normal distributions were fitted to the histograms for visual comparison. Expo-Square shows approximately three times lower mean absolute error as compared to Sinusoid-Sinusoid, given the same average power and capture time.

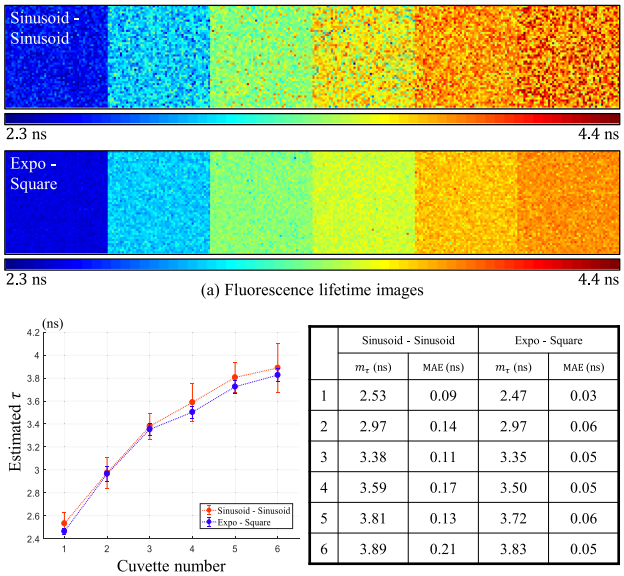

(a) Fluorescence lifetime images

	Sinusoid - Sinusoid		Expo - Square	
	m_τ (ns)	MAE (ns)	m_τ (ns)	MAE (ns)
1	2.53	0.09	2.47	0.03
2	2.97	0.14	2.97	0.06
3	3.38	0.11	3.35	0.05
4	3.59	0.17	3.50	0.05
5	3.81	0.13	3.72	0.06
6	3.89	0.21	3.83	0.05

(b) Statistical results

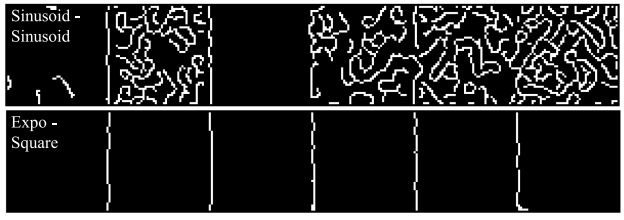

(c) Edge detection results of (a) after smoothing

Fig. 15. **Scanning experimental results with solutions.** (a) Fluorescence lifetime images of six solutions obtained by Sinusoid-Sinusoid (upper) and Expo-Square (lower). (b) Mean values m_τ and mean absolute errors MAE of the measured lifetimes for six solutions. (c) Edge detection results of (a) after applying the same amount of smoothing to both images. Expo-Square achieves considerably higher SNR as compared to Sinusoid-Sinusoid, resulting in robust determination of edges across the solution boundaries.

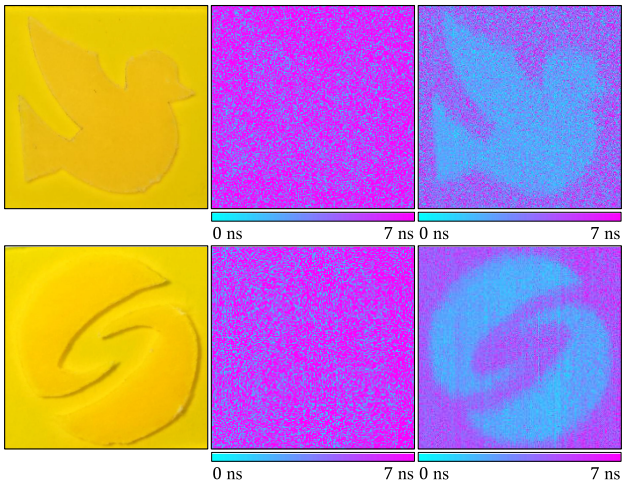

(a) Fluorescent sample (b) Sinusoid - Sinusoid (c) Expo - Square

Fig. 16. **Visual comparisons of fluorescence lifetime images.** (a) Solid fluorescent samples with two lifetimes were made using the fluorescent tape (foreground) and the fluorescent slide (background). The fluorescence lifetime images were obtained by two coding schemes, (b) Sinusoid-Sinusoid and (c) Expo-Square. The boundaries between the foreground and background are invisible with Sinusoid-Sinusoid but clear with Expo-Square.

low light source power (151mA from the laser diode current controller for the star and the bird samples and 155mA for the logo sample), for both coding schemes. The optimal parameter sets determined for these scenes were $\mathcal{P}_{opt} = \{f_0 = 32.5\text{MHz}\}$ and $\mathcal{P}_{opt} = \{f_0 = 6.8\text{MHz}, a = 0.44e9\text{s}^{-1}, \chi = 0.34\}$ for Sinusoid-Sinusoid and Expo-Square, respectively. The boundaries between the foreground and the background are nearly invisible with Sinusoid-Sinusoid (Figure 1(e) and Figure 16(b)) but clearly discernible with Expo-Square (Figure 1(g) and Figure 16(c)).

8.2.3 Comparison of Data Acquisition Times. We compare the data acquisition times of various schemes, in order to achieve a fixed desired lifetime precision. Figure 17(a) compares the data

Schemes	Data acquisition time (ms)		
	Coumarin 6 in ethanol	Rhodamine 110 in ethanol	Fluorescein in ethanol
Sinusoid - Sinusoid	10.00	10.00	10.00
Delta - Square	3.90	3.48	8.08
Expo - Square	1.60	1.45	1.48

(a) Data acquisition time comparison

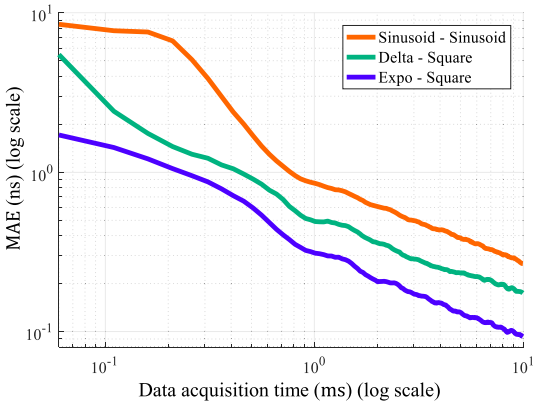

(b) Mean absolute error over the data acquisition time

Fig. 17. **Data acquisition time and lifetime precision comparison.** (a) Data acquisition time to achieve the same lifetime precision. Expo-Square can achieve the same precision as Sinusoid-Sinusoid with only one-seventh data acquisition time. (b) Relationship between the mean absolute error, MAE, of the measured lifetimes for Rhodamine 110 in ethanol with data acquisition time. Expo-Square requires considerably shorter acquisition time than Sinusoid-Sinusoid to achieve the same SNR.

acquisition times between three coding schemes (Sinusoid-Sinusoid, Delta-Square, and Expo-Square) to achieve the same lifetime precision (mean absolute errors) for three solutions (Coumarin 6, Rhodamine 110, and Fluorescein in ethanol). The desired mean absolute error was fixed to the mean absolute error achieved by the Sinusoid-Sinusoid with 10ms data acquisition time: 0.26ns, 0.34ns, and 1.19ns for Coumarin 6, Rhodamine 110, and Fluorescein, respectively. Expo-Square can achieve the same precision as Sinusoid-Sinusoid with only one-seventh data acquisition time. Figure 17(b) shows the relationship between the lifetime precision and the data acquisition time. The mean absolute errors, MAE, of the measured lifetimes of Rhodamine 110 in ethanol were plotted against data acquisition time for three coding schemes. Expo-Square achieves high precision (low mean absolute error) even at very short acquisition times, thus leading to considerable speed-ups in data capture, given a desired level of SNR.

9 LIMITATIONS AND FUTURE WORK

Objective for Lifetime Precision for a Multi-Exponential Decay. The mean lifetime error and the surrogate proposed in the article are intended for mono-exponential decay (single lifetime). However, for certain materials, the fluorescence emission profile is a linear combination of multiple exponential functions (Lakowicz 2006). An important next step is to extend the approaches developed in this article, and design an objective for lifetime precision, and code optimization procedures for materials with multi-exponential fluorescence lifetime decay.

Surrogate for More Than Three Measurements. The surrogate, as defined in Equation (16), is valid only for $K = 3$ measurements since the cross product in Equation (13) is not generally defined when $K > 3$. While this is not a strong practical limitation since the relative performance of two coding schemes remains approximately the same irrespective of K, a promising direction of future research is to derive a surrogate for $K > 3$ measurements.

Optimization of the Surrogate. The proposed surrogate as an objective function is non-convex and non-smooth. Hence, it is challenging to obtain globally optimal solutions for both modulation and demodulation functions in the general case (i.e., when the search space contains all possible coding schemes). A compelling line of research is to seek potentially sub-optimal solutions in a narrowed search space by incorporating various physical constraints like the maximum peak power and the maximum system bandwidth.

ACKNOWLEDGMENTS

The authors would also like to thank Felipe Gutierrez Barragan for calibration of the setup.

REFERENCES

Diego Airado-Rodríguez, Teresa Galeano-Díaz, Isabel Durán-Merás, and Jens Petter Wold. 2009. Usefulness of fluorescence excitation-emission matrices in combination with PARAFAC, as fingerprints of red wines. *Journal of Agricultural and Food Chemistry* 57, 5 (2009), 1711–1720.

Syed Abdullah Aljunid, Gleb Maslennikov, Yimin Wang, Hoang Lan Dao, Valerio Scarani, and Christian Kurtsiefer. 2013. Excitation of a single atom with exponentially rising light pulses. *Physical Review Letters* 111, 10 (2013), 103001.

Philippe I. H. Bastiaens and Anthony Squire. 1999. Fluorescence lifetime imaging microscopy: Spatial resolution of biochemical processes in the cell. *Trends in Cell Biology* 9, 2 (1999), 48–52.

Wolfgang Becker. 2014. *The bh TCSPC Handbook*. Becker & Hickl.

Oscar Beijbom, Tali Treibitz, David I. Kline, Gal Eyal, Adi Khen, Benjamin Neal, Yossi Loya, B. Greg Mitchell, and David Kriegman. 2016. Improving automated annotation of benthic survey images using wide-band fluorescence. *Scientific Reports* 6 (2016), 23166.

Mikhail Y. Berezin and Samuel Achilefu. 2010. Fluorescence lifetime measurements and biological imaging. *Chemical Reviews* 110, 5 (2010), 2641–2684.

Ayush Bhandari, Christopher Barsi, and Ramesh Raskar. 2015a. Blind and reference-free fluorescence lifetime estimation via consumer time-of-flight sensors. *Optica* 2, 11 (Nov. 2015), 965–973. DOI: https://doi.org/10.1364/OPTICA.2.000965

Ayush Bhandari, Christopher Barsi, and Ramesh Raskar. 2015b. Blind and reference-free fluorescence lifetime estimation via consumer time-of-flight sensors. *Optica* 2, 11 (2015), 965–973.

Ayush Bhandari and Ramesh Raskar. 2016. Signal processing for time-of-flight imaging sensors: An introduction to inverse problems in computational 3-D imaging. *IEEE Signal Processing Magazine* 33, 5 (2016), 45–58.

M. J. Booth and T. Wilson. 2004. Low-cost, frequency-domain, fluorescence lifetime confocal microscopy. *Journal of Microscopy* 214, 1 (2004), 36–42.

A. Colasanti, A. Kisslinger, G. Fabbrocini, R. Liuzzi, M. Quarto, P. Riccio, G. Roberti, and F. Villani. 2000. MS-2 fibrosarcoma characterization by laser induced autofluorescence. *Lasers in Surgery and Medicine* 26, 5 (2000), 441–448.

Daniela Comelli, Cosimo D'Andrea, Gianluca Valentini, Rinaldo Cubeddu, Chiara Colombo, and Lucia Toniolo. 2004. Fluorescence lifetime imaging and spectroscopy as tools for nondestructive analysis of works of art. *Applied Optics* 43, 10 (2004), 2175–2183.

Kalyanmoy Deb, Amrit Pratap, Sameer Agarwal, and TAMT Meyarivan. 2002. A fast and elitist multiobjective genetic algorithm: NSGA-II. *IEEE Transactions on Evolutionary Computation* 6, 2 (2002), 182–197.

Michelle A. Digman, Valeria R. Caiolfa, Moreno Zamai, and Enrico Gratton. 2008. The phasor approach to fluorescence lifetime imaging analysis. *Biophysical Journal* 94, 2 (2008), L14–L16.

L. A. Donaldson and K. Radotic. 2013. Fluorescence lifetime imaging of lignin autofluorescence in normal and compression wood. *Journal of Microscopy* 251, 2 (2013), 178–187.

Alan Elder, Simon Schlachter, and Clemens F. Kaminski. 2008. Theoretical investigation of the photon efficiency in frequency-domain fluorescence lifetime imaging microscopy. *JOSA A* 25, 2 (2008), 452–462.

Dan Elson, Jose Requejo-Isidro, Ian Munro, Fred Reavell, Jan Siegel, Klaus Suhling, Paul Tadrous, Richard Benninger, Peter Lanigan, James McGinty, et al. 2004. Time-domain fluorescence lifetime imaging applied to biological tissue. *Photochemical & Photobiological Sciences* 3, 8 (2004), 795–801.

Alessandro Esposito, Hans Gerritsen, Thierry Oggier, Felix Lustenberger, and Fred S. Wouters. 2006. Innovating lifetime microscopy: A compact and simple tool for life sciences, screening, and diagnostics. *Journal of Biomedical Optics* 11, 3 (2006), 034016.

Alessandro Esposito, Hans C. Gerritsen, and Fred S. Wouters. 2007. Optimizing frequency-domain fluorescence lifetime sensing for high-throughput applications: Photon economy and acquisition speed. *JOSA A* 24, 10 (2007), 3261–3273.

A. Esposito, T. Oggier, H. C. Gerritsen, F. Lustenberger, and F. S. Wouters. 2005. All-solid-state lock-in imaging for wide-field fluorescence lifetime sensing. *Optics Express* 13, 24 (2005), 9812–9821.

Ying Fu, Antony Lam, Yasuyuki Matsushita, Imari Sato, and Yoichi Sato. 2014. Interreflection removal using fluorescence. In *European Conference on Computer Vision*. Springer, 203–217.

Mohit Gupta, Andreas Velten, Shree K. Nayar, and Eric Breitbach. 2018. What are optimal coding functions for time-of-flight imaging? *ACM Transactions on Graphics (TOG)* 37, 2 (2018), 13.

Shuai Han, Yasuyuki Matsushita, Imari Sato, Takahiro Okabe, and Yoichi Sato. 2012. Camera spectral sensitivity estimation from a single image under unknown illumination by using fluorescence. In *IEEE Conference on Computer Vision and Pattern Recognition (CVPR'12)*. IEEE, 805–812.

Miles Hansard, Seungkyu Lee, Ouk Choi, and Radu Patrice Horaud. 2012. *Time-of-Flight Cameras: Principles, Methods and Applications*. Springer Science & Business Media.

Samuel W. Hasinoff, Frédo Durand, and William T. Freeman. 2010. Noise-optimal capture for high dynamic range photography. In *IEEE Conference on Computer Vision and Pattern Recognition (CVPR'10)*. IEEE, 553–560.

Felix Heide, Matthias B. Hullin, James Gregson, and Wolfgang Heidrich. 2013. Low-budget transient imaging using photonic mixer devices. *ACM Transactions on Graphics (ToG)* 32, 4 (2013), 45.

Felix Heide, Lei Xiao, Andreas Kolb, Matthias B. Hullin, and Wolfgang Heidrich. 2014. Imaging in scattering media using correlation image sensors and sparse convolutional coding. *Optics Express* 22, 21 (2014), 26338–26350.

J. Michael Hollas. 2004. *Modern Spectroscopy*. John Wiley & Sons.

Matthias B. Hullin, Martin Fuchs, Ivo Ihrke, Hans-Peter Seidel, and Hendrik P. A. Lensch. 2008. Fluorescent immersion range scanning. *ACM Transactions on Graphics* 27, 3 (Aug. 2008), Article 87, 10 pages. DOI: https://doi.org/10.1145/1360612.1360686

Matthias B. Hullin, Johannes Hanika, Boris Ajdin, Hans-Peter Seidel, Jan Kautz, and Hendrik P. A. Lensch. 2010. Acquisition and analysis of bispectral bidirectional reflectance and reradiation distribution functions. *ACM Transactions on Graphics* 29, 4 (July 2010), Article 97, 7 pages. DOI: https://doi.org/10.1145/1778765.1778834

Moon S. Kim, Byoung-Kwan Cho, Alan M. Lefcourt, Yud-Ren Chen, and Sukwon Kang. 2008. Multispectral fluorescence lifetime imaging of feces-contaminated apples by time-resolved laser-induced fluorescence imaging system with tunable excitation wavelengths. *Applied Optics* 47, 10 (2008), 1608–1616.

Joseph R. Lakowicz. 2006. *Principles of Fluorescence Spectroscopy*. Springer.

R. Lange. 2000. *3D Time of Flight Distance Measurement with Custom Solid State Image Sensors in CMOS, CCD Technology*. https://books.google.com/books?id=upMuHwAACAAJ

Lea Lenhardt, Rasmus Bro, Ivana Zeković, Tatjana Dramićanin, and Miroslav D. Dramićanin. 2015. Fluorescence spectroscopy coupled with PARAFAC and PLS DA for characterization and classification of honey. *Food Chemistry* 175 (2015), 284–291.

Yuxiang Lin and Arthur F. Gmitro. 2010. Statistical analysis and optimization of frequency-domain fluorescence lifetime imaging microscopy using homodyne lock-in detection. *JOSA A* 27, 5 (2010), 1145–1155.

Douglas Magde, Gail E. Rojas, and Paul G. Seybold. 1999. Solvent dependence of the fluorescence lifetimes of xanthene dyes. *Photochemistry and Photobiology* 70, 5 (1999), 737–744.

John A. Nelder and Roger Mead. 1965. A simplex method for function minimization. *The Computer Journal* 7, 4 (1965), 308–313.

Austin Nevin, Daniela Comelli, Gianluca Valentini, Demetrios Anglos, Aviva Burnstock, Sharon Cather, and Rinaldo Cubeddu. 2007. Time-resolved fluorescence spectroscopy and imaging of proteinaceous binders used in paintings. *Analytical and Bioanalytical Chemistry* 388, 8 (2007), 1897–1905.

Lucio Pancheri, Nicola Massari, and David Stoppa. 2013. SPAD image sensor with analog counting pixel for time-resolved fluorescence detection. *IEEE Transactions on Electron Devices* 60, 10 (2013), 3442–3449.

Johan Philip and Kjell Carlsson. 2003. Theoretical investigation of the signal-to-noise ratio in fluorescence lifetime imaging. *JOSA A* 20, 2 (2003), 368–379.

Asima Pradhan, Prabir Pal, Gilles Durocher, Luc Villeneuve, Antonia Balassy, Féridoun Babai, Louis Gaboury, and Louise Blanchard. 1995. Steady state and time-resolved fluorescence properties of metastatic and non-metastatic malignant cells from different species. *Journal of Photochemistry and Photobiology B: Biology* 31, 3 (1995), 101–112.

J. Requejo-Isidro, J. McGinty, I. Munro, D. S. Elson, N. P. Galletly, M. J. Lever, M. A. A. Neil, G. W. H. Stamp, P. M. W. French, P. A. Kellett, et al. 2004. High-speed wide-field time-gated endoscopic fluorescence-lifetime imaging. *Optics Letters* 29, 19 (2004), 2249–2251.

Imari Sato, Takahiro Okabe, and Yoichi Sato. 2012. Bispectral photometric stereo based on fluorescence. In *IEEE Conference on Computer Vision and Pattern Recognition (CVPR'12)*. IEEE, 270–277.

S. Schlachter, A. D. Elder, A. Esposito, G. S. Kaminski, J. H. Frank, L. K. Van Geest, and C. F. Kaminski. 2009. mhFLIM: Resolution of heterogeneous fluorescence decays in widefield lifetime microscopy. *Optics Express* 17, 3 (2009), 1557–1570.

L. K. Seah, U. S. Dinish, W. F. Phang, Z. X. Chao, and V. M. Murukeshan. 2005. Fluorescence optimisation and lifetime studies of fingerprints treated with magnetic powders. *Forensic Science International* 152, 2–3 (2005), 249–257.

L. K. Seah, P. Wang, V. M. Murukeshan, and Z. X. Chao. 2006. Application of fluorescence lifetime imaging (FLIM) in latent finger mark detection. *Forensic Science International* 160, 2–3 (2006), 109–114.

Nathan C. Shaner, Gerard G. Lambert, Andrew Chammas, Yuhui Ni, Paula J. Cranfill, Michelle A. Baird, Brittney R. Sell, John R. Allen, Richard N. Day, Maria Israelsson, et al. 2013. A bright monomeric green fluorescent protein derived from Branchiostoma lanceolatum. *Nature Methods* 10, 5 (2013), 407.

Wen Shi, Xiaohua Li, and Huimin Ma. 2014. Fluorescent probes and nanoparticles for intracellular sensing of pH values. *Methods and Applications in Fluorescence* 2, 4 (2014), 042001.

Ewa Sikorska, Tomasz Górecki, Igor V. Khmelinskii, Marek Sikorski, and Jacek Kozioł. 2005. Classification of edible oils using synchronous scanning fluorescence spectroscopy. *Food Chemistry* 89, 2 (2005), 217–225.

Shiwen Sun, Birgit Ungerböck, and Torsten Mayr. 2015. Imaging of oxygen in microreactors and microfluidic systems. *Methods and Applications in Fluorescence* 3, 3 (2015), 034002.

Virginia Torczon. 1997. On the convergence of pattern search algorithms. *SIAM Journal on Optimization* 7, 1 (1997), 1–25.

Tali Treibitz, Zak Murez, B. Greg Mitchell, and David Kriegman. 2012. Shape from fluorescence. In *European Conference on Computer Vision*. Springer, 292–306.

Andreas Velten, Thomas Willwacher, Otkrist Gupta, Ashok Veeraraghavan, Moungi G. Bawendi, and Ramesh Raskar. 2012. Recovering three-dimensional shape around a corner using ultrafast time-of-flight imaging. *Nature Communications* 3 (2012), 745.

Charles W. Wilkerson Jr., Peter M. Goodwin, W. Patrick Ambrose, John C. Martin, and Richard A. Keller. 1993. Detection and lifetime measurement of single molecules in flowing sample streams by laser-induced fluorescence. *Applied Physics Letters* 62, 17 (1993), 2030–2032.

Di Wu, Matthew O'Toole, Andreas Velten, Amit Agrawal, and Ramesh Raskar. 2012. Decomposing global light transport using time of flight imaging. In *IEEE Conference on Computer Vision and Pattern Recognition (CVPR'12)*. IEEE, 366–373.

Qiaole Zhao, Ian T. Young, and Jan Geert Sander De Jong. 2011. Photon budget analysis for fluorescence lifetime imaging microscopy. *Journal of Biomedical Optics* 16, 8 (2011), 086007.

Received June 2018; revised November 2018; accepted March 2019

Supplementary Technical Report: Coding Scheme Optimization for Fast Fluorescence Lifetime Imaging

JONGHO LEE, JENU VARGHESE CHACKO, BING DAI, SYED AZER REZA, ABDUL KADER SAGAR, KEVIN W. ELICEIRI, ANDREAS VELTEN, and MOHIT GUPTA, University of Wisconsin-Madison

1 OVERVIEW

This document provides derivations, explanations, and more results supporting the content of the article submission titled "Coding Scheme Optimization for Fast Fluorescence Lifetime Imaging."

2 FD-FLIM VS. C-TOF IMAGING

In this section, we derive the detailed equations of the measurement intensities for FD-FLIM and C-ToF imaging based on their image formation models when the Sinusoid-Sinusoid coding scheme is used.

2.1 Fluorescence Emission in FD-FLIM and Reflection in C-ToF Imaging with Sinusoidal Illuminations

In FD-FLIM, the system's impulse response $h(t)$ is an exponentially decaying function $h(t) = \frac{1}{\tau}e^{-\frac{t}{\tau}}$ $(t \geq 0)$, while in C-ToF imaging it is a shifted delta function $h(t) = \delta(t - \frac{2d}{c})$, where d is the scene depth and c is the light speed. Let us assume that the light source is modulated with a sinusoid:

$$M(t) = \frac{M_0}{2}\left(1 + \cos\left(2\pi f_0 t\right)\right), \tag{1}$$

where M_0 determines the source power. Then, the fluorescence emission in FD-FLIM or the reflected light in C-ToF imaging at time t observed at the sensor is a scaled and offset version of the convolution of $M(t)$ and $h(t)$:

$$E(t) = \alpha \int_{-\infty}^{\infty} M(s)h(t-s)\,ds + \gamma, \tag{2}$$

where α is a scale factor depending on system parameters and the sample and γ is an offset corresponding to ambient illumination. For the sake of simplicity, assume $\alpha = 1$ and $\gamma = 0$. Then, in FD-FLIM:

$$E^{FLIM}(t) = \frac{M_0}{2}\left(1 + \frac{1}{\sqrt{1 + (2\pi f_0\tau)^2}}\cos\left(2\pi f_0 t - \tan^{-1}(2\pi f_0\tau)\right)\right), \tag{3}$$

and in C-ToF imaging:

$$E^{ToF}(t) = \frac{M_0}{2}\left(1 + \cos\left(2\pi f_0 t - \frac{4\pi f_0 d}{c}\right)\right). \tag{4}$$

In FD-FLIM, the lifetime τ is inherent in both the amplitude attenuation $1/\sqrt{1 + (2\pi f_0\tau)^2}$ and the phase shift $\tan^{-1}(2\pi f_0\tau)$ of $E(t)^{FLIM}$. In C-ToF imaging, the depth d is only in the phase shift, $4\pi f_0 d/c$ of $E^{ToF}(t)$, as shown in Figure 1. Any periodic function can be represented as a sum of sinusoids with different amplitudes and frequencies. When given an arbitrary periodic waveform of the incident light, the reflected light in C-ToF imaging is just the phase-shifted version of the incident light, while the fluorescence emission in FD-FLIM is very complicated due to different amplitude attenuations and phase shifts for different frequency components.

2.2 Intensity Vector Points in the Intensity Space

The intensity vector point $[B_1, \ldots, B_K]$ in the K-dim intensity space is defined with

$$B_i = \int_T E(t)D_i(t)dt \quad (i = 1, \ldots, K), \tag{5}$$

where $D_i(t)$ is the demodulation function with a phase shift of $\phi_i = 2\pi(i-1)/K$. With a sinusoid demodulation function:

$$D_i(t) = \frac{1}{2}\left(1 + \cos\left(2\pi f_0 t - \phi_i\right)\right) \quad (i = 1, \ldots, K), \tag{6}$$

in FD-FLIM:

$$B_i^{FLIM} = \frac{M_0 T}{4}\left(1 + \frac{1}{2\sqrt{1 + (2\pi f_0\tau)^2}}\cos\left(\phi_i - \tan^{-1}(2\pi f_0\tau)\right)\right), \tag{7}$$

and in C-ToF imaging:

$$B_i^{ToF} = \frac{M_0 T}{4}\left(1 + \frac{1}{2}\cos\left(\phi_i - \frac{4\pi f_0 d}{c}\right)\right). \tag{8}$$

Figure 2 shows the several intensity vector points $[B_1, B_2, B_3]$ in the 3D intensity space for FD-FLIM and C-ToF imaging. In Figure 2(a), the intensity vector points corresponding to 16 different τ values uniformly sampled from [0ns, 15ns] with 1ns step size are represented. In Figure 2(b), those corresponding to 16 different d values uniformly sampled from [0m, 1.5m] with 0.1m step size are represented. Two modulation frequencies, 10MHz (upper figure) and 100MHz (lower figure), are used. As the modulation frequency increases, the inter-point distance increases for relatively short τ's and decreases for relatively long τ's in FD-FLIM. On the contrary, the inter-point distance always increases for all d's in C-ToF imaging.

3 MEAN LIFETIME ERROR VS. SURROGATE METRIC FOR DIFFERENT LIFETIME RANGES

Figure 3 shows the comparison between (a) the mean lifetime error and (b) the surrogate metric for different coding schemes with different lifetime ranges. Note that there is a strong correlation between the mean lifetime error and surrogate metric, for all the coding schemes and all the lifetime ranges, over the entire range of modulation frequencies.

0730-0301/2019/06-ART26 $15.00
https://doi.org/10.1145/3325136

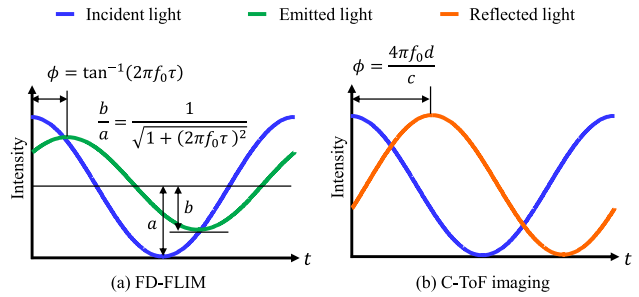

Fig. 1. **Fluorescence emission in FD-FLIM and reflection in C-ToF imaging with sinusoidal illumination.** The lifetime information τ is in both amplitude attenuation b/a and phase-shift ϕ of the emitted light in FD-FLIM, but the scene depth information d is only in phase-shift ϕ of the reflected light in C-ToF imaging.

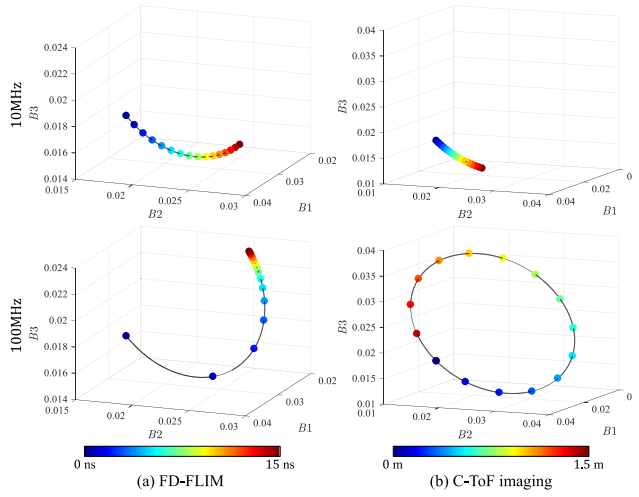

Fig. 2. **Intensity vector points for FD-FLIM and C-ToF imaging in the intensity space.** (a) Intensity vector points for 16 different lifetimes in FD-FLIM, and (b) intensity vector points for 16 different scene depths in C-ToF imaging when the modulation frequency is 10MHz (upper figure) and 100MHz (lower figure).

4 OPTIMIZATION FOR DIFFERENT LIFETIME RANGES

Figure 4 shows the inverse surrogate values (Figure 4(a)) and the related optimal parameter sets (Figure 4(b)) of 12 coding schemes for three different τ ranges $[\tau_1, \tau_2]$ = [1ns, 3ns], [6ns, 8ns], and [11ns, 13ns]. There are several key observations to notice. First, the relative coding scheme performance depends on the lifetime. For example, the coding scheme performance difference between Square-Ham and Expo-Sinusoid decreases when the lifetime increases. Second, the optimal modulation frequency for each coding scheme is inversely related to the lifetime. When the lifetime increases, the optimal modulation frequency decreases. Third, the optimal parameter value of κ for Expo decreases when the lifetime increases. We think this is related to the fact that when the lifetime increases, κ should decrease to maximize the convolution of Expo and the fluorescence response $h(t) = \frac{1}{\tau} e^{-\frac{t}{\tau}}$. Fourth, the optimal modulation frequency of Expo-Square is relatively low as compared with other coding schemes. This is another advantage of using Expo-Square since most FD-FLIM systems are band-limited, and there is, consequently, a limitation in using high modulation frequency.

5 DECODING FLUORESCENCE LIFETIME

A unified lifetime-decoding framework applicable to any coding scheme is essential. In this section, we explain how to decode lifetimes from the measured intensities for the given coding scheme.

5.1 Analytical Approach

Since there are three unknowns, α, β, and τ, we need $K \geq 3$ intensity values to estimate the lifetime. From the image formation model:

$$B_i = \alpha \mathfrak{V}_i(\tau) + \beta \quad (i = 1, \ldots, K), \tag{9}$$

where

$$\mathfrak{V}_i(\tau) = \int_T \left(\int_{-\infty}^{\infty} \frac{M(s)}{\tau} e^{\frac{s-t}{\tau}} \, ds \right) D_i(t) \, dt \tag{10}$$

is the fluorescence correlation function described completely by the modulation function $M(t)$ and the demodulation function $D(t)$. $D_i(t)$ is the phase-shifted demodulation function by $2\pi(i-1)/K$. We can construct the following equation when $K = 3$ with the assumption that $B_2 \neq B_3$:

$$F(\tau) = \frac{\mathfrak{V}_1(\tau) - \mathfrak{V}_2(\tau)}{\mathfrak{V}_2(\tau) - \mathfrak{V}_3(\tau)} = \frac{B_1 - B_2}{B_2 - B_3} = b. \tag{11}$$

Since the only interesting unknown is lifetime τ, we can remove other unknowns by taking a ratio between two consecutive differences of B_i as represented in Equation (11). $F(\tau)$ is a known function determined by a coding scheme, and b is the constant obtained from the intensity measurements. We empirically verified that for all 12 coding schemes used in the optimization, $F(\tau)$ is bijective. Therefore, if we know the coding scheme and the corresponding intensity values, we can estimate the lifetime $\hat{\tau}$ by solving

$$\hat{\tau} = \arg\min_{\tau} |F(\tau) - b| \, . \tag{12}$$

For $K > 3$, we can consider $\binom{K}{3}$ combinations of Equation (11) and take the average of all the obtained lifetimes to estimate the final $\hat{\tau}$. This is one example to estimate the lifetime when $K > 3$, and the optimal algorithm for solving for lifetime is out of our scope.

5.2 Table Look-Up Approach

For each coding scheme, save all pairs of the lifetime value τ and the corresponding $F(\tau)$ in Equation (11) in the table, and find the best matching τ when b is given. Since $F(\tau)$ is bijective, we can estimate the lifetime τ from b without ambiguity.

RunTime Comparison Between Analytical Approach and Table Look-Up Approach. For Sinusoid-Sinusoid and Delta-Sinusoid, the closed-form solution exists for solving for τ. However, in general, there is no closed-form solution for the arbitrary coding scheme, and an iteration-based solver is required to solve for τ in the analytical approach. In this case, a table look-up approach is faster. According to our computation, the table look-up approach with 0.01ns step size in τ index is about 20 times faster than the analytical approach, and, as shown in Figure 5, is just as precise.

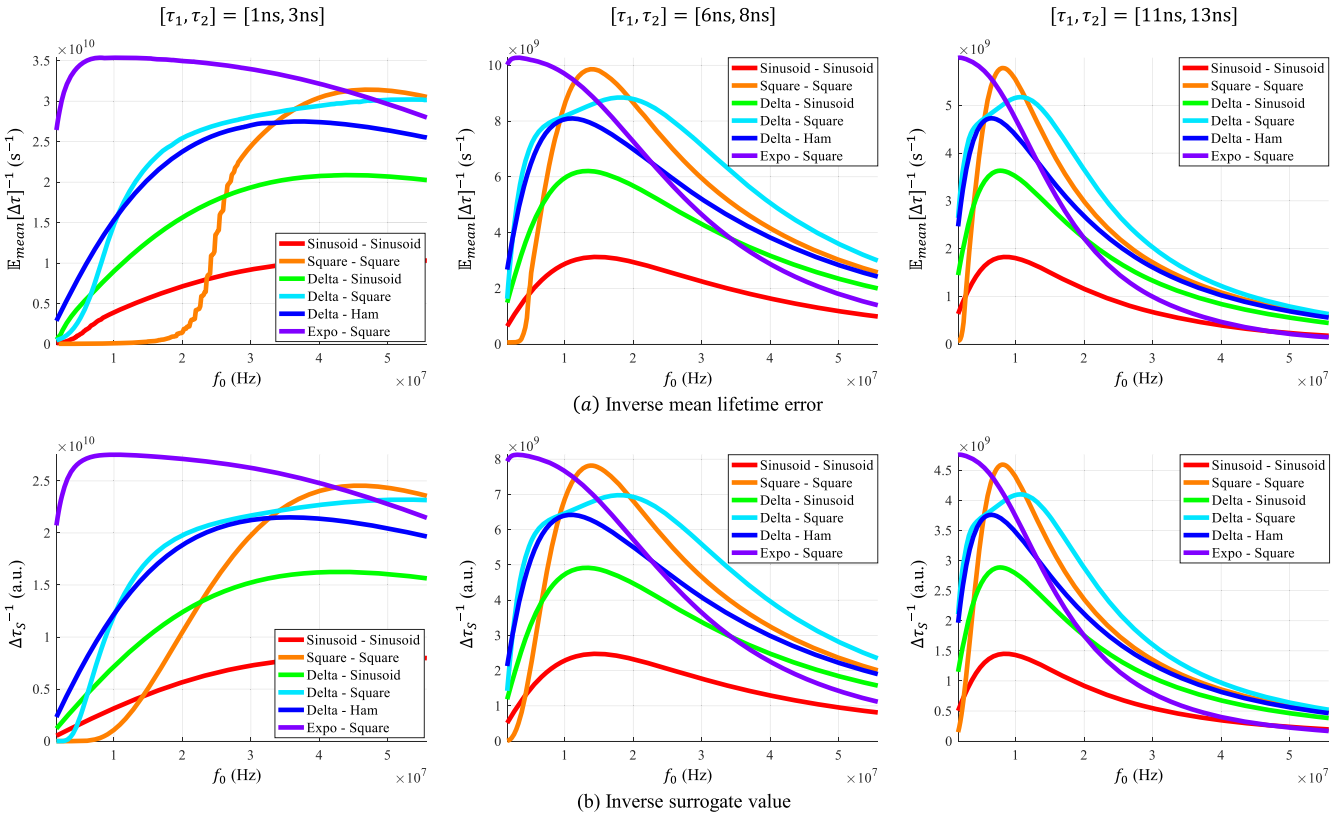

(a) Inverse mean lifetime error

(b) Inverse surrogate value

Fig. 3. **Coding scheme performance comparison according to mean lifetime error and surrogate metric for different lifetime ranges.** (a) Inverse mean lifetime errors $\mathbb{E}_{mean}[\Delta\tau]^{-1}$, and (b) inverse surrogate values $\Delta\tau_S^{-1}$ for three different lifetime ranges, $[\tau_1, \tau_2]$ = [1ns, 3ns], [6ns, 8ns], and [11ns, 13ns]. The surrogate values have a strong correlation with the mean lifetime error across various coding schemes, frequencies, and lifetime ranges.

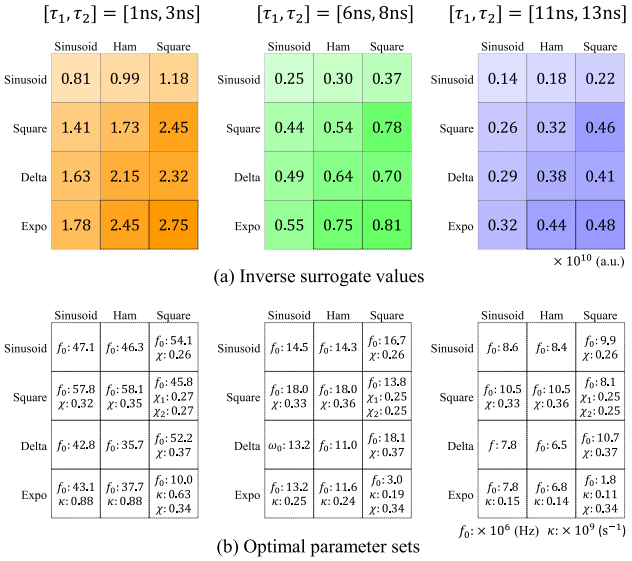

(a) Inverse surrogate values

(b) Optimal parameter sets

Fig. 4. **Optimization results for different τ ranges.** (a) The inverse surrogate values of different coding schemes for different τ ranges. Expo-Square and Square-Square show good performances as compared with other coding schemes. (b) The corresponding optimal parameter sets. The optimal parameter values vary according to the τ ranges.

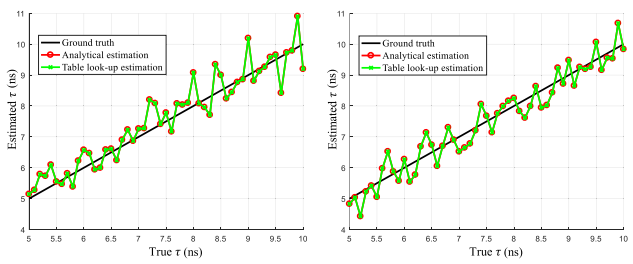

(a) Sinusoid - Sinusoid

(b) Delta - Square

Fig. 5. **Lifetime estimation results using analytical and table look-up approaches.** We added noise to the intensities obtained by two coding schemes: (a) Sinusoid-Sinusoid and (b) Delta-Square ($\chi = 0.5$). Lifetimes can be estimated from the noisy intensities using the analytical approach (red plot) and the table look-up approach (green plot). The table look-up approach is much faster than the analytical approach while showing almost the same estimation results.

5.3 Fluorescence Correlation Functions for Various Coding Schemes

Both analytical approach and table look-up approach require the computation of the fluorescence correlation functions $\mathcal{U}_i(\tau)$ ($i = 1, \ldots, K$) for the given coding scheme to solve for τ using Equation (12). We describe the fluorescence correlation functions for

the coding schemes used in Figure 3. The fluorescence correlation functions for any other coding schemes can be derived similarly. Please note that the fluorescence correlation functions can be also computed numerically without analytical derivations. For the fluorescence correlation computation, we impose two constraints for the coding schemes. The area under the curve of the modulation function $M(t)$ for the period T_0 is P, and the amplitude of the demodulation function $D(t)$ is between 0 and 1. We also assume T in Equation (10) satisfies $T \gg T_0$.

Sinusoid-Sinusoid. The coding scheme is represented as

$$M(t) = \frac{P}{T_0}\left(1 + \cos(2\pi f_0 t)\right), \tag{13}$$

$$D_i(t) = \frac{1}{2}\left(1 + \cos(2\pi f_0 t - \phi_i)\right) \quad (i = 1, \ldots, K), \tag{14}$$

where $\phi_i = 2\pi(i-1)/K$. Then the fluorescence correlation functions $\mathfrak{V}_i(\tau)$ $(i = 1, \ldots, K)$ for Sinusoid-Sinusoid are

$$\mathfrak{V}_i(\tau) = \frac{PT}{2T_0}\left(1 + \frac{1}{2\sqrt{1 + (2\pi f_0 \tau)^2}}\cos(\phi_i - \tan^{-1}(2\pi f_0 \tau))\right). \tag{15}$$

Delta-Sinusoid. The coding scheme is represented as

$$M(t) = P\sum_{n=\infty}^{\infty}\delta(t - nT_0), \tag{16}$$

$$D_i(t) = \frac{1}{2}\left(1 + \cos(2\pi f_0 t - \phi_i)\right) \quad (i = 1, \ldots, K), \tag{17}$$

where $\phi_i = 2\pi(i-1)/K$. Then the fluorescence correlation functions $\mathfrak{V}_i(\tau)$, $(i = 1, \ldots, K)$ for Delta-Sinusoid are:

$$\mathfrak{V}_i(\tau) = \frac{PT}{2T_0}\left(1 + \frac{1}{\sqrt{1 + (2\pi f_0 \tau)^2}}\cos(\phi_i - \tan^{-1}(2\pi f_0 \tau))\right). \tag{18}$$

Delta-Square. The coding scheme is represented as

$$M(t) = P\sum_{n=\infty}^{\infty}\delta(t - nT_0), \tag{19}$$

$$D_i(t) = \frac{1}{2}\left(1 + \mathrm{sqr}(2\pi f_0 t - \phi_i, \chi)\right) \quad (i = 1, \ldots, K), \tag{20}$$

where $\phi_i = 2\pi(i-1)/K$, sqr is a square function whose amplitude is between -1 and 1, and χ is a duty cycle of sqr. If we define $t_i = T_0(i-1)/K$, the fluorescence correlation functions $\mathfrak{V}_i(\tau)$ $(i = 1, \ldots, K)$ for Delta-Square are

$$\mathfrak{V}_i(\tau) = \begin{cases} \frac{PT}{T_0\left(1 - e^{(-\frac{T_0}{\tau})}\right)}\left(e^{-\frac{t_i}{\tau}} - e^{-\frac{t_i+\chi}{\tau}}\right), & \text{if } t_i + \chi \le T_0 \\ \frac{PT}{T_0\left(1 - e^{(-\frac{T_0}{\tau})}\right)}\left(1 - e^{-\frac{t_i - T_0 + \chi}{\tau}} + e^{-\frac{t_i}{\tau}} - e^{-\frac{T_0}{\tau}}\right), & \text{otherwise.} \end{cases} \tag{21}$$

Delta-Ham. The coding scheme is represented as

$$M(t) = P\sum_{n=\infty}^{\infty}\delta(t - nT_0), \tag{22}$$

$$D_i(t) = \text{Hamiltonian functions.} \tag{23}$$

Please refer to Gupta et al. (2018) for the equations of Hamiltonian functions. When $K = 3$, the fluorescence correlation functions $\mathfrak{V}_i(\tau)$ $(i = 1, 2, 3)$ for Delta-Ham are

$$\mathfrak{V}_1(\tau) = PT\frac{6\tau}{T_0^2}\frac{e^{-\frac{T_0}{3\tau}} - e^{-\frac{T_0}{2\tau}}}{1 + e^{-\frac{T_0}{2\tau}}}, \tag{24}$$

$$\mathfrak{V}_2(\tau) = PT\frac{6\tau}{T_0^2}\frac{1 - e^{-\frac{T_0}{6\tau}}}{1 + e^{-\frac{T_0}{2\tau}}}, \tag{25}$$

$$\mathfrak{V}_3(\tau) = PT\left(\frac{1}{T_0} + \frac{6\tau}{T_0^2}\frac{e^{-\frac{T_0}{3\tau}} - e^{-\frac{T_0}{6\tau}}}{1 + e^{-\frac{T_0}{2\tau}}}\right). \tag{26}$$

Square-Square. The coding scheme is represented as

$$M(t) = \frac{P}{2\chi_1 T_0}\left(1 + \mathrm{sqr}(2\pi f_0 t, \chi_1)\right), \tag{27}$$

$$D_i(t) = \frac{1}{2}\left(1 + \mathrm{sqr}(2\pi f_0 t - \phi_i, \chi_2)\right) \quad (i = 1, \ldots, K), \tag{28}$$

where $\phi_i = 2\pi(i-1)/K$, sqr is a square function whose amplitude is between -1 and 1, and χ_1 and χ_2 are duty cycles of sqr for $M(t)$ and $D(t)$, respectively. If we define $t_i = T_0(i-1)/K$, $d_1 = \chi_1 T_0$, and $d_2 = \chi_2 T_0$, the fluorescence correlation functions $\mathfrak{V}_i(\tau)$ $(i = 1, \ldots, K)$ for Square-Square are as follows:

When $0 \le t_i < d_1$,

$$\mho_i(\tau) = \begin{cases} \frac{PT}{\left(\chi_1 T_0^2\right)\left(1-e^{-\frac{T_0}{\tau}}\right)}\left(\tau\left(1-e^{\frac{d_1-T_0}{\tau}}\right)\left(e^{-\frac{t_i+d_2}{\tau}}-e^{-\frac{t_i}{\tau}}\right)+\left(1-e^{-\frac{T_0}{\tau}}\right)d_2\right), & \text{if } t_i+d_2 \le d_1 \\ \frac{PT}{\left(\chi_1 T_0^2\right)\left(1-e^{-\frac{T_0}{\tau}}\right)}\left(\tau\left(1-e^{\frac{d_1-T_0}{\tau}}\right)\left(e^{-\frac{d_1}{\tau}}-e^{-\frac{t_i}{\tau}}\right)+\left(1-e^{-\frac{T_0}{\tau}}\right)(d_1-t_i)+\tau\left(1-e^{\frac{d_1}{\tau}}\right)\left(e^{-\frac{t_i+d_2}{\tau}}-e^{-\frac{d_1}{\tau}}\right)\right), & \text{if } d_1 < t_i+d_2 \le T_0 \\ \frac{PT}{\left(\chi_1 T_0^2\right)\left(1-e^{-\frac{T_0}{\tau}}\right)}\left(\tau\left(1-e^{\frac{d_1-T_0}{\tau}}\right)\left(e^{-\frac{t_i+d_2-T_0}{\tau}}-1+e^{-\frac{d_1}{\tau}}-e^{-\frac{t_i}{\tau}}\right)+\left(1-e^{-\frac{T_0}{\tau}}\right)(d_1+d_2-T_0)+\tau\left(1-e^{\frac{d_1}{\tau}}\right)\left(e^{-\frac{T_0}{\tau}}-e^{-\frac{d_1}{\tau}}\right)\right), & \text{otherwise.} \end{cases} \tag{29}$$

When $d_1 \le t_i \le T_0$,

$$\mho_i(\tau) = \begin{cases} \frac{PT}{\left(\chi_1 T_0^2\right)\left(1-e^{-\frac{T_0}{\tau}}\right)}\left(\tau\left(1-e^{\frac{d_1}{\tau}}\right)\left(e^{-\frac{t_i+d_2}{\tau}}-e^{-\frac{t_i}{\tau}}\right)\right), & \text{if } t_i+d_2 \le T_0 \\ \frac{PT}{\left(\chi_1 T_0^2\right)\left(1-e^{-\frac{T_0}{\tau}}\right)}\left(\tau\left(1-e^{\frac{d_1}{\tau}}\right)\left(e^{-\frac{T_0}{\tau}}-e^{-\frac{t_i}{\tau}}\right)+\left(1-e^{-\frac{T_0}{\tau}}\right)(d_2+t_i-T_0)+\tau\left(1-e^{\frac{d_1-T_0}{\tau}}\right)\left(e^{-\frac{t_i+d_2-T_0}{\tau}}-1\right)\right), & \text{if } T_0 < t_i+d_2 \le T_0+d_1 \\ \frac{PT}{\left(\chi_1 T_0^2\right)\left(1-e^{-\frac{T_0}{\tau}}\right)}\left(\tau\left(1-e^{\frac{d_1}{\tau}}\right)\left(e^{-\frac{t_i+d_2-T_0}{\tau}}+e^{-\frac{T_0}{\tau}}-e^{-\frac{d_1}{\tau}}-e^{-\frac{t_i}{\tau}}\right)+\left(1-e^{-\frac{T_0}{\tau}}\right)d_1+\tau\left(1-e^{\frac{d_1-T_0}{\tau}}\right)\left(e^{-\frac{d_1}{\tau}}-1\right)\right), & \text{otherwise.} \end{cases} \tag{30}$$

Expo-Square. The coding scheme is represented as

$$M(t) = \frac{\kappa P}{e^{\kappa T_0}-1}e^{\kappa t} \quad (0 \le t \le T_0, \kappa \ge 0), \tag{31}$$

$$D_i(t) = \frac{1}{2}\left(1+\mathrm{sqr}(2\pi f_0 t-\phi_i,\chi)\right) \quad (i=1,\ldots,K), \tag{32}$$

where $\phi_i = 2\pi(i-1)/K$, sqr is a square function whose amplitude is between -1 and 1, and χ is a duty cycle of sqr. If we define $t_i = T_0(i-1)/K$, the fluorescence correlation functions $\mho_i(\tau)$ $(i=1,\ldots,K)$ for Expo-Square are

$$\mho_i(\tau) = \begin{cases} \frac{\kappa PT}{(\kappa\tau+1)(e^{\kappa T_0}-1)}\left(\frac{\tau(e^{\kappa T_0}-1)}{1-e^{-\frac{T_0}{\tau}}}\left(e^{-\frac{t_i}{\tau}}-e^{-\frac{t_i+\chi}{\tau}}\right)+\frac{1}{\kappa}\left(e^{\kappa(t_i+\chi)}-e^{\kappa t_i}\right)\right), & \text{if } t_i+\chi \le T_0 \\ \frac{\kappa PT}{(\kappa\tau+1)(e^{\kappa T_0}-1)}\left(\frac{\tau(e^{\kappa T_0}-1)}{1-e^{-\frac{T_0}{\tau}}}\left(1-e^{-\frac{t_i-T_0+\chi}{\tau}}+e^{-\frac{t_i}{\tau}}-e^{-\frac{T_0}{\tau}}\right)+\frac{1}{\kappa}\left(e^{\kappa(t_i-T_0+\chi)}-1+e^{\kappa T_0}-e^{\kappa t_i}\right)\right), & \text{otherwise.} \end{cases} \tag{33}$$

5.4 Example

For Sinusoid-Sinusoid coding scheme when $K=3$,

$$\mho_1(\tau) = \frac{PT}{2T_0}\left(1+\frac{1}{2\left(1+(2\pi f_0\tau)^2\right)}\right), \tag{34}$$

$$\mho_2(\tau) = \frac{PT}{2T_0}\left(1+\frac{1}{2\left(1+(2\pi f_0\tau)^2\right)}\left(\cos\left(\frac{2\pi}{3}\right)+\sin\left(\frac{2\pi}{3}\right)2\pi f_0\tau\right)\right), \tag{35}$$

$$\mho_3(\tau) = \frac{PT}{2T_0}\left(1+\frac{1}{2\left(1+(2\pi f_0\tau)^2\right)}\left(\cos\left(\frac{4\pi}{3}\right)+\sin\left(\frac{4\pi}{3}\right)2\pi f_0\tau\right)\right). \tag{36}$$

Thus,

$$F(\tau) = \frac{\mho_1(\tau)-\mho_2(\tau)}{\mho_2(\tau)-\mho_3(\tau)} = \frac{1-\left(\cos(\frac{2\pi}{3})+\sin(\frac{2\pi}{3})2\pi f_0\tau\right)}{\left(\cos(\frac{2\pi}{3})+\sin(\frac{2\pi}{3})2\pi f_0\tau\right)-\left(\cos(\frac{4\pi}{3})+\sin(\frac{4\pi}{3})2\pi f_0\tau\right)} = b \tag{37}$$

and

$$\tau = \frac{\sqrt{3}}{2\pi f_0\,(2b+1)}. \tag{38}$$

Although τ is solvable in a closed form in the Sinusoid-Sinusoid case, in general, it is required to solve non-linear equations for other coding schemes.

REFERENCE

Mohit Gupta, Andreas Velten, Shree K. Nayar, and Eric Breitbach. 2018. What are optimal coding functions for time-of-flight imaging? *ACM Transactions on Graphics (TOG)* 37, 2 (2018), 13.